

# Transactions of the ASME®

Editor, **T. H. OKIISHI (2003)**  
Associate Editors  
Gas Turbine (Review Chair)  
**E. BENVENUTI (2002)**  
Heat Transfer  
**R. BUNKER (2003)**  
Turbomachinery  
**R. ABHARI (2002)**  
**R. DAVIS (2005)**  
**C. KOCH (2002)**  
**S. SJOLANDER (2005)**

**BOARD ON COMMUNICATIONS**  
Chair and Vice-President  
**OZDEN OCHOA**

**OFFICERS OF THE ASME**  
President, **S. H. SKEMP**

Executive Director, **VIRGIL R. CARTER**

Treasurer, **R. E. NICKELL**

**PUBLISHING STAFF**  
Managing Director, Engineering  
**THOMAS G. LOUGHLIN**

Director, Technical Publishing  
**PHILIP DI VIETRO**

Managing Editor, Technical Publishing  
**CYNTHIA B. CLARK**

Production Coordinator  
**LYNN ROSENFELD**  
Production Assistant  
**MARISOL ANDINO**

Transactions of the ASME, Journal of Turbomachinery (ISSN 0889-504X) is published quarterly (Jan., Apr., July, Oct.) by The American Society of Mechanical Engineers, Three Park Avenue, New York, NY 10016. Periodicals postage paid at New York, NY and additional mailing offices. POSTMASTER: Send address changes to Transactions of the ASME, Journal of Turbomachinery, c/o THE AMERICAN SOCIETY OF MECHANICAL ENGINEERS, 22 Law Drive, Box 2300, Fairfield, NJ 07007-2300.

**CHANGES OF ADDRESS** must be received at Society headquarters seven weeks before they are to be effective. Please send old label and new address.

**STATEMENT from By-Laws.** The Society shall not be responsible for statements or opinions advanced in papers or ... printed in its publications (B7.1, Par. 3).

**COPYRIGHT © 2002** by the American Society of Mechanical Engineers. For authorization to photocopy material for internal or personal use under those circumstances not falling within the fair use provisions of the Copyright Act, contact the Copyright Clearance Center (CCC), 222 Rosewood Drive, Danvers, MA 01923, tel: 978-750-8400, www.copyright.com. Request for special permission or bulk copying should be addressed to Reprints/Permission Department.

**INDEXED** by Applied Mechanics Reviews and Engineering Information, Inc. Canadian Goods & Services Tax Registration #126148048

# Journal of Turbomachinery



Published Quarterly by The American Society of Mechanical Engineers

VOLUME 124 • NUMBER 4 • OCTOBER 2002

## TECHNICAL PAPERS

- 521 **The Use of Sweep and Dihedral in Multistage Axial Flow Compressor Blading—Part I: University Research and Methods Development (2002-GT-30328)**  
Simon J. Gallimore, John J. Bolger, Nicholas A. Cumpsty, Mark J. Taylor, Peter I. Wright, and James M. M. Place
- 533 **The Use of Sweep and Dihedral in Multistage Axial Flow Compressor Blading—Part II: Low and High-Speed Designs and Test Verification (2002-GT-30329)**  
Simon J. Gallimore, John J. Bolger, Nicholas A. Cumpsty, Mark J. Taylor, Peter I. Wright, and James M. M. Place
- 542 **Experimental Investigation of Unsteady Flow Field Within a Two-Stage Axial Turbomachine Using Particle Image Velocimetry (2002-GT-30664)**  
Oguz Uzol, Yi-Chih Chow, Joseph Katz, and Charles Meneveau
- 553 **Flow Nonuniformities and Turbulent “Hot Spots” Due to Wake-Blade and Wake-Wake Interactions in a Multi-Stage Turbomachine (2002-GT-30667)**  
Yi-Chih Chow, Oguz Uzol, and Joseph Katz
- 564 **Analysis of Rotor-Rotor and Stator-Stator Interferences in Multi-Stage Turbomachines (2002-GT-30355)**  
L. He, T. Chen, R. G. Wells, Y. S. Li, and W. Ning
- 572 **Micro Air Injection and Its Unsteady Response in a Low-Speed Axial Compressor (2002-GT-30361)**  
Chaoqun Nie, Gang Xu, Xiaobin Cheng, and Jingyi Chen
- 580 **Turbofan Performance Deterioration Tracking Using Nonlinear Models and Optimization Techniques (2002-GT-30026)**  
K. Mathioudakis, Ph. Kamboukos, and A. Stamatis
- 588 **Effects of the Nature of Excitation on the Response of a Mistuned Bladed Disk Assembly (2002-GT-30430)**  
D. Cha and A. Sinha
- 597 **A Fundamental Model of Mistuning for a Single Family of Modes (2002-GT-30425)**  
D. M. Feiner and J. H. Griffin
- 606 **Optimum Strain Gage Application to Bladed Assemblies (2002-GT-30306)**  
J. Szwedowicz, S. M. Senn, and R. S. Abhari
- 614 **Unsteady Rotor Heat Transfer in a Transonic Turbine Stage (2002-GT-30195)**  
F. Didier, R. Dénos, and T. Arts
- 623 **Effect of Nonuniform Inlet Conditions on Endwall Secondary Flows (2002-GT-30188)**  
K. S. Hermanson and K. A. Thole
- 632 **St and  $c_f$  Augmentation for Real Turbine Roughness With Elevated Freestream Turbulence (2002-GT-30198)**  
Jeffrey P. Bons
- 645 **Separated Flow Transition Under Simulated Low-Pressure Turbine Airfoil Conditions—Part 1: Mean Flow and Turbulence Statistics (2002-GT-30236)**  
Ralph J. Volino
- 656 **Separated Flow Transition Under Simulated Low-Pressure Turbine Airfoil Conditions—Part 2: Turbulence Spectra (2002-GT-30237)**  
Ralph J. Volino

(Contents continued on inside back cover)

This journal is printed on acid-free paper, which exceeds the ANSI Z39.48-1992 specification for permanence of paper and library materials. <sup>TM</sup>  
 85% recycled content, including 10% post-consumer fibers.

- 665 **Predicting Transition Without Empiricism or DNS** (2002-GT-30238)  
Mark W. Johnson
- 670 **Evaluation of Pressure Side Film Cooling With Flow and Thermal Field Measurements—Part I: Showerhead Effects** (2002-GT-30174)  
J. Michael Cutbirth and David G. Bogard
- 678 **Evaluation of Pressure Side Film Cooling With Flow and Thermal Field Measurements—Part II: Turbulence Effects** (2002-GT-30175)  
J. Michael Cutbirth and David G. Bogard
- 686 **Correlation of Film-Cooling Effectiveness From Thermographic Measurements at Enginelike Conditions** (2002-GT-30180)  
S. Baldauf, M. Scheurlen, A. Schulz, and S. Wittig
- 699 **Heat Flux Reduction From Film Cooling and Correlation of Heat Transfer Coefficients From Thermographic Measurements at Enginelike Conditions** (2002-GT-30181)  
S. Baldauf, M. Scheurlen, A. Schulz, and S. Wittig
- 710 **Combined 3-D Flow and Heat Transfer Measurements in a 2-Pass Internal Coolant Passage of Gas Turbine Airfoils** (2002-GT-30214)  
D. Chanteloup, Y. Juaneda, and A. Bölcs
- 719 **Author Index**

# The Use of Sweep and Dihedral in Multistage Axial Flow Compressor Blading—Part I: University Research and Methods Development

Simon J. Gallimore

John J. Bolger

Nicholas A. Cumpsty  
Mem. ASME

Mark J. Taylor

Peter I. Wright

James M. M. Place

Rolls-Royce Plc,  
Derby, DE24 8BJ U.K.

*This paper describes the introduction of 3-D blade designs into the core compressors for the Rolls-Royce Trent engine with particular emphasis on the use of sweep and dihedral in the rotor designs. It follows the development of the basic ideas in a university research project, through multistage low-speed model testing, to the application to high pressure engine compressors. An essential element of the project was the use of multistage CFD and some of the development of the method to allow the designs to take place is also discussed. The first part of the paper concentrates on the university-based research and the methods development. The second part describes additional low-speed multistage design and testing and the high-speed engine compressor design and test.*  
[DOI: 10.1115/1.1507333]

*Keywords:* Multistage, Compressor, Sweep, Dihedral, Design

## Introduction

The design of multistage axial flow compressors has been revolutionized in recent years by the development of three-dimensional multistage viscous calculations (CFD) and the availability of the computational power to allow these methods to be used extensively in the design process. This was demonstrated by Rhie et al. [1] and LeJambre et al. [2] who were the first to publish a description of the use of such techniques in the design of an engine multistage compressor. As part of that work they used multistage CFD to allow them to introduce tangentially bowed stators and rotor hub wall contouring into the design. This was backed up by research testing on similar stator designs reported by Weingold et al. [3] which was carried out on a medium-speed research rig.

This paper describes the elements that went into a similar project at Rolls-Royce. These included research at two universities, integrated 3-D CFD design methods development and high-speed rig testing. It culminated in the successful incorporation of 3-D rotor and stator designs into the core compressors of the Trent 500 engine. An overview of the project and the philosophy adopted is given in the next section.

The use of three-dimensional design concepts is not new. It has long been recognized that such methods can be used to reduce the losses in compressor blade rows. Before the availability of 3-D CFD, “end-bend” designs based on experimental research programs were in use for some years. Examples of this in the open literature include the work of Wisler [4] on a low-speed research compressor and that of Freeman [5], both of which led directly to application in engine compressors. These were based on heuristic concepts applied to blade rows in isolation. Other approaches, incorporating simple models into throughflow methods have been used in industry for multistage compressor design to adapt 2-D to 3-D blade shapes. This approach depends very much on the appropriateness of the model introduced to allow for three-

dimensionality. Multistage CFD takes away this aspect of the problem and allows coupling of the blade rows to be included, avoiding mis-matching in the axial and radial directions. An investigation of such interactions was reported by Graf and Sharma [6] where they showed that a tangentially bowed stator design reduced the stability margin of a compressor by affecting the rotor operation.

Low-speed experimental research into the use of sweep and dihedral in cascades or stages has been the subject of many papers. Breugelmans et al. [7], Breugelmans [8] and Sasaki and Breugelmans [9] investigated a compressor cascade and showed that the endwall losses could be considerably reduced by using dihedral at the ends of the blades. Tweedt et al. [10] used sweep on the stator of a low-speed stage. They showed improved performance although the sweep was achieved by increasing the chord of the stator in the endwall regions which made it difficult to distinguish the effects of sweep alone. More recently, the work of Staubach et al. [11] and Inoue et al. [12] have shown that rotor performance may also be improved by 3-D design. Sweep has been successfully applied to fan rotors at high Mach numbers (Wadia et al. [13], Hah et al. [14]).

## Project Overview

A good understanding of the 3-D flow physics within compressor blade rows is necessary to underpin a fully-3D design philosophy and exploit multistage 3-D Navier-Stokes analysis techniques to their full potential. The close links between Rolls-Royce and the University of Cambridge have led to a succession of Rolls-Royce engineers working for PhD degrees at the Whittle Laboratory. Two such studies are described in Place [15] and Bolger [16]. These research programs have combined experimental work on the low-speed single-stage Deverson compressor, described in Place et al. [17], with computational investigations of 3-D flow phenomena. Such studies have helped to define the framework of 3-D compressor design at Rolls-Royce. Fundamental to this design philosophy is the recognition that each spanwise blade element does not operate in isolation with the flow influenced only

Contributed by the International Gas Turbine Institute and presented at the International Gas Turbine and Aeroengine Congress and Exhibition, Amsterdam, The Netherlands, June 3–6, 2002. Manuscript received by the IGTI, November 20, 2001. Paper No. 2002-GT-30328. Review Chair: E. Benvenuti.

by the local blade geometry and local incidence, but rather in a continuous static pressure field set up by the blade as a whole. (Sudden changes in static pressure can only be the result of intense local three-dimensionality such as tip-leakage vortices.) Endwall blading, therefore, does not operate under the severe streamwise static pressure gradients that two-dimensional cascade calculations would suggest. However, these sections still have to achieve the static pressure rise imposed by the radial equilibrium set up by the bulk of the blade while operating at increased local incidence and reduced inlet dynamic head. The quasi-3-D (Q3D) multistage compressor design methods used in the mid-1980s and early 1990s described by Denton [18] and Place [15] typically neglect endwall boundary layers and other three-dimensional flow features. This leads to the design of blading whose inlet and exit conditions in the endwall regions are significantly different from those generated by the real highly three-dimensional flow. Three-dimensional multistage viscous calculations allow these effects to be addressed through modelling of the 3-D flowfield, giving design choices not previously available.

The project had four main elements. There was a fundamental investigation into the effects of sweep and dihedral using a low-speed single stage research rig at the Whittle Laboratory, University of Cambridge. This was part of a long-term program of research into three-dimensional flow and loss generation in axial flow compressors. In parallel, a multistage CFD method was developed and validated to give good results for the types of compressor to be redesigned. This included improvements to the wall function and turbulence model as well as the introduction of shroud leakage and bleed hole modelling. Blade geometry manipulation and solution post-processing software was wrapped around the solver to form an integrated design system. The initial results from the low-speed research were adapted and used as a basis for multistage low-speed designs which were tested at the University of Cranfield. The designs for the engine compressor were executed in parallel with the low-speed designs and the methods development using information from the research testing. Blading was initially designed for a development of the Trent 800 engine and it is these designs and tests that will be described here. Subsequently, the same techniques were applied to both the intermediate and high pressure compressors for the Trent 500 engine. Throughout the project, the objective was to transfer the benefits from the fundamental university research into the engine compressor designs as quickly as possible.

## CFD Method Development

The philosophy of the multistage CFD development was to create an integrated, rapid design system that was fast enough to be used as an everyday part of an engine project design. Blade geometry manipulation software that reads and writes directly to CFD input files and post-processing software that allows 1-D, 2-D, and 3-D interrogation and comparison of flow solutions was developed and wrapped around the CFD solver. The CFD method is a development of the one described by Denton [19]. A simple sheared H-grid is used with viscosity and turbulence effects included using a thin shear layer approximation to the Navier-Stokes equations and an eddy viscosity mixing length model. The interface between adjacent rotating and stationary blade rows is dealt with by using a mixing plane approach. Tip clearance flows were included by using the 'pinched tip' model, an approach that is common for simple H-meshes. The basic method has been considerably developed by Denton since his original paper was published. In particular, the mixing plane calculation has been improved and the turbulence model has been modified. It is recognized that the solver is not as sophisticated as some that are available. However, it is able to predict changes in the structure and losses of the flowfield, though not always the magnitude of such changes. If the extent of a 3-D separation is under-predicted by the CFD code, then the benefit of reducing the 3-D separation

will also be under-estimated. However, the code has a proven record of highlighting regions of the compressor that require careful design attention.

In this paper we will only describe changes to the method that were introduced by the authors as part of this project and these are highlighted in the following sections. It is important to recognize that the calculations shown in this work do not include modelling of deterministic stresses and overlapping grids. Deterministic stress modelling is available in the code using an approach which is similar to that described by Hall [20], but its use was not found to be necessary in order to achieve satisfactory agreement with the experimental data used in this study. This is different to the approach adopted by Adamczyk [21] and others.

Computational meshes used throughout this study are relatively coarse by today's standards and reflect the fact that the bulk of this work was done a few years ago. Radial and pitchwise meshes typically consisted of 33 points with 100 points in the axial mesh from mixing plane to mixing plane (around 50 on the blade surfaces).

**Wall Shear Stress.** In the original formulation of the code the shear stress on the solid boundaries was determined by assuming that the first grid point away from the surfaces (not the point on the surface) was either in the laminar sub-layer or in the logarithmic part of a turbulent boundary layer. For the mesh densities used in this study the point was in the logarithmic layer. Denton [19] explains how an explicit expression linking the skin friction and Reynolds number was used to obtain the wall skin friction in this case. Early multistage calculations using this model showed that the flow capacity of the compressors considered here was some 4% above that measured on test. It was felt that this discrepancy was due to the underprediction of three-dimensional separations in the blade surface endwall corners due to the relatively large spacing of the grid at the solid surfaces. To improve the prediction of the flow capacity an alternative method of calculating the skin friction was implemented. This assumes that the mesh point lying on the solid surface is at the edge of the laminar sublayer, the thickness of which is determined by a specified value of  $y^+$ . Knowing the velocity and density predicted at this point by the CFD allows the shear stress to be calculated as follows:

$$\tau_w = \frac{\rho V^2}{y^+} \quad (1)$$

A value of  $y^+ = 11$  was taken as being representative of the edge of the laminar sub-layer. This type of formulation has been used previously in a viscous throughflow method by Howard and Gallimore [22] and developed independently for CFD by Grotjans and Menter [23].

**Turbulence Model.** In order to model the Reynolds stress terms in the Reynolds averaged Navier-Stokes equations, it is necessary to make use of some form of turbulence modelling. Typically, this now involves the use of one-equation (Spalart and Allmaras [24]) or two-equation (Launder and Spalding [25]) turbulence models, although considerable success has been achieved with simple algebraic models such as Baldwin and Lomax [26]. The emphasis in the use of this CFD code as part of a 3-D design system was on achieving a rapid and robust design tool, and with this in mind it was decided to make use of a Prandtl mixing length approach which is more consistent with the use of the thin shear layer approximation. All boundary layers are assumed to be fully turbulent. Correct use of the transport equation models would require the calculation of all of the Navier-Stokes terms as well as the computational expense of solving the transport equations for the turbulence quantities; fine grids are usually required to obtain good results.

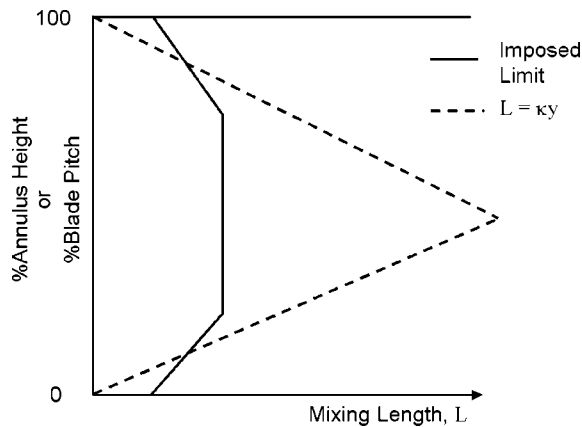


Fig. 1 Schematic diagram of zonal mixing length model

The Prandtl mixing length model makes use of the Boussinesq assumption, that the turbulent shearing stress is proportional to the rate of mean strain. The eddy viscosity representing the action of the turbulence on the mean flow is used to calculate the turbulent shear stress terms to close the system of equations. Initial use of this model (which used  $L = \kappa\gamma$  until cut off at a specified distance from the wall and then held constant) gave poor agreement with test data and it was decided to develop the model by imposing different limits on the mixing length parameter  $L$  in various regions of the flow. A schematic of this zonal approach is given in Fig. 1, with limits imposed in both the pitchwise and spanwise directions. The values of the mixing length limits were calibrated using test data on a wide range of test cases including intermedi-

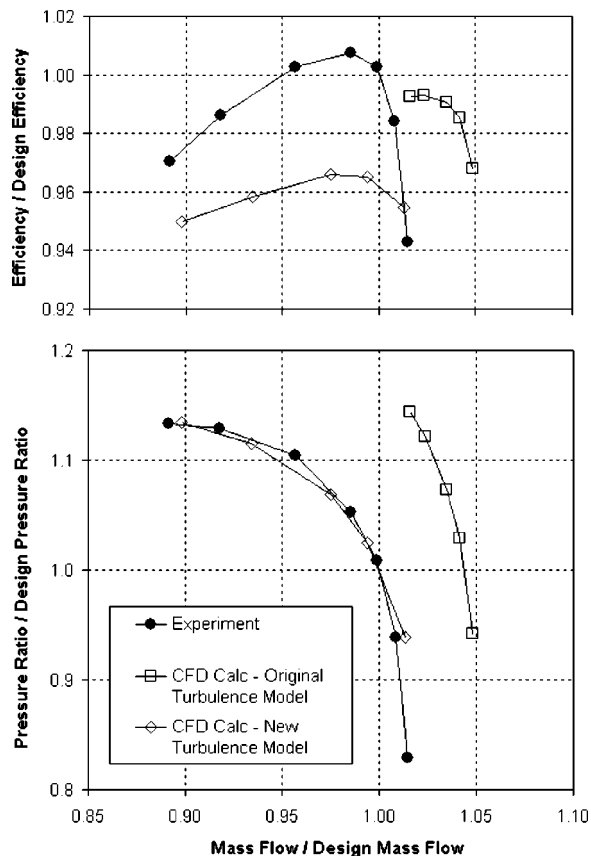


Fig. 2 Calibration of turbulence model with high-speed compressor characteristics

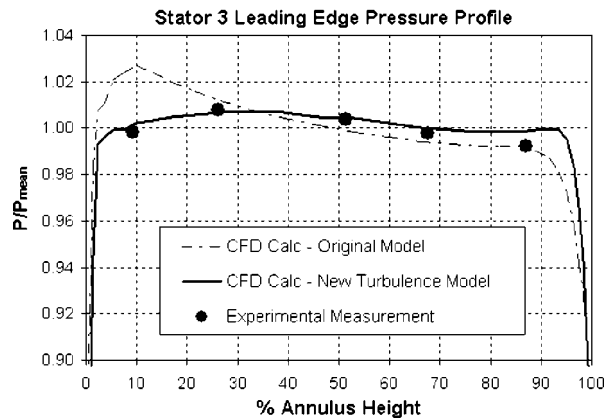
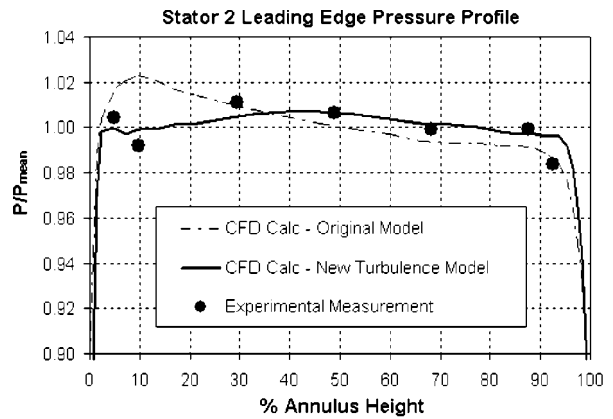


Fig. 3 Calibration of turbulence model with high-speed compressor interstage test data

ate and high pressure compressors, multistage fans and low-speed compressor research rigs. The limits derived depend on the geometry of the machine. Different values are used for rotors, shrouded stators and cantilevered stators. Non-zero mixing lengths in the free-stream regions away from blade and endwall boundary layers go some way to modelling the effects of spanwise mixing in the multistage environment. An added level of flexibility, which allows the limits to vary from row to row, could have been employed but was not found to be necessary for the machines under consideration.

Figure 2 shows overall compressor characteristics for a multistage high pressure compressor comparing results from the code both with and without the zonal modelling approach with test data. The original turbulence model was approximately 4% out on mass flow, while the new zonal modelling approach used together with the wall shear model described in the previous section gives good agreement for the pressure ratio characteristic. The absolute level of efficiency of the compressor is not well predicted and could be improved with a more refined mesh and a more sophisticated turbulence model at the expense of increased computational run-time. However, the shape of the characteristic is in good agreement with test data and, most importantly from the designers' point of view, the peak efficiency flow rate and the shape of the characteristic near stall are well predicted. The reason for the improved match with test data is the improved blockage prediction achieved with the new model. Radial plots of pitchwise-averaged normalized total pressure at two stator inlet test measuring planes are shown in Fig. 3. The improvement in the prediction of the hub corner separation of the upstream rotor is immediately apparent. The calculation method may not predict the correct ef-

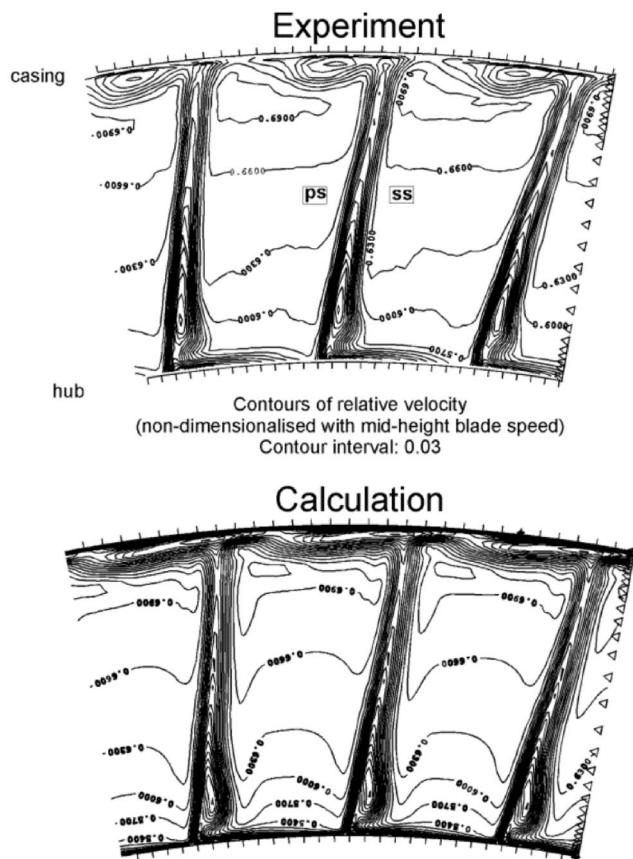


Fig. 4 Comparison of experiment with CFD calculation for low-speed rotor exit flowfield

efficiency, but it does highlight the effect of the development of 3-D separations on the radial profiles, the overall and the individual stage characteristics.

For the code to be effective as a design tool the detailed features of the flowfield must be well reproduced. Extensive use of test traverse data and blade surface statics were used to ensure that the new zonal mixing-length model was accurately predicting the secondary flows, corner separations and clearance flows for each compressor blade type. Figure 4 shows test and predicted contours of relative velocity at rotor exit for a build of the Deverson low-speed research compressor. It is evident that the new turbulence model qualitatively captures the principal features of the flowfield. The fine detail may be slightly different, especially in the tip clearance region, but the overall agreement and flow structures are acceptably close for design purposes.

**Real Geometry Features.** It was found to be important to model the real effects on the flow caused by stator shroud leakage flows, bleed off-take flows and any gaps and leakages present in the annulus. The importance of such flows has been demonstrated on an isolated rotor by Shabbir et al. [27]. These effects were modelled by applying different boundary conditions on the end-walls where there was an opening rather than by applying mesh and CFD to the complicated geometries outside the main annulus in the multistage calculation. The boundary condition consisted of specifying the net mass flow through the open region with the local velocities being determined by the static pressure field predicted by the CFD. This results in flow being able both to enter and to leave the annulus through the open region if the net mass flow through the opening is less than that required to ensure that the velocities everywhere are either directed into or out of the annulus. An example of this is given in Fig. 5, which shows the

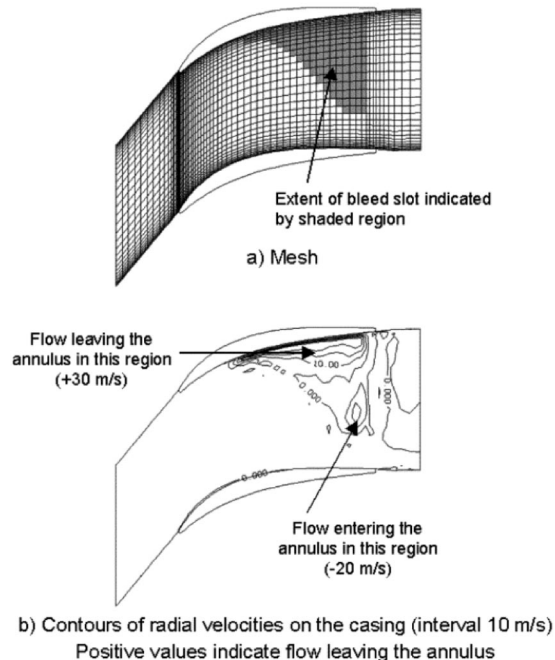


Fig. 5 Improved bleed hole modeling; (a) mesh, (b) contours of radial velocities on the casing (interval 10 m/s). Positive values indicate flow leaving the annulus.

radial velocities calculated through a bleed hole in the casing where the net bleed flow is considerably less than that which the hole has to pass in off-design operation.

The massflow and the change in tangential velocity and temperature through the stator shrouds was calculated using the models of Lewis [28], McGreehan and Ko [29], Wellborn [30] and proprietary methods. A research program was undertaken in the Whittle Laboratory to investigate the interaction effects of these types of flows with the main stream flow. This is described by Demargne and Longley [31] where detailed CFD calculations and cascade experiments of individual shroud flows were undertaken. This confirmed that the main effects were correctly modeled in the 3-D code used for multistage compressor design.

### A Toolkit for 3-D Design

This section describes part of the research undertaken at the Whittle Laboratory in parallel with the CFD method development within Rolls-Royce. Experiments on a conventionally designed (2-D) research stage bladed with modern prescribed pressure distribution aerofoils (similar to “controlled diffusion” described by Pratt & Whitney), together with CFD calculations, were used to develop and understand the complex 3-D flow phenomena in embedded compressor stages. The increased understanding of the loss generation mechanisms and flow structures resulting from this project has led to the development of a 3-D design framework whose elements are described below. The 3-D design toolkit was then subsequently used to design a 3-D stage at the same aerodynamic duty as an existing 2-D stage. This 3-D stage is described later in the paper.

**Spanwise Swirl Distribution.** The spanwise swirl distribution (sometimes referred to as the vortex design) is a major contributor to the overall performance of a multistage machine. Changing the swirl distribution can be considered a 2-D design change and the overall effects on the free-stream radial equilibrium pressure field can be predicted using inviscid throughflow calculations. The use of a free vortex design proved useful in the days before numerical methods were established as it was amenable to manual throughflow calculation and had advantages such

as minimizing stream sheet twisting. However, modern designs use a “controlled vortex” distribution which uses tailored spanwise distributions of rotor work input and stator swirl angle to achieve features regarded as desirable in the multistage environment such as hub-strong total pressure profiles and increased end-wall axial velocity. Three-dimensional multistage CFD is capable of assessing the merits of different vortex designs more completely than earlier throughflow methods.

**Definitions of Re-camber, Dihedral and Sweep.** Under certain circumstances it is beneficial to align the blade leading and/or trailing edges more closely with the local flow direction. A process of modification to do this will be termed re-camber. Such geometry changes have also been described in the literature as “end-bends,” but this term is not employed here as it is often used to describe the simultaneous re-camber of leading and trailing edges and it is desired here to de-couple the two.

The use of three-dimensional stacking has been the source of a large number of experimental and numerical investigations over recent years. A variety of terms have been used to describe stacking line modifications (e.g., lean, sweep, bow, skew) and no consistent nomenclature has emerged from these investigations. There is, therefore, a need to define carefully the conventions adopted during the course of this paper. The terms dihedral and sweep will be used to describe movements of aerofoil sections in the manner shown in Fig. 6. Movements normal to the aerofoil section chord line will be termed dihedral; movements parallel to the aerofoil section chord line will be termed sweep. Dihedral and sweep angles are defined as being the angle made between the endwall normal direction and a straight line drawn between the endwall aerofoil section and the point at which the dihedral and swept sections merge back into the conventional (2-D) stack—the blend point. The dihedral angle is taken to be positive if the suction surface makes an obtuse angle with the endwall. The sweep angle is taken to be positive if the aerofoil sections close to the endwall are moved in the upstream direction. Intermediate blade sections between the endwall and the blend point lie on a curve of defined shape. Other orthogonal definitions of lean and sweep are clearly also valid (e.g. tangential and axial respectively) but these are not used by the present authors. In the context of the present framework, the tangential bowing of the stators described by Weingold et al. [3] can be thought of as a combination of positive dihedral and negative sweep.

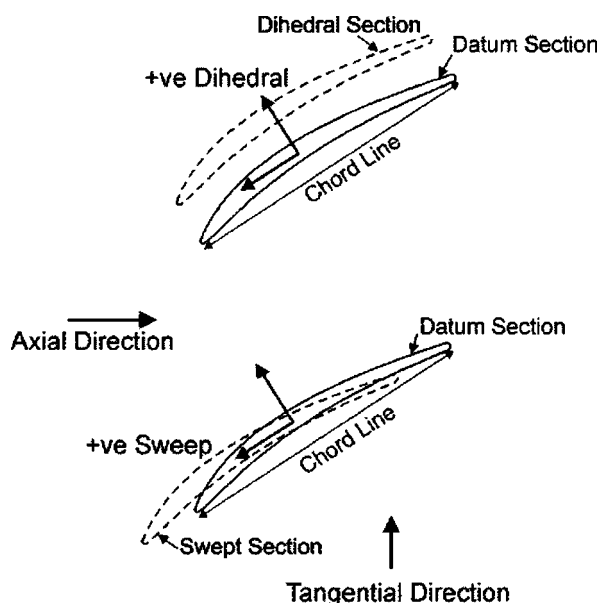


Fig. 6 Definition of dihedral and sweep

The use of a single value to describe the magnitude of geometric dihedral or sweep introduced into the aerofoil is helpful in quantifying the size of change incorporated. However, the real flow experiences a differing amount of aerodynamic dihedral and sweep at each location in the blade passage depending on the local geometry and flow velocity vector. The local dihedral and sweep in the blade passage can be calculated from the 3-D solution using the blade geometry and the pitchwise-averaged velocity vector at each axial and radial position. Plotted as contours these are useful in determining whether geometry changes inadvertently introduce adverse conditions in certain regions of the blade passage.

**Chordwise Camber and Thickness Distributions.** Changing the chordwise shape of the aerofoil sections has often been thought of as a way of affecting the blade force distributions near the endwall sections. There is no doubt that profile re-design can affect the overall pressure field, but only when a significant part of the aerofoil is modified. Such changes are often applied in the mid-span region of 3-D blades to offset the increased loading caused by the 3-D stack and restore profile loss back to 2-D levels. However, modifications concentrated more locally near the endwalls are likely to behave like end-bends, i.e., the change in blade profile is too rapid for the pressure field to adjust to the new blade shape and pressure remains effectively fixed by the mid-span region. Behlke [32] achieved some success with blade profile re-design to reduce separations near endwall regions and Wisler [4] described the use of stators with “twist gradients” near the endwalls. It is likely that all these improvements can be classed in the end-bend category, principally aligning the metal with the flow, and the benefits arose from this rather than the effects associated with two-dimensional blade profile shape.

**Leading Edge Re-Camber (LER).** The viscous forces exerted on the flow by the endwalls and their interaction with the lifting aerofoil create a spanwise profile of axial velocity. This, when combined with the change in frame of reference between rotor and stator and the secondary flows produced by upstream blade rows, cause the flow angle at inlet to the blade rows typically to increase (measured from the axial direction) progressively as the endwall is approached. Aligning the leading edge more to the flow direction may well help to reduce the amount of suction surface deceleration necessary to achieve this pressure rise and prevent the blade suction surface boundary layer from separating.

Having incorporated an increased blade inlet angle into the new aerofoil near the hub and casing it must be decided how to stack the new aerofoil sections radially. The new blade profile sections incorporating re-camber will have different centroid positions to the datum blade and require movement in the axial and tangential direction to align their centroids with those of other sections. However, centroid stacking is not the only option available. Choosing to maintain the same leading edge or trailing edge positions as the datum aerofoil or opting for a conventional centroid radial stack results in different three-dimensional blade shapes. Stacking line choices clearly introduce effects of dihedral and sweep. It must therefore be concluded that LER cannot be thought of as independent from dihedral and sweep. Changing the aerofoil camber to account for endwall boundary layers invariably adds local dihedral and sweep to the endwall sections—how much and at what chordwise position is governed by the amount of re-camber and stack chosen. This is an important observation which is very often overlooked during a blade design. Another beneficial feature of LER is the increase in blade chord introduced if LER is applied while keeping the meridional chord fixed: the true chord will increase as the stagger increases giving higher solidity in the endwall regions.

**Trailing Edge Re-Camber (TER).** The use of trailing edge re-camber is less common than LER, in part because it is not obvious which way to move the trailing edge to improve the flow. Secondary flow analysis might suggest that the flow is over-turned close to the endwalls and under-turned further away. The designer

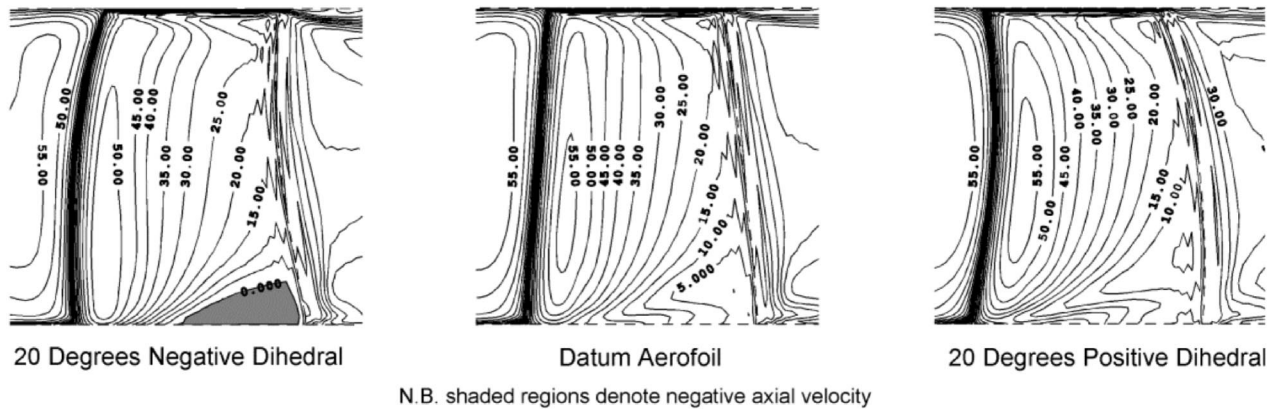


Fig. 7 Computed near-suction surface axial velocity contours for datum and dihedral rotors

could then design a “mirror image” blade angle distribution which counteracts the overturning by the secondary flow in the endwall boundary layer by de-cambering the endwall blade profile and overcambering the sections nearer mid-span. This approach assumes that the secondary flow will do some of the turning in the endwall regions and has been exploited with some success in turbines (e.g., Denton et al. [33]). Another approach might be to accept that there is a cross-passage flow and attempt to align the blade exit angle more with the flow direction by overcambering the trailing edge near the endwall and undercambering it nearer to midspan. This approach has also found some application.

Similar to LER, a change of camber near the trailing edge in the endwalls coupled with the choice of stacking line introduce the effects of dihedral and sweep. TER which decambers the endwall sections might look an attractive proposition but the improvements gained may have more to do with inadvertent introduction of dihedral and sweep effects than they do with aligning the blade trailing edge more closely with the flowfield.

**Dihedral.** The effects of dihedral have been described using lifting line models to simulate blade rows by a number of researchers including Smith and Yeh [34], Cumpsty [35], Weingold et al. [3] and Place [15]. Leaning the lifting line (and consequently its image system in the endwall) generates induced velocities according to the Biot-Savart law. These induced velocities have their strongest effect near where the leaned blade intersects the endwalls. Changes in blade loading caused by the induced velocity field in these regions can have a significant effect on endwall loss generation, as described by Place [15] and demonstrated by Breugelmans et al. [7], Breugelmans [8], Shang et al. [36], Weingold et al. [3] and Sasaki and Breugelmans [9]. The use of dihedral on blades with a tip clearance is beneficial under certain circumstances. Figure 7 shows axial velocities computed by the Denton CFD code close to the suction surface for three candidate rotors for the Deverson low-speed single-stage compressor with  $-20$ ,  $0$  and  $+20$  degrees of dihedral applied at the centroid using a circular arc stacking line. The flowfield also needs to be studied in other views to get a feel for the magnitude of the corner separations. However, for brevity in this paper, only the near-suction surface contours are presented. These give a qualitative assessment of the effects of blade geometry changes. Changes were applied relative to the 2-D datum prescribed pressure distribution blading whose mid-span design parameters are detailed in the Appendix. All sections apart from the mid-height section experience some stacking shifts from a conventional radial centroid stack. Near the hub endwall the positive dihedral blade has increased axial velocity near the trailing edge and lower loss, while the negative dihedral blade exhibits a large corner separation with higher loss and blockage. At the casing the negative dihedral blade demonstrates slightly increased axial velocity towards the

trailing edge due to the increased entrainment of blade surface boundary layer caused by the stronger tip leakage flow. Interrogating the CFD flow solutions further, it is observed that the blade with positive dihedral generates less tip clearance flow blockage and loss while the negative dihedral blade has more. Overall, the positive dihedral reduces the hub corner and tip clearance losses, leading to a fuller velocity profile near the endwalls, but at the expense of increasing the losses near the mid-height region. Surface static pressure distributions close to the rotor hubs are shown in Fig. 8. The  $+20$  deg dihedral blades shows a reduction in blade force and an increase in effective incidence near the endwall while the  $-20$  deg dihedral blade shows the opposite trend. Similar observations can be made at the rotor tip. At mid-span the  $+20$  deg dihedral causes an increase in blade force and a reduction in effective incidence. The opposite trends are observed for negative dihedral.

The use of positive dihedral has been calculated to be beneficial for both fixed and free ends of blades. It provides a method of introducing a rapid reduction in blade force local to the endwalls and alleviates high suction surface deceleration rates in these regions at the expense of increased blade force at mid-span. A redesign of the mid-span blade profile shape to tolerate this increased blade force should result in a net loss reduction for the blade row as a whole. The modifications at mid-span are usually small enough not to penalize the stall range of the blade row as a whole as this tends to be dominated by the endwalls reaching a limiting condition. The reduction in cross-passage pressure gradient near the endwalls can also be utilised to reduce the effects of secondary flow. For conventional blading with small fillet radii, the migration of the endwall boundary layer onto the suction sur-

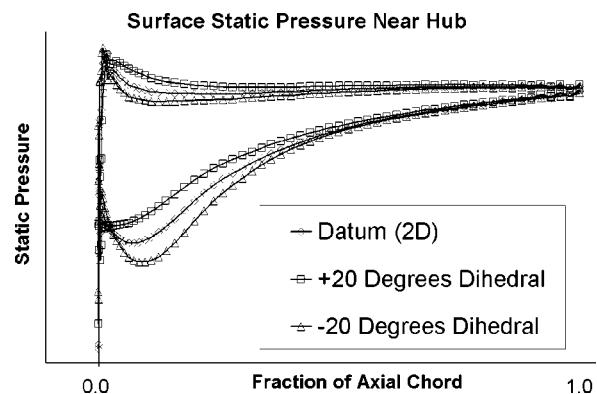


Fig. 8 Computed surface static pressure distributions for datum (2-D) and dihedral rotors



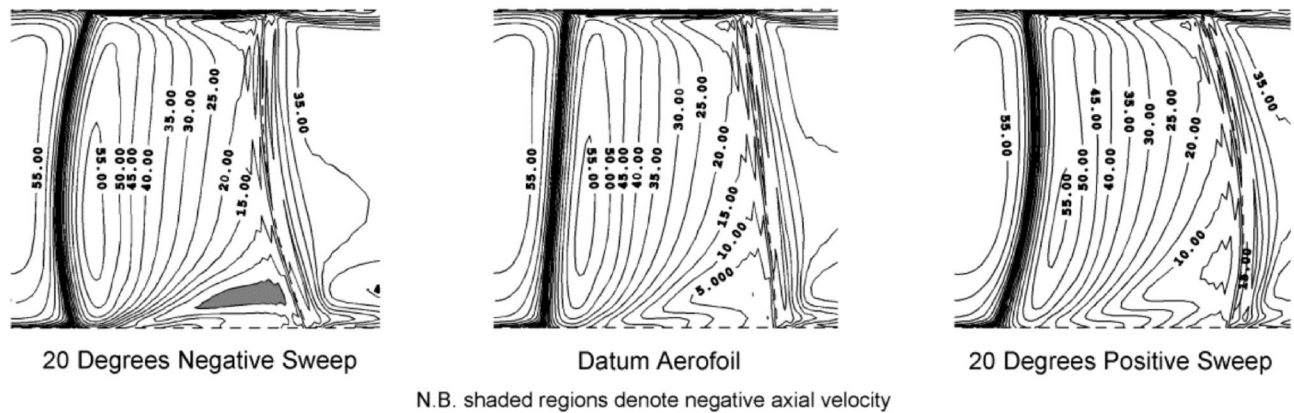


Fig. 9 Computed near-suction surface axial velocity contours for datum and swept rotors

face by the secondary flow is opposed by an increase in pressure at the junction of blade and endwall necessary to divert the tangential component of the endwall flow through 90 degrees into the spanwise direction. The addition of positive dihedral reduces the need for such a large pressure increase and the large fillet radius effect of the positive dihedral encourages the flow to migrate up the span of the blade. Whether there is more or less endwall boundary layer fluid which convects onto the suction surface depends on the relative magnitudes of the reduction in cross-passage pressure gradient caused by the dihedral and the enhanced radial flows of the fluid on the blade surface.

The local increase in static pressure close to the leading edge of a positive dihedral endwall section increases the incidence onto the aerofoil in this region and this can be offset with the introduction of LER to match the blade leading edge more closely with the incoming flow direction. Applying LER to a conventional radially-stacked blade while keeping the same spanwise relationship of centroids introduces negative dihedral near the leading edge and positive dihedral near the trailing edge. However, starting from a positive dihedral aerofoil and applying the same type of LER makes the leading edge more radial and further increases the trailing edge dihedral i.e. the leading edge is not necessarily subjected to negative dihedral.

**Sweep.** Blade sweep has been used in transonic compressor design with the intent of reducing shock losses, analogous to the use of swept wings in external aerodynamic applications. Theory would suggest that the reduction in shock losses would be achieved by either positive or negative sweep, but tests of various transonic rotors demonstrate the advantage of positive sweep in achieving both improved efficiency and flow range. Wadia et al. [13] and Hah et al. [14] described a series of transonic fan designs and subsequent tests where positive and negative sweep were used to influence the conventional blade aerodynamics. They used 3-D calculations to explain the experimental results and described mechanisms which control the spanwise migration of blade surface boundary layer. Wennerstrom [37] described the use of sweep on a transonic fan stator to reduce Mach numbers and increase choke margin near the stator hub. There are few reports of the use of sweep for subsonic compressor blading, however.

The application of sweep for the Deverson single-stage low-speed compressor was investigated numerically for  $-20$ ,  $0$ , and  $+20$  deg swept rotors on circular arc stacking lines. Figure 9 shows computed contours of axial velocity close to the suction surfaces of the datum and swept rotors. Near the hub the positive sweep reduces the region of low axial velocity towards the trailing edge while the negative sweep causes a separation to occur. Surface static pressure distributions near the rotor hubs are shown in Fig. 10. The positive sweep near the hub moves the front part of the suction surface into a higher pressure region which reduces the

effective incidence and peak velocity along the aerofoil chord at the expense of increasing the blade force near the trailing edge. A similar trend is observed near the rotor tip while the opposite trend is observed at midheight. Denton and Xu [38] explained this effect by considering the blade force near the leading edge. End-wall hub sections which are positively swept have no blade above them to support the pressure rise they would generate if the flow were purely two-dimensional. As the pressure gradient perpendicular to the endwall is small compared with the blade-to-blade pressure gradient and the blade force has to fall to zero a short distance above the endwall section, positively swept endwall sections must have reduced leading edge blade force. Towards the trailing edge of positively swept blades, the opposite trend occurs. The blade sections inboard of the endwall section must still maintain blade force as they produce the pressure gradient necessary to turn the flow. This blade force is imposed on the endwall sections which can affect the profile boundary layer development and pressure rise capability. The mid-height region compensates for the blade force changes near the endwalls.

Positively swept endwall sections increase the leading edge blade force and reduce the trailing edge blade force near mid-height. During the parametric rotor study, no significant tip clearance loss reduction was observed for positive sweep. The negatively swept blade arguably achieved the best overall performance thanks to its superior performance over the mid-span region.

At the casing, the lack of improvement predicted in the near suction surface axial velocity contours, including the tip clearance flow, upon the application of positive sweep is disappointing. Conventional wisdom would suggest that reducing the leading edge blade force and peak pressure difference across the blade

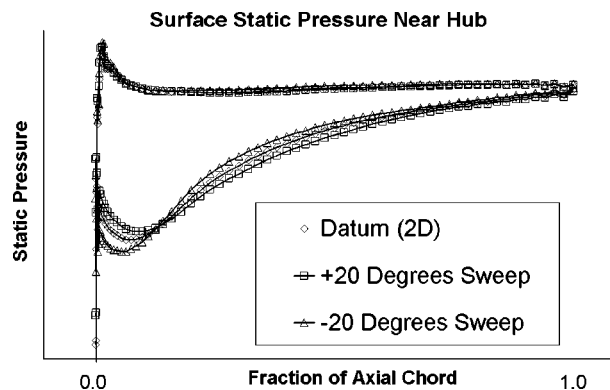


Fig. 10 Computed surface static pressure distributions for datum (2-D) and swept rotors

might prove an advantage, but this has not been realized here. Contours of local aerodynamic lean and sweep in the blade passage from the CFD solution for the three rotors reveal that the aerofoil with positive sweep has a region of negative dihedral close to the blade tip while the negatively swept blade exhibits positive dihedral over the majority of the tip chord. Possible beneficial features of sweep are therefore being offset by the negative dihedral. The introduction of combined dihedral and sweep to reduce the peak pressure difference across the blade tip and redistribute the chordwise blade force in a manner which reduces the overall mixing losses could be effective.

**Stacking Line Shapes.** Off-loading the endwalls can cause an increase in loading over the rest of the span and regions where the dihedral or sweep blends back into the conventional stacking line will attract the migration of boundary layer fluid-secondary flow, caused by the radial pressure gradient set up by the dihedral and sweep on the suction surface. Choosing a circular arc stacking line shares out the increase in mid-height loading over the whole span but, for a given amount of movement of the endwall blade sections, can off-load sections which are well capable of achieving the demanded static pressure rise without boundary layer separation. Biasing the stacking shifts to be more extreme nearer to the endwalls reduces the amount of off-loading experienced by sections further away from the endwall. Care must be taken to ensure that any blend points are not overloaded by a combination of the increase in loading necessary to offset the reduced endwall loading (effectively an inviscid effect) and the migration of boundary layer fluid to these regions under the prevailing pressure gradients (a boundary layer effect).

Similar stacking line observations are reported by Emmerson and Buchanan [39]. They conclude for both a colateral and a skewed inlet boundary layer that the use of a parabolic arc stack with blend points situated away from midspan offered the best calculated potential for loss reduction.

**Endwall Contouring.** The use of endwall contouring to control three-dimensional flows as yet has not been fully exploited for multistage compressors. A notable exception comes from LeJambre et al. [2] who described the use of endwall contouring on rotor hubs which creates a radial force akin to dihedral. The rotor exhibited reduced suction surface separation close to the hub corner, but it was not clear from their paper whether the contouring was axisymmetric or nonaxisymmetric. The use of non-axisymmetric endwall contouring has been used in multistage turbine applications to improve efficiency (Harvey et al. [40]) and is a tool which will become more and more valuable for future highly loaded compressor designs. Its effects can be calculated using 3-D viscous calculations.

### 3-D Blade Design Study

The previous section described a subset of calculations that formed the basis for a re-design exercise applied to the conventional (2-D stacked) prescribed pressure distribution bladed compressor stage on the Deverson low-speed single-stage research compressor. The 3-D stage was designed to have the same flow and stage loading coefficients (see Appendix). The resulting 3-D blade designs are pictured in Fig. 11. The 3-D design was developed in parallel with an experimental study of the performance of the conventional 2-D stage. Detailed flow measurements were made and CFD models of the stage were calibrated with this test data. The models were then interrogated to shed light on the loss generation mechanisms and the 3-D design toolkit was employed to improve the performance of the endwall sections of the rotor and stator. Candidate designs were assessed by interrogating 3-D solutions in the following ways:

In 3-D: flow structures; contours of properties; amount of reverse flow on suction surfaces.

In 2-D: pitchwise-averaged radial profiles; blade surface pressure distributions.

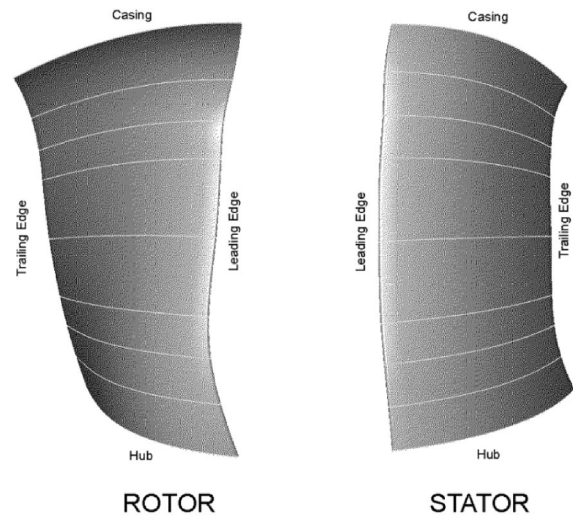


Fig. 11 Front views onto suction surface of 3-D stage

In 1-D: work input, pressure rise and efficiency characteristics; shape of characteristics compared with datum design at throttled conditions.

**3-D Rotor Design.** Oil and dye flow visualisation on the rotor hub revealed evidence of strong cross-passage flow towards the

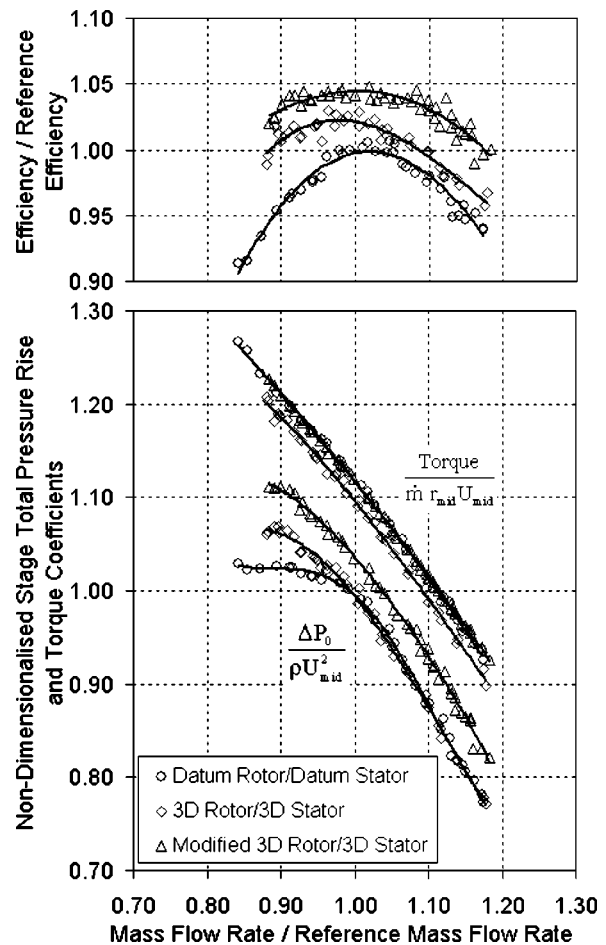


Fig. 12 Comparison of 2-D and modified 3-D stage performance characteristics

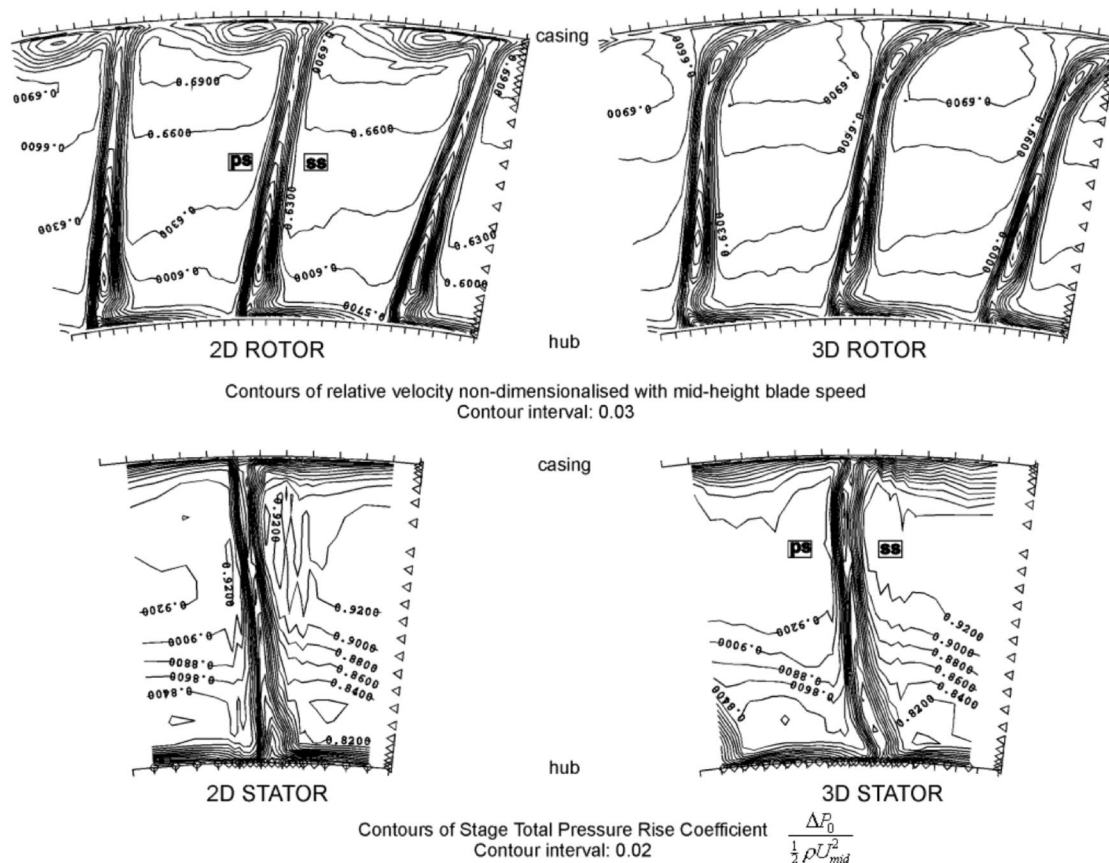


Fig. 13 Comparison of measured 2-D and 3-D blade row exit conditions at design point

suction surface. A saddle point was located on the endwall close to the nose of the aerofoil near the pressure surface, an indication of high incidence and low inlet relative dynamic head. Near stall the stagnation point moved further into the blade passage and the cross-passage flow increased. Other experiments undertaken to define the flowfield included on-rotor surface static pressure measurements, on-rotor flow visualisation, pneumatic area traversing and slant hotwire anemometry. Measured aerofoil surface static pressure distributions near the hub exhibited increased forward loading relative to mid-span but this was by no means excessive.

Calculations also suggested that the rotor hub corner flow is strongly influenced by the cross-passage endwall boundary layer migration. The calculations showed no evidence of flow reversal on the suction surface at design point, but a corner separation grows progressively with reducing flow coefficient. A 3-D design solution which reduces the effects of cross-passage flow and reduces the static pressure on the pressure surface local to the leading edge would reduce the size of the horseshoe vortex and prevent the hub endwall boundary layer from interacting so severely with the blade profile boundary layer. Sweep and LER were chosen as the best combination of modifications to achieve these aims.

Slant hotwire and pneumatic probe area traversing revealed the rotor tip region to be dominated by a loss and blockage core associated with the tip clearance vortex. It was suggested earlier that combined dihedral and sweep may offer tip clearance loss reduction benefits. Both of these features to some extent oppose each other when fixing the resulting effective incidence and it was found necessary also to include LER near the rotor tip to restore the effective incidence back to reasonable levels. The CFD code predicted significant benefits for large dihedral and sweep values so the design space was fully explored and deliberately

extreme amounts of dihedral and sweep were included in the 3-D design.

**3-D Stator Design.** Oil and dye flow visualization combined with pneumatic area traversing and surface static pressure measurements revealed the stator hub region to be sensitive to endwall separation caused by cross-passage flow and excessive deceleration local to the stator suction surface. Incidence near the hub was also observed to be high. Dihedral was employed in the hub region as an effective means of reducing the near endwall deceleration rate and cross-passage flow. Positive dihedral, when combined with LER to address the high incidence, was predicted to offer significant loss reduction. The stator casing region was predicted and measured to be operating at high incidence with only a modest amount of cross-passage flow. Modifications, similar to the stator hub region, were employed to address incidence and suction surface deceleration rate.

**Test Results.** Measured characteristics for the 3-D stage are compared with the 2-D stage in Fig. 12. The 3-D stage performance is significantly better than the 2-D datum build, which had a reasonably respectable peak total-to-total efficiency of  $89\% \pm 1\%$ . However, the 3-D rotor did not give a significant benefit in stage efficiency relative to an intermediate build consisting of the 2-D rotor and 3-D stator. While the 3-D stator is a great success at all operating points, the 3-D rotor performance deteriorates at throttled conditions. The measured exit flow conditions at the design point and near stall operating point are shown in Figs. 13 and 14, respectively. The large amount of tip sweep and dihedral for the rotor which blended out at around 20% immersion has overloaded this part of the blade. The CFD used at the time of the

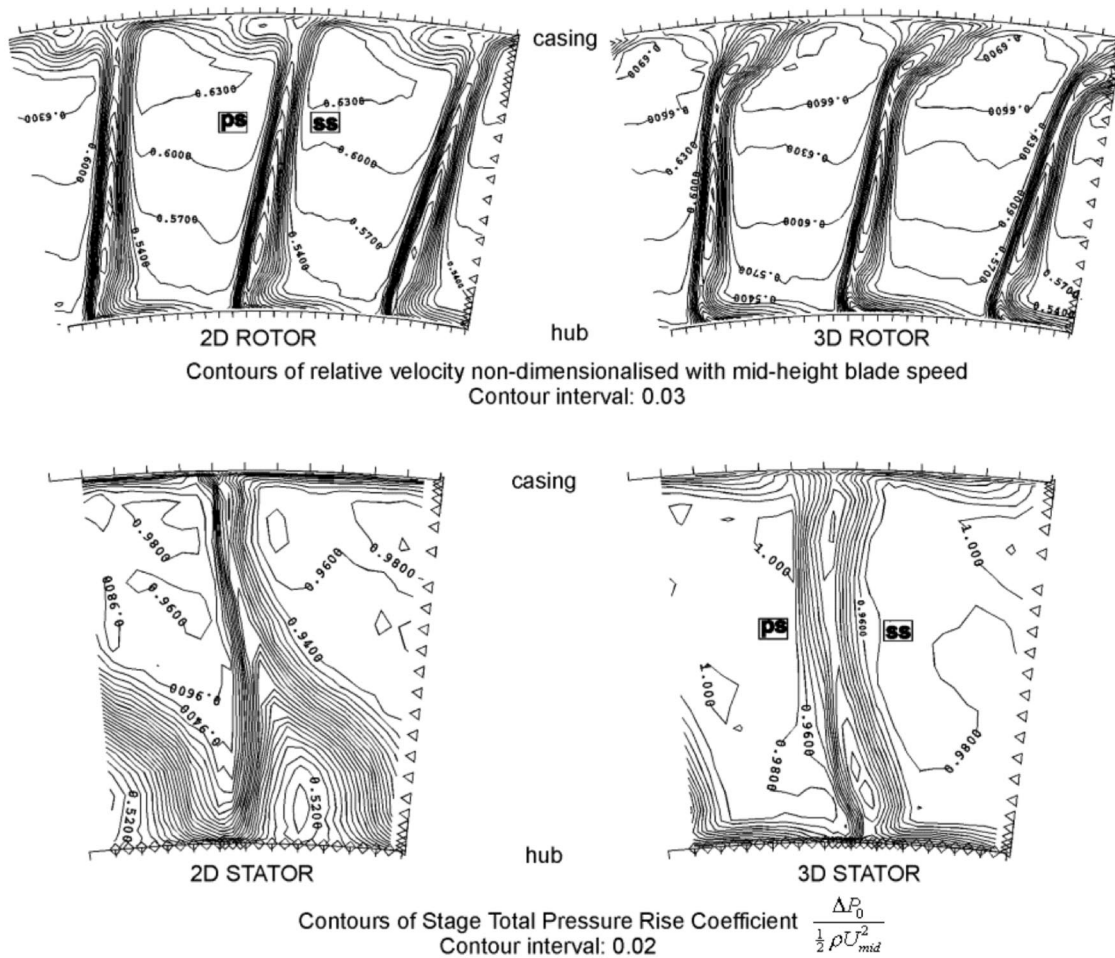


Fig. 14 Comparison of measured 2-D and 3-D blade row exit conditions at a near-stall operating point

design had only hinted at a loss increase in this region and had not warned of a significant loss increase. A further modification was made to the 3-D rotor which sought to redistribute this increase in loading by altering the trailing edge sweep and dihedral. The 3-D rotor was modified by the addition of tip chord to achieve this aim: in the modified rotor the trailing edge was approximately a straight radial line in the meridional view. This blade was tested and yielded significant performance improvements as shown in Fig. 12. It is worth noting that the design described in this paper was done before the design system developments described in the earlier parts of this paper were fully implemented. More recent calculations incorporating the improvements to the wall shear stress and turbulence modelling and using finer meshes have identified the thicker wakes near the blend point in the tip region of the 3D rotor, similar to the measurements.

### Discussion

The work described in Part I of this paper can be divided into two basic elements that are required in order to include 3-D blade designs into engine compressors. The first of these is a 3-D design toolkit that has been established together with some basic principles for designing blades in three dimensions. This was achieved by low-speed experimental research, closely coupled with the use of CFD calculations. The research shows that significant improvements can be made to compressor efficiency by using these techniques. For these techniques to be useful in the compressor design activity it is essential that they can be applied without significantly extending the time taken to deliver the final design solution. This

leads to the second element of the work in which an integrated multistage CFD design system was developed. The emphasis for this part of the work was to allow the designer to re-blade quickly a multistage compressor and run design and off-design constant speed characteristics overnight. This was achieved by keeping the CFD code as fast as possible whilst including important effects such as shroud leakage and bleed slot flows. To this end, a mixing length turbulence model was used, although it was modified in a semi-empirical manner to improve the agreement between predictions and measurements. The use of load sharing software allows the calculations to be distributed to many different computers. Each six-stage calculation takes about 6 hours on a Sun Ultra 10 workstation equipped with a 440 MHz RISC processor. This rapid turnaround and capacity for undertaking many CFD assessments of design proposals brings the use of multistage CFD into the preliminary design phase. Standard profile shapes or prescribed pressure distribution blade profile sections can be generated automatically on the back of a throughflow calculation and these can be used as a starting point for 3-D blade design studies. Three-dimensional CFD calculations are not yet good enough to calculate accurately total pressure loss. Two-dimensional blade-to-blade solvers have been tuned over many years to give accurate predictions for blade profile sections outside of the endwall boundary layer regions. Consequently, a good underlying 2-D design is still necessary to achieve a good overall efficiency target. (Should the 3-D CFD become accurate enough to assess the impact of blade profile shape changes then this constraint is removed.) Currently, however, the 3-D code is used to get a qualitative assessment of the endwall flow behavior and 3D stage

matching and design modifications predicted to improve the end-wall flowfield are regarded as desirable. Consequently, much better information is available to the designer at an early stage in the design so that efficiency and surge margin goals can be achieved. A large reduction in the cost and timescales associated with a rig test development program is realised through extensive filtering of inadequate design solutions before any real commitment to hardware.

In Part II of this paper the application of the design toolkit and the integrated CFD design system to low-speed multistage compressors and high-speed engine compressors is described.

## Conclusions

An integrated multistage CFD design system has been developed that is fast enough to allow such techniques to be routinely used in engine project design. This included modifications to a mixing length turbulence model to improve the agreement with experiment. The CFD code includes the real effects of shroud leakage and bleed flows. In parallel, a 3D design toolkit has been established for the application of 3D features into multistage compressor blading. Improvements in compressor performance due to 3-D design have been demonstrated on a single-stage low-speed research compressor.

## Acknowledgments

The authors would like to thank Professor John Denton of the Whittle Laboratory, University of Cambridge, for use of his CFD code and for help with modifications to it. The authors would also like to thank Mr. Mike Howard of Rolls-Royce Compressor Systems for his help in the preparation of the two papers. The work was supported by the Department of Trade and Industry, the Ministry of Defence, QinetiQ (formerly DERA) and Rolls-Royce Plc. The authors would like to thank them for permission to publish. However, the opinions expressed here are those of the authors and not necessarily those of Rolls-Royce Plc or any other organization.

## Nomenclature

$A$	= annulus area
$H$	= enthalpy
$L$	= mixing length
$P$	= pressure
$U$	= blade speed
$V$	= flow velocity
$V_\tau$	= friction velocity, $\tau_\omega/\rho$
$\dot{m}$	= mass flow rate
$r$	= radius
$y$	= distance from the wall
$y^+$	= $yV_\tau/\nu$
$ps$	= pressure surface
$ss$	= suction surface
$\Delta$	= change across the stage
$\kappa$	= von Karman constant, 0.41
$\nu$	= kinematic viscosity
$\rho$	= density
$\tau_\omega$	= wall shear stress

## Subscripts

0	= stagnation conditions
mid	= mid-span
mean	= area-averaged
$x$	= axial component

## Appendix

### Deverson Rig Controlled Diffusion Blading Design Parameters

Design rpm	500
Hub-casing ratio	0.80
Mean flow coefficient ( $\dot{m}/\rho AU_{mid}$ )	0.510
Mid-span Flow Coefficient ( $V_{x_{mid}}/U_{mid}$ )	0.543
Stage Loading Coefficient ( $\Delta H_0/U_{mid}^2$ )	0.456
Reynolds number (based on rotor mid-span chord)	$2.7 \times 10^5$
Reaction	51.6%
Stage pre-swirl (degrees)	24.5
Rotor Lieblein Diffusion Factor	0.505
Stator Lieblein Diffusion Factor	0.455
Rotor stagger (degrees)	36.4
Stator stagger (degrees)	35.4
Rotor and stator solidity	1.44

## References

- [1] Rhie, C. M., Gleixner, A. J., Spear, D. A., Fischberg, C. J., and Zacharias, R. M., 1995, "Development and Application of a Multistage Navier-Stokes Solver: Part I—Multistage Modelling Using Bodyforces and Deterministic Stresses," ASME Paper 95-GT-342.
- [2] LeJambre, C. R., Zacharias, R. M., Biederman, B. P., Gleixner, A. J., and Yekta C. J., 1995, "Development and Application of a Multistage Navier-Stokes Solver: Part II—Application to a High Pressure Compressor Design," ASME Paper 95-GT-343.
- [3] Weingold, H. D., Neubert, R. J., Behlke, R. F., and Potter, G. E., 1995, "Reduction of Compressor Stator Endwall Losses Through the Use of Bowed Stators," ASME Paper 95-GT-380.
- [4] Wisler, D. C., 1985, "Loss Reduction in Axial Flow Compressors Through Low-Speed Model Testing," ASME J. Eng. Gas Turbines Power, **107**, No. 2, pp. 354–363.
- [5] Freeman, C., 1985, "Effects of Tip Clearance Flow on Compressor Stability and Engine Performance," VKI Lecture Series LS-1985-05.
- [6] Graf, M. B., and Sharma, O. P., 1996, "Effects of Downstream Stator Pressure Field on Upstream Rotor Performance," ASME Paper 96-GT-507.
- [7] Breugelmans, F. A. E., Carels, Y., and Demuth, M., 1984, "Influence of Dihedral on the Secondary Flow in a Two-Dimensional Compressor Cascade," ASME J. Eng. Gas Turbines Power, **106**, July 1984, pp. 578–584.
- [8] Breugelmans, F. A. E., 1987, "Investigation of Dihedral Effects in Compressor Cascades," AGARD CP421, Advanced Technology for Aero Gas Turbine Components, Sept.
- [9] Sasaki, T., and Breugelmans, F., 1997, "Comparison of Sweep and Dihedral Effects on Compressor Cascade Performance," ASME Paper 97-GT-2.
- [10] Tweed, D. L., Okiishi, T. H., and Hathaway, M. D., 1986, "Stator Endwall Leading-Edge Sweep and Hub Shroud Influence on Compressor Performance," ASME Paper 86-GT-197.
- [11] Staubach, J. B., Sharma, O. P., and Stetson, G. M., 1996, "Reduction of Tip Clearance Losses Through 3-D Airfoil Designs," IGTI Asia Conference Paper 96-TA-013.
- [12] Inoue, M., Kuroumaru, M., Furukawa, M., Kinoue, Y., Tanini, T., Maeda, S., and Okuna, K., 1997, "Controlled-Endwall-Flow Blading for Multistage Axial Compressor Rotor," ASME Paper 97-GT-248.
- [13] Wadia, A. R., Szucs, P. N., and Crall, D. W., 1997, "Inner Workings of Aerodynamic Sweep," ASME Paper 97-GT-401.
- [14] Hah, C., Putterbaugh, S. L., and Wadia, A. R., 1998, "Control of Shock Structure and Secondary Flow Field Inside Transonic Compressor Rotors Through Aerodynamic Sweep," ASME Paper 98-GT-561.
- [15] Place, J. M. M., 1997, "Three-Dimensional Flow in Axial Compressors," Ph.D. thesis, University of Cambridge.
- [16] Bolger, J. J., 1999, "Three Dimensional Design of Compressor Blading," Ph.D. thesis, University of Cambridge.
- [17] Place, J. M. M., Howard, M. A., and Cumpsty, N. A., 1996, "Simulating the Multistage Environment for Single Stage Compressor Experiments," ASME J. Turbomach., **118**, pp. 706–716.

- [18] Denton, J. D., 1994, "Designing in Three Dimensions," AGARD Lecture Series 195—Turbomachinery Design using CFD.
- [19] Denton J. D., 1990, "The Calculation of Three Dimensional Viscous Flow Through Multistage Turbomachines," ASME Paper 97-GT-345.
- [20] Hall, E. J., 1997, "Aerodynamic Modeling of Multistage Compressor Flowfields—Part 2: Modeling Deterministic Stresses," ASME Paper 97-GT-345.
- [21] Adamczyk, J. J., 1985, "Model Equations for Simulating Flows in Multistage Turbomachinery," ASME Paper 85-GT-226.
- [22] Howard, M. A., and Gallimore, S. J., 1993, "Viscous Throughflow Modelling for Multi-Stage Compressor Design," ASME J. Turbomach., **115**, pp. 296–304.
- [23] Grotjans, H., and Menter, F. R., 1998, "Wall Functions for General Application CFD Codes," Proc ECCOMAS 98.
- [24] Spalart, P. R., and Allmaras, S. R., 1992, "A One-Equation Turbulence Model for Aerodynamic Flows," AIAA Pap. 92-0439.
- [25] Launder, B. E., and Spalding, D. B., 1974, "The Numerical Computation of Turbulent Flows," Comput. Methods Appl. Mech. Eng., **3**, pp. 269–289.
- [26] Baldwin, B. S., and Lomax, H., 1978, "Thin Layer Approximation and Algebraic Model for Separated Turbulent Flows," AIAA Pap. 78-257.
- [27] Shabbir, A., Celestina, M. L., and Adamczyk, J. J., and Strazisar, A. J., 1997, "The Effect of Hub Leakage Flow on Two High Speed Axial Flow Compressor Rotors," ASME Paper 97-GT-346.
- [28] Lewis, K. L., 1993, "The Aerodynamics of Shrouded Multi-Stage Turbines," Ph.D. thesis, University of Cambridge.
- [29] McGreehan, W. F., and Ko, S. H., 1989, "Power Dissipation in Smooth and Honeycomb Labyrinth Seals," ASME Paper 89-GT-220.
- [30] Wellborn, S., 1996, "Effects of Shrouded Stator Cavity Flows on Multistage Axial Compressor Aerodynamic Performance," NASA CR 198536.
- [31] Demargne, A. A. J., and Longley, J. P., 2000, "The Aerodynamic Interaction of Stator Shroud Leakage and Mainstream Flows in Compressors," ASME Paper 2000-GT-0570.
- [32] Behlke, R. F., 1986, "The Development of a Second Generation of Controlled Diffusion Airfoils for Multistage Compressors," ASME J. Turbomach., **108**, pp. 32–41.
- [33] Denton, J. D., Wallis, A. M., Borthwick, D., Grant, J., and Ritchey, I., 1996, "The Three-Dimensional Design of Low Aspect Ratio 50% Reaction Turbines," Paper S461/008/96, Latest Advances in the Aerodynamics of Turbomachinery with Special Emphasis, upon Secondary Flows, IMechE Seminar, Dec. 9–10, Rugby, U.K.
- [34] Smith, L. H., and Yeh, H., 1963, "Sweep and Dihedral Effects in Axial Flow Turbomachinery," ASME J. Basic Eng., **85**, pp. 401–416.
- [35] Cumpsty, N. A., 1990, "Unresolved Problems in Turbomachine Design—3D Design of Blades," Iowa Turbomachinery Course Notes.
- [36] Shang, E., Wang, Z. Q., and Su, J. X., 1993, "The Experimental Investigations on the Compressor Cascades with Leaned and Curved Blade," ASME Paper 93-GT-50.
- [37] Wennerstrom, A. J., 1984, "Experimental Study of a High Throughflow Transonic Axial Compressor Stage," ASME J. Eng. Gas Turbines Power, **106**(3), pp. 552–560.
- [38] Denton, J. D., and Xu, L., 1998, "The Exploitation of 3D Flow in Turbomachinery Design," The Successful Exploitation of CFD in Turbomachinery Design, IMechE Seminar, London, March 19.
- [39] Emmerson, P. R., and Buchanan, C. R., 1996, "Investigations of Sweep and Lean Effects on a Highly Loaded Compressor Cascade Using a 3-D Viscous Analysis," Defense Research Agency, Farnborough, U.K., DRA/AS/PTD/TR95056/1.
- [40] Harvey, N. W., Brennan, G., Newman, D. A., and Rose, M. G., 2002, "Improving Turbine Efficiency Using Non-Axisymmetric Endwalls: Validation in the Multi-Row Environment and with Low Aspect Ratio Blading," ASME Paper GT-2002-30337.

# The Use of Sweep and Dihedral in Multistage Axial Flow Compressor Blading—Part II: Low and High-Speed Designs and Test Verification

Simon J. Gallimore

John J. Bolger

Nicholas A. Cumpsty  
Mem. ASME

Mark J. Taylor

Peter I. Wright

James M. M. Place

Rolls-Royce Plc,  
Derby, DE24 8BJ UK

*This paper describes the introduction of 3-D blade designs into the core compressors of the Rolls-Royce Trent engine series with particular emphasis on the use of sweep and dihedral in the rotor designs. It follows the development of the basic ideas in a university research project, through multistage low-speed model testing, to their application to the high pressure engine compressor. An essential element of the project was the use of multistage CFD and some of the development of the method to allow the designs to take place is also discussed. Part I of the paper concentrated on the fundamental university-based research and the methods development. Part II describes additional low-speed multistage design and testing and the high-speed engine compressor designs and tests. [DOI: 10.1115/1.1507334]*

*Keywords:* Multistage, Compressor, Sweep, Dihedral, Design

## Introduction

This paper describes a project whose objective was to use multistage 3-D CFD to re-design the core compressors of the Trent engine to improve efficiency. In the first part (Gallimore et al. [1]) some fundamental aerodynamic research into 3-D compressor blade design was described, together with the development of the CFD method. In this paper we will describe the application of this work to the engine compressors. As part of this activity, further low-speed research was carried out on a four-stage rig in order to increase confidence in the engine project designs and further validate the design methodology. The background to this work and previous published experience has been discussed in Part I and so will not be repeated here.

The objective of the project was firmly focused on the re-design of the engine compressors and this had an influence on the approach taken throughout the work. The compressors to be re-designed were existing engine machines that were well understood. In particular, the high pressure (HP) compressor was in use in the Trent 700 and 800 engines. It was decided that the basic axial and radial matching and vortex design of the compressor would not be altered as part of the redesign because these were deemed acceptable in the existing machine. The objective was to improve the efficiency without reducing the stability margin or operating range of the compressor. It was also decided to re-design the engine compressor blading in two steps. In the first, the stator blade rows were redesigned and this was followed by a re-design of the rotor blade rows. The designs were also constrained to be back-compatible with the existing blading so that it would not be essential to have all the 3-D-designed blade rows in the compressor. A mixed set of blading, with some rows being unchanged from the original 2-D design, would be an option if so desired. This would allow some improvements to be made to the engine compressor even if particular 3-D blade rows were not successful. The possible design space for the 3-D designs was thus

constrained to some extent for the engine machines. A similar approach was adopted for the first design of the four-stage low-speed rig but the second low-speed design was allowed more freedom to explore the maximum potential of the design methodology.

## Low-Speed Designs and Test Results

The work on the low-speed four-stage rig was intended to support the engine project designs by confirming the findings of the university research described in Part I and to provide detailed aerodynamic measurements of the multistage flowfield in the 3-D designs, which would not be available from the engine compressor tests. The low-speed designs were conducted at Rolls-Royce in parallel with the high-speed engine design activity. The tests were carried out at Cranfield University on the low-speed four-stage test facility. A description of the rig is available in other publications (e.g., Howard et al. [2]) and so will not be repeated here.

The datum 2-D blading for the designs was taken from a previous research program, which is summarized by Swoboda et al. [3]. Although the design point parameters were not exactly the same as those for the high-speed compressor, it was decided that they were sufficiently close and representative to provide a valid experiment. (The engine Reynolds numbers are an order of magnitude greater than the low-speed rig). The design parameters for the low-speed rig are summarized in Table 1.

Two designs were undertaken and tested. For the first of these the stators were re-designed and then tested with the datum rotors. For the second, both the rotors and the stator blade rows were re-designed. The blade and vane numbers were not altered in the re-designs to avoid the need to manufacture new casing rings and drum fixings.

**3-D Stator Design (VRB1).** For the first low-speed design, designated *Viscous Re-Blade 1* (VRB1), attention was focused on the stator blade rows, which were of a shrouded construction. The design space was restricted to changes in the tangential stack of the aerofoils with associated camber and stagger changes. By not admitting any axial shift of the aerofoil sections, this ensured that

Contributed by the International Gas Turbine Institute and presented at the International Gas Turbine and Aeroengine Congress and Exhibition, Amsterdam, The Netherlands, June 3–6, 2002. Manuscript received by the IGTI, November 20, 2001. Paper No. 2002-GT-30329. Review Chair: E. Benvenuti.

**Table 1 Cranfield University compressor design data**

Rotational Speed	1100 rpm
Hub-casing ratio	0.85
Mid-span Flow Coefficient	0.50
Mid-span Stage Loading, $\Delta H_0/U^2$	0.35
Rotor Reynolds number (based on rotor mid-span chord)	$2.9 \times 10^5$
Reaction	64%
Rotor Mid-span Lieblein Diffusion Factor	0.42
Stator Mid-span Lieblein Diffusion Factor	0.41

the stators would be suitable for use with the existing 2-D rotors, because the axial gaps between adjacent blade rows were maintained.

The multistage CFD method described in Part I was first used to analyze the datum design. All four stages were included in the calculation. Because the method uses a time-marching algorithm the analysis was conducted at a higher blade speed than that used on the rig in order to increase the Mach numbers to around 0.3 and so help the convergence. This is a standard technique in such circumstances and the Mach numbers are low enough not to modify the flowfield significantly. The complete pressure rise characteristic of the machine was calculated and the overall results for the embedded study stage, stage 3, are compared to the datum test results in Fig. 1. The shape of the pressure rise char-

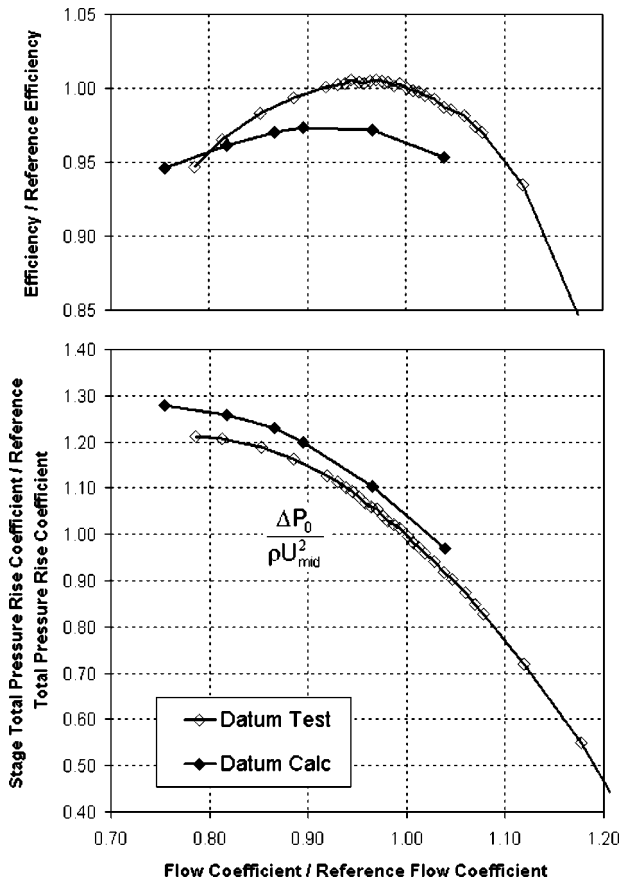


**Fig. 1 Comparison of measured and predicted characteristic for datum compressor**

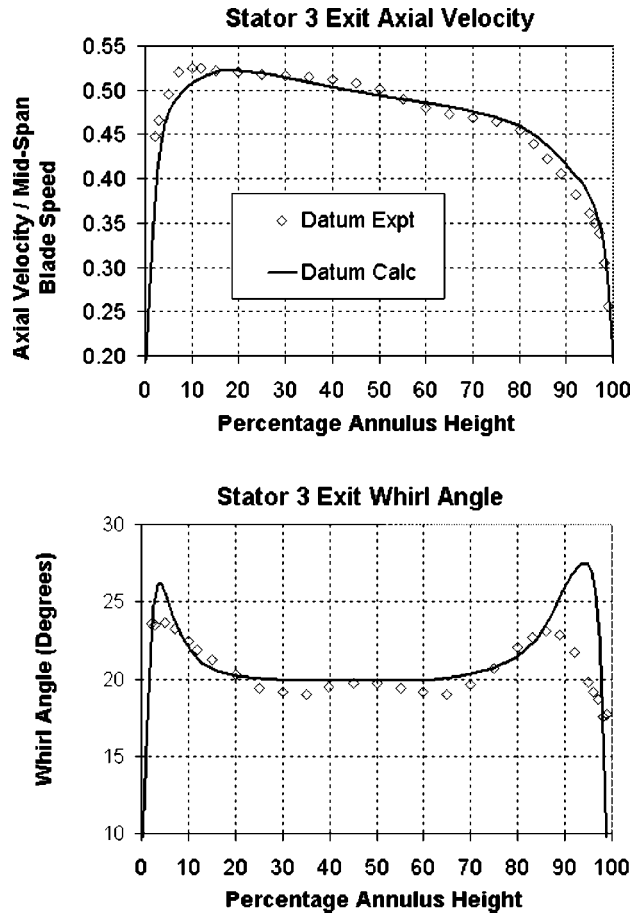


**Fig. 2 Measured and calculated stator 3 exit conditions**

acteristic and the efficiency variation with flow are predicted quite well. Figure 2 compares the predicted and measured axial velocities and flow angles at stator 3 exit at close to the design point. Again, the flow features have been reasonably well predicted by the code. Further improvement to the fine detail could be addressed by more mesh and further tuning of the turbulence model. The agreement with the measured data was considered to be close enough to give confidence that examining the CFD results for regions of the flow that could be improved by re-design of the stators would lead to an improvement in performance. Figure 3 shows contours of the predicted axial velocities just off the suction surface of the third stage rotor and stator at the peak efficiency and near stall conditions. Regions of reverse axial flow are evident in the suction surface endwall corners of the stators and at the rotor hub. These grow as the stall point of the machine is approached. The same picture with the redesigned stators is shown in Fig. 4. This shows that the areas of reverse flow in the stator have been virtually eliminated at the design point and significantly reduced at the stall point. The multistage effect of the change in the stator geometry is evident in the change in the contours in the rotor. This improvement in the flowfield results in a calculated reduction in the losses and a small increase in the peak efficiency. The improved efficiency is evident in the predicted characteristics for the re-designed stators, which are shown in Fig. 5 (which also shows the predicted characteristics for the second re-design, designated VRB2, which is discussed in the next section). There is no significant change to the predicted pressure rise characteristic. A picture of the re-designed stator and the datum stator is shown in Fig. 6.

**3-D Rotor and Stator Design (VRB2).** In the second design, designated VRB2, it was decided that both the rotors and the



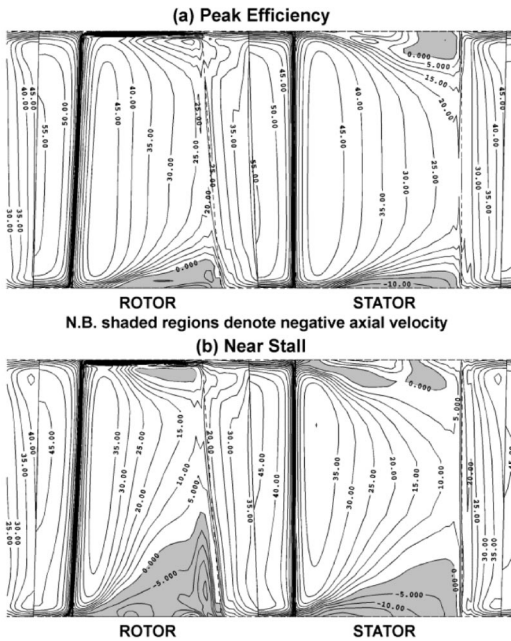


Fig. 3 Contours of axial velocity just off the suction surface for the datum compressor

stators should be re-designed and that axial shifts of the blade sections were to be allowed. This represented considerably more risk than the first design and more than was planned for the engine compressors at that time. However, the objective was to explore more fully the design space with a view to the future. As part of the design it was decided that the solidity could be reduced if required in order to get the maximum efficiency benefit while not compromising the stall range of the compressor. A series of views of the resultant blading is shown in Fig. 7. The rotor has sweep at

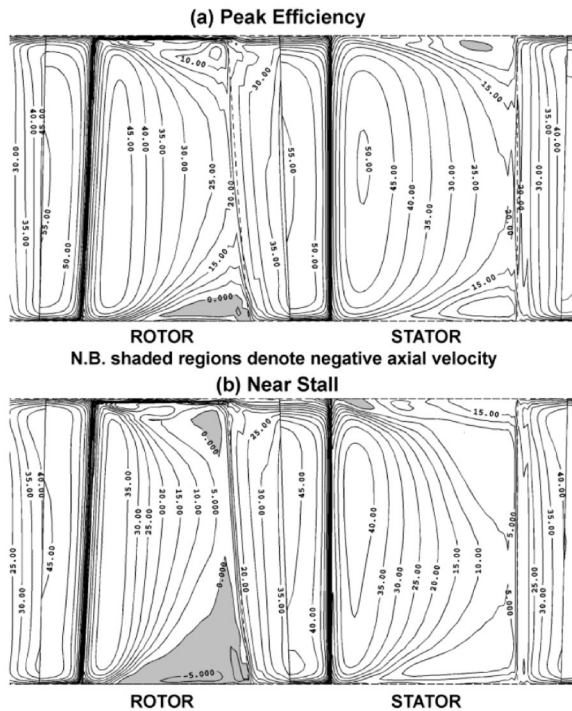


Fig. 4 Contours of axial velocity just off the suction surface for VRB1 compressor

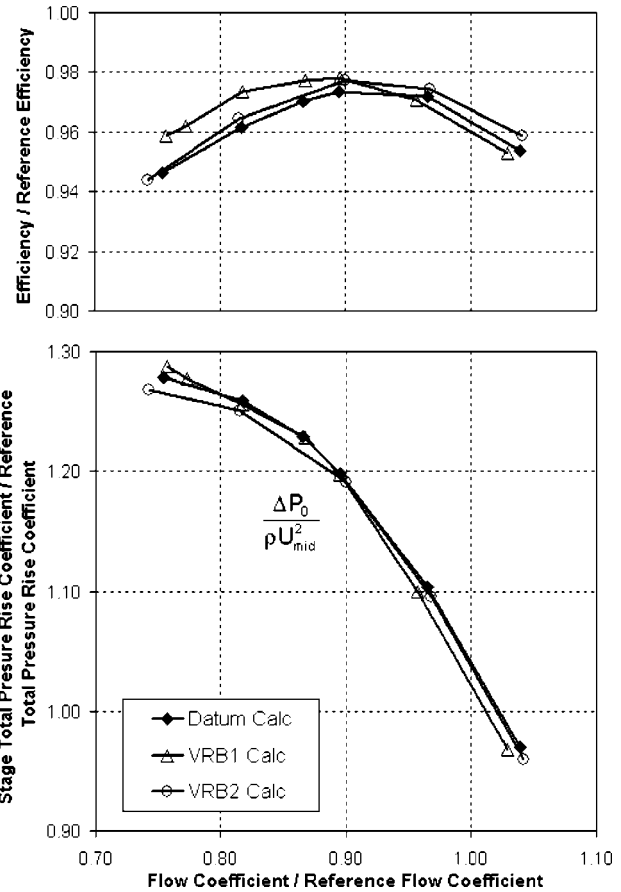


Fig. 5 Predicted characteristics for the datum, VRB1 and VRB2 compressors

the hub and dihedral at the tip. This is based on the work described in Part I, although the modifications at the blade tip were not as extreme as in that rotor design so that the initial problems associated with it could be avoided. The stator has a combination of sweep and dihedral at both ends and the stator chord has been significantly reduced at mid-span. This led to the interesting result that the most severe regions of reverse flow on the stator suction

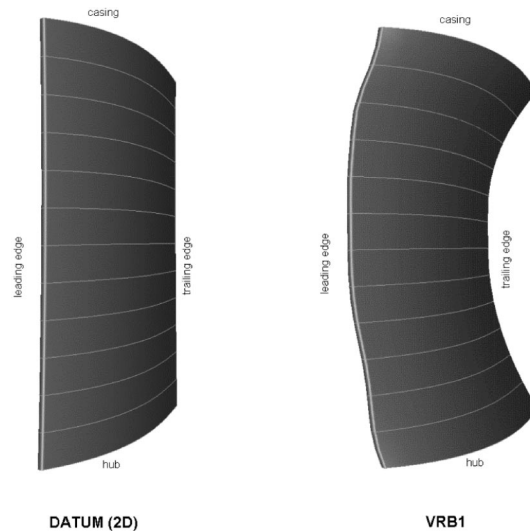


Fig. 6 Axial view onto suction surfaces of datum and VRB1 stators

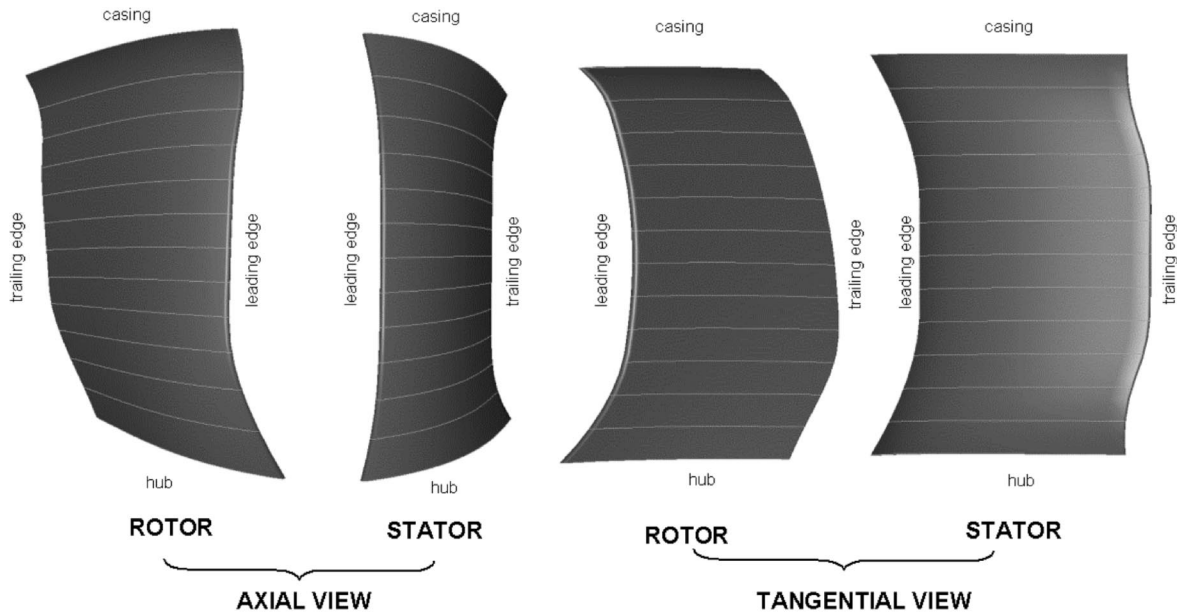


Fig. 7 Axial and tangential views of VRB2 rotors and stators

surface were predicted to occur away from the endwalls, which had been significantly off-loaded by the redesign. This is illustrated in Fig. 8 which shows the regions of reverse flow at the near stall condition. The results should be compared to those given in Fig. 3(b). The rotor re-design has reduced the reverse flow near the hub but has increased the reversed flow over the midheight regions of the blade.

The predicted overall characteristic for VRB2 is shown in Fig. 5, where it is compared to the predictions for the datum and VRB1 designs. The peak efficiency for VRB2 is predicted to be very similar to that of VRB1 and above that for the datum design. At non-dimensionalized flow coefficients above 0.90, VRB2 is calculated to have higher efficiency than the other two designs. For low flows VRB2 is more efficient than the datum but is less efficient than the VRB1 design. There is a slight reduction in the predicted stall range, as indicated by the flatter pressure rise characteristic near stall. This was attributed to the mid-span chord reduction on the VRB2 stator in an attempt to maximise efficiency. Overall, it was judged that the VRB2 design showed sufficient promise to be tested.

**Test Results.** The measured characteristic for the tests of the datum build, the VRB1 and the VRB2 redesigns are shown in Fig. 9. VRB1 gave a 1.3% improvement in peak efficiency with a

small increase in stall margin. VRB2 produced a further 0.9% increase in peak efficiency. The overall efficiency gains are greater than predicted and VRB2 has increased peak efficiency above VRB1, which was not predicted. At low flow coefficients VRB2 has lower efficiency than VRB1, but is still above the datum level, as predicted by the CFD. For high flow coefficients, VRB2 is more efficient than VRB1, as predicted, but VRB1 is more efficient than the datum design whereas the CFD calculated that it

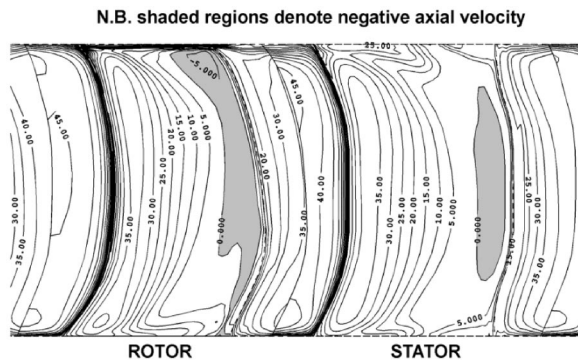


Fig. 8 Contours of axial velocity near stall just off the suction surface for VRB2

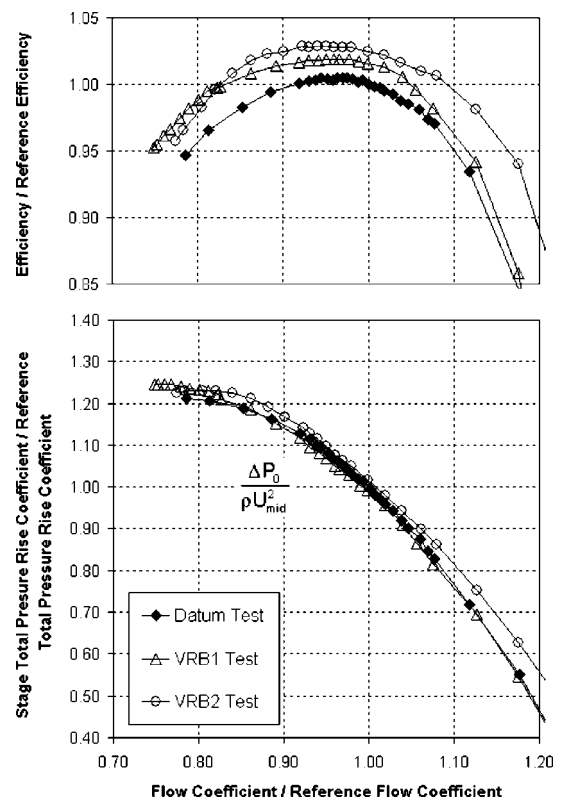


Fig. 9 Measured characteristics for datum, VRB1 and VRB2

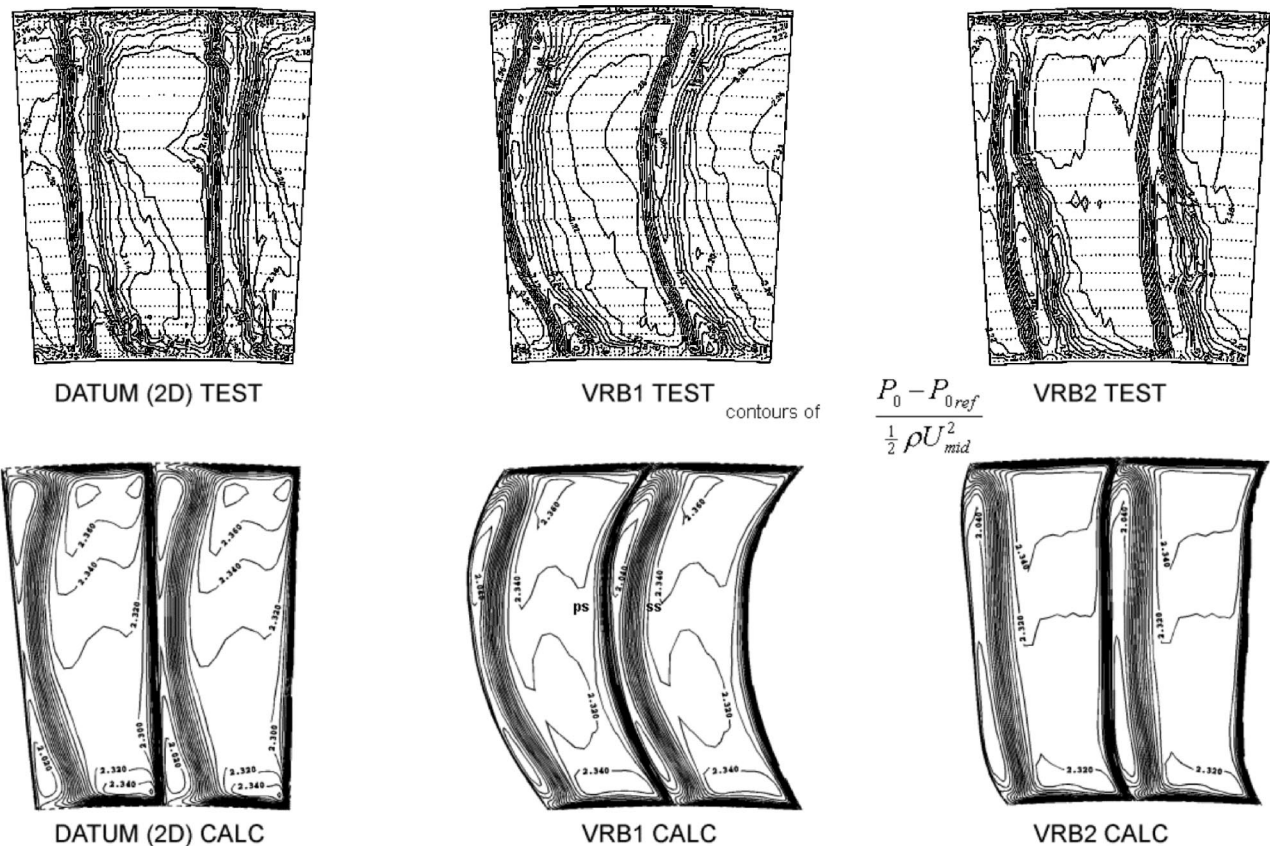


Fig. 10 Measured and calculated contours of stator 3 exit total pressure coefficient for the datum, VRB1 and VRB2 compressors

would be less efficient than the datum. Although the increase in the measured peak efficiency levels is larger than expected, it can be argued that the CFD has predicted the change in the shapes of the efficiency characteristics quite well. VRB1 retains efficiency better at low flows and VRB2 retains efficiency better at the higher flows. Examination of the pressure rise characteristics shows that VRB1 had increased stall range relative to the datum compressor. VRB2 had a stall range that was similar to the datum, despite the reductions of solidity in the design. This indicates that the stalling process for this compressor is dominated by the flow-field in the endwall regions of the machine. The trends in the changes to the stall range can be seen in the CFD predictions, but are not as clear as in the measurements.

Examination of the detailed traverse results showed that the design intent in terms of changes to the flowfield had been achieved. Fig. 10 compares the measured and predicted stator exit total pressure coefficient near stall for the three tests. The trends in the contours are predicted reasonably well. In particular, it is worth observing that for VRB2 the thicker wakes resulting from the region of separation have moved away from the endwalls towards mid-span, as was predicted to happen.

It can be concluded that the design CFD has predicted the direction of the changes measured in the tests, but not the magnitude. The low-speed tests have confirmed the research described in Part I and shown that significant efficiency increases may be obtained with 3-D blading design without significantly reducing surge margin.

### High-Speed Designs and Test Results

For the high-speed designs, a practical approach was adopted which allowed individual blade or vane rows to be retrofitted with the existing 2-D blading if necessary. The consequence of this was

to restrict the axial movements permitted by the aerofoil sections in order to maintain acceptable axial gaps between adjacent rows. In the first section below, the design of the stator blade rows is described. This is followed by a description of the rotor design and then the test results.

The compressor that was modified was the six-stage high-pressure compressor that was already in service in Trent engines. It was axially well-matched so it was decided to retain the existing basic design, and hence vortex design, in the re-designs. The compressor already had modern chordwise thickness and camber distribution aerofoil sections with low profile losses. This type of pressure distribution was retained. The aerofoil thickness-to-chord ratios were also maintained. The re-design consisted of only adjusting the existing blading to take into account the 3-D flow effects predicted to be present in the machine.

**3-D Stator Design.** The re-design of the stators concentrated on the first five stators. The sixth stator (or outlet guide vane) was omitted because this had already been re-designed using single blade row 3-D CFD several years earlier and included 3-D design features which were successful. The design rule adopted for the stators was that there should be no axial shifts applied to the aerofoils so that the meridional view of the compressor would remain unaltered. Reductions in the numbers of stators were to be permitted, provided that the predictions showed that any decrease in solidity would not reduce the surge margin of the machine.

The approach to the design of the aerofoils was very similar to that described above for the low-speed VRB1 design. The blade sections near the endwall were displaced tangentially to form an obtuse angle between the blade suction surface and the annulus walls. The inlet angles of the sections near the wall were increased to reduce local incidence in these regions. The effect of the tangential offset is to introduce negative sweep at the endwalls,

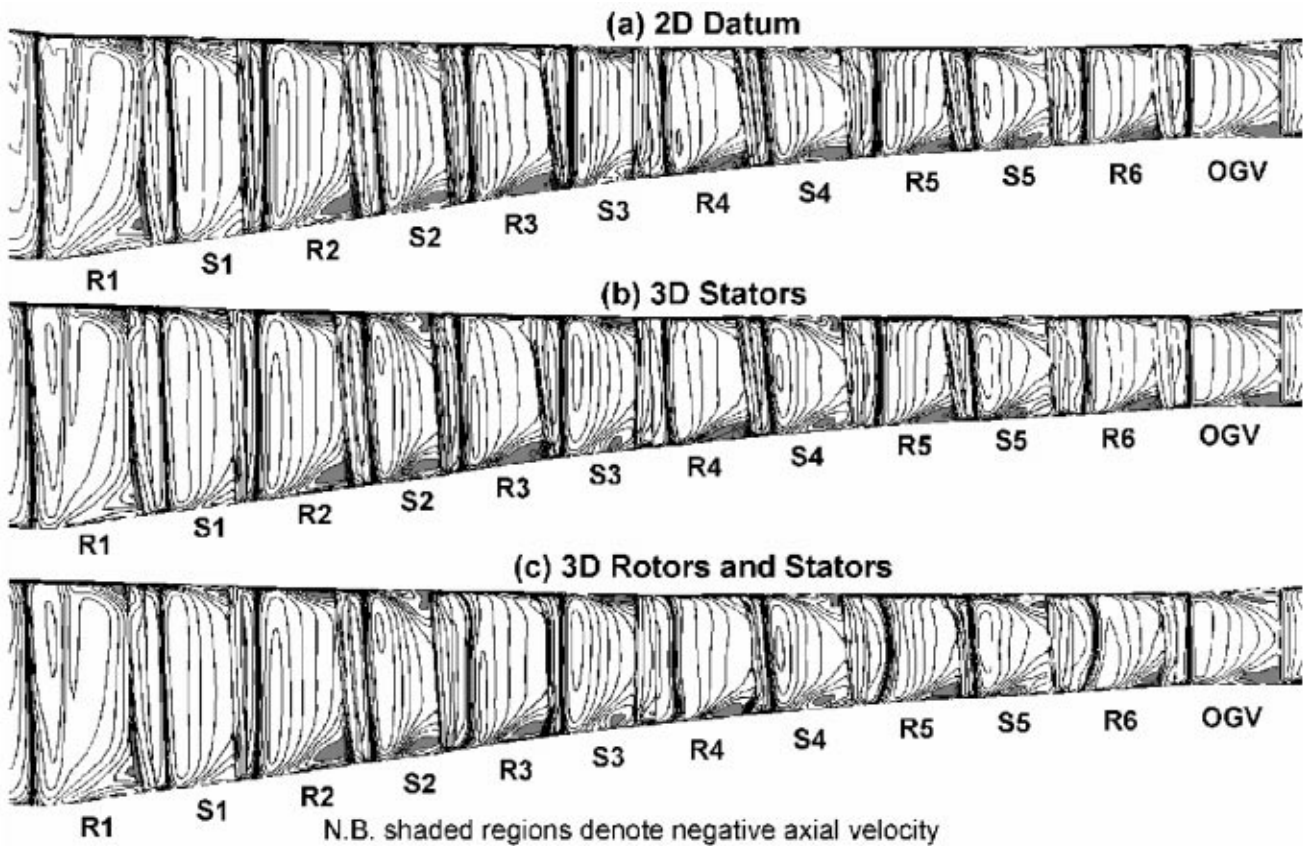


Fig. 11 Contours of axial velocity just off the suction surface for three high-speed compressors at design-speed on the working line—(a) 2-D datum, (b) 3-D stators, (c) 3-D rotors and stators

which tends to increase further the local incidence. This was also taken into account, via the 3-D CFD, and compensated for with the leading edge re-camber. For the first three stators it was found that these modifications off-loaded the endwall sections sufficiently for the number of blades to be reduced. Care was taken to make sure that the amount of tangential offset and the amount of leading edge re-camber for each stator was part of a family.

The criteria for deciding how much modification was to be applied to each row was the amount of reverse flow predicted in the suction surface endwall regions of the stators. This was examined at a range of operating points including the working line and approximate surge line points at design-speed and at part-speed operation (80% aerodynamic speed). An example of the predicted improvement in the flowfield at design-speed on the working line is shown in Figs. 11(a) and (b), which compares axial velocities just off the suction surface for the redesigned stators with the datum 2-D standard. For the first three stators it is not immediately apparent that there is an improvement. However, it must be remembered that the number of aerofoils had been reduced by around 15% so that while the predicted loss in the endwalls is similar for the two cases the mid-span loss has been reduced because of the reduction in solidity. Where the blade numbers were reduced the blade sections were initially re-designed at the reduced solidity using the established 2-D design system. An example of such a stator loss coefficient (total pressure divided by inlet dynamic head) is shown in Fig. 12(a). Figure 12(b) shows an example of the loss reduction for stator 4, where the blade numbers were not changed. This shows the reduction in loss close to the endwalls resulting from the 3-D design. Further away from the endwalls there is a predicted increase in the losses but the CFD calculation suggested that there was a net decrease in the total loss for the blade.

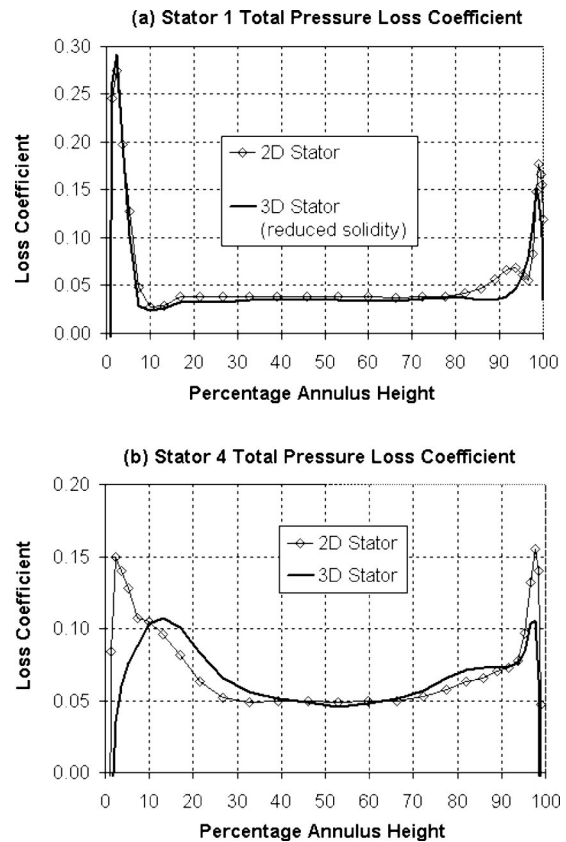


Fig. 12 High-speed compressor predicted stator loss coefficients

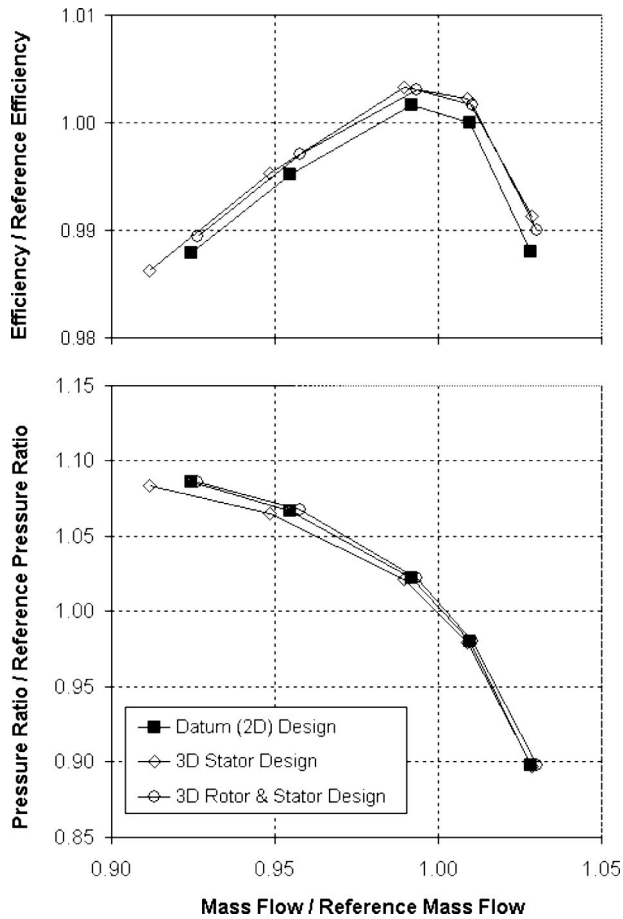


Fig. 13 Calculated high-speed compressor characteristics at design speed

The predicted design-speed overall characteristic for the compressor with the new stators is compared with that for the original blading in Fig. 13 (this figure also shows the predicted characteristic for the re-designed rotors, which are discussed in the next section). This shows that the design intent of keeping the datum compressor behavior has been maintained. In particular, the shape of the characteristics at throttled conditions is similar, indicating that the surge line is likely to be similar for the two machines. At the time the machine was designed, there was no predicted weakening of the characteristic. The slight off-design weakening in the pressure rise curve occurred in later versions of the CFD code after the implementation of the new turbulence and wall shear stress models. Had this weakening been predicted at the time, the design would have been altered slightly to improve the characteristic shape. The predicted increase in efficiency is relatively small, being about 0.3% at the peak, but this was thought sufficient to proceed with the test of the blading.

**3-D Rotor Design.** For the rotor designs a careful examination of the axial gaps in the compressor was undertaken and it was concluded that a certain amount of axial shift of the rotor blade sections could be tolerated. The use of tangential offset was restricted by the stresses caused by the centrifugal effect of the rotation of these blade rows and the balance of the blades on the platforms also needed to be assessed in order to maintain mechanical integrity. These considerations restricted the modifications that could be made to the rotor blades. For the front rotors, the constraints were particularly difficult to stay within and still achieve worthwhile aerodynamic benefits and so the first two rotors were omitted from this design exercise. If a complete re-design of the compressor were to be considered then some of

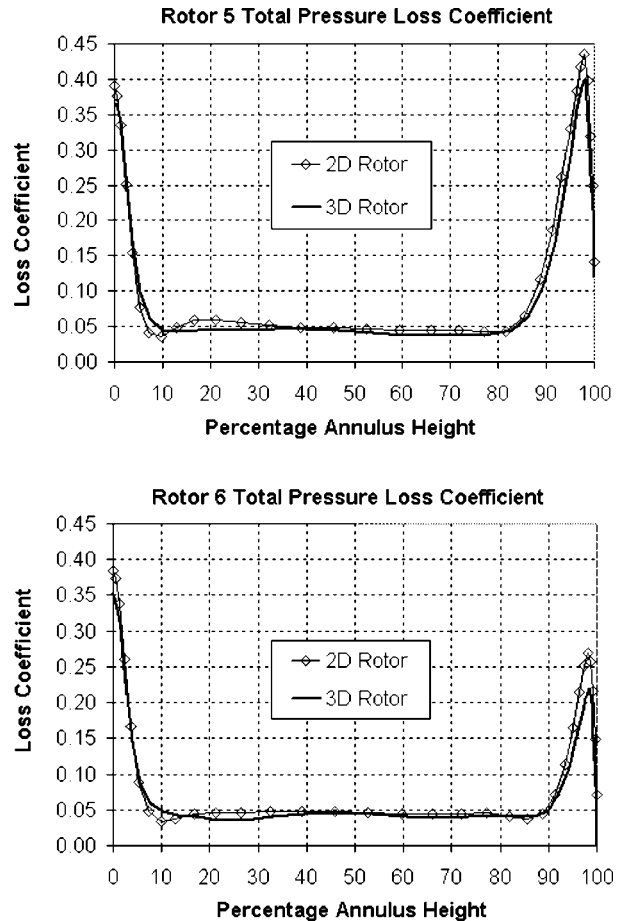


Fig. 14 High-speed compressor predicted rotor loss coefficients

these restrictions could be relaxed. Within the constraints just described, rotors 3 to 6 were modified to have swept hub sections with some leading edge recamber. At the blade tips the sections were moved tangential and normal to the chord line, following the earlier results of the university research and the VRB2 low-speed tests. In order to protect surge margin it was felt that it would be unwise to reduce the number of rotors and so this option was not pursued in the design.

The results of the rotor modifications are shown in Fig. 11(c), where the predicted suction surface velocities for the 2-D and 3-D blading are compared on the working line. The sweep at the rotor hubs has reduced the reverse flow there. It is less clear in Fig. 11 that the modifications at the tip have improved the flow. However, an example in the predicted improvement in the total pressure loss coefficient (relative total pressure loss divided by inlet dynamic head), shown in Fig. 14, indicates that the tip loss has been reduced. The type of blade shape resulting from such 3D modifications is shown in Fig. 15, which shows the blading for the fifth stage as an example.

The predicted design-speed characteristic for the compressor is shown in Fig. 13. Results are shown for the 2-D datum machine, the 3-D stators with the 2-D rotors and the 3-D rotors with the 3-D stators. The pressure ratio characteristic for the 3-D rotors and 3-D stators is predicted to retain the shape of that calculated for the datum compressor, indicating that the surge margin is likely to remain unchanged. The gain in efficiency is predicted to be very similar to that calculated for the 3-D stators alone. However, the experimental evidence from the low-speed testing had suggested

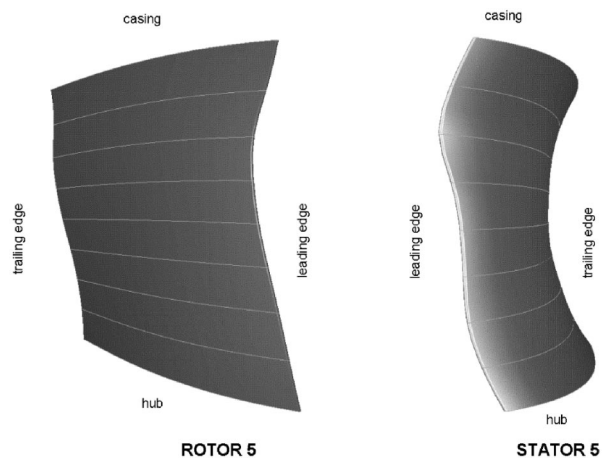


Fig. 15 Axial view of high-speed compressor blading

that the rotor modifications could produce an efficiency improvement and so the high-speed 3-D rotor designs were manufactured and tested.

**Test Results.** The new 3-D blading for the high pressure compressor was evaluated in two rig tests. In the first, the 3-D stators were included. For the second, the 3-D rotors were added to give a test of the full 3-D machine. The rotor running tip clearances were kept the same for all three tests. This can be problematic for high aspect ratio or low hub-to-casing ratio 3-D rotors where the blade changes shape from static to running in an un-

conventional way due to the nonradial stack of the blade profile centroids. This can be allowed for at the design condition (by deriving a static blade shape which runs up to the required shape at the design point) but may introduce different clearances at part-speed and over-speed conditions. For the blades described in this paper this was not a problem as they were sufficiently stiff to avoid this issue. The overall results for the two tests are compared to those from the datum test with 2-D blading in Fig. 16. This shows that the overall objectives of the designs were met, with increased efficiency with no significant loss in surge margin. The 3-D stators gave an improvement of some 0.7% in peak efficiency, considerably more than the 0.3% predicted during the 3-D design. The surge margin increased by a small amount, despite the fact that some of the stators had been removed during the design. The characteristics show that the design-speed flow capacity of the compressor has increased as a consequence of including the 3-D stators. The compressor inlet flow was not being controlled by first stage rotor choking at the design speed. At higher speed, where the rotor 1 does control choking flow, the inlet flows for the three compressor builds were essentially the same. Data at this higher speed has not been presented as it is outside of the engine operating range. Hence, the flow increase cannot be attributed to first rotor flow capacity. The increase in flow at design speed was not predicted and could be due to the under-estimation of the reduction of loss and blockage in the compressor due to the improved stator design. This serves as a warning for future re-design efforts because such axial re-matching of the compressor might lead to detrimental performance.

The test with the 3-D rotors produced an additional 0.2% increase in the peak efficiency, although the predictions indicated that there would be no gain. This was considered acceptable when the constraints imposed on the design by the particular aspects of the project are considered. The surge margin was essentially maintained at the level of the datum compressor, as indicated by the calculations.

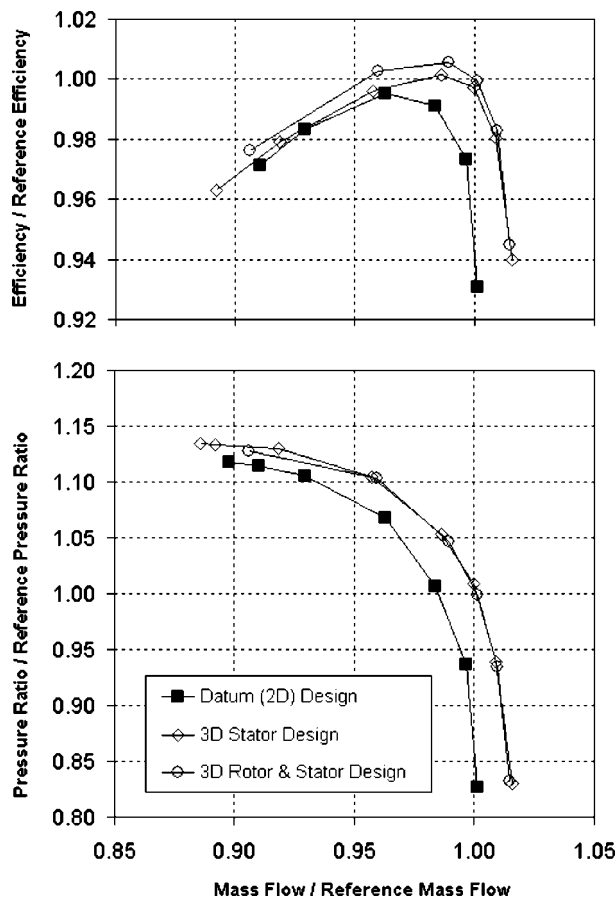


Fig. 16 High-speed compressor measured characteristics at design speed

## Discussion

The results from the high-speed rig tests confirmed that significant improvements can be made to engine compressor efficiency by using 3-D blade designs in both the rotor and stator blade rows. This can be achieved without reducing surge margin even when aerofoil numbers and mid-span solidity are reduced. As far as the authors are aware, this is the first time that hub and casing sweep and dihedral modifications to rotor blades in multistage engine compressors have been used successfully and described in the open literature. The low-speed research and testing and the CFD development were essential elements in the project that allowed ideas to be explored quickly and cheaply before design changes were committed to the engine machine.

The success of the designs described in this paper show that it was not necessary to include deterministic stresses in the multi-stage CFD modeling for these cases in order to make improvements to the compressors. The CFD used in this work did not predict the magnitude of the changes in efficiency but it did indicate that the modifications should improve the efficiency. The test results exceeded expectation in this regard. It was possible to estimate the effect on the surge margin of blade geometry change from the CFD results using overall characteristic shapes and radial profiles of blade row loading parameters. The calculations showed no loss in surge margin and this was supported by the tests.

It should be noted that more sophisticated CFD tools are available for use in an analysis of the final design solution. However, these are not regularly used during the intensive design phase as they hamper the iterative nature of the design process with prohibitive run-times. (Already, the continued growth in computer power begins to erode the last sentence.) The emphasis of the work described here is on a quick turnaround of engine 3-D designs using fast and efficient tools, which capture the essential

physics of the 3-D flow. The designer is guided by 3-D design tools right from the preliminary design phase, rather than at a later stage where it becomes more difficult to change the architecture of a machine.

Since the completion of the work described in this paper the design methodology has been applied to a series of engine compressors with similar good results. In particular, the new intermediate and high pressure compressors for the Trent 500 engine were designed using these techniques. For these machines it was possible to include more modifications to the blades than was possible in the high-speed designs described above because the compressors were designed from the start with 3-D blading included. The resulting blading tended to look more like the low-speed VRB2 design described above. These compressors have been certified, flight-tested, and are expected to enter revenue service in the near future.

## Conclusions

Multistage 3-D CFD has been successfully applied to engine project compressors to give more efficiency without compromising surge margin. The modifications can result in a cost reduction by allowing aerofoil numbers to be reduced. The CFD was not found to be reliable in predicting amounts of efficiency change, though it was found to give reliable indications of the direction of the change. Low-speed research and CFD method development were essential parts of the project. Three-dimensional blade design is now the recognized standard for engine multistage compressors.

## Acknowledgments

The authors would like to thank Professor John Denton of the Whittle Laboratory, University of Cambridge, for help with modifications to his CFD code and Mr. Mike Howard of Rolls-Royce Compressor Systems for his help in the preparation of the two

papers. The work was supported by the Department of Trade and Industry, the Ministry of Defence, QinetiQ (formerly DERA) and Rolls-Royce Plc. The authors would like to thank them for permission to publish. However, the opinions expressed here are those of the authors and not necessarily those of Rolls-Royce Plc or any other organization.

## Nomenclature

$A$	= annulus area
$H$	= enthalpy
$P$	= pressure
$U$	= blade speed
$V$	= flow velocity
$ps$	= pressure surface
$ss$	= suction surface
$\Delta$	= change across the stage
$\rho$	= density

## Subscripts

0	= stagnation conditions
1	= blade row inlet
mid	= mid-span
ref	= reference
rel	= relative frame of blade row

## References

- [1] Gallimore, S. J., Bolger, J. J., Cumpsty, N. A., Taylor, M. J., Wright, P. I., and Place, J. M. M., 2002, "The Use of Sweep and Dihedral in Multistage Axial Flow Compressor Blading Part I: University Research and Methods Development," *ASME J. Turbomach.*, **124**, pp. 521–532.
- [2] Howard, M. A., Ivey, P. C., Barton, J. P., and Young, K. F., 1994, "Endwall Effects at Two Tip Clearances in a Multistage Axial Flow Compressor with Controlled Diffusion Blading," *ASME J. Turbomach.*, **116**, pp. 635–647.
- [3] Swoboda, M., Ivey, P. C., Wenger, U., Gümmer, V., 1998, "An Experimental Examination of Cantilevered and Shrouded Stators in a Multistage Axial Compressor," *ASME Paper 98-GT-282*.

# Experimental Investigation of Unsteady Flow Field Within a Two-Stage Axial Turbomachine Using Particle Image Velocimetry

**Oguz Uzol**  
Mem. ASME

**Yi-Chih Chow**  
Mem. ASME

**Joseph Katz**  
Mem. ASME

**Charles Meneveau**  
Mem. ASME

Department of Mechanical Engineering,  
Johns Hopkins University,  
Baltimore, MD 21218

*Detailed measurements of the flow field within the entire 2nd stage of a two-stage axial turbomachine are performed using particle image velocimetry. The experiments are performed in a facility that allows unobstructed view on the entire flow field, facilitated using transparent rotor and stator and a fluid that has the same optical index of refraction as the blades. The entire flow field is composed of a "lattice of wakes," and the resulting wake-wake and wake-blade interactions cause major flow and turbulence nonuniformities. The paper presents data on the phase averaged velocity and turbulent kinetic energy distributions, as well as the average-passage velocity and deterministic stresses. The phase-dependent turbulence parameters are determined from the difference between instantaneous and the phase-averaged data. The distributions of average passage flow field over the entire stage in both the stator and rotor frames of reference are calculated by averaging the phase-averaged data. The deterministic stresses are calculated from the difference between the phase-averaged and average-passage velocity distributions. Clearly, wake-wake and wake-blade interactions are the dominant contributors to generation of high deterministic stresses and tangential nonuniformities, in the rotor-stator gap, near the blades and in the wakes behind them. The turbulent kinetic energy levels are generally higher than the deterministic kinetic energy levels, whereas the shear stress levels are comparable, both in the rotor and stator frames of references. At certain locations the deterministic shear stresses are substantially higher than the turbulent shear stresses, such as close to the stator blade in the rotor frame of reference. The nonuniformities in the lateral velocity component due to the interaction of the rotor blade with the 1st-stage rotor-stator wakes, result in 13 percent variations in the specific work input of the rotor. Thus, in spite of the relatively large blade row spacings in the present turbomachine, the nonuniformities in flow structure have significant effects on the overall performance of the system. [DOI: 10.1115/1.1509077]*

## Introduction

The unsteadiness in a multi-stage turbomachine is generally described in two parts: The "nondeterministic" (random) unsteadiness, referring to the fluctuations due to turbulence, associated, for example with blade wakes, and "deterministic" (periodic) unsteadiness, referring to fluctuations in the flow field correlated with the shaft frequency (or blade-rate frequency). The overall aerodynamics, vibration and acoustic characteristics of the machine are significantly affected by both forms of unsteadiness.

In the numerical simulations of turbomachinery, unsteady RANS equations have to be solved in order to determine the time (phase) dependent characteristics of the flow field. This approach is still impractical as a design tool for turbomachines with multiple blade rows and varying number of rotor and stator blades. Instead, an "averaged" flow state can be determined by solving the "average-passage" RANS equations, introduced first by Adamczyk [1]. This approach accounts for the effects of the phase-dependent unsteadiness and spatial nonuniformities associated with neighboring blade rows but does not resolve them. Three different averaging operators are being employed, the first being "ensemble averaging," that account for the turbulence and is used also in unsteady RANS. The second operator is "time averaging" that removes the deterministic unsteady flow, covering time scales

that are of the order of the shaft period, including the phase-dependent variations in flow structure. The third operator is "passage to passage averaging", necessary for turbomachinery with varying number of rotors and stators on consecutive stages. When these operators are applied to the Navier-Stokes equations one obtains the average-passage RANS equations. In this formulation each blade row has a steady average-passage flow field, and neighboring blade rows are coupled (replaced with) through circumferentially uniform systems of body forces, energy sources and deterministic stresses (Adamczyk [1], Adamczyk et al. [2,3], Rhie et al. [4], LeJambre et al. [5], Busby et al. [6]). The effects of phase-dependent unsteadiness on the average-passage flow field are accounted for through the "deterministic stresses." These stresses must be modeled in order to obtain a closed system of equations. The mixing plane approach is another simpler method for transferring the information between blade rows using boundary conditions in a plane located between the rows (e.g., Dawes [7], Denton [8]).

Previous studies have reported that deterministic stresses can be of similar or higher magnitude than the Reynolds stresses (Rhie et al. [4], Lejambre et al. [5], Sinha et al. [9]). Therefore, neglecting these interactions may lead to significant errors. Different models for the deterministic stresses have already been proposed (e.g., Adamczyk et al. [2], Van de Wall [10], Meneveau and Katz [11]), but unlike RANS closure models, there are no widely accepted and validated modeling tools. To develop these models one requires a database obtained either from experiments or unsteady RANS involving multistages, the latter introducing uncertainties

Contributed by the International Gas Turbine Institute and presented at the International Gas Turbine and Aeroengine Congress and Exhibition, Amsterdam, The Netherlands, June 3–6, 2002. Manuscript received by the IGTI, December 14, 2001. Paper No. 2002-GT-30664. Review Chair: E. Benvenuti.



related to turbulence closure models. In previous experimental studies, the deterministic stresses have been obtained from single point measurements (hot-wire, hot-film, split hot-film, five hole probe, etc.) and by traversing in between the blade rows and within blade passages (e.g., Prato et al. [12,13], Suryavamshi et al. [14,15]). Recent papers by Sinha and Katz [16] and Sinha et al. [9] provide deterministic stress distributions in a centrifugal pump obtained using 2-D PIV. The present paper provides detailed data on the distributions of deterministic stresses in a multi-stage axial turbomachine.

In order to understand the physical mechanisms and cause and effect relations of the unsteadiness, which lead to improved deterministic stress models, experimental data over the entire flow fields in a multi-stage turbomachine is essential. The axial turbomachinery facility introduced by Uzol et al. [17] and Chow et al. [18,19] enables us to perform 2-D PIV measurements covering an entire stage of a turbomachine, from the rotor inlet to the stator exit. This facility uses transparent rotor and stator blades operating in a solution of NaI, which has the same optical index of refraction as the blades, hence allowing optical access to the entire flow field. Detailed PIV measurements performed in this facility provide the data base for detailed phase-averaged and average-passage velocity distributions, along with the deterministic stresses and turbulence parameters. These measurements cover the entire 2nd stage of a two-stage turbomachine, from the inlet to the rotor to the exit from stator. The present data-base is composed of measurements performed at 500 rpm, at mid span, close to design conditions and at ten different rotor phases relative to the stator blade (every 3 deg), covering an entire rotor passage. The ten phase-averaged flow fields, obtained (each) by averaging 100 instantaneous distributions, are used to calculate the average-passage flow fields both in the stator and rotor frames of references. The deterministic stresses are determined from the difference between the phase averaged and average passage velocity distributions. The causes for the deterministic stresses are identified and compared to the distributions of Reynolds stresses. Finally, the causes of nonuniformities in the average-passage flow field and their impact on the performance of the rotor blade row are presented and discussed.

## Experimental Setup and Procedures

**Facility.** The axial turbomachine test facility enables us to perform detailed and complete PIV measurements at any point within an entire stage including the rotor, stator, gap between them, inflow into the rotor and the wake structure downstream of the stator. To generate such data using optical techniques one needs unobstructed view of the entire domain at any phase angle. This unlimited optical access is facilitated using a rotor and stator made of a transparent material (acrylic) that has the same optical index of refraction as the working fluid, a concentrated solution, 62–64 percent by weight, of NaI in water. This fluid has a specific gravity of 1.8 and a kinematic viscosity of  $1.1 \times 10^{-6} \text{ m}^2/\text{s}$  (i.e., very close to that of water). Thus, the blades become almost invisible, do not obstruct the field of view and do not alter the direction of the illuminating laser sheet required for PIV measurements. Information related to use and maintenance of the NaI solution can be found in [17].

The two-stage axial turbomachine shown in Fig. 1 has four blade rows. There are 12 rotor blades, each with a chordlength of 50 mm, span of 44.5 mm, thickness of 7.62 mm and camber varying from 2.54 mm at the hub to 1.98 mm at the tip. The resulting Reynolds number based on the tip speed and rotor chordlength is  $3.7 \times 10^5$  at 500 rpm, the speed of the present tests. The stators have 17 blades, each with a chordlength of 73.2 mm, span of 44.5 mm, thickness of 11 mm and camber of 6.22 mm. The system is driven by a 25-HP rim-driven motor, preventing the need for a long shaft, and the two rotors are connected by a

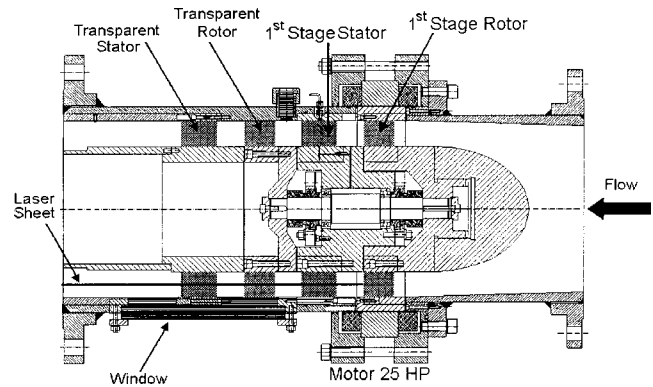


**Fig. 1 Test section of the axial turbomachine; the 2nd-stage rotors and stators are made of transparent acrylic**

common shaft, supported by precision bearings. More details about the facility can be found in [18] and the main geometrical parameters are listed in Table 1.

**PIV Setup and Experimental Procedure.** The measurements cover the entire 2nd stage. Data has been obtained at 10 rotor phases, every three degrees of blade orientation, covering an entire rotor blade passage of 30 deg. In this paper we present data for the midspan plane and at 500 rpm. At least one hundred instantaneous realizations are recorded for each phase and location. For selected cases we record 1000 images in order to obtain converged statistics on the turbulence. The sample area is  $50 \times 50 \text{ mm}^2$ , and as a result several data sets at different axial locations have been collected to cover the entire stage. Data analysis including image enhancement and cross-correlation analysis is performed using in-house developed software and procedures (Roth et al. [20,21]). Adapting these procedures to the current geometry, including modifications to the image enhancement procedures, and removal of the blade trace/signature prior to velocity computations are discussed in [17]. Additional details about the PIV setup, data acquisition system and uncertainty estimates can be found in [19].

## Results and Discussion

**Phase Averaged Flow Fields.** Using the instantaneous measurements, the phase-averaged results are calculated using

$$\bar{u}(x, y, \phi) = \frac{1}{N} \sum_{i=1}^N u_i(x, y, \phi) \quad \bar{v}(x, y, \phi) = \frac{1}{N} \sum_{i=1}^N v_i(x, y, \phi) \quad (1)$$

$$k(x, y, \phi) = \frac{31}{4N} \sum_{i=1}^N [(u_i(x, y, \phi) - \bar{u}(x, y, \phi))^2 + (v_i(x, y, \phi) - \bar{v}(x, y, \phi))^2] \quad (2)$$

**Table 1 The geometrical parameters for the axial turbomachine used in the present experiments (R2 and S2 refer to the 2nd-stage rotor and stator, respectively; S1 is the 1st-stage stator)**

No. of stages	2	R2-S2 axial gap / Rotor axial chord (mid-span)	1.92
No. of rotor blades	12	S1-R2 axial gap / Rotor axial chord (mid-span)	1.95
No. of stator blades	17	Rotor pitch-to-chord ratio (mid-span)	1.34
Hub-to-tip ratio	0.708	Stator pitch-to-chord ratio (mid-span)	0.66

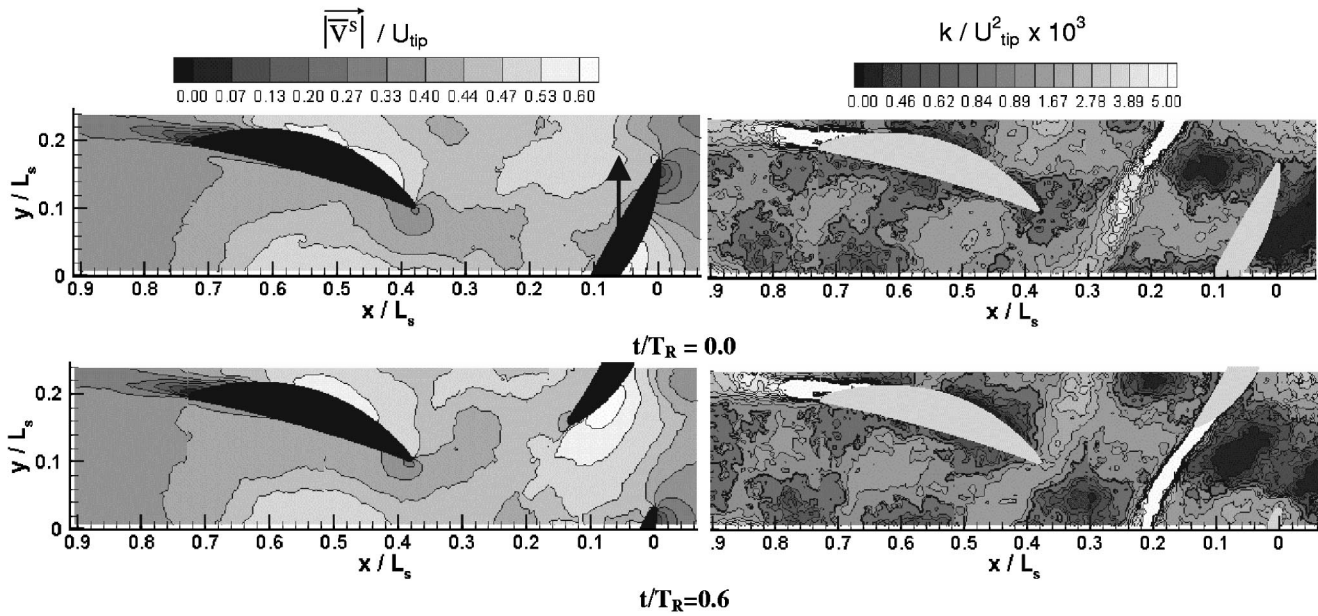


Fig. 2 Phase-averaged velocity in the stator frame of reference ( $|\vec{V}^s|$ ) and turbulent kinetic energy ( $k$ ) at two rotor phases covering the entire 2nd stage.  $U_{\text{tip}}=8$  m/s is the blade tip velocity at 500 rpm,  $L_s=203$  mm is the stage length and  $x=0$  is the rotor leading edge. Arrow shows the rotor direction.

$$-\overline{u'v'}(x,y,\phi) = -\frac{1}{N} \sum_{i=1}^N [u_i(x,y,\phi) - \bar{u}(x,y,\phi)][v_i(x,y,\phi) - \bar{v}(x,y,\phi)] \quad (3)$$

$$\bar{\alpha}(x,y,\phi) = \tan^{-1} \left( \frac{\bar{v}(x,y,\phi)}{\bar{u}(x,y,\phi)} \right) \quad (4)$$

where  $N=100$  is the number of instantaneous vector maps for each phase,  $u$  and  $v$  are the mean streamwise and lateral (almost circumferential, although the light sheet is flat) velocity components, respectively, and  $\phi$  is the phase angle. The  $3/4$  coefficient of  $k$ , the “turbulent kinetic energy,” is selected to account for the variance of the out of plane velocity component assuming that it is an average of the available measured components.

Figure 2 shows the phase averaged velocity and turbulent kinetic energy distributions for two different rotor phases. The high momentum regions on the suction side of the stator blade, along the aft suction side the rotor blade, and in the rotor wake are clearly visible. One can observe the phase-dependent variations of the velocity field, for example on the suction side of the stator blade. At  $t/T_R=0.0$  ( $T_R$  is the rotor blade-passage period) a rotor wake, easily identified in the  $k$  distribution, is impinging on the stator blade and the high momentum region on the suction side is split into two separate zones (Fig. 2). Conversely, at  $t/T_R=0.6$  the rotor wake is not impinging on the stator, and there is only a single high momentum zone on the blade. At this phase one rotor wake is located just upstream of the stator and a second (the one located near the leading edge at  $t/T_R=0.0$ ) impinges on the blade at mid chord, downstream of the high momentum region.

The distributions of turbulent kinetic energy clearly demonstrate that the flow field consists of a lattice of wakes formed both by the blades of the 1st stage, located upstream of the sample area, and by visible blades of the 2nd stage. As the almost horizontally aligned 1st-stage wakes pass through the 2nd stage rotor they are chopped off, creating wake segments. An example of such a 1st stage stator wake segment is evident in the  $k$  distribution  $t/T_R=0.0$ , between the rotor blade and the wake of a previous blade ( $x/L_s=0.25$ ,  $y/L_s=0.1$ ). The 1st-stage stator wake trajectory becomes discontinuous across the rotor wake (and blade) because of

the differences in the velocity magnitude on the suction and pressure sides of the rotor blade. An example of stator wake “shearing” can be seen in the turbulent kinetic energy plot at  $t/T_R=0.6$ . A little less obvious but still evident is the inclined wake of the 1st stage rotor, which is located 6.5 rotor axial chords upstream. At  $t/T_R=0.0$ , it engulfs the leading edge of the 2nd-stage rotor blade, and at  $t/T_R=0.6$  it is located above the emerging blade leading edge.

The 2nd-stage stator blade chops off the incoming rotor wakes, and the resulting train of inclined wake segments is transported through the stator passage. At  $t/T_R=0.0$  (Fig. 2) one can identify two rotor wakes inside the stator passage, a third segment is located at the exit from the passage and another one is approaching the leading edge of the stator blade. The latter is being chopped by the leading edge of the stator at  $t/T_R=0.6$ . The interaction of these wake segments with the stator wake causes phase dependent oscillations of the stator wake trajectory, to a great part due to variations in flow angle within the rotor wake segment [18]. The extent of the high turbulent kinetic energy zone in the core of the stator wake also expands and contracts depending on the location of the intersection with the rotor wake segment. More information can be found in [18,19].

Inherently, the flow field in the rotor frame of reference is also phase dependent. Unfortunately, the field of view of the current experiments ( $50 \times 50$  mm<sup>2</sup>, height of Fig. 2) does not allow us to obtain the entire flow field around a rotor blade from a single phase measurement. For each rotor phase, we can either see the flow around the leading edge or the wake region of the blade. Nevertheless, it is possible to construct the entire flow field by matching corresponding data sets obtained in different phases-rotor orientations relative to the stator. This phase matching procedure can be explained as follows:

To begin, we recall that the experiments are performed in the stator frame of reference. For 12 rotor blades, the rotor blade passage of 30 deg is covered by collecting 10 independent data sets every 3 deg of blade orientation. Hence, assuming rotor passage-to-passage periodicity, the phase that follows phase 10 ( $t/T_R=0.9$ ) would be the same as phase 1 ( $t/T_R=0.0$ ). In the rotor frame of reference, the stator passage is covered in 21.2 deg of rotation since there are 17 stator blades. Therefore, a specific

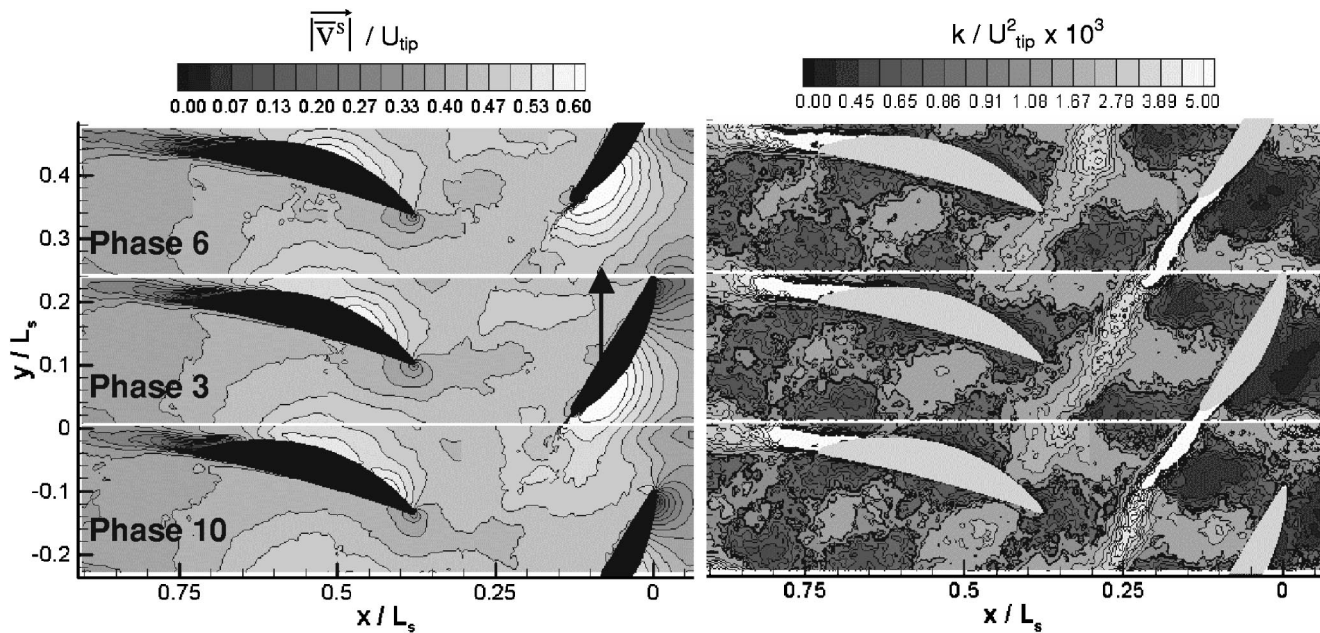


Fig. 3 Matched sets of phase averaged absolute velocity ( $|\vec{V}^s|$ ) and turbulent kinetic energy ( $k$ ) consisting of, from bottom to top, phase 10 ( $t/T_R=0.9$ ), phase 3 ( $t/T_R=0.2$ ) and phase 6 ( $t/T_R=0.5$ ). Arrow shows the rotor direction.

rotor blade is located in almost the same position with respect to the stator every 7th phase of our datasets. For example, the rotor blade in phase 3 (middle set in Fig. 3) is located in phase 10 at almost the same position (0.2 deg difference) with respect to the following stator blade, but in phase 10 (bottom set of Fig. 3) that particular rotor blade and the stator blade that it is facing are out of our field of view. Thus, phases 3 and 10 represent matched conditions of rotor orientation relative to the stator, and in fact, phase 10 shows the wake of the blade in phase 3. Similarly, phase 6 can be positioned on top of phase 3 since it represents matched conditions that have occurred 21 deg of blade orientation before phase 3. This matching procedure allows us to reconstruct the entire flow field in the rotor blade row (Fig. 3). Of course, the inherent assumption of this procedure is that the flow field in rotor passages is periodic. Since the sample phases presented in Fig. 3 are recorded independently, and the mean flow and turbulence structures/features seem to be continuous across the matched sets, the assumption of rotor passage-to-passage periodicity seems to be valid for this turbomachine. The complex flow field with the lattice structure formed by the 1st and 2nd-stage rotor and stator wakes become more evident in Fig. 3.

Matching all the appropriate rotor phases relative to the stator enables us to construct the entire flow field around the rotor blade in the rotor frame of reference, including its inlet and its wake. Figures 4(a), (b), and (c) are the resulting sample distributions of phase-averaged velocity, phase-averaged flow angle and turbulent kinetic energy, respectively, around the rotor blade at two different stator phases. As expected, the flow field in the rotor frame of reference is also dominated by the interaction with the 1st-stage stator and rotor wakes. In phase  $t/T_S=0.286$  ( $T_S$  is the stator passage period) a stator wake, characterized by high  $k$  and low  $\bar{\alpha}$ , is just starting to impinge on the rotor blade. The inclined region with elevated turbulent kinetic energy just above this stator wake is the 1st-stage rotor wake. Another sheared/segmented wake can be identified, one part on the pressure side of the blade and the other near the trailing edge on the suction side. As noted before, the discontinuity in wake trajectory is caused by the differences in velocities on the suction and pressure sides of the blade. In the rotor frame of reference the wake segment on the suction side moves downward faster than the segment on the pressure side. At

$t/T_S=0.858$ , the stator wakes are translated downward, and the stator wake located in the previous set near the leading edge is now chopped off, as it moves at different speeds on both sides of the blade. At  $t/T_S=0.858$ , the rotor blade is also starting to cut through the 1st-stage rotor wake.

The flow non-uniformities associated with wake-blade and wake-wake interactions are discussed in detail in [19]. However, a few examples that have bearings on the present paper should be mentioned. For example, the phase averaged velocity contours  $t/T_S=0.286$  show that there is a low momentum zone accompanied by (mostly) high (negative) flow angle on the pressure side of the rotor blade. This region coincides with the intersection of the 1st-stage stator and rotor wakes. At  $t/T_S=0.858$  the same wake intersection and associated non-uniformities can be seen interacting with the rotor wake, just downstream of the rotor trailing edge (at about  $0.1 < x/L_S < 0.2$ ,  $0.1 < y/L_S < 0.2$ ).

The interaction of the stator wake segments with the 2nd-stage rotor wakes cause phase-dependent meandering of the rotor wake, evident for example, in the upper rotor wake at  $t/T_S=0.286$  (Fig. 4). The wake intersections also involve substantial increase in the magnitude of flow angle towards axial flow in the absolute frame of reference. As demonstrated in [19], the rotor wake is sheared by the non-uniformities in the axial velocity distributions (absolute frame), which are a direct result of the “discontinuities” in the trajectories of the stator wake. This shearing creates a kink in the trajectory of the rotor wake, regions with concentrated vorticity, high turbulence levels and high shear stresses, the latter with a complex structure that resembles the mean strain. Although the wakes diffuse, the regions of elevated turbulence (defined as “turbulent hot spots”) persist far downstream of their origins. In fact, every region of wake intersection has an elevated turbulence level. Two such kinks at wake intersections appear as sudden enlargements in the velocity contours at  $t/T_S=0.286$ , at (0.25,0.25) and at (0.16,0.38) in Fig. 4(a). These complex flow non-uniformities associated with wake-wake and wake-blade interactions are advected downstream, causing phase-dependent variations in flow structure over the entire passage. As demonstrated in the next sections, these phenomena generate high deterministic stresses and considerable variations in the performance of the rotor.

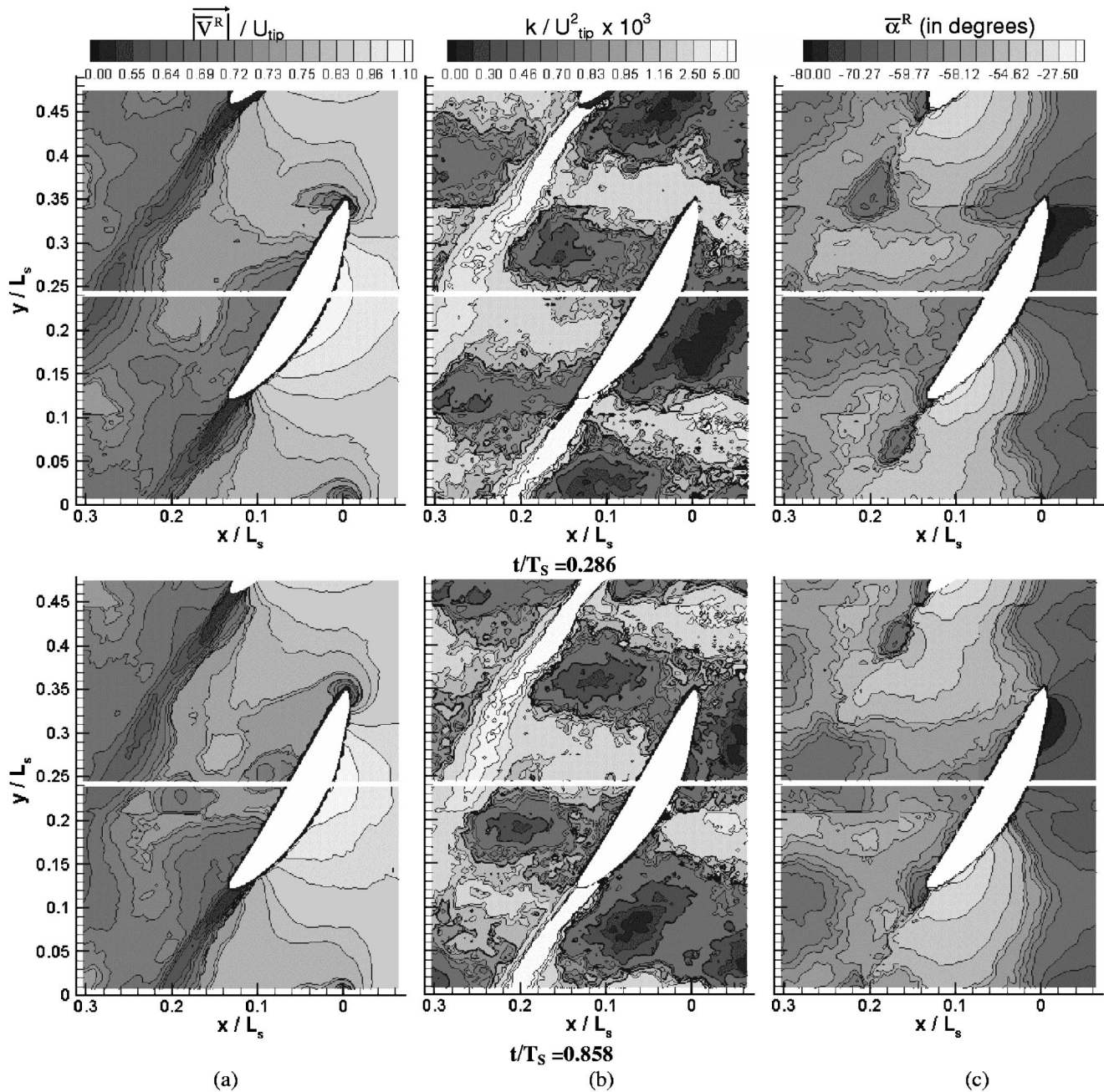


Fig. 4 (a) Phase-averaged velocity in the rotor frame of reference ( $|\bar{V}^R$ ); (b) turbulent kinetic energy; (c) phase-averaged flow angle ( $\bar{\alpha}^R$ ) in the rotor frame of reference around the rotor blade for two different stator phases

**Average Passage Flow Field and Deterministic Stresses.**

The measured phase averaged flow fields at ten different rotor phases, which cover the entire rotor passage every 3 deg of rotor orientation, enable us to calculate the average-passage flow fields and distributions of deterministic stresses both in the rotor and stator frames of references. Recall that each of the present phase-averaged flow fields are ensemble averages of 100 instantaneous realizations. The “average passage” flow fields presented in this section correspond to the “time-averaging” operator applied on the “ensemble-averaged” equations. We do not account for passage-to-passage variations in this study. The average-passage velocity in the stator and rotor frames of references are defined as

$$\hat{u}_i^S(x,y) = \frac{1}{T_R} \int_0^{T_R} \bar{u}_i^S(x,y,t) dt \approx \frac{1}{N_R} \sum_{n=1}^{n=N_R} \bar{u}_i^S(x,y,\phi_{R,n}) \quad (5)$$

$$\hat{u}_i^R(x,y) = \frac{1}{T_S} \int_0^{T_S} \bar{u}_i^R(x,y,t) dt \approx \frac{1}{N_S} \sum_{n=1}^{n=N_S} \bar{u}_i^R(x,y,\phi_{S,n}) \quad (6)$$

where  $N$  is the total number of phase averaged realizations, covering an entire passage, the subscripts  $S$  and  $R$  refer to the stator and rotor passages, respectively, and  $\phi$  is the phase. The superscripts  $S$  and  $R$  refer to frames of reference, and  $u_i$ ,  $i=1,2$  refers to axial and lateral velocity components, respectively. Since the measurements provide a finite number of phases, the blades do not cover each point at the same frequency, and as a result the average-passage data becomes patchy, especially within the passages. To provide a smooth transition and prevent the patchiness, we have to construct additional fields every 0.75 deg of rotor orientation. The process is based on linearly interpolating the ex-

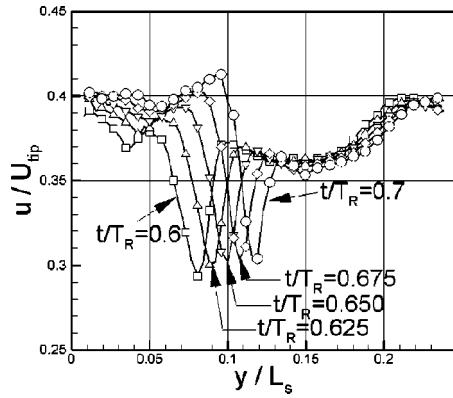


**Fig. 5 Sample comparisons between measured ( $t/T_R=0.6$  and  $0.7$ ) and interpolated ( $t/T_R=0.625, 0.650$  and  $0.675$ ) phase-averaged axial velocity profiles in the rotor wake ( $x/L_S=0.161$ )**

perimental data in points that are circumferentially shifted according to their phase, using weighted averages based on the phase lag. The newly constructed flow field is positioned based on its phase. Since each pair of experimental data sets used for interpolation is spatially shifted, the missing information at the bottom and top edges is completed using the appropriate matched phases, as explained in the previous section (see Fig. 3). Figure 5 shows a sample of measured (at  $t/T_R=0.6$  and  $t/T_R=0.7$ ) and interpolated axial velocity profiles within the wake of the rotor blade in the stator frame of reference. The smooth transition between the two measured distributions is clearly evident.

In determining the average passage flow fields, the points that fall inside the blades are assigned a zero fluid velocity to account for the mass balance of the fluid. This procedure is consistent with the gating function used in the derivation of average-passage equations [1], and is similar to the procedures used by Sinha et al. [9] to calculate the same parameters. The deterministic stress tensors in the stator frame of reference,  $\tau_{ij}^{S\ det}(x,y)$ , and rotor frame of reference,  $\tau_{ij}^{R\ det}(x,y)$ , are calculated from the difference between the phase-averaged and average passage flow fields; i.e.,

$$\tau_{ij}^{S\ det}(x,y) = -\frac{1}{N_R} \sum_{n=1}^{n=N_R} [\bar{u}_i^S(x,y, \phi_{R,n}) - \hat{u}_i^S(x,y)] [\bar{u}_j^S(x,y, \phi_{R,n}) - \hat{u}_j^S(x,y)] \quad (7)$$

$$\tau_{ij}^{R\ det}(x,y) = -\frac{1}{N_S} \sum_{n=1}^{n=N_S} [\bar{u}_i^R(x,y, \phi_{S,n}) - \hat{u}_i^R(x,y)] [\bar{u}_j^R(x,y, \phi_{S,n}) - \hat{u}_j^R(x,y)] \quad (8)$$

$$k_{det}^S = \frac{1}{2} (\tau_{11}^{S\ det} + \tau_{22}^{S\ det}) \quad k_{det}^R = \frac{1}{2} (\tau_{11}^{R\ det} + \tau_{22}^{R\ det}) \quad (9)$$

where  $k_{det}^S$  and  $k_{det}^R$  are the deterministic kinetic energy in the stator and rotor frames of reference, respectively.

Figures 6(a), (b) show the average passage velocity magnitude, deterministic kinetic energy and deterministic shear stress distributions, in the stator and rotor frames of reference, respectively. Consistent with the reference frame, all the rotor phases are averaged out in the stator frame of reference, and all the stator phases are averaged out in the rotor frame of reference. Several observations can be readily made from these distributions:

*In the Stator Frame of Reference (Fig. 6(a)).*

1. The high momentum region on the suction side of the blade and the structure of the stator wake are clearly visible in the average-passage velocity distribution. The boundary layer

on the suction side becomes significantly thicker at  $x/L_S > 0.62$ , but there is no flow separation (no reverse flow), and then generates a large wake zone.

2. Significant tangential nonuniformity in  $\hat{u}_i^S$  exists in the gap between the rotor and the stator. "Potential flow" (nonviscous) effects associated with the presence of the stator blade increase with decreasing distance from the leading edge, particularly at  $x/L_S > 0.32$ . Another major contributor, especially at  $0.13 < x/L_S < 0.3$  (immediately downstream of the rotor passage) is the tangential nonuniformities caused by interactions of the rotor blades with the 1st-stage rotor and stator wakes, discussed briefly in the first part of this paper and in more details in [19]. These (phase-dependent) interactions modulate the distributions of both the momentum being generated by the rotor, and the 1st-stage nonuniformities as they are advected through the rotor passage. Consequently, the distribution and magnitude of the high momentum region forming on the rotor suction side and extending in to the rotor wake (see Figs. 2 and 3), becomes phase dependent. As an illustrating example, in Fig. 2 ( $t/T_R=0.6$ ) and at  $x/L_S=0.2$ , the region with high velocity is bounded on its bottom side (at  $y/L_S=0.14$ ) by a segment of the 1st-stage stator wake. As this phase-dependent high momentum region is advected downstream, it also has a phase-dependent trajectory. Consequently, specific regions in the rotor-stator gap are periodically exposed to high momentum flow, whereas other regions are not, resulting in a nonuniform average passage velocity. The lobe with elevated  $\hat{u}_i^S$  in the rotor-stator gap shows the average trajectory of the high momentum flow. The location of this lobe is affected by the orientation of the rotor blade as it interacts with and modifies the flow nonuniformities generated by the 1st-stage wakes.
3. Tangential nonuniformities in the distributions of deterministic kinetic energy ( $k_{det}^S$ ) and shear stress ( $\tau_{12}^{S\ det}$ ) develop immediately downstream of the rotor passage and extend into the gap between the stator blades. The elevated  $k_{det}^S$  in the rotor-stator gap is a direct result of the complex, phase-dependent wake-wake and blade-wake interactions involving all of the upstream blade rows. These elevated levels are extended into the stator passages, and slowly decay towards the exit from the stator. Examination of the phase averaged data (Figs. 2 and 3) clearly show that the lattice of wakes persists throughout the stator passage, and as discussed before, the wakes even modulate the stator wake.
4. Regions with high positive deterministic shear stress, extending diagonally from (0.25,0.05) to (0.4,0.22), appear upstream of the stator's leading edge and extend into the stator passage, above but not near the suction side of the blade. This phenomenon is caused by phase-dependent unsteadiness related to wake-wake interactions, especially the 1st stage stator and the 2nd-stage rotor (see Fig. 3; also in [19]). High positive  $\tau_{12}^{S\ det}$  indicates strong correlations between negative and positive, axial and lateral, fluctuating (cyclic) phase averaged velocity components. Such an occurrence is an indicator for enhanced "deterministic mixing." Note that the high positive  $\tau_{12}^{S\ det}$  region coincides with the lower edge of the high  $k_{det}^S$  layer. Above it, coinciding with the upper half of the elevated  $k_{det}^S$  layer, the deterministic shear stress is slightly negative. Thus, the high  $k_{det}^S$  region contains layers of shear stresses with opposite signs, a phenomenon that one would expect to find in wakes (or jets). However, the high  $k_{det}^S$  does not coincide with the lobe of high average-passage velocity. This disagreement may be a result of potential flow effects that modify the velocity distribution near the leading edge of the stator.
5. A narrow band of negative deterministic stresses develops along the suction side of the blade boundary layer up to

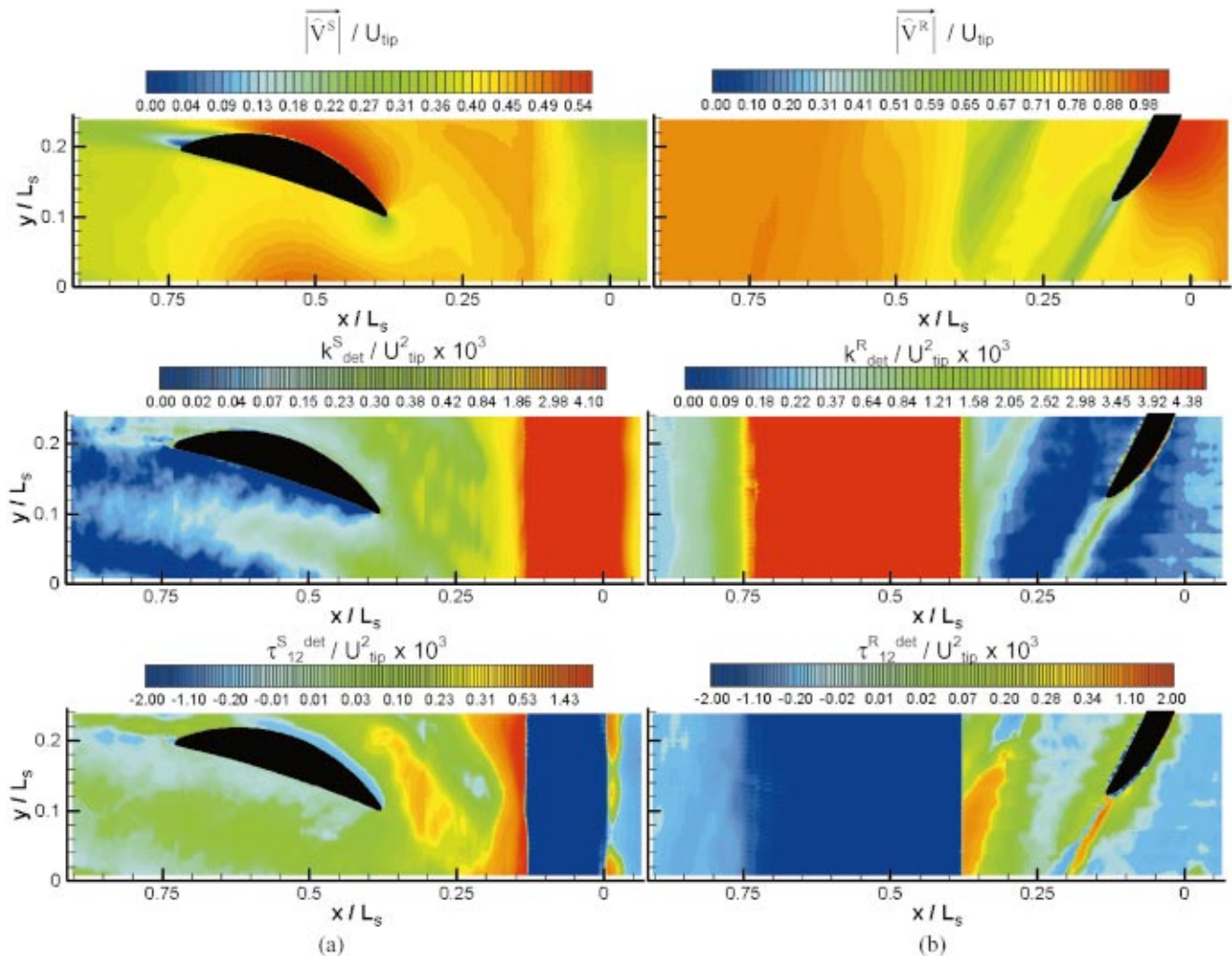


**Fig. 6 (a) Distributions of average passage velocity magnitude ( $|\vec{V}^S|$ ), deterministic kinetic energy ( $k_{\text{det}}^S$ ) and deterministic shear stress ( $\tau_{12}^{S \text{ det}}$ ) in the stator frame of reference; (b) distributions of average passage velocity magnitude ( $|\vec{V}^R|$ ), deterministic kinetic energy ( $k_{\text{det}}^R$ ) and deterministic shear stress ( $\tau_{12}^{R \text{ det}}$ ) in the rotor frame of reference**

about  $x/L_s=0.65$ , and then stops in the region where the boundary layer becomes significantly wider. Phase dependent variations in the flow near the wall, due to interactions with the lattice of wakes of the previous blades, discussed and illustrated briefly earlier in this paper (see also [18]), is the primary cause for this phenomenon. Note that the sign of the stress is *opposite* to the sign of Reynolds shear stresses that would develop in the boundary layer. Preliminary analysis indicates that, the deterministic production in this region as well as within the stator passages is negative, indicating a transport of energy from the phase averaged (unsteady) flow to the average passage flow.

6. In the aft region of the stator suction boundary layer the shear stress changes sign and becomes positive. Downstream of the stator trailing edge one can identify two high stress layers with opposite signs. The regions of high  $k_{\text{det}}^S$  in the stator wake coincide with both layers, i.e. the deterministic kinetic energy is high at the same place that the shear stress is high.

*In the Rotor Frame of Reference, (Fig. 6(b)).*

1. Regions with low average-passage momentum in the rotor frame of reference ( $\hat{u}_i^R$ ) are evident in both rotor wakes that

are located within the sample area. The first is trailing from the blade and the second is generated by another blade located above it.

2. The highest levels of deterministic kinetic energy ( $k_{\text{det}}^R$ ) are found within the rotor wakes. Wake-wake interactions, such as the shearing and bending of the rotor wake by the segmented 1st stage stator, discussed before (and is the primary topic of [19]), are the primary cause for this phenomenon. Elevated levels of  $k_{\text{det}}^R$  can also be seen on the pressure side of the blade. They are a result of phase-dependent variations in velocity that occur as the rotor chops of the 1st-stage stator wake, and cuts through the centerline of the 1st-stage rotor wake. The resulting flow nonuniformities are then convected along the blade surface and interact with the rotor wake, generating the kinks (or meandering of the rotor wake—see Fig. 4), regions with concentrated vorticity and turbulent hot spots [19]. The deterministic kinetic energy levels are also elevated upstream and within the rotor blade passages, mostly due to the transport of wakes generated by the blade of the 1st stage through the passages.
3. Wide regions with low but significant positive deterministic shear stress,  $\tau_{12}^{R \text{ det}}$ , form on both sides of the rotor blade. Examination of the phase average data suggests that these

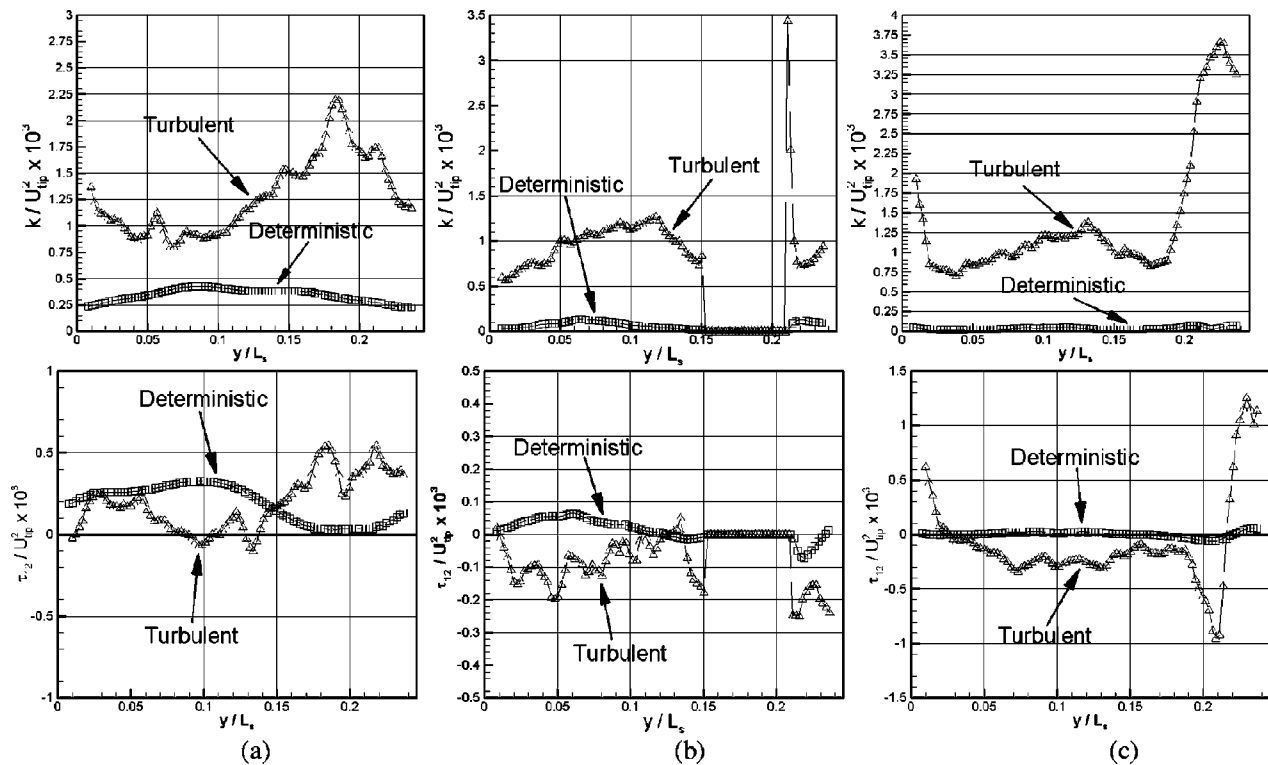


**Fig. 7 Comparisons between  $k$  and  $k_{\text{det}}^S$  (upper row), and between  $-\overline{u'v'}$  and  $\tau_{12}^{S \text{ det}}$  (lower row) at: (a)  $x/L_S=0.271$ , (b)  $x/L_S=0.553$ , and (c)  $x/L_S=0.835$ . Values at  $t/T_R=0.7$  are selected as representatives for the turbulent parameters.**

“halos” are a result of phase-dependent flow nonuniformities, caused by interactions of the rotor blade with the wakes of the 1st-stage (chopping of the 1st stage stator wake and splitting the 1st-stage rotor wake). Clear evidence for these nonuniformities is provided by comparing the two phases in Fig. 4.

- Parallel layers with elevated levels of positive and negative shear stresses develop in the wake of the rotor blade, with the positive layer reaching higher magnitudes. Upstream of the stator passage the shear stress distribution within the (upper) wake becomes completely positive and its magnitude increases. Examination of the phase-averaged velocity distributions and flow angle in this region (not shown, see [18]) indicates that the flow angle within the rotor wake increases (in the absolute frame of reference) just upstream of the stator wake. This angle change alters the sign of the deterministic shear stress.
- Regions of elevated deterministic stresses  $k_{\text{det}}^R$  and  $\tau_{12}^R \text{ det}$  extend downstream of both stator passages. As mentioned before, rotor wake segments transported through the stator passage modify the phase-averaged flow downstream of the stator, and generate deterministic stresses.

#### Comparison Between Turbulent and Deterministic Stresses.

This section compares the distributions and magnitudes of Reynolds stresses to the distributions and magnitudes of deterministic stresses. Recall that the turbulent stresses are calculated from the difference between the instantaneous and phase averaged data, whereas the deterministic stresses are calculated from the difference between the phase averaged and average-passage data. Previous studies have already reported that the deterministic stresses can be of similar or higher magnitude than the turbulent stresses [4,5,9]. Figure 7 compares the present distributions of  $k_{\text{det}}^S$  to  $k$  (at  $t/T_R=0.7$ ), and  $\tau_{12}^{S \text{ det}}$  to  $-\overline{u'v'}$  (also at  $t/T_R=0.7$ ) at three axial locations: 30 percent of the stator axial chord upstream from the stator leading edge, mid stator passage, and 30 percent stator axial

chord downstream from the stator trailing edge. As is evident, in all three axial locations the turbulent kinetic energy levels are much higher than the corresponding deterministic kinetic energy levels. In all three cases, the high  $k$  values are associated with turbulent wakes, the 1st-stage stator wake in Fig. 7(a), the wake lattice in Fig. 7(b), as well as the 2nd-stage stator wake (high peak) and wake lattice (lower broad peak) in Fig. 7(c). The only exception with similar (but still lower) values is the elevated  $k_{\text{det}}^S$  region in the gap between the rotor and the stator. Conversely, the levels of the turbulent and deterministic shear stresses are comparable to each other. At  $x/L_S=0.271$  (upstream of the stator), there is even a region where  $\tau_{12}^{S \text{ det}}$  is higher than  $-\overline{u'v'}$  ( $0.05 < y/L_S < 0.15$ ). As discussed before, wake-wake interactions involving the 1st-stage rotor and stator wakes, as well as the 2nd stage rotor wake, generate high phase-dependent unsteadiness in this region. Within and downstream of the stator passage, the turbulent shear stresses are higher than the deterministic stresses. It is also evident that trends of the Reynolds and deterministic stresses differ substantially.

The turbulent and deterministic stresses in the rotor frame of reference are compared in Fig. 8. It shows the distributions of  $k$ ,  $k_{\text{det}}^R$ ,  $-\overline{u'v'}$  and  $\tau_{12}^R \text{ det}$  at three axial locations, namely 30, 60, and 170 percent of the rotor axial chordlengths downstream from the rotor trailing edge. The third sample is located close to the stator. We use the turbulent kinetic energy and shear stress at  $t/T_R=0.5$ , consistent with the location of the rotor in Fig. 6(b). In all three cases the regions with elevated levels of deterministic kinetic energy are located within the rotor wake: in (a) ( $x/L_S=0.172$ ) and (b) ( $x/L_S=0.212$ ) the wake is generated by the blade shown in the sample area, and in (c) ( $x/L_S=0.355$ ) the wake is generated by the blade above the sample area. Consequently, one can identify corresponding peaks in the distributions of turbulent kinetic energy. As explained before, interactions of the rotor wake with the wakes of the 1st stage are the causes for both. In (a) and (b), the levels of  $k_{\text{det}}^R$  are substantially lower than

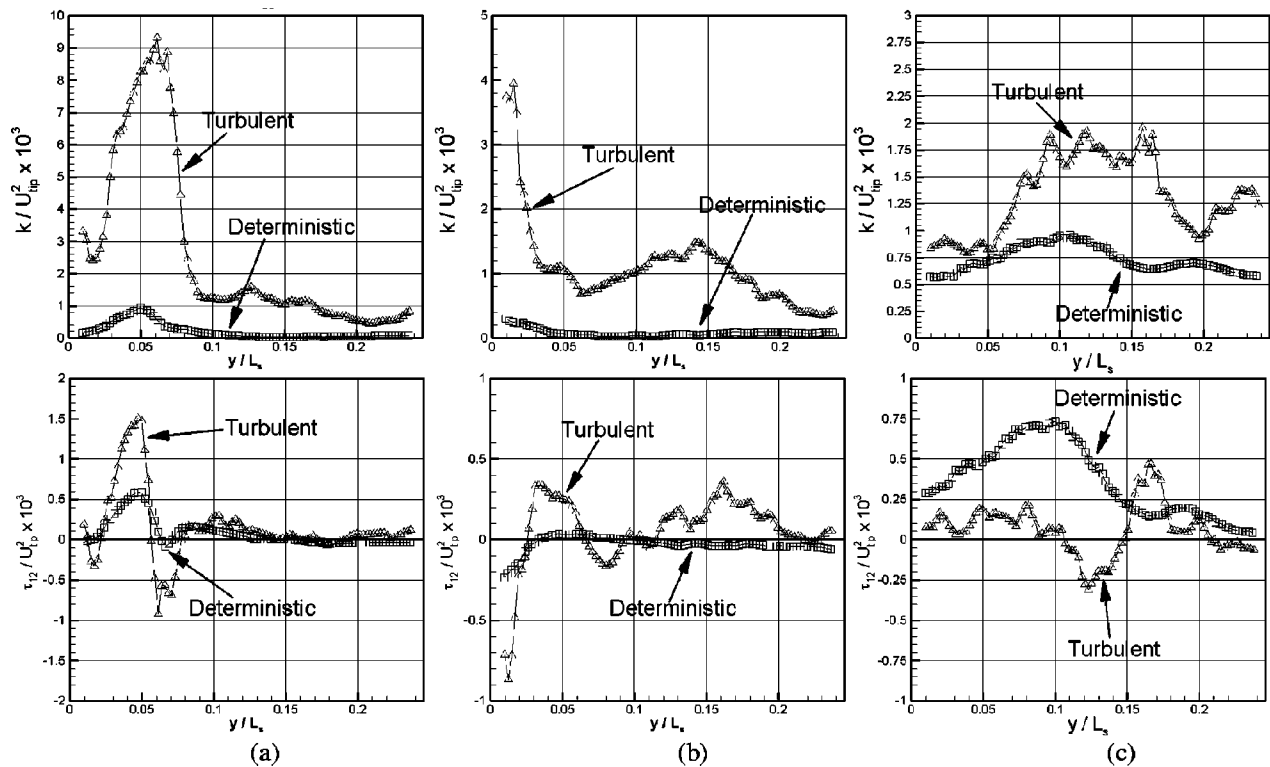


**Fig. 8 Comparisons between  $k$  and  $k_{det}^R$  (upper row), and between  $-\overline{u'v'}$  and  $\tau_{12}^{R det}$  (lower row). (a)  $x/L_s=0.172$ , (b)  $x/L_s=0.212$ , and (c)  $x/L_s=0.355$ . Values at  $t/T_R=0.5$  that correspond to the same rotor location are selected as representatives for the turbulent parameters.**

the levels of  $k$ , whereas in plane (c) the values are comparable. However, the  $k$  distributions contain additional peaks that occur, at least for planes a and b, as the 1st-stage stator wake crosses the sample plane. Interestingly, the  $k$  peaks associated with the rotor wake decay quickly with axial distance, whereas the broader, “far field” wake of the 1st-stage stator maintains almost the same level of turbulent kinetic energy (note the differences in scales).

Close to the rotor blade, at  $x/L_s=0.212$  (Fig. 8(b)), the levels of  $\tau_{12}^{R det}$  are elevated within the rotor wake, but are still lower than the turbulent shear stress. Both stresses have layers with opposite signs, consistent with the previous discussion, although this trend is clearer in the Reynolds stress. At  $x/L_s=0.212$  we miss the positive stress peaks of the wake, but capture the negative peaks at  $y/L_s=0.01$  (see Fig. 6b). Conversely, at  $x/L_s=0.355$ , the plane with the highest values of  $\tau_{12}^{R det}$  in the rotor-stator gap, the deterministic shear stress is significantly higher than the turbulent stress. As noted before, at this location the magnitude of the shear stress is affected by the stator-induced changes to flow angle. In regions outside the rotor wake the deterministic shear stresses are very small.

#### Effect of the Nonuniformities Present in the Average Passage Field on the Work Input.

In this section we examine the effect of flow non-uniformities associated with blade-wake and wake-wake interactions on the performance of rotor, expressed in terms of the work input of the rotor row. Figures 9(a), (b) show the distributions of average-passage lateral velocity components in the stator frame of reference ( $\hat{u}_2^S = \hat{v}^S$ ), downstream and upstream of the rotor row, respectively. The rotor blade row occupies the space between  $x/L_s=0.0$  and  $x/L_s=0.132$ . As is evident from these plots, the distribution of  $\hat{v}^S$  becomes non-uniform in the tangential direction immediately downstream of the rotor row. Although tangential nonuniformities are expected close to the stator blade because of the potential flow effects (Shang et al. [22]), the  $0.14 < x/L_s < 0.21$  region is located

more than 50 percent of the stator axial chord upstream of the stator leading edge. Hence, this region should have minimal potential flow effect associated with the 2nd-stage stator blade. Nevertheless, the non-uniformities are evident. Substantial non-uniformities in  $\hat{v}^S$  occur also upstream of the rotor blade row (Fig. 9(b)). Figure 10 compares the average-passage lateral velocity distributions in two axial planes, one is located 55 percent of the rotor axial chord upstream of the rotor leading edge ( $x/L_s = -0.07$ ), and the other is located 16 percent of the rotor axial chord downstream of the rotor trailing edge ( $x/L_s=0.153$ ). The maximum tangential variation of  $\hat{v}^S/U_{tip}$  downstream of the blade row is 7 percent, and 55 percent upstream of the rotor. We have already established that the nonuniformities upstream of the rotor

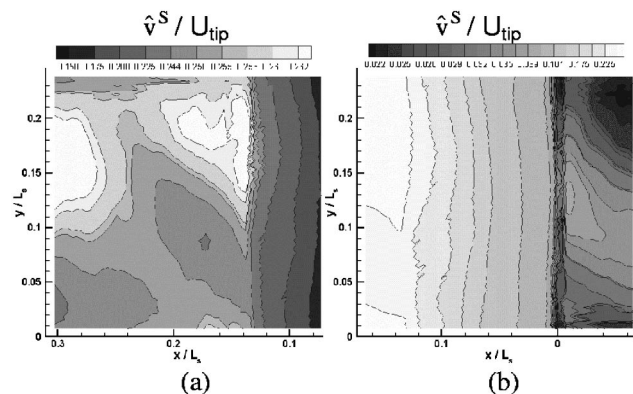


**Fig. 9 Distributions of average passage lateral velocity component.  $\hat{v}^S/U_{tip}$ , (a) downstream and (b) upstream of the rotor blade row. The rotor blade occupies the  $0.0 < x/L_s < 0.132$  region. Flow from right to left.**



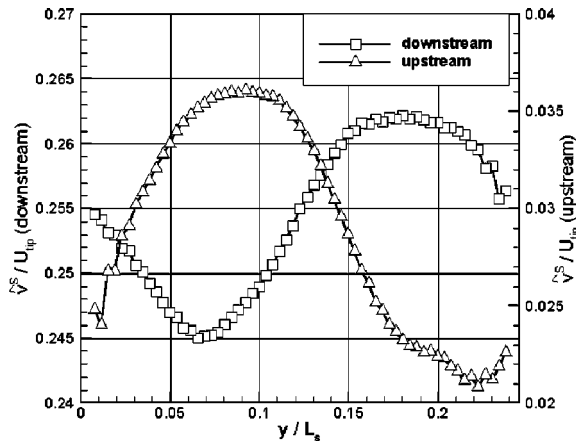


Fig. 10 Distributions of  $\hat{v}^S/U_{tip}$  in sample planes located upstream ( $x/L_s = -0.07$ ) and downstream ( $x/L_s = 0.153$ ) of the rotor blade row

are predominantly caused by the presence of the 1st-stage stator wakes. Within the 1st stage stator wake the lateral velocity is low (the stator is designed to generate an axial flow), whereas in the regions outside of these wakes  $\hat{v}^S/U_{tip}$  is higher, presumably due to a decreased effectiveness with increasing distance from the blade. Downstream of the rotor blade row, the increased lateral velocities in the  $0.13 < y/L_s < 0.245$  region is caused by the interaction of the rotor blade with the 1st-stage rotor and stator wakes, discussed briefly in this paper and is the main topic of [19].

In order to demonstrate the effect of these nonuniformities on the specific work input of the blade row, let's define two parameter  $W_1^*$  and  $W_2^*$

$$W_1^* = \frac{\hat{v}_d^S - \hat{v}_{u,av}^S}{\hat{v}_{d,av}^S - \hat{v}_{u,av}^S} \quad W_2^* = \frac{\hat{v}_d^S - \hat{v}_u^S}{\hat{v}_{d,av}^S - \hat{v}_{u,av}^S} \quad (10)$$

where the subscripts  $u$  and  $d$  refer to the selected planes upstream and downstream of the rotor, respectively, and the subscript "av" refers to average over the tangential direction. Both  $W_1^*$  and  $W_2^*$  are indicators for the tangential nonuniformities in the average specific work input, resulting, in the present case from interactions with the 1st-stage wakes.  $W_2^*$  accounts for the non-uniformity at the inlet to the rotor and  $W_1^*$  does not. Figure 11 shows the distributions of  $W_1^*$  and  $W_2^*$ . The peak-to-peak variations in  $W_1^*$  and

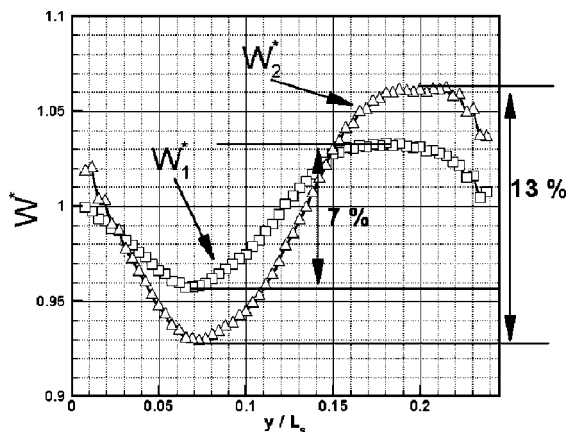


Fig. 11 Tangential nonuniformity in the average passage specific work input ( $W^*$ ) at 16 percent rotor axial chord downstream (at  $x/L_s = 0.153$ ) of the rotor blade row due to the non-uniform average passage lateral velocity distribution

$W_2^*$  are 7 and 13 percent, respectively. These results are a clear indication that the interaction of the rotor blade with the wake of the 1st stage cause substantial variations in the performance of the rotor. This conclusion holds in spite of the relatively high blade spacings of the present turbomachine, a distance of 1.95 times the rotor axial chord from the 1st-stage stator and 6.5 rotor axial chords from the 1st-stage rotor (see Table 1).

## Conclusions

PIV measurements are performed in the 2nd stage of a two-stage axial turbomachine. Phase averaged flow fields are obtained for 10 different rotor phases covering the entire stage. Phase averaged results are then used to obtain the average passage flow fields and distributions of deterministic stress in the entire stage both in the stator and rotor frames of references. The measured phase averaged flow field is extremely complex and appears to consist of a lattice of wakes. Wake-wake and wake-blade interactions cause substantial phase-dependent, nonuniformities and high turbulence both in the rotor and stator frames of references. These phenomena generate high deterministic stresses and considerable variations in the performance of the rotor.

The average-passage flow fields in the stator frame of reference contain substantial tangential non-uniformities in the average-passage velocity, as well as in the distributions of deterministic kinetic energy and shear stress in the rotor-stator gap. Close to the stator blade, the non-uniformity in the velocity distribution is mainly due to the potential field of the stator. However close to the rotor blade within the gap, the non-uniformities are due to the interaction of the 1st-stage rotor and stator wakes with the rotor blades. Tangential nonuniformities and elevated levels of deterministic kinetic energy and shear stress inside the gap is a direct result of the complex, phase-dependent wake-wake and blade-wake interactions involving all of the upstream blade rows. These elevated levels are extended into the stator passages, and slowly decay towards the exit from the stator. The distributions of the deterministic kinetic energy and the shear stress within the gap also show a wake or jet like character, consisting of a high deterministic kinetic energy region and layers of shear stresses with opposite signs. Phase dependent variations in the flow near the suction side of the stator blade results in negative deterministic stresses along the suction side of the blade boundary layer. The sign of the stress is *opposite* to the sign of Reynolds shear stresses that would develop in the boundary layer. Preliminary analysis indicates that, the deterministic production in this region as well as within the stator passages is negative, indicating a transport of energy from the phase averaged (unsteady) flow to the average passage flow. High levels of deterministic kinetic energy and shear stress are also found within the stator wake mainly due to the meandering of the stator wake, resulting from interaction with the wakes generated by upstream blade rows.

In the rotor frame of reference, the deterministic kinetic energy levels are maximum inside the rotor wakes. Wake-wake interactions, such as the shearing and bending of the rotor wake by the segmented 1st-stage stator are the primary cause for this phenomenon. Wide regions with low but significant positive deterministic shear stress form on both sides of the rotor blade. Examination of the phase average data suggests that these "halos" are a result of phase-dependent flow non-uniformities, caused by interactions of the rotor blade with the wakes of the 1st-stage (chopping of the 1st-stage stator wake and splitting the 1st-stage rotor wake). Elevated levels of positive and negative shear stresses also develop in the wake of the rotor blade, with the positive layer reaching higher magnitudes. Upstream of the stator passage the shear stress distribution within the rotor wake becomes completely positive and its magnitude increases, mainly due to phase dependent flow angle variations in this region.

The deterministic stresses are also compared to the turbulent (Reynolds) stresses. It is observed that the turbulent kinetic energy levels are generally higher than the deterministic kinetic energy

levels, whereas the shear stress levels are comparable, both in the rotor and stator frames of reference. At certain locations the deterministic shear stresses are substantially higher than the turbulent shear stresses, such as close to the stator blade in the rotor frame of reference. At this location the magnitude of the shear stress is affected by the stator-induced changes to the flow angle.

The substantial tangential non-uniformities in the lateral velocity component result in 13 percent variations in the specific work input of the rotor. Thus, in spite of the relatively large blade row spacings in the present turbomachine, the nonuniformities in flow structure have significant effects on the overall performance of the system.

It has to be kept in mind that all the measurements reported in this paper are two-dimensional and at mid-span. We have actually recorded 2-D data on two other radial planes (the hub and the tip). Midspan measurements are just the starting point of our studies. Our future measurements will also include 3-D stereoscopic PIV measurements in different radial planes.

## Acknowledgments

This project is sponsored by AFOSR under grant No. F49620-01-1-0010. The program manager is Dr. T. Beutner. Support for construction/assembly of the facility was also provided by ONR, under grant number N00014-99-1-0965. The program officer is P. Purtell. We would also like to thank Yury Ronzhes, Stephen King, Ali Pinarbasi, Madan M. Guin for their contribution to the construction of the facility, and Khoon Ooi from Able Corporation, for designing the rotor and stator blades

## Nomenclature

$k$	=	turbulent kinetic energy
$k_{\text{det}}$	=	deterministic kinetic energy
$L_s$	=	stage length starting from rotor leading edge
$N$	=	total no. of instantaneous samples
NaI	=	sodium iodide
$t$	=	time
$T$	=	blade passing period
$u$	=	instantaneous axial velocity
$U_{\text{tip}}$	=	velocity of rotor blade tip
$v$	=	instantaneous lateral velocity
$ \vec{V} $	=	velocity magnitude
$-u'v'$	=	Reynolds shear stress
$W^*$	=	specific work input variation
$x$	=	axial direction; $x=0$ is the rotor leading edge
$y$	=	lateral direction (almost circumferential, but laser sheet is flat)
$\bar{\alpha}$	=	phase averaged flow angle (yaw angle)
$\phi$	=	rotor phase
$\tau_{ij}^{\text{det}}$	=	deterministic shear stress tensor

## Superscripts

$R$	=	rotor frame of reference
$S$	=	stator frame of reference
$\bar{\phantom{x}}$	=	phase-averaged value
$\hat{\phantom{x}}$	=	average passage value

## Subscripts

1	=	not including upstream nonuniformity
2	=	including upstream nonuniformity
av	=	tangential average
d	=	downstream

u = upstream

## References

- [1] Adamczyk, J. J., 1985, "Model Equation for Simulating Flows in Multistage Turbomachinery," ASME Paper No. 85-GT-226.
- [2] Adamczyk, J. J., Mulac, R. A., and Celestina, M. L., 1986, "A Model for Closing the Inviscid Form of the Average-Passage Equation System," ASME Paper No. 86-GT-227.
- [3] Adamczyk, J. J., Celestina, M. L., Beach, T. A., and Barnett, M., 1990, "Simulation Of Three Dimensional Viscous Flow Within A Multistage Turbine," ASME J. Turbomach., **112**, p. 370.
- [4] Rhie, C. M., Gleixner, A. J., Spear, D. A., Fischberg, C. J., and Zacharias, R. M., 1998, "Development and Application Of A Multistage Navier-Stokes Solver—Part I: Multistage Modeling Using Body Forces and Deterministic Stresses," ASME J. Turbomach., **120**, p. 205.
- [5] Lejambre, C. R., Zacharias, R. M., Biederman, B. P., Gleixner, A. J., and Yetka, C. J., 1998, "Development And Application Of A Multistage Navier-Stokes Solver. Part II: Application To A High Pressure Compressor Design," ASME J. Turbomach., **120**, p. 215.
- [6] Busby, J., Sondak, D., Staubach, B., and Davis, R., 2000, "Deterministic Stress Modeling of a Hot Gas Segregation in a Turbine," ASME J. Turbomach., **122**, p. 62.
- [7] Dawes, W. N., 1992, "Towards Improved Throughflow Capability: The Use of Three-Dimensional Viscous Flow Solvers in A Multistage Environment," ASME J. Turbomach., **114**, pp. 8–17.
- [8] Denton, J. D., 1992, "The Calculation of Three-Dimensional Viscous Flow Through Multistage Turbomachines," ASME J. Turbomach., **114**, pp. 18–26.
- [9] Sinha, M., Katz, J., and Meneveau, C., 2000, "Quantitative Visualization of the Flow in a Centrifugal Pump With Diffuser Vanes-II: Addressing Passage-Averaged and Large-Eddy Simulation Modeling Issues in Turbomachinery Flows," ASME J. Fluids Eng., **122**, pp. 108–116.
- [10] Van de Wall, A. G., Kadambi, J. R., and Adamczyk, J. J., 2000, "A Transport Model for the Deterministic Stresses Associated With Turbomachinery Blade Row Interactions," ASME J. Turbomach., **122**, pp. 593–603.
- [11] Meneveau, C., and Katz, J., 2001, "A Deterministic Stress Model for Rotor-Stator Interactions in Simulations of Passage-Averaged Flow," submitted to ASME J. Fluids Eng.
- [12] Prato, J., Lakshminarayana, B., and Suryavamshi, N., 1997, "Exit Flow Field of an Embedded Stator in a Multi-Stage Compressor," J. Propul. Power, **13**(2), pp. 169–177.
- [13] Prato, J., Lakshminarayana, B., and Suryavamshi, N., 1998, "Steady and Unsteady Three-Dimensional Flow Field Downstream of an Embedded Stator in a Multi-Stage Axial Flow Compressor Part I: Unsteady Velocity Field," ASME Paper No. 98-GT-521.
- [14] Suryavamshi, N., Lakshminarayana, B., and Prato, J., 1998, "Steady and Unsteady Three-Dimensional Flow Field Downstream of an Embedded Stator in a Multi-Stage Axial Flow Compressor Part II: Composite Flow Field," ASME Paper No. 98-GT-522.
- [15] Suryavamshi, N., Lakshminarayana, B., and Prato, J., 1998, "Steady and Unsteady Three-Dimensional Flow Field Downstream of an Embedded Stator in a Multi-Stage Axial Flow Compressor—Part III: Deterministic Stress and Heat Flux Distribution and Average-Passage Equation System," ASME Paper No. 98-GT-523.
- [16] Sinha, M., and Katz, J., 2000, "Quantitative Visualization of the Flow in a Centrifugal Pump With Diffuser Vanes-I: On Flow Structures and Turbulence," ASME J. Fluids Eng., **122**, pp. 97–107.
- [17] Uzol, O., Chow, Y. C., Katz, J., and Meneveau, C., 2001, "Unobstructed PIV Measurements within an Axial Turbo-Pump Using Liquid and Blades with Matched Refracted Indices," 4th International Symposium on Particle Image Velocimetry, Göttingen, Germany, September 17–19; also, 2002, Experiments in Fluids, Aug.
- [18] Chow, Y. C., Uzol, O., Katz, J., and Meneveau, C., 2002, "An Investigation of Axial Turbomachinery Flows Using PIV in an Optically-Unobstructed Facility," presented at 9th Int. Symposium on Transport Phenomena and Dynamics of Rotating Machinery, Honolulu, Hawaii, February 10–14.
- [19] Chow, Y. C., Uzol, O., and Katz, J., 2002, "Flow Nonuniformities And Turbulent "Hot Spots" Due To Wake-Blade And Wake-Wake Interactions In A Multistage Turbomachine," ASME J. Turbomach., **124**, pp. 553–563.
- [20] Roth, G. I., Mascenik, D. T., and Katz, J., 1999, "Measurements of The Flow Structure and Turbulence Within A Ship Bow Wave," Phys. Fluids, **11**(11), pp. 3512–3523.
- [21] Roth, G. I., and Katz, J., 2001, "Five Techniques for Increasing the Speed and Accuracy of PIV Interrogation," Meas. Sci. Technol., **12**, pp. 238–245.
- [22] Shang, T., Epstein, A. H., Giles, M. B., and Sehra, A. K., 1993, "Blade Row Interaction Effects on Compressor Measurements," J. Propul. Power, **9**(4), pp. 569–578.

# Flow Nonuniformities and Turbulent “Hot Spots” Due to Wake-Blade and Wake-Wake Interactions in a Multi-Stage Turbomachine

**Yi-Chih Chow**  
Mem. ASME

**Oguz Uzol**  
Mem. ASME

**Joseph Katz**  
Mem. ASME

Department of Mechanical Engineering,  
Johns Hopkins University,  
Baltimore, MD 21218

*This experimental study provides striking examples of the complex flow and turbulence structure resulting from blade-wake and wake-wake interactions in a multi-stage turbomachine. Particle image velocimetry (PIV) measurements are performed within the entire 2<sup>nd</sup> stage of a two-stage turbomachine. The experiments are performed in a facility that allows unobstructed view of the entire flow field, facilitated using transparent rotor and stator and a fluid that has the same optical index of refraction as the blades. This paper contains data on the phase-averaged flow structure including velocity, vorticity and strain-rate, as well as the turbulent kinetic energy and shear stress, at mid span, for several orientation of the rotor relative to the stator. Two different test setups with different blade geometries are used in order to highlight and elucidate complex phenomena involved, as well as to demonstrate that some of the interactions are characteristic to turbomachines and can be found in a variety of geometries. The first part of the paper deals with the interaction of a 2<sup>nd</sup>-stage rotor with the wakes of both the rotor and the stator of the 1<sup>st</sup> stage. Even before interacting with the blade, localized regions with concentrated mean vorticity and elevated turbulence levels form at the intersection of the rotor and stator wakes of the 1<sup>st</sup> stage. These phenomena persist even after being ingested by the rotor blade of the 2<sup>nd</sup> stage. As the wake segment of the 1<sup>st</sup>-stage rotor blade arrives to the 2<sup>nd</sup> stage, the rotor blades become submerged in its elevated turbulence levels, and separate the region with negative vorticity that travels along the pressure side of the blade, from the region with positive vorticity that remains on the suction side. The 1<sup>st</sup>-stage stator wake is chopped-off by the blades. Due to difference in mean lateral velocity, the stator wake segment on the pressure side is advected faster than the segment on the suction side (in the absolute frame of reference), creating discontinuities in the stator wake trajectory. The nonuniformities in phase-averaged velocity distributions generated by the wakes of the 1<sup>st</sup> stage persist while passing through the 2<sup>nd</sup>-stage rotor. The combined effects of the 1<sup>st</sup>-stage blade rows cause 10–12 deg variations of flow angle along the pressure side of the blade. Thus, in spite of the large gap between the 1<sup>st</sup> and 2<sup>nd</sup> rotors (compared to typical rotor-stator spacings in axial compressors), 6.5 rotor axial chords, the wake-blade interactions are substantial. The second part focuses on the flow structure at the intersection of the wakes generated by a rotor and a stator located upstream of it. In both test setups the rotor wake is sheared by the nonuniformities in the axial velocity distributions, which are a direct result of the “discontinuities” in the trajectories of the stator wake. This shearing creates a kink in the trajectory of the rotor wake, a quadruple structure in the distribution of strain, regions with concentrated vorticity, high turbulence levels and high shear stresses, the latter with a complex structure that resembles the mean strain. Although the “hot spots” diffuse as they are advected downstream, they still have elevated turbulence levels compared to the local levels around them. In fact, every region of wake intersection has an elevated turbulence level.*

[DOI: 10.1115/1.1509078]

## Introduction

The unsteady flow field around and in the wakes of the rotor and stator blades embedded within a multi-stage turbomachine is dominated by the interaction of the upstream rotor and stator wakes with the downstream blades and wakes. These interactions can have a significant impact on the vibration and acoustic characteristics of the machine. Therefore obtaining reliable and detailed experimental data on the interaction of the rotor and stator

blades in a multi-stage turbomachine is critical, not only for understanding the physical mechanisms but also for the development of reliable and accurate computational methods as well.

In a multi-stage turbomachine environment the upstream rotor and stator wakes are chopped into segments as they pass through rotor and stator blade rows. The wake segments are then transported through the rotor-stator gaps and blade passages, while interacting with wakes generated by other blades as well as with the blades themselves. These interactions cause substantial variations in the spatial and temporal distributions of momentum, energy and turbulence across the stage. Numerous numerical and experimental studies have already focused on blade-wake and wake-wake interactions. Numerical studies include unsteady

Contributed by the International Gas Turbine Institute and presented at the International Gas Turbine and Aeroengine Congress and Exhibition, Amsterdam, The Netherlands, June 3–6, 2002. Manuscript received by the IGTI, December 13, 2001. Paper No. 2002-GT-30667. Review Chair: E. Benvenuti.

RANS simulations (e.g., Rai [1], Ho and Lakshminarayana [2], Valkov and Tan [3]). The basic idea behind the steady Average-Passage RANS (Adamczyk [4], Dawes [5], Denton [6], Rhie et al. [7]) is to account for the unsteady interaction using deterministic stress models. Flow nonuniformities associated with “chopping of a wake” and the “negative jet” behind a rotor blade have already been identified in numerical simulations (e.g., [2,3]). These phenomena have also been observed experimentally in 2-D PIV measurements performed by Chow et al. [8].

Experiments investigating unsteady rotor-stator interactions in turbomachines have mostly been performed using single point measurements by traversing between the blade rows and within the blade passages, both in stationary and rotating frames of references. These measurements have been performed using a variety of probes including hot-wire, hot-film, LDV, split hot-film, five-hole pitot, high response pressure transducer, etc. (Chesnakas and Dancy [9], Stauter et al. [10], Zaccaria and Lakshminarayana [11], Prato et al. [12], Suryavamsi et al. [13,14], Sentker and Reiss [15]). Investigations of the effect of upstream wakes on mixing have been performed using “tracer gas technique” (e.g., Li and Cumpsty [16]). Although the amount of experimental data is substantial, inherently, these measurements cannot cover the entire stage, and as a result miss some of the details essential for understanding the complex physical mechanisms involved. Only experimental data that covers the entire flow field in a multi-stage turbomachine can resolve all the “causes and effects.” Thus, in recent years 2-D particle image velocimetry (PIV) is gaining increasing popularity as a means to investigate the flow with turbomachines (Dong et al. [17,18], Day et al. [19], Tisserant and Bruegelmans [20], Gogineni et al. [21], Sanders et al. [22], Sinha et al. [23,24], Wernet [25]). PIV requires optical access for the laser sheet and the camera to the region of interest, whereas the flow field in a multi-stage turbomachine is usually optically obstructed by the blade rows. In addition, light reflections from the blade surfaces and end-walls tremendously affect the quality of images, especially near the boundaries. As a result, previously obtained data in multi-stage axial turbomachines have covered limited areas, away from boundaries and mostly between blade rows. In order to overcome this problem, Uzol et al. [26] and Chow et al. [8] have introduced a new facility that enables unobstructed PIV measurements within an entire stage by matching the optical index of refraction of the blades and the working fluid. This method not only makes it possible to obtain a complete optical access to the entire stage, it also minimizes the light reflection from the boundaries. This paper contains data obtained in this facility.

The PIV measurements are performed within the entire 2<sup>nd</sup> stage of a two-stage axial turbomachine, but the present paper focuses on the flow around and immediately downstream of the rotor blades. Complementary data on the overall flow structure and turbulence within the stage can be found in Uzol et al. [26,27] and Chow et al. [8]. The main objective is to investigate the phase-dependent interactions of wakes generated by the upstream blade rows with the rotor blades and its near wake. As this paper demonstrates, the upstream wakes cause substantial temporal and spatial nonuniformities in the flow structure and turbulence level. These nonuniformities are caused both by the wake of the neighboring stator, as well as by the wake of 1<sup>st</sup>-stage rotor that is located 6.5 rotor axial chords upstream.

## Experimental Setup and Procedures

**Facility.** The axial turbomachine test facility enables us to perform complete PIV measurements at any point within an entire stage including the rotor, stator, gap between them, inflow into the rotor and the wake downstream of the stator. The unobstructed optical access is facilitated using a rotor and stator made of a transparent material (acrylic) that has the same optical index of refraction as the working fluid (concentrated solution, 62–64% by weight, of NaI in water). This fluid has a specific gravity of 1.8

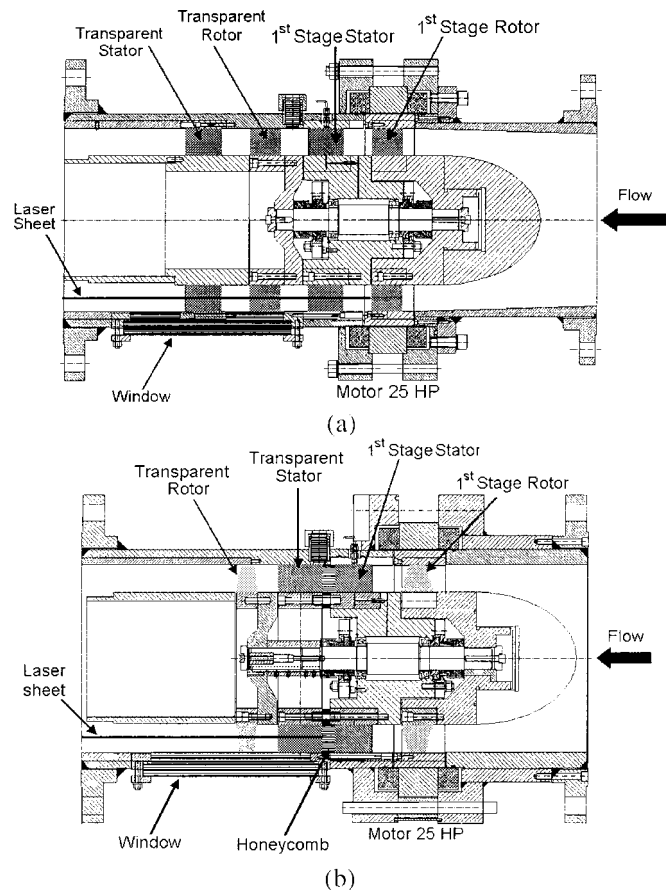


**Fig. 1 The axial turbomachine (a) test setup no. 1 used during most of the present experiments; (b) Test setup no. 2**

and a kinematic viscosity of  $1.1 \times 10^{-6} \text{ m}^2/\text{s}$ , i.e., very close to that of water. Thus, the blades become almost invisible, do not obstruct the field of view, do not alter the direction of the illuminating laser sheet while passing through the blades, and minimize the reflection from the boundaries. Information related to use and maintenance of the NaI solution can be found in [26].

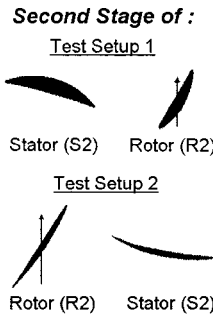
Two different test setups shown in Figs. 1(a), (b) have been utilized to investigate the wake-wake and blade-wake interactions. However, most of the results reported in this paper are obtained using test setup no. 1. The more limited results from test setup no. 2 are used for demonstrating the presence and detailed flow structure around the turbulent “hot spots,” as will be discussed in the following sections.

Test setup no. 1 has four blade rows forming two similar stages. Both rotors has 12 blades, each with a chordlength of 50 mm, span of 44.5 mm, thickness of 7.62 mm and camber varying from 2.54 mm at the hub to 1.98 mm at the tip. The resulting Reynolds number based on the tip speed and rotor chordlength is  $3.7 \times 10^5$  at 500 rpm, the speed of the present tests. The stators have 17 blades, each with a chordlength of 73.2 mm, span of 44.5 mm, thickness of 11 mm and camber of 6.22 mm. The system is driven by a 25-HP rim-driven motor that is connected directly to the 1<sup>st</sup>-stage rotor, preventing the need for a long shaft. The two rotors are connected by a common shaft supported by precision bearings. A shaft encoder and a control system are used for synchronizing our PIV system with the rotor phase. The main geometrical parameters of the axial turbopump test setup no. 1 are listed in Table 1. More details about the facility can be found in [8].

Test setup no. 2 shown in Fig. 1(b) has a different arrangement. The 1<sup>st</sup> stage (rotor and stator) is identical to that of test setup no. 1, but the 2<sup>nd</sup> stage consists of a stator followed by a rotor. A honeycomb with 6-mm-dia openings occupies the entire gap

**Table 1 Geometrical parameters for test setups nos. 1 and 2**

	Test Setup	
	No. 1	No. 2
No. of stages	2	
No. of rotor blades	12	
No. of stator blades	17	
Hub-to-tip ratio	0.708	
R2-S2 axial gap/Rotor axial chord	1.92	1.41
S1-R2 axial gap/Rotor axial chord	1.95	N/A
Rotor pitch-to-chord ratio (mid-span)	1.34	1.34
Stator pitch-to-chord ratio (mid-span)	0.66	0.97
Rotor chord (mm)	50	50
Stator chord (mm)	73.2	50
Rotor and Stator span (mm)	44.5	44.5



between the two stator rows. The purpose of this honeycomb is to reduce the effect of large-scale turbulence generated at the upstream blade rows, and align the flow in the axial direction, consistent with the orientation of the 1<sup>st</sup> stage stator. Similar to test setup no. 1, there are 12 rotor and 17 stator blades (which are also made of transparent acrylic) in the 2<sup>nd</sup> stage. The geometrical parameters of this setup are given in Table 1. The ultimate purpose of this arrangement is to study the stability of swirling wakes, but in this paper the data is used to demonstrate the formation of turbulent hot spots behind the rotor in an environment where the wakes of the 1<sup>st</sup> stage are suppressed by the honeycomb.

**PIV Setup and Experimental Procedure.** Optical access is provided by a window that extends from upstream of the rotor, covering the entire 2<sup>nd</sup> stage and terminating downstream of the stator (Figs. 1(a) and 2). An additional transparent insert enables us to insert a probe containing the laser-sheet optics (Fig. 2). Consequently, we can illuminate any desired plane with a laser sheet from the hub to the tip of the blades, including the tip-gap. The interrogated planes can be parallel or normal to the axis of the turbomachine. The corner window also provides us with an optical access to the interior of the rotor and the stator, which is essential for future, 3-D, HPIV measurements (Zhang et al. [28]).

The PIV setup is shown in Fig. 2. The light source is a 50 mJ/pulse dual-head Nd-YAG laser whose beam is expanded to generate a 1 mm thick light sheet. The flow is seeded using 20% silver coated, hollow glass, spherical particles, which have a mean diameter of 13 μm and an average specific gravity of 1.6, i.e., slightly below that of the working fluid. The images are recorded by a 2048×2048 pixels<sup>2</sup>, Kodak ES4.0, 8-bit, cross-correlation digital camera and stored in a computer. The laser and the camera

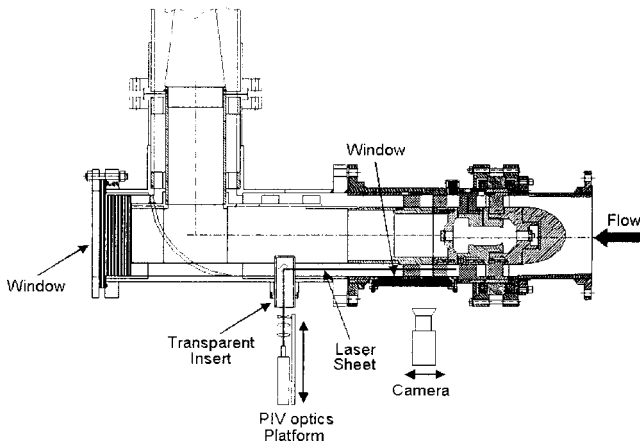


**Fig. 2 Optical access to the test section and the PIV system used in the present experiments**

are synchronized with the orientation of the rotor using a shaft encoder that feeds a signal to a controller containing adjustable delay generators. Consequently, we can acquire data at any desired rotor phase. The controller also monitors the temperature of the facility and the pressure difference that the turbomachine generates.

The measurements involving test setup no. 1 cover the entire 2<sup>nd</sup> stage including the inflow to the rotor, the flow around the rotor, the gap between the rotor and the stator, the flow around the stator and the stator wake. Data has been obtained at 10 rotor phases, every three degrees of blade orientation, which cover an entire rotor blade passage of 30°. In this paper we present data recorded at the mid-span plane and at a rotational speed of 500 rpm. For each condition (phase and location) at least one hundred instantaneous realizations have been recorded. For selected cases we record 1000 realizations in order to obtain converged statistics on the turbulence. The sample area is 50×50 mm<sup>2</sup>, and as a result several (five) data sets at different axial locations with sufficient overlap have been recorded to cover the entire stage. Data analysis includes image enhancement and cross-correlation analysis using in-house developed software and procedures (Roth et al. [29,30]). Adapting these procedures to the current geometry, including specific modifications to the image enhancement procedures, and removal of the blade trace/signature prior to velocity computations are discussed in [26].

The uncertainty in mean displacement in each interrogation window is about 0.3 pixels, provided the window contains at least 5–10 particle pairs. For the typical displacement between exposures of 20 pixels, the resulting uncertainty in instantaneous velocity is about 1.5%. Slip due to the difference between the specific gravity of the particle (1.6) and that of the fluid (1.8) may cause an error of less than 0.2%, i.e., much less than other contributors (Sridhar and Katz [31]).

## Results and Discussion

**Flow Field in the Entire Stage.** Unless specifically stated, most of the data presented in this paper is obtained using test setup no. 1. The phase-averaged data and turbulence parameters are calculated using,

$$\bar{u}(x, y, \phi) = \frac{1}{N} \sum_{i=1}^N u_i(x, y, \phi) \quad (1)$$

$$k(x, y, \phi) = \frac{3}{4} \frac{1}{N} \sum_{i=1}^N [(u_i(x, y, \phi) - \bar{u}(x, y, \phi))^2 + (v_i(x, y, \phi) - \bar{v}(x, y, \phi))^2] \quad (2)$$

$$-\overline{u'v'}(x, y, \phi) = -\frac{1}{N} \sum_{i=1}^N [u_i(x, y, \phi) - \bar{u}(x, y, \phi)] \times [v_i(x, y, \phi) - \bar{v}(x, y, \phi)] \quad (3)$$

$$\bar{\omega}(x, y, \phi) = \frac{\partial \bar{v}(x, y, \phi)}{\partial x} - \frac{\partial \bar{u}(x, y, \phi)}{\partial y} \quad (4)$$

$$\bar{S}_{xy}(x, y, \phi) = \frac{1}{2} \left( \frac{\partial \bar{v}(x, y, \phi)}{\partial x} + \frac{\partial \bar{u}(x, y, \phi)}{\partial y} \right) \quad (5)$$

$$\bar{\alpha}(x, y, \phi) = \tan^{-1} \left( \frac{\bar{v}(x, y, \phi)}{\bar{u}(x, y, \phi)} \right) \quad (6)$$

where  $N=100$  is the number of instantaneous vector maps,  $u$  and  $v$  are the axial and lateral (almost circumferential, although the light sheet is flat) velocity components, respectively, and the overbar indicates an ensemble average. The 3/4 coefficient for  $k$ ,

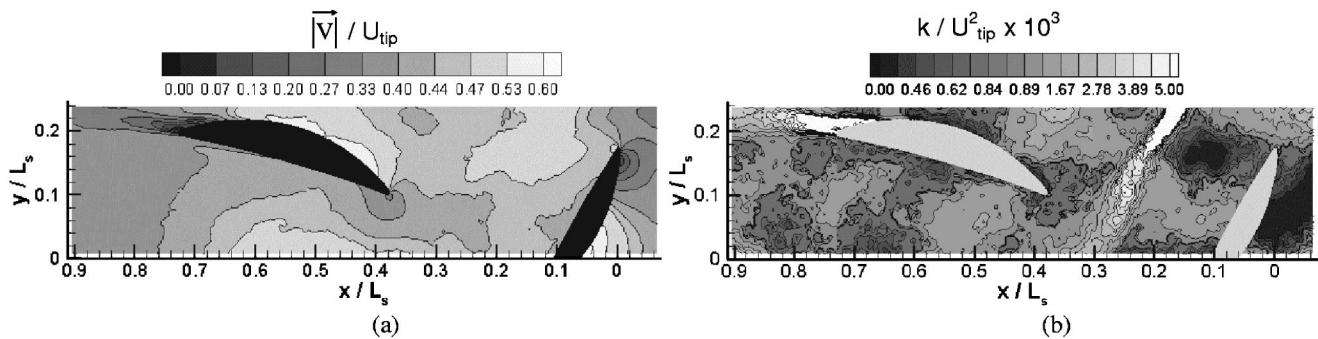


**Fig. 3** (a) Phase-averaged velocity and (b) turbulent kinetic energy distributions at midspan, obtained by combining the results in several measurement domains.  $U_{tip}=8$  m/s is the tip velocity of rotor blade at 500 rpm;  $L_s=203$  mm is the stage length starting from the rotor leading edge.

the “turbulent kinetic energy,” is selected to account for the out of plane velocity component assuming that it is an average of the available measured components.

Sample phase-averaged velocity and turbulent kinetic energy distributions within the entire stage, obtained by combining the data from all the sample areas, are presented in Fig. 3. In the phase-average velocity distribution one can observe the high momentum regions on the suction side of the stator blade, along the aft suction side of the rotor blade and in the near wake of the rotor blade. The latter can be seen in the wake of the rotor blade that is already beyond the sample area and that rotor wake can easily be identified in the  $k$  distribution.

The turbulent kinetic energy plot in Fig. 3(b) reveals four distinct rotor wakes: one trailing behind the rotor blade, the second one impinging on the leading edge of the stator blade, the third one located inside the stator passage and the fourth exiting the stator passage, confined between the two stator wakes. The rotor wakes are transported through the stator passage after they get “chopped off” by the stator blades. The wake of the 2<sup>nd</sup>-stage stator is clearly visible. It follows a thickening of the boundary layer (but no separation, see [26]) near the trailing edge, on the suction side of the stator.

Upstream of the rotor row, on the top and bottom of the right hand side of the contour map, one can see the wakes of 1<sup>st</sup>-stage stator (in this example the lower one is barely visible). These wakes are broken to segments and scooped by the rotor blades. Traces of this wake can be identified all the way to the exit of the next stator as almost horizontal layers of elevated turbulence in the regions between the rotor wakes. Due to differences in velocity on the two sides of the rotor, the 1<sup>st</sup>-stage stator wake is discontinuous across the rotor wake. At the intersection of the rotor and stator wakes, for example above the leading edge of the stator in the sample shown, a wide region of elevated turbulence level forms. As discussed in detail in the following sections, this phenomenon has been observed frequently at intersections of rotor and stator wakes and we will refer to it as a turbulent “hot spot.” A little less obvious, but still evident is the wake of the 1<sup>st</sup> stage rotor (details and clearer illustrations follow). In the phase shown it engulfs the leading edge of the 2<sup>nd</sup>-stage rotor.

**Interaction of the Rotor Blade With Upstream Rotor and Stator Wakes.** Complex wake-blade interactions occur as the 1<sup>st</sup> stage rotor and stator wakes pass through the rotor of the 2<sup>nd</sup> stage. Figure 4 is a sample turbulent kinetic energy distribution (for one of the phases) within the 2<sup>nd</sup>-stage rotor, illustrating the presence of several distinct wake zones generated by the rotor blade and the upstream blade rows. The two 1<sup>st</sup>-stage stator wakes which are aligned almost horizontally on the upper and lower parts of the map, as well as the 2<sup>nd</sup>-stage rotor wake are clearly visible. In addition, in spite of being weaker, one can still identify the 1<sup>st</sup>-stage rotor wake which is inclined between the stator

wakes, and extends just in front of the blade leading edge. The 1<sup>st</sup>-stage stator wake in the lower right corner of the domain is being chopped off by the rotor blade.

Figure 5 shows eight flow parameters at four different phases of the rotor blade, including the phase-averaged axial velocity, lateral velocity, velocity magnitude, absolute flow angle, vorticity and shear strain rate, as well as the turbulent kinetic energy and Reynolds shear stress. The following characteristic patterns exist in all of these distributions:

(a) When the stator wake is not interacting with other blades or wake, it is characterized by low phase-averaged axial velocity, mean vorticity of opposite signs on both sides of the wake, high turbulent kinetic energy, peaking at the center of the wake and shear stresses of opposite signs peaking on both sides of the wake.

(b) The near-field rotor wake is characterized by a high lateral velocity and low axial velocity, resulting in high flow angle. Proceeding across the wake, there is an abrupt change in velocity magnitude, especially near the trailing edge of the blade. The turbulent kinetic energy is very high, with peak values reaching

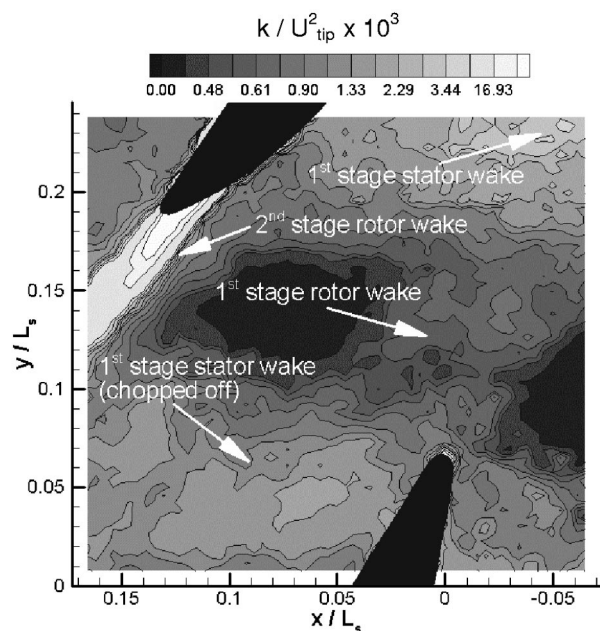


**Fig. 4** Turbulent kinetic energy distribution within the 2<sup>nd</sup>-stage rotor passage, showing the wake of the rotor blade and the wakes of the 1<sup>st</sup> stage (rotor and stator) passing through and interacting with the blades

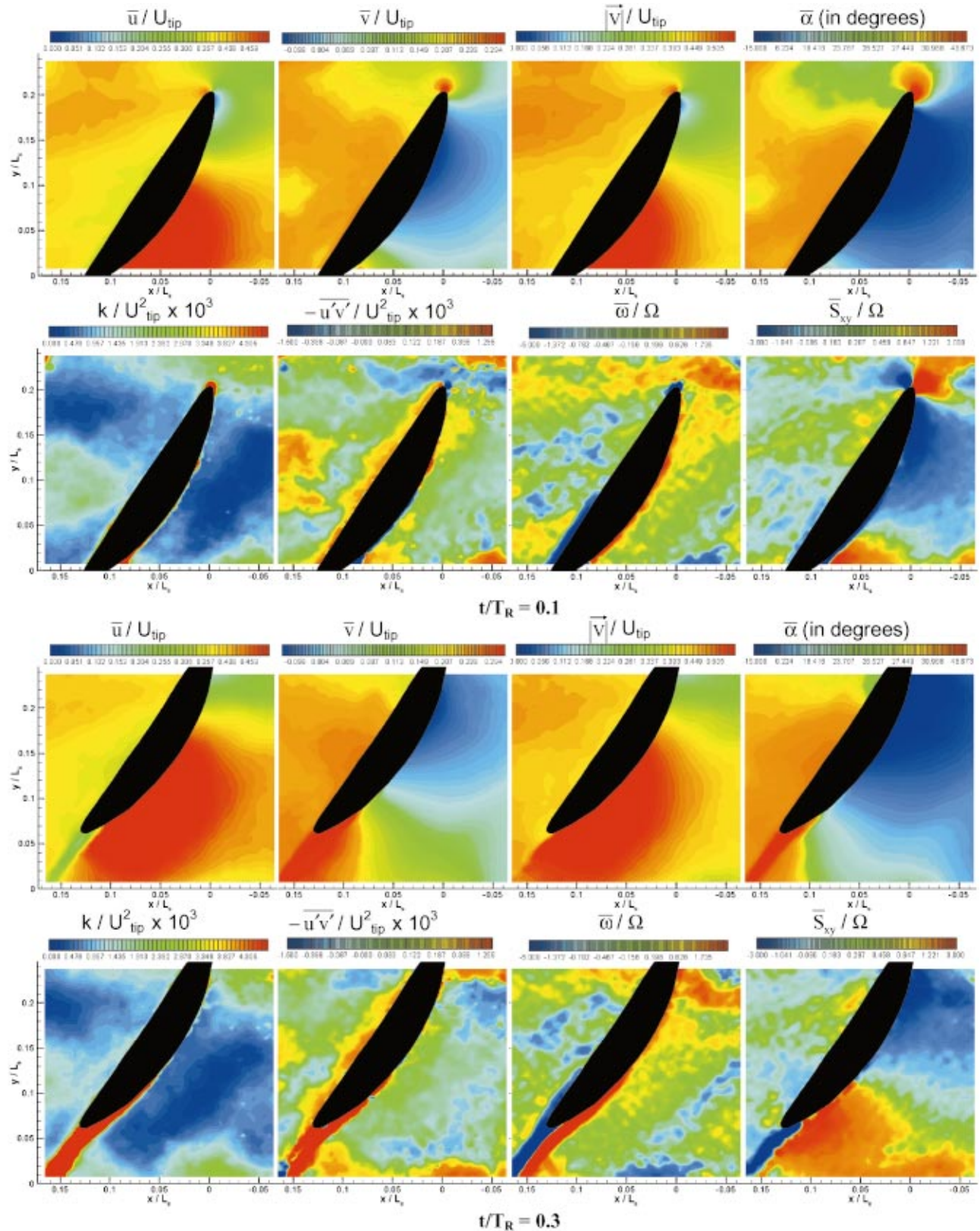


Fig. 5 Distributions of phase averaged: axial ( $\bar{u}$ ) and lateral ( $\bar{v}$ ) velocity components, velocity magnitude ( $|\bar{V}|$ ), flow angle ( $\bar{\alpha}$ ) vorticity ( $\bar{\omega}$ ), and shear strain ( $\bar{S}_{xy}$ ), as well as turbulent kinetic energy ( $k$ ) and Reynolds shear stress ( $-\bar{u}'v'$ ) within the rotor passage of the 2<sup>nd</sup> stage. Data at four rotor phases,  $t/T_R=0.1, 0.3, 0.5$  and  $0.7$ , are presented. Negative vorticity is out of the plane of the paper.

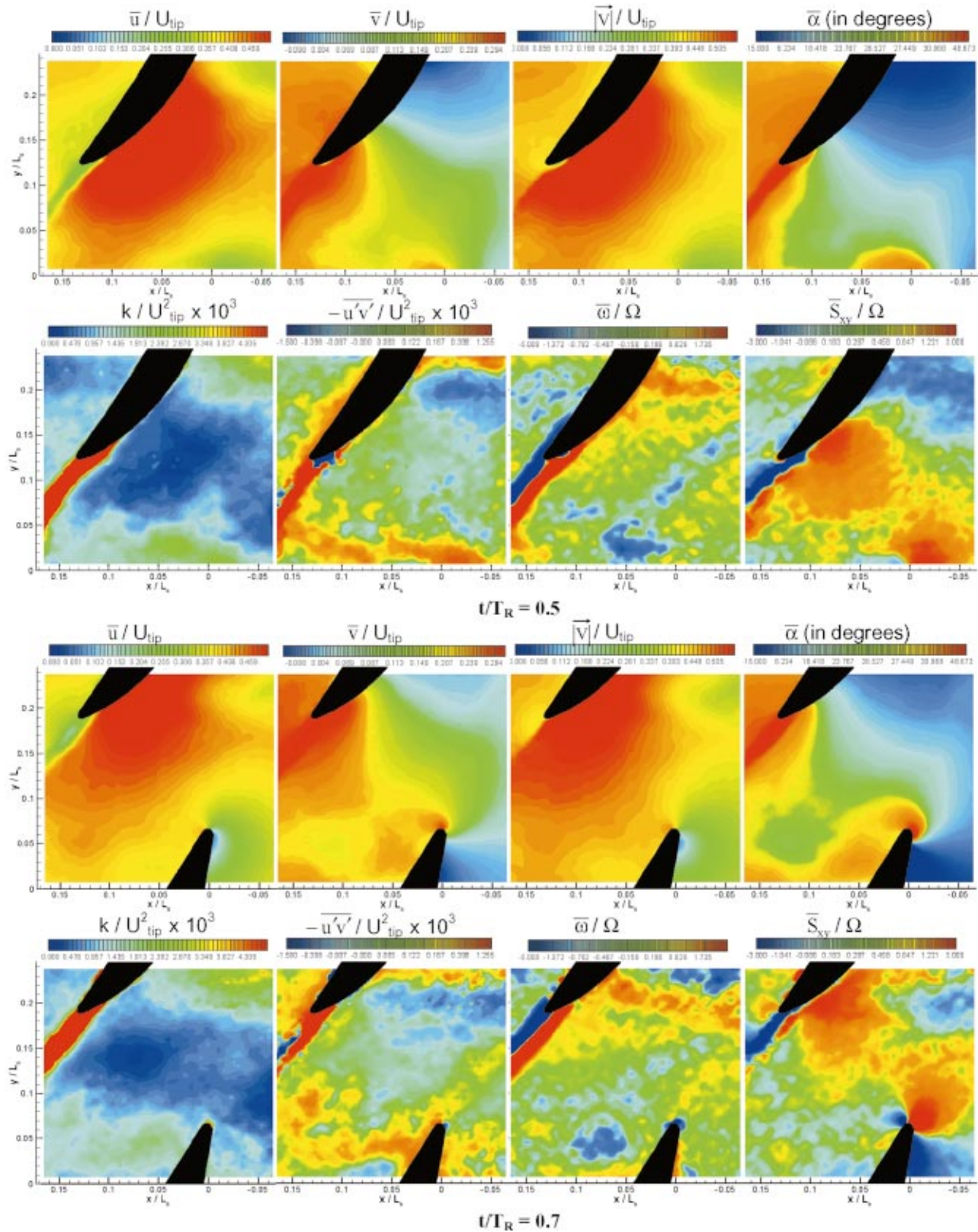


Fig. 5 (continued)

$k/U_{tip}^2 = 39 \times 10^{-3}$ , and the two sides of the wake have relatively high vorticity of opposite signs. The high shear stresses are initially positive throughout the wake and then start having opposite signs.

(c) The wake of the 1<sup>st</sup>-stage rotor is inclined and weaker, but

still has elevated levels of  $k$ , with mean vorticity and Reynolds shear stress with opposite signs on both sides. Before interacting with the rotor blade, the signature of the 1<sup>st</sup>-stage rotor wake is particularly evident at  $t/T_R = 0.3$ , as inclined lines with elevated vorticity and shear stress of opposite signs.



When these wakes interact with each other and with the rotor blade, the result is a very complicated flow field. To illustrate specific phenomena, we follow them across the phases and identify specific cases where they are particularly noticeable.

**Chopping of the Stator Wake.** As it passes through the rotor, the stator wake is chopped-off by the blades. As the  $k$  distributions show most clearly, at  $t/T_R=0.7$  the leading edge of the blade cuts through the wake and at  $t/T_R=0.1$  the high turbulence region is aligned with the pressure side of the blade. Due to difference in mean lateral velocity, the stator wake segment on the pressure side is advected upward faster than the segment on the suction side (in the absolute frame of reference), creating what appears to be a discontinuity across the rotor blade and its wake. This phenomenon is particularly evident in the distribution of  $k$  and axial velocity at  $t/T_R=0.7$ . At the intersection of the blade with the stator wake, the horizontal velocity component is lower, for example on the pressure side of the blade at  $t/T_R=0.3$ .

**Interaction of the 1<sup>st</sup>-Stage Rotor Wake With the 2<sup>nd</sup>-Stage Rotor Blade.** As the wake segment of the 1<sup>st</sup>-stage rotor blade (bounded by the two stator wakes) arrives to the 2<sup>nd</sup> stage, the rotor blades cut through it, separating the region with negative vorticity (left side) that travels along the pressure side of the blade, from most of the region with positive vorticity that remains on the suction side. This process starts at  $t/T_R=0.7$ , and as it progresses at  $t/T_R=0.1, 0.3$ , and  $0.5$ , it creates wide regions with negative vorticity along the pressure side of the blade and positive vorticity on the suction side. The contribution of the blade itself to the vorticity is confined to the flow very near the surface and in the blade wake, consistent with the fact that the boundary layer on the rotor blade remains attached. Cutting through the 1<sup>st</sup>-stage rotor wake, as the  $k$  distributions at  $t/T_R=0.1, 0.3$ , and  $0.5$  confirm, also puts the blade in a wide flow domain with positive Reynolds stress on both sides of the blade, including the pressure side, where the wall generated shear stress should be negative.

**Interaction of the 1<sup>st</sup>-Stage Rotor Wake With the 1<sup>st</sup>-Stage Stator Wake.** Even before interacting with the blade, localized regions with high/concentrated mean vorticity and elevated turbulent kinetic energy form at the intersection of the rotor and stator wakes of the 1<sup>st</sup> stage. This phenomenon can be observed at ( $t/T_R=0.5, x/L_S=0.05, y/L_S=0.025$ ) and ( $t/T_R=0.7, x/L_S=0.075, y/L_S=0.05$ ). Consistent with the forthcoming discussion, we suspect that this phenomenon is a remainder of turbulent hot spots generated at wake-intersections of the 1<sup>st</sup> stage. The concentrated vorticity and elevated turbulence at the intersection persists after being engulfed by the blade ( $t/T_R=0.1, x/L_S=0.15, y/L_S=0.1-0.15$ ). The shear stresses are also high at the same location.

**Nonuniformity in Mean Flow Associated With Wake-Blade Interactions.** The nonuniformities in phase-averaged velocity distributions generated by the wakes of the 1<sup>st</sup> stage persist while passing through the 2<sup>nd</sup>-stage rotor. For example, as the distributions of  $v$  and  $\alpha$  at  $t/T_R=0.1$  and  $0.3$  show (especially the latter), the 1<sup>st</sup>-stage rotor wake increases the lateral velocity component and flow angle along the pressure side of the blade. The stator wake generates regions with low velocity, for example downstream of the leading edge of the rotor blade at  $t/T_R=0.7$ . The combined effect of the 1<sup>st</sup>-stage rotor and stator cause 10–12 deg variations of flow angle along the pressure side of the blade. The nonuniformity in the tangential velocity implies significant effects on the work input of the blade row. Indeed, as discussed in [27], the wake-induced tangential variations in the work input of the present system are about 13%. Thus, the interaction with wakes has a considerable effect on the performance of the turbomachine in spite of the relatively large blade row spacings specified in Table 1. Combining the gaps and the stator passage, the 1<sup>st</sup>-stage rotor trailing edge is located 6.5 rotor axial chords upstream of the 2<sup>nd</sup>-stage rotor. Nonetheless, the wake-blade interactions are substantial.

**Formation of “Kinks” and “Turbulent Hot Spots” due to Wake-Wake Interactions.** We have already mentioned that turbulent hot spots, i.e., localized regions with high turbulent kinetic energy, are generated at the intersection of the 1<sup>st</sup>-stage rotor and stator wakes. This phenomenon was initially observed in a much clearer form during experiments performed using Test Setup No. 2. Subsequent examinations of the data obtained with Test Setup No. 1 have confirmed the existence of these hot spots in both systems. This section focuses on this phenomenon.

The measurements with test setup no. 2 have been performed at 800 rpm, and as of today only a single phase of the rotor blade has been completed (the experiments are in progress). Recall that in this case a honeycomb is inserted in the gap between the 1<sup>st</sup> and 2<sup>nd</sup> stages, and the 2<sup>nd</sup>-stage rotor is located downstream of the stator.

Figure 6 shows the phase-averaged velocity magnitude, flow angle, vorticity and mean shear strain rate as well as the turbulent kinetic energy and Reynolds shear stress distributions in the wake of the 2<sup>nd</sup> rotor. Two rotor wakes, one trailing behind the blade and the other on the top left corner, as well as two horizontally aligned segments of the upstream stator wake located in between the rotor wakes are clearly visible in the distributions of  $k$ . The regions occupied by the stator wake segments can also be identified as the layers with low phase-averaged momentum, low flow angle, significant variations in the magnitude of  $\bar{\sigma}_{xy}$ , as well as vorticity and shear stress with alternating signs on both sides of the wakes.

A peculiar flow phenomenon develops at the intersections of stator and rotor wakes. It consists of:

(a) A distinct peak with high turbulent kinetic energy, leading us to define it as a turbulent “hot spot.” Two such peaks are evident in the sample shown, at ( $x/C_{Rx}=0.62, y/C_{Ry}=0.64$ ) and at (1.6, 1.42), the latter belonging to the wake of another blade. The level of  $k$  within the hot spot at (0.62, 0.64) is about twice the level in the rotor wake in the vicinity of the spot, and about 20 times the level in the (relatively) low turbulence zones outside of the wakes. Below the maximum  $k$  point, there is a “kink” in the trajectory of the rotor wake.

(b) Regions with high and low mean velocity magnitude are located within the rotor wake on both sides of the high turbulence peak, with the highest velocity gradients coinciding with the point of maximum turbulence. Together with two additional local peaks located to the left of the rotor wake, one within the stator wake segment (minimum) and the other above it (maximum), they form a quadruple of local extremums. Parts of the same arrangement can be seen around the second hot spot.

(c) In the wake with a hot spot at (0.62, 0.64), the point with maximum flow angle coincides with the turbulence peak. In the other wake, the angle peak is located slightly above and to the left of the maximum  $k$  point. The distribution of flow angles clearly shows the “kink” in both rotor wakes.

(d) A region with positive vorticity that coincides with the hot spot, giving the impression that the phase-averaged vorticity sheet trailing from the rotor rolls up into a large vortex (0.62, 0.64). The vorticity in the rotor wake path downstream of this point is significantly lower. The rotor wake region with negative mean vorticity seems to circumvent the concentrated positive peak and then splits into two branches, one continuing with the rotor wake and the other aligned with the stator wake. Below the hot spot the rotor wake continues to be divided to layers with positive and negative vorticity. The vorticity peak at (1.6, 1.42) appears already separated from the sheet, but the overall pattern persists.

(e) Discontinuities in the distributions of  $-u'v'$ . In both rotor wakes shown, the region with negative stress has a kink just above the center of high vorticity (and high  $k$ ) region. At the center there is abrupt transition from negative to positive Reynolds stress. Below the hot spot the rotor wake is again divided to layers with negative and positive Reynolds stresses.

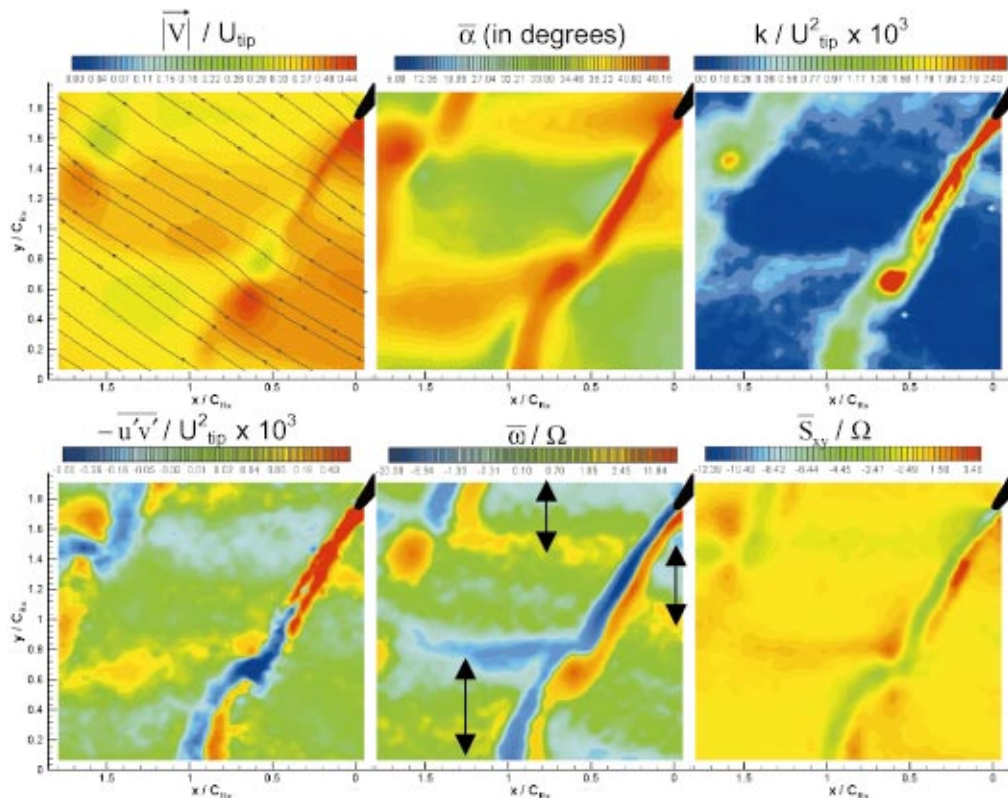


**Fig. 6** Wake-wake interactions as the rotor wake of test setup no. 2 intersects with the stator wake. Shown are the distributions of phase-averaged velocity magnitude ( $|\bar{V}|$ ), flow angle ( $\bar{\alpha}$ ) vorticity ( $\bar{\omega}$ ), and shear strain ( $\bar{S}_{xy}$ ), as well as turbulent kinetic energy ( $k$ ) and Reynolds shear stress ( $-u'v'$ ).  $x=0$  is the rotor trailing edge and  $C_{Rx}=24$  mm is the rotor axial chord.  $U_{tip}=12.8$  m/s is the blade tip speed at 800 rpm. The arrows indicate the location of stator wake segments. Negative vorticity is out of the plane of the paper.

(f) Two layers with negative and positive mean strain-rate extends from the trailing edge of the blade. In the vicinity of the (0.62, 0.64) hot spot (only) the high negative strain rate region has a trajectory that coincides with the layer of high negative Reynolds stress. Almost exactly at the center of the hot spot there are abrupt changes to the strain magnitude. For both rotor wakes shown there are four distinct strain peaks arranged in a quadruple configuration, two with positive peaks and two with negative peaks.

Measurements performed further downstream (not shown), of the rotor blade reveal that the structures developing at the intersection of wakes diffuse but are still clearly evident, at least up to two chordlengths downstream of the rotor blade (future measurements will track them further downstream).

In order to further elucidate the flow structures involved and the reasons for their formation, Figure 7 shows a vector map of the phase-averaged velocity overlaid on the vorticity after subtracting the mean velocity at the center of the (0.62, 0.64) hot spot. The two positive vortices are clearly evident along with the elongated “vortical structure” with negative vorticity trailing behind the blade. Examinations of this plot and Figure 6 indicates that the kink in the blade wake is caused by (related to) discontinuities in the trajectories of the stator wake across the rotor wake caused by differences in velocity in the suction and pressure sides of the rotor blade. Consequently, just below the kink in Fig. 7, the region to the left of the rotor wake is part of a stator wake segment, whereas the region to the right of the rotor wake is not part of the stator wake, and has a significantly higher axial velocity than stator wake segments above and below it. This relatively high  $u$  region pushes part of the rotor wake to the left creating the kink.

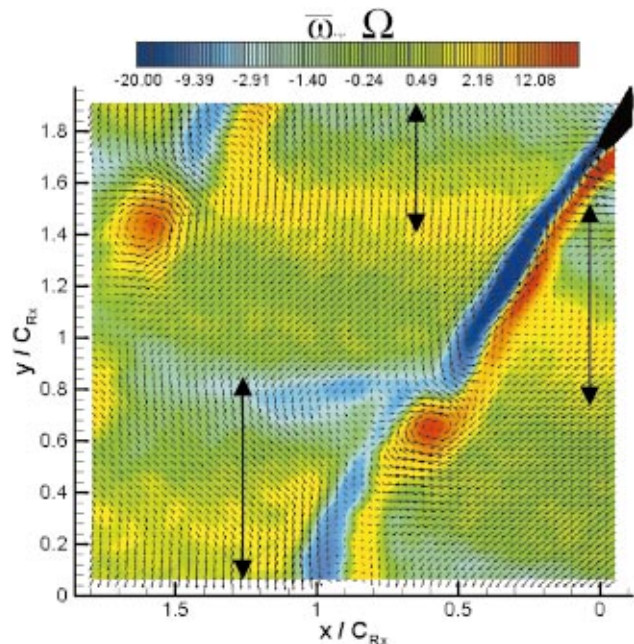


**Fig. 7** A vector map of the velocity relative to the velocity at the center of the (0.62, 0.64) vortex overlaid on the vorticity distribution. The arrows indicate location of the stator wake segments (see also Fig. 6). Negative vorticity is out of the plane of the paper.

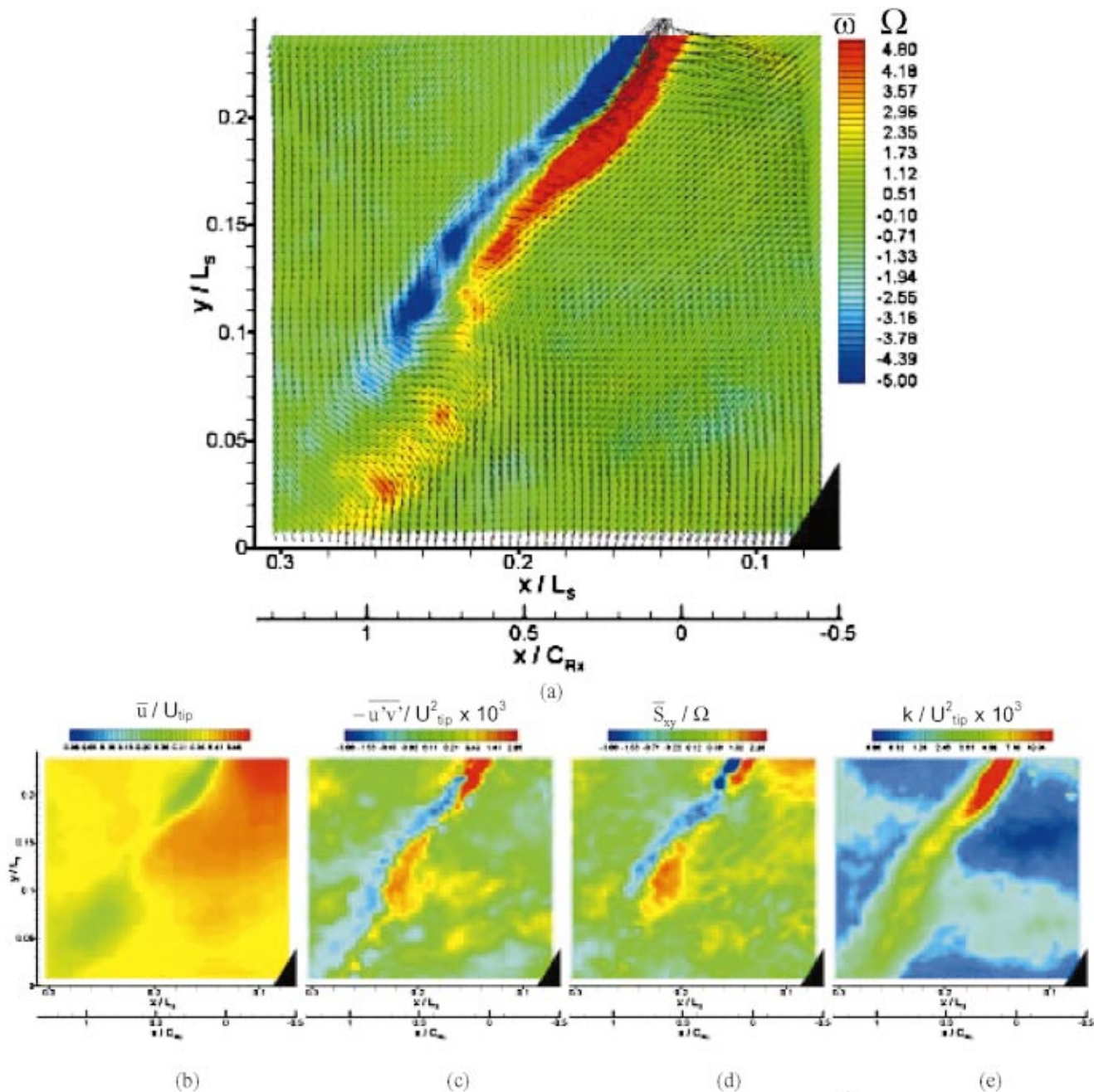


Fig. 8 Phase-averaged flow showing wake-wake interactions and the formation of a kink in the 2<sup>nd</sup>-stage rotor wake of test setup no. 1,  $t/T_R=0.9$ . (a) An enlarged vector map of the velocity relative to the velocity at the center of the (0.16, 0.17) "vortex" overlaid on the vorticity distribution. Negative vorticity is out of the plane of the paper. (b)  $\bar{u} / U_{tip}$  (c)  $-\overline{u'v'} / U_{tip}^2 \times 10^3$  (d)  $\bar{S}_{xy} / \Omega$  (e)  $k / U_{tip}^2 \times 10^3$ .  $x=0$  on the second  $x$ -axis is the rotor trailing edge and  $C_{Rx}=27$  mm is the rotor axial chord.

Since the domain to the left of the point of maximum vorticity in the rotor wake has low momentum (see Fig. 6), the relative flow is diverted either upward (along the axis of the rotor wake) or downward. The upward flow generates the concentrated vortex. Examination of the instantaneous data near the vortex center reveals that the high turbulence level at this location is caused by slight variations in the location of the vortex (meandering) and the high velocity gradients at this location.

As the rotor wake is being shed it is periodically deformed by the local nonuniformities in the advection velocity resulting from the discontinuities in the stator wake. Since these discontinuities are caused by differences in the velocity on the two sides of the blade, their extent are related to the blade loading. Thus, one should expect to find different levels of wake kinking on different

blades, but the phenomenon is an inherent result of the chopping of the stator wake by the rotor. Consequently, one should expect to find similar phenomena in test setup no. 1, except that the additional 1<sup>st</sup>-stage rotor wake, and the fact that it engulfs the 2<sup>nd</sup>-stage rotor complicates matters even further.

Clear indications that the wake kinking and the resulting domains with concentrated vorticity, elevated turbulence levels, variations in shear strain and Reynolds stress for test setup no. 1 are presented in Fig. 8. In this example there are two kinks with the regions containing concentrated positive vorticity centered around (0.16, 0.17) and (0.255, 0.03). The distributions of  $\bar{u}$  and  $k$  confirm that these kinks also occur in regions with velocity mismatch across the rotor wake associated with the discontinuity in stator wakes. The Reynolds stress distributions are also quite simi-

lar. Above the (upper) kink  $-\overline{u'v'}$  is positive, and just above it a layer with negative stress that curves around the center of the vortex forms. Two stress layers with opposite signs appear below the kink. The strain distributions in Fig. 8 are also shifted relative to the vorticity and it is more difficult to identify the quadruple arrangement. However, one can still observe zones with positive strain rate peaks immediately above and below the kink, consistent with the results in Figure 6.

Unlike the distinct positive vortex of test setup no. 2, the upper positive “vortex” of test setup no. 1 (Figure 8(a)) is more elongated and the lower one is spread over a wider area. In fact the positive vorticity area is comparable in shape to the region with negative vorticity. As a result, the velocity gradients near the vortex centers are not as distinct, resulting in broader regions with elevated turbulent kinetic energy ( $k$  is higher everywhere). Consequently, as the wakes of blade setup no. 1 evolve, the broad high  $k$  peaks not necessarily coincide with the positive vorticity peaks. However, they do form and persist, as Fig. 3 shows (as well as data obtained in other phases). Furthermore, we have also identified hot spots at the intersection of the (far field) wakes of the 1<sup>st</sup>-stage rotor and stator as they arrive to the 2<sup>nd</sup>-stage rotor (Fig. 5,  $t/T=0.5$  and  $0.7$ ). Note that this flow phenomenon is different since the 1<sup>st</sup>-stage rotor operates in a wake-free region, and is then chopped by the 1<sup>st</sup>-stage stator. Consequently, one should expect to find some differences in the structure of the interactions, especially since the wake of the present stator is larger and wider than that of the rotor [26,27,8]. The details on these interactions will be the focus of future papers.

## Conclusions

PIV measurements covering the entire 2<sup>nd</sup> stage of a two-stage turbomachine enable us to study the complex flow and turbulence structure resulting from blade-wake and wake-wake interactions in a multi-stage turbomachine. Two blade geometries are used in order to highlight and elucidate complex phenomena involved, as well as to demonstrate that some of the interactions are characteristic to turbomachines and can be found in a variety of geometries. We are not going to repeat here all the details reported in the previous sections. However, some of the main findings should be emphasized.

The first part of the paper deals with the interaction of a 2<sup>nd</sup>-stage rotor with the wakes of both the rotor and the stator of the 1<sup>st</sup> stage. Even before interacting with the blade, localized regions with high/concentrated mean vorticity and elevated turbulent kinetic energy and Reynolds shear stress form at the intersection of the rotor and stator wakes of the 1<sup>st</sup> stage. These phenomena persist even after being chopped by the blade. As the wake segment of the 1<sup>st</sup>-stage rotor blade arrives to the 2<sup>nd</sup> stage, the rotor blades cut through it, separating the region with negative vorticity (left side) that travels along the pressure side of the blade, from most of the region with positive vorticity that remains on the suction side. Cutting through the 1<sup>st</sup>-stage rotor wake also submerges the blade in a wide flow domain with elevated turbulence levels and positive Reynolds stress on both sides of the blade. As it passes through the rotor, the stator wake is chopped-off by the blades. Due to difference in mean lateral velocity, the stator wake segment on the pressure side is advected upward faster than the segment on the suction side (in the absolute frame of reference), creating discontinuities in the wake trajectory.

The nonuniformities in phase-averaged velocity distributions generated by the wakes of the 1<sup>st</sup> stage persist while passing through the 2<sup>nd</sup>-stage rotor. For example, the 1<sup>st</sup>-stage rotor wake increases the lateral ( $\sim$ tangential) velocity component and flow angle along the pressure side of the 2<sup>nd</sup>-stage rotor blade, and the 1<sup>st</sup>-stage stator wake generates regions with low axial velocity. The combined effect of the 1<sup>st</sup>-stage wakes causes 10–12 deg variations of flow angle along the pressure side of the blade, which will result in significant phase-dependent variations in work

input of the blade row. Thus, in spite of the large gap between the 1<sup>st</sup> and 2<sup>nd</sup>-stage rotors (6.5 rotor axial chords), the wake-blade interactions are substantial.

The second part focuses on the details of the flow structure at the intersection of the wakes generated by a rotor and a stator located upstream of it. The honeycomb separating the 1<sup>st</sup> and 2<sup>nd</sup> stages of setup no. 2 enables us to obtain a clearer picture on the flow/turbulence structure, but the same phenomena persist in both systems. In both cases the rotor wake is sheared by the non-uniformities in the axial velocity distributions, which are a direct result of the “discontinuities” in the trajectories of the stator wake across the rotor wake. This shearing creates a kink in the trajectory of the rotor wake, a quadrupole structure in the distribution of strain, regions with concentrated vorticity, high turbulence levels and high shear stresses (the latter with a complex structure that resembles the mean strain). The instantaneous data near the vortex center reveals that the high turbulence level is greatly affected by variations in the location of the vortex (meandering) and the high velocity gradients at this location. Although the “hot spots” diffuse as they are advected downstream, they still have elevated turbulence levels compared to the local levels around them. In fact, it seems that every region of wake intersection has an elevated turbulence level. We plan to follow the evolution and dissipation of these hot spots in future papers. It has to be kept in mind that all the measurements reported in this paper are two-dimensional and at mid-span. We have actually recorded 2-D data on two other radial planes (the hub and the tip). Mid-span measurements are just the starting point of our studies. Our future measurements will also include 3-D stereoscopic PIV measurements in different radial planes.

## Acknowledgments

This project is sponsored in part by ONR under grant number N00014-99-1-0965, managed by P. Purtell and in part by AFOSR under grant No. F49620-01-1-0010, managed by T. Beutner. The ONR program is part of a joint effort involving W. Blake (NSWC/Carverock), H. Atassi (U. of Notre Dame) and Y. T. Lee (NSWC/Carverock). We would like to thank Yury Ronzhes, Stephen King, Ali Pinarbasi and Madan M. Guin for their contribution to the construction of the facility. We would also like to thank K. Ooi from Able Corporation, for designing the rotor and stator blades of test setup no. 1, as well as Y. T. Lee for designing the blades of test setup no. 2.

## Nomenclature

$C_{Rx}$	= rotor blade axial chord
$k$	= turbulent kinetic energy
$L_s$	= stage length starting from the rotor leading edge
$N$	= total number of instantaneous samples
NaI	= sodium iodide
$\overline{s}_{xy}$	= phase averaged mean shear strain rate
$t$	= Time
$T_R$	= rotor blade passing period
$u$	= instantaneous axial velocity
$\bar{u}$	= phase averaged axial velocity
$U_{tip}$	= velocity of rotor blade tip
$v$	= instantaneous lateral velocity
$\bar{v}$	= phase-averaged lateral velocity
$ \bar{V} $	= Phase-averaged velocity magnitude
$-\overline{u'v'}$	= Reynolds shear stress
$x$	= axial direction, $x=0$ is rotor leading edge
$y$	= lateral direction (almost circumferential, but laser sheet is flat)
$\bar{\alpha}$	= phase-averaged flow angle (yaw angle)
$\phi$	= rotor phase
$\Omega$	= angular velocity of rotation in rad/s
$\bar{\omega}$	= phase-averaged vorticity

## References

- [1] Rai, M. M., 1987, "Navier-Stokes Simulation Of Rotor/Stator Interaction Using Patched And Overlaid Grids," *J. Propul. Power*, **3**, pp. 387–396.
- [2] Ho, Y. H., and Lakshminarayana, B., 1995, "Computation of Unsteady Viscous Flow Through Turbomachinery Blade Row due to Upstream Rotor Wakes," *ASME J. Turbomach.*, **117**, pp. 541–552.
- [3] Valkov, T. V., and Tan, C. S., 1998, "Effect of upstream rotor vortical disturbances on the time-average performance of axial compressor stators: Part I—Framework of technical approach and wake-stator blade interactions," *ASME J. Turbomach.*, **121**, pp. 377–386.
- [4] Adamczyk, J. J., 1985, "Model Equation for Simulating Flows in Multistage Turbomachinery," *ASME Paper No. 85-GT-226*.
- [5] Dawes, W. N., 1992, "Towards Improved Throughflow Capability: The Use of Three-Dimensional Viscous Flow Solvers in A Multistage Environment," *ASME J. Turbomach.*, **114**, pp. 8–17.
- [6] Denton, J. D., 1992, "The Calculation of Three-Dimensional Viscous Flow Through Multistage Turbomachines," *ASME J. Turbomach.*, **114**, pp. 18–26.
- [7] Rhie, C. M., Gleixner, A. J., Spear, D. A., Fischberg, C. J., and Zacharias, R. M., 1998, "Development and Application Of A Multistage Navier-Stokes Solver. Part I: Multistage Modeling Using Body Forces and Deterministic Stresses," *ASME J. Turbomach.*, **120**, p. 205.
- [8] Chow, Y. C., Uzol, O., Katz, J., and Meneveau, C., 2002, "An Investigation of Axial Turbomachinery Flows Using PIV in an Optically-Unobstructed Facility," presented at 9th Int. Symposium on Transport Phenomena and Dynamics of Rotating Machinery, Honolulu, Hawaii, February 10–14.
- [9] Chesnakas, C. J., and Dancey, C. L., 1990, "Three-component LDA measurements in an Axial Flow Compressor," *J. Propul. Power*, **6**(4), p. 474–481.
- [10] Stauter, R. C., Dring, R. P., and Carta, F. O., 1990, "Temporally and Spatially Resolved Flow in a Two-Stage Axial Compressor Part I: Experiment," *ASME Paper No. 90-GT-259*
- [11] Zaccaria M. A., and Lakshminarayana B., 1995, "Unsteady Flow Field due to Nozzle Wake Interaction with the Rotor in an Axial Flow Turbine Part I: Rotor Passage Flow Field," *ASME Paper No. 95-GT-295*
- [12] Prato, J., Lakshminarayana B., and Suryavamshi N., 1998, "Steady and Unsteady Three-Dimensional Flow Field Downstream of an Embedded Stator in a Multi-Stage Axial Flow Compressor Part I: Unsteady Velocity Field," *ASME Paper No. 98-GT-521*
- [13] Suryavamshi N., Lakshminarayana B., and Prato J., 1998, "Steady and Unsteady Three-Dimensional Flow Field Downstream of an Embedded Stator in a Multi-Stage Axial Flow Compressor—Part II: Composite Flow Field," *ASME Paper No. 98-GT-522*
- [14] Suryavamshi N., Lakshminarayana B., and Prato J., 1998, "Steady and Unsteady Three-Dimensional Flow Field Downstream of an Embedded Stator in a Multi-Stage Axial Flow Compressor Part III: Deterministic Stress and Heat Flux Distribution and Average-Passage Equation System," *ASME Paper No. 98-GT-523*
- [15] Sentker, A., and Riess, W., 2000, "Experimental Investigation of Turbulent Wake-Blade Interaction in Axial Compressors," *Int. J. Heat Fluid Flow*, **21**, pp. 285–290.
- [16] Li, Y. S., and Cumpsty, N. A., 1991, "Mixing in Axial Flow Compressors Part I: Test Facilities and Measurements in a Four Stage Compressor," *ASME J. Turbomach.*, **113**, pp. 161–165.
- [17] Dong, R., Chu, S., and Katz, J., 1992, "Quantitative Visualization of the Flow within the Volute of a Centrifugal Pump Part A: Technique," *ASME J. Fluids Eng.*, **114**, p. 390–395.
- [18] Dong, R., Chu, S., and Katz, J., 1992, "Quantitative Visualization of the Flow within the Volute of a Centrifugal Pump Part B: Results and Analysis," *ASME J. Fluids Eng.*, **114**, p. 396–403.
- [19] Day, K. M., Lawless, P., and Fleeter, S., 1996, "Particle Image Velocimetry Measurements in a Low Speed Research Turbine," *AIAA Pap.*, No. 96-2569.
- [20] Tisserant, D., and Breugelmans, F. A. E., 1997, "Rotor Blade-to-Blade Measurements Using Particle Image Velocimetry," *ASME J. Turbomach.*, **119**, pp. 176–181.
- [21] Gogineni, S., Goss, L., Copenhaver, W., and Gorrell, S., 1997, "Development of Digital Two-Color PIV for Turbomachinery Applications," *AIAA Pap.*, No. 97-0494.
- [22] Sanders, A. J., Papalia, J., and Fleeter, S., 1999, "A PIV Investigation of Rotor-IGV Interactions in a Transonic Axial Flow Compressor," 35th AIAA/ASME/SAE/ASEE Joint Propulsion Conference & Exhibit, June 20–23, Los Angeles, CA, *AIAA Pap.*, No. 99-2764.
- [23] Sinha, M., and Katz, J., 2000, "Quantitative Visualization of the Flow in a Centrifugal Pump With Diffuser Vanes-I: On Flow Structures and Turbulence," *ASME J. Fluids Eng.*, **122**, pp. 97–107.
- [24] Sinha, M., Katz, J., and Meneveau, C., 2000, "Quantitative Visualization of the Flow in a Centrifugal Pump With Diffuser Vanes-II: Addressing Passage-Averaged and Large-Eddy Simulation Modeling Issues in Turbomachinery Flows," *ASME J. Fluids Eng.*, **122**, pp. 108–116.
- [25] Wernet, M. P., 2000, "Development of Digital Particle Imaging Velocimetry for use in Turbomachinery," *Exp. Fluids*, **28**, pp. 97–115.
- [26] Uzol, O., Chow, Y. C., Katz, J., and Meneveau, C., 2001, "Unobstructed PIV Measurements within an Axial Turbo-Pump Using Liquid and Blades with Matched Refracted Indices," 4th International Symposium on Particle Image Velocimetry, Göttingen, Germany, September 17–19, 2001; also, 2002, *Exp. Fluids*, Aug.
- [27] Uzol, O., Chow, Y. C., Katz, J., and Meneveau, C., 2002, "Experimental Investigation Of Unsteady Flow Field Within a Two-Stage Axial Turbomachine Using Particle Image Velocimetry," *ASME J. Turbomach.*, **124**, pp. 542–552.
- [28] Zhang, J., Tao, B., and Katz, J., 1997, "Turbulent Flow Measurement In A Square Duct With Hybrid Holographic PIV," *Exp. Fluids*, **23**, pp. 373–381.
- [29] Roth, G. I., Mascenik, D. T., and Katz, J., 1999, "Measurements of The Flow Structure and Turbulence Within A Ship Bow Wave," *Phys. Fluids*, **11**(11), pp. 3512–3523.
- [30] Roth, G. I., and Katz, J., 2001, "Five Techniques for Increasing the Speed and Accuracy of PIV Interrogation," *Meas. Sci. Technol.*, **12**, pp. 238–245.
- [31] Sridhar, G., and Katz, J., 1995, "Drag and Lift Forces on Microscopic Bubbles Entrained by a Vortex," *Phys. Fluids*, **7**, pp. 389–399.

L. He  
T. Chen<sup>1</sup>

School of Engineering,  
University of Durham,  
Durham, DH 1 3LE, UK

R. G. Wells

Y. S. Li

W. Ning

Compressor Group,  
Industrial Gas Turbines,  
ALSTOM Power,  
Lincoln, LN5 7FD, UK

# Analysis of Rotor-Rotor and Stator-Stator Interferences in Multi-Stage Turbomachines

*A nonlinear harmonic methodology is adopted to analyze interactions between adjacent stages in multi-stage compressors. Of particular interest are the effects of circumferential "aperiodic" distributions and the relative circumferential positioning ('clocking') of blades. The main feature of the present approach is that both the aperiodic and clocking effects are very efficiently included with circumferential "steady" harmonic disturbances. Consequently, a single run of the nonlinear harmonic solver using a single-passage domain can produce the whole annulus unsteady and aperiodic time-averaged flow field. In addition, performance variation at any clocking position can be obtained simply by post-processing the result. A case study is presented for a two-and-half-stage transonic compressor, and the present results show much stronger rotor-rotor interaction than stator-stator interaction. A mechanism leading to strong rotor-rotor interference seems to be the interaction between upstream rotor wakes and the downstream rotor passage shock waves. A rotor-rotor clocking study illustrates a qualitatively different loss variation with respect to clocking position in a transonic flow compared to that in a subsonic flow.*

[DOI: 10.1115/1.1508382]

## 1 Introduction

Computational fluid dynamics (CFD) methods for steady flow analysis of isolated blade rows can now be routinely used on a daily basis in compressor designs. The market forces to reduce both design cycle time and manufacturing costs lead to a stricter requirement to enhance the current design capability for multi-stage machines. The trend for more compact (higher loading) designs requires improvement of our current understanding and predictive capability of stage matching/interactions in a steady and/or unsteady manner in a multi-stage environment. It is recognized that full-scale unsteady Navier-Stokes simulations of all deterministic temporal and spatial nonuniformity can provide useful information to form a basis to help our understanding of unsteady effects (e.g., Giles, [1], Arnone and Pacciani [2]). However, this kind of multi-passage time-dependent simulations would need large computing resources, and are not feasible to be used in a daily design environment. The main factors on computational efficiency of multi-stage time-domain unsteady CFD solvers in comparison to a steady flow solution are: (a) the requirement for a multi-passage/whole annulus domain, due to inherent rotor-stator relative motion and effectively arbitrary blade counts in different bladerows; and (b) the requirement for a time-accurate integration scheme.

There are basically two different kinds of approaches to multi-stage CFD modeling currently available for a design purpose. The first approach follows the mixing-plane treatment originally proposed by Denton and Singh [3], in which circumferential non-uniformity is mixed-out "instantly" at a rotor-stator interface. It should be emphasized that though one may choose different flow variables to be mixed out, the mixing process should be solely dictated by the conservation laws, and consequently there must be a mixing loss generated at the interface. In addition to this mixing loss generated at the interface somehow artificially, the unsteady transportation of the disturbances and the subsequent interaction effects on the adjacent bladerows would be completely lost. The

second approach follows the framework proposed by Adamczyk [4,5] to account for bladerow interaction effects on time-averaged and passage-averaged flows by including the deterministic stress terms. Compared to the mixing-plane approach, Adamczyk's approach can include much more interbladerow interaction mechanisms, but its superiority over the former depends on how the deterministic stress terms are modeled. In addition to Adamczyk's own model, there have been various recent efforts in identifying efficient ways of providing closure of these extra stress terms, either by using simple quasi-steady models (Rhie et al. [6]), semi-analytical models (van de Wall et al., 2000 [7]) or by time-domain simulations (e.g., Hall, [8], Dorney and Sharma [9]).

The present work is aimed at using an efficient and accurate computational method to obtain the deterministic stress terms for a multi-stage environment. As a starting point, our main intention is that the modeling methodology should be based on solving the unsteady Navier-Stokes equations without resorting to expensive time-accurate integrations of the equations in multi-passage domains. To this end, the frequency-domain-based nonlinear harmonic approach has been adopted. The methodology was initially developed for blade aeroelastic calculations (Ning and He [10], He and Ning [11]) and more recently extended to calculating rotor-stator interactions (Chen et al. [12]). One particular issue to be addressed here is how to include rotor-rotor and stator-stator interactions in terms of the aperiodicity and clocking in the single-passage harmonic calculation for arbitrary blade counts. Furthermore, previous studies on clocking effects have been largely confined to stator rows. One might ask, does a rotor-rotor interaction behave in the same way as a stator-stator one?

## 2 Flow Physical and Numerical Modeling

**2.1 Baseline Steady Viscous Flow Model.** For convenience of simulating flows in multiple-bladerow turbomachinery, a cylindrical co-ordinate  $(x, \theta, r)$  in an absolute system is adopted. For a rotor bladerow, this would avoid the extra terms related to the Coriolis term etc., and is preferred for convenience of the treatment at a rotor-stator interface. A mesh around a rotor row will be seen as a moving mesh in the absolute system. An integral form of the 3-D unsteady Reynolds-averaged Navier-Stokes equations over a moving finite volume is

<sup>1</sup>Currently, Mechanical Engineering Dept, Imperial College, London, UK

Contributed by the International Gas Turbine Institute and presented at the International Gas Turbine and Aeroengine Congress and Exhibition, Amsterdam, The Netherlands, June 3–6, 2002. Manuscript received by the IGTI, September 21, 2001. Paper No. 2002-GT-30355. Review Chair: E. Benvenuti.

$$\begin{aligned} \frac{\partial}{\partial t} \int \int \int_{\delta V} U \cdot dV + \oint \oint_{\delta A} [Fn_x + (G - Uv_{mg})n_\theta + Hn_r] \cdot dA \\ = \int \int \int_{\delta V} S_i \cdot dV + \oint \oint_{\delta A} [V_x n_x + V_\theta n_\theta + V_r n_r] \cdot dA \quad (1) \end{aligned}$$

where  $U$ ,  $F$ ,  $G$ , and  $H$  are the standard conservative variable and inviscid flux vectors.  $v_{mg} = \Omega r$  is the grid moving velocity and the extra inviscid flux term  $Uv_{mg}$  accounts for the contribution to the fluxes due to moving grids.  $S_i$  is the inviscid source term to include the centrifugal effect for maintaining a circumferential movement in the radial momentum equation. Detailed formulations for these viscous stress terms can be found elsewhere (e.g., Hoffmann et al. [13]). For turbulent flows, the Baldwin-Lomax mixing-length model is currently used to close the Reynolds stresses.

On solid blade/endwall surfaces, the log-law is applied to determine the surface shear stress and the tangential velocity is left to slip. This treatment is preferred for 3-D multi-stage calculations because of the relatively coarse meshes to be used. Both over rotor tip clearance and under stator hub clearance effects are included typically using one to three mesh cells. At the inlet to the multi-stage computational domain, stagnation parameters and flow angles are specified. At the exit, the pitchwise mean static pressure at each spanwise section is specified, and the local upstream-running characteristic is formulated to drive the pitchwise average pressure to the specified value, while the local pitchwise nonuniformity is determined by the downstream-running characteristic.

The governing equations are discretized in space using the cell-centred finite volume scheme, together with the blended 2nd and 4th-order artificial dissipation to damp numerical oscillations. The baseline time-marching method solves the discretized 3-D unsteady Navier-Stokes equations in a multi-passage and multi-row domain by using the four-stage Runge-Kutta scheme, accelerated by a time-consistent multi-grid technique (He [14]). For steady as well as harmonic unsteady flow variables as introduced later, the time term in Eq. (1) should be regarded as a pseudo one, and is used purely for the sake of facilitating efficient steady flow time-marching methods, such as the conventional local time-stepping and multi-grid techniques.

In a multi-bladerow domain, computational meshes are fixed to blades. Relatively moving rotor and stator meshes are patched together at an interface. In the baseline steady solver for multi-stage flows, we adopt the mixing-plane approach [3,15] to mix out all circumferential nonuniformities. Hence, there are no sources of deterministic unsteadiness, leading to a pure steady flow in each bladerow. The present implementation of the mixing-plane treatment follows a nonreflective procedure by Saxer and Giles [16]. At each spanwise section, the ‘‘mixed-out’’ variables at both the rotor and stator sides are flux-averaged. The difference in the mixed-out variables across the interface represents a jump in characteristics. The procedure is to drive characteristic jumps to zero in a nonreflective manner, leading to conservation of total mass, momentum and energy fluxes across the interface, when the pseudo-time-marching solution is converged.

**2.2 Nonlinear Harmonic Model.** An unsteady flow variable can be decomposed into a time-averaged part and an unsteady perturbation, e.g.,

$$U = \bar{U} + U' \quad (2)$$

Substituting the foregoing expression for the conservative variables into the integral form of the unsteady Navier-Stokes equations and time-averaging them, the resultant time-averaged equations are given as

$$\begin{aligned} \oint \oint_{\delta A} [\bar{F}n_x + (\bar{G} - \bar{U}v_{mg})n_\theta + \bar{H}n_r] \cdot dA = \int \int \int_{\delta V} \bar{S}_i \cdot dV \\ + \oint \oint_{\delta A} [\bar{V}_x n_x + \bar{V}_\theta n_\theta + \bar{V}_r n_r] \cdot dA \quad (3) \end{aligned}$$

Note that the time-averaged equations include extra deterministic stress terms [4,5] compared to the steady flow equations. These deterministic stress terms depend on the solution to the unsteady perturbations. Consider that an unsteady disturbance consisting of  $N_F$  harmonic components each of which has a frequency  $\omega_k$

$$U'(x, \theta, r, t) = \sum_{k=1}^{N_F} (\tilde{U}_k e^{i\omega_k t} + \tilde{U}_{-k} e^{-i\omega_k t}) \quad (4)$$

where  $\tilde{U}_k$  and  $\tilde{U}_{-k}$  are a pair of complex conjugates. Then a set of equations for each harmonic component can be obtained by collecting all the terms at its frequency, noting that only those with positive frequencies need to be solved. These together with their conjugates will enable the reconstruction of the full unsteadiness in a time domain as defined in Eqs. (4) and (2).

For any two unsteady velocity components defined in Eq. (4), the deterministic stress term is calculated by summing the products of the real parts and imaginary parts of the complex amplitudes (e.g., for  $u$  and  $v$ )

$$\overline{u'v'} = 2 \sum_{k=1}^{N_F} [(\tilde{u}_k)_r (\tilde{v}_k)_r + (\tilde{u}_k)_i (\tilde{v}_k)_i] \quad (5)$$

If only a single harmonic mode is included, the nonlinear harmonic method is in fact the same as a harmonic balance approach. When multiple frequencies (including higher harmonics of a fundamental) are considered, a full harmonic balance formulation will include the 1st-order (quasi-linear) terms as well as the cross-coupling terms as given by Hall et al. [17]. In the present work, we assume that the unsteady effects are largely dominated by the first order terms, and only include these quasi-linear terms in the harmonic balancing. The treatment is the same as the previous work for rotor-stator interaction [12], which implies that unsteady disturbances with different frequencies will only interact with the time-averaged flow through the deterministic stress terms. The equations for all harmonics are now effectively quasi-linear, i.e. they are in a linear form based on the *time-averaged* flow. The resultant equations with respect to the  $N_F$  harmonic components are

$$\begin{aligned} \int \int \int_{\delta V} i\omega \cdot \tilde{U}_k \cdot dV \\ + \oint \oint_{\delta A} [\tilde{F}_k n_x + (\tilde{G}_k - \tilde{U}_k v_{mg})n_\theta + \tilde{H}_k n_r] \cdot dA \\ = \int \int \int_{\delta V} (\tilde{S}_i)_k \cdot dV + \oint \oint_{\delta A} [\tilde{V}_x n_x + \tilde{V}_\theta n_\theta + \tilde{V}_r n_r]_k \cdot dA \\ (k=1, 2, \dots, N_F) \quad (6) \end{aligned}$$

Similar to the steady flow mixing-plane calculations, a nonlinear harmonic calculation needs only a single blade-to-blade passage domain for a multistage calculation. For the time-averaged equations, the same boundary conditions are specified as for a steady flow. For the harmonic perturbation equations, the phase-shift periodic condition is implemented at the periodic boundaries of a single-passage domain. 1-D nonreflecting boundary conditions are adopted at both inlet and exit far-field boundaries for the harmonic perturbations.

By introducing the pseudo time-dependence in Eq. (6), the whole system consisting of both the time-averaged and unsteady

perturbation equations can be integrated in the pseudo time. This simultaneous time-marching process mimics the physical interaction and provides a strong coupling between the time-averaged and the unsteady parts. Hence, the strong coupling approach should be beneficial from a stability and convergence viewpoint. Details of the formulations and the simultaneous coupling solution between the time-averaged flow and the unsteady perturbations can be found in the previous papers [10–12].

**2.3 Interface Treatment for Rotor-Stator Interaction.** At a rotor-stator mesh interface, the first point to note is that steady circumferential spatial nonuniformity in one bladerow will be sensed as an unsteady disturbance in the other. Based on this consideration, the spatial Fourier transform is firstly carried out at its upstream and downstream interface boundaries for each bladerow, and these spatial Fourier components are used to define the unsteady harmonic disturbances in the boundary conditions of the corresponding adjacent bladerows.

Take a bladerow domain embedded in a multi-stage compressor for example. At its inlet, incoming wake (vorticity and entropy) perturbations, in velocities (axial, tangential, and radial), pressure and density, are produced by a spatial Fourier transform of the time-averaged pitchwise nonuniform field at the outlet of the upstream row. While at the outlet from this bladerow under consideration, upstream running potential (pressure wave) disturbances can be produced by a spatial Fourier transform of the time-averaged nonuniform field at the inlet to the adjacent downstream row. Each of the upstream and downstream unsteady harmonic disturbances can then be specified in the nonreflective boundary condition treatment.

As far as the time-averaged flow is concerned, the original Saxer and Giles approach [11] has been modified to include the deterministic stresses due to flow unsteadiness in the total fluxes. The deterministic stress terms are conveniently updated using the real and imaginary parts of harmonic amplitudes of unsteady disturbances at both inlet and exit. The rest of the procedure will follow exactly the same way as that in a mixing-plane steady flow solution.

**2.4 Rotor-Rotor (Stator-Stator) Interaction.** Consider only the situation with a rotor-rotor interaction. The procedure and discussion presented here apply equally to stator-stator interactions. It is noted firstly that the effects of rotor-rotor interactions depend on the blade counts. This is highlighted in two extreme cases: (a) both rotors have the same number of blades, and (b) two rotors have such different blade counts that a relative circumferential position between two blades in the two rotors respectively can only repeat after the whole annulus (e.g., 20 blades in rotor-1 and 21 in rotor-2).

Let's consider a two-stage compressor consisting of rotor-1, stator-1, rotor-2 and stator-2.  $N_{R1}$  and  $N_{R2}$  are denoted to be the numbers of blades for rotor-1 and rotor-2, respectively. If both rotors have the same blade count, every blade passage in one rotor row will see the same pattern of spatial disturbance from the other rotor blade row. Hence, the rotor-rotor interaction pattern will be periodic with the wavelength being one blade pitch. This is the case in which we should have the maximum range of varying relative circumferential positioning (clocking or indexing) of blades in the two rotor rows, and expect to have the maximum clocking effect.

The clocking effect can, however, be significantly reduced when the two rotors have different blade counts. For example, if  $N_{R1}=21$  blades and  $N_{R2}=20$ , then adjacent passages in rotor-2 will have slightly different circumferential positions, relative to the blades in rotor-1, and the maximum clocking range would only be 1/20 blade pitch. In this case, although the clocking effect is expected to be negligible, the passages in each rotor row will not be spatially periodic in the circumferential direction. This aperiodic effect needs to be assessed if an average-passage approach is adopted. The point to bear in mind is that as far as rotor-2 is

concerned, although the magnitude of velocity deficit of wakes from rotor-1 might be smaller than those from the immediate upstream stator row, the wavelength of the aperiodic disturbance could be much longer. Since the axial decay rate of a disturbance is closely related to its circumferential length scale (rather than its amplitude), disturbances of long circumferential length scales even with small amplitudes may have comparable, if not more, effects on downstream stages than those with larger amplitudes but shorter circumferential wave length.

In the framework of the present nonlinear harmonic approach, a necessary issue to be addressed is how to specify the rotor-1 wake disturbances at the inlet of rotor-2 domain. Note that in the stator-1 frame, "steady" (time-averaged) rotor-1 wakes are seen as the unsteady disturbances in the form of a circumferential traveling wave with a phase-shifted periodicity. Thus, in the stator domain any unsteady disturbance in the same traveling wave form with the phase-shift periodicity should be seen as "steady" in the rotor frames. Hence, it follows that the unsteady disturbances at stator-1 exit should correspond to the rotor-1 wake disturbances. Currently, pitchwise phase-averaged amplitudes of unsteady disturbances at the exit of stator-1 domain are adopted as the amplitudes of the rotor-1 wake disturbances as seen at the inlet of the rotor-2 domain.

Having identified at rotor-2 inlet the upstream disturbance from rotor-1, we have to consider how to deal with the passage-average effect, if each passage in rotor-2 will see a different rotor-1 wake when both rotors have different blade counts. In this case, the flow variables in the averaged-passage would be

$$\bar{U}_{pa} = \frac{1}{N_{R2}} \sum_{n=1}^{N_{R2}} \bar{U}_n \quad (7)$$

Interestingly, this spatial-averaging of an aperiodic steady flow is equivalent to a time-averaging of  $N_{R2}$  snapshots in a single-passage of rotor-2, if rotor-1 were made to rotate very slowly (in a quasi-steady manner) relative to rotor-2. This consideration leads to a very simple and efficient implementation to include the rotor-rotor interaction in the nonlinear harmonic approach. In practice, the calculations for this quasi-steady "rotating" disturbance  $\bar{U}_{pa}$  are obtained in the same procedure as for other unsteady disturbances except for setting a zero frequency.

Once having obtained the quasi-steady harmonic perturbation field  $\bar{U}_{pa}$  in a single passage domain of the rotor-2 flow field due to the "slowly rotating" disturbance at its inlet, we can reconstruct the corresponding spatially aperiodic time-averaged flow field in the whole annulus. The time-average flow variable in passage  $n$  is given by

$$\bar{U}_n = \bar{U} + \bar{U}_{pa} e^{i(n-1)\sigma} + \bar{U}_{-pa} e^{-i(n-1)\sigma} \quad (8)$$

where,  $\sigma = (N_{R1}/N_{R2}) \cdot 2\pi$  is the inter blade phase angle, i.e., the spatial phase shift between adjacent blade passages. Then, the passage-average flow for rotor-2 can be easily obtained from Eq. (7). The corresponding aperiodic perturbation for passage  $n$  is

$$\hat{U}_n = \bar{U}_n - \bar{U}_{pa} \quad (9)$$

which can be used to work out the aperiodic deterministic stresses due to the passage-averaging. Note that when both rotors have the same blade count ( $N_{R1}=N_{R2}$ ), the foregoing aperiodic perturbation will reduce to zero.

The procedure lends itself naturally and automatically to evaluating the clocking effect. If the clocking effect is to be analyzed, the results with different clocking positions can be easily reconstructed based on the quasi-steady harmonic perturbation due to the very slow rotation of rotor-1 relative to the rotor-2. For instance, the flow field with the clocking position  $Z$  is

$$\bar{U}_z = \bar{U} + \bar{U}_{pa} e^{iz\sigma} + \bar{U}_{-pa} e^{-iz\sigma} \quad (10)$$



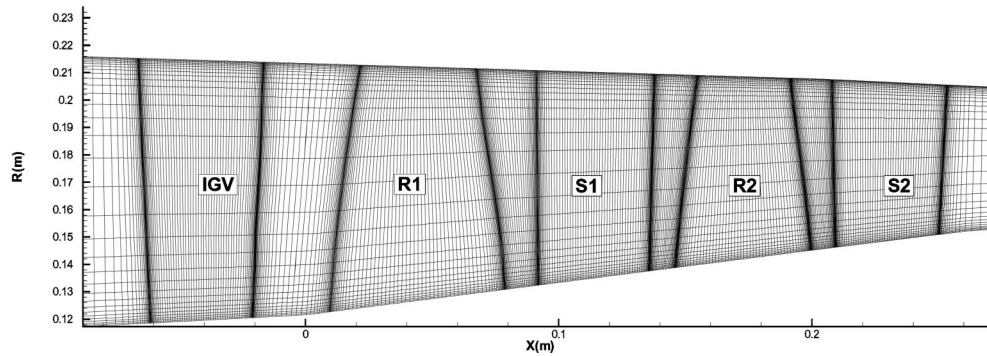


Fig. 1 Meridional mesh for ALSTOM 2.5-stage compressor

where  $Z = \Delta y / \text{pitch}$ , and  $\Delta y$  is measured from the reference point corresponding to the quasi-steady field,  $\bar{U} + \bar{U}_{pa} + \bar{U}_{-pa}$ .

It is worthwhile noticing that the clocking effect in a full range of relative circumferential positions between two rotors can now be evaluated by post-processing the result from just one single calculation. The procedure has no limitation on blade counts. The gain in computational efficiency is substantial compared to a general situation when a multi-passage time-domain calculation will have to be executed for each clocking position of interest. Thus, the approach is able to efficiently include the rotor-rotor (stator-stator) interaction effects for practical blade configurations and flow conditions relevant to designs of multi-stage turbomachines. Although the computational examples presented here are for compressor blading, this method is directly applicable to turbines.

### 3 Results and Discussions

The test case used in this study is a 2.5-stage transonic compressor (IGV+stage 1 and 2), as described previously by Wells et al.[18], Li and Wells [19]. It has blade counts, 26:17:30:21:30 for the five blade rows. A simple H-mesh is used with a patched interface between adjacent bladerows. Its meridional mesh is shown in Fig. 1. Local mesh refinements are made around the leading edge, trailing edge, near blade surfaces and end walls for each bladerow. Total mesh number is about 0.5 million, with roughly 95, 33, 33 cells in the axial, circumferential and radial directions for each blade row. The tip leakage over the rotors is included with two radial mesh cells and the hub leakage under the stators with one mesh cell.

**3.1 Baseline Steady Flow Solution.** The mixing-plane steady solver has been applied to analyze the 2.5-stage transonic compressor, and compared against the experimental data reported by Wells et al.[18]. The overall performance characteristic lines are shown in Fig. 2, where the mass flow is normalized by the choke mass flow at design speed. The choke mass flow at design speed has been predicted to be about 1.5% higher than the experimental data, similar predictions by other codes were also reported [19]. At 80, 90, and 100% design speeds, the calculations can be pushed to near the experimental stall/surge conditions. Both total pressure ratio and polytropic efficiency characteristic lines are reasonably well predicted for the conditions from 80 to 100% of design speed, with less than 1% efficiency difference compared to the experimental data.

**3.2 Unsteady Results of Overall Performance.** The nonlinear harmonic approach has been adopted to simulate the 3-D unsteady flow of the compressor with the original blade counts. As discussed earlier, the task of unsteady analysis would be extremely time-consuming for conventional whole-annulus nonlinear time-marching methods.

Previous investigations have shown that two–three harmonic orders of unsteady perturbation are sufficient to represent the

wake disturbance generated from an upstream bladerow. In the present work, we use two orders of the harmonic perturbations in both rotor-1 and rotor-2 domains to simulate the downstream running stator wakes, and three orders in stator-1 and stator-2 domains to simulate the downstream running rotor wakes given the relatively higher steady loading on rotors. Also, three orders of harmonics have been included in the rotor-2 domain for rotor-rotor interaction and 2 orders in the stator-2 domain for stator-stator interaction.

Including all these unsteady perturbations, a nonlinear harmonic calculation consumes about eight times more CPU for each pseudo-time step than that for the steady solution. Starting from a converged steady solution, a converged unsteady solution requires roughly half of the total time steps needed for a steady solution to converge from scratch. So on average, an unsteady solution using the nonlinear harmonic approach consumes four to five times

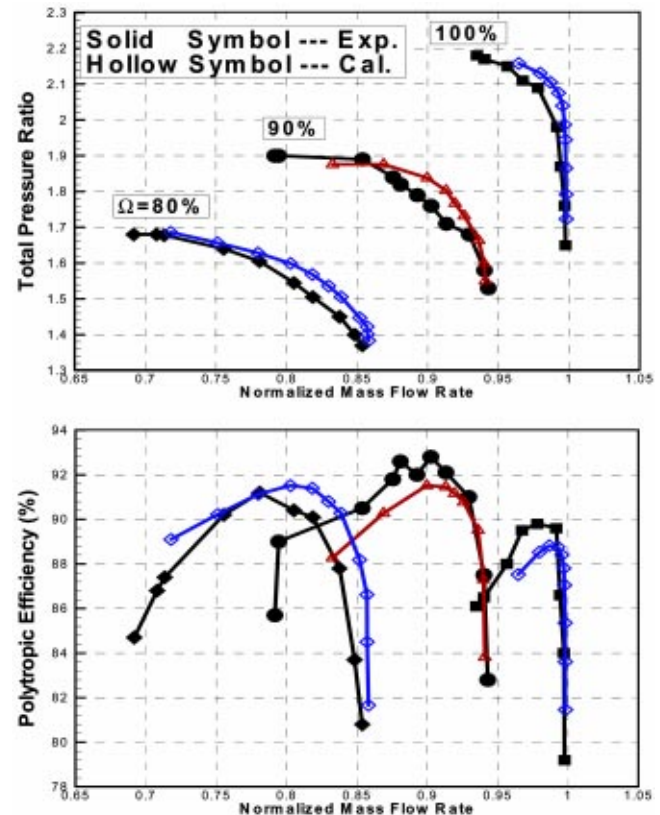


Fig. 2 Performance lines calculated by baseline steady solver

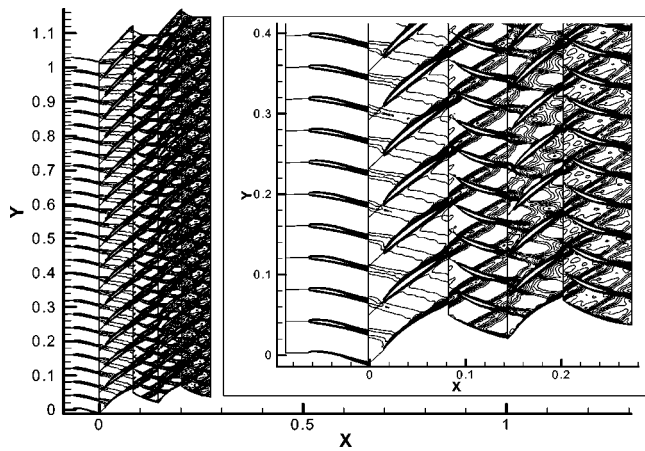


Fig. 3 Entropy contours on midspan section (left: whole domain, right: close-up)

more CPU compared to a steady solution. As a result, a computation of a 3-D unsteady flow in five blade rows (with a mesh density of 100k per passage) can be obtained in a matter of five-seven days using a single processor SGI Power Challenger workstation. This is far more efficient than conventional multi-passage time-domain calculations.

Figure 3 shows the instantaneous entropy contours at the midspan sections. The instantaneous snapshot on the multi-passage domain is reconstructed from a single-passage solution, and illustrates all the downstream running disturbances associated with wakes shed from both stators and rotors. The disturbances pass through all the interfaces quite smoothly. The validity of the interface treatment in the 3-D sense can also be demonstrated by the instantaneous entropy contours on axial planes just before and after the interface between stator-1 and rotor-2, as shown in Fig. 4. Again, this aperiodic multi-passage snapshot is reconstructed from the single-passage result according to the phase-shifted periodicity. At this interface, two disturbances, wakes from stator-1 and those from rotor-1 are included. Note that the blade wakes shed from stator-1 are almost radially straight, as indicated by the corresponding dense radial entropy contours. On the other hand, rotor-1 wakes are radially leaned (anticlockwise) toward the suction surface as a result of blade twist, which can be clearly identified by these more diffused entropy contours. In addition, we can

Table 1 Calculated compressor efficiencies

	Steady	Unsteady
80% Speed	89.66%	89.73%
Design Speed	88.23%	88.30%

see that the rotor-1 wakes are clearly stretched by the suction/pressure surface velocity difference of stator-1 (as indicated in Fig. 3), which is consistent with the distorted rotor-1 wakes seen at the stator-1 exit (Fig. 4(a)). The small wiggles of the rotor-1 wakes after the interface (Fig. 4(b)) are due to the truncated harmonic approximation.

The 3-D unsteady viscous results for the compressor have been obtained at the design condition for 100% speed with the flow through both rotors being transonic, and the peak efficiency condition for 80% speed (subsonic flow for all rows). The overall time-averaged performances at the two conditions show very small differences in comparison with the steady results, as shown in Table 1. We can see that the time-averaged efficiency predicted by the nonlinear harmonic approach is only 0.07% higher than that predicted by the steady method at the design condition, and it is 0.06% at the peak efficiency condition for 80% speed. The differences in other overall performance parameters (pressure ratios and mass flow rates) between the steady and unsteady solutions are also very small. Given the present unsteady calculation includes several bladerow interaction mechanisms, one does wonder whether this indifference is because all mechanism are of negligibly small amplitudes or something else. Some further analysis and discussions presented as follows are helpful in addressing this issue.

**3.3 Stator-Stator Clocking.** The original blade counts of the stator rows of the two stages (30:30) would lead to periodic time-averaged flow patterns in both rows and we should have the maximum (one blade pitch) clocking range. This effect of clocking the two stator rows is examined by post-processing the time-averaged result from the nonlinear harmonic computation presented earlier. The polytropic efficiency (at stator-2 exit) dependence on the clocking position is shown in Fig. 5(a) at a 80% rotation speed condition, and in Fig. 5(b) for the design speed. Note that for both conditions, the flows around the stators are always subsonic though those around rotors are transonic at the design speed and purely subsonic at 80% speed. As we can see, the stator clocking shows very little effect on the perfor-

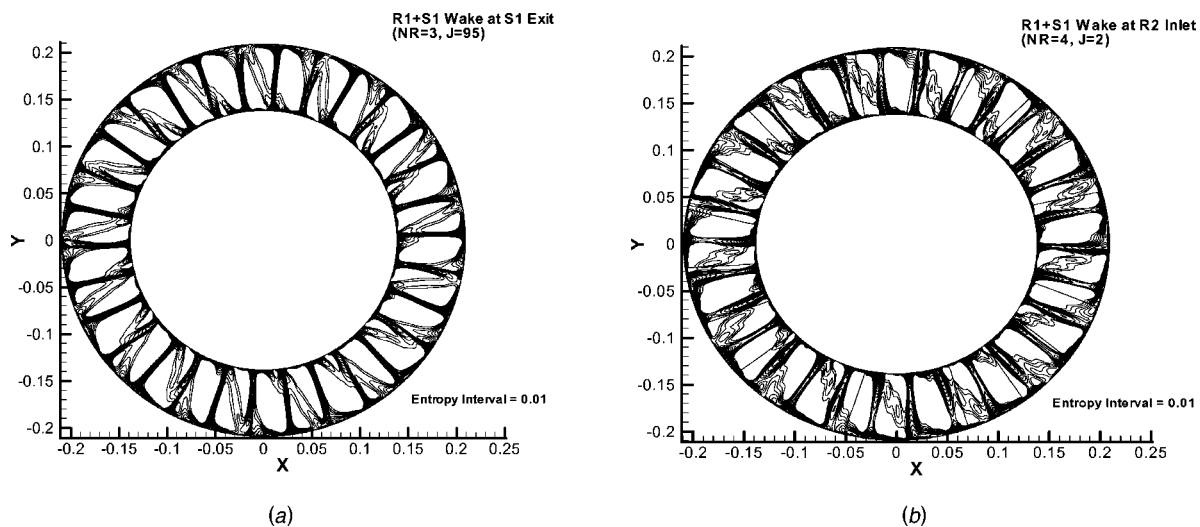


Fig. 4 Entropy contours on stator-1/rotor-2 interface (viewed from upstream, superimposed wakes shed from radial stator-1 and anticlockwise leaned rotor-1 blades) (a) stator-1 exit plane; (b) rotor-2 inlet plane

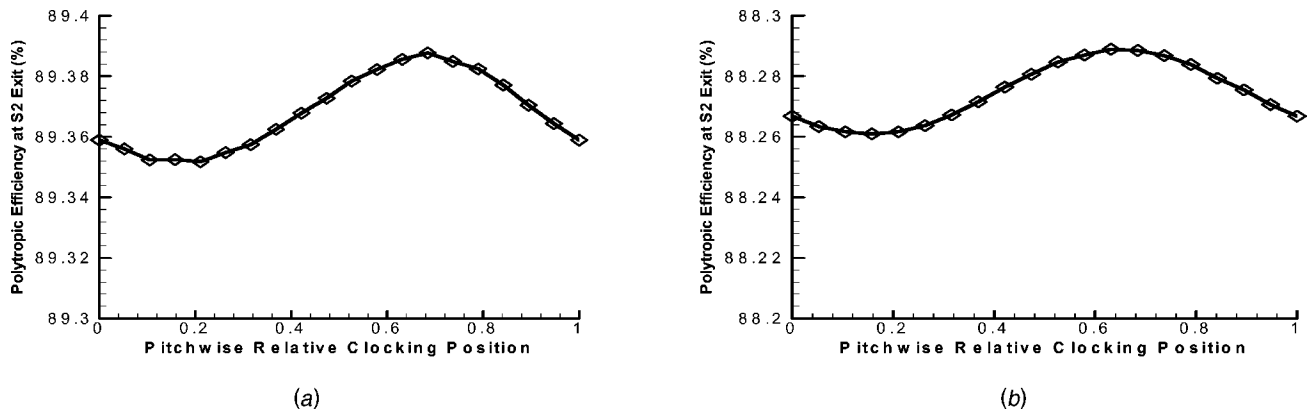


Fig. 5 Time-averaged efficiency variation due to stator-stator clocking—(a) 80% rotor speed; (b) 100% rotor speed

mance. In both cases, the maximum efficiency variation is well below 0.1. In addition, the shapes and the peak positions of the efficiency variations at the two conditions look almost the same, indicating the similarity of behaviors at high and low speed conditions. This suggests that the behavior of stator-stator clocking based on the results obtained at low speeds, e.g., the experimental data by Barankiewicz and Hathaway [20] should be expected to be qualitatively valid at high speeds.

**3.4 Rotor-Rotor Interaction (Aperiodic Flow).** It can be seen that the rotor wakes are stronger and more persistent than those shed by the stators (Fig. 4). The rotor blade counts for the two stages are 17:21, so the time-averaged flow field in rotor-2 should be aperiodic. Figure 6 shows the time-averaged efficiencies in the 21 blades passages of rotor-2 at the two speed conditions, clearly showing the aperiodic pattern with four lobes resulting from the difference of the rotor blade numbers. The efficiency is calculated based on the time-averaged stagnation pressure and stagnation temperature, which is shown to be consistent with the time-averaged values of unsteady entropy in terms of  $\text{Exp}(-S/R)$ .

It is noted that the aperiodic circumferential efficiency variation due to rotor-rotor interaction (Fig. 6) is much larger than that due to stator-stator clocking (Fig. 5). In the subsonic case, the peak-peak efficiency difference is 0.65% and that in the transonic case is 0.55%. This aperiodic passage-passage variation in time-averaged flow field will need to be taken into account when one is to calculate (or measure) time-averaged performance of a rotor

row, which means that time-resolved data in only one blade passage would not be sufficient to produce the averaged performance results for the bladerow involved.

**3.5 Rotor-Rotor Clocking.** All the computational results we have so far obtained illustrate that the rotor-rotor interaction effects are much stronger than stator-stator interaction. The question is if there might be any underlining mechanism for this.

Some further calculations were carried out to specially examine the effect as well as the mechanisms of rotor-rotor clocking. As we discussed earlier, the maximum clocking range (one blade pitch) can be achieved if both bladerows have the same blade count. Based on this consideration, the blade number of rotor-1 has been increased from 17 to 21 (i.e., equal to that of rotor-2). It should be pointed out that no attempt was made to rescale the rotor blades to achieve the original solidity, and only 2-D calculations on the mid-span section were performed with this modified blade count. Again, the two distinctive conditions (80 and 100% speed), corresponding to subsonic or transonic flows in both rotors, were considered.

The efficiency variations due to the full range of rotor-rotor clocking are shown in Fig. 7. At the subsonic condition, the peak-peak difference in the efficiency measured at rotor-2 exit is 0.16% (Fig. 7(a)). However, the maximum variation at the transonic condition is 0.46% (Fig. 7(b)). It is also noticed that, unlike the results of stator-stator clocking (Fig. 5) the shapes of the efficiency curves with respect to the clocking positions are very different at the two flow conditions. In fact, they are almost

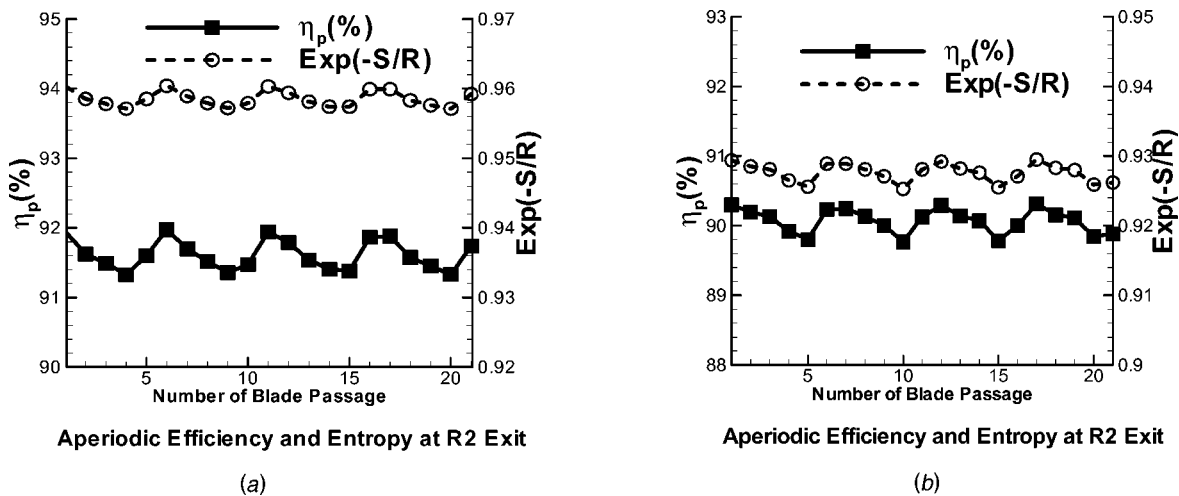
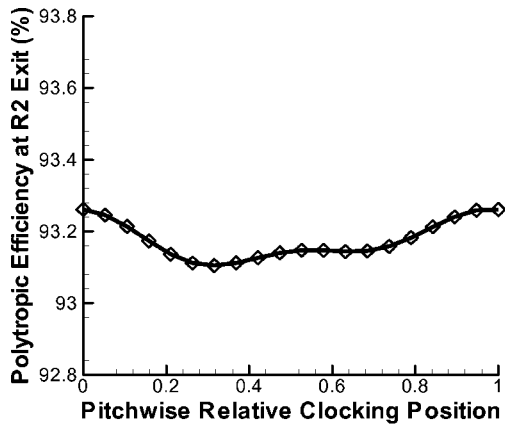
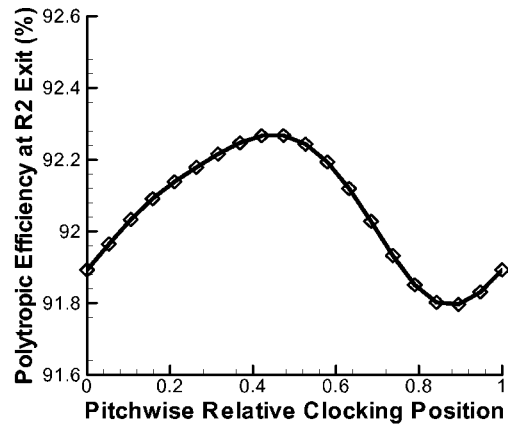


Fig. 6 Time-averaged efficiency/loss in 21 passages of rotor-2 (original rotor-rotor blade counts, 17:21)—(a) subsonic flow (80% speed); (b) transonic flow (100% speed)



(a)



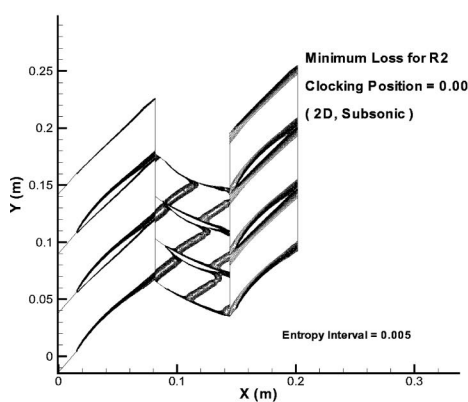
(b)

**Fig. 7 Efficiency variation due to rotor-rotor clocking (2-D mid-span section, rotor-rotor blade counts 21:21)—(a) subsonic flow; (b) transonic flow**

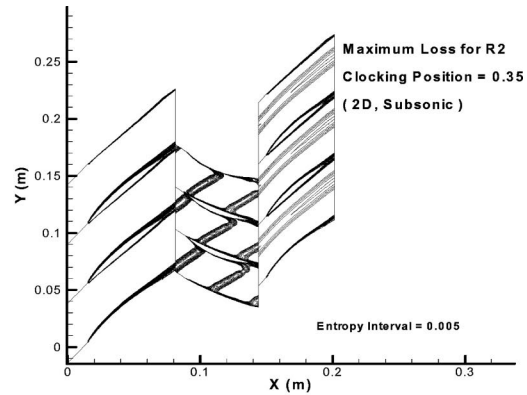
anti-phase, with the minimum efficiency clocking position in the subsonic flow (Fig. 7(a)) closely corresponding to that of the maximum efficiency in the transonic one (Fig. 7(b)).

The entropy contours at these peak clocking positions can be used to throw some lights on the corresponding mechanisms of the rotor-rotor clocking effects, as shown Figs. 8 and 9. In these

figures, the entropy contours in rotors-1 and rotor-2 are based on time-averaged values. There are several points we should note from these entropy contours. At the subsonic flow conditions, the minimum loss clocking position corresponds to that when the upstream rotor wake hits the downstream rotor blade and mixes with its boundary layer (Fig. 8(a)), and the maximum loss corresponds

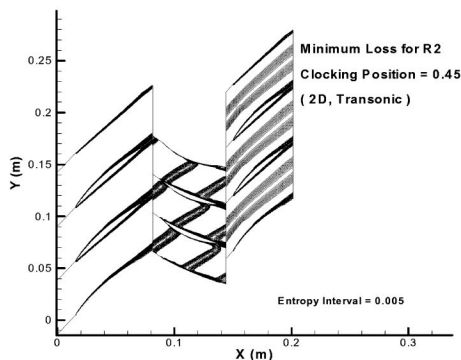


(a)

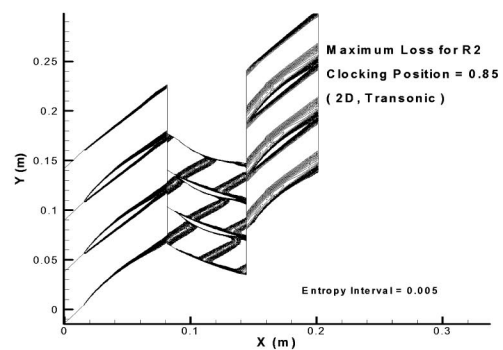


(b)

**Fig. 8 Entropy contours at rotor-rotor clocking positions with maximum and minimum losses in subsonic flow (rotor1-stator1-rotor2 configuration)—(a) minimum loss; (b) maximum loss**



(a)



(b)

**Fig. 9 Entropy contours at rotor-rotor clocking positions with maximum and minimum losses in transonic flow (rotor1-stator1-rotor2 configuration)—(a) minimum loss; (b) maximum loss**

to that when an upstream wake passes through the middle passage (Fig. 8(b)). The present rotor-clocking results at the subsonic condition are similar to typical previous computational results of compressor stator-clocking (e.g., [21]). This behavior might simply be attributed to that the largest velocity difference between a wake and its surrounding (hence the highest mixing loss) would result from the wake passing through mid-passage.

We have a completely different picture for the transonic flow (Fig. 9). The overriding factor seems to be the existence of the passage shock in rotor-2. Note that now the most lossy clocking position is when the upstream wake passes through the rotor-2 passage just over the suction surface, where the shock strength is at its highest (Fig. 9(b)). In keeping with the argument of Denton [22], the mixing loss will be increased when a wake is subject to an adverse pressure gradient since the low momentum fluid inside the wake will be slowed down further leading to a larger velocity deficit. It then follows that a wake passing across a stronger shock wave would produce higher mixing loss. In the present case, the rotor passage shock wave is at its highest strength in the region outside the suction surface boundary layer. The signature of the wake-shock interaction is clearly identifiable in the entropy contours (Fig. 9(b)). We also note that the rotor-2 shock is quickly weakened off as it extends from the suction surface toward the mid-passage. Interestingly, the minimum loss now corresponds to the clocking position when the wake passes through the mid-passage (Fig. 9(a)), which is the most lossy position in the subsonic case. There does not seem to be a simple explanation why this should be the case, since based on the discussion on the subsonic case, we would expect that at the minimum loss, rotor-1 wakes should be closer to the pressure surface of the rotor-2 blade.

## Concluding Remarks

A method for including rotor-rotor (stator-stator) interactions of multi-stage compressors has been presented, based on the nonlinear harmonic method of solving the 3-D unsteady Navier-Stokes equations in the frequency domain. The method calculates efficiently unsteady and time-averaged flows in a multi-stage turbomachinery environment with arbitrary blade-counts. With a single-run of the present multi-stage unsteady solver in a single-passage for each bladerow, we can obtain the circumferentially aperiodic unsteady flow field for the whole annulus. In addition, time-averaged performance variation at any clocking position can be evaluated by simply post-processing the single-run result.

A case study has been carried out for a 2.5-stage transonic compressor. The computational results illustrate that rotor-rotor interaction effects are considerably stronger than those due to stator-stator interactions. The maximum efficiency variation due to stator-stator clocking is found to be less than 0.1%, while the passage-to-passage aperiodic efficiency variation due to rotor-rotor interaction can be as high as 0.7%. A further computational study on rotor-rotor clocking indicates a qualitatively different rotor-rotor interaction mechanism in a transonic flow compared to that in a subsonic flow.

## Acknowledgments

The authors would like to acknowledge ALSTOM Power for the continuous financial and technical support to the project and for the permission to publish this work. Useful discussions with John Adamczyk during Li He's recent visit to NASA Glenn Research Center are much appreciated.

## Nomenclature

$P$  = static pressure  
 $u, v, w$  = axial, tangential and radial flow velocities  
 $F, G, H$  = axial, tangential and radial flux vector  
 $U$  = conservative variable vector  
 $P_p$  = blade-to-blade pitch

$\rho$  = fluid density  
 $\tau$  = viscous stress components  
 $\Omega$  = rotating speed  
 $\omega$  = angular frequency  
 $\sigma$  = inter-blade phase angle

## Subscripts

$i$  = imaginary part  
 $k$  = unsteady disturbance index  
 $n$  = blade index  
 $r$  = real part  
 $x, \theta, r$  = cylindrical polar co-ordinates  
 $pa$  = passage-averaged

## Superscripts

$-$  = time-averaged  
 $'$  = unsteady perturbation  
 $\sim$  = complex harmonic amplitude

## References

- [1] Giles, M. B., 1988, "Calculation of Unsteady Wake/Rotor Interaction," *J. Propul. Power*, **4**, pp. 356–362.
- [2] Arnone, A., and Pacciani, R., 1996, "Rotor/Stator Interaction Analysis Using the Navier-Stokes Equations and Multigrid Method," *ASME J. Turbomach.*, **118**, pp. 679–689.
- [3] Denton, J. D., and Singh, U. K., 1979, "Time-Marching Methods for Turbomachinery Flow Calculations," VKI—LEC-SER-1979-7, von Karman Inst for Fluid Dynamics, Belgium.
- [4] Adamczyk, J. J., 1985, "Model Equations for Simulating Flows in Multistage-Turbomachinery," ASME Paper 85-GT-226.
- [5] Adamczyk, J. J., 1999, "Aerodynamic Analysis of Multistage Turbomachinery Flows in Support of Aerodynamic Design," IGTI Scholar Lecture, ASME Paper 99-GT-80.
- [6] Rhie, C. M., Gleixner, A. J., Spear, D. A., Fischberg, C. J., and Zacharias, R. M., 1998, "Development and Application of a Multistage Navier-Stokes Solver, Part 1: Multistage Modelling Using Bodyforces and Deterministic Stresses," *ASME J. Turbomach.*, **120**(2), pp. 205–214.
- [7] Van de Wall, A. G., Kadambi, J. R., and Adamczyk, J. J., 2000, "A Transport Model for the Deterministic Stress Associated with Turbomachinery Blade Row Interactions," *ASME J. Turbomach.*, **122**(4), Oct.
- [8] Hall, E. J., 1997, "Aerodynamic Modelling of Multistage Compressor Flow Fields," ASME Paper 97-GT-344.
- [9] Dorney, D. J., and Sharma, O. P., 1997, "Evaluation of Flow Field Approximations for Transonic Compressor Stages," *ASME J. Turbomach.*, **119**, pp. 445–451.
- [10] Ning, W., and He, L., 1998, "Computation of Unsteady Flows Around Oscillating Blades Using Linear and Non-Linear Harmonic Euler Methods," *ASME J. Turbomach.*, **120**(3), pp. 508–514.
- [11] He, L., and Ning, W., 1998, "Efficient Approach for Analysis of Unsteady Viscous Flows in Turbomachines," *AIAA J.*, **36**(11), pp. 2005–2012.
- [12] Chen, T., Vasanthakumar, P., and He, L., 2001, "Analysis of Unsteady Blade Row Interaction Using Nonlinear Harmonic Approach," *J. Propul. Power*, **17**, No. 3, May, pp. 651–658.
- [13] Hoffmann, K., Chiang, S., Siddiqui, S., and Papadakis, M., 1996, "Fundamental Equations of Fluid Mechanics," Engineering Education Systems, U.S.A.
- [14] He, L., 2000, "3-D Navier-Stokes Analysis of Rotor-Stator Interactions in Axial-flow Turbines," *Proc. IMech. E, Part A*, **214**, pp. 13–22, Jan.
- [15] Denton, J. D., 1992, "The Calculation of Three-Dimensional Viscous Flow Through Multistage Turbomachine," *ASME J. Turbomach.*, **114**(1), pp. 18–26.
- [16] Saxer, A. P., and Giles, M. B., 1993, "Quasi-Three-Dimensional Nonreflecting Boundary Conditions for Euler Equations Calculations," *J. Propul. Power*, **9**(2), pp. 263–271.
- [17] Hall, K. C., Thomas J. P., and Clark W. S., 2000, "Computation of Unsteady Nonlinear Flows in Cascades using a Harmonic Balance Technique," 9th In. Symposium on Unsteady Aerodynamics and Aeroelasticity of Turbomachines, Lyon, France, Sept.
- [18] Wells, R. G., Baty, G., Carchedi, F., and Wood, G. R., 1989, "The Design and Test of a Two Stage Transonic Axial Flow Compressor," ASME Paper 89-GT-164.
- [19] Li, Y. S. and Wells, R. G., 1999, "The Three-Dimensional Aerodynamic Design and Test of a Three-Stage Transonic Compressor," ASME Paper 99-GT-68.
- [20] Barankiewicz, W. S., and Hathaway, M. D., 1997, "Effects of Stator Indexing on Performance in a Low Speed Multi-Stage Axial Compressor," ASME Paper 97-GT-496.
- [21] Dorney, D. J., Sharma, O. P., and Gundy-Burlet, K. L., 1998, "Physics of Airfoil Clocking in a High-Speed Axial Compressor," ASME Paper 98-GT-82.
- [22] Denton, J. D., 1993, "Loss Mechanisms in Turbomachines," IGTI Scholar Lecture, ASME Paper 93-GT-435.

# Micro Air Injection and Its Unsteady Response in a Low-Speed Axial Compressor

Chaoqun Nie

Gang Xu

Xiaobin Cheng<sup>1</sup>

Jingyi Chen

Institute of Engineering Thermophysics,  
Chinese Academy of Sciences,  
Beijing, China

*A new approach, steady micro air injection from the casing, is proposed to improve the stability of a three-stage low-speed axial compression system. Although the injection rate is designated to be only a few ten thousandth of the compressor flow rate, such an injection is able to trigger the unsteady response and thus lower the mass flow rate at stall for up to 5.83%. At the same time, it keeps the steady compressor characteristic with no injection unchanged. In order to verify that the compressor response is indeed unsteady, experiments at various injection configurations are performed, which include different injection angles, axial gaps between injector and blade leading edge, radial penetration of injector and the amount of injected air. Evidences of the unsteady response are further demonstrated through dynamic signal analysis using a wavelet-based method to show the behavior of early flow disturbances under the influence of injection. Numerical analyses performed at near stall condition show that the tip clearance vortices do response to the micro-injection, and thus delay the inception of stall. [DOI: 10.1115/1.1508383]*

## 1 Introduction

The phenomenon of flow instability in the compression system, typically rotating stall and surge, has been a long-standing problem of concern for the turbomachinery industry for years. The traditional measure to alleviate the danger this phenomenon brings about to the compressor operation is to set the compressor design point with a margin away from the estimated stability boundary. Another well developed and still developing measure is the different configuration of casing treatment, which would shift the stability boundary to the lower flow rate range though the penalty in efficiency is often accompanied. The third measure, which is an emerging technology since more than ten years ago, is based on the "smart engine" concept and typified by the active control technique to suppress the compressor flow instability in its early inception (Epstein et al. [1]). In the course of developing this technique, a number of innovative ideas have been continuously updated, in particular in the research of stall inception, system modeling, numerical flow computation and the data processing methods. This technique can now be implemented through schemes of active cancellation, shifting compressor characteristic and/or the operability enhancement. The authors believe that many of these developments are important background information for further tackling the problem, in spite that the original goal of active control has not yet been fully realized due to the complexity of the flow physics and the control technique itself. One of the recent highlights on the successes and lessons of this multidisciplinary research was given by Greitzer [2].

Among these developments, the air injection in the tip region of compressor annulus, as a variation of casing treatment, has recently received greater attention to control the compressor instability and improve the performance as a whole. The design principle of the injection could be either active or passive (Day [3], Goto [4], Behnken et al. [5], Weigl et al. [6], Suder et al. [7]), and to the authors' interest, all of them have been successful to certain extent. This should imply that the unsteady characteristics of the compression system have undergone some favorable change even though the control measure is a steady one. In other words, a

mechanism of unsteady response would exist in the compressor when the steady injection acts on the unsteady phenomenon of flow instability, the rotating stall. It is also interesting to note that for many years the passive control has been designed by the empirical approach through a trade-off for the improvement of compressor performance. But it is now being developed to the more rational approach by judging the blade passage flow parameters, e.g., the redistribution of the incidence and blade loading [7]. However, the approach of flow analyses up to now, either experimental or numerical, remains a steady one. On the other hand, for the case of active control, the design approach is inherently unsteady, but mostly based on the linear development of stall waves rather than the unsteady flow parameters on the scale of blade passages.

Two consequences could be drawn from the above argument on the unsteady response. Since the action really needed for control of the flow instability is only on the unsteady part of the flow, the amount of the injected air for the steady injection can be dramatically reduced. This is perceptible because the behavior of a highly nonlinear system may be influenced even by a slight variation of boundary condition and this is the case for compression systems operating at near stall conditions. Another consequence is that the steady compressor characteristic with no injection should not be influenced by such tiny injected air and thus could keep its shape unchanged. It is obvious that both of these propositions, if they work well, would make this micro injection approach very attractive for its use in the practical application.

When this idea was initiated, some experimental work was tried on a two-stage low-speed axial compressor rig. Three tubes with 2-mm inner diameter were bent to form simple injectors which were inserted into the near region of compressor casing via the existing holes originally used for pressure probes. The radial penetration of the injector is about 2 mm from the outer casing. The preliminary result was very encouraging (Xu et al. [8]). Therefore, a new casing was designed to better accommodate the injectors and the measurement and a new program for the more complete study of this approach was restarted. The main goals of the program are twofold. One is to further confirm and demonstrate the beneficial effect of micro air injection to the compressor stability enhancement. The other is to illustrate and clarify the compressor unsteady response perceived as the underlying mechanism of such enhancement. The results of this study will be reported in the present paper.

<sup>1</sup>Institute of Acoustics.

Contributed by the International Gas Turbine Institute and presented at the International Gas Turbine and Aeroengine Congress and Exhibition, Amsterdam, The Netherlands, June 3–6, 2002. Manuscript received by the IGTI, October 25, 2001. Paper No. 2002-GT-30361. Review Chair: E. Benvenuti.

In Section 2, the experimental axial compressor facility now extended to three stages, the measurement scheme and the injector geometry are first described. The improvement of compressor performance in terms of its stability enhancement is demonstrated in Section 3 for different amounts of injected air and at different operating speeds. In Section 4, the unsteady response underlying this improvement is verified by varying the injection configuration against the base one. The dynamic behavior of this unsteady response is further clarified in Section 5 through analyzing the stall and its precursory signals using a two-dimensional wavelet method developed by the authors. To complement the experimental results, numerical study at the near stall condition has been performed for the effect of micro-injection on the flow structure in the tip region and outlined in Section 6. Finally, the paper is concluded following suggestions for the future work.

## 2 Description of Experiment Program

**2.1 Low-Speed Axial Compressor Test Rig.** The experiment was conducted in a three-stage version of the test rig driven by a 18.5KW AC motor with its speed controlled by a frequency converter. The blading identical for three stages is of practical high-pressure compressor design. Its design specifications are given in Table 1 and its side view and schematic layout can be seen in Figs. 1 and 2.

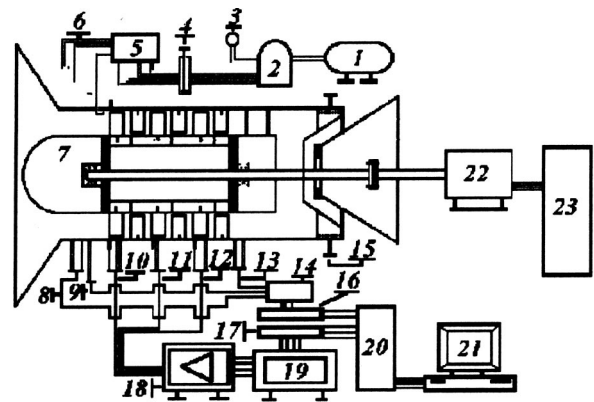
**2.2 Injector Design and Injection System.** Tubes with 2 mm inner diameter were adapted as the injectors and machined to the shape as shown in Fig. 3. The machined tubes made each injector having the same dimension and easier for its correct positioning. The injectors were deployed in front of the first rotor

**Table 1 Specifications of the three-stage low-speed axial compressor**

Rotational speed (rpm)	2400
Mass flow rate (kg/s)	2.6
Pressure rise coefficient	2.32
Outer diameter (mm)	500
Hub-tip ratio	0.75
Rotor tip clearance (% of tip chord)	3.4
Axial gap of rotor-stator and stage (mm)	8
Blade number of rotor and stator	60
Midspan chord of rotor and stator (mm)	33.3
Aspect ratio of rotor and stator	1.86
Rotor midspan stagger (deg)	44
Stator midspan stagger (deg)	23



**Fig. 1 Side view of compressor test rig**



1. Air Compressor 2. Air tank 3. Pressure meter 4. Control valve  
5. Flow meter 6. Injectors 7. Three-stage axial compressor  
8. 13. Static pressure taps 9. 3-hole probe 10. 11. 12. Transducers (XCS-190)  
14. Steady sensor box 15. Cone valve 16. 17. BNC Connectors (BNC-2090)  
18. Amplifiers (8300AU) 19. Data recorder (XR-7000)  
20. Data acquisition board (PCI-6071E) 21. Computer  
22. Motor 23. Inverter (IPF-18.5)

**Fig. 2 Schematic of compressor rig, measurement and injection system**

and their position can be varied in relation to the rotor blade leading edge (axial gap) and to the outer wall of the casing (radial penetration). The angular position can also be varied as axially aligned or rotated around the axial direction. Four injectors equally spaced circumferentially were used at a time throughout the experiment (Fig. 4). The injection system shown in Fig. 2 includes air compressor, air tank, manometer, control valve, flow

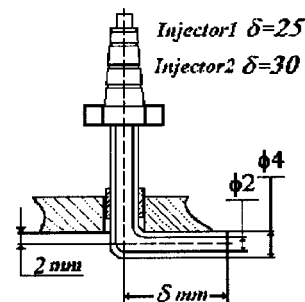


**Fig. 3 Injector design (dimensions in mm)**

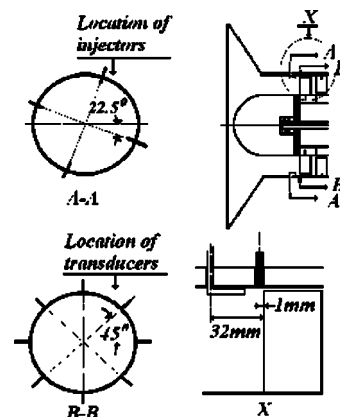


**Fig. 4 Position of injectors and pressure transducers**

Table 2 Summary of experimental results at various injection configurations

Configurations	Mass flow coefficient at stall	% decrease of mass flow at stall	Pressure coefficient at stall	% increase of pressure coefficient at stall	Note (2400 rpm for all)
No injection	0.4138		2.323		0° injection angle 2 mm radial penetration 7 mm axial gap
Injected flow 0.019%	0.4086	1.26	2.331	0.34	
Injected flow 0.045%	0.4008	3.14	2.341	0.78	
Injected flow 0.056%	0.3897	5.83	2.358	1.51	
No injection	0.4134		2.323		Injected flow 0.045% 2 mm radial penetration 2 mm axial gap
+15° injection angle	0.4203	-1.67	2.320	-0.13	
0° injection angle	0.3932	4.89	2.343	0.86	
-15° injection angle	0.3893	5.83	2.349	1.12	
No injection	0.4102		2.317		Injected flow 0.045% 0° injection angle 2 mm axial gap
2 mm injector penetration	0.3912	4.63	2.351	1.47	
4.5 mm injector penetration	0.3949	3.73	2.335	0.78	
7 mm injector penetration	0.4037	1.59	2.328	0.48	

meter and the injectors. The flow meter specially chosen for the micro flow rate is of thin-plate orifice type with its measurement range up to 20 cu. L/m.

**2.3 Measurement.** To evaluate the stability improvement, the overall compressor performance in terms of total-to-static pressure rise coefficient ( $\Delta p/0.5\rho U^2$ ) and flow coefficient ( $V_x/U$ ) is measured through eight on casing static pressure taps around the annulus both at inlet and outlet of the compressor,

where  $U$  refers to the blade speed at mean radius. To study the unsteady response of the compressor, eight pressure transducers (Kulite XCS-190) are equally spaced around the casing wall in front of the first rotor. In addition, a 3-hole traverse probe is inserted 3 mm in front of the first rotor to measure the inlet velocity distribution with and without injection. Figure 4 shows the position of injectors and transducers and the schematic of data acquisition system is shown in Fig. 2.

**2.4 Test Procedure.** The compressor throttling was made through the exit rotary cone valve mounted on the shaft and regulated manually when the stall is approached. When the compressor was running with injection, the desired amount of injection is obtained by matching the pressure in the air tank and the opening of control valve, so that the pressure in the air tank could be kept constant in the whole throttling process. For a given geometry of

injector, the maximum amount of air injection is limited by the size and safety of the tank, and is about 15 cu. L/min in the present experiment which is 0.056% of the design mass flow of the compressor.

### 3 Improvement of Compressor Performance

**3.1 Compressor Performance at Different Amounts of Injected Flow.** We first compare the compressor performance with and without injection at the design operating speed of 2400 rpm. The injected flow varies from 5-15 cu. L/m which is only 0.019–0.056% of the compressor design flow rate. The injectors were aligned along axial direction. The axial gap and radial penetration of the injectors were set at 7 and 2 mm, respectively. As shown in Fig. 5, the compressor with no injection was running into stall at flow coefficient of 0.4138 and the pressure coefficient of 2.323. With injection (the injected flow added to the measured compressor inlet flow), while being able to keep the shape of compressor characteristic unchanged, the stability boundary of the compressor was much improved. For the case of 0.045% injection, the compressor entered into stall at flow coefficient of 0.4008 and the pressure coefficient of 2.341. The stable working mass flow was decreased by 3.14% and the pressure coefficient increased by 0.78%. These results as well as results shown in following parts of the paper are all summarized in Table 2. As can be expected and

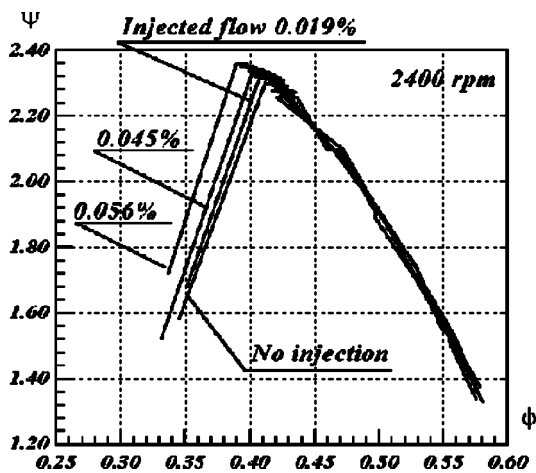


Fig. 5 Compressor performance with and without injection (including various amounts of injection)/0 deg injection, 2 mm radial penetration, 7 mm axial gap

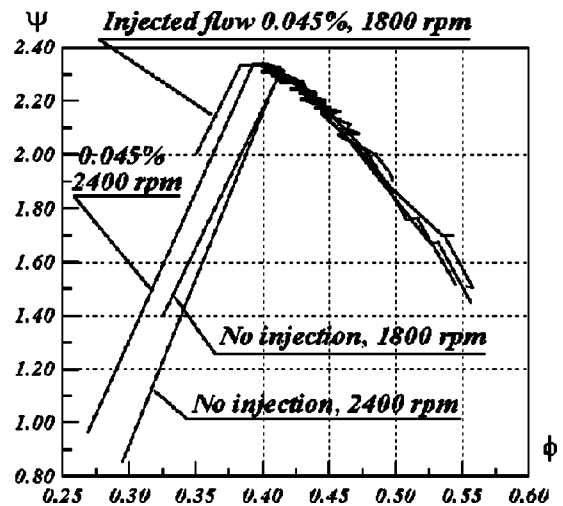


Fig. 6 Compressor performance at different operating speed/0 deg injection, 2 mm radial penetration, 7 mm axial gap



shown in Fig. 5, this beneficial effect keeps increasing with the increased amount of injected flow. When the injected flow increased to 0.056% of the main flow, 5.83% decrease of mass flow at stall was obtained with 1.51% increase of the pressure coefficient at stall. Experiment with further higher amount of injected flow was not performed because of the aforementioned limitation of the injection system. It can be expected that this trend would go on in some extent when the injected flow is dramatically increased from micro amount of some ten thousandth of the compressor main flow to the amount of some hundredth as shown by the classic injection scheme cited in the introduction. But then the cost of injected air and the possible efficiency penalty, plus the complexity of the control scheme if it is active, have to be considered and compromised with the obtainable margin of stability improvement.

**3.2 Compressor Performance at Different Operating Speed.** In another comparison, Fig. 6 shows that the compressor stability could be further improved when the micro injection executed at lower operating speed. This is encouraging yet it dictates the need for testing the effectiveness of micro injection on the high-speed machine. While such test will be included in the future work, the worry for the effectiveness may not be that much because the unsteady control mechanism for the micro injection as will be outlined in the following sections is different from that for the classic steady injection.

#### 4 Verification of Unsteady Response

**4.1 Micro Injection at Various Injection Angles.** As shown in Fig. 7, the injector could rotate to either side from the axial direction. The positive and negative injection angles correspond to with and against the direction of rotor revolution. From the result in Fig. 8 and summarized in Table 2, in comparison with the axial zero degree injection, the stability could be further enhanced with  $-15$  deg injection and no effective with  $+15$  deg injection. A simple steady flow explanation that the negative injection angle corresponds to the increase of the flow incidence cannot be the case, because it would increase the flow separation and thus the stability goes to deteriorate. Further attempt of explanation along the same line, but considering that the flow incidence is actually decreasing under the negative injection angle because of the higher velocity of injected flow (e.g.,  $V_{jet} = 64$  m/s for 0.045% injected flow compared to  $V_x = 22$  m/s of the compressor inlet velocity), is not supportive either. Since if this were the case, the flow incidence will be decreasing for all tested injection angles at all injection flow rates covering the negative incidence range so wide that will contradict results for the trend and the effect of stability improvement. In fact, the tiny amount of injection would not be sufficient enough to influence the inlet velocity pattern. Moreover, the injector was positioned so close to the blade leading edge that the measurement of the inlet velocity

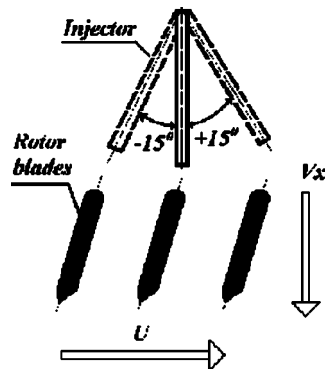


Fig. 7 Various injection angles

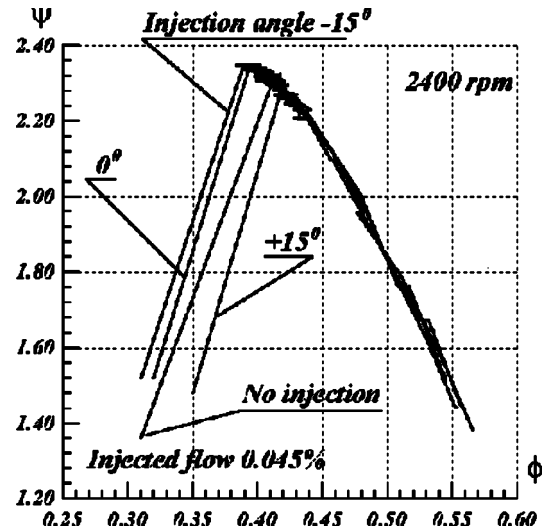


Fig. 8 Compressor performance at various injection angles/2 mm radial penetration, 2 mm axial gap

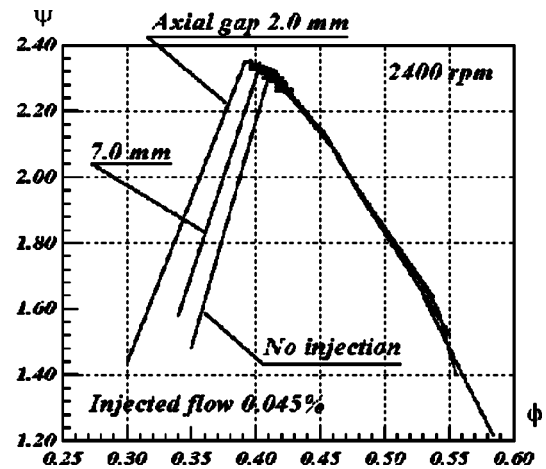


Fig. 9 Compressor performance with different axial location of injectors/0 deg injection, 2 mm radial penetration

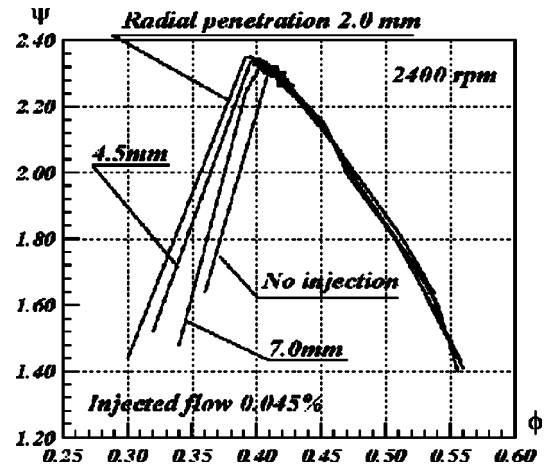


Fig. 10 Compressor performance with different radial penetration of injectors/0 deg injection, 2 mm axial gap

could not detect any change when micro injection occurs and under whatever the injection angles. Therefore the steady flow explanation was finally discarded. One explanation we then postulate is that the injector may act as a pilot high momentum external flow source ( $V_{jet}/U_t=1.02$  for 0.045% injection and  $V_{jet}/U_t=1.27$  for 0.056% injection, where  $U_t$  is the blade speed at tip), being able to suppress the possible early disturbances in the tip region of the compressor, which would otherwise grow up to the stall cells. The small size covered by the injected flow would be just enough to influence the early flow disturbances, which are thought to initiate the evolution process of stall and currently described in detail in the paper of Lin et al. [9]. As four injectors were deployed in the experiment, any initial disturbance will meet the injected flow four times in one rotor revolution, the time which should be sufficient to not let the disturbance to grow. In the following sections, further evidences will be provided to support this postulation.

**4.2 Micro Injection With Different Axial Gap Between Injector and Blade Leading Edge.** Based on the foregoing postulation, one could expect that locating the injector closer to the blade leading edge would increase the effect of injected flow to the flow disturbances in the blade passage. This was indeed the case as shown in Fig. 9 where evident gain of stability for 2 mm axial gap (4.89% decrease of mass flow at stall) was obtained compared with 7 mm gap (3.14% decrease of mass flow at stall). This was the reason in Fig. 8 of previous Section 4.1, that for the sake of more clarity, the comparison was made at 2 mm gap instead of 7 mm. It is also worthy to note that further reducing the gap will lead to the over rotor tip injection scheme which is perhaps another possibility to enhance the effect of micro injection.

**4.3 Micro Injection With Different Radial Penetration of Injectors.** As indicated by some of the previous research and will be also discussed in the CFD analysis in this paper, the tip clearance vortex plays an important role for the stall inception (Hoying et al. [10]). Therefore, if the injector goes further inside from the tip region, the effect of compressor unsteady response to the micro injection would be reduced. Figure 10 shows such comparison that 7 mm radial penetration of the injector indeed diminishes the improving effect of injection (numbers are summarized in Table 2). The result as such could also imply that the compressor is tip critical in relation to the stall inception.

**4.4 Micro Injection With Circumferentially Agglomerated Injectors.** Instead of discrete arrangement, the four injectors were closely spaced circumferentially within 30 deg. As shown in Fig. 11, this agglomerated arrangement reduced the effect of micro injection. A possible explanation is that it reduces the chance any disturbance can face the action of the injector in one revolution time, the point already mentioned in Section 4.1.

## 5 Dynamic Behavior of Unsteady Response

**5.1 Stall Inception Behavior With and Without Injection.** So far the verification of unsteady response outlined in Section 4 was of intuitive character, by proof and disproof approach. However, the result in the next section will provide a direct verification by showing the picture of flow disturbances in the stalling process under various injection configurations. We start from demonstrating the basic behavior of the rotating stall and its inception for the tested compressor. Figure 12 compares the time-domain pressure signals recorded from eight on-shroud pressure transducers (one transducer was in defect and its signal was missing) in front of the first rotor for the cases with and without injection. In both cases, the flow disturbances in a form of short-scale pips in the pressure signals appeared spontaneously, preceded the establishment of stall cells. After the pips became more organized and propagated circumferentially at 0.63 of rotor speed, in less than four rotor revolution times, the stall cells could finally evolved and rotated at 0.4 of rotor speed. Such behavior as can be seen from Fig. 12 is

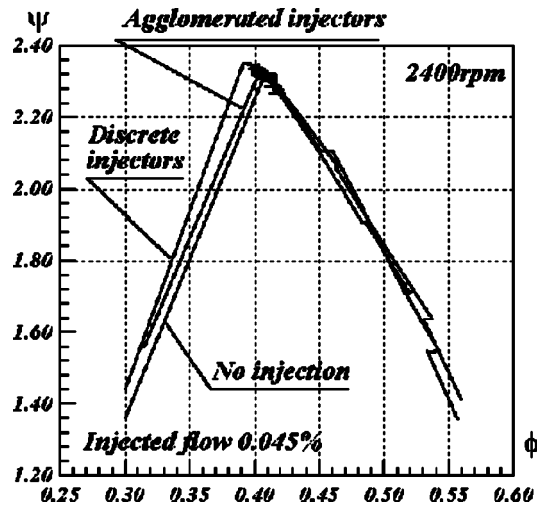
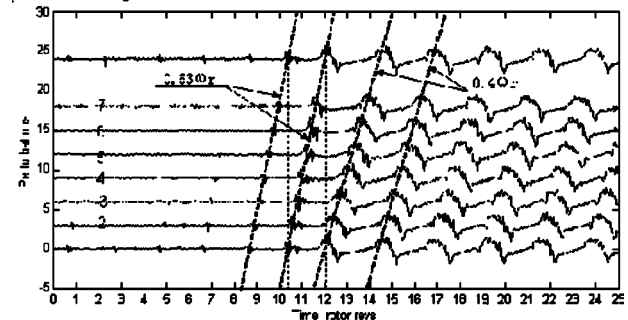


Fig. 11 Compressor performance with circumferentially agglomerated injectors/0 deg injection, 2 mm radial penetration, 2 mm axial gap

the same with and without injection. Corresponding frequency characteristics as shown in Fig. 13 should be also the same for both cases. The dominant frequency component is 40 Hz for rotor speed before stall and 16 Hz for stall cells. This indicates that the micro-injection is able to postpone the stall inception as shown in previous sections but not alter the basic behavior of stall once it appears.

**5.2 Two-Dimensional Wavelet Analysis for Various Injection Configurations.** The objective of this analysis is to uncover the behavior of flow disturbances in the stalling process and find out their link with the effect of micro injection on delaying the stall inception. A two-dimensional wavelet-based method de-

### Without injection:



### With injection:

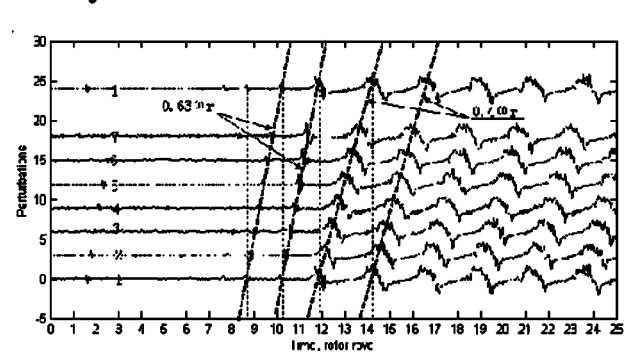
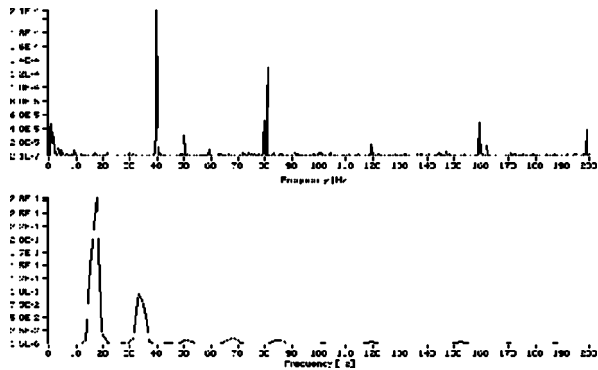
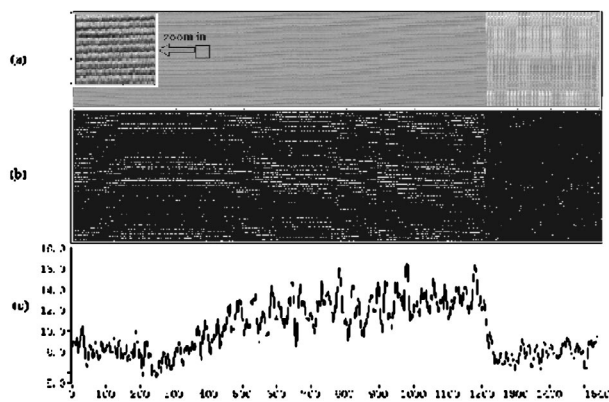


Fig. 12 Pressure signals in the time domain at various circumferential locations with and without injection/2400 rpm



**Fig. 13 Pressure spectra in the frequency domain before and after stall/2400 rpm, without injection**

veloped by Cheng et al. [11] was chosen as the suitable tool for this purpose. This method was aimed to reveal the changing pattern of flow disturbances expressed through different scale of singularities in the signals analyzed. Pressure signals recorded by a single dynamic transducer were first reconstructed to form a time-space (circumferential direction) intensity image interpreted to represent the character of flow changing with time and space. The two-dimensional wavelet transform was then applied for the image processing at different scales so that any weak change of the image can be recognized. In previous research, the method has been successfully tested for capturing early flow disturbances in the stalling process long before the appearance of pips and stall cells. Using this method, Fig. 14 shows the result analyzed for the case without injection. Figure 14(a) is the reconstructed image from pressure signals measured in front of the rotor where the density in the plot represents the value of the pressure with brighter color for higher pressure. The horizontal time scale is in rotor revolution and vertical space scale in a range of one circumference around the compressor. An apparent vertical boundary between the pre-stall and developed stall regions is visible at the time of 1200 rotor revolutions. The black-white strips shown in the magnified portion of pre-stall region are formed by the pressure changes across each blade passage. This image is then processed at different scales using wavelet transform and the spots of singularities can be plotted as seen in Fig. 14(b), which is the result for small scale (about half of the blade pitch) being chosen to represent the behavior of flow disturbances. In order to give a quantitative measure for the numbers of image singularities, the spots are summed up and shown in Fig. 14(c) as a curve of spot quantities over time. The increasing trend of this curve indicates the increase in the number of small-scale disturbances long before



**Fig. 14 Time-space image of pressure signals and image processing via 2-D wavelet transform/2400 rpm, without injection**

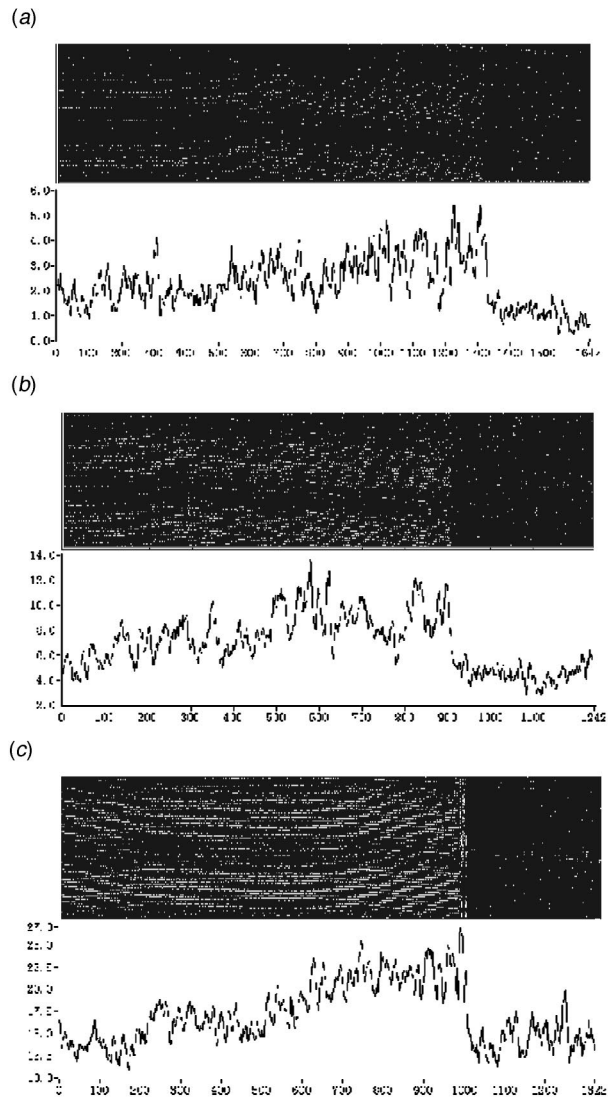


**Fig. 15 Image processing of pressure signals via 2-D wavelet transform/2400 rpm, different injection angles, 2 mm radial penetration, 2 mm axial gap—(a)  $-15$  deg injection, (b)  $0$  deg injection, (c)  $+15$  deg injection**

the final inception of few pips and stall cells as seen from Fig. 12. Once the full stall takes place, the small-scale disturbances evolve abruptly into large-scale stall cells, and therefore the curve in Fig. 14(c) falls down. (A rising curve, not shown here, was obtained when the image processed at large-scale of several blade pitches which represent the scale of stall cells.) In the following analysis, we will focus on the small-scale singularity plots and compare their behavior under different injection configurations. From Fig. 15 for a comparison at different injection angles, judging by the number of bright spots in the plots and by the level on vertical coordinate of the curve, it is evident that the spot quantities are significantly reduced from the cases of  $+15$ ,  $0$ , to  $-15$  deg. This is a clear indication that the corresponding small-scale disturbances are decreasing with the injection angles that have the increasing gain of the compressor stability. Similar results were also obtained when comparing the singularity plots for the injection under different axial gaps and radial penetrations but omitted here for brevity.

## 6 Numerical Study of Unsteady Response

**6.1 Computation Scheme.** Having shown the effect of micro injection on the compressor performance and on the early flow

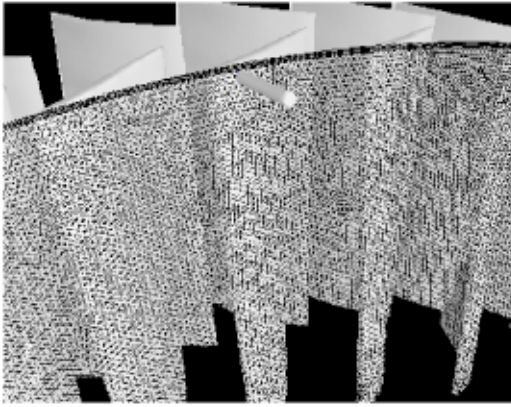


Fig. 16 Computation geometry and grid points on the slipping plan between injector and rotor

disturbances in the stalling process, a question still remains of how the micro injection interacts with the flow in blade passages. Therefore the blade passage flow in the compressor tip region with and without injection was studied by numerical simulation. A three-dimensional unsteady viscous scheme was then applied for one stage of the tested compressor. FLUENT UNS with the standard SIMPLE core method was used. Since the objective of this simulation was simply to reveal the variation of the flow structures under the influence of micro injection, a near stall condition was chosen. This significantly simplified the computation, yet it was still able to capture the key features of the blade passage flow fields with and without micro injection and uncover the influence of such injection on tip clearance vortices, which were considered as the mechanism that triggered the instability. The pressure coefficient of 0.67 was chosen, which was quite close to the stall point in the first stage performance curve of the tested compressor (not shown here for brevity). Based on the actual numbers of four injectors and 60 rotor and stator blades, the computation for the numbers of 1:15:15 can be accepted to simulate the unsteady injector-rotor-stator flow. The speed of injected flow was also given the same as in the test case which is of 3 cu. L/m flow rate per injector. For the unsteady computation, a second-order time accuracy scheme is used and the time resolution in each blade passage is 20 steps. RNG-k- $\epsilon$  turbulence model and a non-equilibrium wall function were applied to simulate the complex tip flow. The computation domain was divided into three subdomains: injector, rotor and stator, with two slipping planes one in-between injector-rotor and the other rotor-stator, and with the rotor sub-domain rotated at 2400 rpm. The grids contain a total of

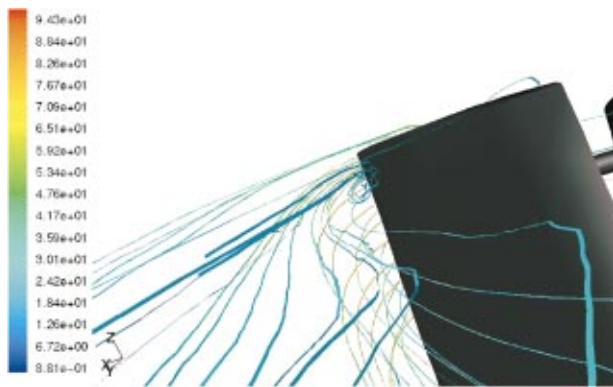


Fig. 17 Three-dimensional view of traces of tip clearance vortex without injection

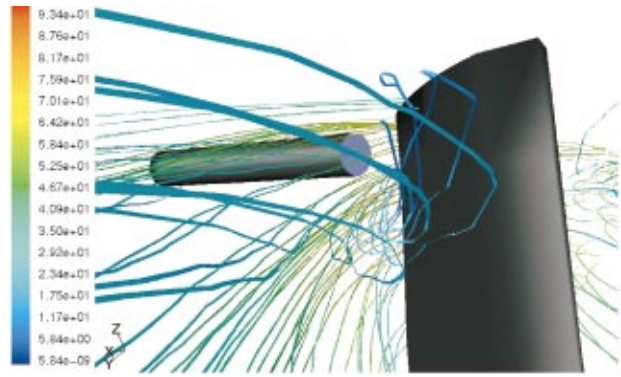


Fig. 18 Three-dimensional view of traces of tip clearance vortex with injection

1490 thousands nodes, with unstructured grids for the rotor blade passage (densified in the vicinity of rotor inlet) and five layers structured grids in the tip clearance region. Figure 16 shows the computation geometry and the grid points on the slipping plan between the injector and rotor.

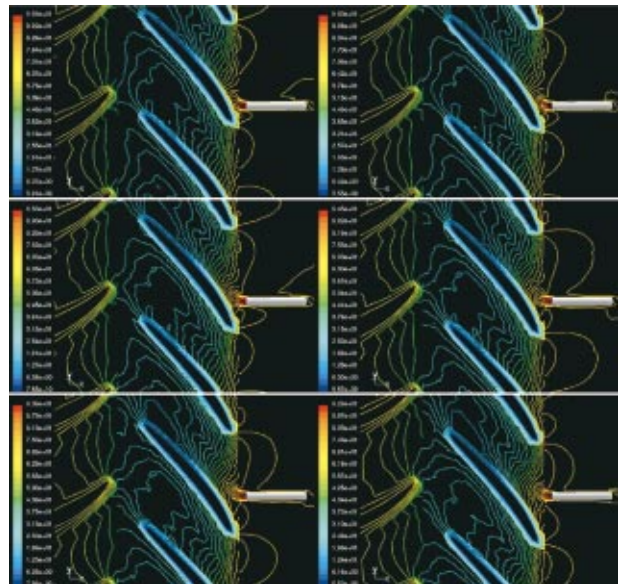


Fig. 19 Instantaneous relative velocity contours

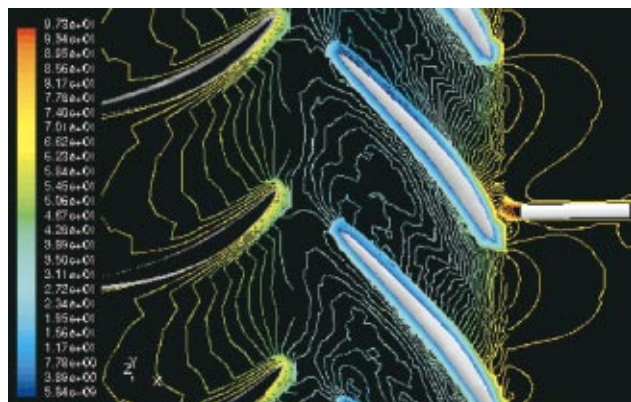


Fig. 20 Localized injected flow scrubbing velocity field near suction surface of blade

**6.2 Computation Results.** We first compare the structure of tip clearance vortex computed for the cases with and without injection. In a three-dimensional view of Figs. 17 and 18, in front of the blade tip region, particle traces are released from a 5 deg sector (the angle of blade-to-blade is 6 degrees) with its relative position fixed to the rotor blade. For the case of no injection as shown in Fig. 17, the tip clearance vortices can be seen near the front part of suction surface of the blade, with their traces further extended downstream and bend at the stator inlet. Other traces also seen in Fig. 17 are tip leakage traces towards the neighboring blade tip and the traces cross blade leading edge towards downstream. Figure 18 is the case with injection chosen for the moment of the apparent effect of injected flow. The picture of the traces in Fig. 18 is generally the same as in Fig. 17, only it is viewed from different angle following the relocation of the tip clearance vortices. However, the location of the vortices with injection is now shifted further downstream obviously pushed by the injected flow. Therefore, as the stall inception is usually accompanied with the tip clearance vortex moving forward, the effect of micro injection in delaying this process could be anticipated. The next question is to what extent the micro injection effects the blade passage flow as a whole. This question could be qualitatively answered from the instantaneous picture of relative velocity contours on the outer blade-to-blade surface of revolution and shown in Fig. 19. Depending on the relative position of injector to the blade passage, the effect of injector is different, but all rather localized (see the magnified picture of velocity contour in Fig. 20), and thus the overall blade passage flow pattern is not influenced.

## 7 Future Work

The authors believe that further clarification of the unsteady flow mechanism under micro injection lies in understanding the blade passage flow details in the tip region of the compressor. One specific question is how the shift of the leakage vortex downstream may lead to the weakening of early flow disturbances. This is also the key issue nowadays in order to elucidate the flow mechanism of rotating stall inception. In this context, as the effect of micro injection was found in relation to the flow disturbances appeared much earlier than any type of stall inception, we believe the outcome of micro injection would be still favorable even if the compressor was modal; but the case was not tested because the compressor did not depict modal type stall inception in present test conditions. On the other hand, in complement to the flow mechanism study, parameter optimization can play the role not only to verify the effect of injection, but also to better locate the injectors and to help designing the practically usable injection scheme. The micro injection scheme also poses a new challenge for the system modeling taken consideration of the interaction between large scale (compression system) and small scale (micro injection) into account. As a result, the role of minor change of boundary condition (micro injection) in changing the behavior of nonlinear compression system would be resolved.

## 8 Conclusions

A new approach, steady micro air injection, is proposed and experimentally verified for its effect on improving the compressor stability. The injection flow rate is only 0.045–0.056% of the compressor main flow and 3.14–5.83% benefit in extending the stability boundary can be attained. In the meantime, the steady compressor characteristic with no injection remains unchanged. This result shows a mechanism of unsteady response of the compressor to the micro injection, which is different from the steady flow understanding so far adopted for the steady flow injection scheme. This unsteady response was proved and interpreted through three different ways: experiment under various injection configurations, wavelet analysis for unsteady flow disturbances and numerical computation at the near stall condition. The main results can be summarized as following:

- Varying the injection configuration, such as injection angles, axial gaps and radial penetration of injector, etc., was implemented as a proof and disproof means for the unsteady response. The experimental result not only verifies the effect of injection and furnishes a way for its further improvement, but also supports a postulation that the compressor responds to the micro injection in such a way that it could clear up the tip flow disturbances before they grow up.
- The two-dimensional wavelet-based method offers a viable tool to capture the flow disturbances appeared much earlier than the final inception of pressure pips and stall cells. It is also able to uncover the behavior of the flow disturbances, judging the time-varying number of singularities obtained through processing the reconstructed pressure image. The result proved the interaction of the micro injection on early flow disturbances that a decreasing number of singularities were obtained corresponding to the injection configuration with the increasing gain of the compressor stability.
- A three-dimensional unsteady viscous flow computation to simulate the injector-rotor-stator flow at near stall condition provides an added interpretation for the mechanism of micro injection in effecting the rotor tip flows. It can be shown that although the effect of injected flow is rather localized in relation to the overall blade passage flow, it could shift the position of tip clearance vortex towards downstream and thus delay the inception of stall.

Encouraged by the results reported herein and with the future research going on, it can be hoped that this new approach could become one of the new choices for improving the compressor stability, a problem of long concern for turbomachine designers.

## Acknowledgment

The research in this paper is funded by the project of National Basic Research Plan and the project of Innovative Research, Chinese Academy of Sciences. These supports are gratefully acknowledged. The authors would like to thank Dr. Choon S. Tan, Dr. Feng Lin and Dr. Liping Xu for their insightful discussions and suggestions. The contribution of Mr. Yuchuan Niu, Zhiting Tong in carrying on the experimental program is also gratefully acknowledged.

## References

- [1] Epstein, A. H., Williams, J. E., and Greitzer, E. M., 1989, "Active Suppression of Aerodynamic Instabilities in Turbomachinery," *J. Propul. Power*, **5**(2), pp. 204–211.
- [2] Greitzer, E. M., 1998, "Smart Jet Engines—Case History of a Multidisciplinary Research Program," *JSME Int. J. Series B*, **41**, No. 1.
- [3] Day, I. J., 1993, "Active Suppression of Rotating Stall and Surge in Axial Compressors," *ASME J. Turbomach.*, **115**, pp. 40–47.
- [4] Goto, A., 1994, "Suppression of Mixed-Flow Pump Instability and Surge by the Active Alteration of Impeller Secondary Flows," *ASME J. Turbomach.*, **116**, pp. 621–634.
- [5] Behnken, R. L., Leung, M., and Murray, R. M., 1997, "Characterizing the Effects of Air Injection on Compressor Performance for Use in Active Control of Rotating Stall," *ASME 97-GT-316*.
- [6] Weigl, H. J., Paduano, J. D., Frechette, L. G., Epstein, A. H., Greitzer, E. M., Bright, M. M., and Strazisar, A. J., 1998, "Active Stabilization of Rotating Stall and Surge in a Transonic Single Stage Axial Compressor," *ASME J. Turbomach.*, **120**, pp. 625–636.
- [7] Suder, K. L., Hathaway, M. D., Thorp, S. A., Strazisar, A. J., and Bright, M. B., 2000, "Compressor Stability Enhancement using Discrete Tip Injection," *ASME 2000-GT-650*.
- [8] Xu, G., Cheng, X., Nie, C., and Chen, J., 2001, "Unsteady Response to the Tip Injection in a Low-Speed Axial Compressor," *Proc., 5th ISAIIF*, Vol. 1, pp. 349–358, Gdansk, Poland.
- [9] Lin, F., Chen, J., and Li, M., 2001, "Experimental Investigation on Unsteady Rotor Tip Flows in a High Speed Compressor Throttled to Stall," *ASME 2002-GT-30360*.
- [10] Hoying, D. A., Tan, C. S., Vo, H. D., and Greitzer, E. M., 1998, "Role of Blade Passage Flow Structures in Axial Compressor Rotating Stall Inception," *ASME 98-GT-588*.
- [11] Cheng, X., Chen, J., and Nie, C., 1999, "Investigation on the Precursor Behavior of Compressor Rotating Stall through Two-Dimensional Wavelet Transform," *Proc. ICET*, pp. 278–284, Beijing, China.

# Turbofan Performance Deterioration Tracking Using Nonlinear Models and Optimization Techniques

**K. Mathioudakis**  
Associate Professor

**Ph. Kamboukos**  
Research Assistant

**A. Stamatis**  
Research Associate

Laboratory of Thermal Turbomachines,  
National Technical University of Athens,  
Athens 15710, Greece

*A method of identifying the gradual deterioration in the components of jet engines is presented. It is based on the use of an engine model which has the capability to adapt component condition parameters, so that measured quantities are matched. The main feature of the method is that it gives the possibility to identify performance deviations in a number of parameters larger than the number of measured quantities. This is achieved by optimizing a cost function which incorporates not only measurement matching terms, but also terms expressing various constraints resulting from the physical knowledge of the deterioration process. Time series of data representing deterioration scenarios are used to demonstrate the method's capabilities. The test case considered is a twin spool partially mixed turbofan, representative of present-day large civil aeroengines. Implementation aspects, related to both the measurement set and the identification algorithms are discussed. An interpretation of the output of the method in function of different parameters entering the diagnostic problem is presented. [DOI: 10.1115/1.1512678]*

## Introduction

Deterioration of the performance of jet engines with time results from a number of physical mechanisms. The ability of the user to identify the current condition of a deteriorated engine is a key factor to ensuring reliable operation and optimal usage.

The ability to forecast deterioration and the importance of producing models providing such a possibility has been discussed by Zaita et al. [1]. Using existing information, they have proposed a method to incorporate the effect of various deterioration mechanisms in individual component performance models as well as into the overall engine model. The work was motivated by the need to assess engine capability and overall mission performance for various environments at different instants in the engine life.

A different view point is taken when an existing engine in service deteriorates with time. The possibility to identify the amount of deterioration of individual components and assess its effect on overall performance provides information, which is valuable for improving cost effectiveness of maintenance actions.

Condition monitoring and diagnostic techniques using aerothermodynamic performance data, is the means to obtain such information. Doel [2] has commented on the features of approaches used, while presenting a particular analysis tool that can be used for this purpose. Performance diagnostic methods for identifying deterioration have also been presented by Barwell [3], Urban and Volponi [4], and Volponi [5].

Finally, an area of interest to the engine designer is the incorporation of condition tracking algorithms in engine controls. The desire is to optimize engine control, by taking into account the current engine condition, providing thus improved control capability for more efficient operation and longer life. Lietzau and Kreiner [6] have discussed controls related aspects.

The present paper introduces a method that allows the identification of the condition of a deteriorated engine, from existing measurement data records. It offers several advantages over other methods used today, mainly because of its ability to track deteriora-

tion using a limited number of measurements for relatively large deterioration levels and without the need for a-priori estimation of component condition parameters.

Before presenting the method a brief overview of existing works related to engine deterioration is given, in order to be able to assess some of the considerations used in our formulation.

## Deterioration Mechanisms

Deterioration of jet engine performance is caused by several mechanisms, which are different for the different engine components.

The main types of geometry changes causing compressor performance deterioration are tip clearance increase, airfoil shape change and surface quality change. Rubs can be responsible for clearance changes, erosion and corrosion can change airfoil shape and surface quality, while fouling changes mainly surface quality and secondarily shape. Turbines suffer from the same main types of changes, but in this case shape changes have a more direct and pronounced effect on swallowing capacity. Vane trailing edge bowing and trailing edge erosion are effects that may increase swallowing capacity, while affecting efficiency at the same time. Swallowing capacity can decrease in the case deposits are formed on the airfoils surface. Combustors, finally, do not usually contribute substantially to performance deterioration. A common feature of all cases is the reduction in component efficiency. Swallowing capacity reduces for compressors while it can either reduce or increase in turbines.

Different causes and mechanisms of performance deterioration of jet engines are reviewed in [1]. Degradation in both land and aero gas turbines is also reviewed by Kurz and Brun [7], who pointed out differences in mechanisms for the two types. Industrial gas turbine deterioration has been discussed by Diakunchak [8].

Concerning now the overall effect of deterioration on engine performance, a number of works has been published over the years. Work has been performed during the 1970s and early 1980s at NASA, mainly on the JT9D and CF6 engines. Olsson and Stromberg [9], for example, have reported overall trends in performance deterioration and the repartition of deviations to the engine components. Similar information about the CF6 has been

Contributed by the International Gas Turbine Institute and presented at the International Gas Turbine and Aeroengine Congress and Exhibition, Amsterdam, The Netherlands, June 3–6, 2002. Manuscript received by the IGTI, November 11, 2001. Paper No. 2002-GT-30026. Review Chair: E. Benvenuti.

reported by Fasching and Stricklin [10]. Work has been done in other organizations also, as for example reported by Sasahara [11] and Danielsson [12] for the JT9D and Glennly [13] for a helicopter engine. All these works contain data on engine deterioration with time, which provide information exploited later in the present paper.

### A Model as a Tool Supporting the Diagnosis

The technique presented here relies on the existence of an engine performance model, that can simulate operation of either healthy or faulty engine.

For the purpose of the present analysis an engine is considered as a system, whose operating point is defined by means of a set of variables, denoted as  $u$ . The health condition of its components is represented through the values of a set of "health" parameters, contained in a vector  $f$ . The system is observed through measured variables (speeds, pressures, temperatures, etc.), contained in a vector  $Y$ . The operating engine establishes a relationship between these parameters, which can be expressed through a functional relation:

$$Y = F(u, f) \quad (1)$$

A computer model materializing this relation can reproduce the values of any thermodynamic quantity measured along the engine gas path. It is interesting to note that by assigning appropriate values to the components of vector  $f$ , the effect of engine component faults or deterioration on measured quantities can be reproduced.

A schematic representation of the generation of measurements by an engine model, simulating healthy or faulty engine performance is shown in Fig. 1. A specific engine performance model, described by Stamatis et al. [14], will be employed for illustrating the method proposed here. It represents a twin spool, partially mixed turbofan, with a configuration typical of contemporary

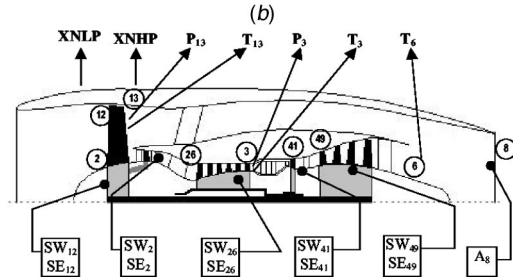
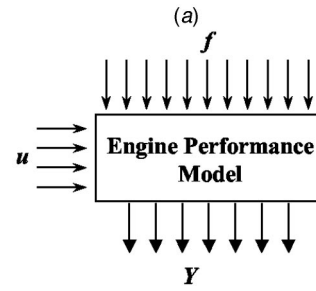


Fig. 1 (a) Generation of measured quantities by a model, (b) example set of measurements and parameters on a civil turbofan

large civil engines. Measurements that can be taken from the turbofan and can also be produced by the model are shown in the lower part of Fig. 1.

This particular set of measurements, being representative of a measurement set in today's engines of this type, will be used in the test cases reported in the paper. Noise is added to model predictions to simulate actual measurements. Gaussian noise is employed with standard deviation for each measurement as follows:

Sensor	$P_{amb}$	P1	T1	WFE	XNLP	XNHP	$P_{13}$	$P_3$	$T_3$	$T_6$	$T_{13}$
3 sigma	100 Pa	100 Pa	2 K	2 gr/S	6 rpm	12 rpm	300 Pa	5 KPa	2 K	2 K	2 K

These values are representative of current measurement possibilities.

Parameters employed to characterize the condition of each component are a flow factor SW and an efficiency factor SE. They determine how component flow capacity and efficiency are modified with respect to a reference condition. For a component with entrance at station  $i$  of the engine, we define

$$\text{Flow factor: } SW_i = (W_i \cdot \sqrt{T_i/p_i}) / (W_i \cdot \sqrt{T_i/p_i})_0 \quad (2a)$$

$$\text{Efficiency factor: } SE_i = \eta_i / (\eta_i)_0 \quad (2b)$$

These factors for all engine components constitute the vector  $f$  and are shown in Fig. 1. The use of such factors for describing the health condition of engine components has been discussed by Stamatis et al. [15].

### Condition Determination: Formulation of the Nonlinear Diagnostic Problem

The purpose of a diagnostic method is to determine the values of component health parameters of an engine (vector  $f$ ), when a set of measured quantities (vector  $Y$ ) is available for given operating conditions (vector  $u$ ). The first condition used to set up a system of equations for solving such a problem is the requirement that the quantities measured on the engine are reproduced in the

best possible way. A mathematical condition expressing this requirement is that the following expression must obtain a minimum value:

$$OF_Y = \sum_{i=1}^M \left( a_i \frac{Y_i^{calc} - Y_i^g}{Y_i^g} \right)^2 \quad (3)$$

Coefficients  $a_i$  can be chosen appropriately to give more weight to measurements with smaller uncertainty. For a given operating point and set of measurements  $Y^g$  this expression is a function of health parameters. The values of health parameters can thus be determined by solving an optimization problem.

The possibility to derive a unique solution for  $f$  depends on how the number  $M$  of independent measurements is related to the number  $N$  of unknown  $f$  components.

- If  $N \leq M$ , the least-squares problem of minimizing  $OF_Y$  is solved and a unique solution is derived. For  $N = M$ , an alternative is to solve the system of  $M$  nonlinear equations  $Y(f) = Y^g$ , (zero minimum for  $OF_Y$ ).
- If  $N > M$ , then an infinite number of solutions exist. By as-

signing to  $N-M$  components of  $f$  arbitrary values,  $M$  equations can be solved to produce a unique solution for the remaining  $M$  components.

Unfortunately this last situation is usually encountered in practice: a limited number of measurements is available, while a larger number of health parameters needs to be determined for fully characterizing the condition of the engine. In order to be able to produce a solution for  $f$  some additional relations are needed.

The choice of additional relations will be guided by the particular properties of condition changes for engine deterioration:

- (a) Performance parameters of all components decrease, apart from turbine flow functions which can either decrease or increase.
- (b) Changes are gradual, namely the values of health parameters change slowly with time and abrupt changes are not expected.

These general features make a distinction between deterioration identification and component fault detection: component faults are usually concentrated around one particular component or area of the engine and may appear suddenly.

Condition (a) gives a set of inequalities that have to be satisfied by the solution and thus bound the search domain for a solution

$$\Delta \eta \leq 0 \text{ for all components, } \Delta q \leq 0 \text{ for compressors} \quad (4)$$

These constraints are implemented in the optimization procedure described later though the evaluation of appropriate penalty functions.

Condition (b) can be materialized through a probabilistic reasoning. For example, if parameters are assumed to be Gaussian random variables the most probable variation will have to minimize a norm of vector  $f$ . An example of such a norm is:

$$OF_f = \sum_{j=1}^N \left( b_j \frac{f_j - f_j^r}{f_j^r} \right)^2 \quad (6)$$

Coefficients  $b_j$  can be used to give more weight to parameters with smaller uncertainty. This last requirement is the one used for formulation of Kalman-type methods (as, for example, described in [2]). It must be commented here that this is a rather arbitrary condition and is simply related to statistics of the quantities involved. It does not necessarily reflect the physics of the deterioration process. It can, however, lead to realistic parameters estimation, if it is satisfied simultaneously with the requirement of minimal measurements deviations, Eq. (3).

In view of these facts, an approach of minimizing a function produced by a combination of the expressions of measurements deviations and minimum norm of  $f$  would be expected to provide the means for estimating the components of  $f$ . From studies in estimation theory, it has been found that it is useful to include in the objective function a term of sum of absolute values, since this term may improve the numerical behavior of the estimation procedure by increasing its robustness (see related comments by Grodent and Navez [16]). The function that was chosen to be minimized after taking into account all the previous considerations is as follows:

$$F = \sum_{i=1}^M \left[ \frac{Y_i^{\text{calc}}(f) - Y_i^g}{Y_i^g \sigma_{Y_i}} \right]^2 + C_A \cdot \sum_{j=1}^N \left| \frac{f_j - f_j^r}{f_j^r \sigma_{f_j}} \right| + C_S \cdot \sum_{j=1}^N \left[ \frac{f_j - f_j^r}{f_j^r \sigma_{f_j}} \right]^2 \quad (7)$$

All deltas are weighted by the inverse of the standard deviation of the corresponding quantity. Weight factors  $C_A$ ,  $C_S$  are also included, for the possibility to change the relative importance of the two groups of terms. The reference values  $f^r$  of the health indices can be chosen to represent a "best" guess of the values to be determined. An obvious first guess would be the values for the healthy engine  $f^0$ .

## Implementation of a Solution Algorithm

We will now discuss some particular features of the procedure we employ for implementation of a minimization algorithm and the derivation of a diagnosis.

**Measurement Smoothing.** Smoothing measurement data prior to feeding them to the diagnostic algorithm significantly improves its performance. The smoothing operation that is used here is applied on the values of measurements deltas and not on the measurements themselves.

The first reason for this choice is that the raw measurements arriving from the engine vary not only because of noise but also because of operating point variation. If the measurements were smoothed directly, this variation should be taken into account by an appropriate model. Using deltas eliminates this need, because the dependence of delta on the operating point is very weak when neighboring operating conditions are considered. Additionally, deltas characterize the phenomena to be identified (deterioration), by exhibiting a consistent evolution with usage time of the engine.

It is recalled here that a measurement delta is defined as follows:

$$\Delta Y = 100 \times \frac{Y - Y^0}{Y^0} \quad (8)$$

$Y^0$  is the value that  $Y$  would obtain if the engine is at a known condition (for example, new and clean). It is provided by an engine simulation model, for the same set point parameters (vector  $u$ ) as those corresponding to  $Y$ .

An example of variation of a measured quantity and its delta is shown in Fig. 2. The actual measurement undergoes a significant variation, even though data from typical cruise are considered. Observation of the value itself does not reveal clearly the presence of deterioration. The delta on the other hand shows a clear trend corresponding to the engine deterioration. If a dependence on operating point exists, it is very weak and anyway smaller than the level of noise. We consider thus that

$$\Delta Y = \Delta Y(f), \quad f = f(t)$$

where  $t$  is the time of usage of the engine (that could be expressed as hours of operation, number flight cycles or other suitable quantity)

A further consideration for measurement deltas is that since they represent small deviations from a known condition, they can be assumed to relate linearly to component parameter deviations

$$[\Delta Y] = [J] \cdot [\Delta f] \quad (9)$$

$[J]$  is the Jacobian matrix for the operating point considered. This relation implies that if component parameter deviations  $\Delta f$  vary in a certain way with usage time, the above relation will establish the way of variation of  $\Delta Y$ .

Coming now to the way  $\Delta f$  vary with time of usage of the engine, it can be claimed that their variation with time can be considered to be of the form of a low degree polynomial, a linear approximation being rather satisfactory. This point is supported by published data [9–13]. On this basis, data from a deteriorating

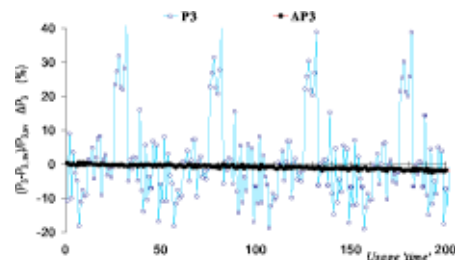


Fig. 2 Time evolution of  $p_3$  and  $\Delta p_3$  on a deteriorating engine



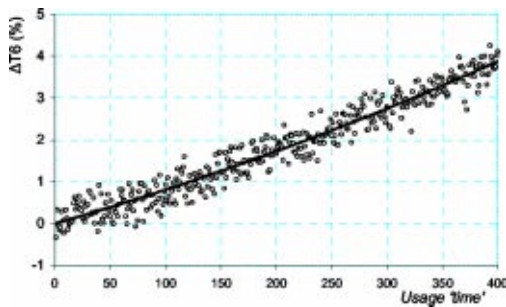


Fig. 3 Time evolution of  $\Delta T_6$  and best fit line for smoothing

engine, at certain operating conditions, can be smoothed by passing through them a best fit line. An example of the time evolution of delta of a measured quantity and the best fit line used to smooth the data is shown in Fig. 3.

Once a smooth evolution has been established, measurements are reconstituted from the reference values and the smoothed delta at each instant in time

$$Y_i^{\text{smooth}} = Y_i^0 \cdot \left( 1 + \frac{\Delta Y_i^{\text{smooth}}}{100} \right) \quad (11)$$

**Choice of Reference Values  $f^r$ .** A feature of weighted least squares is the dependence of the obtained solution on the initial value of health coefficients. The initial values are taken into account in the form of the components of vector  $f^r$  in Eq. (6). If, for example,  $f^r$  is taken to be equal to  $f^0$ , namely the values for an intact engine, the solution that will be derived will essentially involve nonzero terms in Eq. (6). For measurements from a faulty engine, zeroing of the measurements term would require the parameters to be different from those of the healthy engine and therefore the parameter term to be nonzero. This of course does not exclude the possibility to obtain a correct solution. Even though the parameter term will be nonzero, it is possible that the correct solution is achieved, if it corresponds to the nonzero minimum of the corresponding terms. This is demonstrated in a particular example we use for interpretation of the method results, presented in the Appendix.

On the other hand, if  $f^r$  has the values of the parameters that correspond to the faulty condition by which the measurements were generated, then the solution will provide exactly these values. For these values the objective function becomes zero, which is essentially its global minimum, as it is a positive defined function. In this respect the closer the initial estimations of  $f^r$  to the actual solution, the closer the estimated values will be to the solution.

These facts are taken into account in the way we choose to update the values of  $f^r$  as successive estimations with time are performed. When an engine deteriorates with usage, the condition of the components changes very slowly. This suggests that a good choice for reference factors at each time instant is the value of the

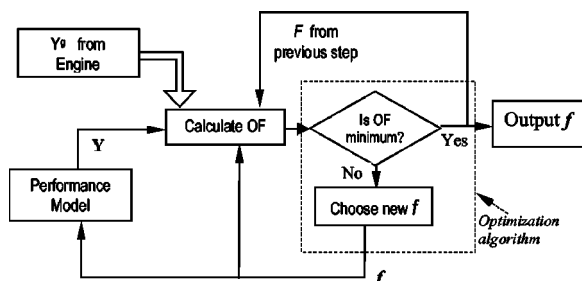


Fig. 4 Procedure for health parameters determination

same factors obtained at the previous time instant. Actually, instead of using the raw estimation at the latest point a filter is applied to the previously estimated values to derive the reference for the current estimation. The flow chart of the procedure for each point in time is shown in Fig. 4.

The approach followed here has two features different from existing linear gas path analysis tools: It is purely nonlinear, as it uses the engine nonlinear model for deltas estimation and it includes explicit weight terms  $C$  which add flexibility to the estimation process.

### Application of the Method

In order to examine how the method performs, it has been tested on a set of data representative of actual engine deterioration. The data have been produced in the frame of a European research project (Curnock [17]) and represent deterioration trends similar to ones actually observed on engines in service. Four hundred data points are provided, representing some typical flight profiles, repeated as an engine deteriorates over time. The typical set of seven measured aforementioned quantities (Fig. 1) has been used as an input to the method.

The results of the estimation by this method, compared to the actual component parameter trends that produced the measurements are shown in Fig. 5. Most parameter trends are closely followed. The accuracy of prediction of the final values of the individual health parameters at the end of the examined period can be assessed from inspection of Fig. 6. It is observed that the component deterioration magnitude is closely estimated.

In order to understand why some parameters are closely estimated while others are not, the response of the algorithm to unit deviations of individual parameters has been examined. Figure 7 shows the values of parameters estimated by processing measurement produced by the engine model, with each individual health parameter disturbed by 1%. The elements of the matrix in this figure can be interpreted as follows:

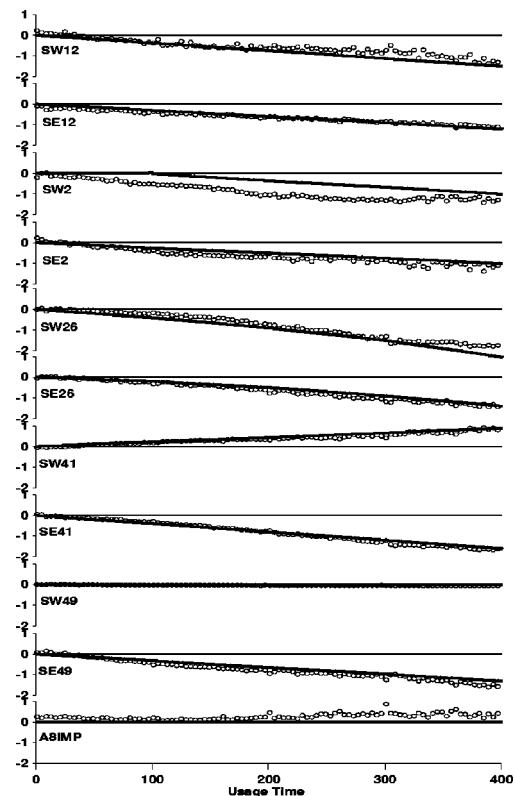


Fig. 5 Actual and estimated health parameters evolution in a deteriorating engine (—actual, ○ estimated)

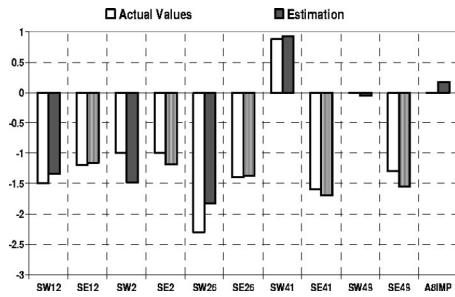


Fig. 6 Comparison of actual and estimated health parameters at the end of the period analyzed

- Inspection of rows reveals the possibility of the method to identify isolated changes. If a row contains only a value close to 1 for the changed parameter and very small values of the remaining ones, e.g., SW12, SE12, then this parameter would be well identifiable, when it deviates alone. This would be for example the case of an isolated component fault. Parameters which are not well identifiable as stand alone deviations, such as SE2, SW2, spread information to neighboring ones. This implies that other deviations will not be clearly identifiable if all parameters are expected to vary, as in the case of deterioration.

- Inspection of columns, shows if the estimation of a particular parameter is influenced by deviations on other parameters. This is an indication on how good the estimation will be when more deviations are present. SE12 and SE41 are the ones that are expected to be most clearly identified, while SW2, SW26, SE26, SW49 are expected to be much depending on the values of other deviations rather than their own.

Since this matrix provides a picture of the diagnostic ability of the algorithm for both isolated faults and generalized deterioration, it will be termed *diagnostic response matrix*. It would ideally be equal to the identity matrix.

A result that gives an indication of the importance of these effects is the estimated values for a case that all parameters have simultaneously changed by 1%, and is shown in Fig. 8. Parameters that contain different contributions in the columns of Fig. 7 are the ones exhibiting the largest difference from the actual value. These observations indicate that looking at the response to measurements produced by disturbing individual parameters (as for example done by Doel [18]) may be an indicator as to how a method responds to individual component faults but cannot indicate response to deterioration, when all components deviate.

Coming back to Fig. 7, a result which may be surprising at a first glance is that some parameters are very accurately estimated. It is known that weighted least squares tend to spread more the estimated deviations of single component parameters. The present authors assess that the improvement in concentrating estimated values is due to some features particular to the present approach. Using weight coefficients on the terms containing parameter del-

Disturbed	Estimated values										
Parameter	SW12	SE12	SW2	SE2	SW26	SE26	SW41	SE41	SW49	SE49	ASIMP
f1: SW12	-1.006	0	-0.001	0	0	0	-0.001	0	0	-0.001	-0.006
f2: SE12	0	-1.000	0	0	0	0	0	0	0	0	0.001
f3: SW2	-0.127	0	-0.051	-0.006	-0.453	-0.145	0.054	-0.002	-0.389	-0.003	-0.104
f4: SE2	0	0	-0.824	-0.338	-0.280	-0.277	-0.001	-0.001	0.250	-0.004	0.000
f5: SW26	-0.001	0	-0.001	0	-0.999	0	0	0	0.001	0.000	-0.001
f6: SE26	0	0	-0.001	0	0	-1.000	0	0	0	-0.001	0
f7: SW41	-0.001	-0.005	0	0	0	0	-1.000	0	0	0	-0.002
f8: SE41	0	-0.005	-0.007	0	0	0	-0.001	-0.995	-0.061	-0.047	-0.003
f9: SW49	0	0	0	0	0	0	0	0	-0.999	0.001	0.001
f10: SE49	-0.006	0	-0.001	0	0	0	-0.001	-0.002	0.004	-0.999	-0.006
f11: ASIMP	0	0	0	0	0	0	0	0	0	0	-1.000

Fig. 7 Estimated health parameter deviations, for data produced from unit disturbances on every individual parameter



Fig. 8 Estimated parameter deviations, for measurements produced by disturbing all health parameters by 1%

tas is such a feature. It was found that very small values of this coefficient produce more accurate estimates. For such values minimization of the objective function requires predominantly minimization of measurement deviations. This means that practically all measurement deviations must be close to or equal to zero, implying that solutions will lie on the hypersurface defined by this set of equations. The final solution is then found as the point on that surface with a minimum distance from the reference condition, as expressed through the norm used. The expression for this norm was also found to influence the estimation accuracy.

In order to facilitate the understanding of the behavior of the solution to the diagnostic problem considered here, an interpretation of the behavior of weighted least squares in comparison to the accurate solution of the diagnostic problem is given in the Appendix.

## Discussion

The results presented above were derived using a certain formulation of the solution algorithm. We will now discuss some aspects with respect to the general validity of the procedure.

First, linear functions were used for smoothing of the input data. This is not a limitation, since any kind of function can be employed. It must be pointed out, however, that the linear function can always be used as long as small deviations are considered. This means that if the procedure is applied before deterioration becomes very severe, the linear approximation is sufficient. A piecewise linear approximation can be used for any kind of deviation.

The approach proposed is useful for estimating the condition of individual components, and thus giving the possibility to have at any moment along the engine life an adapted model accurately representing engine operation. Such a model is useful for adjusting engine operating limits but also for adapting control schedules for optimal operation. The question is how many points are necessary for producing a picture of engine deterioration. For the noise levels used in our investigation, it was found that at least 50 points are needed before the deterioration rate can be captured. Sample results for two parameters are shown in Fig. 9, from estimations based on 50, 100, 200, 300, and 400 points. Evolution of some parameters is captured very precisely even with a small number of points while for others a larger number of points is needed. Estimation is better for parameters that can be better identified, according to the observations made on the diagnostic response matrix, in the previous section.

The accuracy of estimation of the method presented may be significantly improved if additional measurements are used. The estimation results presented above were based on the typical set of seven measurements. When the method was tested on different deterioration scenarios, this time involving a change of LPT flow function, it was observed that change of this parameter cannot be captured from this set of measurements. Addition of pressure measurements at HP compressor inlet and between the turbines gave the possibility to capture this parameter too ([2] reports that such

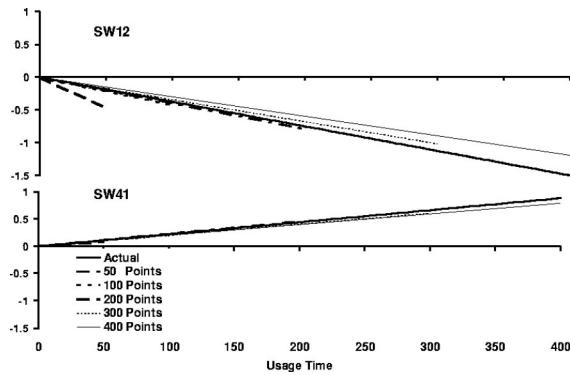


Fig. 9 Deterioration estimation based on different numbers of data points (different instants along the engine life)

measurements can be done on-wing). Estimations of SW49 using 7 and 9 measurements are shown in Fig. 10. The clear improvement with the additional measurements is observed.

The possibility to derive accurate information about all component parameters from a limited number of measurements has been demonstrated by the research group of the present authors, through the technique of gas path analysis at discrete operating points (Stamatis et al. [19]). Data from a limited number of sensors at several discrete operating points can be exploited, to derive a larger number of parameters. The potential of this method has been further examined in recent studies (Kobayashi and Simon [20], Groenstedt [21], Gulati et al. [22]). In the present study data from neighboring operating conditions were used. Even though deltas have a dependence on operating point, such a dependence has been assumed to be weak and comparable to the level of noise, in the present case. Therefore no attempt was made to examine the possibility of exploiting discrete operating points data for parameter estimation.

Finally, in the investigation reported in the foregoing, it has been assumed that the measurement data are free from sensor errors (bias). It is assumed that data have already passed a first check and reading errors have been recovered. The method can also cope with the detection of measurement errors, in the same way as linear methods. The values of the weight parameter  $C$  would have to be adjusted for optimizing the ability of detecting sensor errors. Sensor error detection is favored by larger values of this parameter. Such an investigation, however, is beyond the scope of the present paper. The only comment is that the possibility to vary relative weights through parameter  $C$  may provide an additional flexibility to existing techniques.

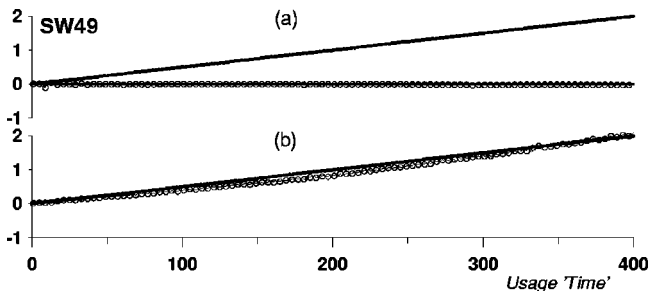


Fig. 10 LPT deterioration estimation by using (a) 7 measurements, (b) 9 measurements. (—actual, ○ estimated)

## Conclusions

A method for assessing the condition of an engine due to gradual performance deterioration has been presented. The method is based on a nonlinear optimization procedure, with a formulation of the least-squares type.

It was shown that by smoothing the deltas of measurements at certain operating conditions and using a recursive estimation of health parameters, it is possible to achieve good estimations for a measurement data set typical of engines in service today. The accuracy of the estimated values can be improved when additional measurements are used.

A way of assessing the diagnostic potential for either isolated faults or generalized deterioration was introduced, though the observation of the “diagnostic response” matrix.

A simplified formulation was used to interpret the behavior of solutions of methods of this type and explain the mechanism of their derivation.

Various aspects of implementation of the method, related to its practical application were discussed.

## Acknowledgments

The work for this paper has been carried out in the frame of project BR PR CT 97-0601 (OBIDICOTE) and financial support of the Commission of the European Union is gratefully acknowledged.

## Nomenclature

A8IMP	= exhaust area
EPM	= engine performance model
HPC	= high-pressure compressor
HPT	= high-pressure turbine
LPT	= low-pressure turbine
$f$	= vector of engine component health parameters
$P_i$	= total pressure at station $i$ of engine
$SE_i$	= efficiency factor (Eq. 2(b))
$SW_i$	= flow factor (Eq. 2(a))
$T_i$	= total temperature at station $i$ of engine
$u$	= vector of quantities defining operating point
WFE	= fuel flow rate
$W_i$	= mass flow at position $i$ of engine
XNHP	= high-pressure shaft rpm
XNLP	= low-pressure shaft rpm
$Y$	= vector of measured quantities
$\Delta Y$	= percentage deviation of magnitude $Y$ from nominal value, Eq. (8)
$\eta_i$	= efficiency of component with entrance at station $i$
$\sigma_f$	= normalized standard deviation of $f$
$\sigma_y$	= normalized standard deviation of $Y$

## Subscripts, Superscripts

0	= quantity referring to intact engine
$g$	= given value of quantity, e.g., from measurement
$i$	= position along engine, Fig. 1

## Appendix

**Interpretation of Weighted Least-Squares Solutions.** The behavior of the solution to the problem of minimization of Eq. (6), in function of the values of the parameters contained in this expression, can be understood by considering a simplified situation, with one measurement and two unknown component parameters.

We consider the engine used as a test case in the paper and we consider the following situation: We want to monitor the condition of the HP turbine through the measurement of compressor delivery pressure  $P_3$ . In order to be able to derive an analytical solution, we consider that we have small deviations and we use only

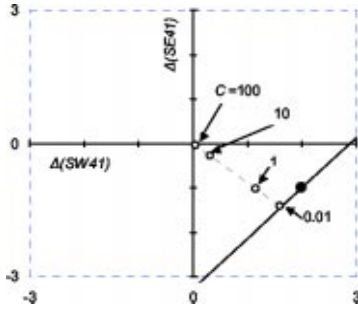


Fig. 11 Solution of minimizing Eq. (12), for different values of  $C$ ; (— line for given  $\Delta P_3$ . - - - locus of solutions. ● actual fault)

the sum of squares in expression (6). The function that has to be minimized, in order to obtain  $f_7$  and  $f_8$  ( $SW_{41}$  and  $SE_{41}$  for our test case) is the following:

$$OF = \left( \frac{P_3}{P_3^g} - 1 \right)^2 + C \left[ \frac{\sigma_{f_8}^2}{\sigma_{f_7}^2} \left( \frac{f_7}{f_7^r} - 1 \right)^2 + \left( \frac{f_8}{f_8^r} - 1 \right)^2 \right] \quad (12)$$

The standard deviation  $\sigma_{p_3}$  has been omitted in this expression, as it has been included in the constant  $C$  which express the relative magnitude of the two terms to be minimized.  $C$  also embeds  $\sigma_{f_8}^2$ , as the investigation that follows has shown that it is the relative weights of the terms in the brackets that matter and not their absolute values. Minimization of this expression is equivalent to satisfying the equations

$$\frac{\partial(OF)}{\partial f_7} = 0, \quad \frac{\partial(OF)}{\partial f_8} = 0 \quad (13)$$

The assumption of small derivations allows the expression of  $P_3$  derivations in terms of  $SW_{41}$  and  $SE_{41}$

$$\Delta(p_3) = J_1 \Delta f_7 + J_2 \Delta f_8 \quad (14)$$

$$\text{where: } J_1 = \frac{f_7^0}{P_3^g} \cdot \frac{\partial p_3}{\partial f_7}, \quad J_2 = \frac{f_8^0}{P_3^g} \cdot \frac{\partial p_3}{\partial f_8}$$

Using Eq. (A1), and substituting for  $\Delta p_3$  from Eq. (14). Eqs. (13) give a linear system of equations, with unknowns  $\Delta f_7$  and  $\Delta f_8$ .

An analytical solution is given as an example. For the case of equal standard deviations, the system of Eqs. (13) becomes

$$\begin{aligned} (J_1^2 + C) \Delta f_7 + J_1 J_2 \Delta f_8 &= J_1 \Delta Y^g + C \Delta f_7^r \\ J_1 J_2 \Delta f_7 + (J_2^2 + C) \Delta f_8 &= J_2 \Delta Y^g + C \Delta f_8^r \end{aligned} \quad (15)$$

and its solution

$$\Delta f_7 = (J_1 \Delta Y^g + (J_2^2 + C) \Delta f_8^r - J_1 J_2 \Delta f_7^r) / (J_1^2 + J_2^2 + C)$$

$$\Delta f_8 = (J_2 \Delta Y^g + J_1 J_2 \Delta f_7^r - (J_1^2 + C) \Delta f_8^r) / (J_1^2 + J_2^2 + C)$$

$$\text{where } \Delta f_i^r = (f_i^r - f_i^0) / f_i^0, \quad \Delta Y^g = (Y^g - Y^0) / Y^0$$

We consider the example of a high-pressure turbine deteriorated by erosion, that caused a 2% mass flow capacity increase and 1% efficiency drop:  $\Delta f_7 = \Delta(SW_{41}) = +2\%$ .  $\Delta f_8 = \Delta(SE_{41}) = -1\%$ .

Using the engine model we produce the deviation in  $p_3$  and we use the system of two equations derived in the foregoing, to solve and determine  $\Delta f_7$ ,  $\Delta f_8$ . The solution obtained for several values of the constant  $C$  are shown in Fig. 11. On the same figure, the straight line corresponding to the linearized relation between parameters and measurement. Eq. (14), is shown. (For this particular

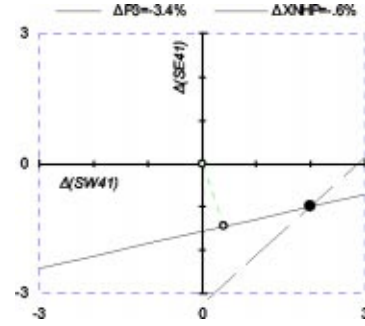


Fig. 12 Estimated solutions for  $\Delta SW_{41}$ ,  $\Delta SE_{41}$  when  $XNHP$  is given; (● actual solution)

example Eq. (14) becomes:  $\Delta P_3 = -1.19 \Delta f_7 + 1.06 \Delta f_8$ .) The point representing the actual component deterioration that has produced the measurement deviation is also shown.

It is observed that the locus of solutions is a line drawn from the origin (perpendicular to the  $\Delta P_3$  line, for equal standard deviations). For small values of  $C$ , the solution is close to the  $\Delta P_3$  line, but as  $C$  increases it moves away from it and closer to the origin. This figure explains how the least squares can produce a solution that is close to the actual values, even though one measurement only is available and is used to determine two parameters. It also shows that small values of  $C$  produce solutions that are essentially closer to the actual one.

The choice of a particular measurement is related to how closely the actual solution is approximated. For example, if  $XNHP$  were used instead of  $P_3$ , the estimated values would be further away from the actual solution, as shown in Fig. 12. The locus of solutions, with two points, one for small and one for large value of  $C$  are shown. The line for the equation corresponding to  $\Delta XNHP$  is also drawn. If both measurements were available, the precise solution would have been found from the intersection of the two lines.

The solution is also influenced by the relative magnitudes of standard deviations of the two estimated parameters. Figure 13 shows how the solution varies for different relative magnitudes. Depending on the proportion of standard deviations, the solution can be closer to or farther from the actual one. Increasing one standard deviation moves the solution closer to the corresponding axis. A particular proportion makes the solution equal to the actual one. Although this proportion could be useful for tuning the method, it will not produce an accurate solution for other faults, linked to different relative magnitudes of mass flow and efficiency deltas. A specific ratio of standard deviations provides a close approximation for faults causing the same relative deltas. This ratio does not necessarily correspond to the actual values, as they would have been derived by measurement error propagation.

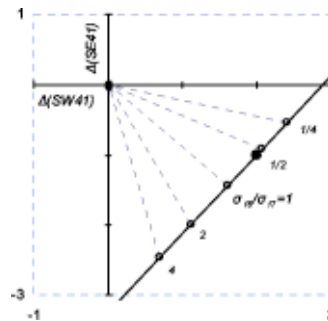


Fig. 13 Loci of solutions for different proportions of standard deviations; given  $\Delta P_3$ . (● actual solution)

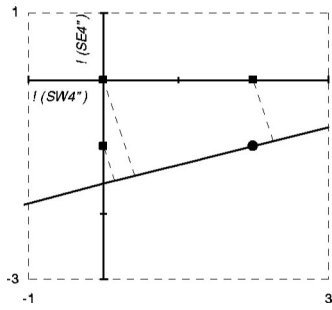


Fig. 14 Loci of solutions for different initial values of health parameters (■); given XNHP; (● actual solution)

The influence of the choice of initial values for  $f$  is demonstrated in Fig. 14. The loci of solutions for different values of  $C$  have the same slope, but originate from different locations, namely the point corresponding to the initial values. A further observation is that if one of the two health parameters has a predominant influence on the measurement (the line for the measurement forms a large angle with its axes), then estimation of this parameter is much less sensitive to the choice of initial value. Figure 14 shows that estimated values of  $\Delta(SE_{41})$  vary much less than values of  $\Delta(SW_{41})$ , for the different choices of initial point. Obviously, if a line is perpendicular to an axis, the parameter on this axis is precisely estimated, but the other one cannot be estimated at all.

The preceding discussion shows that the method produces a solution, irrespective of the actual cause of a measurement deviation. A deviation caused by one component, would thus be attributed to more than one, through the solution consisting of more than one parameter deviations. How much of the deviation will be distributed to each one depends on the slope of the line, for the case of two parameters given as an example here. It is through such a mechanism that single-component deviations are distributed to others, as for example presented in [18] and observed earlier in the paper.

The previous observations are based on a linear relation between measurement and parameter deviations. This is chosen because it gives the possibility to easily assess the influence of the various factors involved in the estimation. The nonlinear method of the paper can also be used to demonstrate these observations. Figure 15 provides the same information as Figs. 11 and 13, using the nonlinear method, including the results of the linear method

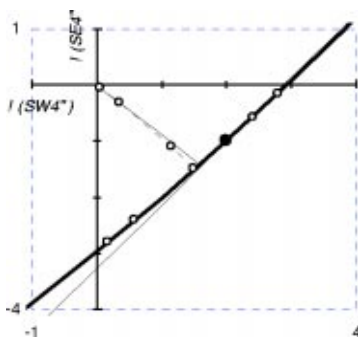


Fig. 15 Comparison of solutions by linear and the nonlinear algorithm (— linear, — nonlinear)

for comparison. Although the linear relations produce the same trend and are thus suitable for interpreting the solution, the nonlinear ones provide values which differ. The difference increases as the deviation from the point used as reference increases. The nonlinear approach can accurately capture deviations, even though they may be of a sizeable magnitude.

As a final comment, the foregoing analysis can be used to interpret even situations with multiple measurements and component parameters, as long as the number of parameters exceeds the number of measurements by one. In that case,  $N-1$  parameters can be expressed in function of the  $N$ th one; so for each one of them, one equation with two unknowns is formulated, which could be studied as in the foregoing. The examination of sensitivity of the method to individual parameter disturbances, reported in the body of the paper, substitutes for such a study.

## References

- [1] Zaita, A. V., Baley, G., and Karlsons, G., 1998, "Performance Deterioration Modeling in Aircraft Gas Turbine Engines," *ASME J. Eng. Gas Turbines Power*, April, **120**, pp. 344–349.
- [2] Doel, D., 1994, "TEMPER—a Gas Path Analysis Tool for Commercial Jet Engines," *ASME J. Eng. Gas Turbines Power*, Jan, **116**, pp. 82–89.
- [3] Barwell, M. J., 1987, "COMPASS—Ground Based Engine Monitoring Program for General Applications," *SAE Technical Paper* 871734.
- [4] Urban, L. A., Volponi, A. J., 1992, "Mathematical Methods Of Relative Engine Performance Diagnostics," *SAE Trans.*, **101** Aerospace Technical Paper 922048.
- [5] Volponi A., Sensor Error Compensation in Engine Performance Diagnostics, *ASME Paper* 94-GT-58.
- [6] Lietzau, K., Kreiner A., "Model Based Control Concepts For Jet Engines," *ASME Paper* 2001-GT-0016.
- [7] Kurz, R., and Brun, K., 2001, "Degradation in Gas Turbine Systems," *ASME J. Eng. Gas Turbines Power*, **123**, Jan, pp. 70–77.
- [8] Diakunchak, I. S., 1992, "Performance Deterioration in Industrial Gas Turbines," *ASME J. Eng. Gas Turbines Power*, **114**, pp. 161–168.
- [9] Olsson, W. J., Stromberg, W. J., 1981, *Aircraft Engine Diagnostics*, NASA Lewis Res. Center, pp. 43–61, Jan. 1981, Contract No. NASA 3-20632.
- [10] Fasching, W. A., Stricklin, R., 1982, *CF6 Jet Engine Diagnostics Program: Final Report*, NASA/CR-165582.
- [11] Sasahara, O., 1985, *JT9D Engine/Module Performance Deterioration Results from Back to Back Testing*, Paper ISABE 85-7061.
- [12] Danielsson, S. G., 1977, "Gas Path Analysis Applied to Pre And Post Overhaul Testing of JT9D Turbofan Engine," Paper SAE 770993.
- [13] Glenn, D. E., 1988, *Gas Path Analysis And Engine Performance Monitoring in a Chinook Helicopter*, Paper 25, AGARD-CP-448, Engine Condition Monitoring, Technology and Experience.
- [14] Stamatis A., Mathioudakis K., Ruiz J., Curnock B., 2001, 'Real time engine model implementation for adaptive control & performance monitoring of large civil turbofans,' *ASME Paper*, 2001-GT-0362.
- [15] Stamatis, A., Mathioudakis, K., Papailiou, K. D., 1990, "Adaptive Simulation of Gas Turbine Performance," *ASME J. Eng. Gas Turbines Power*, Apr. **112**, pp. 168–175.
- [16] Grodent, M., Navez, A., 2001, *Engine Physical Diagnosis Using A Robust Parameter Estimation Method*, 37th AIAA/ASME/SAE/ASEE Joint Propulsion Conference And Exhibit, July 8–11, Salt Lake City, UT., Paper AIAA-2001-3768.
- [17] Curnock, B., 2001, *OBIDICOTE Programme Work Package 4 Steady-State Test Cases for Engine Deterioration*, Rolls Royce report, Document No. DNS78608, May.
- [18] Doel, D., 1994, "An Assessment of Weighted-Least-Squares Based Gas Path Analysis," *ASME J. Eng. Gas Turbines Power*, Apr., **116**, pp. 366–373.
- [19] Stamatis, A., Mathioudakis, K., Berios, G., Papailiou, K., 1991, "Jet Engine Fault Detection with Differential Gas Path Analysis at Discrete Operating Points," *J. Propul. Power*, **7**, (6), Nov./Dec. pp. 1043–1048.
- [20] Kobayashi, T., Simon, D., 2001, *A Hybrid Neural-Genetic Algorithm Technique for Aircraft Engine Performance Diagnostics*, 37th AIAA/ASME/SAE/ASEE Joint Propulsion Conference and Exhibit, 8–11 July, Salt Lake City, Utah, Paper AIAA-2001-3763.
- [21] Groenstredt, T. V., 2001, *A Multi Point Gas Path Analysis Tool for Gas Turbine Engines With A Moderate Level of Instrumentation*, XV ISABE, Bangalore, India, September 3–7, Paper ISABE-2001-1139.
- [22] Gulati, A., Taylor, D., Singh, R., 2001, *Multiple Operating Point Analysis Using Genetic Algorithm Optimization for Gas Turbine Diagnostic*, XV ISABE, Bangalore, India, September, 3–7, 2001, Paper ISABE-2001-1139.

# Effects of the Nature of Excitation on the Response of a Mistuned Bladed Disk Assembly

D. Cha  
A. Sinha

Department of Mechanical Engineering,  
The Pennsylvania State University,  
University Park, PA 16802

*In this paper, responses of a mistuned bladed disk assembly are examined and compared for three types of excitations: uncorrelated narrow band random excitations, correlated narrow band random excitations and sinusoidal excitations with unknown (time-invariant and random) amplitudes. Analytical techniques are also developed to compute the statistics of responses for these types of excitations. Effects of correlations of narrow band excitations are investigated in details. It has been found that the response statistics for correlated narrow band random excitations can be viewed in terms of the concepts related to the response to a deterministic engine order excitation. [DOI: 10.1115/1.1508385]*

## 1 Introduction

The effects of mistuning have received a wide attention in the existing literature [1–8] because small variations in the modal properties of blades can lead to a large difference in the forced response of each blade. While most of studies deal with deterministic sinusoidal excitations, the nature of excitation has been found to be random in many applications [9–12]. Sogliero and Srinivasan [1] considered white noise excitations and computed the mean-square displacement by Monte-Carlo simulations. Cha and Sinha [8] have developed analytical techniques to compute the statistics of the responses for white noise and narrow band random excitations. It has been shown that the impact of mistuning can be significant when the frequency bandwidth of random excitation is small. They assumed that external forces on blades are statistically independent of each other, and found that there are many frequencies at which mean square response of the blade attains maximum values. However, unlike white noise excitations, a narrow band random force has a dominant frequency and may have correlations with excitations experienced by other blades. For a deterministic engine order excitation, external forces are related by a constant interblade phase angle and there is only one resonant frequency for the forced response. Therefore, it is desirable to study the effects of correlations among narrow band random forces on the statistics of the response and determine how responses differ from those to uncorrelated narrow-band random excitations. In particular, following questions arise: (i) Can there be a single resonance for correlated narrow band excitations? (ii) Will the sensitivity of response to mistuning be higher or lower for correlated narrow band excitations? (iii) Are concepts related to deterministic engine order excitations applicable to correlated narrow band excitations?

In this paper, effects of correlations of narrow band random excitations on the system response are investigated. Correlated narrow-band excitations are obtained as outputs of coupled band pass filters with white noises as inputs. The base patterns of narrow band excitation correlations are developed using the concepts related to the response to a deterministic engine order excitation. It has been shown that correlations of general narrow band excitations can be represented as a linear combination of these basic patterns. Features of responses for correlated narrow band random excitations are compared with those of sinusoidal excitations with unknown amplitudes which represent standard engine order excitations where the amplitude and phase are considered as time

invariant random variables. This type of excitation corresponds to time-invariant circumferential pressure field with unknown or random magnitudes.

The model of the bladed disk assembly is chosen to be as shown in Fig. 1 [3,4,8]. This model represents the fundamental mode of vibration for each blade. The modal mass of each blade is considered to be identical and represented by  $m_i$ . And the modal stiffness of the  $i$ th blade is represented by  $k_i$ . The mechanical coupling between adjacent blades due to the disk's flexibility has been represented by a spring with the stiffness  $K_c$ . The damping coefficient  $c$  is used to represent the structural and aerodynamic damping.

First, analytical techniques to compute the statistics of forced response are presented for two types of excitation: sinusoidal excitations with unknown amplitudes and correlated narrow-band random excitations. Then the influence of correlations of narrow band random excitations on the system response is described.

## 2 Formulation

Let  $M$ ,  $K$  and  $C$  be mass, stiffness and damping matrices, respectively. The system of governing differential equations can be written as follows:

$$M\ddot{x} + C\dot{x} + Kx = F(t) \quad (1)$$

The mistuning phenomenon is simulated by considering the perturbations in the stiffness matrix alone. If the stiffness matrix for the corresponding tuned system is  $K_0$

$$K = K_0 + \delta K \quad (2)$$

where  $\delta K$  is the random deviation in the stiffness matrix due to mistuning. Here,  $\delta K$  is a diagonal matrix with diagonal elements

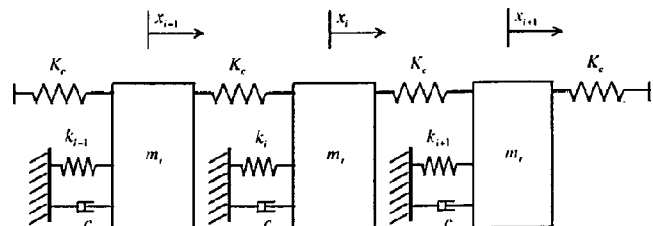


Fig. 1 Model of a bladed disk assembly

Contributed by the International Gas Turbine Institute and presented at the International Gas Turbine and Aeroengine Congress and Exhibition, Amsterdam, The Netherlands, June 3–6, 2002. Manuscript received by the IGTI, March 4, 2002. Paper No. 2002-GT-30430. Review Chair: E. Benvenuti.

as  $\delta k_1, \delta k_2, \dots, \delta k_n$ . It is assumed that random variables  $\delta k_i (i=1, 2, \dots, n)$  are independent and have Gaussian distributions with zero mean.

**2.1 Sinusoidal Excitations With Unknown Amplitudes.** If the external force vector,  $F(t)$ , is assumed to correspond to a particular engine order excitation for the time-invariant random circumferential pressure field, then the amplitudes of sine and cosine components of the force on each blade,  $\alpha_c$  and  $\beta_c$ , can be considered as time invariant random variables; i.e.,

$$F_i(t) = \alpha_c \sin(\omega t + \psi_i) + \beta_c \cos(\omega t + \psi_i) \quad (3)$$

where

$$\alpha_c = \alpha_{c0} + \delta\alpha_c, \quad (4a)$$

$$\beta_c = \beta_{c0} + \delta\beta_c \quad (4b)$$

$$\alpha_{c0} = E[\alpha_c], \quad (4c)$$

$$\beta_{c0} = E[\beta_c] \quad (4d)$$

$$\psi_i = \frac{2\pi r(i-1)}{n}, \quad (r = \text{engine order excitation}) \quad (4e)$$

The steady-state response can be written as

$$x_i(t) = A_{xi} \sin \omega t + B_{xi} \cos \omega t \quad (5)$$

where  $A_{xi}$  and  $B_{xi}$  are also time invariant random variables. The vectors of response amplitudes and external force amplitudes can be defined as

$$x_a = [A_{x1} \ B_{x1} \ \dots \ A_{xn} \ B_{xn}]^T \quad (6)$$

$$F_a = [a_1 \ b_1 \ \dots \ a_n \ b_n]^T \quad (7)$$

where

$$a_i = \alpha_c \cos \psi_i - \beta_c \sin \psi_i, \quad (8a)$$

$$b_i = \alpha_c \sin \psi_i + \beta_c \cos \psi_i \quad (8b)$$

Substituting Eqs. (3) and (5) into Eq. (1) and equating the components of  $\cos \omega t$  and  $\sin \omega t$ , a system of  $2n$  algebraic equations is obtained. These equations can be described as

$$(H_0 + \delta H)x_a = F_a \quad (9)$$

The matrix  $H_0$  consists of the elements of  $M$ ,  $C$  and  $K_0$ , whereas the matrix  $\delta H$  consists of the elements of  $\delta K$ . Let the correlation matrix of external force amplitudes be defined as

$$R_{fa} = E[F_a F_a^T] \quad (10)$$

where  $E[\ ]$  is the expected value. The correlation matrix of response amplitudes is then obtained as

$$R_{xa} = E[x_a x_a^T] = (H_0 + \delta H)^{-1} R_{fa} (H_0 + \delta H)^{-T} \quad (11)$$

The expressions for the elements of  $R_{fa}$  are provided in Appendix A. Since the matrix  $H_0$  is nonsingular for a damped system, Eq. (11) yields

$$R_{xa} = (I_{2n} + H_0^{-1} \delta H)^{-1} H_0^{-1} R_{fa} H_0^{-T} (I_{2n} + H_0^{-1} \delta H)^{-T} \quad (12)$$

Equation (12) can be expanded as follows:

$$R_{xa} = (I_{2n} - H_0^{-1} \delta H + (H_0^{-1} \delta H)^2 - \dots) H_0^{-1} R_{fa} H_0^{-T} \quad (13)$$

$$(I_{2n} - \delta H H_0^{-T} + (\delta H H_0^{-T})^2 - \dots)$$

Neglecting higher order terms,  $R_{xa}$  can be expressed as follows

$$R_{xa} = R_{0a} - H_0^{-1} \delta H R_{0a} - R_{0a} \delta H H_0^{-T} \quad (14)$$

where

$$R_{0a} = H_0^{-1} R_{fa} H_0^{-T} \quad (15)$$

The mean square value of response amplitude of a mistuned system is defined as follows:

$$R a_i = E[A_{xi}^2 + B_{xi}^2] = (R_{xa})_{2i-1, 2i-1} + (R_{xa})_{2i, 2i} \quad (16)$$

Due to mistuning,  $R a_i$  is a random variable. Hence, the mean value of response amplitude square,  $\mu_{Ra}$ , is defined as

$$(\mu_{Ra})_i = E[R a_i] = E[(R_{xa})_{2i-1, 2i-1}] + E[(R_{xa})_{2i, 2i}] \quad (17a)$$

And, the standard deviation of response amplitude square,  $\sigma_{Ra}$ , is defined as

$$(\sigma_{Ra}^2)_i = E[(R a_i - (\mu_{Ra})_i)^2] = E[R a_i^2] - (\mu_{Ra})_i^2 \quad (17b)$$

where

$$E[R a_i^2] = E[(R_{xa})_{2i-1, 2i-1} + (R_{xa})_{2i, 2i}]^2$$

$$= E[(R_{xa})_{2i-1, 2i-1}^2] + E[(R_{xa})_{2i, 2i}^2]$$

$$+ 2E[(R_{xa})_{2i-1, 2i-1} (R_{xa})_{2i, 2i}] \quad (18)$$

Expressions for  $(\mu_{Ra})_i$  and  $(\sigma_{Ra}^2)_i$  are provided in Appendix B.

## 2.2 Correlated Narrow-Band Random Excitations

*Generation of Correlated-Narrow Band Random Excitations.* Correlated narrow-band excitations,  $g_i(t)$ , can be obtained as outputs of a multi-dimensional band-pass filter subjected to white noise excitations  $w_i(t)$ ; i.e.,

$$\ddot{g} + C_F \dot{g} + K_F g = K_F w(t) \quad (19)$$

where

$$C_F = 2\xi_F \omega_F C_R \quad (20a)$$

$$K_F = \omega_F^2 I_n \quad (20b)$$

$$g(t) = [g_1(t) \ g_2(t) \ \dots \ g_n(t)]^T \quad (20c)$$

$$w(t) = [w_1(t) \ w_2(t) \ \dots \ w_n(t)]^T \quad (20d)$$

and  $C_R$  is a positive definite matrix. When  $C_R$  is the identity matrix, the multi-dimensional band-pass filter, Eq. (19), is reduced to uncoupled  $n$  band pass filters with damping ratio  $\xi_F$  and natural frequency  $\omega_F$ . In other words,  $g_i$  is independent of  $g_j (i \neq j)$  if  $C_R$  is the identity matrix. The correlation matrix of white noise excitations is given as follows:

$$R_w(\tau) = E[w(t)w(t+\tau)^T] = Q_0 \delta(\tau) I_n \quad (21)$$

where  $Q_0$  is the intensity and  $\delta(\tau)$  is the dirac-delta function.

Let  $V$  be the normalized eigenvector matrix of the matrix  $C_F$ . By the linear transformation

$$g = Vy \quad (22)$$

Equation (19) can be changed to a system of  $n$  decoupled equations as follows:

$$\ddot{y} + V^T C_F V \dot{y} + \omega_F^2 y = \Phi(t) \quad (23)$$

where

$$V^T C_F V = \text{diag}[2\xi_{b1}\omega_{b1} \ 2\xi_{b2}\omega_{b2} \ \dots \ 2\xi_{bn}\omega_{bn}] \quad (24a)$$

$$\Phi(t) = \omega_F^2 V^T w(t) \quad (24b)$$

Note that  $V^T C_F V$  is a diagonal matrix. Due to the orthonormality condition of normalized eigenvector matrix

$$V^T V = V V^T = I_n \quad (25)$$

Next, the correlation matrix of transformed white noise excitations can be calculated as follows:

$$R_\Phi(\tau) = E[\Phi(t)\Phi(t+\tau)^T] = \omega_F^4 Q_0 \delta(\tau) I_n \quad (26)$$

The elements of the correlation matrix of transformed narrow-band excitations is then obtained [13] as

$$R_{y_i y_j}(\tau) = E[y_i(t)y_j(t+\tau)]$$

$$= \int_{-\infty}^{\infty} \int_{-\infty}^{\infty} h_i(\lambda_1)h_j(\lambda_2)R_{\Phi_i \Phi_j}(\tau+\lambda_1-\lambda_2)d\lambda_1d\lambda_2$$
(27)

where  $R_{\Phi_i \Phi_j}(\tau)$  is the  $(i, j)$  element of  $R_{\Phi}(\tau)$

$$R_{\Phi_i \Phi_j}(\tau) = E[\Phi_i(t)\Phi_j(t+\tau)]$$
(28)

and  $h_i(t)$  is the unit impulse response of the  $i$ th decoupled band-pass filter system; i.e.,

$$h_i(t) = \frac{1}{\omega_F \sqrt{1 - (\xi_{bi}\omega_{bi}/\omega_F)^2}} e^{-\xi_{bi}\omega_{bi}t}$$

$$\times \sin(\omega_F \sqrt{1 - (\xi_{bi}\omega_{bi}/\omega_F)^2}t), \quad (t > 0)$$
(29)

Mean square values of transformed narrow-band excitations are obtained from Eq. (27) by setting  $\tau=0$

$$R_{y_i y_j}(0) = \begin{cases} 0 & (i \neq j) \\ \frac{Q_0 \omega_F^2}{4 \xi_{bi} \omega_{bi}} & (i = j) \end{cases}$$
(30)

The correlation matrix of transformed narrow-band excitation can be written as

$$R_y(0) = \frac{Q_0 \omega_F^2}{2} (V^T C_F V)^{-1}$$
(31)

Using Eqs. (22) and (24a), the correlation matrix of actual narrow-band random forces is obtained as below,

$$R_g = E[g(t)g(t)^T]$$

$$= V R_y(0) V^T = \frac{Q_0 \omega_F^2}{2} V (V^T C_F^{-1} V) V^T$$

$$= \frac{Q_0 \omega_F}{4 \xi_F} C_R^{-1}$$
(32)

Therefore, the coupled structure of band-pass filter,  $C_R$ , can be easily calculated when the correlation matrix of external forces,  $R_g$ , is known.

$$C_R = \frac{4 \xi_F}{Q_0 \omega_F} R_g^{-1}$$
(33)

*Response to Correlated Narrow-Band Excitations.* Let a state vector be selected as

$$z^T = [g^T \quad \dot{g}^T \quad x^T \quad \dot{x}^T]$$
(34)

Then, Eqs. (1) and (19) can be represented as

$$\dot{z} = Az + Bw(t)$$
(35)

where

$$A = \begin{bmatrix} 0 & I_n & 0 & 0 \\ -K_F & -C_F & 0 & 0 \\ 0 & 0 & 0 & I_n \\ M^{-1} & 0 & -M^{-1}K & -M^{-1}C \end{bmatrix},$$
(36a)

$$B = \begin{bmatrix} 0 \\ K_F \\ 0 \\ 0 \end{bmatrix}$$
(36b)

Since  $E[w_i(t)] = 0$ , it has been shown that  $E[z_i(t)] = 0$ . Let  $P$  be the correlation matrix of state variables; i.e.,

$$P = E[z(t)z(t)^T]$$
(37)

**Table 1 System parameters**

$m_i = 0.0114 \text{ kg}, \quad c = 1.45 \text{ Ns/m}, \quad k_s = 430000 \text{ N/m}, \quad K_c = 45430 \text{ N/m}$
---

Then the correlation matrix  $P$  satisfies the following system of algebraic equations under steady-state conditions [14].

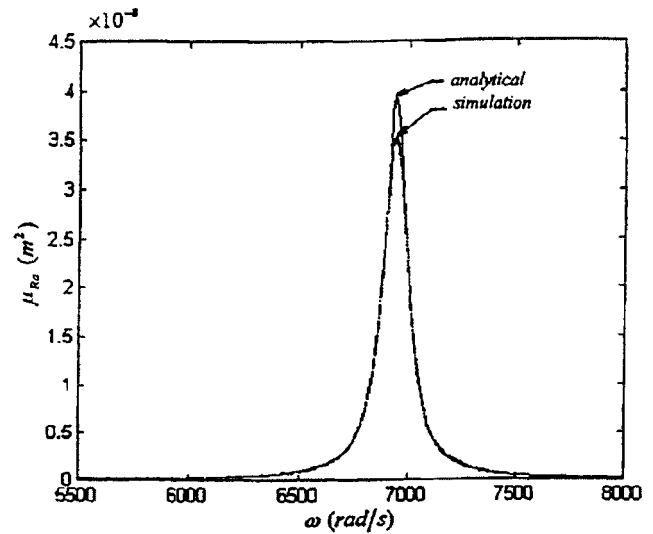
$$AP + PA^T = B_R$$
(38)

where

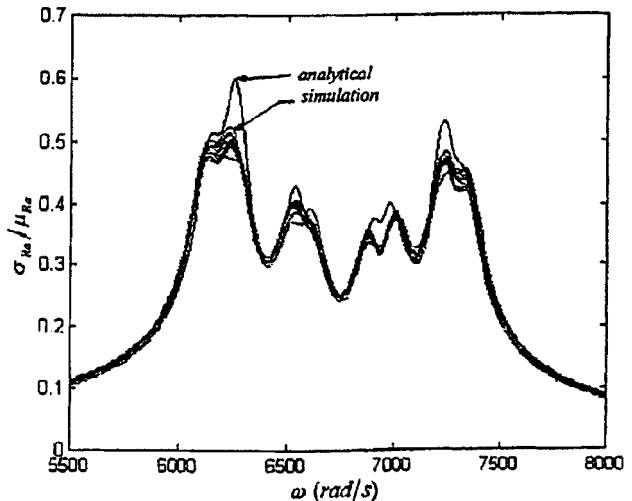
$$B_R = -BQ_0B^T$$
(39)

Equation (38) is called the Lyapunov equation and can be easily solved using the MATLAB routine [15] "lyap." The variance of the system response,  $(\sigma_x^2)_i$ , can be obtained from the correlation matrix  $P$ ; i.e.,

$$(\sigma_x^2)_i = E[x_i^2] = (P)_{2n+i, 2n+i}$$
(40)



(a)



(b)

**Fig. 2 (a)  $\mu_{Ra}$  as a function of  $\omega$ , (b)  $\sigma_{Ra}/\mu_{Ra}$  as a function of  $\omega$ ; (sinusoidal excitations with unknown amplitudes)**



Because of mistuning,  $\sigma_x^2$  are random variables. Hence, it is desirable to predict mean and standard deviation of  $\sigma_x^2$ . Using the Taylor's series expansion, the solution of Eq. (38) for a mistuned system can be approximated as follows:

$$P = P_0 + \sum_{i=1}^n \frac{\partial P}{\partial k_i} \delta k_i \quad (41)$$

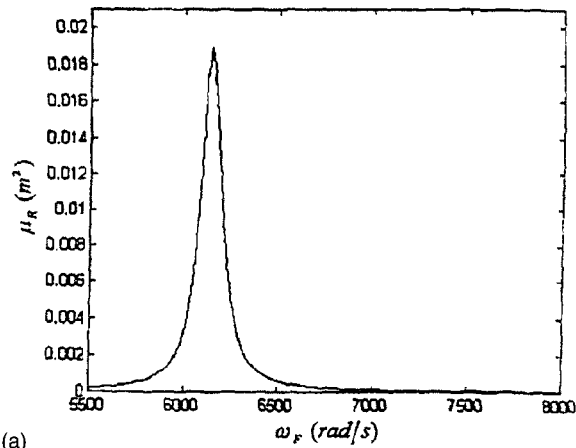
where  $P_0$  is the correlation matrix of the perfectly tuned system. Note that the higher order terms of the Taylor's series expansion are neglected. The validity of this approximation has been established by Cha and Sinha [8].  $\partial P / \partial k_i$  is a solution of the following linear algebraic equation which is obtained by differentiating Eq. (38) with respect to  $k_i$ ; i.e.,

$$A_0 \frac{\partial P}{\partial k_i} + \frac{\partial P}{\partial k_i} A_0^T = - \left( \frac{\partial A}{\partial k_i} P_0 + P_0 \frac{\partial A^T}{\partial k_i} \right) \quad (42)$$

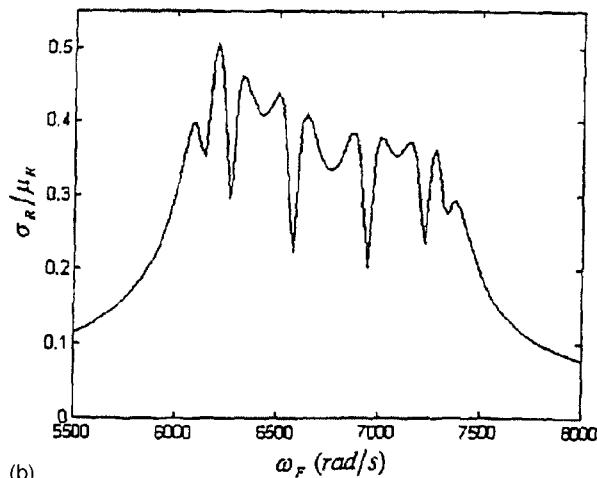
Note that  $\partial A / \partial k_i$  and  $\partial A^T / \partial k_i$  can be calculated analytically. The matrix  $P_0$  is known by solving Eq. (38) for a perfectly tuned system. Hence, the right-hand side of Eq. (42) is known, and Eq. (42) is the Lyapunov equation which can be again solved by using the MATLAB routine "lyap." From Eq. (41), the mean and the standard deviation of response variance can be easily calculated as follows:

$$(\mu_R)_i = E[P_{2n+i, 2n+i}] \quad (43a)$$

$$(\sigma_R^2)_i = E[P_{2n+i, 2n+i}^2] - (\mu_R)_i^2 \quad (43b)$$



(a)



(b)

Fig. 3 (a)  $\mu_R$  as a function of  $\omega_F$ , (b)  $\sigma_R / \mu_R$  as a function of  $\omega_F$ ; (correlated excitation, pattern 0)

where the expressions for  $(\mu_R)_i$  and  $(\sigma_R^2)_i$  are provided in Appendix C.

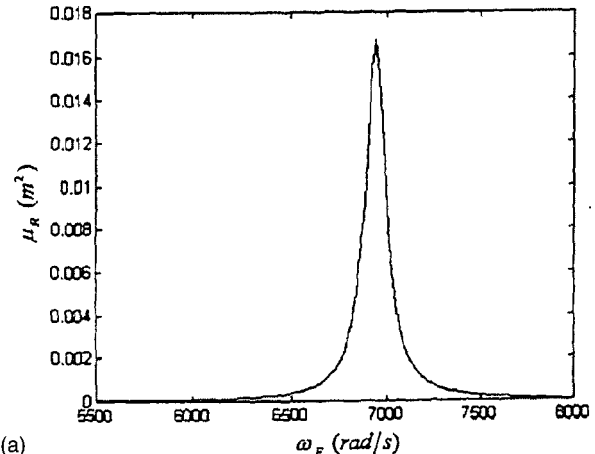
### 3 Numerical Results

The nominal values of modal parameters are chosen from the paper by Griffin and Sinha [16], and are presented in Table 1. The number of blades is selected to be equal to ten. The standard deviation of each blade's modal stiffness is taken to be 8000 N/m, which corresponds to about 1 percent mistuning in terms of the ratio of standard deviation and mean value of the modal frequency of each blade.

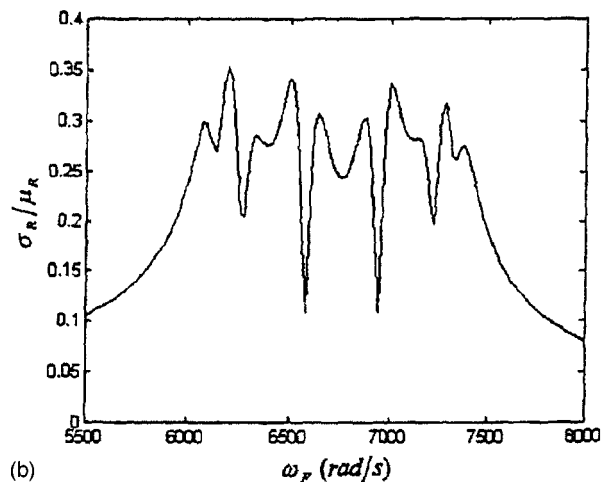
In Section 3.1, the statistics of response are calculated for sinusoidal excitations with unknown amplitudes whereas effects of correlations of narrow-band excitations on the response variance are investigated in Section 3.2.

#### 3.1 Sinusoidal Excitations With Unknown Amplitudes.

In order to verify the accuracy of the analytical technique, the mean and the standard deviations of the square of each blade's amplitude,  $\mu_{Ra}$  and  $\sigma_{Ra}$ , are obtained by solving Eq. (11) for Monte Carlo simulations and compared with analytical results obtained from Eq. (17). The MATLAB command "randn" [15] is used to generate the variations in modal stiffnesses. It yields random numbers which have Gaussian distribution with zero mean and specified standard deviation. For the Monte-Carlo simulation, a large number (arbitrarily chosen to be 1000) of bladed disk assemblies are considered. It is assumed that the mean and the variance of random variable  $\alpha_c$  and  $\beta_c$  of Eq. (3) are unity and



(a)



(b)

Fig. 4 (a)  $\mu_R$  as a function of  $\omega_F$ , (b)  $\sigma_R / \mu_R$  as a function of  $\omega_F$ ; (correlated excitation, pattern 3)

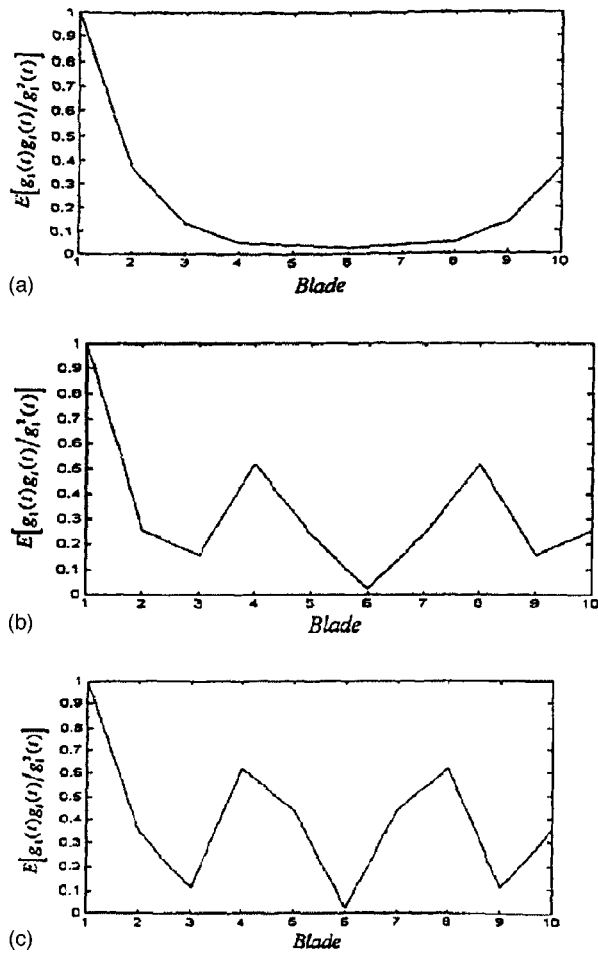


Fig. 5 The correlations of narrow-band excitation (a) case 1, (b) case 2, (c) case 3

deviations of  $\alpha_c$  and  $\beta_c$  are independent of each other; i.e.,  $\alpha_{c0} = \beta_{c0} = 1N$ ,  $E[\delta\alpha_c^2] = E[\delta\beta_c^2] = 1N^2$ , and  $E[\delta\alpha_c\delta\beta_c] = 0$ . The engine order excitation,  $r$ , is assumed as three.

In Fig. 2, the simulation and analytical results for the  $\mu_{Ra}$  and the  $\sigma_{Ra}/\mu_{Ra}$  of the system are plotted as a function of the excitation frequency  $\omega$ . It can be seen that analytical results compare well with those from numerical simulations. The number of peaks of  $\mu_{Ra}$  is only one. It indicates that a vigorous vibration of blades can occur when the natural frequency of the bladed disk assembly is equal to the frequency of external force and the number of nodal diameters is equal to the number of engine order,  $r$ . This triple-coincidence condition of resonance [17] can be obtained from the Campbell diagram. However, the number of peaks in plots for  $\sigma_{Ra}/\mu_{Ra}$  is related to the number of blades. It reflects the fact that repeated natural frequencies of a tuned system split due

Table 2 Components of six base correlation patterns

Correlation	pattern 0	pattern 1	pattern 2	pattern 3	pattern 4	pattern 5
Uncorrelated	0.1	0.2	0.2	0.2	0.2	0.1
Case 1	0.2209	0.3119	0.1957	0.1262	0.0968	0.0485
Case 2	0.3370	0.1543	0.0462	0.3110	0.1280	0.0235
Case 3	0.4070	0.1034	0.0671	0.3719	0.0371	0.0135

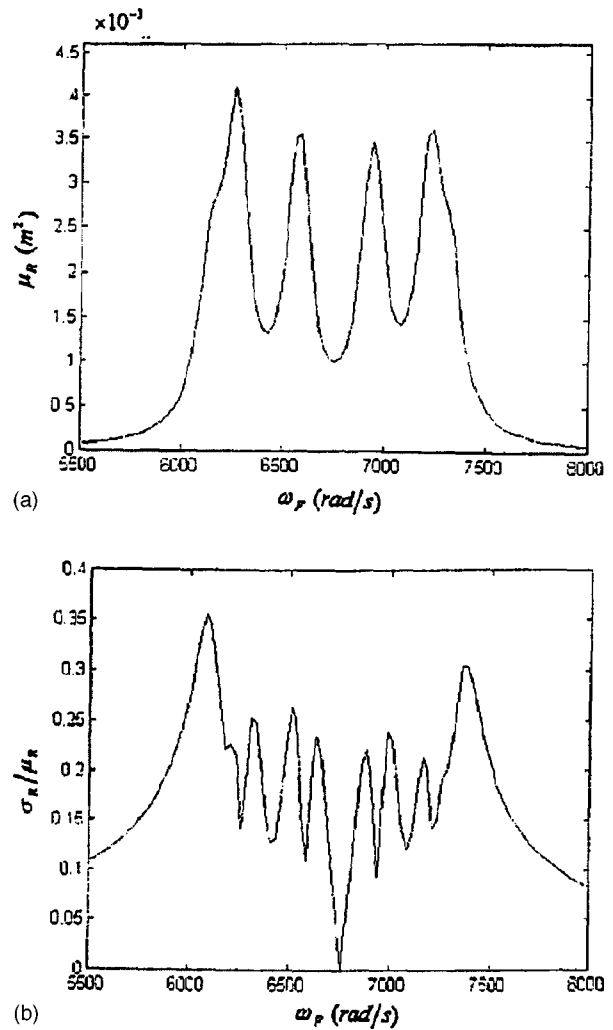


Fig. 6 (a)  $\mu_R$  as a function of  $\omega_F$ , (b)  $\sigma_R/\mu_R$  as a function of  $\omega_F$ ; (uncorrelated excitations)

to mistuning. On a Pentium P-75, the computation times required for numerical simulation and analytical technique are 285 min and 22 s for each  $\omega$ , respectively.

**3.2 Correlated Narrow-Band Random Excitations.** It is assumed that each blade experiences the same intensity of excitation and the correlation between any two blade forces is same if relative positions of corresponding blades are same; i.e.,

$$E[g_i^2(t)] = E[g_j^2(t)] \quad (44a)$$

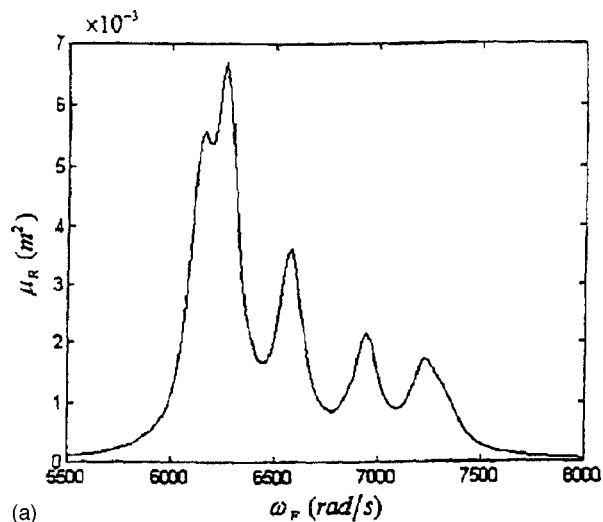
$$E[g_i(t)g_j(t)] = E[g_{i+k}(t)g_{j+k}(t)] \quad (44b)$$

$$E[g_i(t)g_{i+j}(t)] = E[g_i(t)g_{i-j}(t)] \quad (44c)$$

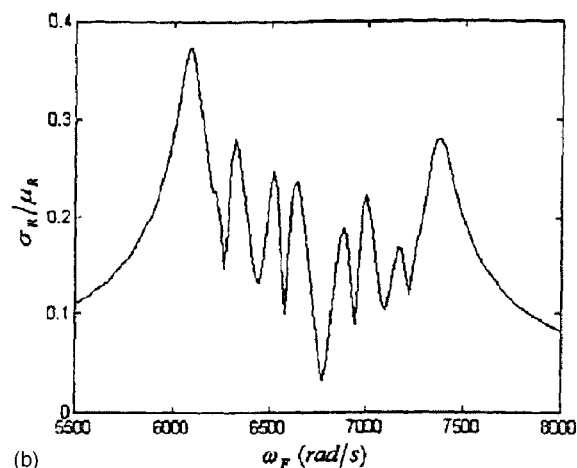
Therefore, the correlation matrix,  $R_g$ , is a symmetric circular matrix and six elements of the first row of  $R_g$  can represent the entire matrix  $R_g$  when the number of blades equals ten. Based on the constant interblade phase angles of deterministic engine order excitations, six base patterns of excitation correlations are developed as follows:

$$R_g(1,i) = E[g_1(t)g_i(t)] = \cos\left(\frac{2\pi(i-1)}{n}p\right)$$

where  $p$ =pattern number. To calculate the coupled structure of band pass filter  $C_R$  which is related to the inverse of  $R_g$ , the elements of  $R_g$  are slightly modified so that the rank of  $R_g$  is equal



(a)



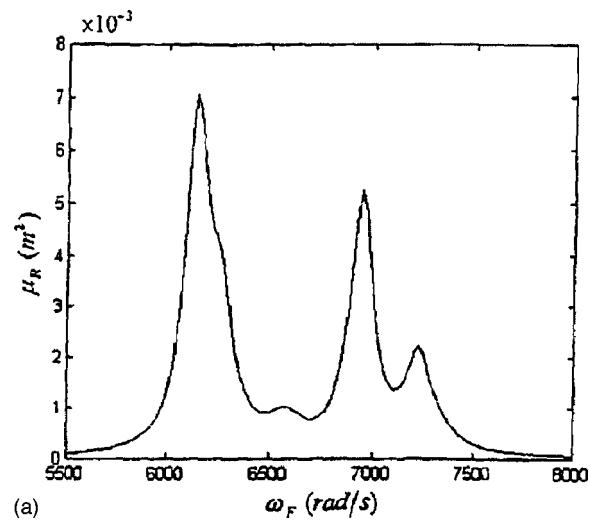
(b)

Fig. 7 (a)  $\mu_R$  as a function of  $\omega_F$ , (b)  $\sigma_R/\mu_R$  as a function of  $\omega_F$ ; (correlated excitations, case 1)

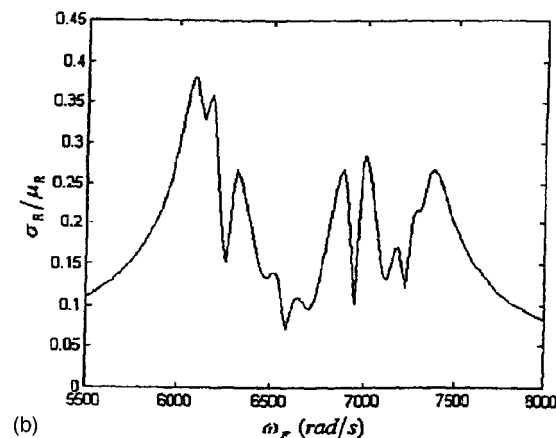
to the number of blades. For example, the cross-correlations,  $E[g_i(t)g_j(t)]$ , of the 0th pattern have been chosen as 0.99 instead of 1.

With given correlations of excitations, the analytical results of  $\mu_R$  and  $\sigma_R/\mu_R$  are calculated from Eq. (43); e.g., Figs. 3 and 4 for  $p=0$  and 3, respectively. The numerical value for  $\xi_F$  is chosen as 0.001 and the intensity of external white noise excitation,  $Q_0$ , is assumed as unity. It is found that the number of peaks of  $\mu_R$  is only one and the resonant frequency is same as that for the case of the corresponding engine order excitation which can be obtained from the Campbell diagram. It indicates that correlations of excitations are important factors for the response of a tuned system. However, features of  $\sigma_R/\mu_R$  do not change significantly and the number of peaks is same as the number of blades.

Six base patterns corresponding to  $p=0, 1, 2, 3, 4,$  and  $5$  can be considered as a basis to describe a general correlated excitation. Three cases of correlation matrix,  $R_g$ , are arbitrarily considered and are shown in Fig. 5. For the case 1, the force on each blade is moderately correlated only with forces on adjacent blades. The  $R_g$  of case 3 is a minor change of case 2 and both excitations are related to the 3rd correlation pattern,  $p=3$ . These three cases of correlated excitations and the independent narrow band excitations are resolved by the six base patterns. The results are shown in Table 2. For independent narrow-band excitations, each pattern has an equal importance. Weightings of patterns 1 to 4 are twice those of patterns 0 and 5 because they correspond to repeated



(a)



(b)

Fig. 8 (a)  $\mu_R$  as a function of  $\omega_F$ , (b)  $\sigma_R/\mu_R$  as a function of  $\omega_F$ ; (correlated excitations, case 2)

natural frequencies of the bladed disk assembly. For the case 1, patterns 0, 1 and 2 are dominant while patterns 0 and 3 are dominant for cases 2 and 3. The analytical results of uncorrelated excitation and these three correlated cases are plotted in Figs. 6–9. The dominant peaks of  $\mu_R$  match well with the weighting factors of correlation patterns in Table 2. From the responses of cases 2 and 3, Figs. 8 and 9, it is found that a small variation in  $R_g$  does not significantly change the features of responses  $\mu_R$  and  $\sigma_R$ . While the number of peaks of  $\mu_R$  depends on the nature of the excitation correlation, the number of peaks of  $\sigma_R/\mu_R$  is always related to the number of blades. Since  $\sigma_R/\mu_R$  is a measure of impact of mistuning, it implies that the mistuning effect is not sensitive to the correlation pattern of excitation.

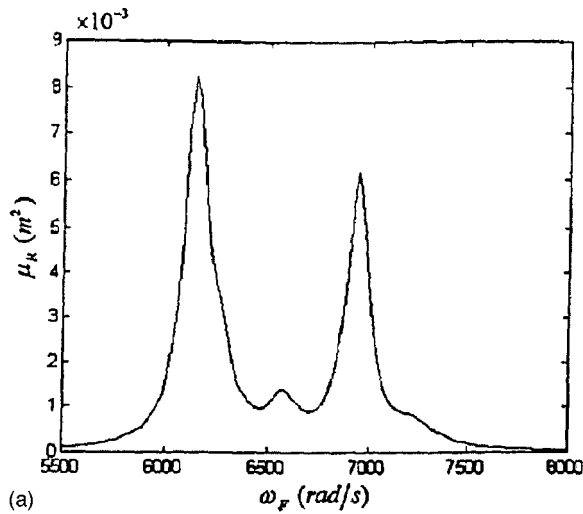
From the comparison of responses of the uncorrelated excitation with the responses of six base correlation patterns, it is found that the peak value of the mean of response variance,  $\mu_R$ , is significantly increased for six base patterns. Therefore, the Lyapunov equation, Eq. (38), for the tuned system is expressed as three coupled algebraic equations to study the effect of cross-correlations of excitations.

$$A_1 P_1 + P_1 A_1^T = -B_1 \quad (45a)$$

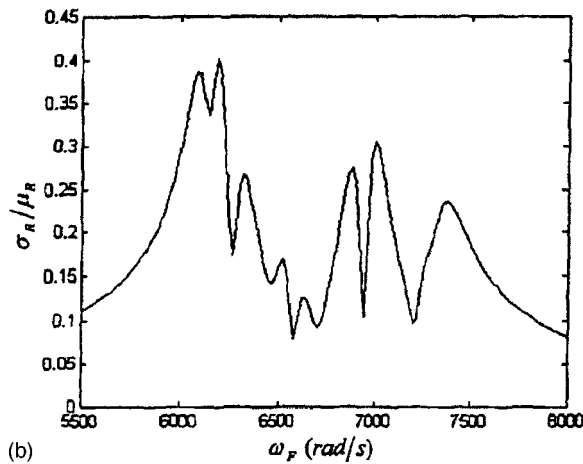
$$A_1 P_2 + P_2 A_3^T = -B_2 \quad (45b)$$

$$A_3 P_3 + P_3 A_3^T = -B_3 \quad (45c)$$

where



(a)



(b)

Fig. 9 (a)  $\mu_R$  as a function of  $\omega_F$ , (b)  $\sigma_R/\mu_R$  as a function of  $\omega_F$ ; (correlated excitations, case 3)

$$A_1 = \begin{bmatrix} 0 & I_n \\ -K_F & -C_F \end{bmatrix}, \quad (46a)$$

$$A_2 = \begin{bmatrix} 0 & 0 \\ M^{-1} & 0 \end{bmatrix} \quad (46b)$$

$$A_3 = \begin{bmatrix} 0 & I_n \\ -M^{-1}K_0 & -M^{-1}C \end{bmatrix} \quad (46c)$$

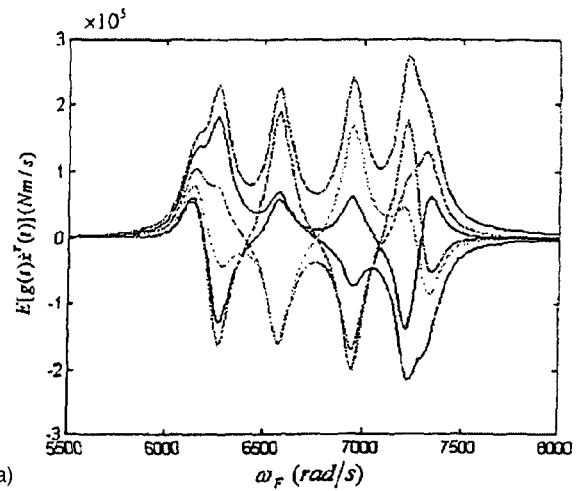
$$P_1 = E \begin{bmatrix} gg^T & g\dot{g}^T \\ \dot{g}g^T & \dot{g}\dot{g}^T \end{bmatrix}, \quad (47a)$$

$$P_2 = E \begin{bmatrix} gx^T & g\dot{x}^T \\ \dot{g}x^T & \dot{g}\dot{x}^T \end{bmatrix} \quad (47b)$$

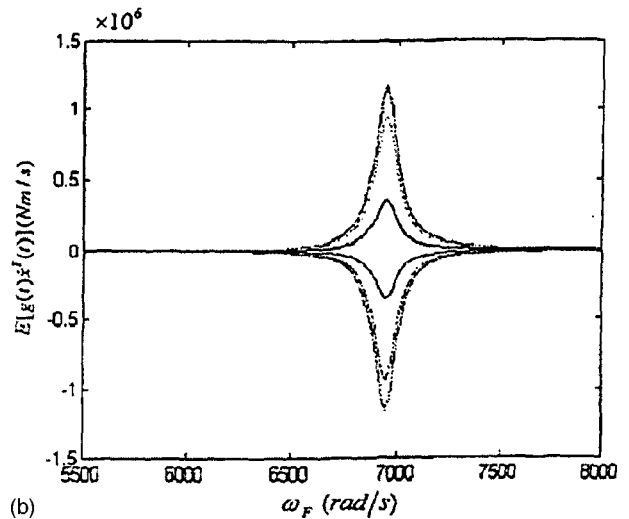
$$P_3 = E \begin{bmatrix} xx^T & x\dot{x}^T \\ \dot{x}x^T & \dot{x}\dot{x}^T \end{bmatrix} \quad (47c)$$

$$B_1 = \begin{bmatrix} 0 & 0 \\ 0 & K_F Q_0 K_F^T \end{bmatrix}, \quad (48a)$$

$$B_2 = \begin{bmatrix} 0 & E[gg^T]M^{-T} \\ 0 & E[\dot{g}g^T]M^{-T} \end{bmatrix} \quad (48b)$$



(a)



(b)

Fig. 10  $E[g\dot{x}^T]$  as a function of  $\omega_F$ ; (a) uncorrelated excitation, (b) correlated excitation, pattern 3

$$B_3 = \begin{bmatrix} 0 & (M^{-1}E[gg^T])^T \\ M^{-1}E[gx^T] & M^{-1}E[\dot{g}\dot{x}^T] + (M^{-1}E[g\dot{x}^T])^T \end{bmatrix} \quad (48c)$$

The intensity of narrow-band excitations,  $E[gg^T]$ , is obtained from Eq. (45a). Note that the elements of  $E[g\dot{g}^T]$  and  $E[\dot{g}g^T]$  are zero, [18]. The correlation matrix  $P_2$  can be calculated from Eq. (45b). Then, the response variance of blades,  $E[xx^T]$ , can be obtained from Eq. (45c). It is found that the effective input intensity for this dynamic system only depends on  $E[gx^T]$  and  $E[g\dot{x}^T]$ .

For the uncorrelated excitation and the 3rd pattern of correlated excitation, Figs. 6 and 4 as examples.  $E[gg^T]$ ,  $E[gx^T]$  and  $E[g\dot{x}^T]$  have been computed. With the change of  $\omega_F$ , the nominal intensity of excitation,  $E[gg^T]$ , is of same order for both types of excitation. However, the elements of  $E[gx^T]$  and  $E[g\dot{x}^T]$  for the 3rd correlation pattern are significantly increased near the resonance frequency while those of uncorrelated excitation show multiple peaks and distributed over the range of the natural frequencies, for example, Fig. 10. These results explain that the  $\mu_R$  for each of six base patterns has a single peak, Figs. 3 and 4, and its magnitude is significantly increased compared to that for independent narrow band excitations, Fig. 6.

#### 4 Conclusions

Analytical techniques have been developed to study the effects of nature of excitations on the response of a mistuned bladed disk

assembly. In addition, basic concepts are developed to interpret the statistics of responses due to correlated narrow band excitations.

It is found that the number of peaks of mean-square response  $\mu_R$  depends on correlations of the narrow-band random excitations and the dominant peaks of  $\mu_R$  are matched well with weighting factors of the base correlation patterns which are very close to tuned modes with constant interblade phase angles. For uncorrelated narrow-band excitations, there are many frequencies at which values of  $\mu_R$  are maximum, whereas only a single resonance is found if the correlation pattern corresponds to one of the engine order excitations. For an engine order excitation with unknown (time-invariant and random) amplitudes, the mean of the square of response amplitude ( $\mu_{Ra}$ ) also shows a single resonance. Mistuning effects represented by the curves of  $\sigma_R/\mu_R$  and  $\sigma_{Ra}/\mu_{Ra}$  do not change significantly by the excitation correlations and have always multiple peaks which are related to the number of blades.

## Nomenclature

- $A$  = system matrix in state space analysis  
 $A_{xi}, B_{xi}$  = amplitude of sinusoidal response of  $i$ th blade  
 $B$  = input matrix in state space analysis  
 $B_R$  = input matrix of Lyapunov equation  
 $C$  = damping matrix  
 $c$  = damping coefficient of each blade  
 $E[\ ]$  = expected value  
 $F(t)$  = external force vector  
 $F_a$  = sinusoidal force vector, defined in Eq. (7)  
 $g(t)$  = narrow band excitation vector  
 $H_0, \delta H$  = defined in Eq. (9)  
 $h_i(t)$  = impulse response of  $i$ th decoupled band-pass filter system  
 $I_n$  = identity matrix  
 $K$  = stiffness matrix  
 $K_c$  = coupling stiffness between adjacent blades  
 $k_0$  = modal stiffness of each blade for tuned system  
 $k_i$  = modal stiffness of  $i$ th blade  
 $M$  = mass matrix  
 $m_i$  = modal mass of each blade  
 $n$  = no. of blades  
 $P$  = correlation matrix of state variables  
 $Q_0$  = intensity of white noise excitation  
 $Ra$  = mean square value of response amplitude, defined in Eq. (16)  
 $R_{fa}$  = correlation matrix of sinusoidal force vector, defined in Eq. (10)  
 $R_w(\tau)$  = correlation matrix of white noise excitations  
 $R_{xa}$  = correlation matrix of sinusoidal response vector, defined in Eq. (11)  
 $R_y(\tau)$  = defined in Eq. (31)  
 $R_\Phi(\tau)$  = defined in Eq. (26)  
 $r$  = engine order excitation  
 $V$  = normalized eigenvector matrix  
 $w(t)$  = white noise excitation vector  
 $x_a$  = sinusoidal response vector, defined in Eq. (6)  
 $x_i$  = displacement of  $i$ th blade  
 $y_i$  = defined by Eq. (22)  
 $z$  = state vector  
 $\alpha_c, \beta_c$  = unknown amplitudes of sinusoidal excitations  
 $\delta k$  =  $k_i - k_0$   
 $\sigma_{xi}$  = standard deviation of  $i$ th blade's displacement  
 $\sigma_R$  = defined in Eq. (43b)  
 $\sigma_{Ra}$  = defined in Eq. (17b)  
 $\mu_R$  = defined in Eq. (43a)  
 $\mu_{Ra}$  = defined in Eq. (17a)  
 $\Phi(t)$  = transformed force vector  
 $\xi_F$  = damping ratio of band-pass filter  
 $\psi_i$  = phase shift of engine order excitation of  $i$ th blade

$\omega_F$  = resonant frequency of band-pass filter

## Appendix A

**Computation of the Correlation Matrix of External Force Amplitudes.** The external forces are defined as

$$F_i(t) = \alpha_c \sin(\omega t + \psi_i) + \beta_c \cos(\omega t + \psi_i) = a_i \sin \omega t + b_i \cos \omega t \quad (49)$$

where

$$a_i = \alpha_c \cos \psi_i - \beta_c \sin \psi_i, \quad (50a)$$

$$b_i = \alpha_c \sin \psi_i + \beta_c \cos \psi_i \quad (50b)$$

The elements of the correlation matrix of external force amplitude are defined as

$$\begin{aligned} E[a_i a_j] &= E[(\alpha_c \cos \psi_i - \beta_c \sin \psi_i)(\alpha_c \cos \psi_j - \beta_c \sin \psi_j)] \\ &= E[\alpha_c^2] \cos \psi_i \cos \psi_j + E[\beta_c^2] \sin \psi_i \sin \psi_j \\ &\quad - E[\alpha_c \beta_c] \sin(\psi_i + \psi_j) \end{aligned} \quad (51)$$

$$\begin{aligned} E[b_i b_j] &= E[(\alpha_c \sin \psi_i + \beta_c \cos \psi_i)(\alpha_c \sin \psi_j + \beta_c \cos \psi_j)] \\ &= E[\alpha_c^2] \sin \psi_i \sin \psi_j + E[\beta_c^2] \cos \psi_i \cos \psi_j \\ &\quad + E[\alpha_c \beta_c] \sin(\psi_i + \psi_j) \end{aligned} \quad (52)$$

$$\begin{aligned} E[a_i b_j] &= E[(\alpha_c \cos \psi_i - \beta_c \sin \psi_i)(\alpha_c \sin \psi_j + \beta_c \cos \psi_j)] \\ &= E[\alpha_c^2] \cos \psi_i \sin \psi_j - E[\beta_c^2] \sin \psi_i \cos \psi_j \\ &\quad + E[\alpha_c \beta_c] \cos(\psi_i + \psi_j) \end{aligned} \quad (53)$$

where

$$E[\alpha_c^2] = E[(\alpha_{c0} + \delta\alpha)^2] = \alpha_{c0}^2 + E[\delta\alpha^2] \quad (54a)$$

$$E[\beta_c^2] = E[(\beta_{c0} + \delta\beta)^2] = \beta_{c0}^2 + E[\delta\beta^2] \quad (54b)$$

$$E[\alpha_c \beta_c] = E[(\alpha_{c0} + \delta\alpha)(\beta_{c0} + \delta\beta)] = \alpha_{c0} \beta_{c0} + E[\delta\alpha \delta\beta] \quad (54c)$$

## Appendix B

**Calculation of  $(\mu_{Ra})_i$  and  $(\sigma_{Ra}^2)_i$  for Sinusoidal Excitations With Unknown Amplitudes.** From Eq. (14)

$$R_{xa} = R_{0a} - H_0^{-1} \delta H R_{0a} - R_{0a} \delta H H_0^{-T} \quad (55)$$

Because

$$\begin{aligned} (H_0^{-1} \delta H R_{0a})_{i,j} &= \sum_{l=1}^n ((H_0^{-1})_{i,2l-1} (R_{0a})_{2l-1,j} \\ &\quad + (H_0^{-1})_{i,2l} (R_{0a})_{2l,j}) \delta k_l \end{aligned} \quad (56)$$

$$\begin{aligned} (R_{0a} \delta H H_0^{-T})_{i,j} &= \sum_{l=1}^n ((R_{0a})_{i,2l-1} (H_0^{-1})_{j,2l-1} \\ &\quad + (R_{0a})_{i,2l} (H_0^{-1})_{j,2l}) \delta k_l \end{aligned} \quad (57)$$

Equation (55) can be expressed as

$$(R_{xa})_{i,j} = (R_{0a})_{i,j} - \sum_{l=1}^n (\delta R_{xa})_{i,j,l} \delta k_l \quad (58)$$

where

$$\begin{aligned} (\delta R_{xa})_{i,j,l} &= (H_0^{-1})_{i,2l-1} (R_{0a})_{2l-1,j} + (H_0^{-1})_{i,2l} (R_{0a})_{2l,j} \\ &\quad + (R_{0a})_{i,2l-1} (H_0^{-1})_{j,2l-1} + (R_{0a})_{i,2l} (H_0^{-1})_{j,2l} \end{aligned} \quad (59)$$

Since  $E[\delta k_i] = 0$ , it is obvious that  $E[(R_{xa})_{i,i}] = (R_{0a})_{i,i}$ ; and it can be shown that

$$E[(R_{xa})_{i,i}^2] = (R_{0a})_{i,i}^2 + E[\delta k^2] \sum_{l=1}^n (\delta R_{xa})_{i,i,l}^2 \quad (60)$$

$$E[(R_{xa})_{i,i}(R_{xa})_{j,j}] = (R_{0a})_{i,i}(R_{0a})_{j,j} + E[\delta k^2] \sum_{l=1}^n (\delta R_{xa})_{i,i,l}(\delta R_{xa})_{j,j,l} \quad (61)$$

The matrix  $H_0$  and  $\delta H$  for the system shown in Fig. 1 are

$$H_0 = \begin{bmatrix} h_1 & h_3 & -h_2 & 0 & 0 & 0 & \cdots & -h_2 & 0 \\ -h_3 & h_1 & 0 & -h_2 & 0 & 0 & \cdots & 0 & -h_2 \\ -h_2 & 0 & h_1 & h_3 & -h_2 & 0 & \cdots & 0 & 0 \\ 0 & -h_2 & -h_3 & h_1 & 0 & -h_2 & \cdots & 0 & 0 \\ \cdot & \cdot & \cdot & \cdot & \cdot & \cdot & \cdots & \cdot & \cdot \\ \cdot & \cdot & \cdot & \cdot & \cdot & \cdot & \cdots & \cdot & \cdot \\ \cdot & \cdot & \cdot & \cdot & \cdot & \cdot & \cdots & \cdot & \cdot \\ -h_2 & 0 & 0 & 0 & 0 & 0 & \cdots & h_1 & h_3 \\ 0 & -h_2 & 0 & 0 & 0 & 0 & \cdots & -h_3 & h_1 \end{bmatrix} \quad (62)$$

$$\delta H = \text{diag}[\delta k_1 \quad \delta k_1 \quad \delta k_2 \quad \delta k_2 \quad \cdots \quad \delta k_n \quad \delta k_n] \quad (63)$$

where

$$h_1 = k_0 + 2K_c - m_i \omega^2, \quad (64a)$$

$$h_2 = K_c, \quad (64b)$$

$$h_3 = -c \omega \quad (64c)$$

## Appendix C

### Expressions for $\mu_R$ and $\sigma_R^2$ .

1 The mean of response correlation;  $(\mu_R)_i$

$$(\mu_R)_i = E \left[ (P_0)_{2n+i,2n+i} + \sum_{l=1}^n \frac{\partial P_{2n+i,2n+i}}{\partial k_l} \delta k_l \right] = (P_0)_{2n+i,2n+i} \quad (65)$$

because

$$E[\delta k_l] = 0. \quad (66)$$

2 The standard deviation of response correlation;  $(\sigma_R)_i$

$$(\sigma_R^2)_i = E[P_{2n+i,2n+i}^2] - (\mu_R)_i^2 \quad (67)$$

where

$$\begin{aligned} E[P_{i,i}^2] &= E \left[ \left( P_{0i,i} + \sum_{l=1}^n \frac{\partial P_{i,i}}{\partial k_l} \delta k_l \right)^2 \right] \\ &= E[(P_0)_{i,i}^2] + E \left[ \left( \sum_{l=1}^n \frac{\partial P_{i,i}}{\partial k_l} \delta k_l \right)^2 \right] \\ &\quad + 2E \left[ P_{0i,i} \left( \sum_{l=1}^n \frac{\partial P_{i,i}}{\partial k_l} \delta k_l \right) \right] \end{aligned} \quad (68)$$

and

$$E[(P_0)_{i,i}^2] = (P_0)_{i,i}^2 \quad (69)$$

$$E \left[ \left( \sum_{l=1}^n \frac{\partial P_{i,i}}{\partial k_l} \delta k_l \right)^2 \right] = E[\delta k^2] \sum_{l=1}^n \left( \frac{\partial P_{i,i}}{\partial k_l} \right)^2 \quad (70)$$

$$E \left[ P_{0i,i} \left( \sum_{l=1}^n \frac{\partial P_{i,i}}{\partial k_l} \delta k_l \right) \right] = 0. \quad (71)$$

## References

- [1] Sogliero, G., and Srinivasan, A. V., 1980, "Fatigue Life Estimates of Mistuned Blades Via a Stochastic Approach," *AIAA J.*, **18**(3), pp. 318–323.
- [2] Griffin, J. H., and Hoosac, T. M., 1984, "Model Development and Statistical Investigation of Turbine Blade Mistuning," *ASME J. Vib., Acoust., Stress, Reliab. Des.*, **106**, pp. 204–210.
- [3] Sinha, A., 1986, "Calculating the Statistics of Forced Response of a Mistuned Bladed Disk Assembly," *AIAA J.*, **24**(11), pp. 1797–1801.
- [4] Sinha, A., and Chen, S., 1989, "A Higher-Order Technique to Calculate the Statistics of Forced Response of a Mistuned Bladed Disk Assembly," *J. Sound Vib.*, **130**(2), pp. 207–221.
- [5] Wei, S.-T., and Pierre, C., 1988, "Localization Phenomena in Mistuned Assemblies With Cyclic Symmetry—Part I: Free Vibration, Part II: Forced Vibration," *ASME J. Vib., Acoust., Stress, Reliab. Des.*, **110**, pp. 429–449.
- [6] Lin, C.-C., and Mignolet, M. P., 1997, "An Adaptive Perturbation Scheme for the Analysis of Mistuned Bladed Disks," *ASME J. Eng. Gas Turbines Power*, **119**, pp. 153–160.
- [7] Whitehead, D. S., 1998, "The Maximum Factor by Which Forced Vibration of Blades Can Increase Due to Mistuning," *ASME J. Eng. Gas Turbines Power*, **120**, pp. 115–119.
- [8] Cha, D., and Sinha, A., 1998, "Statistics of Response of a Mistuned Bladed Disk Assembly Subjected to White Noise and Narrow Band Excitation," *ASME Paper*, 98-GT-379.
- [9] Whitehead, D. S., 1960, "The Analysis of Blade Vibration Due to Random Excitation," Reports and Memoranda No. 3253, Cambridge Univ.
- [10] Haupt, U., Rautenberg, M., and Abdel-Hamid, A. N., 1988, "Blade Excitation by Broad-Band Pressure Fluctuations in a Centrifugal Compressor," *ASME J. Turbomach.*, **110**, pp. 129–137.
- [11] Minkiewicz, G., and Russler, P., 1997, "Dynamic Response of Low Aspect Ratio Blades in a Two Stage Transonic Compressor," *33rd AIAA/ASME/SAE/ASEE/SME Joint Propulsion Conference and Exhibit, AIAA paper 97-3284*.
- [12] Sanders, A. J., and Fleeter, S., 1997, "Variability of Rotor Wake Interactions and Airfoil Unsteady Aerodynamics," *Proc., ASME Aerospace Division*, AD-Vol. 55, pp. 411–418.
- [13] Papoulis, A., 1966, *Probability, Random Variables and Stochastic Processes*, McGraw-Hill, New York, NY.
- [14] Sinha, A., 1990, "Friction Damping of Random Vibration in Gas Turbine Engine Airfoils," *Int. J. Turbo Jet Engines*, **7**, pp. 95–102.
- [15] *MATLAB Manual*, 1995 The MathWorks, Inc., MA.
- [16] Griffin, J. H., and Sinha, A., 1985, "The Interaction Between Mistuning and Friction in the Forced Response of Bladed Disk Assemblies," *ASME J. Eng. Gas Turbines Power*, **107**, pp. 205–211.
- [17] Huang, W.-H., 1981, "Free and Forced Vibration of Closely Coupled Turbomachinery Blades," *AIAA J.*, **19**(7), pp. 918–924.
- [18] Cha, D., 1999, "Statistics of Response of a Mistuned and Frictionally Damped Bladed Disk Assembly Subjected to Random Excitation," Ph.D. thesis, The Pennsylvania State University, University Park, PA.

# A Fundamental Model of Mistuning for a Single Family of Modes

D. M. Feiner

e-mail: dfein@andrew.cmu.edu

J. H. Griffin

e-mail: jg9h@andrew.cmu.edu

Department of Mechanical Engineering,  
Carnegie Mellon University,  
Pittsburgh, PA 15213

*A new reduced order model of mistuned bladed disk vibration is presented. This new approach is shown to accurately represent the response of real turbine geometries when only a single family of modes is excited. Yet its mathematical form is even simpler than that of a mass-spring model. Because it requires only minimal input data, this model is much easier to use than previous reduced order methods. Furthermore, its simplicity allows the fundamental parameters that control mistuning to be readily identified.*

[DOI: 10.1115/1.1508384]

*Keywords:* Mistuning, Blade Vibration, Reduced Order Model, Forced Response, Modeling

## 1 Introduction

The resonant amplitudes of turbine blades are generally very sensitive to small variations in the blade properties. Therefore, the small blade variations that result from manufacturing tolerances and wear cause some blades to have a significantly increased vibratory response and fail from high cycle fatigue. This phenomenon, referred to as the mistuning problem, has been studied extensively. Srinivasan [1] provides a comprehensive review of the topic.

In much of the mistuning research, bladed disks are modeled by lumped parameter mass-spring systems [2–6]. The simplicity of these models allows researchers to study trends or produce analytical results that provide physical insight into the mistuning problem. Furthermore, their low computational cost allows them to be used effectively for Monte Carlo simulations. However, these types of systems are extremely sensitive to slight errors and the lumped parameter models are not sufficiently accurate to capture the true behavior of a real bladed disk. As a consequence, the lumped parameter models offer a means of qualitative, not quantitative analysis.

An alternative approach for modeling mistuned bladed disks would be to use finite element-based reduced order methods. These models can accurately calculate the response of a real bladed disk geometry with computational costs that are comparable to mass-spring models. Two order-reduction approaches have been developed: one was a component mode synthesis and one was based on using a subset of nominal modes (SNM). The original reduced order models employed component mode synthesis, which analyzed the blades and the disk as separate substructures [7–10]. More recently, Yang and Griffin [11] developed a simpler approach (subset of nominal modes) that allowed the bladed disk to be analyzed as a single structure. Their method, SNM, reduced the degrees of freedom in the equations of motion by representing the mistuned system modes as a limited sum of the nominal or tuned system modes. However, while these models can effectively analyze true blade and disk geometries, they are still too mathematically complicated to provide physical insight into the mistuning problem. Furthermore, they are often difficult to use because they require as input a significant amount of data that must first be generated from finite element analyses of the tuned system and then incorporated into the reduced order model.

In this paper we present a new model of mistuned bladed disks that can accurately represent the mistuned response of real turbine geometries. It is applicable when the modes that are excited are part of an isolated family in which the strain energy is primarily in the blades. Once the new model is derived, it provides a mathematical formulation that is even simpler than that resulting from the use of mass spring models. Because of its simplicity, one may readily identify the fundamental parameters that control mistuned response. For this reason, we refer to this approach as providing a fundamental mistuning model (FMM).

FMM is basically an extension of SNM that takes advantage of how the SNM formulation may be simplified when the nominal modes used in the representation are limited to a single family. From experience with SNM, we know that a single family of modes often works quite well [11]. An example of where FMM will usually be applicable is in representing mistuning in the “first bending” modes. The term, first bending, is used by blade designers to refer to the lowest frequency modes in the bladed disk because the deformation in the blades is fairly similar to that of a cantilevered beam in its first bending mode.

We will find that when SNM is simplified to produce the fundamental model, it requires only two sets of parameters in order to accurately predict the mistuned modes and natural frequencies of the system. One parameter set consists of the nominal frequencies of the tuned system. This completely characterizes the bladed disk. The second set of parameters consists of the deviations of the individual blade frequencies from their tuned value (frequency deviations). This completely characterizes the mistuning. In addition, if we specify the engine order of the excitation and the modal damping we can predict the amplitude magnification that will be caused by mistuning. Thus, we will see that the only parameters that affect mistuning in an isolated family of modes are: the nominal frequencies of the tuned system, the frequency deviations of the mistuned blades, the modal damping, and the engine order of the excitation.

Since FMM requires only minimal input data, it is extremely simple to use. The tuned system frequencies can be obtained from a standard cyclic symmetric finite element analysis. The only other necessary input, the blade frequency deviations, may either be measured for a specific rotor or randomly generated for Monte Carlo simulations.

This paper is presented as follows. Section 2 provides the theoretical basis for FMM. In Section 3, two benchmark cases are discussed. The first case uses a simplified blade geometry to explore FMM’s ability to capture the effects of general mistuning; i.e., the bladed disk is simultaneously subjected to geometric, den-

Contributed by the International Gas Turbine Institute and presented at the International Gas Turbine and Aeroengine Congress and Exhibition, Amsterdam, The Netherlands, June 3–6, 2002. Manuscript received by the IGTI, January 30, 2002. Paper No. 2002-GT-30425. Review Chair: E. Benvenuti.

sity, and elastic modulus variations. The second benchmark examines the accuracy of FMM when it is used to model a turbine blade with a more realistic geometry. In each case, the FMM calculations of the mistuned frequencies, modes, and forced response are compared with finite element analyses. Then, Section 4 explores the limitations of FMM. Lastly, the key attributes of the method are summarized in Conclusions.

## 2 Theory

This section presents the mathematical basis of the fundamental mistuning model, FMM. We assume that we are dealing with an isolated family of modes in which the strain energy is primarily in the blades. This will allow us to make a number of simplifying assumptions as we progress through the derivation. The validity of the resulting model will be corroborated through the numerical studies in Section 3.

Section 2.1 of this section describes how the SNM approach [11] is used to reduce the order of the mistuned free-response equations and formulate the problem in terms of reduced order sector matrices. Section 2.2 relates the sector matrices to mistuned blade frequencies. Section 2.3 simplifies the resulting mathematical expressions and summarizes the FMM approach.

**2.1 Reduction of Order.** Consider a mistuned, bladed disk in the absence of an excitation. By assuming a harmonic, undamped, steady-state response, the equations of motion can be written as

$$[(\mathbf{K}^\circ + \Delta\mathbf{K}) - \omega_j^2(\mathbf{M}^\circ + \Delta\mathbf{M})]\boldsymbol{\phi}_j = 0 \quad (1)$$

where  $\mathbf{K}^\circ$  and  $\mathbf{M}^\circ$  are the tuned system mass and stiffness matrices.  $\Delta\mathbf{K}$  and  $\Delta\mathbf{M}$  are the variations in the stiffness and mass matrices due to mistuning. The vector  $\boldsymbol{\phi}_j$  is the  $j$ th mistuned mode, and  $\omega_j$  is its corresponding natural frequency.

In SNM, the mistuned modes are represented as a weighted sum of a limited number of nominal system modes [11]; i.e.,

$$\boldsymbol{\phi}_j = \sum_{m=0}^{N-1} \beta_{jm} \boldsymbol{\phi}_m^\circ \quad (2)$$

where  $\beta_{jm}$  is a weighting factor, and  $\boldsymbol{\phi}_m^\circ$  is the  $m$ th nominal system mode normalized with respect to the tuned mass matrix. Alternatively, (2) may be expressed in matrix notation as

$$\boldsymbol{\phi}_j = \boldsymbol{\Phi}^\circ \boldsymbol{\beta}_j \quad (3)$$

where  $\boldsymbol{\beta}_j$  is a vector of weighting factors, and  $\boldsymbol{\Phi}^\circ$  is a matrix whose columns are the tuned system modes; i.e.,  $\boldsymbol{\Phi}^\circ = [\boldsymbol{\phi}_0^\circ \boldsymbol{\phi}_1^\circ \dots \boldsymbol{\phi}_{N-1}^\circ]$ . Substituting (3) into (1) and premultiplying by  $\boldsymbol{\Phi}^{\circ H}$ , where H is the Hermitian, yields the reduced order problem

$$[(\Lambda^\circ + \Delta\hat{\mathbf{K}}) - \omega_j^2(\mathbf{I} + \Delta\hat{\mathbf{M}})]\boldsymbol{\beta}_j = 0 \quad (4)$$

Physically,  $\Lambda^\circ$  represents the modal stiffness matrix and  $\mathbf{I}$  represents the modal mass matrix. However, since the modes are normalized with respect to the mass matrix,  $\Lambda^\circ$  is simply a diagonal matrix of the tuned system eigenvalues,<sup>1</sup> and  $\mathbf{I}$  is the identity matrix.  $\Delta\hat{\mathbf{K}}$  and  $\Delta\hat{\mathbf{M}}$  are the variations in the modal stiffness and modal mass matrices caused by stiffness and mass mistuning

$$\Delta\hat{\mathbf{K}} = \boldsymbol{\Phi}^{\circ H} \Delta\mathbf{K} \boldsymbol{\Phi}^\circ \quad (5)$$

$$\Delta\hat{\mathbf{M}} = \boldsymbol{\Phi}^{\circ H} \Delta\mathbf{M} \boldsymbol{\Phi}^\circ \quad (6)$$

By consolidating the modal mass and stiffness variations into one term, (4) can be written as

$$(\Lambda^\circ + \hat{\mathbf{A}}_j)\boldsymbol{\beta}_j = \omega_j^2 \boldsymbol{\beta}_j \quad (7)$$

where

<sup>1</sup>An eigenvalue is equal to the square of the natural frequency of a mode.

$$\hat{\mathbf{A}}_j = \Delta\hat{\mathbf{K}} - \omega_j^2 \Delta\hat{\mathbf{M}} \quad (8)$$

In this form, each mistuned frequency,  $\omega_j$ , has a corresponding mistuning matrix,  $\hat{\mathbf{A}}_j$ . However, assuming that the subset of nominal modes  $\boldsymbol{\Phi}^\circ$  used in the SNM representation consists of a single family of modes in which the strain energy is primarily in the blades, the mistuned frequencies will be closely spaced. Thus, all of the  $\omega_j$  in (8) are nearly equal and can be approximated by an average of the tuned system frequencies,  $\omega_{\text{avg}}$ . Therefore, the  $\hat{\mathbf{A}}_j$  will be approximated by the single mistuning matrix

$$\hat{\mathbf{A}} = \Delta\hat{\mathbf{K}} - \omega_{\text{avg}}^2 \Delta\hat{\mathbf{M}} \quad (9)$$

Thus, (7) becomes

$$(\Lambda^\circ + \hat{\mathbf{A}})\boldsymbol{\beta}_j = \omega_j^2 \boldsymbol{\beta}_j \quad (10)$$

In the next section we will relate the matrix  $\hat{\mathbf{A}}$  to the frequency deviations of the mistuned blades.

### 2.2 Relating Mistuning to Blade Frequency Deviations.

In order to determine mistuned modes and frequencies from (9), the mistuning matrix,  $\hat{\mathbf{A}}$ , must first be calculated. One possible approach is to calculate  $\hat{\mathbf{A}}$  directly from its definition, which is very similar to the method used by SNM. However, these calculations are fairly tedious because they involve the extraction of data from finite element models and the multiplication of large matrices. In addition, they require knowledge of how the mass and stiffness matrices vary from one sector to the next—information that we typically do not have. Instead, FMM uses approximations to relate  $\hat{\mathbf{A}}$  directly to the blade-alone frequency deviations.

Relating  $\hat{\mathbf{A}}$  to frequency deviations is a three-step process. First, the mistuning matrix is expressed in terms of the mode shapes of an individual sector. Then, the sector modes are related to their corresponding cantilevered blade mode. Finally, the resulting blade-mode terms in  $\hat{\mathbf{A}}$  are expressed in terms of the frequency deviations of the blades.

*Relating Mistuning to Sector Modes.* Consider the mistuning matrix,  $\hat{\mathbf{A}}$ , as defined by Eq. (9). This matrix is formed by taking a product of the tuned system modes with the mistuned stiffness and mass matrices, Eqs. (5) and (6). This product can be taken on a sector-by-sector basis; i.e.,

$$\hat{\mathbf{A}} = \sum_{s=0}^{N-1} \hat{\mathbf{A}}^{(s)} \quad (11)$$

where  $\hat{\mathbf{A}}^{(s)}$  is the contribution to  $\hat{\mathbf{A}}$  from the  $s$ th sector. The sectors are numbered from 0 to  $N-1$  where  $N$  is the number of blades on the disk.

From (9),  $\hat{\mathbf{A}}^{(s)}$  is

$$\hat{\mathbf{A}}^{(s)} = \Delta\hat{\mathbf{K}}^{(s)} - \omega_{\text{avg}}^2 \Delta\hat{\mathbf{M}}^{(s)} \quad (12)$$

where  $\Delta\hat{\mathbf{K}}^{(s)}$  and  $\Delta\hat{\mathbf{M}}^{(s)}$  are the  $s$ th sector contributions to the modal stiffness and mass variations

$$\Delta\hat{\mathbf{K}}^{(s)} = \boldsymbol{\Phi}^{\circ(s)H} \Delta\mathbf{K}^{(s)} \boldsymbol{\Phi}^{\circ(s)} \quad (13)$$

$$\Delta\hat{\mathbf{M}}^{(s)} = \boldsymbol{\Phi}^{\circ(s)H} \Delta\mathbf{M}^{(s)} \boldsymbol{\Phi}^{\circ(s)} \quad (14)$$

in which  $\Delta\mathbf{K}^{(s)}$  and  $\Delta\mathbf{M}^{(s)}$  are the physical variations in the stiffness and mass matrices for the  $s$  blade-disk sector, and  $\boldsymbol{\Phi}^{\circ(s)}$  is the portion of tuned mode matrix,  $\boldsymbol{\Phi}^\circ$ , that corresponds to the  $s$ th sector.

Substituting (13) and (14) into (12) produces an expression for  $\hat{\mathbf{A}}^{(s)}$  in terms of the physical mass and stiffness variation of a sector and the tuned sector modes

$$\hat{\mathbf{A}}^{(s)} = \boldsymbol{\Phi}^{\circ(s)H} (\Delta\mathbf{K}^{(s)} - \omega_{\text{avg}}^2 \Delta\mathbf{M}^{(s)}) \boldsymbol{\Phi}^{\circ(s)} \quad (15)$$

Considering only a single element of the matrix  $\hat{\mathbf{A}}^{(s)}$ , (15) implies



$$\hat{\mathbf{A}}_{mn}^{(s)} = \boldsymbol{\phi}_m^{\circ(s)H} (\Delta \mathbf{K}^{(s)} - \omega \Delta \mathbf{M}^{(s)}) \boldsymbol{\phi}_n^{\circ(s)} \quad (16)$$

where  $\boldsymbol{\phi}_m^{\circ(s)}$  and  $\boldsymbol{\phi}_n^{\circ(s)}$  are the modes in the  $m$ th and  $n$ th columns of  $\boldsymbol{\Phi}^{\circ(s)}$ . Thus, the mistuning matrix has been expressed in terms of the tuned modes and mistuning of individual sectors.

**Relating Sector Modes to Blade Mode.** In the SNM formulation the tuned system modes are written in complex, traveling wave form [11]. When the tuned system modes are expressed in this manner, the amplitudes of every blade in a mode are the same, but each blade has a different phase. Therefore, the part of the mode corresponding to the  $s$ th sector can be written in terms of the same mode on the 0th sector, multiplied by an appropriate phase shift; i.e.,

$$\boldsymbol{\phi}_m^{(s)} = e^{ism2\pi/N} \boldsymbol{\phi}_m^{\circ(0)} \quad (17)$$

where  $i = \sqrt{-1}$ . In (17) it is assumed that the modes are ordered in the pattern

$$\left\{ \begin{array}{cccccccc} \boldsymbol{\phi}_0^{(s)} & \boldsymbol{\phi}_1^{(s)} & \boldsymbol{\phi}_2^{(s)} & \cdots & \boldsymbol{\phi}_{N/2}^{(s)} & \boldsymbol{\phi}_{N/2+1}^{(s)} & \cdots & \boldsymbol{\phi}_{N-1}^{(s)} \\ (0) & (1B) & (2B) & \cdots & \left(\frac{N}{2}\right) & \left(\left(\frac{N}{2}-1\right)F\right) & \cdots & (1F) \end{array} \right\} \quad (18)$$

where the second row in (18) indicates the nodal diameter and direction of the corresponding mode that lies above it. **B** denotes a backward traveling wave, defined as a mode with a positive phase shift from one sector to the next, and **F** denotes a forward traveling wave, defined as a mode with a negative phase shift from one sector to the next. Note that the modes are numbered from 0 to  $N-1$ .

Substituting (17) into (16) results in an expression for the elements of the sector mistuning matrix in terms of the 0th sector modes

$$\hat{\mathbf{A}}_{mn}^{(s)} = e^{is(n-m)2\pi/N} \boldsymbol{\phi}_m^{\circ(0)H} (\Delta \mathbf{K}^{(s)} - \omega_{\text{avg}}^2 \Delta \mathbf{M}^{(s)}) \boldsymbol{\phi}_n^{\circ(0)} \quad (19)$$

Because the tuned modes used as a basis are an isolated family of modes that have most of their strain energy in the blades, the sector modes of all nodal diameters look nearly identical and can be approximated by their corresponding blade-alone mode as indicated schematically in Fig. 1. Applying the blade mode approximation for the sector modes in (19),  $\hat{\mathbf{A}}_{mn}^{(s)}$  can be written as

$$\hat{\mathbf{A}}_{mn}^{(s)} = \left( \frac{\omega_{\text{avg}}^2}{N(\omega_b^{\circ})^2} \right) e^{is(n-m)2\pi/N} [\mathbf{b}^{\circ H} (\Delta \mathbf{K}^{(s)} - \omega_{\text{avg}}^2 \Delta \mathbf{M}^{(s)}) \mathbf{b}^{\circ}] \quad (20)$$

where  $\mathbf{b}^{\circ}$  is the corresponding tuned blade-alone mode, normalized with respect to the blade mass matrix, and  $\omega_b^{\circ}$  is its natural frequency. The factor

$$\omega_{\text{avg}}^2 / (N(\omega_b^{\circ})^2)$$

scales the blade mode terms so that they have approximately the same strain energy as the sector modes they replace.

**Introduction of Blade Frequency Deviation.** Finally, the bracketed terms of (20) may be related to the frequency deviations of the individual blades. Consider a mistuned blade that is clamped at its base. The free-response equation of motion is

$$[(\mathbf{K}^{\circ(s)} + \Delta \mathbf{K}^{(s)}) - \omega_b^2 (\mathbf{M}^{\circ(s)} + \Delta \mathbf{M}^{(s)})] \mathbf{b} = 0 \quad (21)$$

where the mass and stiffness matrices are matrices of a single blade-disk sector,  $\mathbf{b}$  is the mistuned blade mode of interest, and  $\omega_b$  is its corresponding natural frequency. Since it was assumed that this family of modes is isolated the frequencies of the blades are not close together. As a result, it can be shown that the mode shapes remain essentially unchanged by the perturbation in the mass and stiffness matrices [12]; i.e.,

$$\mathbf{b} = \mathbf{b}^{\circ} \quad (22)$$

Substituting (22) into (21) and pre-multiplying by  $\mathbf{b}^{\circ H}$  yields,

$$\mathbf{b}^{\circ H} (\Delta \mathbf{K}^{(s)} - \omega_b^2 \Delta \mathbf{M}^{(s)}) \mathbf{b}^{\circ} = \omega_b^2 - \omega_b^{\circ 2} \quad (23)$$

where  $\omega_b^{\circ}$  is the tuned blade frequency. By factoring the right-hand side of (23) into  $(\omega_b + \omega_b^{\circ})(\omega_b - \omega_b^{\circ})$ , the expression can be approximated by,

$$\omega_b^2 - \omega_b^{\circ 2} \approx 2\omega_b^{\circ} \Delta \omega_b \quad (24)$$

in which  $\Delta \omega_b$  is the fractional change in the blade frequency, given by  $\Delta \omega_b = (\omega_b - \omega_b^{\circ}) / \omega_b^{\circ}$ . Since the sector mode's strain energy is primarily in the blades,  $\omega_b \approx \omega_{\text{avg}}$ . By making this substitution on the left side of (23) and substituting (24) on the right side, the expression reduces to a simplified approximation for the bracketed terms of (20).

$$\mathbf{b}^{\circ H} (\Delta \mathbf{K}^{(s)} - \omega_{\text{avg}}^2 \Delta \mathbf{M}^{(s)}) \mathbf{b}^{\circ} \approx 2\omega_b^{\circ} \Delta \omega_b \quad (25)$$

Substituting (25) into (20) results in an expression that relates the elements of the sector  $s$  mistuning matrix to the frequency deviation of the  $s$ th blade

$$\hat{\mathbf{A}}_{mn}^{(s)} = \frac{2\omega_{\text{avg}}^2}{N} e^{is(n-m)2\pi/N} \Delta \omega_b^{(s)} \quad (26)$$

where the superscript on  $\Delta \omega_b$  is introduced to indicate that the frequency deviation corresponds to the  $s$ th sector. These sector contributions may be summed to obtain the elements of the mistuning matrix

$$\hat{\mathbf{A}}_{nm} = \frac{2\omega_{\text{avg}}^2}{N} \sum_{s=0}^{N-1} e^{is(n-m)2\pi/N} \Delta \omega_b^{(s)} \quad (27)$$

**2.3 The Simplified Form of the Fundamental Mistuning Model.** FMM solves the eigenvalue problem (10) to calculate the system's mistuned mode shapes and frequencies. The matrix of this eigenvalue problem contains two terms: a diagonal matrix consisting of the tuned system eigenvalues,  $\lambda$ , and the mistuning matrix,  $\mathbf{A}$ . In Section 2.2, the elements of  $\mathbf{A}$  were expressed in terms of the frequency deviation of the individual blades. In this section we will further simplify these expressions.

Consider the exponential term in (27). Due to periodicity and aliasing effects, it takes on only  $N$  distinct values. It can be written in terms of the dummy index,  $p$

$$e^{is(n-m)2\pi/N} = e^{isp2\pi/N} \quad (28)$$

where

$$p = \begin{cases} (n-m) & n \geq m \\ (n-m) + N & n < m \end{cases}$$

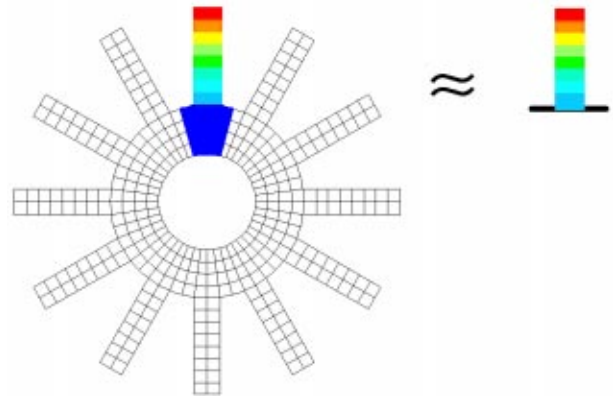


Fig. 1 Near equivalence of sector mode and blade mode

Note that  $p$  ranges from 0 to  $N-1$ . Substituting (28) into (27) produces

$$\hat{\mathbf{A}}_{nm} = 2\omega_{\text{avg}}^2 \left[ \frac{1}{N} \sum_{s=0}^{N-1} e^{isp2\pi/N} \Delta\omega_b^{(s)} \right] \quad (29)$$

Observe that the bracketed term of (29) is a form of the discrete Fourier transform (DFT). In this case, it is the  $p$ th DFT of the blade frequency deviations  $\Delta\omega_b^{(s)}$ , which we will denote as  $\bar{\omega}_p$ ; i.e.,

$$\bar{\omega}_p = \left[ \frac{1}{N} \sum_{s=0}^{N-1} e^{isp2\pi/N} \Delta\omega_b^{(s)} \right] \quad (30)$$

By substituting (30) into (29),  $\hat{\mathbf{A}}$  may be expressed in the simplified matrix form

$$\hat{\mathbf{A}} = 2\omega_{\text{avg}}^2 \bar{\mathbf{\Omega}} \quad (31)$$

where

$$\bar{\mathbf{\Omega}} = \begin{bmatrix} \bar{\omega}_0 & \bar{\omega}_1 & \cdots & \bar{\omega}_{N-1} \\ \bar{\omega}_{N-1} & \bar{\omega}_0 & \cdots & \bar{\omega}_{N-2} \\ \vdots & \vdots & \ddots & \vdots \\ \bar{\omega}_1 & \bar{\omega}_2 & \cdots & \bar{\omega}_0 \end{bmatrix} \quad (32)$$

$\bar{\mathbf{\Omega}}$  is a matrix containing the discrete Fourier transforms of the blade frequency deviations. Note that  $\bar{\mathbf{\Omega}}$  has a circulant form, in which each column is equal to the previous column rotated down a row. Therefore, it has only  $N$  distinct values.

Substituting (31) into (10) produces the most basic form of the eigenvalue problem that may be solved to determine the modes and natural frequencies of the mistuned system.

$$(\mathbf{\Lambda}^\circ + 2\omega_{\text{avg}}^2 \bar{\mathbf{\Omega}}) \boldsymbol{\beta}_j = \omega_j^2 \boldsymbol{\beta}_j \quad (33)$$

Equations (32) and (33) represent the functional form of the fundamental mistuning model.  $\mathbf{\Lambda}^\circ$  is a diagonal matrix of the nominal system eigenvalues, ordered in accordance with (18). The eigenvalues are equal to the squares of the natural frequencies of the tuned system. This matrix contains all the nominal system information required to calculate the mistuned modes. Note that the geometry of the system does not directly enter into this expression. The term representing mistuning in (33),  $2\omega_{\text{avg}}^2 \bar{\mathbf{\Omega}}$ , is a simple circulant matrix that contains the discrete Fourier transforms of the blade frequency deviations, pre-multiplied by a scaling coefficient. The scaling coefficient is  $2\omega_{\text{avg}}^2$  where  $\omega_{\text{avg}}$  is the average value of the tuned system frequencies.

The eigenvalues of (33) are the squares of the mistuned frequencies, and the eigenvectors define the mistuned mode shapes through (3). In fact, because the tuned modes have been limited to a single family and appear in  $\Phi^\circ$  in a certain order, we can approximately calculate the distortion in the mistuned mode shapes without knowing anything specific about  $\Phi^\circ$ . The reason for this is the assumption that all of the tuned system modes on the zeroth sector look nearly the same; i.e.,  $\boldsymbol{\phi}_m^{(0)} \approx \boldsymbol{\phi}_n^{(0)}$ . Then (2) and (17) imply that if the  $j$ th mistuned mode is given by  $\boldsymbol{\beta}_j = [\beta_{j0}, \beta_{j1}, \dots, \beta_{j,N-1}]^T$  then the physical displacements of the  $s$ th blade in this mode are proportional to

$$x_{js} = \sum_{m=0}^{N-1} \beta_{jm} e^{ism2\pi/N} \quad (34)$$

### 3 Numerical Results

We wrote a computer program to implement the theory presented in the last section. The program also incorporates a simple modal summation algorithm to calculate the bladed disk's forced response. The modal summation assumes constant modal damping. The basic modal summation algorithm was chosen to bench-

mark the forced response because a similar algorithm may be used as an option in the commercial finite element code ANSYS that we were using as a benchmark. Clearly, FMM can be used with more sophisticated methods for calculating the forced response, such as the state-space approach used in SNM [11].

This section presents two benchmark tests of the fundamental mistuning model code. The first case examines the model's ability to handle general mistuning in which the blades are simultaneously subjected to geometric, density, and modulus variations. This is an interesting test case since the theory indicates that the dynamic response depends only on the blades' frequency deviation and not on the physical cause of the mistuning. The first test is performed using a simplified blade geometry that is readily represented with a relatively small number of degrees of freedom.

The second case investigates FMM's effectiveness in representing a more realistic blade geometry. In addition, the geometry is also studied by using a mass spring representation to gauge the relative accuracy of the two methods. This is a natural comparison since a mass-spring representation is the only widely used modeling approach that has a similar level of simplicity as FMM. We will compare results from FMM and the mass-spring model with a finite element benchmark.

#### 3.1 General Mistuning Benchmark.

Consider the bladed disk model shown in Fig. 2. The system was designed with long beamlike blades in order to provide a simple test case in which the natural frequencies of the first bending family of modes are isolated. Figure 3 shows the system natural frequencies and identifies the isolated family. Thus, the first bending family satisfies the assumptions of the fundamental mistuning model, and is a good candidate for a benchmark test. The bladed disk was constructed from a coarse grid of plate elements to keep the total number of degrees of freedom in the model low. This allowed a benchmark finite element analysis of the entire rotor to be performed with minimal difficulty.

The bladed disk was mistuned by independently varying each blade's length, density, and Young's modulus. These variations were applied randomly, with 0.2, 0.8, and 0.8% standard deviations in length, density and modulus, respectively. These standard deviations were chosen so that each type of perturbation would have a comparable effect on the blade frequency deviations.

The dynamic response of the mistuned bladed disk was then calculated by two different methods: a full finite element analysis using the commercially available ANSYS finite element code, and

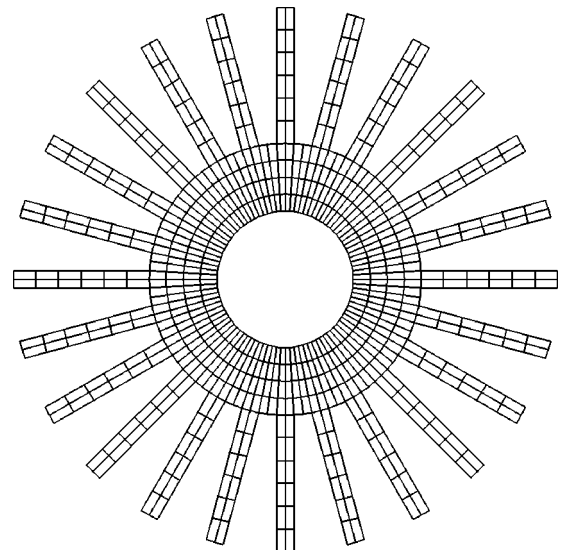


Fig. 2 Finite element model of bladed disk system

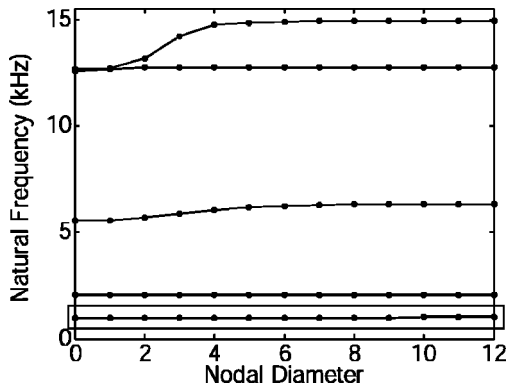


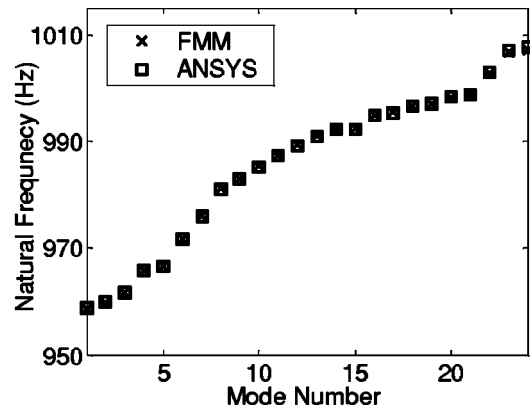
Fig. 3 Tuned system frequencies

FMM. The ANSYS calculations serve as a benchmark to assess the accuracy of the FMM method. The input data for the FMM analysis, the tuned system frequencies and the deviations of the individual blade frequencies from their tuned value, were also calculated by using ANSYS. In practice, the frequency deviations of the individual blades could be measured in bench tests. The discrete Fourier transform of the deviations in blade frequency was calculated to form the fundamental mistuning model of this system, the eigenvalue problem of (33). The eigenvalue problem was solved using a standard numerical algorithm, and then the eigenvectors were converted to physical mode shapes through (34).

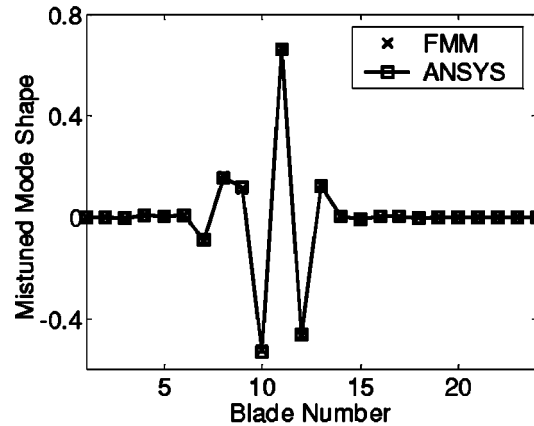
The FMM performed well in this test. The reduced order model's prediction of the mistuned frequencies is shown in Fig. 4(a), along with the benchmark results. Observe that the model gave an accurate estimate of the mistuned frequencies: the maximum error in the reduced order model's frequency prediction was less than 0.05 percent. In addition, FMM also accurately calculated the mistuned mode shapes. By mode shape we mean the displacement of the tip of each blade when plotted as a function of the blade number, i.e. its circumferential location on the disk. For example, a representative mode is depicted in Fig. 4(b).

The bladed disk was then subjected to various engine order excitations. In each case, it was assumed that all modes had a damping ratio of 0.5%. The generalized force in each mistuned mode was calculated and the modes summed to determine the amplitude of each blade as a function of the excitation frequency. The results were normalized by dividing by the amplitude of the tuned system at resonance. Thus, an amplitude greater than one indicates that a blade's response is higher than that of the tuned system at resonance. The same type of calculation was also performed by using a harmonic excitation option in ANSYS. Figure 5 shows a representative result from these calculations. For clarity, we plotted the response of only the high responding blade, the median responding blade, and the low responding blade. The forced response calculated from the fundamental model matched the ANSYS results quite well: at the peak response frequency, the FMM prediction of the highest blade's response differed from that predicted by ANSYS by only 2%. Thus, in this example, the blade frequency deviations used by FMM provide a reasonably accurate, simple method of characterizing a bladed disk that had geometric, density, and modulus mistuning.

**3.2 Realistic Geometry Benchmark.** In the previous example, it was shown that FMM could accurately calculate a bladed disk's mistuned response based only on blade frequency deviations, without regard for the physical cause of the mistuning. However, a beamlike blade model was used in order to minimize the computational cost. Therefore, it is useful to consider an additional test case that shows that FMM can accurately analyze a more realistic geometry.



(a)



(b)

Fig. 4 Representative results of generally mistuned bladed disk—(a) mistuned frequency; (b) mode shape of 17th mode

Consider the 3-D finite element model of the HPT blade-disk sector shown in Fig. 6. There are 24 sectors in the full system. This model was developed by approximating the features of an actual turbine blade and provides a reasonable test of FMM's ability to represent a realistic blade geometry. This system has an

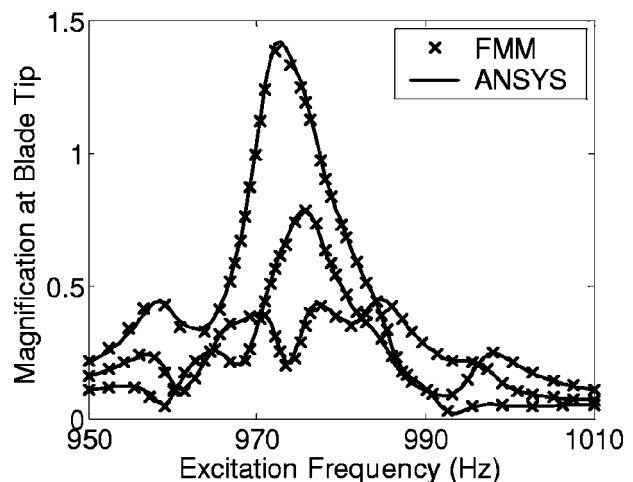


Fig. 5 Blade amplitude as a function of excitation frequency for a 3rd engine order excitation



Fig. 6 Finite element model of bladed disk sector

isolated first bending family of modes with closely spaced frequencies, as shown in Fig. 7. Consequently, we should be able to represent its response with FMM.

As a benchmark, we performed a finite element analysis of the full-mistuned rotor using ANSYS. The bladed disk was mistuned by randomly varying the elastic moduli of the blades with a standard deviation that was equal to 1.5% of the tuned system's elastic modulus.

We then constructed an equivalent mass-spring model with one degree-of-freedom per sector [6]. Each mass was set to unity and the stiffness parameters were obtained through a least squares fit of the tuned natural frequencies. Figure 8 shows the tuned frequencies of the system along with the frequencies of the best-fit mass-spring model. Note that while the mass-spring model was able to capture the higher nodal diameter frequencies fairly well, it had great difficulty with the low nodal diameter frequencies. This discrepancy arises because the natural frequencies of the single degree-of-freedom mass-spring system have the form

$$\omega_n = \sqrt{[k + 4k_c \sin^2(n\pi/N)]/m} \quad (35)$$

where  $m$  is the blade mass,  $k$  and  $k_c$  are the base stiffness and coupling stiffness,  $n$  is the nodal diameter of the mode, and  $N$  is the number of blades. However, the actual frequencies of the finite element model have a significantly different shape when plotted as a function of nodal diameters. In contrast, FMM takes the actual finite element frequencies as input parameters, and therefore is guaranteed to match the tuned system's frequencies exactly.

The mass-spring model was then mistuned by adjusting the base stiffness of the blades to correspond to the modulus changes used in the finite element model. The mistuned modes and forced response were then calculated with both FMM and the mass-spring model, and compared with the finite element results.

The mistuned frequencies predicted by FMM and ANSYS are quite similar, Fig. 9(a). However the mass-spring model had some significant discrepancies, especially in the low frequency modes. FMM and ANSYS also predict essentially the same mistuned mode shapes, e.g., see Fig. 9(b). In contrast, the mass-spring model did a poor job of matching the finite element mode shapes, even on modes whose frequencies were accurately predicted. For example, the mode plotted in Fig. 9(b) corresponded to the 18th frequency, as highlighted in Fig. 9(a). Note that the mass-spring

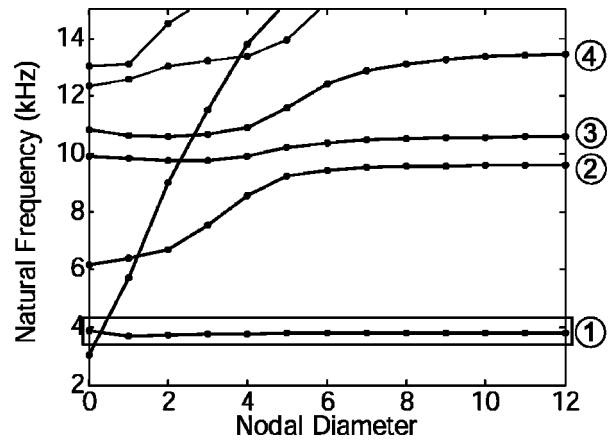


Fig. 7 Tuned system frequencies of the first four families of modes

model accurately predicted this frequency. However, it is clear from Fig. 9(b) that the mass-spring model still did a poor job of matching the finite element mode shapes.

The predicted modes were then summed to obtain the system's forced response to various engine order excitations. Figure 10(a) shows the amplitudes predicted by the mass-spring model and ANSYS for a representative case. For clarity, only the high responding, median responding, and low responding blades are plotted. Observe that the mass-spring model provided a poor prediction of the system's forced response. However, the results from FMM agreed well with those computed by ANSYS, as shown in Fig. 10(b). The prediction by FMM of the highest blade response differed from that predicted by ANSYS by only 1.6%. Thus, FMM can provide accurate predictions of the mode shapes and forced response of a turbine blade with a realistic geometry.

#### 4 Limitations

The fundamental mistuning model was derived from the subset of nominal modes theory by applying three simplifying assumptions: only a single, isolated family of modes is excited, the strain energy of that family's modes is primarily in the blades, and the family's frequencies are closely spaced. In addition, one corollary of these assumptions is that the blade's motion looks very similar among all modes in the family. As demonstrated in the previous section, FMM works quite well when these assumptions are met.

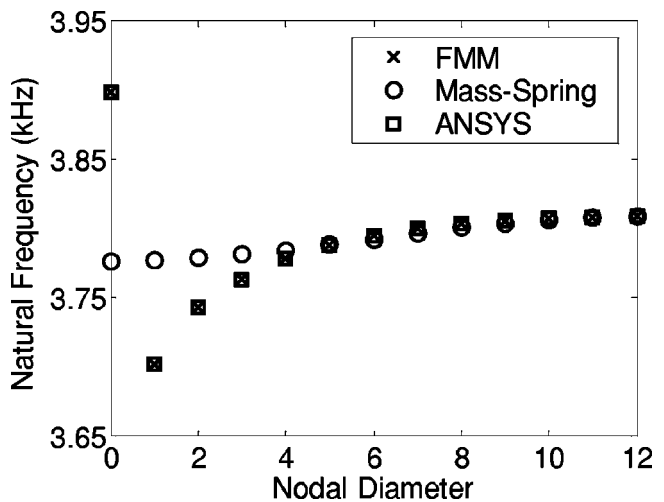
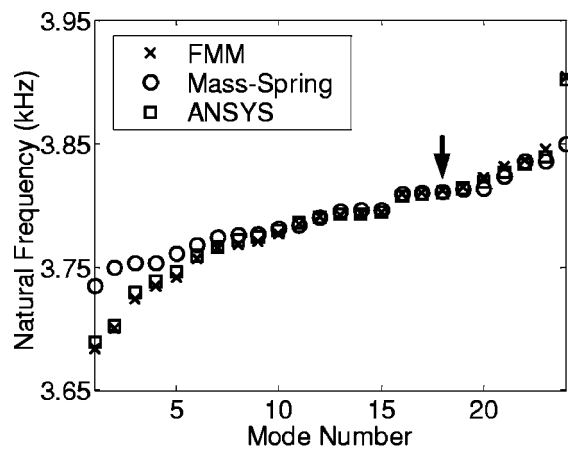
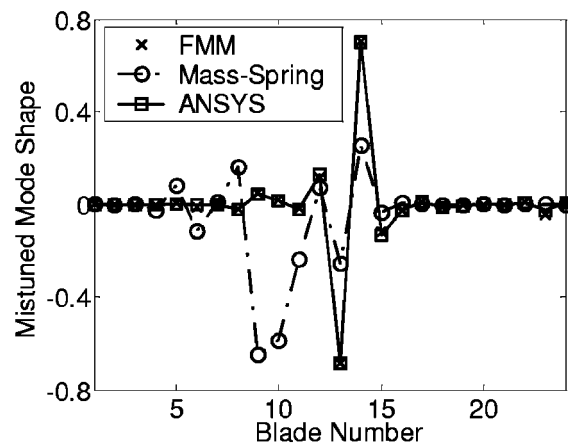


Fig. 8 Tuned system frequencies of the fundamental family of modes



(a)



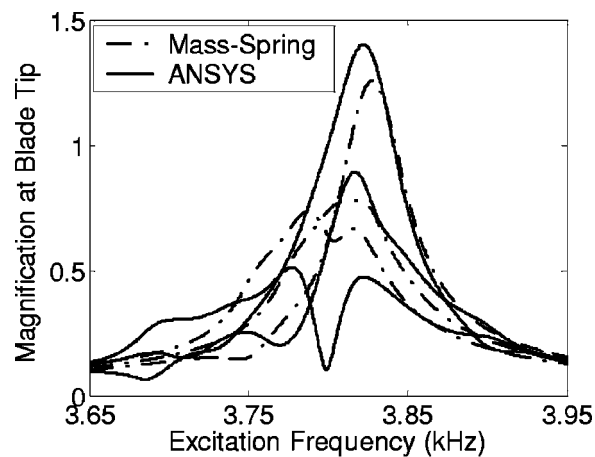
(b)

Fig. 9 Representative results of realistic mistuned bladed disk—(a) mistuned frequency; (b) mode shape of 18th mode

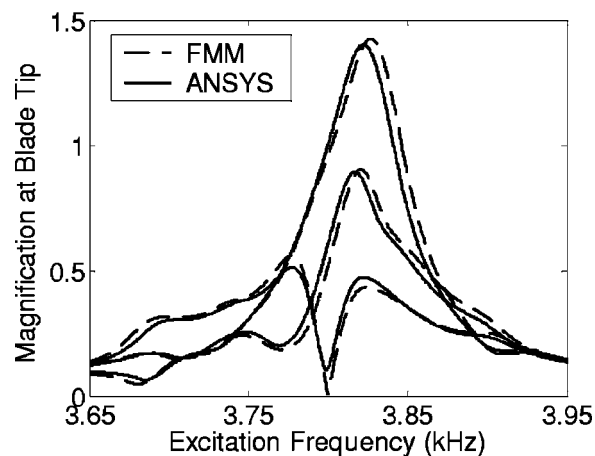
However, these ideal conditions are usually only found in the fundamental modes of a rotor. The higher frequency families are often clustered close together, have a significant amount of strain energy in the disk, and span a large frequency range. Furthermore, veerings are quite common, causing a family's modes to change significantly from one nodal diameter to the next. Therefore, in this section we explore the limitations of FMM to identify when the method works effectively in high frequency regions and when it fails.

To examine the limitations of FMM, we used the realistic HPT model studied in the previous section, see Fig. 6. Note that since we are interested in studying FMM's limitations, we did not take any great care in assigning modes to families. Therefore, some crossings shown in Fig. 7 may in fact be veerings. However, since such errors are easily made in practice, it is useful to include them in the limitation study. For reference, four mode families are numbered along the right side of Fig. 7.

Notice that except for the fundamental modes, the families undergo a significant frequency increase between 0 and 6 nodal diameters. The steep slopes in this region suggest that the modes have a large amount of strain energy in the disk. Furthermore, the high modal density in this area makes it likely that some modes were assigned to the wrong family. Therefore, the modes of a single family will likely change significantly from one nodal diameter to the next. Figure 11 illustrates this behavior for the third mode family. Figure 11 shows how the circumferential ( $\theta$ ) and out-of-plane ( $z$ ) motion of the blade tip's leading edge changes



(a)



(b)

Fig. 10 Blade amplitude as a function of excitation frequency for a 7th engine order excitation—(a) mass-spring response; (b) FMM response

from the 0 nodal diameter mode to the 12 nodal diameter mode. Observe that the  $\theta$  and  $z$  components of the mode shape change significantly between 0 and 6 nodal diameters. Therefore, the assumptions of FMM are violated throughout these low nodal diameter regions. Thus, we would not expect FMM to accurately predict the mistuned frequencies or shapes of these modes. As a result, FMM would not provide accurate forced response predictions when these modes are heavily excited.

To illustrate this limitation of the model, we used FMM to predict the forced response of families 2, 3, and 4 to a 2nd engine-order excitation. Since that engine order would primarily excite the low nodal diameter modes of each family, and those modes violate the assumptions of FMM, we do not expect the model to perform well in this instance. The FMM predictions were compared with finite element results calculated in ANSYS. Figures 12(a), (b) and (c) show the response of the 2nd, 3rd, and 4th families, respectively. For clarity, each plot shows only the low responding blade, the median responding blade, and the high responding blade. Observe that as expected, the FMM results differ significantly from the ANSYS response in both peak amplitudes and overall shape of the response. Thus, when a mode lies in a region where there is uncertainty as to what family a mode belongs, veering, or high slopes on the frequency versus nodal diameter plot, FMM cannot accurately predict its mistuned frequency or mode shape. Therefore, FMM does not work effectively for engine orders that excite modes in these regions.

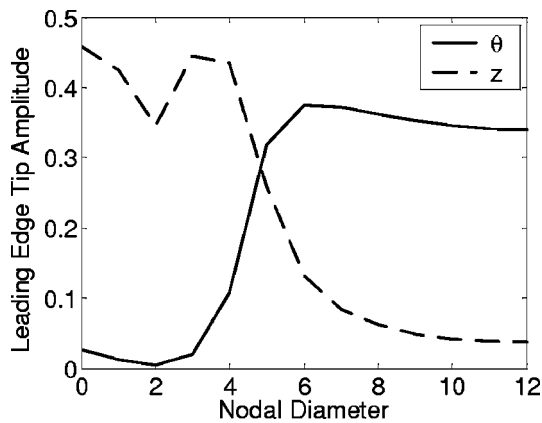


**Fig. 11** Leading-edge tip displacements for the third family of modes

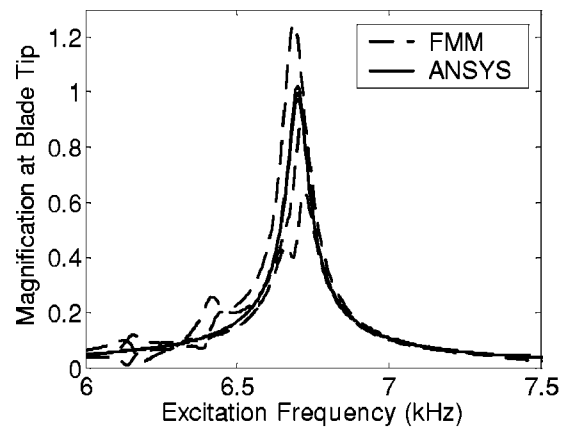
However, there are regions in high frequency modes where FMM works quite well. Over the higher nodal diameter regions the slopes in the frequency versus nodal diameter plot (Fig. 7) are very small, indicating that the modes have most of their strain energy in the blades. Furthermore, the flat regions are well isolated from other families of modes. Therefore, the blade's motion is very similar from one nodal diameter to the next. This can be seen in Fig. 11, which indicates that the  $\theta$  and  $z$  components of the blade tip motion remain fairly constant over the higher nodal diameter regions. Thus, the FMM assumptions are satisfied for these high nodal diameter modes, and it is possible that FMM might capture the physical behavior of these modes better than it did for low engine orders.

To explore this possibility, we used FMM to predict the forced response of families 2, 3, and 4 to a 7th engine order excitation. The FMM results are compared against a finite element benchmark performed in ANSYS. Figures 13(a), (b), and (c) show the responses of families 2, 3, and 4, respectively. For clarity, each plot shows only the low responding blade, the median responding blade, and the high responding blade. Observe that in all three cases, the FMM predictions captured the overall shape of the response curves as well as the peak amplitudes to within 6 percent. Therefore, for this test case we find that when a mode lies in a flat region at the upper end of a frequency versus nodal diameter plot, its response can be reasonably well predicted by FMM.

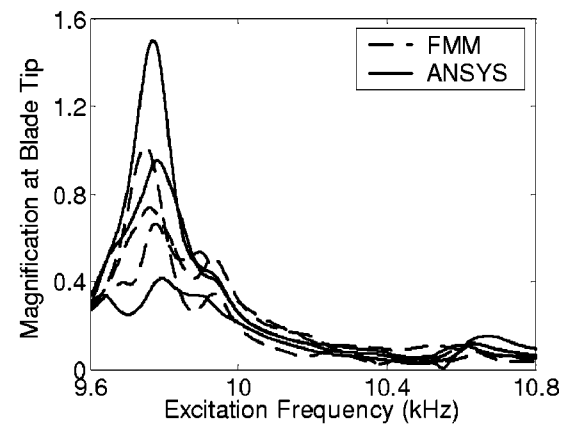
## 5 Conclusions

A new reduced order model of mistuned bladed disks was developed. It is applicable when we have an isolated family of modes in which the strain energy is primarily in the blades. This approach is called a fundamental mistuning model (FMM) because it reduces the mistuning problem to its most fundamental elements and provides physical insights into the mistuning problem. Specifically, it shows that the tuned system frequencies and blade-alone frequency deviations are the only parameters that determine the modes and natural frequencies of the system when it is mistuned. Neither the physical geometry of the system nor the physical causes of the blade frequency deviations are important. The only additional information needed to compute the effect of mistuning on the forced response is the modal damping ratio and the engine order of the excitation.

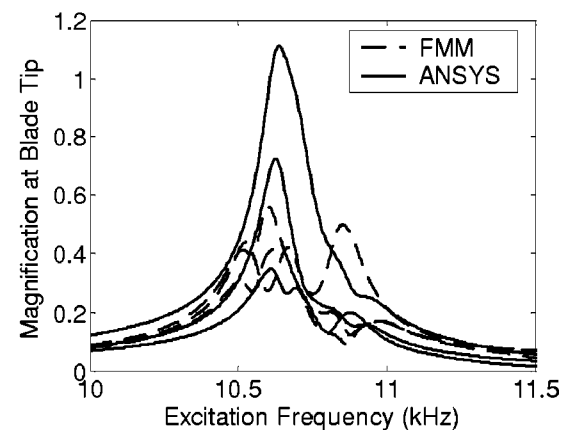
This result makes the fundamental mistuning model extremely simple to use. The only data that must be obtained from a finite element analysis are the natural frequencies of the tuned system modes. Unlike other reduced order models, FMM does not require the transfer of any cumbersome finite element data such as mode shapes or stiffness matrices. Thus, the fundamental mistuning



(a)



(b)

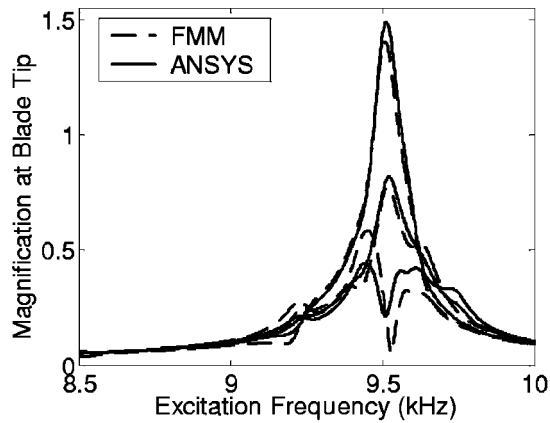


(c)

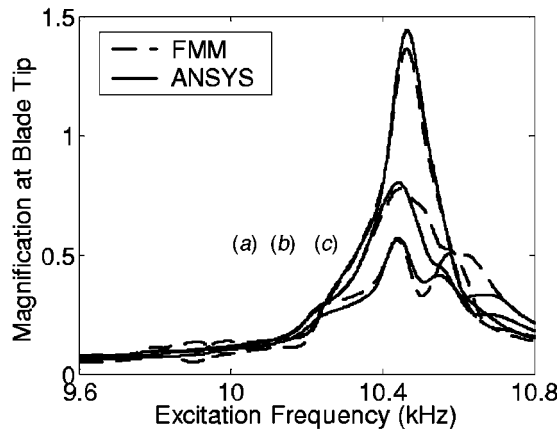
**Fig. 12** Blade amplitude as a function of excitation frequency for a 2nd engine order excitation—(a) family 2, (b) family 3, (c) family 4

model maintains the simplicity and low computational cost of a mass spring model while capturing all the important aspects of the physical system.

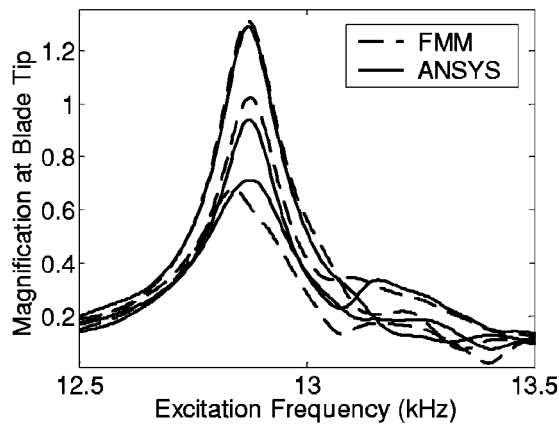
Because of its simplicity, FMM provides us with an approach for making bladed disks less sensitive to mistuning—at least in isolated families of modes. Two of the input parameters to FMM can be estimated from past experience, i.e., the scatter in the blade frequencies and the amount of damping in the system. Once the engine order of the excitation is known, then from FMM the only parameters that affect the mistuned response are the frequencies of



(a)



(b)



(c)

**Fig. 13** Blade amplitude as a function of excitation frequency for a 7th engine order excitation—(a) family 2, (b) family 3, (c) family 4

the tuned system modes. Consequently, the sensitivity of the system to mistuning can be changed only to the extent that physical changes in the bladed disk geometry affect these frequencies. For example, if the disk were designed to be more flexible, then the frequencies of the tuned system would be spread over a broader range, and this might reduce the system's sensitivity to mistuning.

The fundamental mistuning model provides a simple, but accurate method for assessing the effect of mistuning on forced response when we have an isolated family of modes. However, we still need the more complex reduced order models to analyze mistuned response in regions of frequency veering, high modal density and cases of disk-dominated modes. Nonetheless, the simplicity of the Fundamental Mistuning Model makes it a powerful tool for evaluating preliminary designs and provides new insights into the basic physics of the mistuning problem.

### Acknowledgments

The authors wish to thank Dr. N.-E. Kim of Carnegie Mellon University for providing the initial benchmarks used in the development of FMM. These benchmarks were essential to refining the FMM method. The authors would also like to express our appreciation to Mr. S. Yamakawa of Carnegie Mellon University for providing a high quality mesh of the HPT model that was used to validate FMM.

### References

- [1] Srinivansan, A. V., 1997, "Flutter and Resonant Vibration Characteristics of Engine Blades," *ASME J. Eng. Gas Turbines Power*, **119**(4), pp. 742–775.
- [2] Dye, R. C. F., and Henry, T. A., 1969, "Vibration Amplitudes of Compressor Blades Resulting from Scatter in Blade Natural Frequencies," *ASME J. Eng. Power*, **91**(3), pp. 182–188.
- [3] Ewins, D. J., 1969, "The Effects of Detuning Upon the Forced Vibrations of Bladed Disks," *J. Sound Vibr.* **9**(1), pp. 65–79.
- [4] Griffin, J. H., and Hoosac, T. M., 1984, "Model Development and Statistical Investigation of Turbine Blade Mistuning," *ASME J. Vibr., Acoust., Stress, Reliab. Des.*, **109**, pp. 204–210.
- [5] Wei, S. T., and Pierre, C., 1988, "Localization Phenomena in Mistuned Assemblies with Cyclic Symmetry, Part II: Forced Vibrations," *ASME J. Vibr., Acoust., Stress, Reliab. Des.*, **110**(4), pp. 429–438.
- [6] Rivas-Guerra, A. J., and Mignolet, M. P., 2001, "Local/Global Effects of Mistuning on the Forced Response of Bladed Disks," *ASME Paper 2001-GT-0289*, International Gas Turbine Institute Turbo Expo, New Orleans, LA.
- [7] Irretier, H., 1983, "Spectral Analysis of Mistuned Bladed Disk Assemblies by Component Mode Synthesis," *Vibrations of Bladed Disk Assemblies*, Proc. ASME 9th Biennial Conference on Mechanical Vibration and Noise, Dearborn, MI, pp. 115–125.
- [8] Kruse, M. J., and Pierre, C., 1996, "Forced Response of Mistuned Bladed Disks Using Reduced-Order Modeling," *Proc. 37th AIAA/ASME/ASCE/AHS/ASC Structures, Structural Dynamics, and Materials Conference*, Salt Lake City, UT, **4**, pp. 1938–1950.
- [9] Yang, M.-T., and Griffin, J. H., 1997, "A Reduced Order Approach for the Vibration of Mistuned Bladed Disk Assemblies," *ASME J. Eng. Gas Turbines Power*, **119**(1), pp. 161–167.
- [10] Castanier, M. P., Ottarsson, G., and Pierre, C., 1997, "A Reduced Order Modeling Technique for Mistuned Bladed Disks," *J. Vibr. Acoust.*, **119**(3), pp. 439–447.
- [11] Yang, M.-T., and Griffin, J. H., 1999, "A Reduced Order Model of Mistuning Using a Subset of Nominal Modes," *ASME Paper 99-GT-288*, International Gas Turbine Institute Turbo Expo, Indianapolis, IN.
- [12] Yang, M.-T., and Griffin, J. H., 1997, "A Normalized Modal Eigenvalue Approach for Resolving Modal Interaction," *ASME J. Eng. Gas Turbines Power*, **119**(3), pp. 647–650.

**J. Szwedowicz**  
Thermal Machinery Lab,  
ABB Turbo Systems Ltd.,  
CH-5401 Baden, Switzerland  
e-mail: jaroslaw.szwedowicz@ch.abb.com

**S. M. Senn**

**R. S. Abhari**

Turbomachinery Lab,  
Swiss Federal Institute of Technology,  
Zurich, Switzerland

# Optimum Strain Gage Application to Bladed Assemblies

*Optimum placements of the strain gages assure reliable vibration measurements of structural components such as rotating blades. Within the framework of cyclic vibration theory, a novel approach has been developed for computation of the optimum gage positions on tuned bladed disks regarding the determined sensitivity, orthogonality, gradient and distance criteria. The utilized genetic algorithm optimization tool allows for an effective numerical search of suitable solutions of the defined optimization function. A rotating impeller disk represented by a cyclic finite element model demonstrates the application of this method. The present technique can be easily applied to other structural components requiring optimal strain gage instrumentation. [DOI: 10.1115/1.1506957]*

## Introduction

A major goal in the development process of rotating turbomachinery turbine blades is to prevent them from high cyclic fatigue (HCF) failure. Within an HCF design and analysis system, the maximal dynamic blade stresses are usually obtained from the correlation between the numerical modal (free vibration) results and dynamic strain measurements. These vibratory strains are transferred from the gages either by slip rings or telemetry during engine tests with the blade prototype. Vibrations of the blade can be characterized with an adequate number of strain gages placed on the airfoil contour. In most papers given in literature, gage locations and orientations are determined by using the numerical mode shapes (e.g., Kielb and Abhari [1]) or from experimental stress analysis (e.g., Purcell [2]). The strain gage is then instrumented close to the peak stress location for the mode of interest. This qualitative technique may lead into data inaccuracy because of ambiguous mode identification occurring frequently for shrouded disks, blades assembled on flexible disks, or high engine orders. A limited number of papers about the optimum strain gage instrumentation can be found in literature (e.g., Studer [3], Nichol [4], Sensmeier and Nichol [5–7]). Nichol's and Sensmeier's work delivers a very systematic investigation and application of the strain gage optimization. Also, Nichol and Sensmeier give a thorough review of the available literature. Nearly all available literature deals with strain gage instrumentation for a single blade. Griffin's [8] approach, being an exception, could be extended for the gage optimization for an entire bladed disk represented by a lumped model of the mistuned springs and masses.

In recent years, a considerable attention has been paid to the issue of the reduction of component and engine development cost. A considerable reduction of these costs could be achieved through a decrease of the number of tests that would be required to verify the design. This reduction in the amount of tests could be accomplished through the optimization of the used strain gages characterizing the blade and disk vibrations and minimizing experimental uncertainty. In this paper, a numerical method for the determination of the optimum gage placement is presented for both a single blade and tuned disk assembly. In this approach, four criteria are applied to find the optimum which are 1) mode gage orthogonality, 2) strain gage sensitivity, 3) low strain gradient, and 4) distance principle among gages. These four criteria assure the determination of an arbitrary number of sensors placed optimally on the structure of interest. To fulfill these strain gage criteria, an objective function is introduced, which is then optimized through a genetic algorithm. To illustrate the developed procedure, a radial compressor disk is modeled for the optimum instrumentation. The

dynamic behavior of a tuned impeller is obtained from the finite element computation of the cyclic sector of the entire disk. A presented example of eight strain gages placed optimally on the curved pressure side of the impeller blade illustrates the approach used for the operation of the developed numerical tool. Finally, the optimization results for two strain gages on both the single rigidly clamped airfoil and the entire impeller model are compared to each other. The results of this comparison clearly demonstrate the need for the inclusion of the full blade disk assembly in optimum strain gage placements.

## The Cyclic Finite Element Formulation

External excitations acting on the rotating blades induce two traveling waves propagating circumferentially in opposite directions within the bladed disk. The superposition of these waves generates a harmonic disk vibration defined by its natural period, which depends on the system mass and stiffness. In reality the bladed disk is a system of  $N$  blades, whose geometry slightly differs from each other due to manufacturing tolerances, resulting in the mistuning effect. In the design process, the blade mistuning is not a deterministic quantity. In practice, the tuned system of the coupled blades is usually taken into account for the numerical assessment of the static and dynamic behavior of the blade under design.

The tuned bladed disk vibration is represented efficiently using a single blade with complex boundary conditions (Thomas [9]). For the shrouded or snubbed blades, the frictional and cyclic boundary conditions should be separated from each other for computing reliable disc eigenfrequencies, which significantly depend on the real contact between the shrouds (Szwedowicz [10]). Neglecting dissipation effects, eigenfrequencies  $f_{n,j} = \omega_{n,j}/2\pi$  (where  $\omega_{n,j}$  denotes circular frequency) of the disk assembly are calculated from

$$(K(\Omega, n) - \omega_{n,j}^2 M(n))z^{(\ell)} = 0 \quad (1)$$

where the blade complex mass  $M$  and stiffness  $K$  matrices depend on nodal diameter number  $n=0,1,\dots,N/2$  for even  $N$  or  $(N-1)/2$  if  $N$  is an odd number. Additionally, regarding the rotational speed  $\Omega$  of the turbine, the stiffening effect is included in the stiffness matrix  $K$ .

For each mode  $j$  with nodal diameter  $n$  (besides  $n=0$  and  $n=N/2$ ), two identical eigenfrequencies are computed from Eq. (1) which correspond to two possible model shapes  $z^{(\ell)}$  of the cyclic sector  $\ell$ . As it is illustrated in Fig. 1, the harmonic deformation of the successive cyclic sector  $\ell+1$  of the disc is determined from

$$z^{(\ell+1)} = z^{(\ell)} e^{i2\pi n/N}, \quad i = \sqrt{-1} \quad (2)$$

In this paper, the rotating impeller containing  $N=9$  cyclic sectors (see Fig. 1(a)) is considered. The cyclic finite element (FE) model representing this impeller is shown in Fig. 1(b). The eigen-

Contributed by the International Gas Turbine Institute and presented at the International Gas Turbine and Aeroengine Congress and Exhibition, Amsterdam, The Netherlands, June 3–6, 2002. Manuscript received by the IGTI, October 30, 2001. Paper No. 2002-GT-30306. Review Chair: E. Benvenuti.



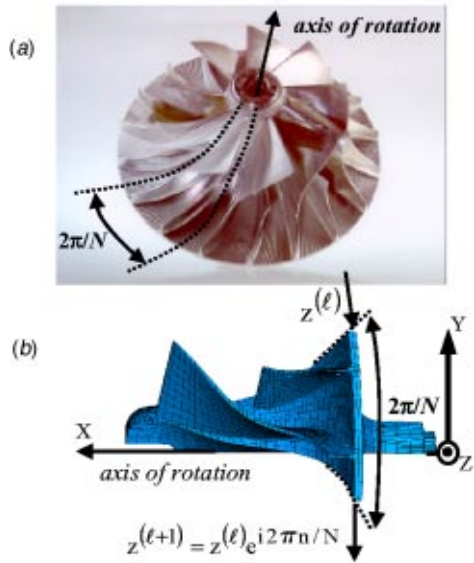


**Fig. 1** The rotational periodic structure of  $N=9$  cyclic sectors (a) and its cyclic finite element representation (b), where  $n$  is a nodal diameter number and  $\ell$  indicates a number of a cyclic sector

frequencies and mode shapes of the rotating impeller are computed with the general purpose ABAQUS FE computer system [11].

A complex blade geometry can be represented easily with a parabolic FE mesh. However, the governing equations of the problem are solved in a piecewise approximation manner. The FE results are given mainly on nodes representing deformations of the structure. In this paper, the numerical accuracy of the FE results is not discussed as this issue can be dealt with the accessible known refinement techniques (e.g., Zeng [12]). When taking into consideration the reliable mesh refinement in the region of the strain gage instrumentation, their optimal placements are then searched among the nodes on the blade contour.

### Gage Dynamic Strain on Blade Contour

Nodal strain and stress tensors, obtained from the FE calculation, are expressed in the spatial Cartesian FE reference system. By free vibration analysis, the external force does not act on the structure. Thus, the normal relative dynamic stress should be equal to zero in the normal direction  $z'$  (see Fig. 2) to the local airfoil contour around the particular node. In the FE practice, this stress is close to zero because of an applied finite size of elements on the airfoil contour. Since this element size approaches infinite small dimensions (e.g., using a dynamic substructuring FE technique), then the local normal stress will be equal to zero. In prac-

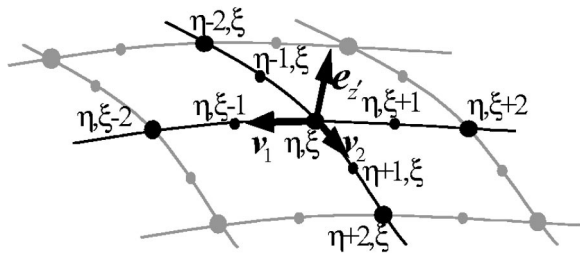


**Fig. 2** FE mesh on the airfoil contour with the indicated nodal local reference system  $x'y'z'$ , where the bigger and smaller circles denote the corner and mid-nodes, respectively

tical applications, the normal dynamic stresses on the airfoil contour are much smaller than the tangential ones. Finally, the nodal stress state on the airfoil contour is reduced to two-dimensional case as it is expressed by

$$S' = T^T S T = \begin{bmatrix} \sigma_{x'x'} & \tau_{x'y'} & 0 \\ & \sigma_{y'y'} & 0 \\ \text{sym.} & & 0 \end{bmatrix} \quad (3)$$

where  $T$  is the nodal transformation matrix from the global Cartesian  $XYZ$  (Fig. 1(a)) into the local nodal  $x'y'z'$  reference system and matrix  $S$  is the nodal stress tensor in the  $XYZ$  system, whereby  $\sigma_{x'x'}$ ,  $\sigma_{y'y'}$  and  $\tau_{x'y'}$  are normal and shear stresses, respectively in the local  $x'y'z'$  reference system on the airfoil contour. The nodal transformation matrix  $T$  is expressed by

$$T = [e_{x'}, e_{y'}, e_{z'}] \quad (4)$$

where  $e_{x'}$ ,  $e_{y'}$  and  $e_{z'}$  are the units vectors of the local nodal reference system  $x'y'z'$ . Regarding the fine rectangular parabolic FE mesh on the airfoil contour, the tangential  $v_1$  and  $v_2$  vectors of the nodal local system can be obtained from distances of corner node  $(\eta, \xi)$  in relation to mid-node nodes  $(\eta, \xi-1)$  and  $(\eta+1, \xi)$ , as it is illustrated in Fig. 2. Unit vector  $e_{z'}$  normal to the airfoil contour is then determined from

$$e_{z'} = [e_{z'1}, e_{z'2}, e_{z'3}]^T = \frac{v_1 \times v_2}{\|v_1 \times v_2\|} \quad (5)$$

where  $e_{z'1}$ ,  $e_{z'2}$  and  $e_{z'3}$  are computed components of unit vector  $e_{z'}$ . Considering the normal vector system, the other unit vectors of the nodal local system  $x'y'z'$  are calculated by

$$e_{y'} = [e_{z'1}, -e_{z'2}, 0]^T \quad (6)$$

and

$$e_{x'} = e_{y'} \times e_{z'} \quad (7)$$

For an isotropic linear elastic material with no preferred directions, Hook's law gives strains on the airfoil contour as

$$\begin{Bmatrix} \varepsilon_{x'x'} \\ \varepsilon_{y'y'} \\ \varepsilon_{x'y'} \end{Bmatrix} = \frac{1}{E} \begin{bmatrix} 1 & -\nu & 0 \\ & 1 & 0 \\ \text{sym.} & & E/G \end{bmatrix} \begin{Bmatrix} \sigma_{x'x'} \\ \sigma_{y'y'} \\ \tau_{x'y'} \end{Bmatrix} \quad (8)$$

where  $E$ ,  $G$ , and  $\nu$  are elastic modulus, shear modulus and Poisson's ratio, respectively. For nodal diameter  $n \in (0, (N-1)/2)$ , the real and imaginary parts of each strain component are obtained from the cyclic FE computation and the nodal complex dynamic strain components are expressed by

$$\begin{aligned} \varepsilon_{x'x'}^c(\eta, \xi, n, j) &\equiv \varepsilon_{x'x'}^{re}(\eta, \xi, n, j) + i \varepsilon_{x'x'}^{im}(\eta, \xi, n, j) \\ \varepsilon_{y'y'}^c(\eta, \xi, n, j) &\equiv \varepsilon_{y'y'}^{re}(\eta, \xi, n, j) + i \varepsilon_{y'y'}^{im}(\eta, \xi, n, j) \\ \varepsilon_{x'y'}^c(\eta, \xi, n, j) &\equiv \varepsilon_{x'y'}^{re}(\eta, \xi, n, j) + i \varepsilon_{x'y'}^{im}(\eta, \xi, n, j) \end{aligned} \quad (9)$$

Arguments of these complex strain components in Eq. (9) are determined as

$$\begin{aligned} \alpha_{x'x'}(\eta, \xi, n, j) &\equiv \arctan \left( \frac{\varepsilon_{x'x'}^{im}}{\varepsilon_{x'x'}^{re}} \right) \\ \alpha_{y'y'}(\eta, \xi, n, j) &\equiv \arctan \left( \frac{\varepsilon_{y'y'}^{im}}{\varepsilon_{y'y'}^{re}} \right) \\ \alpha_{x'y'}(\eta, \xi, n, j) &\equiv \arctan \left( \frac{\varepsilon_{x'y'}^{im}}{\varepsilon_{x'y'}^{re}} \right) \end{aligned} \quad (10)$$

For the eigenfrequency  $f_{n,j}$  obtained from Eq. (1), the behavior of the complex dynamic strain components in the time domain are

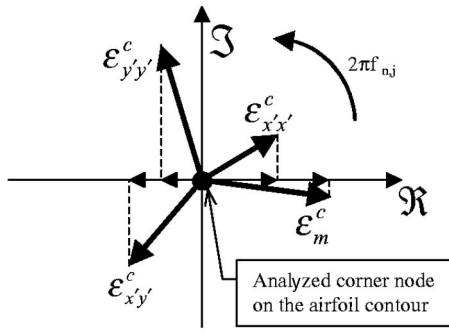


**Fig. 3** Illustration of nodal complex dynamic strain components of the cyclic FE system in the complex domain

illustrated in Fig. 3. Substituting the complex by trigonometric notation, the nodal dynamic strain components are then rewritten in the time domain by

$$\begin{aligned}
 \varepsilon_{x'x'}(\eta, \xi, n, j, t) &= \Re\{(\varepsilon_{x'x'}^{re} + i\varepsilon_{x'x'}^{im})\exp(i2\pi f_{n,j}t)\} \\
 &= |\varepsilon_{x'x'}^c| \cos(2\pi f_{n,j}t + \alpha_{x'x'}) \\
 \varepsilon_{y'y'}(\eta, \xi, n, j, t) &= \Re\{(\varepsilon_{y'y'}^{re} + i\varepsilon_{y'y'}^{im})\exp(i2\pi f_{n,j}t)\} \\
 &= |\varepsilon_{y'y'}^c| \cos(2\pi f_{n,j}t + \alpha_{y'y'}) \\
 \varepsilon_{x'y'}(\eta, \xi, n, j, t) &= \Re\{(\varepsilon_{x'y'}^{re} + i\varepsilon_{x'y'}^{im})\exp(i2\pi f_{n,j}t)\} \\
 &= |\varepsilon_{x'y'}^c| \cos(2\pi f_{n,j}t + \alpha_{x'y'})
 \end{aligned} \quad (11)$$

where  $t$  indicates time.

Regarding an optimal orientation of the strain gage on the airfoil contour, the dynamic strain components  $\varepsilon_{x'x'}^c$ ,  $\varepsilon_{y'y'}^c$ , and  $\varepsilon_{x'y'}^c$  have to be recalculated along an arbitrary direction within the nodal local reference system  $x'y'z'$ . Applying a rule of Mohr's circle (Timoshenko and Goodier [13]), the complex dynamic strain  $\varepsilon_m^c$  along direction  $m$  corresponding to the axis of the strain gage is determined from

$$\begin{aligned}
 \varepsilon_m(\eta, \xi, \varphi, n, j, t) &= |\varepsilon_{x'x'}^c| \cos(2\pi f_{n,j}t + \alpha_{x'x'}) \cos^2(\varphi) \\
 &+ |\varepsilon_{y'y'}^c| \cos(2\pi f_{n,j}t + \alpha_{y'y'}) \sin^2(\varphi) \\
 &+ |\varepsilon_{x'y'}^c| \cos(2\pi f_{n,j}t + \alpha_{x'y'}) \sin(\varphi) \cos(\varphi)
 \end{aligned} \quad (12)$$

where  $\varphi$  defines the measurement axis  $m$  in the nodal local reference system  $x'y'z'$  as it is shown in Fig. 4.

For each angle  $\varphi$ , the dynamic strain  $\varepsilon_m$  in direction  $m$  is the superposition of three harmonic vibrations of the same eigenfrequency  $f_{n,j}$  and various amplitudes and phase delays (see

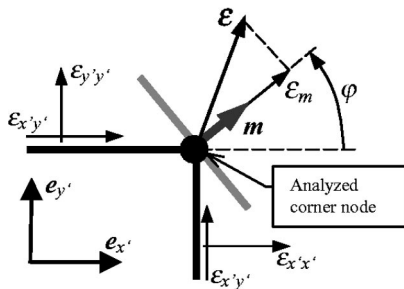


**Fig. 4** Orientation of the 'measurement' axis of the strain gage in the nodal local reference system  $x'y'z'$

Eq. (12)). Thus, the vibration of this strain  $\varepsilon_m$  is described by the same eigenfrequencies  $f_{n,j}$  and its maximal amplitude is obtained from

$$\frac{\partial \varepsilon_m(\eta, \xi, \varphi, n, j, t)}{\partial t} \equiv 0 \quad (13)$$

by determining  $t_{\max}$  when the maximal amplitude of strain  $\varepsilon_m$  occurs in the time domain as

$$t_{\max} = -\frac{1}{\omega_{n,j}} \arctan \frac{a_{xx} \sin \alpha_{x'x'} + a_{yy} \sin \alpha_{y'y'} + a_{xy} \sin \alpha_{x'y'}}{a_{xx} \cos \alpha_{x'x'} + a_{yy} \cos \alpha_{y'y'} + a_{xy} \cos \alpha_{x'y'}} \quad (14)$$

where

$$\begin{aligned}
 a_{xx} &= -|\varepsilon_{x'x'}^c| \cos^2 \varphi, \quad a_{yy} = -|\varepsilon_{y'y'}^c| \sin^2 \varphi, \\
 a_{xy} &= -|\varepsilon_{x'y'}^c| \sin \varphi \cos \varphi
 \end{aligned} \quad (15)$$

For disk mode  $(n, j)$ , the maximal dynamic resulting strain  $\varepsilon_{x-\max}$  of the analyzed node  $(\eta, \xi)$  can be calculated with Eq. (12) by substituting  $t_{\max}$  and the best orientation  $\varphi_{\max}$  obtained from the partial differential as

$$\left. \frac{\partial \varepsilon_m(\eta, \xi, \varphi, n, j, t)}{\partial \varphi} \right|_{t=t_{\max}} \equiv 0 \Rightarrow \varphi_{\max} \quad (16)$$

For all considered disk modes, the maximal resulting dynamic strain  $\varepsilon_{\max}$  in gage on the airfoil contour is determined from

$$\varepsilon_{\max}(n, j) \geq \varepsilon_{x-\max}(\eta, \xi, n, j) \quad \forall \eta, \xi \quad (17)$$

### Criteria for Optimal Positions of Strain Gages

Strain gage positions and orientations on the airfoil contour should assure the identification of all disc modes of interest during the measurement. This may be problematic for bladed disk assemblies whose mode shapes and eigenfrequencies are similar to each other for different nodal diameter vibrations. Therefore, some criteria are required in the identification process of the disc modes. Following Sensmeier's and Nichol's [5–7] as well as Studer's [3] work for rigidly clamped blades, four criteria, such as: gage orthogonality, sensitivity, strain gradient and distance, are used and extended to the bladed discs in this paper.

**Criteria of the Gage Orthogonality.** For a cyclic symmetrical structure like a tuned bladed assembly, their mode shapes are orthogonal relative to each other. In experiments, vibrations of the rotating disk can be measured only with a few strain gages. In the case of  $\Lambda$  number of the strain gages applied on the bladed disk, reduced vibration vectors of the disk assembly are then obtained for all measured mode shapes. The measured mode shapes can be identified by calculating the reduced MAC (modal assurance criteria) from

$$\theta_{(n,i),(k,h)} = \frac{\phi_{n,j}^{*T} \cdot \phi_{k,h}}{\|\phi_{n,j}\| \cdot \|\phi_{k,h}\|} \quad (18)$$

where  $n \neq k = 0, 1, \dots, N/2$  or  $(N-1)/2$ ,  $j \neq h = 1, 2, \dots, J$  (where  $J$  indicates the required number of the measured disk family vibrations) and  $\phi_{n,j}^{*T}$  is the conjugate transformed reduced vibration vector given by

$$\phi_{n,j} = \begin{Bmatrix} \varepsilon_m(\eta_1, \xi_1, \varphi_1, n, j, t_{\max 1}) \\ \varepsilon_m(\eta_2, \xi_2, \varphi_2, n, j, t_{\max 2}) \\ \vdots \\ \varepsilon_m(\eta_\Lambda, \xi_\Lambda, \varphi_\Lambda, n, j, t_{\max \Lambda}) \end{Bmatrix} \quad (19)$$

Since for all  $\Lambda$  strain gages the determined  $\theta_{(n,i),(k,h)}$  scalars are minimal and close to zero for all considered mode shapes  $(n, j)$

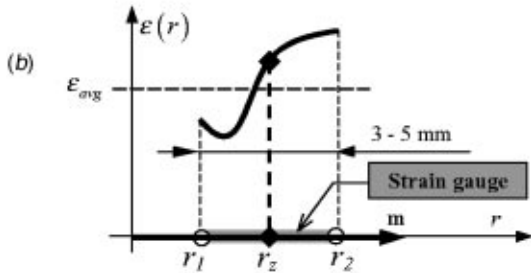
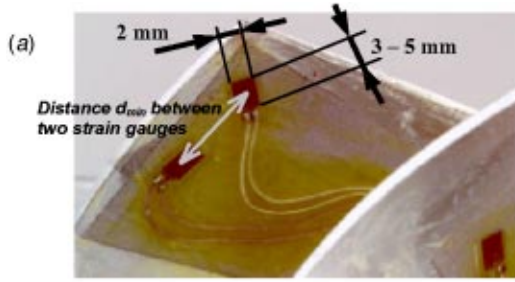


Fig. 5 Example of the impeller instrumented with strain gages (a) and illustration of the strain variation along the gage (b)

and  $(k, h)$ , the orthogonality criteria is fulfilled. Then, the measured mode shapes can be identified for the applied configuration of  $\Lambda$  strain gages.

**Criteria of the Gage Sensitivity.** In the best case, the strain gage is applied close to the peak stress location for the blade mode shape of interest. Due to nodal diameter number  $n = 0, 1, 2, \dots, N/2$ , disk mode number  $J$  of interest is usually higher than number  $\Lambda$  of the applied strain gages. On the other hand, dynamic peak stresses can often be found in regions of high temperature or on disk parts with nonregular contour geometry, impossible for the gage instrumentation. Therefore, strain gages have to be applied in airfoil region of dynamic strains, where magnitudes are high enough in relation to the strain peak of the analyzed mode shape. This relation is called the gage sensitivity and it is obtained from

$$\varepsilon_{\Lambda, \max} = \max \left[ \frac{\varepsilon_m(\eta_1, \xi_1, \varphi_1, n, j, t_{\max 1})}{\varepsilon_{\max}(n, j)}, \dots, \frac{\varepsilon_m(\eta_{\Lambda}, \xi_{\Lambda}, \varphi_{\Lambda}, n, j, t_{\max \Lambda})}{\varepsilon_{\max}(n, j)} \right] \quad (20)$$

where  $\varepsilon_{\max}(n, j)$  is strain peak of disk mode  $(n, j)$  obtained from the free vibration FE computation. Concerning a probable damage of any strain gage, the lower gage sensitivity is also determined from

$$\varepsilon_{\Lambda, \min} = \min \left[ \frac{\varepsilon_m(\eta_1, \xi_1, \varphi_1, n, j, t_{\max 1})}{\varepsilon_{\max}(n, j)}, \dots, \frac{\varepsilon_m(\eta_{\Lambda}, \xi_{\Lambda}, \varphi_{\Lambda}, n, j, t_{\max \Lambda})}{\varepsilon_{\max}(n, j)} \right] \quad (21)$$

Since both upper  $\varepsilon_{\Lambda, \max}$  and lower  $\varepsilon_{\Lambda, \min}$  sensitivity factors approach 1, the criteria of the gage sensitivity is fulfilled.

**Criteria of the Strain Gradient<sup>1</sup>.** The length of the applied strain gages are generally between 3 and 5 mm, as it is shown in Fig. 5(a). The strain gage measures averaging strain  $\varepsilon(r_z)$  determined from

$$\varepsilon_{\text{avg}} = \frac{1}{|r_2 - r_1|} \int_{r_1}^{r_2} \varepsilon(r) dr \quad (22)$$

between position  $r_1$  and  $r_2$  (Fig. 5(b)) along instrumentation direction  $m$  shown in Fig. 4, where point  $r_z$  corresponds to node  $(\eta, \xi)$ . To avoid unexpected measurement errors, sharp strain gradients should not take place within the region of the gage application. Assuming constant relative relations of the dynamic strains among the nodes in the time domain, a gradient of the dynamic strain distribution around node  $(\eta, \xi)$  is evaluated from

$$\psi(\eta, \xi, n, j) = \max \left\{ \left| \frac{\varepsilon_m(\eta, \xi + 1, \varphi_{\xi}, n, j) - \varepsilon_m(\eta, \xi - 1, \varphi_{\xi}, n, j)}{\chi(\eta, \xi + 1) - \chi(\eta, \xi - 1)} \right|, \left| \frac{\varepsilon_m(\eta, \xi, \varphi_{\xi}, n, j) - \varepsilon_m(\eta, \xi - 1, \varphi_{\xi}, n, j)}{\chi(\eta, \xi) - \chi(\eta, \xi - 1)} \right|, \left| \frac{\varepsilon_m(\eta, \xi + 1, \varphi_{\xi}, n, j) - \varepsilon_m(\eta, \xi, \varphi_{\xi}, n, j)}{\chi(\eta, \xi + 1) - \chi(\eta, \xi)} \right|, \left| \frac{\varepsilon_m(\eta + 1, \xi, \varphi_{\eta}, n, j) - \varepsilon_m(\eta - 1, \xi, \varphi_{\eta}, n, j)}{\chi(\eta + 1, \xi) - \chi(\eta - 1, \xi)} \right|, \left| \frac{\varepsilon_m(\eta, \xi, \varphi_{\eta}, n, j) - \varepsilon_m(\eta - 1, \xi, \varphi_{\eta}, n, j)}{\chi(\eta, \xi) - \chi(\eta - 1, \xi)} \right|, \left| \frac{\varepsilon_m(\eta + 1, \xi, \varphi_{\eta}, n, j) - \varepsilon_m(\eta, \xi, \varphi_{\eta}, n, j)}{\chi(\eta + 1, \xi) - \chi(\eta, \xi)} \right| \right\} \quad (23)$$

where angles  $\varphi_{\xi}$  and  $\varphi_{\eta}$  determine in the local system  $x'y'z'$  of node  $(\eta, \xi)$  orientations of the nodal vectors between  $(\eta, \xi - 1)$  and  $(\eta, \xi)$  nodes as well as between  $(\eta - 1, \xi)$  and  $(\eta, \xi)$  nodes, respectively. The vector lengths among corner node  $(\eta, \xi)$  and four mid-nodes  $(\eta - 1, \xi)$ ,  $(\eta + 1, \xi)$ ,  $(\eta, \xi - 1)$  and  $(\eta, \xi + 1)$ , shown in Fig. 4, are calculated from their coordinates  $\chi$  (see Eq. (23)). For all considered modes  $(n, j)$  of interest, the maximal strain gradient  $\psi_{\max}$  in the gage instrumentation region is obtained from

$$\psi_{\max} \geq \psi(\eta, \xi, n, j) \forall \eta, \xi, n, j \quad (24)$$

Finally, for each mode  $(n, j)$  and contour node  $(\eta, \xi)$  the relative strain gradient  $\psi_{\max}^0$  is determined from dividing of Eq. (23) by scalar  $\psi_{\max}$  given in Eq. (24). Since the relative strain gradient approaches zero, the criteria of the gage gradient is fulfilled.

**Criteria of the Strain Distance.** Concerning different technical aspects of the strain gage application on the rotating disk assemblies, a minimal distance  $d_{\min}$  among adjacent strain gages has to be kept (see Fig. 5(a)). Therefore, an additional distance criteria is taken into account as

$$\|\chi(\eta_a, \xi_a) - \chi(\eta_b, \xi_b)\| \geq d_{\min} \quad (25)$$

where  $\chi(\eta_a, \xi_a)$  and  $\chi(\eta_b, \xi_b)$  are coordinates of strain gages  $a$  and  $b$ , respectively. The minimal distance  $d_{\min}$  is established according to the specific gage instrumentation process.

Since the number  $N$  of the blades in the measured disc assembly is higher than the number  $\Lambda$  of the required strain gages, the distance criteria can be neglected. Then, the strain gages can be applied on different blades however, the blade mistuning aspect must be then considered.

## Strain Gage Optimization Function

Optimal positions of  $\Lambda$  number of the strain gages on the bladed disk can be searched according to the previously mentioned four criteria. The application of the straightforward search rule for either minimal or maximal values of these criteria does

<sup>1</sup>In this paper the strain gage misalignment is not considered, because it is caused by errors in the strain gage instrumentation. Thus, this problem is analyzed by post-processing of the strain gage data obtained from the measurement.

not assure the optimal solution for all  $\Lambda$  required strain gages. Therefore, an optimization function based on the gage placement criteria has to be determined.

**Optimization Function for Single Strain Gage.** Considering the application of only one strain gage, the orthogonality and distance criteria can be omitted. An optimization function  $\Phi(\eta, \xi, \varphi)$  is then developed from the relative gage sensitivity  $\varepsilon_{\Lambda=1, \max}$  and gradient  $\psi_{\max}^0$  factors (see Eqs. (20) and (24)) and it can be expressed as

$$\Phi(\eta, \xi, \varphi) = \prod_{n=0}^{N/2} \prod_{j=1}^J |\varepsilon_m(\eta, \xi, \varphi, n, j)|^{\beta_\varepsilon} \cdot \gamma_\varepsilon(n, j) \cdot \delta(|\varepsilon_m(\eta, \xi, \varphi, n, j)| - \varepsilon_{\min}) \cdot |1 - \psi(\eta, \xi, n, j)|^{\beta_\psi} \cdot \gamma_\psi(n, j) \cdot \delta(\psi_{\max} - |\psi(\eta, \xi, n, j)|) \quad (26)$$

where the leap function  $\delta$  is given by

$$\delta(a) = \begin{cases} 1 & \text{for } a \geq 0 \\ 0 & \text{for } a < 0 \end{cases} \quad (27)$$

and the weight factors are

$$\beta_\mu \in (0, \infty), \quad \gamma_\mu(n, j) \in (0, 1), \quad \mu \equiv \begin{cases} \varepsilon \\ \psi \end{cases} \quad (28)$$

In terms of growing magnitudes of  $\beta_\varepsilon$  and  $\beta_\psi$  factors in Eq. (26), the sensitivity or gradient criteria may be amplified respectively in the optimization process. In the same way, certain disk modes become minor or principal in the analysis of the sensitivity or gradient criteria, since  $\gamma_\varepsilon(n, j)$  or  $\gamma_\psi(n, j)$  factors are equal to 0 or 1, respectively. The term  $\delta(|\varepsilon_m(\eta, \xi, \varphi, n, j)| - \varepsilon_{\min})$  in Eq. (26) allows elimination from the optimization process these gage orientations  $\varphi$  along which the determined strains  $\varepsilon_m$  are below the allowable minimal strain  $\varepsilon_{\min}$ . In the same manner, the term  $\delta(\psi_{\max} - |\psi(\eta, \xi, n, j)|)$  eliminates these nodes from the optimization, whose nodal strain gradients are higher than the allowable maximal one  $\psi_{\max}$ . For different orientations  $\varphi \in < 0 \text{ deg}, 180 \text{ deg}$  the optimization function  $\Phi$  is illustrated in Fig. 6 for a single node.

#### Optimization Function for $\Lambda$ Number of Strain Gages.

Since  $\Lambda$  strain gages are required in the measurement, all four gage criteria have to be taken into consideration by creating the optimization function  $\Psi_\Lambda$ . As it is presented in Fig. 6, the applied logarithmic scale is more reasonable in searching any local maximums of the optimization function  $\Psi$ . In this approach, optimization function for  $\Lambda$  number of strain gages is created directly in the logarithmic domain and it can be expressed as

$$\Phi_{\Lambda, \log} \equiv \log \Phi_\Lambda = 2000 + \sum_{n=0}^{N/2} \sum_{j=1}^J \left\{ \beta_\varepsilon \log |\varepsilon_{m, \max}(\Delta_1, \varphi_1, \dots, \Delta_\Lambda, \varphi_\Lambda, n, j)| + \log \gamma_\varepsilon(n, j) + \log \delta_{lg}(|\varepsilon_{m, \max}(\Delta_1, \varphi_1, \dots, \Delta_\Lambda, \varphi_\Lambda, n, j)| - \varepsilon_{\min}) + \beta_\psi \sum_{i=1}^\Lambda \{ \log |1 - \psi(\Delta_i, n, j)| + \log \delta_{lg}(\psi_{\max} - |\psi(\Delta_i, n, j)|) \} + \log \gamma_\psi(n, j) \right\} + \sum_{\forall \{(n, j), (k, h)\}} \log(1 - \theta_{\{(n, j), (k, h)\}}) + \sum_{\forall (a, b)} \log \delta_{lg}(\|\chi(\eta_a, \xi_a) - \chi(\eta_b, \xi_b)\| - d_{\min}) \quad (29)$$

where an arbitrary value of 2000 is only added for avoiding negative values of the  $\Psi$  during the search. Moreover, in Eq. (29)  $\Delta_i = (\eta_i, \xi_i)$  denote nodal positions (Fig. 2) and

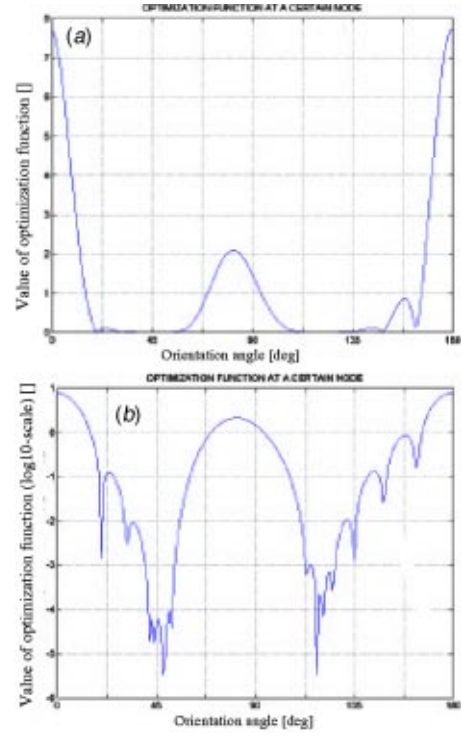


**Fig. 6 Optimization function  $\Psi$  of a single node for different orientations  $\varphi$  (where values  $\Psi$  are multiplied by  $1 \times 10^3$ )—(a) values  $\Psi$  in the linear scale, (b) values  $\Psi$  in the logarithmic scale**

$$\delta_{lg}(a) = \begin{cases} 1 & \text{for } a \geq 10^{-30} \\ 10^{-30} & \text{for } a < 10^{-30} \end{cases} \quad (30)$$

In addition, the following conditions must be fulfilled

$$\begin{aligned} \forall |\varepsilon_{m, \max}| < 10^{-30} &\Rightarrow \varepsilon_{m, \max} = 10^{-30}, \\ \forall |1 - \psi(\Delta_i, n, j)| < 10^{-30} &\Rightarrow |1 - \psi(\Delta_i, n, j)| = 10^{-30}, \\ \forall 1 - \theta_{\{(n, j), (k, h)\}} < 10^{-30} &\Rightarrow 1 - \theta_{\{(n, j), (k, h)\}} = 10^{-30} \end{aligned}$$

The orthogonality term  $(1 - \theta_{\{(n, j), (k, h)\}})$  in the  $\Psi_\Lambda$  (see Eq. (29)) is set to 0 or 1, since two specific modes  $(n, j)$  and  $(k, h)$  are identical or orthogonal to each other, respectively. The last term of Eq. (29) becomes zero, if the distance criteria between two strain gages  $a$  and  $b$  is not satisfied.

Values of the  $\Psi_\Lambda$  varies between 0 and 2001. In this domain  $\Lambda$  maxima of the function  $\Psi_\Lambda$  have to be found to get  $\Lambda$  number of optimal placements of the strain gages. The discrete character of the optimization function  $\Psi_\Lambda$  does not allow close form of analytical solutions. Therefore, a genetic algorithm (Goldberg [14]) is used, being previously recommended for the strain gage optimization by Sensmeier and Nichol [7] as well as by Simpson and Hansen [15]. The detailed description of the genetic algorithm (GA) procedure applied for searching optimal placements of the blade strain gages can be found in Sensmeier's and Nichol's work [7]. To illustrate an effectiveness of the GA procedure, an example of the airfoil contour represented by  $100 \times 100$  nodes is considered for the optimal application of 10 strain gages. The strain gage orientation  $\varphi$  is examined discretely from 0 deg up to 180 deg with an increment angle  $\Delta\varphi$  of 1 deg what gives 180 calculations per each node. A total number of all possible positions is determined from

$$\binom{100 \cdot 100}{10} \cdot 180^{10} = 9.8 \cdot 10^{55}$$

With such a large number of search operations, the GA procedure is a very effective optimization tool. For a relatively short CPU time requirement,<sup>2</sup> the GA delivers 10 suitable results of the optimization function for the 10 strain gage positions in relation to its optimal value.

### Examples of Instrumentation

To demonstrate the developed approach of the strain gage optimization, the impeller disk shown in Fig. 1(a) is taken into account. Eight strain gages have to be applied optimally on the impeller regarding all nodal diameters  $n$  from 0 up to 4 and all disk vibration modes  $j$  up to 6. Because the amount of the required strain gages ( $\Lambda=8$ ) is smaller than the number of disk sectors ( $N=9$ ), the gage distance criteria is neglected within the optimization function  $\psi_{\Lambda=8}$  (see Eq. (29)). The blade pressure side is used for the strain gage instrumentation. Here, 636 mid-nodes and 224 corner-nodes are selected from the spatially curved pressure side (see the dashed line in Fig. 7) and then used in the numerical analysis. For an increment angle  $\Delta\varphi$  of 0.175 deg,  $1.66 \times 10^{38}$  possible placements must be evaluated to reach the optimum of the function  $\Psi_{\Lambda=8}$ .

With 600 chromosomes, the GA optimization is ended on the 440-th generation with 264'000 determinations of the  $\Psi_{\Lambda=8}$ , which is significantly less than the amount of all possible placements of  $1.66 \times 10^{38}$ . Thus, the GA optimization process may not have found the exact optimum of the function, but it provides an appropriate solution according to the considered four gage criteria. The obtained appropriate placements of eight strain gages are presented in Fig. 7 and detailed results are given in the Appendix. Values of the population's for the maximum and average fitness are shown in Fig. 8. Up to the 100th generation, the maximum population increases rapidly and then it grows slowly. Also, the average fitness (Fig. 8) rises significantly below the 100th generation. Afterwards the average fitness oscillates stochastically around a constant average value. This oscillation is induced by the degeneration due to very small magnitudes of the optimization function.

Finally, an optimization result for  $\Lambda=2$  strain gages is compared to the strain gage placements obtained from the qualitative techniques, which is based on the visual peak stress assessment of the rigidly clamped vane (the hub is omitted). As it is presented in Fig. 9, one strain gage position obtained from the qualitative technique is located very close to the gage placement predicted with the GA. The other qualitatively determined position, however, is

<sup>2</sup>The computation lasts few minutes on the standard Unix workstation.

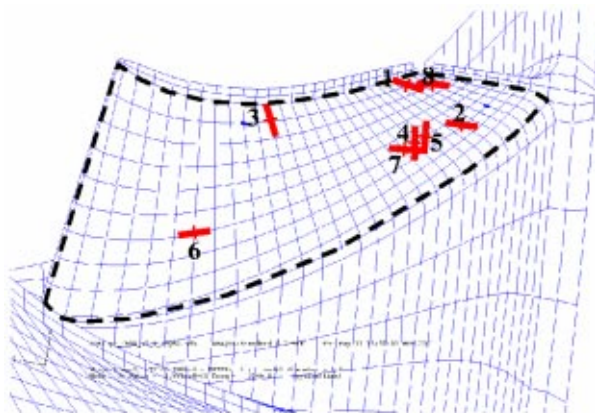


Fig. 7 The spatially curved pressure side of the impeller vane with the eight calculated optimal strain gage placements (nodes on the surface indicated with a dashed line are used in the optimization)

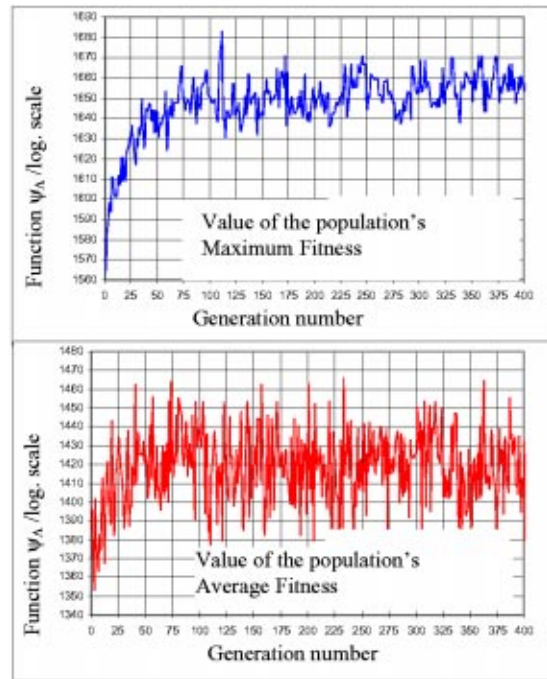


Fig. 8 Values of population's for the maximum (upper figure) and average (bottom figure) fitness from the GA process

located on a different place to the position proposed by the current procedure (see Fig. 9). For the optimized and qualitative gage placements, the optimization function  $\psi_{\Lambda=2}$  is equal to 1450.9 (see Fig. 9) and 1276.1, respectively. Thus, the gage positions obtained from the traditional technique considering the rigidly

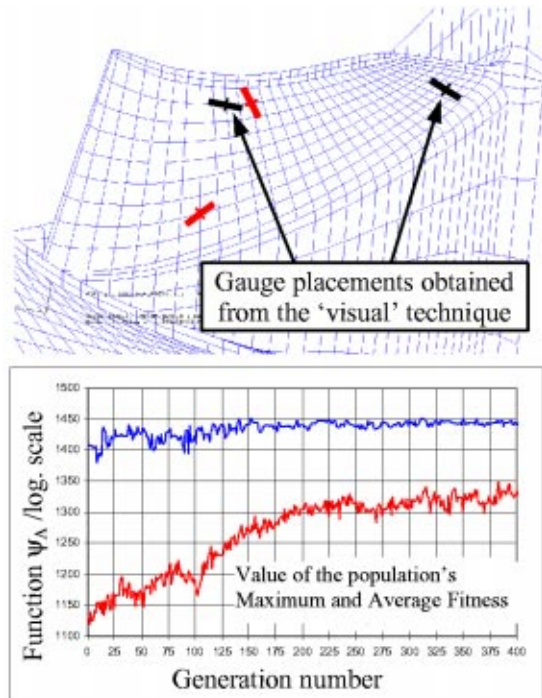


Fig. 9 Comparison of the gage positions obtained from the GA procedure and qualitative technique (upper figure), where the lower figure presents the maximum and average fitness for the optimized gage locations

clamped blade are worse than the placements proposed from the present approach, accounting for the disc vibration and the GA procedure.

## Conclusions

In relation to literature dealing with the rigidly clamped blade, a novel methodology and numerical tool are proposed for the optimum placements of strain gages on the rotating bladed disks. In this approach, the tuned disk assemblies were taken into ac-

count. This approach can be applied to any structure requiring strain gage instrumentation. Only preliminary verification of this tool is discussed in this paper. Additional utilization of this tool is planned together with experimental confirmation.

## Acknowledgment

The authors thank the Thermal Machinery Lab of ABB Turbo Systems, Switzerland for the support and permitting the publication of this paper.

## Appendix

```
*****
GENERATION = 440
Maximum value of the objective function = 1687.053
Average value of the objective function = 1392.851
Minimum MAX strain = 0.3620
Minimum Angle = 0.2702
Average MAX strain = 0.636
Average Angle = 46.10
Number of mutations = 161773
Number of crossover = 79734
```

ST GAUGE POSITION [-]	NODE LABEL [-]	NODE COORD X1 [cm]	COORD X2 [cm]	X3 [cm]	GRID COORD S [-]	COORD T [-]	ORIENT PHI [deg]	VECTOR V1 [cm]	V2 [cm]	V3 [cm]
1	49216	154.5	60.1	18.9	48	2	70.2	0.93687	0.10509	0.33351
2	48984	145.0	57.5	8.7	46	14	16.5	0.26434	0.17348	0.94870
3	46808	119.9	57.8	32.2	20	2	48.6	0.66581	0.38537	0.63890
4	48306	131.5	56.2	12.9	38	12	148.3	-0.54257	0.05333	0.83832
5	48478	135.1	56.7	12.1	40	12	152.2	-0.48553	0.09384	0.86917
6	45898	86.3	45.5	35.9	10	12	130.2	-0.74377	-0.20974	0.63468
7	48134	127.8	55.7	13.7	36	12	173.7	-0.14212	0.15776	0.97720
8	49550	159.2	60.0	16.2	52	4	114.5	-0.91069	-0.00903	0.41300

### STRAIN AMPLITUDES, NORMED

MODE NR.	N	J	POS 1	POS 2	POS 3	POS 4	POS 5	POS 6	POS 7	POS 8	MAX
1	0	1	0.0563	0.4306	0.0042	0.2603	0.2909	0.0534	0.4690	0.0101	0.4690
2	0	2	0.0801	0.1876	0.0050	0.0691	0.0802	0.2918	0.4118	0.0591	0.4118
3	0	3	0.0185	0.3713	0.0227	0.1641	0.1647	0.1343	0.3677	0.1272	0.3713
4	0	4	0.0400	0.0890	0.0619	0.1888	0.1594	0.4444	0.0448	0.0558	0.4444
5	0	5	0.0236	0.1047	0.0640	0.3057	0.3005	0.4145	0.1697	0.0349	0.4145
6	0	6	0.0893	0.1642	0.0115	0.0142	0.0041	0.3620	0.3416	0.0654	0.3620
7	1	1	0.0815	0.2384	0.7310	0.2291	0.2271	0.0889	0.0450	0.0374	0.7310
8	1	2	0.0815	0.2383	0.7072	0.2291	0.2349	0.0889	0.0450	0.0374	0.7072
9	1	3	0.1808	0.1577	0.8872	0.0969	0.1139	0.0316	0.1319	0.0292	0.8872
10	1	4	0.1808	0.1532	0.8872	0.0969	0.1139	0.0316	0.1319	0.0292	0.8872
11	1	5	0.0836	0.3674	0.5495	0.4761	0.4534	0.6264	0.6667	0.0225	0.6667
12	1	6	0.0806	0.4236	0.6027	0.4811	0.4838	0.4516	0.6741	0.0228	0.6741
13	2	1	0.2014	0.2714	0.7196	0.2738	0.2507	0.1802	0.0515	0.0494	0.7196
14	2	2	0.2013	0.0951	0.6639	0.3156	0.2996	0.1802	0.0515	0.0494	0.6639
15	2	3	0.1740	0.0979	0.8734	0.0552	0.0323	0.2126	0.2839	0.0262	0.8734
16	2	4	0.1739	0.2041	0.8733	0.0553	0.0323	0.2127	0.2838	0.0261	0.8733
17	2	5	0.1050	0.0986	0.7796	0.3700	0.3472	0.2213	0.4205	0.0995	0.7796
18	2	6	0.1887	0.2201	0.8784	0.0801	0.0569	0.2215	0.3078	0.0217	0.8784
19	3	1	0.3267	0.3304	0.6235	0.3204	0.2951	0.8898	0.0900	0.0677	0.8898
20	3	2	0.3266	0.1550	0.5644	0.4015	0.3832	0.2940	0.0900	0.0677	0.5644
21	3	3	0.1880	0.2440	0.8546	0.0726	0.0400	0.2850	0.2730	0.0630	0.8546
22	3	4	0.1948	0.2524	0.8853	0.0752	0.0415	0.5891	0.2827	0.0608	0.8853
23	3	5	0.1789	0.2559	0.2066	0.1618	0.1209	0.4553	0.3971	0.0311	0.4553
24	3	6	0.1771	0.2536	0.8704	0.1603	0.1198	0.3120	0.3933	0.0310	0.8704
25	4	1	0.0699	0.1415	0.0956	0.3637	0.3492	0.3815	0.0947	0.2278	0.3815
26	4	2	0.0285	0.0269	0.0094	0.0019	0.0035	0.5965	0.0394	0.0694	0.5965
27	4	3	0.0503	0.0558	0.0134	0.0535	0.0368	0.4649	0.1863	0.0075	0.4649
28	4	4	0.0063	0.3556	0.0917	0.1403	0.1334	0.4588	0.0717	0.2476	0.4588
29	4	5	0.0132	0.4738	0.0643	0.0592	0.0657	0.2910	0.3211	0.2192	0.4738
30	4	6	0.0805	0.1366	0.0071	0.0070	0.0098	0.3772	0.3204	0.0472	0.3772

### ORTHOGONALITY

MODE NR.	MODE NR.	ANGLE [deg]
1	2	36.662386
1	3	16.839481
:		
:		
etc.		

## References

- [1] Kielb, J. J., and Abhari, R. S., 2001, "Experimental Study of Aerodynamic and Structural Damping in a Full-Scale Rotating Turbine," ASME Paper 2001-GT-0262.
- [2] Purcell, T. E., May 1996, "Dynamic Stress Analysis of Gas Turbine Rotor Airfoil Using Thermoelastic Techniques," Exp. Tech., pp. 9–13.
- [3] Studer, A., 1980, "Messortbestimmung für Schaufelschwingungsmessungen mit Dehnmessstreifen (Estimation of Strain Gauge Placements for Blade Vibration Measurement)," *ABB Turbo Systems Ltd., Technischer Bericht HTX-ST 80024*, Baden.
- [4] Nichol, K. L., 1991, "Strain-Gage Placement Considerations for Dynamic Data Analysis," *American Institute of Aeronautics and Astronautics*, AIAA-91-1250, Tennessee.
- [5] Sensmeier, M. D., and Nichol, K. L., 1998, "Minimizing Vibratory Strain Measurement Error," *Proceedings of the 1998 International Gas Turbine & Aeroengine Congress & Exhibition*, 98-GT-257, Stockholm.
- [6] Sensmeier, M. D., and Nichol, K. L., 1998, "Numerical Strain Gage Representation," *American Institute of Aeronautics and Astronautics*, AIAA-98-1720, Tennessee.
- [7] Sensmeier, M. D., and Nichol, K. L., 1998, "Optimum Placement of Sensors for Vibration Measurements on Turbine Engine Blades," *American Institute of Aeronautics and Astronautics*, AIAA-98-1849, Tennessee.
- [8] Griffin, J. H., April 1992, "Optimizing Instrumentation When Measuring Jet Engine Blade Vibration," ASME J. Eng. Gas Turbines Power, **114**, pp. 217–221.
- [9] Thomas, D. L., 1974, "Standing Waves in Rotationally Periodic Structures," J. Sound Vib., **37**, pp. 288–290.
- [10] Szwedowicz, J., 1999, "Cyclic Finite Element Modeling of Shrouded Turbine Blades Including Frictional Contact," ASME Paper 99-GT-92.
- [11] ABAQUS/Standard, 2001, User's Manual Vol. I-III, Hibbit, Karlsson & Sorensen, Inc., USA.
- [12] Zeng, F. L., 1991, "On Adaptive Finite Element Procedures for Static and Dynamic Problems," Chalmers University of Technology, Ph.D. thesis, Publication 91:15, Goteborg, Sweden.
- [13] Timoshenko, S. P., and Goodier, J. N., 1984, *Theory of Elasticity*, 3rd Ed., McGraw-Hill International Book Company, London.
- [14] Goldberg, D. E., 1989, "*Genetic Algorithms in Search, Optimization and Machine Learning*," Addison-Wesley, New York.
- [15] Simpson, M. T., and Hansen, C. H., 1996, "Use of Genetic Algorithms for Optimizing Vibration Actuator Placement for Minimizing Sound Transmission Into Enclosed Spaces," SPIE Vol. 2717, pp. 409–421.

# Unsteady Rotor Heat Transfer in a Transonic Turbine Stage

F. Didier

R. Dénos  
Mem. ASME

T. Arts

Von Karman Institute for Fluid Dynamics,  
Rhode Saint Genèse, Belgium

*This experimental investigation reports the convective heat transfer coefficient around the rotor of a transonic turbine stage. Both time-resolved and time-averaged aspects are addressed. The measurements are performed around the rotor blade at 15, 50, and 85% span as well as on the rotor tip and the hub platform. Four operating conditions are tested covering two Reynolds numbers and three pressure ratios. The tests are performed in the compression tube turbine test rig CT3 of the von Karman Institute, allowing a correct simulation of the operating conditions encountered in modern aero-engines. The time-averaged Nusselt number distribution shows the strong dependence on both blade Mach number distribution and Reynolds number. The time-resolved heat transfer rate is mostly dictated by the vane trailing edge shock impingement on the rotor boundary layer. The shock passage corresponds to a sudden heat transfer increase. The effects are more pronounced in the leading edge region. The increase of the stage pressure ratio causes a stronger vane trailing edge shock and thus larger heat transfer fluctuations. The influence of the Reynolds number is hardly visible. [DOI: 10.1115/1.1505850]*

## Introduction

One of the key parameters for the improvement of the thermal efficiency of the gas turbine cycle is the increase of the turbine inlet temperature. The upper limit will be reached when the combustion will be performed at stoichiometric conditions. Cooling systems are used to allow the operation of the HP stages at temperatures above the melting temperature of the blade material. The limitation is due to the fact that the gain in cycle efficiency due to the turbine inlet temperature increase is balanced by the loss of efficiency due to the cooling system.

The design of a blade cooling scheme requires the knowledge of the convective heat transfer coefficient distribution around the blade profile. Experimental research in this field started many years ago in cascades. For rotors, more realistic configurations were obtained with rotating bars (Ashworth et al. [1], Doorly and Oldfield [2]) or shock generation devices (Popp et al. [3]) upstream of a cascade. More recently, investigations were performed in dedicated turbine stage test rigs (e.g., Guenette et al. [4], Dunn et al. [5], Hilditch et al. [6], Moss et al. [7], Dénos [8]).

Measurements in linear cascades allowed the effects of Mach number, Reynolds number and turbulence intensity to be studied separately. Many studies can be found in the literature, such as those by Arts et al. [9]. They showed the strong link between heat transfer coefficient and Mach number distribution around the blade. An accelerating flow stabilizes the boundary layer and maintains a slightly thickening protective layer between the hot gas and the blade. A decelerating flow destabilizes it and may promote transition and higher heat transfer. The increase of the Reynolds number causes an overall increase of the heat transfer coefficient due to higher flow velocity or density. It also tends to move upstream the transition onset. High free stream turbulence tends to enhance the overall heat transfer rate due to a higher mixing of the flow in the boundary layer. The most visible effect is the displacement of the onset of transition towards the leading edge of the blade on the suction side. On the pressure side the boundary layer remains laminar at low turbulence level. However, at higher turbulence levels, one observes a tendency to transition and a turbulent state may be reached close to the trailing edge.

Rotating bar systems were widely used to simulate the effect of vane wakes and vane trailing edge shocks on the rotor blade flow

field. Doorly and Oldfield [2], put in evidence a heat transfer peak associated with the passage of the shock from the crown to the leading edge on the suction side of the blade. The authors observed a recirculation bubble and identified shortly after the shock passage a turbulent spot traveling at a speed related to the free stream velocity. Johnson et al. [10,12], recorded very high and sharp heat transfer variations with amplitudes of up to three times the mean level, due to direct shock impingement on the blade. The highest variations were recorded between the crown and the leading edge, i.e., in the region that is swept periodically by the vane trailing edge shock. The amplitude of the fluctuations decreases when going from the crown towards the leading edge. The waves were reflected many times in the blade passage, leading to several weaker peaks on the heat flux traces. They proposed a simple model to calculate the heat transfer rate from the pressure fluctuation, based on isentropic compression and change of density in the boundary layer. The model predicted with good accuracy the variations due to the shock on the suction side. They also showed the existence of a "vortical bubble" formed at the leading edge when the shock impinged perpendicularly on the wall. Depending on the location of formation, it would then be convected on either the pressure side or the suction side, and would cause both a transient increase in the surface heat flux and an enhancement in the mean level.

The unsteady heat transfer on the rotor of a fully scaled transonic turbine was measured by Guenette et al. [4]. The results were compared with linear cascade results for the same rotor profile with passing bars, Ashworth et al. [1]. The time-averaged heat transfer levels in the two experiments were very similar. The amplitude of the fluctuations induced by the shock was larger in the turbine than in the cascade. However, the similarity of the results between the two experiments lead to the idea that the heat transfer process at midspan on this transonic rotor was mainly two-dimensional. A two-dimensional Navier-Stokes prediction, with transition set at a point near the leading edge ( $x/s=0.01$ ) gave good results for the mean rotor heat transfer levels.

More recently, Moss et al. [7] performed unsteady pressure and heat flux measurements in a high-pressure turbine. They used Johnson's et al. [10,11] boundary layer compression model and another model assuming a constant heat transfer coefficient and isentropic gas temperature change to predict the heat flux history. Both models gave quite realistic results compared to the measured values. Moss et al. [12] made extensive measurements at five different heights on the same rotor blade. By running the rotor in reverse rotation without stator vanes, and by using data from cas-

Contributed by the International Gas Turbine Institute and presented at the International Gas Turbine and Aeroengine Congress and Exhibition, Amsterdam, The Netherlands, June 3–6, 2002. Manuscript received by the IGTI, September 21, 2001. Paper No. 2002-GT-30195. Review Chair: E. Benvenuti.



**Table 1 Typical stage geometrical characteristics**

	Stator	Rotor
Number of blades	43	64
Chord	72.3 mm	48.4 mm
Axial chord	43.2 mm	39.6 mm
Hub radius	344.5 mm	339.4 mm (at exit)
Tip radius	395.2 mm	395.2 mm

cade experiments, they showed that the wake had very little effect on the time averaged heat transfer, because the boundary layer was transitional or turbulent almost from the leading edge. The presence of the horseshoe vortex at hub was put in evidence.

The goal of the present study is to investigate the convective steady and unsteady heat transfer around the rotor blade profile of a transonic turbine stage. In a previous program, the influences of rotational speed, axial gap between stator and rotor and vane coolant ejection on the unsteady pressure field were investigated, Dénos et al. [13]. In the frame of the present study, these parameters are kept constant. Instead, the stage pressure ratio and the Reynolds number are varied in order to investigate their influence under the transonic regime. The former measurement locations at 50% span are also extended to 15, 50, 85% span as well as to the blade tip and hub platforms.

**The Turbine Stage**

The turbine stage is composed of 43 cylindrical vanes and 64 twisted blades. The main geometrical characteristics of the stage are listed in Table 1. The vanes are internally cooled ( $\dot{m}_c = 3\%$  of overall mass flow) with ejection at the trailing edge on the pressure side. The rotor was designed with a meridional flow channel divergence of 10% at hub in order to reduce the axial outlet velocity and to minimize the secondary losses. The turbine stage was tested in the VKI short duration compression tube facility CT3. This facility is capable of simulating Reynolds and Mach numbers, gas/wall and gas/coolant temperature ratios of modern aero-engine HP turbines (see Sieverding and Arts [14]).

The heat transfer on the rotor blade was investigated at 15, 50, and 85% of the blade height. At each height, 24 thin film gages mounted on ceramic inserts are distributed along the blade profile, as shown in Fig. 1 at 50%. The geometry of the rotor blade at different sections is shown in the same figure. In parallel to heat transfer measurements, pressure measurements were carried out with 72 Kulite fast response pressure transducers, located at the same positions as the thin film gages.

Full details on the turbine test rig, the turbine stage and the instrumentation were reported by Dénos [8]. The stage inlet turbulence level amounts to 1.6% and is much lower than that encountered in real engines.

**Data Processing**

The measurement technique consists in recording the blade surface temperature increase during a blowdown test that produces a

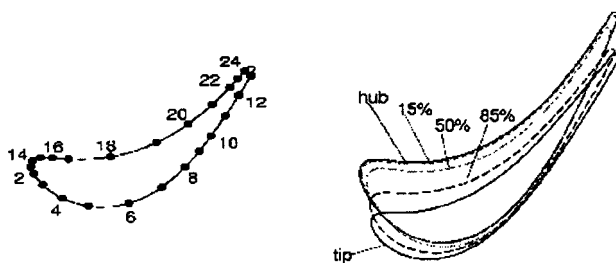


**Fig. 1 Gage distribution and geometry of the Brite rotor**

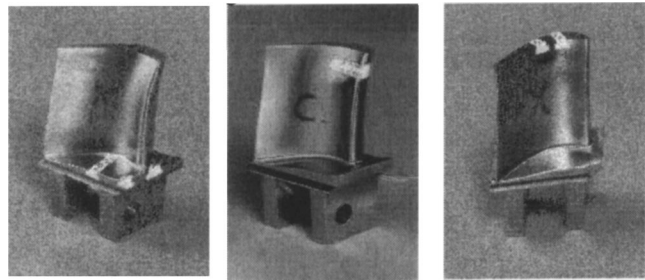


**Fig. 2 Thin film gages on Macor insert at hub platform, 85% span and blade tip**

sudden gas temperature change, the blade being initially at ambient temperature. The blade surface temperature history is measured with a platinum thin film gage resistor implemented on an insulating ceramic insert (see Fig. 2). The testing time ( $\sim 0.5$  s) is so short that the inner extremity of the insert stays at ambient temperature during the blowdown. The gas temperature is monitored with a type K thermocouple. Typical evolutions of these temperatures during the blowdown are depicted in Fig. 3 (top graph). The heat flux  $\dot{q}$  (see bottom of Fig. 3) is obtained by solving the 1-D unsteady conduction equation with a Crank-Nicholson scheme across the insert. The boundary conditions are the wall temperature history and a constant temperature at the inner side of the insert.

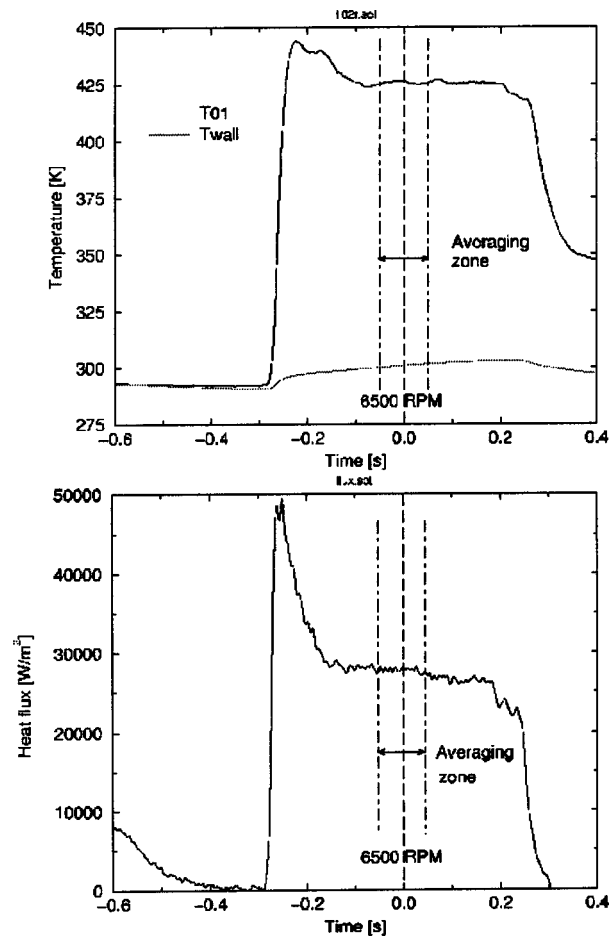


**Fig. 3 Typical temperature evolution in the test section and heat flux on the rotor blade**

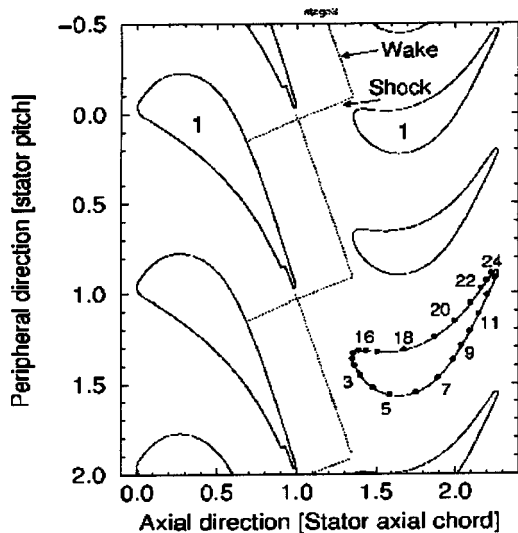


Fig. 4 Phase reference and shock-wake system

The gage signal carries two types of information, i.e., at the blowdown time scale, referred to as time-averaged, and at the blade passing frequency, referred to as time-resolved. The two components are recorded and processed separately. The time-averaged values are obtained with a signal sampled at 1500 Hz and low-pass filtered at 750 Hz. The heat flux is then averaged over a time period of about 100 ms around the design rotational speed of 6500 rpm. The time-resolved traces are high-pass filtered at 100 Hz and sampled at 300 kHz. The surface temperature fluctuations occurring at the vane passing frequency (4660 Hz) being small, they are amplified before being digitized on a 12 bit data acquisition system. The signals are naturally low pass filtered at 78 kHz by the limit of the opto-electronic transmission system (Sieverding et al. [15]). A phase locked average procedure is then applied to the heat flux traces including three rotor revolutions (129 vane passages).

The relative position of the rotor with respect to the stator is known at any time thanks to a diode that gives a pulse at every rotor revolution. The phase-locked averaged traces will be presented as a function of the vane reduced pitch referred to as phase  $\varphi$  in the following.  $\varphi=0$  when the stacking axis of the rotor blade is aligned with the one of the vane;  $\varphi=1$  when the blade has completed one stator pitch traverse (blade labeled 1 in Fig. 4). All signals were corrected for the phase delays induced by the instrumentation and transmission boards.

For similarity purposes, the results will be reported as Nusselt numbers:

$$Nu = \frac{\dot{q}c}{k_g(T_g - T_w)}$$

where  $c$  is the rotor chord at the corresponding height and  $T_g$  is the corresponding relative inlet total temperature calculated from the measured  $T_{01}$  upstream of the stage and the design velocity triangles. At nominal conditions, typical values for the rotor rela-

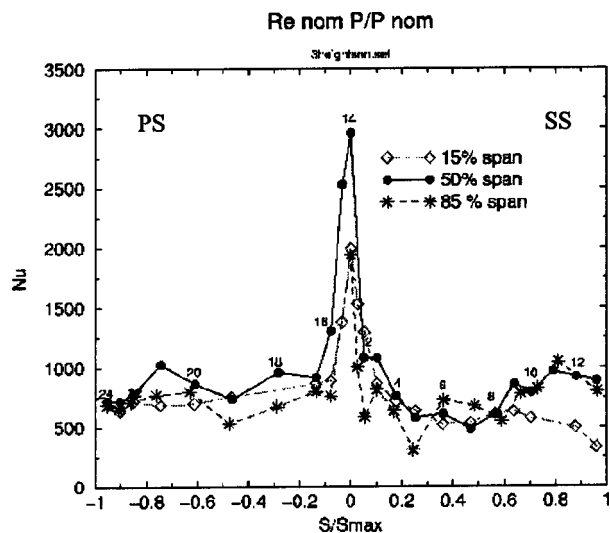


Fig. 5 Time-average Nusselt number at the three investigated heights for nominal conditions

tive inlet total temperature and the wall surface temperature are 370 and 300 K, respectively. The air conductivity  $k_g$  is estimated at the gage temperature.

The overall uncertainty on the Nusselt number was evaluated based on the work of Camci [16] and is estimated to be of the order of  $\pm 5\%$  of the mean value.

### Test Conditions

The measurement campaign consisted in four different operating conditions covering two Reynolds numbers and three pressure ratios. The high and low pressure ratios are, respectively, representative of a highly loaded single stage high pressure turbine and the first stage of a two stage turbine. The high Reynolds number condition was achieved by increasing the stage inlet total pressure. Table 2 summarizes the four operating conditions at 15, 50, and 85% height. In the perspective of testing a 1&1/2 stage configuration, the temperature for the Re high condition was increased from 440 to 480 K to allow a sufficient  $T_{\text{gas}}/T_{\text{wall}}$  on the second stator. A small change of the dimensionless rotor speed  $N/\sqrt{T_{01}}$  results ( $-4.2\%$ ).

### Time-Averaged Nusselt Number Distributions

The Nusselt number distributions around the rotor blade at nominal conditions for the three investigated spans are compared in Fig. 5. Some of the points are averages of up to three tests. Based on 7 measurement locations, the obtained repeatability was of the same order than the uncertainty ( $\pm 5\%$  of the mean value). Levels ranging between 2000 and 3000 are observed in the leading edge region while the average level further downstream on the pressure and suction sides is of the order of 800.

In the front region of the blade, the boundary layer is very thin and the heat transfer depends mainly on the Reynolds number and the free stream turbulence. The highest value is observed at 50%

Table 2 Some characteristics of the flow at 15, 50, and 85% height for the four running conditions

			15 %		50 %		85 %	
	$P_{01}/P_{s3}$	$Re_{2c}$	$M_2$	$Re_{2R} [10^5]$	$M_2$	$Re_{2R} [10^5]$	$M_2$	$Re_{2R} [10^5]$
<i>Re nom P/P nom</i>	3.04	$1.01 \cdot 10^6$	1.08	3.46	1.03	2.99	0.98	2.72
<i>Re nom P/P low</i>	2.32	$0.99 \cdot 10^6$	0.99	3.17	0.95	2.72	0.90	2.46
<i>Re high P/P nom</i>	3.08	$1.26 \cdot 10^6$	1.10	4.53	1.04	3.95	0.99	3.61
<i>Re high P/P high</i>	4.07	$1.26 \cdot 10^6$	1.11	4.62	1.06	4.04	1.01	3.70

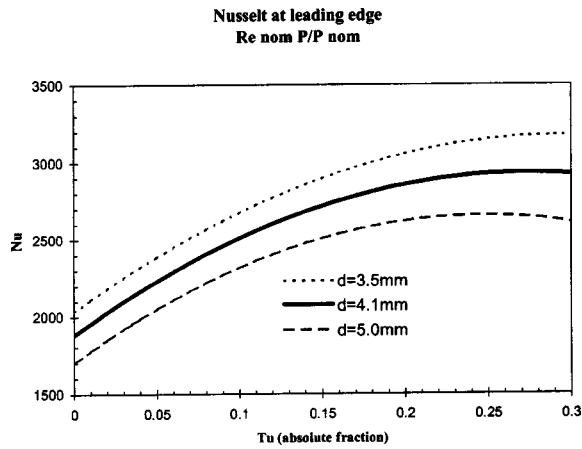


Fig. 6 Prediction of Nusselt number at leading edge according to Lowery and Vachon experimental law for cylinders in cross-flows

span. According to the Reynolds numbers at stator exit (Table 2), the highest value should be seen at 15% of the span and the lowest at 85%. This is probably due to the fact that the gages are not located exactly at the stagnation point. The rate of decrease around the stagnation point being very large, it is difficult to conclude on the differences observed in this region.

In cascade tests, the Nusselt number at the stagnation point of a blade can well be predicted using correlations by measurements around cylinders in cross flows (Camci and Arts, [17]). For example, the correlation of Lowery and Vachon [18], has been used to predict the Nusselt number at the stagnation point at midspan for nominal conditions

$$Nu_d = Re_d^{1/2} (1.01 + 2.624((Tu Re_d^{1/2})/100) - 3.07((Tu Re_d^{1/2})/100)^2)$$

The leading edge can be approximated by a circle of 4.1 mm diameter. Two others diameters, 3.5 and 5.0 mm, are also investigated because the leading edge is more elliptic than circular. The estimated Nusselt number is plotted in Fig. 6 as a function of the turbulence intensity. Although the correlation holds up to 14% turbulence intensity, the formula was extrapolated to 30%. For comparison with our experiments, the Nusselt number is calculated using the rotor chord length. This explains why it is the lowest for the highest diameter. With the diameter of 4.1 mm, a turbulence intensity in excess of 10% is needed in order to reach values of Nusselt number above 2500. To reach the value of 3000 measured at 50% span, unrealistic levels of isotropic turbulence under steady conditions have to be considered (~25%). In the present experiment, it is difficult to define turbulence intensity since the flow is submitted to periodic wake and shock ingestion at a rate of 4660 Hz. It can be concluded that this unsteadiness may enhance considerably the heat transfer rate at the stagnation point with respect to a steady flow case with isotropic turbulence. An unsteady quasi 3-D Navier and Stokes stage computation by Michelassi et al. [19] predicted instantaneous turbulence intensity levels in excess of 30% at the leading edge when the wake was passing. Note that in the case of [12], without vane exit trailing edge shock, the use of another correlation (Kays [20]) for laminar flows over cylinders in cross flows over predicted the Nusselt number at the rotor leading edge.

On the suction side, at 50% span (Fig. 5), the link between the Nusselt number distribution and the Mach number distribution appears clearly. Figure 7 shows the isentropic Mach number based on the measured local static pressure and the relative total pressure at rotor inlet. The convex curvature and the favorable pressure gradient have a stabilizing effect on the boundary layer,

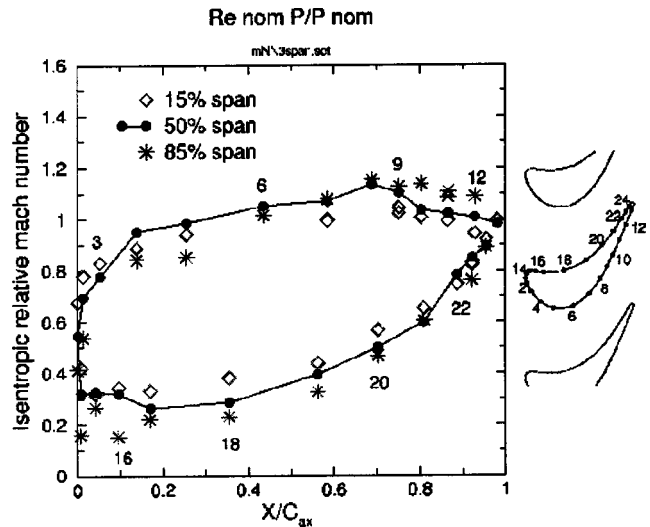


Fig. 7 Mach number distribution at 15, 50, and 85% height for nominal conditions

which thickens progressively. As result, the Nusselt number decreases up to points 7–8. After point 9, the flow is decelerated. This may promote a transitional state and an increase of the heat transfer rate. On the rear suction side, the Mach number remains almost constant, the boundary layer continues to thicken and the Nusselt number decreases accordingly.

These trends appear clearly in cascade tests, with a uniform and steady inlet flow (for example, [9]). The situation is quite different in the case of a rotor that chops periodically (here 4600 times per second) the vane wakes and trailing edge shocks. One can imagine that the boundary layer state may change several thousands of time per second from laminar to turbulent depending on wake and shock interactions with the boundary layer. The terms laminar, turbulent or transitional may then take a kind of statistical meaning rather than indicating a perpetual state. Although the shock and wake ingestions constitute large destabilizing factors, it seems that the boundary layer remains laminar until gages 7–8, probably due to the quite low Reynolds number ( $Re_{3R} = 0.5 \cdot 10^6$ ). Nevertheless, the time-averaged Nusselt number for this part is higher than what one would expect for the case of a permanent laminar boundary layer because of the shock that sweeps the blade from the crown towards the leading edge (seen until gage 5, cf. unsteady part).

The heat transfer on the suction side at 15 and 85% span, is also closely linked to the inlet conditions and to the acceleration rate. On the first part of the suction side, until gage 5, the heat transfer is higher at 50% span. At location 3 at 85% span one observes a peak in the Nusselt number. The same behavior is seen at 50% span but with less amplitude. At location 6, the Nusselt number increases at 15 and 85% span due to a deceleration of the flow just before. On the rear part of the suction side, the level of heat transfer is almost the same at 50 and 85% span with the same tendencies (deceleration between gages 8 and 9) while at 15% span the Nusselt number is much lower due probably to the lower rate of deceleration of the flow.

Around the blade leading edge, the pressure surface boundary layer develops on a convex surface in a region of accelerating flow. In this region, it behaves as on the suction side. The Nusselt number decreases rapidly. After the leading edge region, the curvature changes from convex to concave. At this point a separation bubble could appear, especially at 85% span around gage 16, where the flow is strongly decelerated, but it was not detected. The Nusselt number continues to decrease progressively. After this point of singularity in curvature, the boundary layer state and hence the heat transfer rate are mainly determined by the destabi-

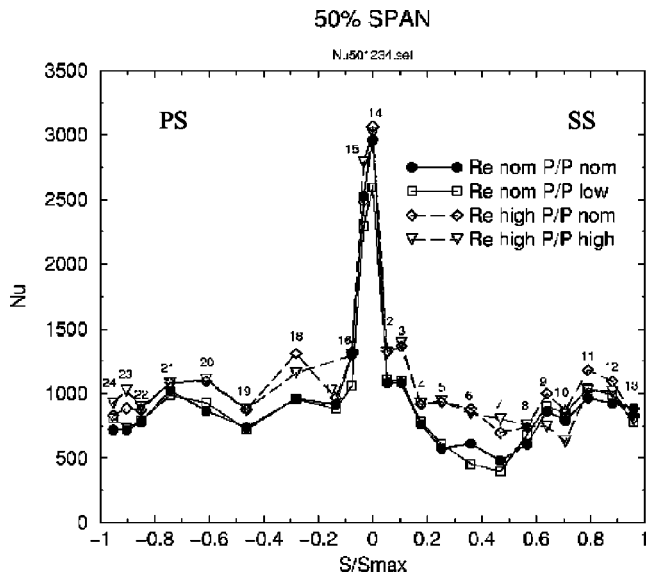


Fig. 8 Nusselt number distribution at 50% for the different running conditions

lizing effects of the concave curvature and the free stream turbulence counteracting the favorable streamwise pressure gradient. In [12], the heat transfer at the beginning of the suction and pressure surface was the lowest at midspan and was increasing going down to the hub. The higher levels at 5 and 10% span were possibly attributed to the horseshoe vortex, which seems to have no influence here at 15%. In the central part of the pressure side, the Nusselt number is globally higher at 50% span than at 15 and 85% span. At the rear pressure side, the boundary layer is re-accelerated. It stabilizes and thickens, leading to the decrease of the Nusselt number.

In Fig. 8, the conditions Re nom  $P/P$  nom and Re high  $P/P$  nom are compared at 50% span. The higher Reynolds number causes a global enhancement of the heat transfer coefficient as expected. A sign of earlier transition is noticed on the suction side (location 5) and is also observed at 15% span. At the leading edge, the maximum measured value is lower at high Reynolds than at nominal Reynolds. Again this could be attributed to the fact that the gage is not exactly at the stagnation point. Moreover, the design relative rotor inlet angle is not exactly the same for the two conditions. This is due to the fact that the temperature at Re high is 480 K instead of 440 K at Re nom. The vane exit Mach numbers are similar but the stator exit velocity has increased due to a higher speed of sound ( $a = \sqrt{\gamma r T}$ ).

On the pressure side, for any of the three spans, the Mach number distribution does not change significantly when the pressure ratio is reduced from  $P/P$  nom to  $P/P$  low. As a result, no significant differences appear in the corresponding heat transfer distributions. The behavior of the suction side boundary layer is basically a function of the different acceleration rates. At 50%, the flow is continuously accelerated for both conditions until location 7 (Fig. 9). This results in almost exactly the same Nusselt number distribution. At low pressure ratio the flow is then decelerated from location 8 until the trailing edge, while for nominal pressure ratio, the flow is accelerated further until location 8. It is decelerated only from location 9 until the trailing edge. As a consequence, the heat transfer is higher for low pressure ratio at the rear part of the suction side.

Similar behaviors commented for the low pressure ratio are observed when comparing the conditions Re high  $P/P$  nom with Re high  $P/P$  high. They are particularly visible at midspan where the flow is still accelerated until location 10 on suction side for the higher pressure ratio.

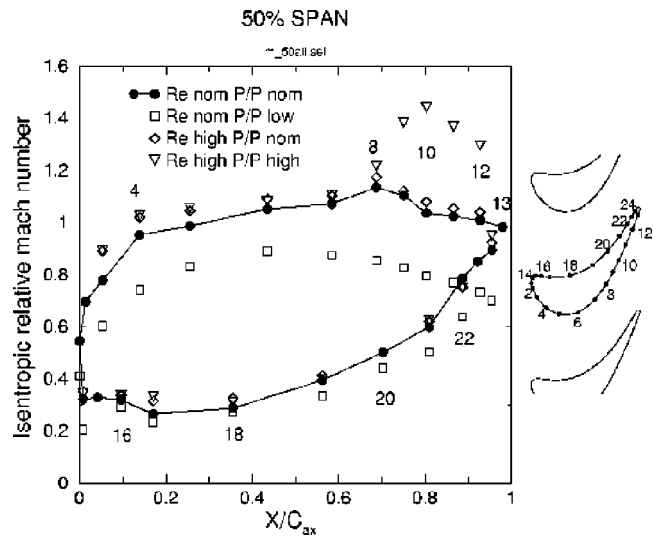


Fig. 9 Mach number distribution at midspan for the different running conditions

As will be shown later in the section dealing with time-resolved measurements, the reduction of the pressure ratio causes a large decrease of the amplitude of the heat transfer fluctuations in the leading edge region at 50% span due to the reduction of the shock strength. This is particularly the case when changing from  $P/P$  nom to  $P/P$  low. At nominal conditions, the amplitude of the fluctuations is much smaller at 50% than at 15% also due to the stronger shock that exists at hub (radial equilibrium, higher Mach number at hub). Coming back to the time-averaged distributions, the reduction of the pressure ratio from  $P/P$  nom to  $P/P$  low causes a lower heat transfer in the leading edge region at 15% only. However, there is no noticeable difference at 50% although the vane exit Mach number decreases from the  $M_2 = 1.03$  to  $M_2 = 0.95$ . Contrary to expectations, this Mach number difference was not sufficient to isolate the effect of the wake from that of the static pressure gradient. This is possibly due to the fact that on one side, when the pressure ratio is reduced, the shock strength is reduced and one would expect lower heat transfer levels due to the reduction of the boundary layer perturbations but on the other side, the reduction of the pressure ratio also reduces the acceleration of the front suction side and this tends to increase the heat transfer rate. Apparently, at 15%, the predominant effect is the reduction of the shock strength. At 50%, the two effects are in balance.

The Nusselt number distribution on the tip of the rotor blade is reported in Fig. 10 at 4 points placed along the camberline. The Nusselt number is calculated using the blade chord at tip. Unfortunately gage 1 was broken and the condition Re high  $P/P$  high was not tested. Note that the tip clearance measured under running conditions increases from the leading edge to the trailing edge (from 0.2 to 0.5 mm). The level of Nusselt number is comparable to the one on the pressure side at 85%. The increase of Nusselt number at gage 5 can be explained by higher transverse velocities in the relative frame in the rear part of the blade tip. This is a typical feature of a tip clearance flow as shown, for example, by Heider et al. [21]. On the rear part of the blade tip, the flow is dominated by the pressure difference between the pressure side and the suction side and a jet that is almost perpendicular to the camberline results, that drives the tip leakage vortex. One can clearly observe the enhancement of the heat transfer with increasing Reynolds number.

The Nusselt number distribution on the rotor hub platform along a line located in the "middle" of the channel is shown in Fig. 11. The Nusselt number is calculated using the blade chord at hub. Here again, the enhancement of the Nusselt number with

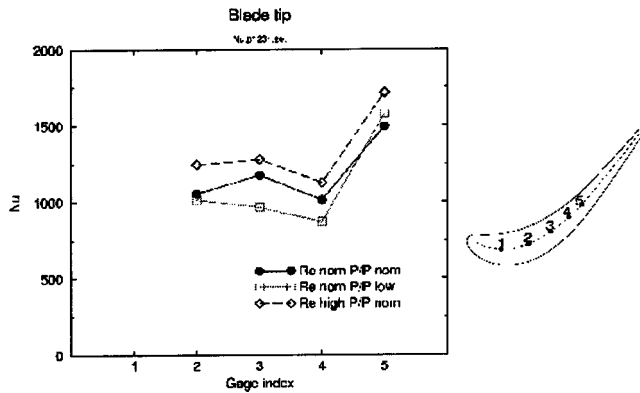


Fig. 10 Nusselt number distribution at blade tip for the different running conditions

increasing Reynolds number is observed. To comment properly the heat transfer distribution, one would need the static pressure distribution over the platform surface together with the streamlines. These streamlines are directed from pressure side to suction side due to the sweeping of the hub passage vortex on the platform.

### Time-Resolved Nusselt Number

This part focuses on the phase-locked averaged traces of the Nusselt number. Note that phase-locked average eliminates all the fluctuations that are not at vane passing frequency. As a consequence, it gives only a restricted view of the flow field. The root mean square (RMS) and the correlation coefficient are additional indications on the nonperiodic components of the signal. The correlation coefficient is obtained by performing a linear regression between the magnitude of the phase-locked average and the magnitude of the raw signal. A coefficient of 1 means that the raw signal is equal to the phase-locked average, i.e., purely periodic fluctuations without random unsteadiness.

The minimum-maximum envelope of the phase locked averaged Nusselt number, the mean RMS over one vane passing event and the correlation coefficient at 50% span for Re nom  $P/P$  nom are plotted in Fig. 12. The highest value of the correlation coefficient reaches 0.7 only at the leading edge whereas for pressure, this coefficient was reaching 0.98 [13]. It is believed that this low correlation coefficient in the leading edge region is due to a poor signal to noise ratio. This is also most probably the major cause for the high overall level of RMS. In the Laplace domain, thus by restriction in the frequency domain, the wall heat flux is linked to the surface temperature by:  $\dot{q}_w(s) = \sqrt{\rho c_p k T(s)} \sqrt{s}$ ,  $s$  being the

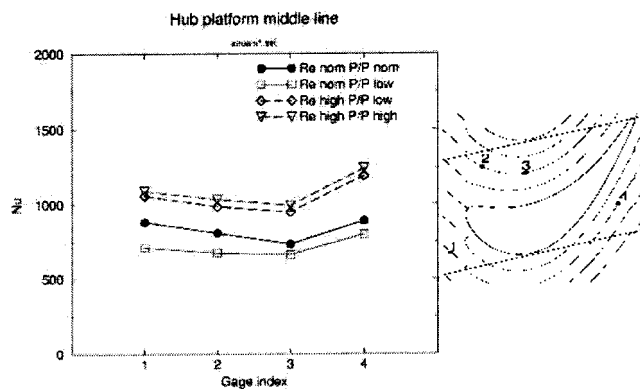


Fig. 11 Nusselt number distribution at hub platform middle line for the different running conditions

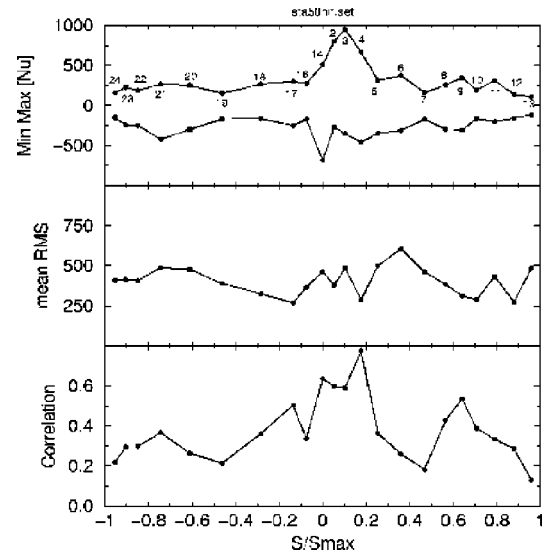


Fig. 12 Statistics for unsteady Nusselt number at 50% span for nominal conditions.

Laplace variable (see Schultz and Jones [22]). This means that, for example, if a 1 Hz periodic heat flux fluctuation causes a surface temperature change of amplitude  $A$ , a 4660 Hz fluctuation (the vane passing frequency) will result in a surface temperature change of amplitude  $\sqrt{T}/\sqrt{4660} \cdot A = 0.014 \cdot A$ . Because the surface temperature fluctuation is used to derive the heat flux, a large amplification of the signal is performed at high frequency in order to obtain a proper resolution of the fluctuations resulting in a low signal to noise ratio.

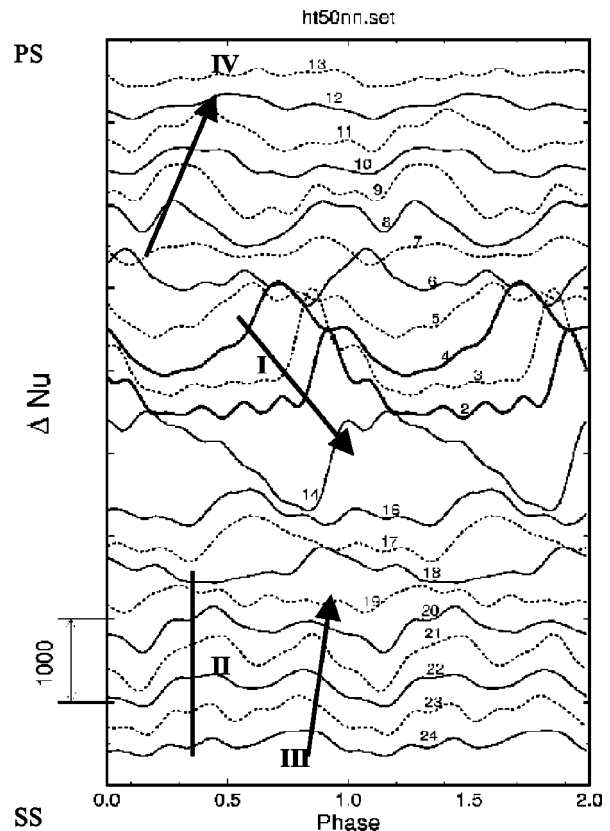


Fig. 13 Unsteady traces at 50% span for nominal conditions

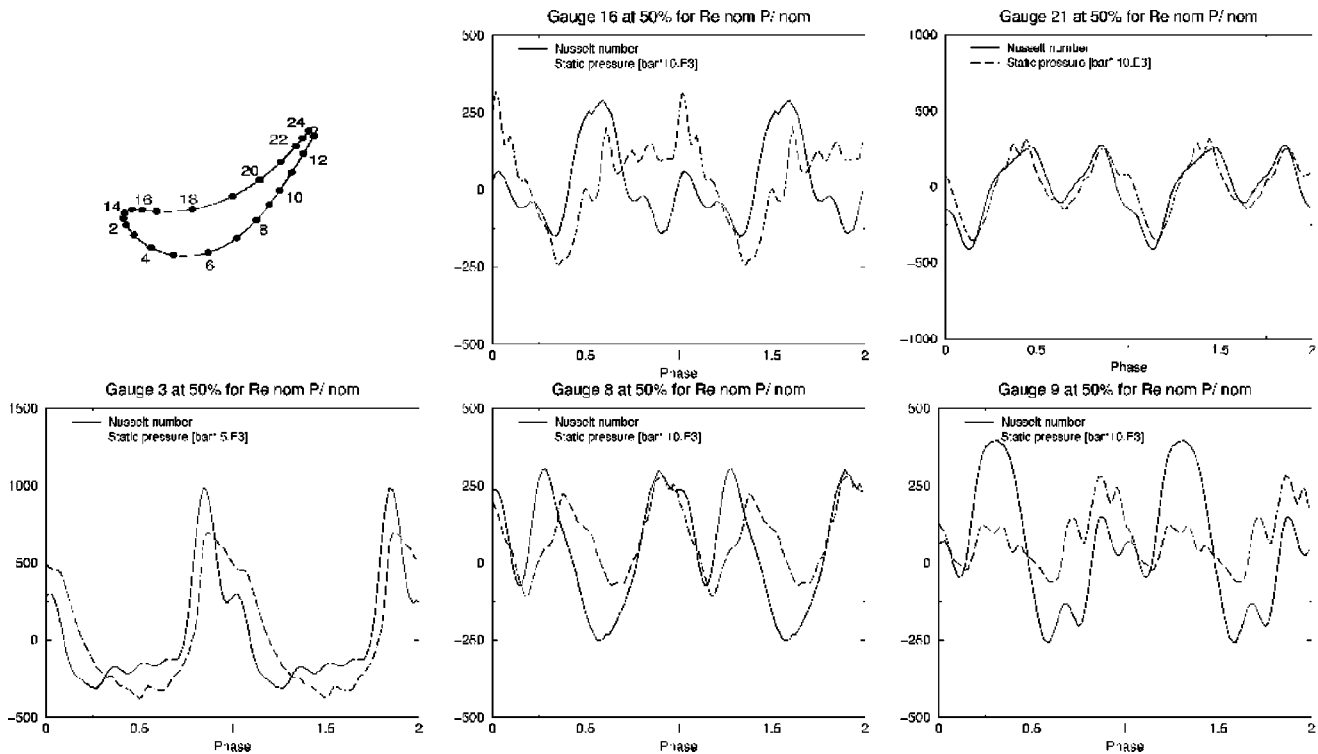


Fig. 14 Minimum and maximum of Nusselt number fluctuations at 15, 50, and 85% span for nominal conditions

For all the conditions, the correlation coefficient is maximum in the leading edge region, where the largest variations of heat transfer are encountered because of the periodic sweeping of the vane trailing edge shock.

Figure 13 shows the unsteady Nusselt number variation over two vane passing events at 50% span for Re high  $P/P$  nom. The phase-locked averaged traces are reported at the 24 measurement locations with sensors 24 to 14 from the rear pressure side to the leading edge and sensors 1 to 13 along the suction side back to the trailing edge. Although the mean value of the phase-locked averaged traces is zero, an offset was added to every curve according to the location of the flux the curvilinear abscissa of the blade.

On the front suction side, a steep gradient that travels from the crown (gauge 4) towards the leading edge (gauge 14) can be identified (see *I* on Fig. 13). This is due to the sweeping of the vane trailing edge shock as the rotor blade traverses the vane pitch (see schematic on Fig. 4). The amplitude of the fluctuations (Fig. 14) varies depending on the measurement location: the highest amplitudes are seen in the vicinity of the crown (gauge 3) and decrease towards the leading edge (gauge 14) similarly to [10]. In this region, the heat flux varies in a similar way to the static pressure as shown in Fig. 15. The two traces are in phase and the shapes exhibit some similarities.

In the regions where the shock does not impinge directly, the magnitudes of the fluctuations are much lower. The last position on the suction side affected directly by the vane trailing edge shock seems to be location 5. The traces from gauges 7 to 12 have a different pattern with two fluctuations per period. A comparison of the Nusselt number fluctuations with the static pressure fluctuations (Fig. 15) shows that at least one of the peaks in a period is in phase. On the rear pressure side, from location 19 to 24 in Fig. 13, the traces exhibit two fluctuations per period. Similarly to the pressure, the first fluctuations of the traces (*II*) are in phase while the second fluctuation (*III*) seems to propagate upstream. The Nusselt number and static pressure fluctuations at location 21 are compared in Fig. 15.

For gauge 16, a wide peak appears around phase  $\varphi=0.6$  and

another small one at phase  $\varphi=1.0$ . The peak at  $\varphi=1.0$  is caused by a direct shock impingement while the one at  $\varphi=0.6$  is due to a shock reflection coming from the leading edge of the adjacent blade [13]. The evolution of these phenomena in the central part of the pressure side can be followed from location 16 to 18. Here again the heat flux follows the static pressure variation (Fig. 15). On the rear suction side, a phenomena that is convected downstream can be identified (*IV*).

The Nusselt number minimum-maximum envelopes at 15, 50, and 85% height for nominal conditions are reported in Fig. 14. The largest fluctuations are observed at 15% height. Due to the

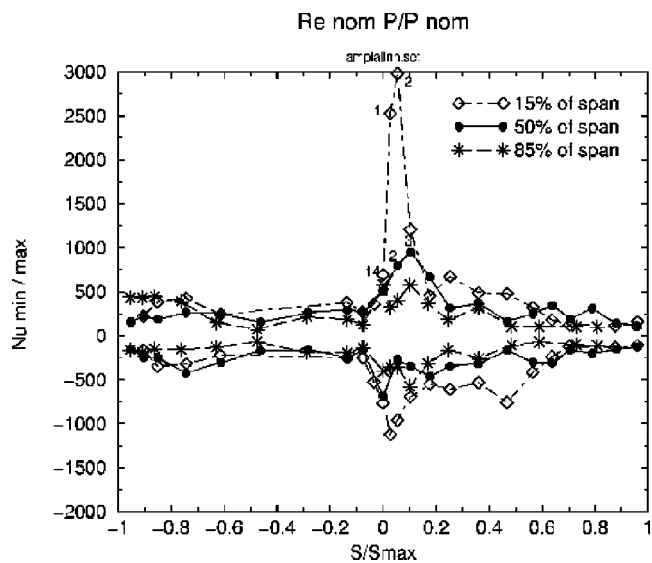


Fig. 15 Comparison of Nusselt number with static pressure fluctuations

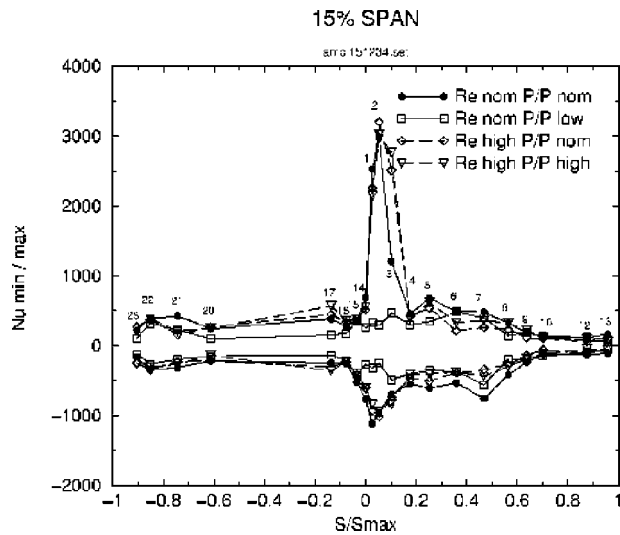


Fig. 16 Minimum and maximum of Nusselt number fluctuations at 15% span for the different conditions

radial equilibrium, the Mach number at stator exit increases towards the hub and thus the shock strength at the vane trailing edge.

One of the striking aspects of the minimum-maximum envelope is the dissymmetry between the maximum and the minimum. The highest peaks are positive. At Re nom  $P/P$  nom the peak values in the leading edge region at 15% (gage 2), 50 and 85% span (gage 3) are 3000, 900 and 600 respectively. At 15%, the peak value is of the same order as the time averaged value at the stagnation point (gage 14) and much larger than the time-averaged value at the same location. This means that in these locations (1, 2, and 3), the instantaneous heat flux can increase up to 3 times the time-averaged value.

On the suction side, the amplitude at 15% is still important until gage 7. Note that the geometry of the section changes from hub to tip (Fig. 1) and not only the strength but also the incidence of the vane trailing edge varies. As a result, the areas that are directly affected by the shock change with the rotor span. Beyond gage 7, the amplitudes are of the same order of magnitude for the three spanwise positions.

Figures 16 and 17 show the magnitude of the fluctuations for the four running conditions at 15 and 50% height respectively. Apparently, the Reynolds number has no important effect on the unsteady heat transfer. The shapes and the amplitudes of the fluctuations are very similar for the conditions Re high  $P/P$  nom and Re nom  $P/P$  nom due to little difference in the stator exit Mach number  $M_2$ . The change in amplitude of gage 3 at 15% span and of gages 2, 3, 4, and 5 at 50% span could be explained by the change in incidence of the flow for the Re high condition.

For the low pressure ratio, the vane exit Mach number is not transonic anymore. Since there are probably no shocks or very weak ones (Table 2), no high peaks are observed. However, the highest amplitudes are encountered around the leading edge region. Globally, the amplitudes are lower than for nominal pressure ratio at the three different heights.

The traces have almost the same shape and the same amplitude when raising the stage pressure ratio from  $P/P$  nom to  $P/P$  high, at Re high (almost same stator exit Mach number  $M_2$ ). Nevertheless, slightly higher amplitudes are seen for  $P/P$  high on the first half of the suction side at 15% span, and at 50% span on the leading edge and on the rear suction side.

## Conclusions

The presence of periodic fluctuations due to shocks and wakes results in very high levels of time-averaged heat transfer at the

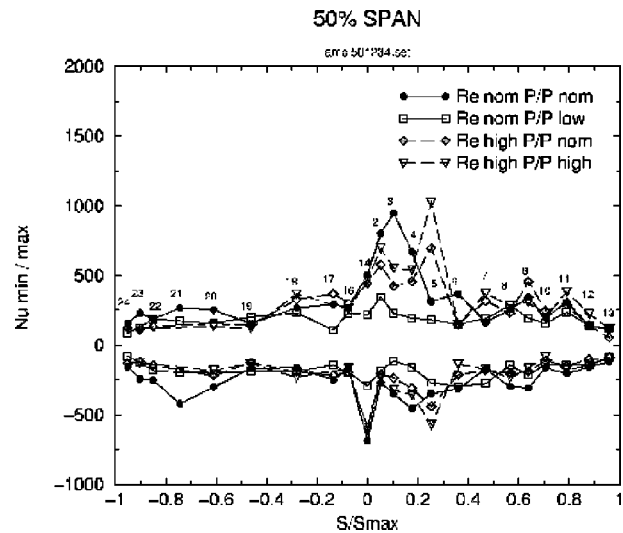


Fig. 17 Minimum and maximum of Nusselt number fluctuations at 50% span for the different conditions

rotor stagnation point at 50% span. Compared with the case of a steady rotor inlet with isotropic turbulence, unrealistic levels of turbulence intensity would be required to achieve the same heat transfer level.

The distribution of the time-averaged Nusselt number around the blade is closely related to the Mach number distribution. An accelerating flow stabilizes the boundary layer and lowers the heat transfer rate whereas a deceleration enhances it.

The variation of the pressure ratio of the stage causes changes in the relative inlet conditions to the rotor blades. The Mach number distribution is modified accordingly due to a change of incidence of the inlet flow field and of the rotor exit Mach number. These variations explain the changes in the distribution of the heat transfer coefficient around the blade. The increase of the Reynolds number enhances the overall heat transfer rate. The observed heat transfer levels are in between a laminar flow and a turbulent flow. This can be explained by the periodic ingestion of pressure discontinuities linked to the vane trailing edge shock and of wakes that carry patches of flow with a higher turbulence level.

On the blade tip, the heat transfer increases significantly at the rear due to a strong transverse tip flow in this region.

The unsteady heat transfer on the front of the rotor blade is mostly dictated by the impingement of the shock coming almost axially from the vane trailing edge. This impingement enhances greatly the heat flux downstream of its impact. When the strength of the shock is reinforced, like, for example, at the hub where the vane exit Mach number is higher, the amplitude of the fluctuations increases significantly. A decrease of the stage pressure ratio causes the vane exit Mach number to drop below  $M_2=1$  and reduces greatly the amplitude of the fluctuations. Surprisingly, the differences observed on the time-averaged distributions are small. The effect of the Reynolds number on the amplitude of the unsteady heat transfer coefficient is small. The rear part of the blade is not directly affected by the vane trailing edge shock, but one or two fluctuations per vane passage event are recorded.

The gathered data should be useful for the validation of unsteady 3-D computations.

## Acknowledgments

The research was carried out under contract for the European Commission as part of the BRITE EuRAM III BE97-4440 project "Turbine Aero-Thermal External Flows." The authors wish to ac-

knowledge this financial support as well as the contributions of the industrial partners ALSTOM POWER, FIAT AVIO, ITP, SNECMA and TURBOMECA.

## Nomenclature

$a$  = speed of sound  
 $c$  = tangential chord  
 $c_p$  = specific heat  
 $k$  = thermal conductivity  
 $\dot{m}$  = mass flow  
 $M$  = Mach number  
 $N$  = rotor rotational speed  
 $Nu$  = Nusselt number  $hc/k$   
 $P$  = pressure  
 $Re$  = Reynolds number  $\rho vc/\mu$   
 $T$  = temperature  
 $U$  = velocity  
 $\varphi$  = phase [0–1] vane pitch  
 $\mu$  = viscosity  
 $\rho$  = density

## Subscripts

$c$  = coolant  
 $0$  = total quantity  
 $s$  = static quantity  
 $1$  = stator inlet  
 $2$  = stator outlet, rotor inlet  
 $3$  = rotor outlet  
 $R$  = relative to the rotor frame  
 $s$  = stator  
 $r$  = rotor  
 $ax$  = axial direction  
 $g$  = gas  
 $w$  = wall

## References

- [1] Ashworth, D. A., LaGraff, J. E., Shultz, D. L., and Grindrod, K. J., 1985, "Unsteady Aerodynamic and Heat Transfer Processes in a Transonic Turbine Stage," *ASME J. Eng. Gas Turbines Power*, **107**, pp. 1022–1030.
- [2] Doorly, D. J., and Oldfield, M. L. G., 1985, "Simulation of the Effect of Shock Wave Passing on a Turbine Rotor Blade," *ASME J. Eng. Gas Turbines Power*, **107**, pp. 998–1006.
- [3] Popp, O., Smith, D. E., Bubb, J. V., Grabowski, III, Diller, T. E., Schetz, J. A., and Ng Wing-Fai, 2000, "Investigation of Heat Transfer in a Film Cooled Transonic Turbine Cascade, Part II: Unsteady Heat Transfer." *ASME Paper 2000-GT-0202*.
- [4] Guenette, G. R., Epstein, A. H., Giles, M. B., Haines, R., and Norton, R. J. G., 1989, "Fully Scaled Transonic Turbine Rotor Heat Transfer Measurements" *ASME J. Turbomach.*, **111**, pp. 1–7.
- [5] Dunn, M. G., Seymour, P. J., Woodward, S. H., Georges, W. K., and Chupp, R. E., 1989, "Phase-resolved Heat-Flux Measurements on the Blade of a Full-Scale Rotating Turbine," *ASME J. Turbomach.*, **111**, pp. 8–19.
- [6] Hilditch, M. A., Smith G. C., Anderson, S. J., and Chana, K. S., 1995, "Unsteady Measurements in an Axial Flow Turbine Stage," *Proc., 85th propulsion and energetics panel symposium on loss mechanism and unsteady flows in turbomachines*, Derby, U.K.
- [7] Moss, R. W., Sheldrake, C. D., and Ainsworth, R. W., Smith, A. D., and Dancer, S. N., 1995, "Unsteady Pressure and Heat Transfer Measurements on a Rotating Blade Surface in a Transient Flow Facility," *85th Propulsion and Energetic Panel Symposium on Loss Mechanism and Unsteady Flows in Turbomachines*, Derby, UK, 1995. AGARD CP No. 571.
- [8] Dénos, R., 1996, "Investigation of the Unsteady Aerothermal Flow Field in the Rotor of a Transonic Turbine," Ph.D. thesis, IVK-University of Poitiers
- [9] Arts, T., Rouvroit, Arts, T., Lambert de, M., 1992, "Aerothermal performance of a 2D highly loaded transonic turbine nozzle guide vane—a test case for inviscid and viscous flow computations," *ASME Paper No. 90-GT-358*, *ASME J. Turbomach.*, **114**(1), pp. 147–154.
- [10] Johnson, A. B., Rigby, M. J., Oldfield, M. L. G., Ainsworth, R. W., and Oliver, M. J., 1989, "Surface Heat Transfer Fluctuations on Turbine Rotor Blade due to Upstream Shock Wave Passing," *ASME J. Turbomach.*, **111**, pp. 105–115.
- [11] Johnson, A. B., Oldfield, M. L. G., Rigby, M. J., and Giles, M. B., 1990, "Nozzle Guide Vane Shock Wave Propagation and Bifurcation in a Transonic Turbine Rotor," *ASME Paper No. 90-GT-310*.
- [12] Moss, R. W., Ainsworth, R. W., and Garside, T., 1998, "Effect of Rotation on Blade Surface Heat Transfer: An Experimental Investigation," *ASME J. Turbomach.*, **120**, pp. 530–540.
- [13] Dénos, R., Arts, T., Paniagua, G., Michelassi, V., and Martelli, F., 2001, "Investigation of the Unsteady Rotor Aerodynamics in a Transonic Turbine Stage," *ASME Paper No. 2000-GT-0435*, *ASME J. Turbomach.*, **123**, p. 81–89.
- [14] Sieverding, C. H., and Arts, T., 1992, "The VKI compression Tube Annular Cascade Facility CT3," *ASME paper 92-GT-336*.
- [15] Sieverding, C. H., Vanhaeverbeek, C., and Schulze, G., 1992, "An Optoelectronic Data Transmission System for Measurements on Rotating Turbomachinery Components" *ASME Paper 92-GT-337*.
- [16] Camci, G., 1985, "Experimental and Theoretical Study of Film Cooling on a Gas Turbine Blade," Ph.D. thesis, Katholieke Universiteit Leuven/von Karman Institute.
- [17] Camci, G., and Arts, T., 1985, "Experimental Heat Transfer Investigation Around the Film-Cooled Leading Edge of a High-pressure Gas Turbine Rotor Blade," *ASME J. Eng. Gas Turbines Power*, **107**, pp. 1016–1021.
- [18] Lowery, G. W., and Vachon, R. I., 1975, "The Effect of Turbulence on Heat Transfer from Heated Cylinders," *Int. J. Heat Mass Transf.*, **18**, pp. 1229–1242.
- [19] Michelassi, V., Martelli, F., Dénos, R., Arts, T., and Sieverding, C. H., 1999, "Unsteady Heat Transfer in Stator-Rotor Interaction by Two Equation Turbulence Model," *ASME J. Turbomach.*, *ASME Paper 98-GT-243*, **121**, pp. 436–447.
- [20] Kays, W., 1966, *Convective Heat and Mass Transfer*, McGraw-Hill, New York, NY
- [21] Heider, R., Duboué, J. M., Petot, B., Billonnet, G., Couaillier, V., and Liamis, N., 1993, "Three-Dimensional Analysis of Turbine Rotor Flow Including Tip Clearance," *ASME Paper 93-GT-111*.
- [22] Schultz, D. L., and Jones, T. V., 1973, "Heat Transfer Measurements in Short Duration Facilities," AGARDograph no 165.



# Effect of Nonuniform Inlet Conditions on Endwall Secondary Flows

**K. S. Hermanson**

Alstom Power (Switzerland),  
CH-5401 Baden, Switzerland

**K. A. Thole**

Mem. ASME,  
Mechanical Engineering Department,  
Virginia Polytechnic Institute and State  
University,  
Blacksburg, VA 24060

*Exit combustor flow and thermal fields entering downstream stator vane passages in a gas turbine engine are highly nonuniform. These flow and thermal fields can significantly affect the development of the secondary flows in the turbine passages contributing to high platform heat transfer and large aerodynamic losses. The flow and thermal fields combine to give nonuniform total pressure profiles entering the turbine passage which, along with the airfoil geometry, dictate the secondary flow field. This paper presents an analysis of the effects of varying total pressure profiles in both the radial and combined radial and circumferential directions on the secondary flowfields in a first-stage stator vane. These inlet conditions used for the first vane simulations are based on the exit conditions predicted for a combustor. Prior to using the predictions, these CFD simulations were benchmarked against flowfield data measured in a large-scale, linear, turbine vane cascade. Good agreement occurred between the computational predictions and experimentally measured secondary flows. Analyses of the results for several different cases indicate variations in the secondary flow pattern from pitch to pitch, which attributes to the rationale as to why some airfoils quickly degrade while others remain intact over time. [DOI: 10.1115/1.1505849]*

## Introduction

Turbine inlet conditions in a gas turbine engine generally consist of temperature and velocity profiles that vary in the radial (spanwise for a linear cascade) and circumferential (pitchwise) directions resulting from combustor exit conditions. Depending on the conditions, these nonuniform profiles can have a strong influence on the nature of the secondary flows in the turbine platform region, also referred to as the endwall region. Secondary flows cause aerodynamic losses, high convective heat transfer, and make it difficult to film-cool the endwall region. These nonuniformities arise from combustor designs that contain film-cooling holes and/or slots to cool the liner and slots at the combustor-turbine interface. Several other factors contribute to the nonuniformities including the interaction of the liner cooling scheme, such as film-cooling holes, and the large dilution holes that are placed in the liner surface. There is also a dependency of the nonuniformities on the fuel and air mass flows in the combustor. Given that there is not always the same number of airfoils as dilution jets, this can cause a nonrepeating pattern for the turbine.

To determine the effects of combustor exit conditions on the secondary flowfields that develop in the passage of a nozzle guide vane, a progression of computations is presented in which increasingly more complicated effects were modeled. First, a uniform temperature with a two-dimensional boundary layer was simulated to compare with available experimental data. Second, several temperature and velocity profiles were simulated in which these profiles were assumed to vary only in the spanwise (radial) direction. The results of these studies indicated the importance of the incoming total pressure gradient. Third, total pressure profiles exiting the combustor (as predicted through CFD) were used as inlet profiles to the turbine vane for isothermal conditions. Clocking studies were also done to determine the effect of slightly shifting the profiles for this third case. The computations representing the first two cases were previously presented by Hermanson and Thole [1] but are briefly presented in this paper to provide a base-

line understanding of these effects. All of the simulations were computed for a turbine vane geometry whereby the engine Reynolds number has been matched at low-speed conditions. Low-speed conditions were computed to allow direct comparison with measured flow fields for these same conditions in a large-scale wind tunnel simulation.

The following sections present a brief discussion of past studies, the CFD methodology and validation, the inlet profiles studied, and results of the study focusing on the relationship between inlet total pressure profiles and resulting secondary flows.

## Past Studies

An increased understanding of the nature of endwall secondary flows has been and continues to be a major objective of research in the gas turbine industry. Numerous papers have been published discussing experimental and computational results in the endwall region. Reported results focus on heat transfer, secondary flow measurements, passage pressure loss measurements, and flow visualization, but there is only a small amount of documentation existing that analyzes these quantities in combination with the effect of spanwise and pitchwise gradients entering the first stage turbine vane from the combustor.

In 1947, Munk and Prim [2] showed that one would expect no changes in the streamline pattern and no distortion of a hot streak in the stator passage presuming a constant total pressure at the inlet to the stator. Much later, Lakshminarayana [3] investigated thermally driven secondary flows using a steady, inviscid theoretical analysis. The derived expressions indicated that gradients in total temperature will only generate secondary vorticity when there are accompanying radial gradients of entropy (total pressure) or Mach number. In the case of a constant Mach number, normal vorticity and total temperature gradients nullify each other. Although this condition is not realistic in a turbine engine, it is essential in understanding the control of secondary flows.

With the knowledge that there is some viscous-dominated region along the approaching platform to a turbine vane, a number of endwall secondary flow models were developed for an approaching turbulent boundary layer. Langston [4], Sharma and

Contributed by the International Gas Turbine Institute and presented at the International Gas Turbine and Aeroengine Congress and Exhibition, Amsterdam, The Netherlands, June 3–6, 2002. Manuscript received by the IGTI, December 11, 2001. Paper No. 2002-GT-30188. Review Chair: E. Benvenuti.

Butler [5], Takeishi, et al. [6], and Goldstein and Spores [7] all proposed models and, although the models vary in complexity, each contains as a minimum:

- a leading edge horseshoe vortex formed from the inlet boundary layer which separates into the pressure-side and suction-side legs, and
- the passage vortex having the same sense of rotation as the pressure side leg of the horseshoe vortex developed due to the airfoil curvature.

The basic secondary flow models discussed generally assume a turbulent boundary layer profile along the approaching platform to the blade or vane. In realistic engine conditions, however, the combustor exit profile can contain large gradients in temperature and pressure in the spanwise and pitchwise directions. In fact, Barringer et al. [8] documented an experimentally simulated gas turbine combustor that showed wide variations in the pressure field that had little resemblance to the turbulent inlet boundary layer profile commonly assumed. Large temperature gradients created by film-cooling jets in the combustor liner were also reported.

While the experimental studies by Butler, et al. [9] and Shang et al. [10] have considered non-uniform inlet temperature profiles, the only experimental study to have considered whether there is an effect of a total pressure variation was that by Stabe et al. [11]. Stabe et al. simulated a liner flow through the use of a Combustor Exit Radial Temperature Simulator (CERTS). The CERTS used circumferential slots with no dilution holes. It was clearly identified from this study that changes did occur in the total pressure when using the CERTS as compared to not using the CERTS. Details are not available, however, for comparing the effects of the two different total pressure profiles on the secondary flowfield development and temperature distortion within the stator vane section.

Based on these studies, there is a clear need for an understanding of how total pressure variations at the inlet to a turbine vane section affect the development of the secondary flowfields. The work presented in this paper provides the first open literature study on the effects of radially and circumferentially varying inlet conditions on the secondary flow fields in a nozzle guide vane passage.

**Turbine Vane Design and CFD Methodology.** This section describes the turbine vane geometry that was studied and the methodology used to study the nonuniform inlet conditions to the turbine. While the profiles that varied in the radial direction alone were based on engine measurements, the computations for the radial/circumferential variations were performed in a two-step process. First, the combustor was simulated considering only the combustor geometry. Second, these combustor exit profiles were used as inlet boundary conditions for the turbine vane simulation. Note that low-speed conditions were simulated for the vane to allow for direct comparisons with simulations and experimental data previously acquired at nominally the same conditions except with a uniform flow field and a turbulent boundary layer on the approaching endwall.

**Turbine Airfoil Description.** The airfoil geometry used for these studies was a commercial first-stage stator vane, previously described by Radomsky and Thole [12,13] and Kang and Thole [14]. The characteristics of the vane geometry and flow conditions are summarized in Table 1. The vane is two-dimensional with the midspan cross-sectional geometry modeled along the entire span of the vane. The CFD simulations were computed for incompressible, viscous, low-speed conditions, thereby matching the Reynolds number but not the Mach number distribution. The effect of not matching the Mach number was addressed in Hermanson and Thole [15], which indicated similar secondary flowfield features between low and high Mach number cases. The primary effect of the Mach number is that the vane becomes slightly foreloaded for

**Table 1 Geometric and flow conditions for stator vane**

Scaling factor	9
Scaled-up true chord	59.4 cm
Pitch/true chord	0.77
Span/true chord	0.93
$Re_{in}$	$2.4 \times 10^5$
$Re_{exit}$	$1.2 \times 10^6$
Axial / true chord, $C_x/C$	0.48
Inlet Angle	$0^\circ$
Trailing edge angle	$72^\circ$

the low Mach number case and aftloaded for the high Mach number case. The effect of being foreloaded is such that the secondary flows are slightly stronger. For both the CFD analysis and wind tunnel experiments, the exit Reynolds number based on chord and exit velocity was  $Re_{ex} = 1.2 \times 10^6$ .

The CFD simulations for the combustor were completed as described previously by Malecki, et al. [16]. The mesh generator used was the commercially available ICEM while the flow solver used was Allstar. Allstar is a proprietary derivative of the National Combustion Code (Liu and Quealy [17]) that is a pressure-based, finite volume, flow solver, which uses the conservative form of the discretized governing equations. Centered differencing was used with second order accuracy. A standard  $k-\epsilon$  turbulence model with wall functions for near-wall modeling was used for the combustor simulations.

The CFD simulations for the turbine vane section were completed with a commercial software package by Fluent, Inc. [18]. Fluent is a pressure-based, incompressible flow solver for unstructured meshes. Second-order discretization was used for the Reynolds Averaged Navier Stokes (RANS) equations as well as the energy and turbulence equations. Fluent is especially applicable to three-dimensional endwall flows because the unstructured mesh capabilities allow the complex geometry of the stator vane to be modeled and because the code allows for solution-adaptive grids based on flow gradients to achieve grid-independent results.

The computational domain for the low speed simulations is depicted in Fig. 1. A domain representing one vane pitch was used to study grid independence, benchmarking of turbulence models, and effects of radial inlet profiles. Computations for three vane pitches were required to match the periodicity of the pitchwise

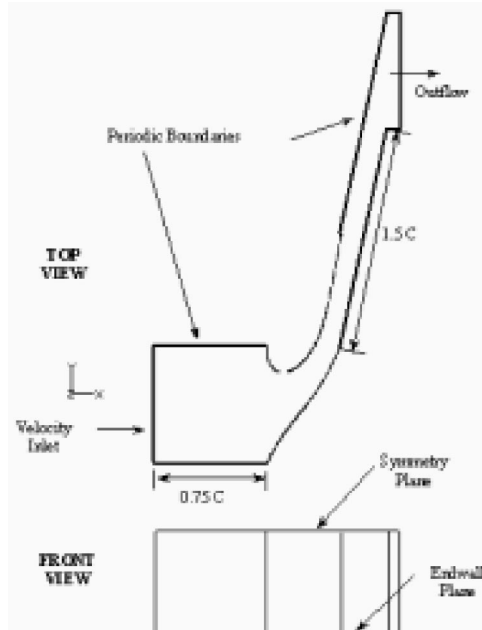


**Fig. 1 Computational domain for single-passage studies**

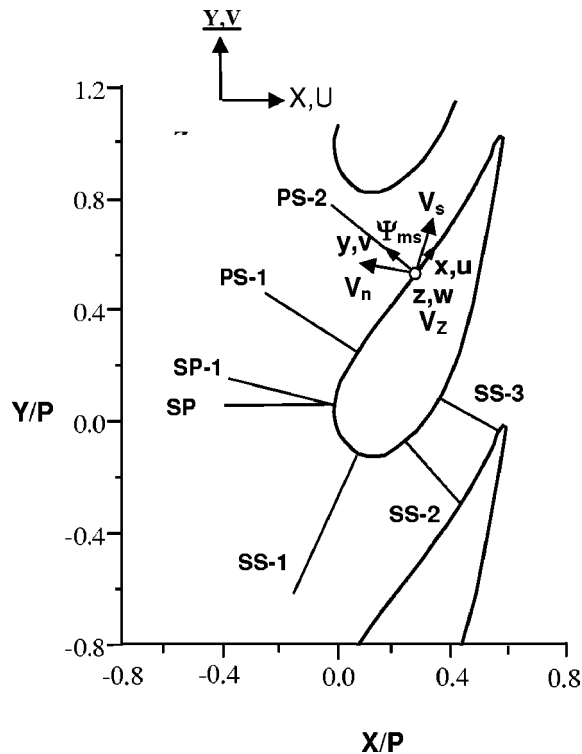


**Fig. 2 Locations and coordinates for benchmarking CFD with experimental measurements**

and spanwise varying inlet condition obtained from the combustor simulations. The inlet boundary condition was placed 75% of a true chord length ( $0.75C$ ) upstream of the blade stagnation and the outlet boundary condition was placed  $1.5C$  downstream along a line directed with the exit flow angle of the vane. Note that this location for the inlet boundary condition was also used as the location to set the combustor exit conditions as the inlet conditions for the turbine vane simulations. No additional dilution or cooling flows were applied downstream of the inlet boundary plane since the combustor simulations had already taken those effects into account. Since the combustor simulations did not include the effect of the vane on the flowfield, however, it was necessary to set the inlet conditions at 75% of a true chord upstream where the vane no longer affects the mean inviscid velocity.

Periodic boundary conditions were placed between the inlet, blade surface, and outlet. The vane was split across the pitch at the location of the dynamic stagnation point. The periodic boundary has been devised at the outlet of the domain to avoid highly skewed cells at the outflow/periodic surface intersection (shown in Fig. 1). A symmetry condition was applied at the vane midspan while a wall boundary condition was used to represent the end-wall. The placement of the inlet and outlet boundary conditions was determined by two-dimensional CFD analyses of the midspan freestream flow.

The primary interest of this study was to discern the horseshoe vortex legs and the passage vortex convecting through the turbine vane passage. Figure 2 shows locations where the flow field predictions of the secondary flows will be compared in this paper. Note that these flow planes are placed normal to the surface with the exception of the SP plane which is parallel with the incoming axial velocity component. The vectors of the secondary velocity components were determined by transforming the local velocities ( $u$ ,  $v$ , and  $w$  in Fig. 2) aligned with the plane of interest into the mean flow direction ( $V_s$ ,  $V_n$ , and  $V_z$ ). The transformation, defined by equations in the Nomenclature, is based on the midspan 2-D flowfield and quantifies the deviation to the midspan velocity

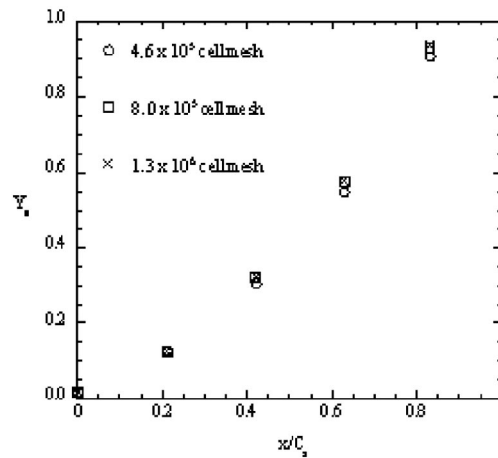


**Fig. 3 Grid sensitivity studies showing the total pressure loss through the passage**

components away from the inviscid region. These secondary flow vectors are plotted using the components normal to the mean flow direction ( $V_n$ ,  $V_z$ ). For clarity, the component of velocity,  $V_n$ , is zero at the midspan since this plane has a purely streamwise flow component.

Grid-independence was verified through a study using three different mesh sizes for a single periodic domain. For the coarsest mesh, consisting of  $4.6 \times 10^5$  cells, the number of cells was conserved by placing the inlet and outflow boundary conditions closer to the vane than presented in Fig. 1 (at one-half chord upstream and one-half chord downstream) with a coarser node spacing at the mid-plane. Two more refined grids were used in this study, with the inlet and outlet boundary conditions illustrated in Fig. 1 ( $0.75C$  upstream and  $1.5C$  downstream), consisting of  $8 \times 10^5$  cells and  $1.3 \times 10^6$  cells.

As a check on the grid sensitivity, the average total pressure losses at several different positions through the cascade passage were calculated. Figure 3 compares the total pressure loss coefficients for all three mesh sizes. To compare the loss for each of the cases in this study the loss was calculated based on mass averaged values at the inlet. The total pressure loss results indicate that there are almost no differences between the two largest mesh sizes and an underprediction for the smallest mesh size. There is only a 0.66% difference between the two largest meshes at  $X/C=0.4$ . For these studies the  $8 \times 10^5$  cell mesh size was considered to be grid-independent. In addition, the secondary flow structures were compared to experiments for the various mesh sizes indicating sufficient grid resolution for secondary flow development predictions.

Prior to simulating various temperature and velocity profiles, the flow field predictions for the nozzle guide vane were validated through comparisons using laser Doppler velocimeter (LDV) measurements of Kang and Thole [14]. The standard  $k-\epsilon$  (Lauder and Spalding [19]) and RNG  $k-\epsilon$  (Yakhot et al. [20]) turbulence models were benchmarked in the leading edge stagnation plane [1] showing that the RNG  $k-\epsilon$  model provided the most accurate prediction of the horseshoe vortex roll-up from the models considered. Note that no changes were made to the recommended constants for any of the computations that were performed. The RNG  $k-\epsilon$  model was expected to provide more accurate results since it contains additional terms in the transport equations for  $k$  and  $\epsilon$  that are more suitable for stagnation flows and flows with high streamline curvature. The computational results of the RNG  $k-\epsilon$  model were also compared to experimental data on six additional planes along the vane. Results for the Plane SS-1 (see Fig. 2) are presented in Figs. 4(a)-(b) with the experimental measurements to demonstrate the good agreement further

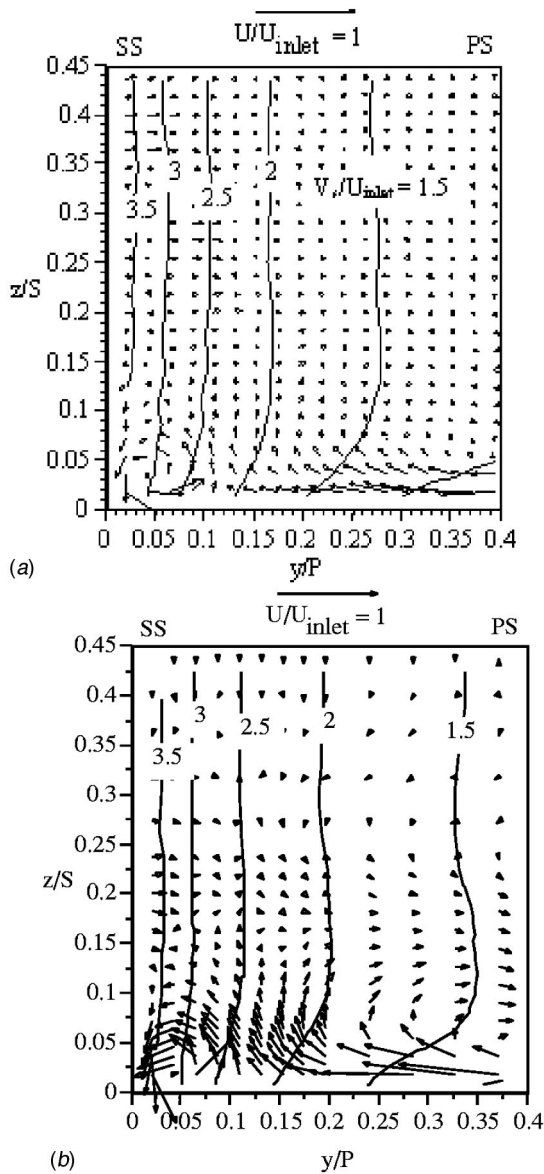


Fig. 4 Predicted (a) and measured (b) secondary velocity vectors and streamwise velocity contours in plane SS-1

downstream in the passage where both the passage vortex and suction side horseshoe vortex dominate near the endwall. The most notable difference seen in each of the planes is that the vortex is located slightly higher off the endwall, 1–3% of the span, in the CFD analysis as compared with the experiments. The reason for this difference may be attributed to deficiencies in the near-wall turbulence modeling.

### Scaling Inlet Profiles to Low-Speed Conditions

Prior to computing the nozzle guide vane flows from both radially and circumferentially varying profiles (two-dimensional profiles), studies of radially (spanwise) variations alone (one-dimensional) were performed to attain a more complete understanding of the physical nature of endwall secondary flows. By applying a combination of inlet conditions to the successfully benchmarked computational domain, the effects of velocity, temperature, pressure, and Mach number could be analyzed. A summary of these cases is given in Table 2. Note that all cases were computed for an inlet Reynolds number,  $Re_{inlet}$ , of approximately  $2.4 \times 10^5$ .

Table 2 Summary of CFD test matrix

Case	$\delta/S$	$\delta_{th}/S$	$T_{wall}/T_{max}$	$T_{wall}/T_{ave}$
1	0.091	-	1	1
2	0.091	0.32	0.63	0.73
3	~0	0.32	0.63	0.73
4	Figure 6	-	1	1
5	Figure 7	-	1	1

Profiles of velocity and temperature varying only in the radial direction previously presented in [1] are represented in cases 1–3 in Table 2 and shown in Figs. 5(a)–(b). The baseline case, case 1, directly modeled wind tunnel conditions, thus a 99% boundary layer thickness of 9.1% span was applied at the inlet. This 9.1% span boundary layer profile was generated using the 2-D boundary layer code, TEXSTAN (Crawford [21]) also for the turbulent quantities. In case 2, a temperature profile is applied in combination with the baseline boundary layer thickness to monitor effects of temperature gradient. A temperature gradient is applied with constant velocity (case 3). The temperature gradient is approximately linear from 0–32% span (endwall to freestream) based on experimentally measured engine pattern factor profiles (Kvasnak [22]). The temperature gradient used for cases 2 and 3 is similar to that used by Boyle and Giel [23]. The mass-averaged total temperature for each case is equal to the constant temperature of the baseline case.

The inlet profiles used in cases 4 and 5, shown in Figs. 6(a)–(c) and 7(a)–(c) simulate pitchwise and spanwise varying inlet conditions. Note that  $Y/P=0, 1.5$  and  $3$  are located at vane stagnation locations. Contours of normalized total pressure are shown at the inlet plane (Figs. 6(a), 7(a)) and the plane SP for each vane (Figs. 6(b), 7(b)). The local velocity normalized by the average value is shown in Figs. 6(c) and 7(c). Profiles of pressure, velocity, and

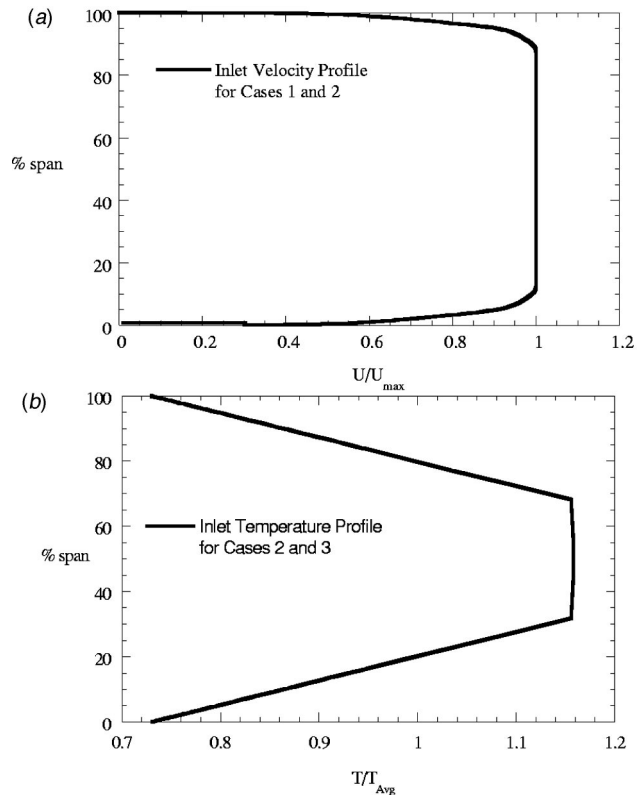


Fig. 5 Inlet conditions for the radially varying velocity (a) and temperature (b) profiles

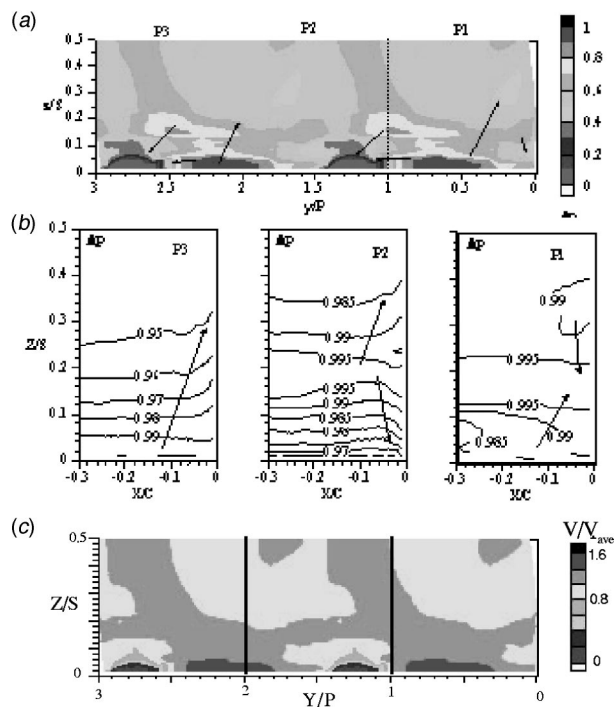


Fig. 6 Inlet boundary conditions for case 4.

temperature were obtained from the combustor CFD simulations and used to determine the velocity profiles. Due to the nature of the coupled solver for highly compressible flows the total and static pressure profiles of the combustor at engine conditions could not be simulated simultaneously. Since the previous study [1] concluded that the total pressure gradients approaching the vane are the driving factor for secondary flow development,

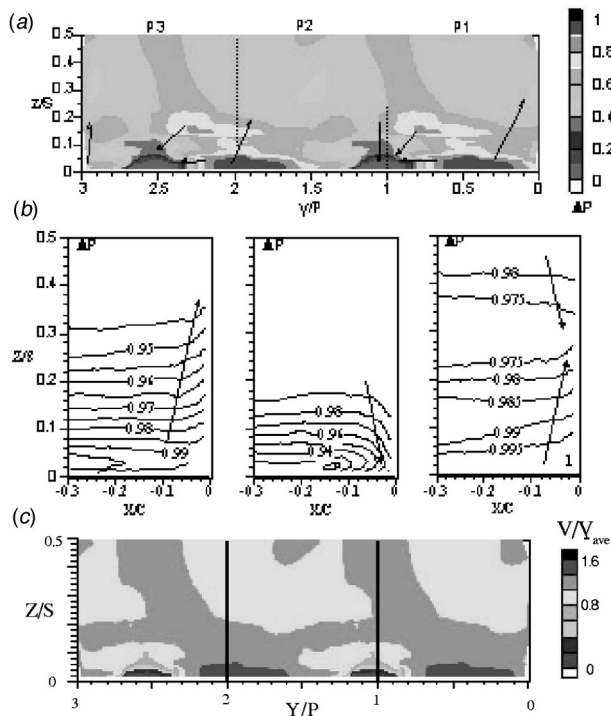


Fig. 7 Inlet boundary conditions for case 5

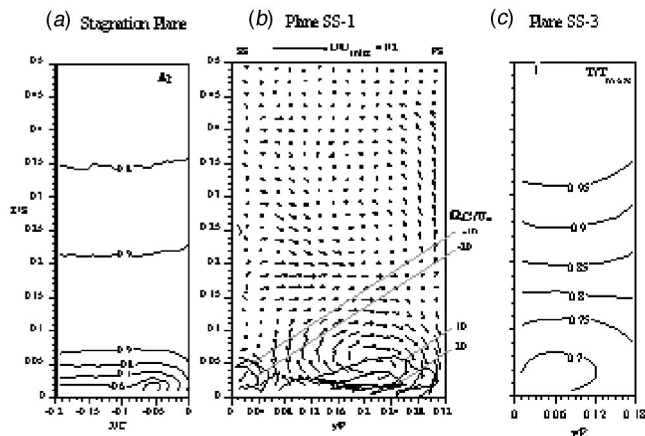


Fig. 8 CFD predictions of total pressure (a), secondary flow vectors with streamwise vorticity contours (b), and temperature contours (c) for case 2

scaled total pressure gradients from the computations of the engine combustor were simulated. The scaling was accomplished by calculating a velocity profile from the predicted total pressure and temperature profiles of the combustor exit assuming a constant static pressure (midspan value of engine simulations). The velocity profile was normalized by the average velocity exiting the combustor. This normalized profile, along with the average velocity required to match the inlet Reynolds number for the vane, was used to calculate the inlet conditions for the simulations. Since the inlet boundary condition for the CFD simulations also has a constant static pressure, the velocity profile imposed allowed for the total pressure gradients of the engine condition to be matched.

The resulting velocity profiles (note that the temperature was considered isothermal) were applied across three vane pitches with periodic boundary conditions applied outside of these three passages. The difference between cases 4 and 5 is simply a shift of the profiles that was 22% of one vane pitch. This shift provided a systematic comparison of the effect of the total pressure profiles. Two cases were considered so that nearly every combination of high and low velocity approaching the vane stagnation could be analyzed. A constant static temperature and pressure was applied in order to model a total pressure profile representing the characteristics of the jets. Although the profile at the combustor exit is not symmetric about the mid-span, the condition was assumed in the CFD simulations in order to achieve a reasonable size mesh of  $2 \times 10^6$  cells.

### Effects of Radially Varying Total Pressure Profiles

Prior to presenting results of the effect of both pitchwise/ spanwise gradients on secondary flow development, a summary of cases 1–3 will be given. This is meant to provide the necessary baseline understanding on the effects of profiles varying normal to the endwall. For this purpose the focus will be on cases 1–3 summarized in Table 2.

Normalized total pressure contours at the leading edge, Plane SP (Figs. 8(a) and 9(a)) graphically display the relationship between stagnation pressure gradients and secondary flows further in the passage, Plane SS-1 (Figs. 8(b) and 9(b)). These secondary flow planes can be compared directly to those of case 1, which was previously shown in Fig. 4(a) for an isothermal flow with a boundary layer thickness that was 9% of the span. The total pressure gradient for the case 1 simply decreases towards the endwall because of the slower velocities in the boundary layer. The presence of a total pressure gradient such that the total pressure decreases as it approaches the endwall drives the flow towards the endwall. This results in the formation of the horseshoe/passage vortex for cases 1 and 2. For case 3, however, in which the total

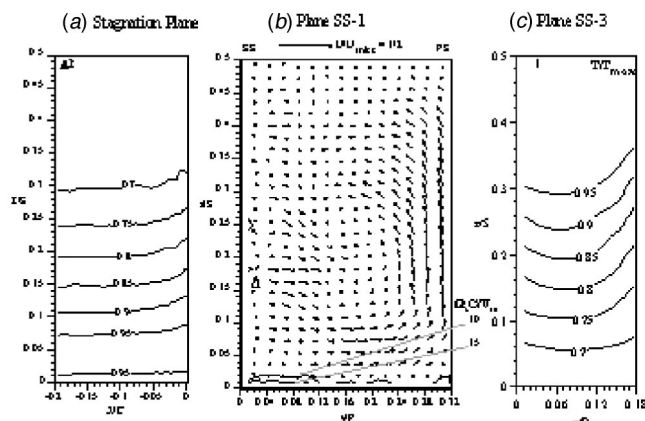


**Fig. 9** CFD predictions of total pressure (a), secondary flow vectors with streamwise vorticity contours (b), and temperature contours (c) for case 3

pressure is lower at the midspan, there is a reversed, counter-rotating vortex extending from the endwall to midspan. With a constant inlet Mach number (not shown in this paper), Hermanson and Thole [1] showed that no secondary flow vortex structures result since the total pressure is uniform. For the uniform Mach number case, there is, however a component of velocity sweeping from the pressure to suction sides of the vane.

Secondary flows near the endwall show only a slight difference from the baseline case even though there is a variation in the total temperature profiles (Figs. 4(a) and 8(b)). The real difference that occurs between these cases is further away from the endwall and towards the midspan where the flow actually forms another vortex. The larger counterrotating vortex predicted in cases 2–3 is a result of the temperature profile prescribed at the inlet which causes a negative gradient in total pressure from endwall to midspan. As seen in the streamwise vorticity contours, the temperature profile and resulting vortex has only a minimum effect on the streamwise vorticity relative to the vorticity generated near the wall.

Of particularly important interest in this parametric study are the distortions of the temperature profiles caused by the secondary flows. The temperature gradients exiting the combustor, sometimes referred to as hot streaks, are distorted by the secondary flow patterns in the first stage stator and create unsteadiness in the rotor downstream. These temperature profiles in combination with a greater turning angle further complicate the endwall secondary flow pattern in the rotor. Normalized total temperature distributions on Plane SS-3 (far downstream in the passage) are shown in Figs. 8(c) and 9(c) for the two previously described cases. The temperature contours closely correspond to the secondary flow patterns that have been described. For case 2 (Fig. 8(c)) the temperature contours are skewed near the endwall with migration of the warmer fluid toward the pressure surface at the endwall region and the cooler fluid near the suction surface. Also, in the region where the fluid is moving up the pressure surface towards the midspan the temperature contours are then skewed in this direction.

Temperature distributions in Plane SS-3 for case 3 are shown in Fig. 9(c). Again, the temperature contours are similar to the secondary flow pattern. For case 3 the endwall region experiences the lowest temperatures across the plane. The cooler temperatures are now moving up along the pressure surface with only a small effect on the suction surface.

The temperature distortions exiting the stator vane bring additional complications to the flowfield in the rotor vane. Both Butler et al. [9] and Dorney et al. [24] observed a strong migration of the warmer fluid to the pressure side and cooler fluid on the suction side in rotor vanes. (Both studies assumed inlet conditions similar

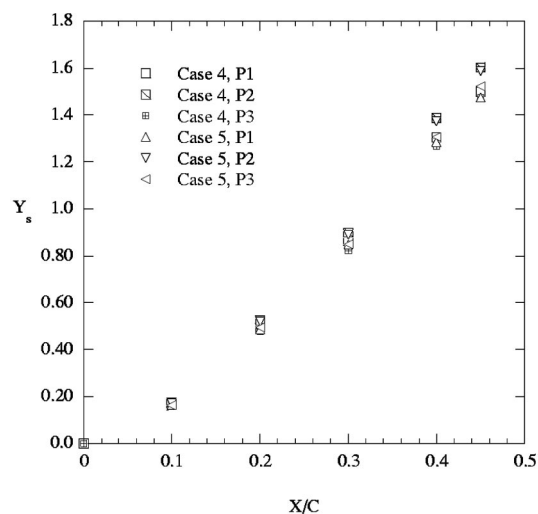


**Fig. 10** Total pressure loss through the vane passages

to case 2.) This separation of the hot and cold fluid is already in existence at the exit of the stator vane and is then exemplified as the secondary flow pattern continues in the rotor vane.

The work of Butler et al. [9] can be related to the significance of the total pressure gradient influencing secondary flows. Through measurements of CO<sub>2</sub> distribution, they observed no significant difference in secondary flows with application of a temperature gradient. No difference was expected however, since the inlet total pressure profile remained the same as in the baseline case with no temperature gradient. Although the flow pattern did not change, the temperature gradients at the exit of the stator vane did become distorted. This led to a difference in the inlet total pressure gradients to the rotor, additional unsteadiness, and subsequently a large difference in secondary flow patterns as exhibited by the CO<sub>2</sub> distributions inside the rotor.

### Effects of Pitchwise and Spanwise Total Pressure Profiles

Two CFD simulations, cases 4 and 5, were analyzed to determine the effect of a combination of pitchwise and spanwise varying inlet conditions on endwall secondary flows. These cases consider a velocity profile with constant temperature in order to achieve an inlet total pressure profile representative of that of the cooling jets from the combustor. As presented in the previous section, the inlet total pressure is the driving factor in determining endwall flows. Although temperature distortions cannot be assessed using this method the pitchwise varying development of secondary flows can be evaluated. The total pressure profiles for case 4 and case 5 have regions of high and low pressure near the endwall to about 15% span (shown in Figs. 6(a) and 7(a)). Due to the periodicity of the velocity profile each computational case simulated three vane pitches. The vane pitch for each case will be referred to by P1, P2, P3, with P1 corresponding to  $y/P=0$ .

The mass averaged total pressure loss through each of the six vane passages is shown in Fig. 10. These were calculated by averaging the inlet quantities across each pitch rather than averaging over the entire inlet so that a true comparison between pitches can be made. Figure 10 shows that the largest losses (by nominally 10% above P1 and P3) occurred in P2 for both cases. By looking at the total pressure loss based on averaged values at the inlet, the loss coefficients at the entrance to the passage are approximately zero. Therefore, the loss associated with the inlet profile is essentially equal for each case, and the excess loss in P2 (cases 4 and 5) must be due to secondary flows occurring in the passage.

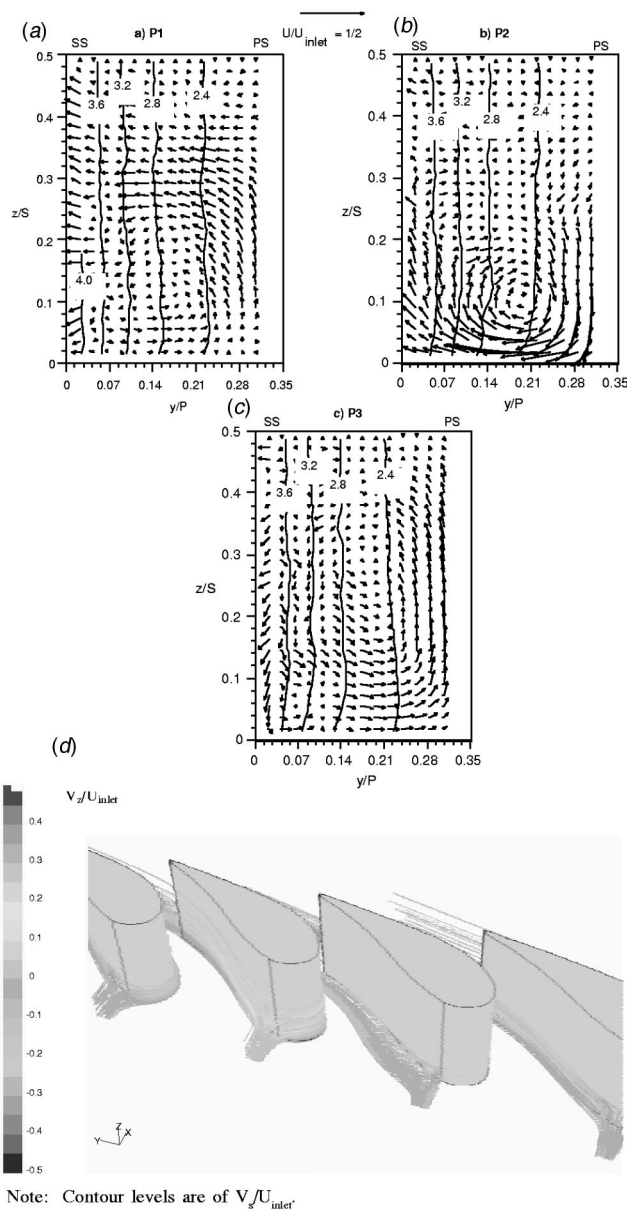


**Fig. 11 Case 4 secondary velocity vectors and streamwise velocity contours for each passage (a)–(c) and streamlines (d)**

The flowfield and streamwise velocity on plane SS-1 for each of the passages in case 4 is presented in Figs. 11(a)–(c) with the streamline patterns as shown in Fig. 11(d), while case 5 is shown in Figs. 12(a)–(d). The flowfields in each of the six passages exhibit a unique flow pattern demonstrating the effect of the pitch-wise varying gradients. Elements of the flowfields presented in the spanwise varying parametric study can be detected. Both the magnitude and direction of the endwall vortices are very different even between neighboring pitches.

The flowfield in P1 of case 4 reveals a similar pattern to case 3. Flow is moving up the pressure surface of the vane and there is a very strong  $V_n$  component toward the suction side at about 30% span. There is no sign of the pressure side horseshoe vortex (PSH) or suction side horseshoe vortex (SSH). In the next passage, P2, the flowfield does exhibit the passage vortex as seen in case 1. This vortex occurs further off the endwall, further from the pressure surface, and occupies a larger region of the endwall than previously documented, however the flow down the pressure surface and across the endwall indicates the presence of the passage

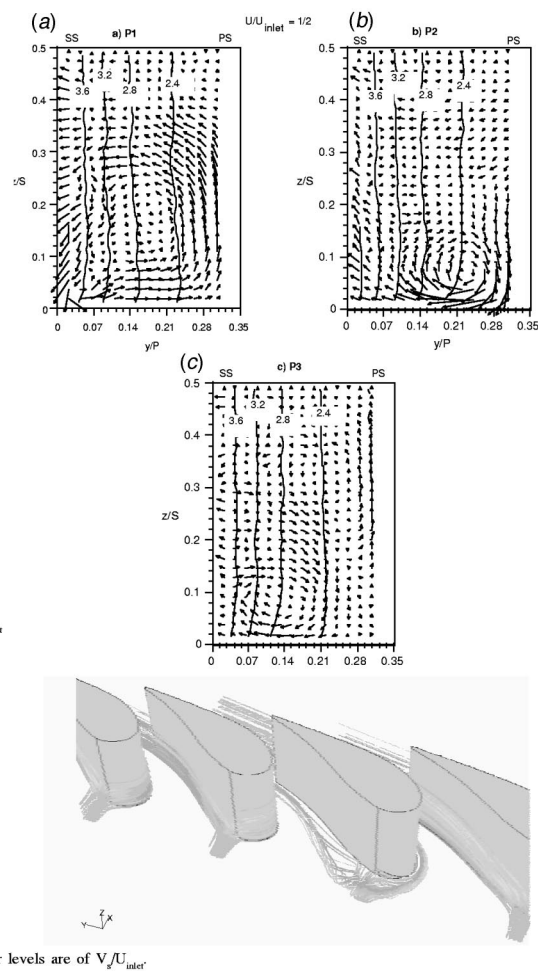


**Fig. 12 Case 5 secondary velocity vectors and streamwise velocity contours for each passage (a)–(c) and streamlines (d)**

vortex. In this case, there is no SSH near the suction surface, and the flow across the endwall continues to encounter the suction surface. Passage P3 again shows a flowfield with similarities to case 3 with flow moving towards the midspan along the pressure surface. This counter rotating vortex occupies a greater area of the passage than is shown in P1. The streamwise velocity contours show that the largest amounts of skewing occur near the vane endwall for the conditions where the cross-flow velocity component exists.

Although the inlet profile was shifted by only  $Y/P=0.22$  between cases 4 and 5, very different flowfields are shown in Figures 12(a)–(c) from what was seen in Figs. 11(a)–(c). P1 (Fig. 12(a)) has flow moving up the pressure surface to form a large vortex similar to P1 in case 4, but this time the SSH is present in the suction side-endwall juncture. A flowfield representing a passage vortex is again seen in P2 (Fig. 12(b)). This vortex occurs closer to the endwall and pressure surface showing more similarity to case 1. There is no SSH revealed in the vector plot for P2. There are only very small magnitudes of secondary flows on P3, but the pattern, which does exist is possibly the most complex demonstrated on any of the passages. A vortex resembling the passage vortex is present near the suction surface up to about 15% span. On the pressure surface, also at about 15% span, flow is directed toward the midspan in the opposite direction of the vortex near the endwall. Again, for these simulations the streamwise velocity shows that the streamwise flow is affected most in P2 due to the large secondary flows.

In order to explain the flow phenomena depicted in Figs. 11 and

12 the gradients in total pressure in the leading edge stagnation plane for each passage again must be examined. In this analysis the gradients in total pressure across the pitch are just as important and must also be the focus. Recall that the static pressures at the inlet are approximately constant for these cases. Figures 6 and 7 present the normalized pitchwise total pressure gradients (a) with the normalized spanwise gradients in Plane SP (b) for P1, P2, and P3 for cases 4 and 5.

The locations of the stagnation planes are indicated in Figs. 6(a) and 7(a) by dashed lines. Arrows indicate the tendency of flow to move from regions or pockets of higher pressure to lower pressure. The high-pressure gradients located at  $y/P=0.8$  would be expected to drive flow in the pitchwise direction towards the lower pressure region. Similarly, flow from 15% span should have a strong component of spanwise velocity towards the endwall. Much smaller magnitudes of secondary flows are expected at  $y/P=0$  due to only small pressure gradients. This plot shows that the flow will already have a 3-D nature as it moves 75% of a chord length from the inlet boundary to the vane stagnation with a very thin boundary layer developing along the endwall. These gradients will also become more distorted as they are accelerated inside the vane passage.

Spanwise gradients for case 4, Fig. 6, also indicate (by arrows) the favorable direction of flow due to the total pressure profile. Both P1 and P3 have profiles such that the flow may divide at 20% span and move up or down the vane. The movement here will also depend on the pitchwise distortions, which move the flow in the out-of-plane direction of the plot. Flow should move up the vane surface at P3. Note that the magnitude of the pressure gradients in the spanwise direction are quite small relative to the pitchwise gradients. The spanwise gradients are also small relative to the inlet conditions of the spanwise varying inlet profiles (cases 1–3).

The pitchwise total pressure gradients for case 5 are again marked with vane spacing and predicted flow in Fig. 7. Since this pressure profile is the same as in Fig. 6 with a 22% shift, the same basic motions can be expected as flow approaches the vane. Once the vane is encountered, however, the interaction with the stagnation and pressure/suction surfaces creates different flowfields from case 4.

The flowfields can be further predicted for case 5 by looking at the pressure gradients in plane SP, Fig. 7. The profile at P1 should drive flow up the vane surface to at least 30% span where an adverse pressure gradient is then encountered. The spanwise pressure gradients in P2 greatly resemble a boundary layer profile, such as that in case 1. The gradients occur up to almost 20% span in this case, but with a smaller pressure deficit than shown for case 1 (Fig. 7). The profile of P3 should also direct flow towards the midspan at the leading edge.

## Conclusions

Prior to studying the effects of inlet conditions on secondary flows, CFD results from a baseline case were benchmarked against the flowfield measurement indicating good agreement. The effects of both purely radial and combined radial/circumferential inlet profiles on the development of secondary flows were determined from a parametric study. Four cases with various combinations of inlet velocity and temperature profiles were compared with the baseline case to determine the effect of spanwise temperature gradients. Application of a temperature gradient in combination with an inlet boundary layer reduced the streamwise vorticity and spanwise velocity associated with the secondary flows. Flow also moved up the vane surface forming a large counterrotating vortex above the boundary layer to the midspan. A temperature gradient applied at the inlet with a constant velocity resulted in large vortex rotating in the opposite direction as the passage vortex with flow moving away from the endwall up the vane surface. This vortex had very little streamwise vorticity. A con-

stant Mach number at the inlet showed no vortex formation. The total pressure gradient is the driving factor for determining the magnitude of secondary flows in the passage.

Temperature contours showed that the secondary flow pattern distorts the temperature for each case. With a temperature gradient and a turbulent inlet boundary layer there was a migration of the cooler temperature to the suction surface. The cooler temperatures moved up the pressure surface in the case of a temperature profile with a constant inlet velocity. Since there were no secondary flows with a constant inlet Mach number there was also very little temperature distortion.

Secondary flow patterns were predicted for two cases with a pitchwise and spanwise total pressure gradient. Six very unique flow patterns resulted from the inlet profile. Characteristics of the flows could be compared with and predicted from the cases analyzed that considered only spanwise inlet profiles. In one passage, flow moved up the vane surface while in the neighboring passage the classic flow pattern depicted in flow models was formed. Again, the flow patterns were a function of the total pressure gradients in the leading edge region in both the spanwise and pitchwise directions. In regions of low spanwise pressure gradient at the leading edge there was very little streamwise vorticity downstream in the passage.

The results from the pitchwise and spanwise varying profiles have not been previously documented. The results demonstrate the need to consider realistic combustor exit profiles in stator design. It may be possible to align high and low pressure regions exiting the combustor with the first stage stator to minimize the resulting secondary flows. The presented results also provide reasoning for gas turbine field experience revealing that some airfoils show heavy degradation leading to a shorter life while neighboring components remain intact over time.

## Acknowledgments

The authors would like to acknowledge Pratt & Whitney for their support of this work. In particular, the authors would like to thank Jason Norris who performed the combustor simulations. The authors also acknowledge that this work was completed at the University of Wisconsin where K. Hermanson completed her MS degree.

## Nomenclature

$C$	= true chord of stator vane
$k$	= turbulent kinetic energy
$Ma$	= Mach number
$\dot{m}$	= mass flow through passage
$n$	= coordinate normal to inviscid streamline
$p$	= static pressure
$P$	= pitch
$P_o$	= total pressure
$Re$	= Reynolds number, $CU/\nu$
$s$	= coordinate aligned with inviscid streamline
$S$	= span of stator vane
$T_s$	= static temperature
$U$	= freestream velocity
$U, V,$	
$W$	= absolute velocity components
$u, v,$	
$w$	= secondary flow plane, transformed velocity components
$V_s$	= streamwise velocity, $u \cos \psi_{ms} + v \sin \psi_{ms}$
$V_n$	= normal velocity, $-u \sin \psi_{ms} + v \cos \psi_{ms}$
$V_z$	= spanwise velocity, $w$
$X, Y,$	
$Z$	= absolute, stationary, coordinate system
$x$	= distance normal to secondary flow plane
$y$	= distance tangent to secondary flow plane



$Y_s$  = pressure loss coefficient,  
 $\int \int \rho u [2(p_{o,\text{inlet}} - p_o / \rho U_{\text{inlet}}^2)] dA / \dot{m}$   
 $\delta$  = boundary layer thickness  
 $\Delta P$  = normalized pressure,  
 $\varepsilon$  = dissipation  
 $\nu$  = viscosity  
 $\rho$  = density  
 $\Omega_s$  = streamwise vorticity,  $\Omega_x \cos(\psi_{ms}) + \Omega_y \sin(\psi_{ms})$   
 $\Omega_x$  = x-vorticity,  $\partial W / \partial Y - \partial V / \partial Z$   
 $\Omega_y$  = y-vorticity,  $\partial U / \partial Z - \partial W / \partial X$   
 $\psi_{ms}$  = midspan turning angle,  $\tan^{-1}(v_{ms} / u_{ms})$

### Subscripts

inlet = value at 0.7 C upstream of vane  
max = maximum value in profile  
mid = value at vane midspan  
ex = value at vane exit  
avg = mass-averaged value

### References

- [1] Hermanson, K., and Thole, K. A., 1999, "Effect of Inlet Profiles on Endwall Secondary Flows," *J. Propul. Power*, **16**, No. 2, pp. 286–296.
- [2] Munk, M., and Prim, R. C., 1947, "On the Multiplicity of Steady Gas Flows Having the Same Streamline Pattern," *Proc., National Academy of Sciences*, Vol. 33.
- [3] Lakshminarayana, B., 1975, "Effects of Inlet Temperature Gradients on Turbomachinery Performance," *ASME J. Eng. Power*, **97**, p. 64.
- [4] Langston, L. S., 1980, "Crossflows in a Turbine Cascade Passage," *ASME J. Eng. Power*, **102**, p. 866.
- [5] Sharma, O. P., and Butler, T. L., 1987, "Predictions of Endwall Losses and Secondary Flows in Axial Flow Turbine Cascades," *ASME J. Turbomach.*, **109**, p. 229.
- [6] Takeishi, K., Matsuura, M., Aoki, S., and Sato, T., 1990, "An Experimental Study of Heat Transfer and Film Cooling on Low Aspect Ratio Turbine Nozzles," *ASME J. Turbomach.*, **112**, pp. 488–496.
- [7] Goldstein, R. J., and Spores, R. A., 1988, "Turbulent Transport on the Endwall in the Region Between Adjacent Turbine Blades," *ASME J. Heat Transfer*, **110**, pp. 862–869.
- [8] Barringer, M. D., Richard, O. T., Walter, J. P., Stitzel, S. M., and Thole, K. A., 2002, "Flow Field Simulations of a Gas Turbine Combustor," *ASME Paper 2001-GT-0170*, *ASME J. Turbomach.*
- [9] Butler, T. L., Sharma, O. P., Joslyn, H. D., and Dring, R. P., 1989, "Redistribution of an Inlet Temperature Distortion in an Axial Flow Turbine Stage," *J. Propul. Power*, **5**, No. 1, pp. 64–71.
- [10] Shang, T., Guenette, G. R., Epstein, A. H., and Saxer, A. P., 1995, "The Influence of Inlet Temperature Distortion on Rotor Heat Transfer in a Transonic Turbine," *AIAA Pap.*, No. 95-36318.
- [11] Stabe, R. G., Whitney, W. J., and Moffitt, T. P., 1984, "Performance of a High-Work Low Aspect Ratio Turbine Tested with a Realistic Inlet Radial Temperature Profile," *NASA Technical Memorandum 83655*, *AIAA Pap.*, No. 84-1161.
- [12] Radomsky, R., and Thole, K. A., 2000, "Highly Turbulent Flowfield Measurements Around a Stator Vane," *ASME J. Turbomach.*, **122**, pp. 255–262.
- [13] Radomsky, R., and Thole, K. A., 2000, "High Freestream Turbulence Effects in the Endwall Leading Edge Region," *ASME J. Turbomach.*, **122**, pp. 699–708.
- [14] Kang, M., and Thole, K. A., 2000, "Flowfield Measurements in the Endwall Region of a Stator Vane," *ASME J. Turbomach.*, **122**, pp. 458–466.
- [15] Hermanson, K., and Thole, K. A., 2000, "Effect of Mach Number on Secondary Flow Characteristics," *Int. J. Turbo Jet Engines*, **17**, pp. 179–196.
- [16] Malecki, R. W., Rhie, C. M., McKinney, R. G., Ouyang, H., Syed, S. A., Colket, M. B., Madabhushi, R. K., 2001, "Application of An Advance CFD-Based Analysis System to the PW6000 Combustor to Optimize Exit Temperature Distribution—Part I: Description and Validation of the Analysis Tool," *ASME 2001-GT-0062*.
- [17] Liu, N. S., and Quealy, A., 1999, "NCC—A Multidisciplinary Design/Analysis Tool for combustion Systems," *NASA/CP-1999-208757*, pp. 183–188.
- [18] Fluent Inc., *Fluent User's Guide*, Version 4.2., 1996, NH.
- [19] Launder, B. E., and Spalding, D. B., 1974, "The Numerical Computation of Turbulent Flows," *Comput. Methods Appl. Mech. Eng.*, **3**, pp. 269–289.
- [20] Yakhot, V., Orszag, S., Thangman, S., Gatski, T. B., and Speziale, C. G., 1992, "Development of Turbulence Models for Shear Flows by a Double Expansion Technique," *Phys. Fluids A*, **4**(7), p. 1510.
- [21] Crawford, M. E., "Simulation Codes for Calculation of Heat Transfer to Convectively-Cooled Turbine Blades," set of 4 lectures in *Convective Heat Transfer and Film Cooling in Turbomachinery*, T. Arts, ed., Lecture Series 1986-06, von Karman Institute for Fluid Dynamics, Rhode-Saint-Genese, Belgium.
- [22] Kvasnak, W., 1997, personal communication.
- [23] Boyle, R. J., and Giel, P. W., "Prediction of Nonuniform Inlet Temperature Effects on Vane and Rotor Heat Transfer," *ASME Paper 97-GT-133*.
- [24] Dorney, D. J., Davis, R. L., Edwards, D. E., and Madavan, N. K., 1992, "Unsteady Analysis of Hot Streak Migration in a Turbine Stage," *J. Propul. Power*, **8**, No. 2, pp. 520–529.

# St and $c_f$ Augmentation for Real Turbine Roughness With Elevated Freestream Turbulence

**Jeffrey P. Bons**  
Air Force Institute of Technology,  
Wright-Patterson AFB, OH 45433

*Experimental measurements of skin friction ( $c_f$ ) and heat transfer (St) augmentation are reported for low speed flow over turbine roughness models. The models were scaled from surface measurements taken on actual, in-service land-based turbine hardware. Model scaling factors ranged from 25 to 63, preserving the roughness height to boundary layer momentum thickness ratio for each case. The roughness models include samples of deposits, TBC spallation, erosion, and pitting. Measurements were made in a zero pressure gradient turbulent boundary layer at two Reynolds numbers ( $Re_x = 500,000$  and  $900,000$ ) and three freestream turbulence levels ( $Tu = 1\%$ ,  $5\%$ , and  $11\%$ ). Measurements at low freestream turbulence indicate augmentation factors ranging from 1.1–1.5 for  $St/St_o$  and from 1.3–3.0 for  $c_f/c_{f_o}$  ( $St_o$  and  $c_{f_o}$  are smooth plate values). For the range of roughness studied (average roughness height,  $k$ , less than 1/3rd the boundary layer thickness) the level of  $c_f$  augmentation agrees well with accepted equivalent sandgrain ( $k_s$ ) correlations when  $k_s$  is determined from a roughness shape/density parameter. This finding is not repeated with heat transfer, in which case the  $k_s$ -based St correlations overpredict the measurements. Both  $c_f$  and St correlations severely underpredict the effect of roughness for  $k^+ < 70$  (when  $k_s$ , as determined by the roughness shape/density parameter, is small). A new  $k_s$  correlation based on the rms surface slope angle overcomes this limitation. Comparison of data from real roughness and simulated (ordered cones or hemispheres) roughness suggests that simulated roughness is fundamentally different from real roughness. Specifically,  $k_s$  values that correlate  $c_f$  for both simulated and real roughness are found to correlate St for simulated roughness but overpredict St for real roughness. These findings expose limitations in the traditional equivalent sandgrain roughness model and the common use of ordered arrays of roughness elements to simulate real roughness surfaces. The elevated freestream turbulence levels produce augmentation ratios of 1.24 and 1.5 ( $St/St_o$ ) and 1.07 and 1.16 ( $c_f/c_{f_o}$ ) compared to the  $Tu = 1\%$  flow over the smooth reference plate. The combined effects of roughness and elevated freestream turbulence are greater than their added effects suggesting that some synergy occurs between the two mechanisms. Specifically, skin friction augmentation for combined turbulence and roughness is up to 20% greater than that estimated by adding their separate effects and 8% greater than compounding (multiplying) their separate effects. For heat transfer augmentation, the combined effect of turbulence and roughness is 5% higher than that estimated by compounding their separate effects at high freestream turbulence ( $Tu = 11\%$ ). At low turbulence ( $Tu = 5\%$ ), there is a negative synergy between the two augmentation mechanisms as the combined effect is now 13% lower than that estimated by compounding their separate effects. [DOI: 10.1115/1.1505851]*

*Keywords:* Roughness, Turbulence, Turbine

## Introduction and Background

Modern land-based turbine airfoils operate in severe environments with high temperatures and near critical stresses. Highly turbulent combustor exit flows spew hot combustion products and other airborne particulates at the turbine surfaces for more than 20,000 hours before regularly scheduled maintenance. Due to this harsh operating environment, turbine surfaces experience significant degradation with service. Measurements reported previously by this author [1] and others [2–4] indicate an order of magnitude or greater increase in rms roughness is typical for a first stage high pressure turbine vane or blade.

For over twenty years, the effects of these elevated levels of surface roughness on turbomachinery performance have been studied at all practical levels; from fundamental flat-

plate wind tunnel research, to multi-blade cascade facilities, to full-up system level tests. These studies all support the expected result that roughness increases surface drag and heat transfer (though to varying degrees). For turbomachinery, this translates to higher heat loads, accelerated part degradation, and lower stage efficiencies.

At the system level, Blair [5] was perhaps the first to report roughness-related increases in St on a rotating turbine facility. In his study, premature boundary layer transition combined with other roughness-induced effects to produce a nearly 100% increase in St for some cases. Guo et al. [6] also reported a two-fold increase in heat transfer for a factor of 25 increase in roughness height (Rz) on their fully scaled nozzle guide vane facility. In their studies with compressors and pumps, Boynton et al. [7], Suder et al. [8], and Ghenaïet et al. [9] all observed 3–5 points loss in efficiency with roughened blades. With the exception of Ghenaïet et al., who actually simulated metal erosion due to sand ingestion, all of these system-level tests have been conducted using-

Contributed by the International Gas Turbine Institute and presented at the International Gas Turbine and Aeroengine Congress and Exhibition, Amsterdam, The Netherlands, June 3–6, 2002. Manuscript received by the ICTI, November 2, 2001. Paper No. 2002-GT-30198. Review Chair: E. Benvenuti.

uniformly distributed roughness (e.g., sand or painted-on particulates).

Sand and powders have also been used to simulate rough surfaces in turbine cascades, where more detailed blade surface measurements can be made [10–12]. These studies have each documented effects similar to those of their system-level counterparts; accelerated boundary layer transition, increased heat transfer, and increased blade losses. A fourth cascade study by Abuaf et al. [13] explored the benefits of metal polishing processes and found that a factor of three reduction in centerline-averaged roughness produced up to a 15% reduction in blade surface integrated heat transfer at some Reynolds numbers.

Unlike system and cascade level tests, flat-plate wind tunnel testing has explored a broader spectrum of surface roughness characterizations. In addition to sand roughness experiments [2,14], researchers have used distributed cylinders [15,16], spherical segments [17,18], cones [19,20], and pedestals [21]. In each case, the roughness element size and spacing was selected to match a predetermined set of roughness statistical parameters. This set could include traditional parameters such as  $Ra$  or  $Rz$  ( $Rz=k$ , the mean roughness height) or more sophisticated characterizations such as correlation length [17], rms deviation of surface slope angles [2], or a roughness shape/density parameter [20] in combination with other parameters. The majority of these researchers have also correlated their findings in terms of the equivalent sandgrain roughness,  $k_s$ , in an effort to translate their characterizations of turbine roughness into the much wider array of roughness encountered in pipe flows and external aerodynamics. A notable exception to this is the work of Taylor et al. [17] which has pursued a discrete-element model (DEM) to evaluate distributed roughness elements. Both methods ( $k_s$  and DEM) have met with varying degrees of success when brought to bear at the cascade and system level. Consequently, designers and operators continue to make significant allowances (safety margins) for uncertainty when calculating heat transfer or losses in operating rough turbines.

It is possible that part of this difficulty in modeling lies with the fact that different roughness-producing mechanisms (deposits, erosion, pitting, and coating spallation) have unique surface features. For example, as shown in [1], pitting and spallation have large roughness recesses below the surface mean line while deposits are characterized by peaks above the mean line. Fundamental fluid dynamics research (most recently by Kithcart and Klett [22]) has shown that recesses have a more marked effect on  $St$  than on  $c_f$  when compared with hills of equivalent dimensions. This is attributed to the reduced drag and enhanced three-dimensional flows (vortices) associated with recesses versus peaks. Nuances such as this can easily be lost when 1 or 2 roughness parameters are used to characterize a wide variety of rough surfaces with discrete, uniform elements. This then creates biases in the final roughness correlation which accentuate one type of roughness while de-emphasizing another.

One way to avoid this bias generated by distributed roughness characterizations of “real” roughness is to employ scaled replicas of actual turbine surfaces in fundamental wind tunnel testing. Results can then be evaluated without bias to a particular dominant shape or spacing. The objective of the present study is to begin building such a database. Accordingly, a diverse (though certainly not comprehensive) collection of six actual surface roughness samples (from [1]) were scaled and tested in a flat plate wind tunnel. Both  $c_f$  and  $St$  were measured and comparisons were made with contemporary roughness correlations found in the open literature. Correlations were also attempted with a number of the roughness parameters cited in previous studies and the most promising candidates were identified.

In addition, it is natural for the turbine designer to be suspicious of data taken in the often pristine laboratory environment. Thus, the relevance of laboratory findings to the actual turbine operating environment is of critical importance. One of the significant fea-

tures of turbine flow fields that could have a synergistic effect with roughness in freestream turbulence. There have been very few studies which have considered the coupled effects of freestream turbulence and surface roughness. Turner et al. [11] found the effect of grid-generated ( $\sim 7\%$ ) turbulence to be similar to a two order of magnitude increase in  $Ra$  (as determined by the blade mean heat transfer coefficient). The combined effect of turbulence and roughness was approximately additive. A similar finding was reported by Bogard et al. [20] for turbulence levels up to 17%. Finally, the results reported by Hoffs et al. [12] using 5 and 10% turbulence in a cascade facility with rough blades lack sufficient detail to determine whether roughness and turbulence effects are complementary. However, the effects of the two different mechanisms on heat transfer are clearly shown to be distinct and significant. The present study expands the existing database to include both  $St$  and  $c_f$  measurement at 5 and 11% freestream turbulence. Again, these measurements are taken using scaled “real” roughness models versus the simulated roughness characterizations (e.g., sand or cones) employed in previous studies.

## Surface Roughness Measurement and Fabrication

In preparation for the current study, nearly 100 land-based turbine components were assembled from four manufacturers: General Electric, Solar Turbines, Siemens-Westinghouse, and Honeywell (formerly Allied-Signal) Corporation. The articles were selected by each manufacturer to be representative of surface conditions generally found in the land-based gas turbine inventory. Chord dimensions on the assembled blades and vanes ranged from 2 to 20 cm and included samples with thermal barrier coatings (TBC). In order to respect proprietary concerns of the manufacturers, strict source anonymity has been maintained for all data presented in this publication.

Extensive 2-D and 3-D surface measurements were made on the assembled hardware [1] using a Taylor-Hobson Form Talysurf Series 2 contact stylus measurement system. This device uses a  $1.5\ \mu\text{m}$  radius diamond-tipped conical stylus to follow the surface features for a given part. The instrument has a maximum horizontal stroke of 50 mm and can measure a total vertical range of 2 mm with a precision of 32 nm. 3-D measurements were made by indexing the part by specified increments in the horizontal direction perpendicular to the stroke of the contact stylus. Increments from 5 to 40 microns were used to map out regions from  $1\times 1$  mm square to  $40\times 40$  mm square for various components. Once a 3-D map was taken, the Talymap™ software was used to remove the part’s form with a polynomial least squares surface fit. With the form removed, the relevant statistics could be extracted from the roughness data. Evaluations were conducted to compute the centerline averaged roughness,  $Ra$ , the rms roughness,  $Rq$ , the maximum peak-to-valley roughness,  $Rt$ , the skewness,  $Sk$ , and the kurtosis,  $Ku$ , as defined in the following ( $y_{\text{mean}}=0$ ):

$$Ra = \frac{1}{N} \sum_{i=1}^N |y_i| \quad (1)$$

$$Rq = \sqrt{\frac{1}{N} \sum_{i=1}^N y_i^2} \quad (2)$$

$$Rt = y_{\text{max}} - y_{\text{min}} \quad (3)$$

$$Sk = \left\{ \frac{1}{N} \sum_{i=1}^N y_i^3 \right\} \frac{1}{Rq^3} \quad (4)$$

$$Ku = \left\{ \frac{1}{N} \sum_{i=1}^N y_i^4 \right\} \frac{1}{Rq^4} \quad (5)$$

Each 3-D map was also evaluated in smaller subsets (or cutoffs) to estimate  $Rz$ , the average of the local  $Rt$  values over the entire

map.  $R_z$  is commonly used as an estimate of the average roughness height,  $k$ . The 3-D maps were then evaluated using 2-D autocorrelations in both the streamwise and cross-stream directions. The correlation lengths,  $\lambda_c$ , were calculated as the distance at which the autocorrelation functions fell to a value of 0.1. In addition, by dissecting the 3-D surface map into its 200 to 1000 individual 2-D traces, the local surface slope angles between each measurement point could be calculated. The sum of these angles over the entire 3-D surface was then used to compute the rms deviation of surface slope angles,  $\alpha_{rms}$ , considered by some [2,20] to be an important roughness parameter.  $\alpha_{rms}$  was calculated for both the streamwise and cross-stream directions.

One final measurement made from the 3-D surface maps was the roughness shape/density parameter,  $\Lambda_s$ . This parameter was developed by Sigal and Danberg [23] to correlate the  $k_s$  estimation process to both the spacing and shape of roughness elements. The parameter was derived for use with two and three dimensional roughness elements (e.g., ribs or cones) mounted to a smooth surface. It is defined as

$$\Lambda_s = \frac{S}{S_f} \left( \frac{A_f}{A_s} \right)^{-1.6} \quad (6)$$

where  $S$  is the reference area of the sample surface (without roughness),  $S_f$  is the total frontal surface area of the roughness elements on the sample.  $A_s$  is the windward wetted surface area of a roughness element, and  $A_f$  is the frontal surface area of a roughness element. Since the surfaces being evaluated in this study were real roughness surfaces rather than ordered cones or hemispheres, the calculation of  $A_f$ ,  $S_f$ , and  $A_s$  was adapted accordingly. To do so, each cell of the 3-D surface height matrix was evaluated independently to determine its windward frontal area and windward wetted area (=0 for leeward facing cells). Since no four adjacent nodes that define a cell in the height matrix are at exactly the same elevation, no cell escaped this evaluation. This is equivalent to presuming that the surface is a collection of dissimilar roughness elements with no gaps. Accordingly, the  $A_f$  and  $A_s$  are computed as the average value from all the cells determined in this manner.  $S_f$  is the sum of all cell  $A_f$  values. Performing the calculation cell by cell in this manner removed any subjectivity that might have been introduced by selecting only conically shaped peaks above some critical height in the surface height matrix. The values of  $\Lambda_s$  were then used to estimate  $k_s$  for each surface using a curve fit to data assembled by Sigal and Danberg and repeated in [20].

$$\log\left(\frac{k_s}{k}\right) = -1.31 \log(\Lambda_s) + 2.15 \quad (7)$$

This same cell-by-cell computation yielded yet another area ratio found to be of some importance in this study. This is the total wetted surface area (both windward and leeward) to smooth surface area ratio ( $S_w/S$ ).

Of the 25 3-D maps reported in [1], six were selected for this study. These include one pitted surface, two coated/spalled surfaces, one fuel deposit surface, and two erosion/deposit surfaces. The statistics for the scaled models of each of the six surfaces are contained in Table 1. Representative 2-D traces from each surface are shown in Fig. 1. (Note: the vertical dimension has been magnified to show roughness features.) The first is a surface that exhibited severe pitting. It is pockmarked with 40-80  $\mu\text{m}$  deep craters (unscaled dimensions), each with a width-to-depth ratio of 10 to 20. The second surface is a TBC coated surface that exhibited intermittent debond without spallation. This created an undulating surface with a regular pattern of peaks and valleys not unlike closely packed spherical segments. Surface no. 3 is a TBC surface which experienced extensive spallation. Surface no. 4 is an example of fuel deposits that are elliptical in shape and aligned with the streamwise flow direction. The last two surfaces are representative of combined erosion and deposits with smaller, more jagged roughness elements than surface no. 4.

**Table 1 Statistics and measurements for six scaled rough surfaces. (Notes:  $k_s$  from Eq. (7), " $k^+$  actual" estimated for actual hardware at  $Re_x=2 \times 10^6$ , " $k^+$  model" for model surfaces at  $Re_x=900,000$  in tunnel, " $k_{adj}$ " and " $k_{adj}^+$ " as defined in report.)**

	Surface Type	Model Scaling	Ra (mm)	$R_z \cong k$ (mm)	Rt (mm)	Rq (mm)
1	Pitted	28.5	0.12	1.14	2.08	0.19
2	TBC debond	25	0.30	1.67	2.01	0.36
3	TBC spalled	28.1	0.84	4.51	6.43	1.04
4	Deposit	34.25	1.17	5.96	7.30	1.44
5	Dep/Erosion	62.7	0.46	3.10	4.05	0.58
6	Erosion	57.7	0.52	3.83	4.23	0.65

	Sk	K	$\lambda_c$ (mm)	$\alpha_{rms}$ (deg)	$S_w/S$	$\Lambda_s$
1	-2.54	14.56	6.62	7.23	1.016	1075
2	0.01	2.45	8.1	5.48	1.009	1957
3	-0.65	3.12	28.6	16.4	1.08	111
4	0.11	2.2	14.5	20.6	1.224	35.1
5	0.33	3.00	4.1	24.1	1.197	29.3
6	0.02	3.00	4.0	25.3	1.198	22.07

	$R_z/\theta$	$k_s$ (mm) (Eqn 7)	$k^+$ actual	$k^+$ model	$k_{sadj}$	$k_{adj}^+$
1	0.57	0.017	0.7	0.66	0.51	20
2	0.84	0.011	0.4	0.40	0.40	15
3	2.26	1.32	24	63	2.9	135
4	2.98	7.95	480	415	6.2	322
5	1.55	5.24	299	274	6.3	330
6	1.92	9.39	535	515	8.8	481

To scale these six surfaces for wind tunnel testing, two parameters were monitored: the roughness height to boundary layer momentum thickness ratio ( $R_z/\theta$ ) and the roughness regime as defined by  $k^+$  ( $Re_k$  in some texts). To properly compute these two parameters for the turbine hardware used in this study would have required a detailed knowledge of the operating environment (pressures, temperatures, etc...) for each of the measured blades. Using this operational data, a boundary layer calculation could be performed to compute  $\theta$  (for  $R_z/\theta$ ) and  $u_\tau$  (for  $k^+$ ). Since operational data was not supplied by the manufacturers, estimates of these parameters were made as follows. For all cases, the blade Reynolds number,  $Re_c$ , was approximated at  $2 \times 10^6$ . This is in the range of values considered typical for high pressure turbine vanes/blades as reported by other researchers [4,13]. The local momentum thickness at the given 3-D map's chordwise location was then estimated using a zero pressure gradient, incompressible, turbulent boundary layer correlation from the leading edge to that point on the blade [ $\delta/x = 0.16 Re_x^{-1/7}$  or  $\delta/c = 0.16(x/c)^{6/7} Re_c^{-1/7}$  and  $\theta \cong 0.097 \delta$  from a power-law-boundary layer profile]. Admittedly,

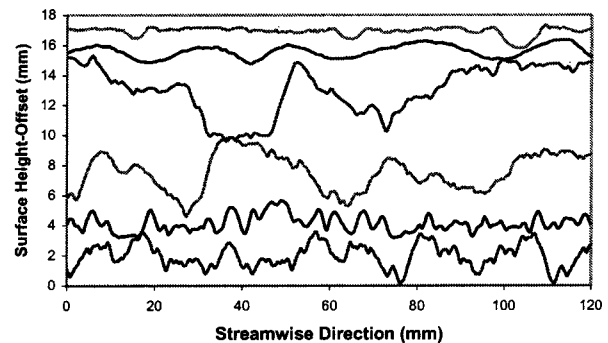


**Fig. 1 Sample 2-D traces from each of the six scaled roughness surfaces. Surfaces nos. 1 to 6 ordered from top to bottom. Traces are offset vertically to eliminate overlap.**

this estimate is an oversimplification. Turbine blade boundary layers are not turbulent from the leading edge and they are subject to pressure gradients, transonic Mach numbers, freestream turbulence, and (of course) roughness. Yet, the range of  $Rz/\theta$  estimates obtained by this method (0.5 to 3) are comparable to those obtained by more sophisticated means [20,21] (see Table 1). Moreover, even a more rigorous, fully-scaled computational estimate on a smooth blade geometry would not account for the boundary layer altering effects of the surface roughness and may not be more accurate. Finally, the goal of this study is not to assess engine-specific roughness effects but rather to use realistic turbine roughness to develop an improved physical understanding that will benefit the entire turbine industry. So, the simple estimates were deemed appropriate and adequate.

From this estimate for  $\theta$ , the ratio  $Rz/\theta$  was computed and the necessary scaling was determined for each 3=D map. At the nominal  $Re_x$  of  $9 \times 10^5$  used in this study, the boundary layer momentum thickness in the wind tunnel is approximately 2 mm ( $Re_\theta \approx 1500$ ). This mandated scalings between 25 and 63 depending on the model (Table 1).

Because of the inherent difficulty with trying to match 2 parameters simultaneously for a wide variety of surfaces, the  $k^+$  roughness scaling was monitored to insure operation in the same roughness regime for the actual part and the scaled model. Nikuradse [24] classified roughness into three regimes: aerodynamically smooth ( $k^+ < 5$ ), transitionally rough ( $5 < k^+ < 70$ ), and completely rough ( $k^+ > 70$ ). In the smooth regime, roughness is not a factor and  $c_f$  is only a function of Re. In the completely rough regime, roughness dominates  $c_f$  which becomes essentially independent of Re. Finally, in the transitionally rough regime  $c_f$  is a function of both roughness and Re. Again, for the present study a standard, zero-pressure gradient boundary layer correlation for  $c_f$  ( $c_f = 0.026 Re^{-1/7}$ ) was used to estimate  $k^+$  ( $k^+ = Re_c (k_s/c) \sqrt{c_f/2}$ ) for each surface. Use of the Sigal-Danberg  $k_s$  correlation (Eq. (7)) insured that  $k_s$  scaled directly with  $k$  ( $Rz$ ) the result being that  $k^+$  was in the same regime for each surface and its scaled model. Both  $k^+$  estimates are listed in Table 1 and are calculated using  $k_s$  values obtained from Equation 7. For the actual blade  $k^+$ , empirical estimates for  $c_f$  and  $Re_c$  were employed as outlined in the foregoing, whereas the model  $k^+$  is obtained using values from the experiment.

Once properly scaled, plastic roughness models were fabricated using a StrataSys Inc. GenSys Xi 3-D printer. The printer has a maximum part fabrication size of  $200 \times 300 \times 200$  mm and creates models by extruding plastic in 0.3 mm thick layers to slowly build up the part. The typical wind tunnel roughness model was composed of six individual roughness panels ( $140 \text{ mm} \times 120 \text{ mm}$  each) with a mean thickness of 6 mm. Arranged three abreast, the panels nearly fill the wind tunnel test section width of 380 mm. If after scaling the 3-D roughness map there was insufficient area to fill the entire wind tunnel test section ( $280 \text{ mm} \times 360 \text{ mm}$ ), the roughness data were mirrored until the minimum area requirements were satisfied.

## Description of Experimental Facility

**Wind Tunnel Facility.** The research facility used for the experiments is shown in Fig. 2. The open loop wind tunnel uses a main flow blower to provide a nominal mass flow of 1.2 kg/s to the test section. A heat exchanger at the main flow blower discharge can be used to vary the flow temperature from 18–54°C. The main flow enters a conditioning plenum of 0.6 m diameter before reaching the rectangular test section. This conditioning plenum has one layer of perforated aluminum plate followed by 7.6 cm of honeycomb straightener, and three layers of fine screen. A circular-to-rectangular foam nozzle conducts the flow from the plenum cross-section to the 0.24 m by 0.38 m test section. With this conditioning, 2-D flow uniformity of  $\pm 3\%$  in velocity is ob-

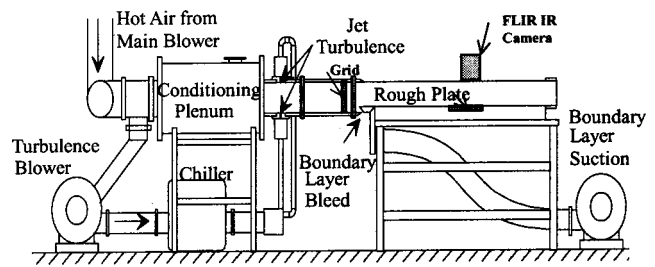
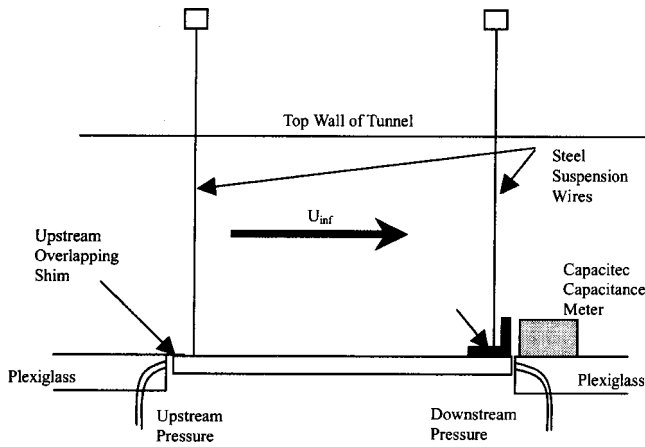


Fig. 2 Schematic of flat plate wind tunnel at AFRL in heat transfer measurement configuration

tained over the center 0.32 m of the test section span. Without employing turbulence generation devices, the freestream turbulence level at the test section was 1%.

At 1.22 m from the plenum exit a knife-edge boundary layer bleed with suction removes the bottom 1.27 cm of the growing boundary layer, making the aspect ratio (span/height) of the final test section approximately 1.7. The top wall of this final section pivots about its forward end in order to adjust the pressure gradient in the tunnel. For the tests presented here, the wall was adjusted to produce zero freestream acceleration over the roughness test panels. At 2.54 cm from the boundary layer suction point, a 1.6-mm-dia cylinder spans the test section to trip the boundary layer to turbulent. This is approximately the height of a fictitious turbulent boundary layer starting from the knife-edged bleed. The leading edge of the roughness panel sections are located 1.04 m from the boundary layer suction point. The roughness panels (generally six panels make a single set) are installed in a 0.28-m streamwise gap in the lower wall. The tunnel then continues 0.62 m beyond the trailing edge of the roughness panels. Accordingly, the flow experiences a transition from a smooth to rough wall condition at the leading edge of the roughness panels. This experimental setup departs from traditional roughness experiments in which the entire development length of the boundary layer is roughened. Studies by Antonia and Luxton [25] and more recently by Taylor and Chakroun [26] show that this smooth to rough transition results in an initial overshoot in  $c_f$  and St followed by a fairly rapid adjustment to the appropriate rough-wall values. Both researchers report an adjustment length equivalent to 3–4 boundary layer thicknesses with up to 20% initial overshoot. To mitigate the effect of this transition region, the heat transfer data were taken on the downstream half of the roughness section (beyond the expected adjustment length). The  $c_f$  measurement, however, was made using a bulk method (as described in the forthcoming) and represents an average value over the entire roughness panel set. To reduce the influence of the initial overshoot, the leading edge of the roughness panels were faired over the initial 20 mm. Nonetheless, the effect could not be altogether eliminated and its influence on the measured value of  $c_f$  was not assessed. That said, the actual turbine roughness measurements reported by Bons [1] and Taylor [3] do show rapid spatial variations in surface roughness. So, this experimental configuration may be more representative of the real turbine blade surface than a fully rough wall from the leading edge of the tunnel.

Freestream turbulence is generated using two distinct methods. For high turbulence generation, a “Tee” located upstream of the conditioning plenum inlet leads to a bypass blower, which generates a bypass flow in parallel with the main flow. This bypass flow is reinjected from two opposing rows of holes located on the top and bottom of the test section, 1.02 m upstream of the boundary layer bleed. A heat exchanger in the bypass line is used to remove the heat of compression from the bypass flow. This jet-injection turbulence generation device produces a turbulence level of 11% at the roughness panels. A standard square-bar grid was used to



**Fig. 3 Schematic of floating panel  $c_f$  measurement apparatus on AFRL wind tunnel**

obtain a lower turbulence level of 5%. The grid is composed of 1.34 cm square bars spaced 6 cm apart and is located 0.2 m upstream of the boundary layer bleed.

Flow velocity is measured using a single-element hot-wire anemometer. A co-located flow thermocouple with 0.3 mm bead diameter is used for flow temperature measurement. The two instruments are mounted on a 3-axis traverse system located atop the wind tunnel. A magnetically encoded linear position indicator affixed to the traverse was used to determine the probe position to within  $2.5 \mu\text{m}$ . Uncertainty in the velocity measurement stems primarily from the calibration fit accuracy. When compared to a co-located Kiel probe velocity measurement, the error is within  $\pm 1.5\%$  at flow rates of interest.

**$c_f$  Measurement.** A number of researchers have struggled with the complexities of making drag measurements over rough surfaces. Two common methods relying solely on velocity measurements are a boundary layer momentum balance and log-region curve fitting. For a zero streamwise pressure gradient flow, the change in boundary layer momentum thickness ( $\theta$ ) can be related directly to  $c_f$  by  $c_f = 2d\theta/dx$ . This is the momentum balance method. It requires a minimum of two velocity profiles separated by a streamwise distance ( $dx$ ) over the rough surface. The second method assumes the presence of a log-linear region in the rough wall turbulent boundary layer velocity profile (when plotted in wall units). This “log-law” region has been shown to be present in rough wall data, though the log-region constant ( $B$ ) is typically adjusted as a function of  $k_s$ . Both of these methods require assumptions to be made about the  $y=0$  wall elevation, which is problematic for rough surfaces. Considering this and other drawbacks of velocity-based  $c_f$  measurements, Acharya et al. [2] concluded that, “an accurate independent measurement of  $c_f$  is thus of central importance to any experiment on rough-wall boundary layers.” Based on this conclusion, Acharya et al. employed a force-balance to measure the actual skin friction force on a roughness coupon in their flowfield.

Following this reasoning, the present work uses a hanging element balance to obtain  $c_f$ . The balance configuration is shown in Fig. 3. Four 0.25-mm-dia, 0.7 m long Nichrome wires attached to an apparatus atop the tunnel allow the roughness panels to be freely suspended in the floor of the wind tunnel. The wires are located outside the wind tunnel and are affixed to the four corners of a metal support plate upon which the six plastic roughness panels are mounted. When air is flowing in the tunnel, the plate moves downstream under the applied shear force. This motion was a maximum of 1.9 mm for the roughest panel tested (with turbulence). This horizontal plate motion is accompanied by a slight vertical plate motion ( $2.6 \mu\text{m}$  for the maximum case) of the heavy support plate which produces the necessary restoring force.

For small-angle motions such as this, the restoring force is approximately linear with streamwise plate deflection. Using a string-pulley apparatus with fractional gram weights, this restoring force was calibrated over the full range of deflections observed in practice. The plate deflection was measured using a Capacitec Model no. 4100-S capacitance meter mounted to the side of the test plate, outside the tunnel walls. The meter is stationary, while a parallel metal bracket is mounted to the moving panel. The air gap between the stationary meter face and the parallel bracket face is the capacitor thickness. The required ground loop from the moving bracket to the power supply and meter is formed using the metal suspension wires. In this way, no friction is added to the plate motion due to the meter. The wire-pulley calibration is remarkably linear and repeatable with least squares correlation coefficients of 0.9999 and repeatable slopes within  $\pm 1.5\%$ .

The test plate is suspended with a 0.5 mm gap at the leading edge and a trailing edge gap which is 0.5 mm greater than the maximum expected excursion. These gaps allow unrestrained motion of the plate under the applied shear force. The gaps also permit differential pressure forces to affect the net displacement of the test plate. To mitigate these pressure forces, the leading edge gap was covered with a 0.05-mm thick stainless steel sheet with 7 mm overlap with the roughness panels. The initial 10 mm of each panel was smooth to accommodate this overlap without interference. Despite this precaution, differential pressures still accounted for 5–15% of the net plate motion. To calculate this component of the force, three pressure taps were installed at mid-plate thickness on the adjoining stationary plexiglass pieces, both upstream and downstream of the suspended aluminum support plate with the roughness panels. The three pressure taps were ganged together to produce mean pressures for both the leading and trailing edge of the free-floating test section. A Druck LPM-5481 low pressure transducer was used to monitor this differential pressure and deduct it from the total displacement (force) measured by the Capacitec meter. With these precautionary measures, smooth plate  $c_f$  values were found to be within 5% of standard correlations. Repeatability was within  $\pm 2.8\%$  (for 1% Tu) and bias uncertainty was estimated at  $\pm 0.00022$  for the smooth plate measurement of  $c_f = 0.00354$  at  $Re_x = 900,000$ . The operation of the Druck transducer and Capacitec meter were found to be very sensitive to temperature, greatly affecting the quoted uncertainty. As such, the main flow heat exchanger was employed to maintain constant room temperature to within  $\pm 0.5^\circ\text{C}$  during testing.

**St Measurement.** For the heat transfer measurements, a FLIR Thermacam SC 3000 infrared camera system is mounted with the lens fit into a hole in the plexiglass ceiling of the tunnel. The camera has a sensitivity of  $0.03^\circ\text{C}$  (at  $30^\circ\text{C}$ ) and allows framing rates of approximately one Hz. At the focal distance of 37 cm, the camera field of view is roughly  $70 \times 90$  mm. This limited field of view is centered at a distance of 1.20 m from the leading edge of the tunnel floor. This puts the mean streamwise position of the heat transfer measurement roughly 2 cm downstream of the center of the roughness panels ( $x = 1.18$  m). The  $320 \times 240$  pixels of the FLIR camera allowed excellent resolution of the roughness features during the transient experiments. For the measurements reported in this study, however, the surface temperatures were simply area-averaged to obtain the representative surface temperature history required for St determination.

The Stanton number was determined from this surface temperature history using the method of Schulz and Jones [27]. This technique uses Duhamel’s superposition method to calculate the surface heat flux given the surface temperature history. It assumes the panels are a semi-infinite solid at constant temperature at time  $t=0$ . To accomplish this, the entire test section was soaked at room temperature for several hours before testing. Using the main flow heat exchanger, a hot-gas air flow was then initiated instantaneously while monitoring the freestream velocity and temperature as well as the average surface temperature (with the IR cam-

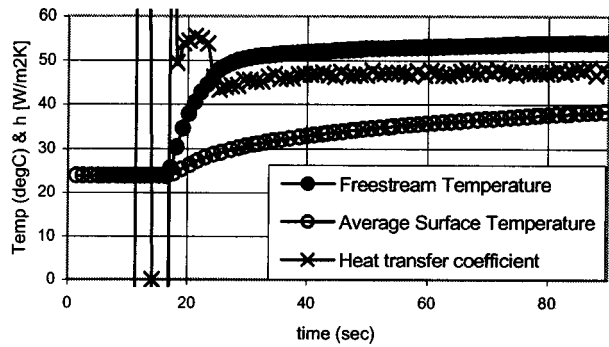


Fig. 4 Typical temperature and  $h$  histories during transient test

era). The heat transfer coefficient ( $h$ ) at the  $i$ th time step was then calculated using the expression from Schultz and Jones.

$$h_i = \frac{1}{T_\infty - T_{s_i}} \left[ \frac{2\kappa}{\sqrt{\pi\alpha}} \sum_{j=1}^i \frac{T_{s_j} - T_{s_{j-1}}}{\sqrt{t_i - t_j} + \sqrt{t_i - t_{j-1}}} \right]$$

In this expression, the summation is made over all steps prior to the  $i$ th time step. A typical  $h$  history calculation using this method is shown in Fig. 4. As shown, after some initial instability due to random temperature fluctuations over the initial time steps, the history settles down to a near constant value. The figure also shows the transient flow and surface temperatures over the same time history. The thermophysical properties, thermal conductivity ( $\kappa$ ) and thermal diffusivity ( $\alpha = \kappa/\rho c_p$ ), for the plastic panels were determined using a National Standards conductivity meter and calorimeter. The measurements yielded the following values:  $\kappa = 0.226 \text{ W/mK} \pm 5\%$  and  $c_p = 1913 \text{ J/kgK} \pm 3\%$ . The plastic density is  $1207 \text{ kg/m}^3 \pm 2\%$ .

For heat transfer measurements, the hanging  $c_f$  balance was removed and the six roughness panels were mounted on a 12-mm-thick plexiglass sheet. This plexiglass sheet has approximately the same thermophysical properties as the plastic panels to avoid thermal wave reflections at the contact surface. A thermocouple sandwiched between the panels and the plexiglass sheet indicated a slight rise in temperature after approximately 30 s for the typical test case. Thermocouples mounted to the underside of the plexiglass support sheet showed no significant change within the total test time of approximately 90 s. This confirmed the use of the semi-infinite conduction assumption in the data processing. Uncertainties due to surface radiation were eliminated by performing an in-place calibration with the panels soaked at various temperatures over the range of tunnel operation. Thermocouples mounted in the test panel assured uniform temperatures to within  $\pm 0.5^\circ\text{C}$  during this calibration. The average of these thermocouple readings was then correlated to the average surface temperature as recorded by the infrared camera. This measured difference between the actual temperature and the recorded infrared temperature was used to adjust the recorded temperature histories during transient testing. In this way, radiation heat transfer losses are accounted for in the final temperature history. The infrared measurement was also sensitive to the temperature of the air between the roughness panels and the receiving optics, since radiation from the plate to the camera is partially absorbed by the surrounding air as a function of temperature. The FLIR software accounts for this by allowing the user to input the ambient air temperature. Since the heat transfer test was transient, this input was adjusted in post-processing to track the freestream temperature from the flow thermocouple as a function of time.

By meticulously accounting for various losses as outlined above, smooth plate  $St$  values were found to be within 3% of a

standard correlation. Repeatability was within  $\pm 3\%$  and bias uncertainty was estimated at  $\pm 0.00008$  for the smooth plate measurement of  $St = 0.00215$  at  $Re_x = 900,000$ .

## Results and Discussion

The results are presented in order of increasing complexity. First, the smooth plate data are presented to verify that the wind tunnel facility meets the accepted standards for a zero-pressure gradient, turbulent boundary layer. Following this, the rough plate data are presented in detail. A smaller subset of this data is contained in [28] with limited discussion. Finally, the elevated turbulence data are presented for the smooth and rough panels in that order.

**Smooth Baseline.** The smooth plate  $St$  and  $c_f$  data are presented in Figs. 5 and 6 for two Reynolds numbers. Standard flat plate correlations for  $c_f$  and  $St$  [29] are also indicated on the plots as follows:

$$c_f = \frac{0.026}{Re_x^{1/7}} \quad (8)$$

$$St = \frac{0.5c_f}{Pr_t + \sqrt{0.5c_f[5Pr_t + 5 \ln(5Pr_t + 1) - 14Pr_t]}} \quad (9)$$

The smooth plate data shows agreement to within 5 and 3% of the  $c_f$  and  $St$  correlations, respectively.

**Effect of "Real" Roughness.** The same figures also show the  $c_f$  and  $St$  values obtained for the six rough panels at the same two  $Re_x$  values.  $St$  augmentation ratios ( $St/St_0$ ) vary from 1.1–1.5 and  $c_f/c_{f_0}$  varies from 1.3–3.0 (a factor of 3–4 times greater augmentation). This  $St$  augmentation can only be partially explained by

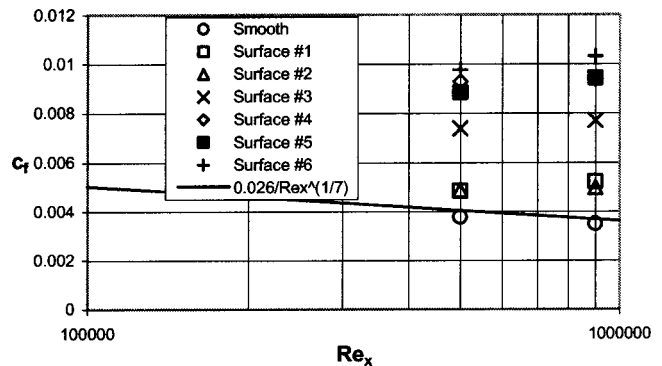


Fig. 5 Skin friction versus Reynolds number for smooth and rough panels

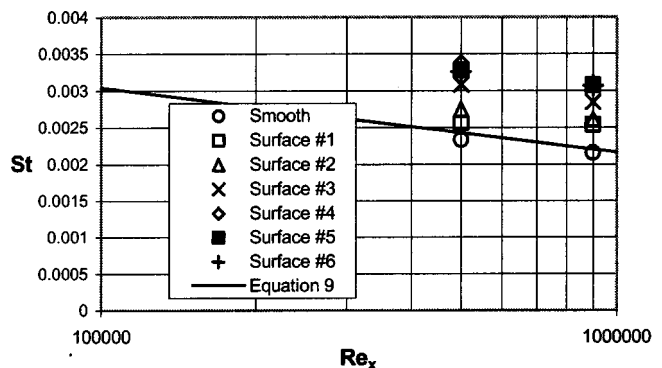


Fig. 6 Stanton number versus Reynolds number for smooth and rough panels

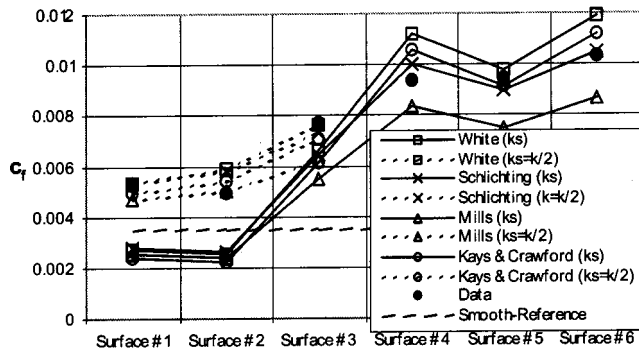


Fig. 7 Skin friction for rough panels compared to standard roughness correlations. Each correlation shown using  $k_s$  from Eq. (7) over all surfaces. Surfaces 1–3 also shown for  $k_s = k/2$  (dashed lines). Data for  $Re_x = 900,000$  only.

the increased wetted surface area of the rough panels ( $S_w/S$ ), which ranges from 1.01–1.22 (Table 1). As indicated previously, empirical correlations for  $c_f$  and  $St$  of rough surfaces have universally been developed based on experimental data with either sand roughness or uniform arrays of roughness elements. Even the uniform roughness array data are generally converted to equivalent sandgrain roughness,  $k_s$ , before correlation. So, in order to assess how well these correlations apply to the “real” roughness in this study, the  $k_s$  from each roughness type must be determined. These values were computed based on  $\Lambda_s$  (Eq. (7)) and are tabulated in Table 1.

A comparison with four  $c_f$  roughness correlations is shown in Fig. 7 for the data at  $Re_x = 900,000$ . These correlations are respectively:

$$c_f = [1.4 + 3.7 \log(x/k_s)]^{-2} \quad \text{from White [30]}$$

$$c_f = 0.168 [\ln(84\delta/k_s)]^2 \quad \text{from Kays and Crawford [31]}$$

$$c_f = [2.87 + 1.58 \log(x/k_s)]^{-2.5} \quad \text{from Schlichting [32]}$$

$$c_f = [3.476 + 0.707 \log(x/k_s)]^{-2.46} \quad \text{from Mills [29]}$$

The smooth  $c_f$  value is indicated as a dashed line in Fig. 7 for reference. As shown, the correlations bound the data for all but the first three surfaces. It should be noted that these correlations were all developed using data in the fully rough regime ( $k^+ > 70$ ). Referencing the model  $k^+$  data in Table 1, it is clear that the first three surfaces in the plot do not meet this criterion. Hence, the correlations significantly underpredict  $c_f$  for these panels (even falling below the smooth reference at very low  $k^+$ ). The fact that the  $c_f$  correlations nicely bracket the experimental data in the fully rough regime suggests that  $k_s$  (as estimated using  $\Lambda_s$  in Eq. (7)) might be an appropriate parameter for  $c_f$  prediction of “real” rough surfaces in this regime. In the other roughness regimes, however, the  $k_s$  values obtained using Eq. (7) are clearly inappropriate. Most notable are the two “aerodynamically smooth” plates ( $k^+ < 5$ ) which are clearly not smooth. In this regime, an equivalent roughness parameter directly related to the characteristic roughness height, (e.g.,  $k_s = k/2$ ), is perhaps more appropriate. If this simple relation is substituted for the Eq. (7)  $k_s$  formulation in cases where it yields  $k_s < k/2$ , the results are closer to reality. Predictions with each of the four correlations using this minimum threshold for  $k_s$  are also included in the figure with dashed lines. Similar results are found for the  $c_f$  data at  $Re_x = 500,000$ , where the  $Rz/\theta$  ratios are slightly smaller and the  $k^+$  values are about half of their level at  $Re_x = 900,000$ .

The  $St$  data are presented in the same manner in Fig. 8. In this case, three correlations are used for comparison:

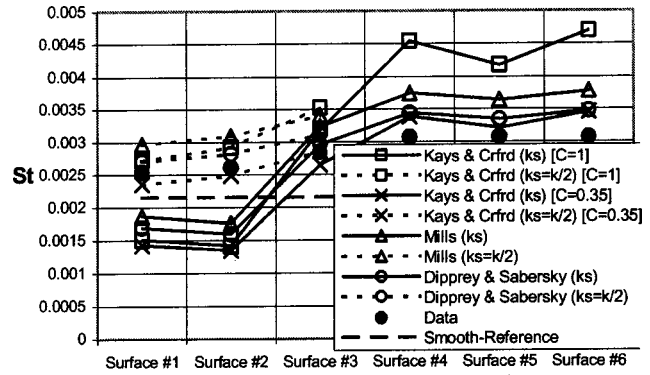


Fig. 8 Stanton number for rough panels compared to standard roughness correlations. Each correlation shown using  $k_s$  from Eq. (7) over all surfaces. Surfaces 1–3 also shown for  $k_s = k/2$  (dashed lines). Data for  $Re_x = 900,000$  only.

$$St = \frac{0.5c_f}{Pr_t + \sqrt{0.5c_f} (k^+)^{0.2} Pr^{0.44}/C}$$

from Kays and Crawford [31]

$$St = \frac{0.5c_f}{1 + \sqrt{0.5c_f} (5.19k^+)^{0.2} Pr^{0.44} - 8.5}$$

from Dipprey and Sabersky [33]

$$St = \frac{0.5c_f}{Pr_t + \sqrt{0.5c_f} (4.8k^+)^{0.2} Pr^{0.44} - 7.65}$$

from Wassel and Mills [34]

For the reference  $c_f$  value required in each correlation, one could use either experimental data (since it is available in this study) or one of the empirical correlations. Since the  $St$  correlations are intended for use as a predictive tool, it was deemed most useful to base  $St$  on a  $c_f$  correlation rather than on data. For this reason, the Schlichting  $c_f$  correlation was employed since it had the best match to the experimental data in the  $k_s > k/2$  regime of Fig. 7 (average 4.5% difference with data). Kays and Crawford suggest  $C = 1$  in their correlation based on a fit to data obtained with closely packed spheres. Since this value gave extremely large  $St$  predictions, the constant  $C$  was arbitrarily dropped to a value of 0.35 to better match the present “real” roughness models (both cases are shown on the plot). The Kays and Crawford correlation predictions thus adjusted are not a significant improvement over the Dipprey and Sabersky results which are obtained without any special tailoring. Both predict values of  $St$  which are roughly 10% higher than the data in the  $k_s > 70$  regime. Again, in the region  $k_s < k/2$ , the  $k_s$ -based correlations are clearly inappropriate when using Eq. (7) to determine  $k_s$  for these “real” roughness models. The more reasonable results using the minimum threshold of  $k_s \geq k/2$  in this region are indicated in Fig. 8 as they were in Fig. 7.

The fact that using the  $k_s(\Lambda_s)$  correlation appears to be inadequate to span the entire range of real roughness in this study led to a closer examination of this formulation for  $k_s$ . In order to assess the appropriateness of the Sigal-Danberg correlation,  $k_s$  was adjusted to the value required to exactly match the Schlichting  $c_f$  correlation with the experimental data for each of the six panels. This  $k_{sadj}$  (nondimensionalized by  $k$ ) is plotted vs.  $\Lambda_s$  in Fig. 9 (data for both Reynolds numbers). Also shown are the log fit (Eq. (7)) and the Schlichting [32] and Hosni et al. [18] simulated roughness data compiled in Bogard et al. [20]. The data in the figure show that in the fully rough regime the real roughness models follow the Eq. (7) fit to the simulated roughness data. Whereas, for the models with  $\Lambda_s > 100$ , there is a large dis-



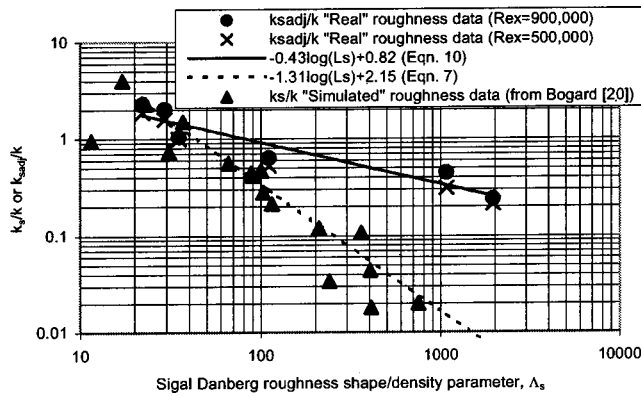


**Fig. 9** Equivalent sandgrain correlation data versus fit. Data from Bogard et al. [20] with accompanying fit (Eq (7)). Data from “real” roughness surfaces at both Reynolds numbers with accompanying fit (Eq. (10)).

crepancy between “real” roughness and simulated roughness. An alternate log fit to the “real” roughness data is also indicated on the figure.

$$\log\left(\frac{k_{sadj}}{k}\right) = -0.43 \log(\Lambda_s) + 0.82 \quad (10)$$

This substantial difference between real and simulated roughness  $k_s$  estimates led to the consideration of alternate geometrical dependencies for  $k_s$  that might unify the entire data set. As such, each of the statistical parameters in Table 1 was independently correlated with the  $k_{sadj}$  values for the six panels. Table 2 contains the correlation coefficient of a least squares fit to the resultant data. Different fitting functions were attempted in each case (linear, logarithmic, and polynomial) and the most successful attempt is included in the table. The results clearly show that  $Rz$  ( $\approx k$ ),  $Ra$ ,  $\lambda$ ,  $Sk$ , and  $K$  do not correlate well with the  $k_{sadj}$  parameter. This may explain why Eq. (7) (which estimates  $k_s$  as a function of  $k$  and  $\Lambda_s$ ) has difficulty for some of the roughness samples. When  $\Lambda_s$  alone is correlated directly against  $k_{sadj}$ , the result is quite good (see Table 2). Surprisingly,  $\alpha_{rms}$  and  $S_w/S$  perform as well or better than  $\Lambda_s$  as parameters of choice for this data set. Of these three,  $\alpha_{rms}$  is the easiest to obtain for real turbine roughness, requiring only a handful of 2-D traces, while determining  $S_w/S$  and  $\Lambda_s$  require full 3-D surface maps. Figure 10 contains the  $k_{sadj}$  versus  $\alpha_{rms}$  data and the associated fit:

$$k_{sadj} = -0.0261 \alpha_{rms} + 0.0138 (\alpha_{rms})^2 \quad (11)$$

This parameter was first reported by Acharya et al. [2] and has received only limited attention in the literature. The reader is cautioned to be careful in the application of Eq. (11) inasmuch as the data set is extremely limited (only six data points thus far). Also, the surface angles were determined from data acquired using a contact stylus, sampled every 5–40  $\mu\text{m}$ . Both of these factors will influence the resultant value of  $\alpha_{rms}$ . Finally, one can readily con-

**Table 2** Correlation coefficient values for least squares fit to  $k_{sadj}$  versus various parameters

Parameter	Fit Type	Correlation Coefficient, $R^2$
$\alpha_{rms}$	2 <sup>nd</sup> order polynomial	0.958
$S_w/S$	Linear	0.892
$\Lambda_s$	Logarithmic	0.899
$Rz \equiv k$	Linear	0.41
$Sk$	Linear	0.36
$K$	Logarithmic	0.23
$Ra$	Linear	0.13
$\lambda_c$	2 <sup>nd</sup> order polynomial	0.099

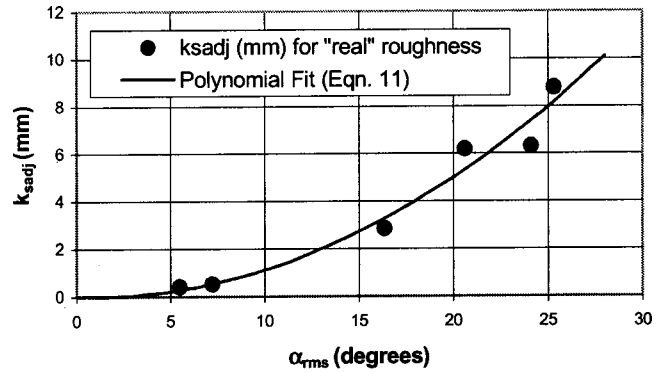


**Fig. 10** Equivalent sandgrain ( $k_{sadj}$  as determined by matching Schlichting  $c_f$  prediction with “real” roughness data) versus rms surface slope angle ( $\alpha_{rms}$ ) with polynomial fit (Eq. (11)).

struct surfaces with widely disparate roughness heights that could register identical  $\alpha_{rms}$  on a single 2-D trace (e.g., right-angle cones of 1 mm height separated by 2 mm versus right angle cones of 10 mm height separated by 20 mm). Clearly this cannot mean that the two would have the same  $k_s$  if both were in a 10-mm-thick boundary layer. So, this correlation must be considered applicable only in the range of  $0.5 < Rz/\theta < 3$  used in this study. It would also be limited to roughness that is locally fairly uniform (such as the panels studies) as opposed to widely spaced, isolated roughness elements which would register widely varying  $\alpha_{rms}$  levels from trace to trace. Despite these limitations, it is encouraging to note that the correlation has the correct physical behavior, as  $\alpha_{rms}$  approaches zero ( $k_s \rightarrow 0$ ). Until further validation can be obtained over a wider array of surfaces, it is only presented as a candidate for calculating  $k_s$  for real roughness.

The foregoing discussion has been focused exclusively on matching  $c_f$ . Of course, it is of interest to see if the same selection of  $k_{sadj}$  (matching the Schlichting  $c_f$  correlation) also brings the experimental St data in line with the corresponding St correlations. Figure 11 shows the St correlation values for the six panels where both  $c_f$  and  $k^+$  correspond to the new  $k_{sadj}$  values. Of the three St correlations considered in Fig. 8, only Dipprey and Sabersky’s is shown in the figure since it showed the most promise in Fig. 8 (without tailoring). It is also the oldest and most comprehensive data set of the three. (Both Kays and Crawford and Wassel and Mills based their correlations at least partially on the Dipprey and Sabersky findings.) This correlation still overpredicts five of the six panels by an average of 10%, while the no. 2 surface is matched to within 1%. This curious result prompted a closer inspection of the model surfaces. Each of the six surfaces is

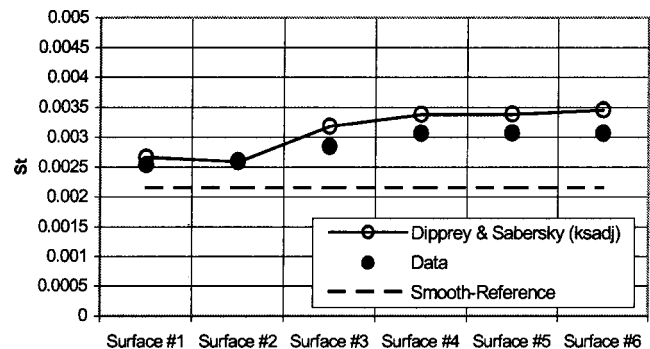


**Fig. 11** Stanton number for “real” roughness panels compared to Dipprey and Sabersky correlation using  $k_{sadj}$  and  $c_f$  from Schlichting. Data for  $Re_x=900,000$  only.

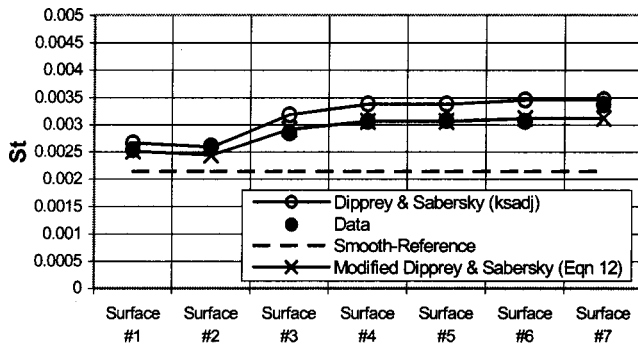


**Fig. 12 Stanton number for six “real” rough panels + cone surface (no. 7) compared to Dipprey and Sabersky correlation using  $k_{sadj}$  and  $c_f$  from Schlichting. Also, modified Dipprey and Sabersky correlation (Eq. (12)). Data for  $Re_x=900,000$  only.**

quite unique (as shown by the traces in Fig. 1), but surface no. 2 has an order or regularity that makes it clearly distinct. As mentioned earlier, this intermittently debonded TBC surface has an undulating surface character not unlike that of closely-packed spherical segments. As such, it is most like the simulated roughness surface using cones or spheres or the close-packed sandgrain surfaces on which the correlations (like Dipprey-Sabersky) are based. Perhaps these correlations consistently overpredict the “real” roughness St precisely because they were developed with simulated (versus real) surface roughness. So, even if the  $k_s$  of the “real” roughness surface is adjusted to match the Schlichting  $c_f$  correlation value, the Dipprey-Sabersky St correlation based on the same  $k_s$  will always be high for “real” roughness. Whereas if  $k_s$  is determined for a simulated rough surface with ordered roughness elements, both the  $c_f$  and St correlations would be accurate.

To test this hypothesis, a 7th model surface was fabricated consisting of densely packed cones with the following dimensions: height=2 mm, base diameter=5 mm, spacing=5 mm. The  $\Lambda_s$  and  $\alpha_{rms}$  values for this surface are 20.2 and 24.6 deg, respectively, a close match to surface no. 6 (22.1 and 25.3 deg). When the  $k_s$  for this new cone surface is adjusted to match the Schlichting  $c_f$  correlation, the St correlation of Dipprey-Sabersky matches the data to within 3% (Fig. 12). This startling result provides at least a preliminary indication that the hypothesis proposed in the foregoing is worthy of further investigation. If proven to be more generally true, it would suggest that simulated rough surfaces with ordered roughness elements can be used to model either the heat transfer behavior or the skin friction behavior of “real” turbine roughness, but not both simultaneously. A physical explanation for this may be related to the 3-D vortical secondary flow patterns that are generated by regular roughness elements. These secondary flows are known to enhance St with little or no effect on  $c_f$  [35]. The randomness and wide range of scales present in “real” roughness may serve to break up these secondary flows and reduce St for the same  $c_f$ . A possibly related mechanism was reported by Pinson and Wang [36] regarding roughness-induced boundary layer transition. They noted that when large roughness elements were followed by small roughness elements, boundary layer transition was actually suppressed compared to the case of large roughness elements followed by a smooth surface. Their explanation was that the smaller roughness elements break up flow disturbances generated by the larger roughness elements, thus suppressing their amplification and subsequent transition. This same mechanism may partially inhibit the heat transfer augmentation of secondary flows induced by large roughness peaks on real roughness surfaces.

If the first constant in the denominator of the Dipprey-Sabersky

St correlation is increased from 5.19 to 5.96, the match with the “real” roughness panels is within  $\pm 2\%$  (also shown on Fig. 12). The new correlation would then be

$$St = \frac{0.5c_f}{1 + \sqrt{0.5c_f(5.96k^{+0.2}Pr^{0.44} - 8.5)}} \quad (12)$$

Of course, this correlation now underpredicts the St for the two ordered surfaces (nos. 2 and 7) by approximately 7%.

Incidentally, the  $k_{sadj}$  for surface no. 7 does fall in line with the  $k_s$  versus  $\alpha_{rms}$  correlation shown in Fig. 10 (Eq. (11)), further suggesting that  $\alpha_{rms}$  may be a suitable candidate for unifying simulated and real roughness correlations for  $k_s$  insofar as  $c_f$  is concerned. Given the above findings, even if such a unifying correlation were derived and verified, there would still be a discrepancy with regard to St.

Though the above findings are presented for  $Re_x=900,000$  only, similar results were obtained at the lower Reynolds value. Only minor modifications to the  $k_{sadj}$  values were required (Fig. 9) and the St overprediction for the “real” roughness surfaces was nearly identical. The  $Re_x=500,000$  data also fall along the Eq. (11) curve fit for  $k_s$  versus  $\alpha_{rms}$ .

**Effect of Freestream Turbulence.** Boundary layer velocity profiles taken at midspan near the test section leading edge are shown in Fig. 13 for three levels of freestream turbulence: 1% (nominal), 5% (grid-generated), and 11% (jet-generated). Also shown in the figure are the turbulence levels in the boundary layer. Note that in the highest turbulence case, the turbulence level in the freestream approaches the level of turbulence associated with the near wall peak. This feature has been determined by other researchers to significantly alter the momentum and energy transport of the turbulent boundary layer.

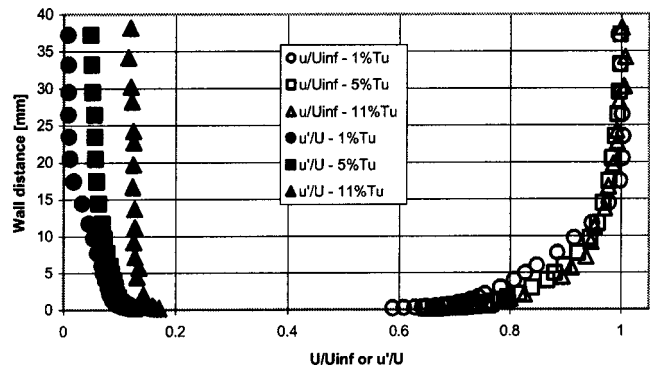


**Fig. 13 Mean and fluctuating velocity profiles at roughness surface leading edge. Three levels of freestream turbulence: 1, 5, and 11%. Data for  $Re_x=900,000$ . (Sparse data presentation for clarity.)**

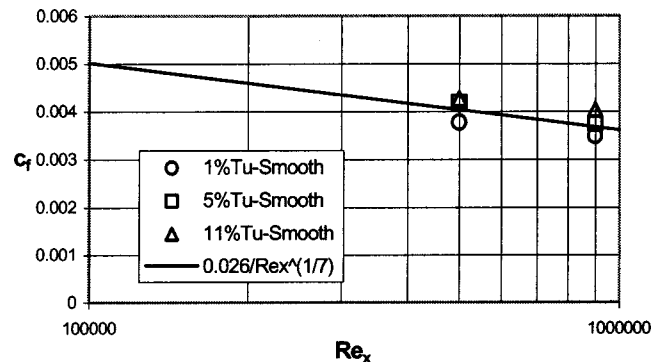


**Fig. 14 Skin friction versus Reynolds number for smooth surface at  $Tu=1, 5,$  and  $11\%$**

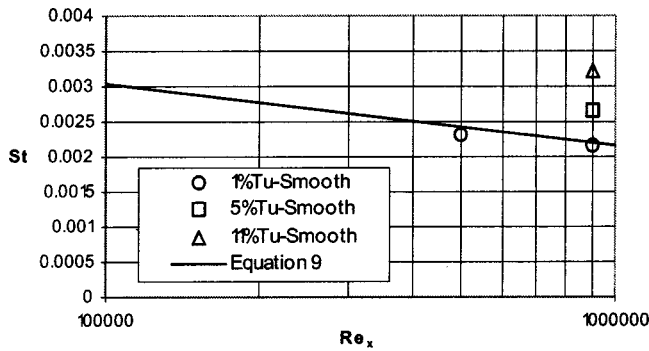


**Fig. 15 Stanton number versus Reynolds number for smooth surface at  $Tu=1, 5,$  and  $11\%$ . Elevated turbulence data for  $Re=900,000$  only.**

The levels of  $c_f$  and  $St$  augmentation produced on the smooth test plate due to the two levels of freestream turbulence are shown in Figs. 14 and 15 and tabulated in Table 3. The table also contains the efficiency factor,  $\eta$ , defined as the ratio of  $St$  augmentation to  $c_f$  augmentation,  $(St/St_0)/(c_f/c_{f0})$ . The  $St$  augmentation range with turbulence is comparable to that generated by the “real” roughness in the previous portion of this report. The  $c_f$  augmentation, on the other hand, is less than one third of the  $St$  augmentation in this case. This is in stark contrast to the augmentation results with roughness where  $c_f/c_{f0}$  was up to four times  $St/St_0$ . The physical explanation for this is that increases in  $c_f$  due to roughness are primarily due to form drag on the individual roughness elements. There is no heat transfer analog to this form drag component of  $c_f$  augmentation, thus  $c_f/c_{f0}$  is two to four times greater than  $St/St_0$  for rough surfaces.

In the case of freestream turbulence, augmentation occurs due to increased momentum and energy exchange with the freestream. There are no alternate mechanisms for surface drag in this case. The finding that freestream turbulence favors heat transfer augmentation over  $c_f$  augmentation is consistent with data presented by other researchers. Pedisius et al. [37] reported efficiency factors ( $\eta$ ) from 1.10 to 1.15 for grid generated turbulence up to 8% over a smooth plate. Maciejewski and Moffat [38] reported  $St/St_0$  values up to 1.80 for their free jet turbulence with over 15%  $Tu$ . The associated  $c_f/c_{f0}$  was estimated at 1.10, yielding  $\eta \approx 1.64$ . Blair [39] proposed an empirically-based correlation to capture this preference for  $St$  over  $c_f$  using a correction to the popular Reynolds analogy ( $2St/c_f \approx 1$ ). His correlation (developed for grid turbulence with up to 7%  $Tu$ ) is

$$\frac{2St}{c_f} = 1.18 + 0.013Tu \quad (13)$$

where the freestream turbulence level ( $Tu$ ) is in percent. This correlation yields estimates of  $\eta=1.06$  at 5%  $Tu$  and  $\eta=1.12$  at 11%  $Tu$ , grossly underestimating the present results. A more appropriate  $Tu$  coefficient to fit the present data would be 0.040. Baskaran et al. [40] likewise found an up to 100% increase in this turbulence coefficient in their grid-generated turbulence data.

In addition to the increase in  $Tu$  that accompanies the change in turbulence generation mechanism from the square-bar grid to the opposing jets in the current study, the integral lengthscale also

**Table 3  $St$  and  $c_f$  augmentation ratios for smooth plate with freestream turbulence ( $Re_x=900,000$ )**

	$Tu = 5\%$	$Tu = 11\%$
$St/St_0$	1.24	1.50
$c_f/c_{f0}$	1.07	1.16
$\eta = (St/St_0)/(c_f/c_{f0})$	1.16	1.30
$Tu/(L_\infty^u/\delta+2)$	0.93	1.71

more than doubles (from 2.4 to 5 cm). Blair [39] and Simonich and Bradshaw [41] have both studied the role of turbulence scale in skin friction and heat transfer augmentation. The physical explanation offered is that larger scale turbulence has difficulty influencing the momentum and energy exchange near the wall due to damping at the solid surface. Thus, Simonich and Bradshaw reported reductions in  $c_f$  and  $St$  augmentation as lengthscale increased at constant  $Tu$ . They were first to suggest dividing  $Tu$  by a lengthscale factor ( $\alpha=L_\infty^u/\delta+2$ ) to account for this effect.  $L_\infty^u$  is the dissipation lengthscale, measured to be 6.7 and 8.8 cm over the roughness plate in this facility (for grid and jet generated turbulence respectively). Values of  $Tu/\alpha$  are included in Table 3. Thole and Bogard [42] combined their own jet-generated turbulence data with that of a number of previous researchers, plotting  $\Delta c_f/c_{f0}$  and  $\Delta St/St_0$  versus  $Tu/\alpha$  in the manner suggested by Simonich and Bradshaw. The reader is referred to Fig. 12 of the Thole and Bogard report where the present  $\Delta c_f/c_{f0}$  data fall in line with the four data sets shown. The  $\Delta St/St_0$  data, however, are nearly double the results of Thole and Bogard, falling more in line with the results of Sahm and Moffat [43] presented in the figure. As such, the smooth plate data with freestream turbulence reported in this study appear to be within the range of results reported in previous studies.

There are a number of different methods to assess the combined effects of roughness and freestream turbulence on  $c_f$  and  $St$ . Of critical importance to the designer is whether results with freestream turbulence alone can be simply added to results with roughness alone to approximate the effect when both are present. If true, this would imply a lack of synergy between the two augmentation mechanisms. This is attractive to the designer because it allows correction factors to be simply superposed without additional parametric testing. One way to determine the degree to which these two mechanisms are synergistic is to compare the augmentation results obtained with both mechanisms present to that achieved by either adding or compounding their individual effects. For example, if the smooth plate  $c_f$  augmentation due to freestream turbulence was 20% and the  $c_f$  augmentation of a rough plate (without turbulence) was 30%, the additive prediction method would result in a combined effect of 50%. For the same case, the compound method would predict a combined effect of 56%. These three methods of comparison are outlined algebraically for  $c_f$  as follows:

$$\text{Synergistic: } \frac{c_{fRTu} - 1}{c_{f0}} \approx \frac{\Delta c_f}{c_{f0}} \quad (14)$$

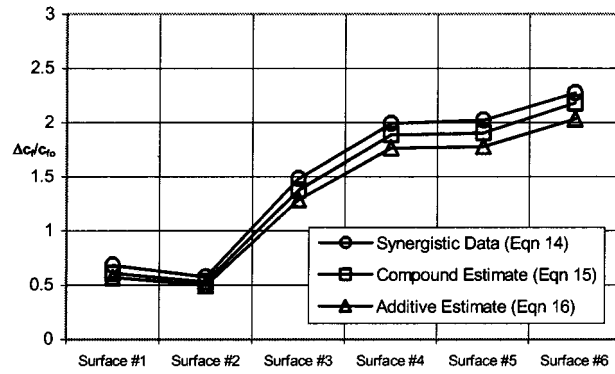
$$\text{Compound: } \frac{c_{fR} c_{fTu} - 1}{c_{f0} c_{f0}} \quad (15)$$

$$\text{Additive: } \left( \frac{c_{fR} - 1}{c_{f0}} \right) + \left( \frac{c_{fTu} - 1}{c_{f0}} \right) \quad (16)$$

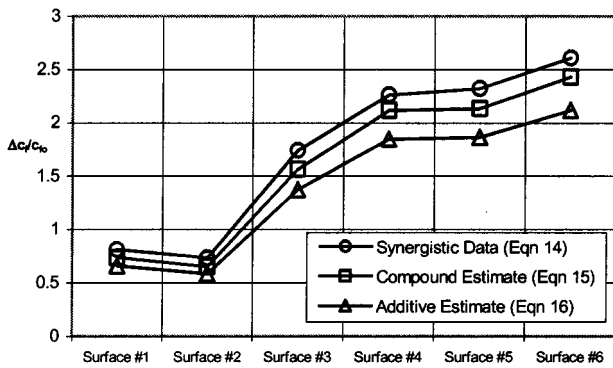
The subscripts  $R$ ,  $Tu$ , and  $RTu$  represent  $c_f$  measurements with roughness only, turbulence only, and the two effects combined respectively. Identical expressions can be written for  $St$  as well. Figures 16(a)–(d) contain these measures (for  $c_f$  and  $St$ ) for all 6 samples in Table 1 at the two elevated  $Tu$  levels.

In all four figures, the additive predicted effects are less than the synergistic (or actual combined) effects. The average discrepancy is 1% for the 5%  $Tu$   $\Delta St/St_0$  results, 13% for the 5%  $Tu$   $\Delta c_f/c_{f0}$  results, and roughly 20% for the two 11%  $Tu$  cases. Even when the compound prediction is used, the results are on average 5% low for  $\Delta St/St_0$  (at 11%  $Tu$ ) and 7.5% low for  $\Delta c_f/c_{f0}$  (at both 5% and 11%  $Tu$ ). This suggests that there is indeed some physical coupling mechanism between the two effects that is responsible for the added enhancement when they are combined.

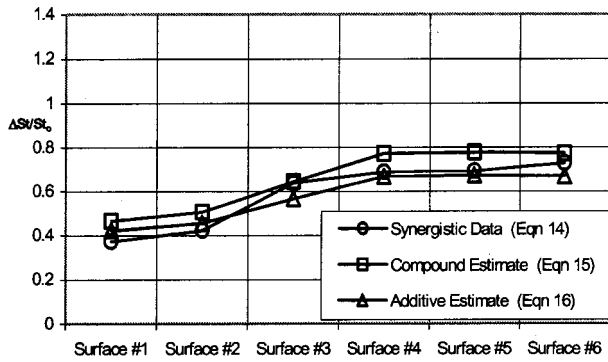
In the case of skin friction, freestream turbulence and roughness have competing effects on the near wall momentum distribution. When plotted in wall units, the log region of the smooth-wall, low-turbulence velocity plot is suppressed by roughness and en-



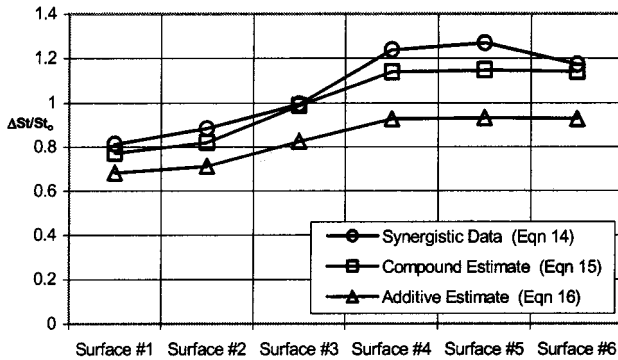
(a)



(b)



(c)



(d)

**Fig. 16 Comparison of combined (synergistic) roughness/turbulence effects on  $c_f$  and  $St$  with estimates using added and compounded individual effects of roughness alone and turbulence alone.  $c_f$  data for six rough surfaces at (a)  $Tu=5\%$  and (b)  $Tu=11\%$   $St$  data at (c)  $Tu=5\%$  and (d)  $Tu=11\%$ . All at  $Re_x=900,000$  only.**

hanced by turbulence. As such, it would be unlikely that a synergy could be occurring in the near wall shear itself. The likely candidate for coupling is the form drag associated with the roughness elements themselves. For the panels in this study, all roughness peaks are smaller than 1/3rd of the boundary layer thickness. The majority of the peaks are situated around the momentum thickness, approximately 1/10th of the boundary layer thickness. In this region of a rough-wall turbulent boundary layer, the momentum is relatively depressed. Accordingly, peaks in this region of the boundary layer have a reduced drag signature due to the lower dynamic pressure available. Since freestream turbulence has a tendency to enhance the near-wall momentum (Fig. 13), the drag on roughness elements would increase synergistically. Since this form drag is such a large component of the overall  $c_f$  augmentation due to roughness, this is a probable explanation for the observed synergy.

The results with heat transfer are less tractable. At 5%  $Tu$ , the additive effect is only slightly less than the synergistic effect on  $St$  (1% less on average). This is consistent with results reported by Turner et al. [11] when 7–8%  $Tu$  was added to their rough-surfaced cascade facility. They found the combined effect to be approximately additive, though boundary layer transition was a complicating factor that could not be isolated and removed from the results. At the higher turbulence level of 11% in this study, however, the additive result undershoots the synergistic effect by an average of 20%. This does not follow the conclusion of Bogard et al. [20] that at high turbulence levels the effects are essentially additive as well. In their core-simulated roughness study, Bogard et al. reported average turbulence levels of 13% and the individual effects on heat transfer were  $\Delta St/St_0 \approx 30\%$  for turbulence and  $\Delta St/St_0 \approx 60\%$  for roughness. The additive effect from these two is 90% while the compound effect is 108%. Their reported synergistic effect was 100%, essentially midway between the two computations. So, the data may show some synergy after all. Perhaps the combined effect is nonlinear and there exists some threshold turbulence level at which synergy begins to be apparent.

This conjecture is supported by the  $\Delta St/St_0$  results for the compound predictions in Figs. 16(c)-(d). In this case, there is actually a negative synergy (average of -13%) between roughness and turbulence at 5%  $Tu$ . This means that if the net effect of the two individual augmentation mechanisms is compounded, the results is greater than the effect in "real life." Since secondary (vortical) flows have been identified as a critical feature of  $St$  augmentation in roughness, it may be that low freestream turbulence levels disrupt the natural formation of shed vorticity from roughness peaks and valleys. Whatever the explanation, the effect is clearly limited since at the higher turbulence level of 11% synergy is once again positive (the synergistic result is 5% greater than the compound result on average for this case).

This nonlinear behavior in  $St$  augmentation between 1, 5, and 11% freestream turbulence is evidenced when comparing efficiency factors as well. As mentioned in the introduction, previous work with regular arrays of dimples and hemispheres by Kithcart and Klett [22] showed that  $\eta$  increases (i.e.,  $\Delta St$  is larger for an equivalent  $\Delta c_f$ ) as roughness elements become more recessed below the mean surface height. In their study, dimple arrays measured an  $\eta$  of 0.75 or greater whereas hemispheres with identical spacing and radius measured  $\eta \approx 0.5$ . For a "real" rough surface the statistical skewness ( $Sk$ ) provides a quantitative measure of the relative concentration and size of peaks and valleys. As reported in [1], a large positive skewness denotes large protrusions above the mean and is typical of surfaces with deposits or erosion. A large negative skewness denotes recesses or cavities typical of pitting or spallations.

Figure 17 shows the efficiency factors versus skewness for all six roughness panels in this study. Data for each of the three levels of  $Tu$  (1, 5, and 11%) is presented. Polynomial curve fits to each set of data are superposed on the plot. These fits exclude the data points near  $\eta \approx 0.9$  with  $Sk \approx 0$  as these correspond to surface no. 2.

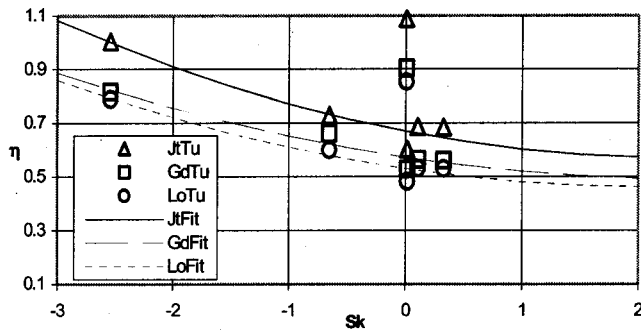


**Fig. 17 Efficiency factor,  $\eta = (St/St_0)/(c_f/c_{f0})$ , versus statistical skewness of roughness. Data for six rough surfaces at  $Tu=1, 5$ , and  $11\%$  for  $Re=900,000$  only. Polynomial fits to all but surface no. 2 data.**

This surface was identified earlier as having an augmented heat transfer more typical of simulated roughness rather than “real” roughness. The curves highlight a noticeable trend to higher  $\eta$  with decreasing  $Sk$ , as expected based on the Kitchart and Klett results. As anticipated, surface no. 2 does not follow this trend. The curves also underscore a distinct difference between the two levels of freestream turbulence.  $5\%$   $Tu$  has only a limited effect on  $\eta$  (increase by roughly  $0.04$ ) while  $11\%$   $Tu$  results in an average increase of  $0.15$  in  $\eta$ . Clearly, between the grid-generated low turbulence and jet-generated high turbulence, some mechanism comes to bear to alter the energy and momentum exchange in this turbulent boundary layer. More work is needed to determine if the observed behavior is a function of turbulence level, roughness type, turbulent lengthscale, or some combination of these parameters.

## Summary and Conclusions

Heat transfer and skin friction measurements have been made on roughness panels in a low-speed, zero pressure gradient wind tunnel. The roughness panels are scaled models of actual turbine surfaces rather than the traditional simulated roughness using sand or ordered arrays of cones or spherical segments. Results indicate that this “real roughness” is distinctly different from simulated roughness. Standard roughness correlations for both  $St$  and  $c_f$  have been evaluated and new correlations are proposed in some cases. The combined effect of freestream turbulence and roughness is also evaluated in detail for these “real roughness” models. Based on the findings, the following conclusions are made:

1 Roughness effects on skin friction are 2–4 times as significant as those on heat transfer.

2 Standard correlations (e.g., from Schlichting) provide a good estimate for  $c_f$  augmentation due to roughness when the roughness is in the fully rough regime ( $k^+ > 70$ ). This conclusion is based on the use of the Sigal and Danberg correlation for  $k_s$  as a function of  $k$  and  $\Lambda_s$  (a shape/density roughness parameter).

3 Standard correlations (e.g., from Dipprey and Sabersky) overpredict rough surface  $St$  by  $10\%$  when the roughness is in the fully rough regime ( $k^+ > 70$ ). Again,  $k_s$  is calculated as a function of  $k$  and  $\Lambda_s$ .

4 Existing  $St$  and  $c_f$  correlations severely underpredict the effect of real roughness when  $k^+ < 70$ . This discrepancy is related to the dependence of  $k_s$  on  $k$ . An alternative formulation for  $k_s$  as an exclusive function of the rms surface slope angle ( $\alpha_{rms}$ ) is proposed to replace the Sigal Danberg formulation over the range of roughness included in this study ( $0.5 < k/\theta < 3$ ).

5 Even when  $k_s$  is adjusted to match the Schlichting  $c_f$  correlation with the experimentally measured values,  $St$  correlations based on this  $k_s$  are still too large by  $10\%$ . This observation is true for the “real” roughness models but not for “simulated” (cone)

roughness models, in which case this  $k_s$  gives an excellent  $St$  match between data and correlations. This observation highlights a distinct difference between “real” and “simulated” roughness. If shown to be more generally true, it would suggest that simulated rough surfaces with ordered roughness elements can be used to model either the heat transfer behavior or the skin friction behavior of “real” turbine roughness, but not both simultaneously.

6 Freestream turbulence effects on heat transfer are roughly three times as significant as those on skin friction, the opposite of roughness effects.

7 When turbulence and roughness are both present, synergies are generated which create larger effects on  $c_f$  and  $St$  than those obtained by adding (or compounding) their individual effects. This difference can reach  $20\%$  when compared to a simply additive approach to account for both effects. An exception to this is the combined effect on  $St$  at low turbulence levels. In this case, negative synergies appear to be present when both roughness and turbulence are present.

## Acknowledgments

The author is indebted to numerous personnel at the four industrial partners for providing the turbine hardware. Primary among these are: Dr. Boris Glezer formerly of Solar Turbines, Dr. Ron Bunker and Mr. Paul Stuttmann at General Electric, Mr. Mohan Hebbar at Siemens-Westinghouse, and Dr. William Troha and Mr. Shawn Pollock of Honeywell Corporation. The author would also like to acknowledge those who assisted in the collection of this data. Captain Jess Drab and 2Lt Christine Ellering at the Air Force Institute of Technology and Cadets Nathan Loucks and Dick Jansen of the United States Air Force Academy. In addition, collaborations with Dr. Keith Hodge and Dr. Steve McClain at Mississippi State University and Drs. Richard Rivir and Rolf Sondergaard of the Air Force Research Lab are appreciated. The testing was conducted at the Air Force Research Lab Aero-thermal research laboratory with technical support from Mr. William Nilson, Mr. Jay Anderson, and Mr. Andy Pitts. The assistance of Ms. Nikki Widmor at the University of Dayton Research Institute in determining the plastic properties is gratefully acknowledged. This work was sponsored by the US Department of Energy—National Energy Technology Laboratory through a cooperative agreement with the South Carolina Institute for Energy Studies at Clemson University. The views expressed in this article are those of the author and do not reflect the official policy or position of the United States Air Force, Department of Defense, or U.S. Government.

## Nomenclature

- $A_f$  = windward frontal surface area of roughness elements on sample
- $A_s$  = windward wetted surface area of roughness elements on sample
- $c_f$  = skin friction coefficient,  $\tau_w / (0.5\rho U_\infty^2)$
- $c$  = blade/vane chord
- $c_p$  = specific heat at constant pressure
- $h$  = convective heat transfer coefficient
- $k$  = average roughness height ( $\approx Rz$ )
- $k_s$  = equivalent sandgrain roughness
- $k = k_s u_\tau / \nu = Re_k$
- $Ku$  = kurtosis of height distribution (Eq. (5))
- $L_\infty^u$  = dissipation lengthscale of turbulence
- $N$  = number of points in profile record
- $Pr$  = Prandtl number ( $\nu/\alpha$ ) ( $\approx 0.71$ )
- $Pr_t$  = turbulent Prandtl number ( $\approx 0.9$ )
- $Ra$  = centerline average roughness (Eq. (1))
- $Re_x$  = Reynolds number ( $U_\infty x/\nu$ )
- $Re_c$  = Reynolds number based on blade chord and exit conditions
- $Rq$  = rms roughness (Eq. (2))

$Rt$  = maximum peak to valley roughness (Eq. (3))  
 $Rz$  = average peak to valley roughnesses  
 $S$  = surface area of sample without roughness  
 $S_f$  = total frontal surface area of sample  
 $S_w$  = total wetted surface area of sample  
 $Sk$  = skewness of height distribution (Eq. (4))  
 $St$  = Stanton number,  $h/(\rho c_p U_\infty)$   
 $T$  = temperature [ $^{\circ}C$ ]  
 $t$  = time [s]  
 $Tu$  = freestream turbulence,  $u'/U_\infty$  [%]  
 $U_\infty$  = freestream velocity  
 $U$  = mean velocity (m/s)  
 $u'$  = fluctuating velocity (rms)  
 $u_\tau$  = friction or shear velocity  $\sqrt{\tau_w/\rho}$   
 $x$  = streamwise distance from tunnel floor leading edge  
 $y$  = surface height coordinate after removal of polynomial fit to surface curvature  
 $\alpha$  = thermal diffusivity ( $\kappa/\rho c_p$ )  
 [also  $\alpha = L_\infty^2/\delta + 2$  for  $Tu/\alpha$ ]  
 $\alpha_{rms}$  = rms deviation of surface slope angles  
 $\delta$  = boundary layer thickness  
 $\eta$  = efficiency factor ( $St/St_0/c_f/c_{f0}$ )  
 $\kappa$  = thermal conductivity  
 $\lambda_c$  = correlation length  
 $\Lambda_s$  = roughness shape/density parameter (Eq. (6)) [also  $L_s$ ]  
 $\nu$  = kinematic viscosity  
 $\theta$  = boundary layer momentum thickness  
 $\rho$  = density  
 $\tau_w$  = wall shear  
 $\nu$  = kinematic viscosity

## Subscripts

adj = adjusted  $k_s$  value required to match Schlichting  $c_f$  correlation to data  
 max = maximum height in profile record  
 min = minimum height in profile record  
 $o$  = smooth plate reference at low freestream turbulence  
 $R$  = roughness effects only  
 $RTu$  = roughness and freestream turbulence effects  
 $s$  = surface value  
 $Tu$  = freestream turbulence effects only  
 $\infty$  = freestream value

## References

- Bons, J. P., Taylor, R., McClain, S., and Rivir, R. B., 2001, "The Many Faces of Turbine Surface Roughness," *ASME J. Turbomach.*, **23**, pp. 739–748.
- Acharya, M., Bornstein, J., and Escudier, M., 1986, "Turbulent Boundary Layers on Rough Surfaces," *Exp. Fluids*, No. 4, pp. 33–47.
- Taylor, R. P., 1990, "Surface Roughness Measurements on Gas Turbine Blades," *ASME J. Turbomach.*, **112**(1), pp. 175–180.
- Tarada, F., and Suzuki, M., 1993, "External Heat Transfer Enhancement to Turbine Blading due to Surface Roughness," *ASME Paper 93-GT-74*.
- Blair, M. F., 1994, "An Experimental Study of Heat Transfer in a Large-Scale Turbine Rotor Passage," *ASME J. Turbomach.*, **116**(1), pp. 1–13.
- Guo, S. M., Jones, T. V., Lock, G. D., and Dancer, S. N., 1998, "Computational Prediction of Heat Transfer to Gas Turbine Nozzle Guide Vanes with Roughened Surfaces," *ASME J. Turbomach.*, **120**(2), pp. 343–350.
- Boynton, J. L., Tabibzadeh, R., and Hudson, S. T., 1993, "Investigation of Rotor Blade Roughness Effects on Turbine Performance," *ASME J. Turbomach.*, **115**, pp. 614–620.
- Suder, K. L., Chima, R. V., Strazisar, A. J., and Roberts, W. B., 1995, "The Effect of Adding Roughness and Thickness to a Transonic Axial Compressor Rotor," *ASME J. Turbomach.*, **117**, pp. 491–505.
- Ghenaiet, A., Elder, R. L., and Tan, S. C., "Particles Trajectories through an Axial Fan and Performance Degradation due to Sand Ingestion," *ASME Paper No. 2001-GT-497*.
- Bammert, K., and Sandstede, H., 1980, "Measurements of the Boundary Layer Development along a Turbine Blade with Rough Surfaces," *ASME J. Eng. Power*, **102**, pp. 978–983.
- Turner, A., Tarada, F., and Bayley, F., 1985, "Effects of Surface Roughness on Heat Transfer to Gas Turbine Blades," *AGARD-CP-390*, pp. 9-1 to 9-9.
- Hoffs, A., Drost, U., and Boles, A., 1996, "Heat Transfer Measurements on a Turbine Airfoil at Various Reynolds Numbers and Turbulence Intensities Including Effects of Surface Roughness," presented at ASME IGTI in Birmingham, U.K., June 1996, *ASME Paper No. 96-GT-169*.
- Abuaf, N., Bunker, R. S., and Lee, C. P., 1998, "Effects of Surface Roughness on Heat Transfer and Aerodynamic Performance of Turbine Airfoils," *ASME J. Turbomach.*, **120**(3), pp. 522–529.
- Pinson, M. W., and Wang, T., 2000, "Effect of Two-Scale Roughness on Boundary Layer Transition over a Heated Flat Plate: Part I — Surface Heat Transfer," *ASME J. Turbomach.*, **122**(2), pp. 301–307.
- Goldstein, R., Eckert, E., Chiang, H., and Elovic, E., 1985, "Effect of Surface Roughness on Film Cooling Performance," *ASME J. Eng. Gas Turbines Power*, **107**, pp. 111–116.
- Pinson, M. W., and Wang, T., 1997, "Effects of Leading Edge Roughness on Fluid Flow and Heat Transfer in the Transitional Boundary Layer over a Flat Plate," *Int. J. Heat Mass Transf.*, **40**(12), pp. 2813–2823.
- Taylor, R. P., Scaggs, W. F., and Coleman, H. W., 1988, "Measurement and Prediction of the Effects of Nonuniform Surface Roughness on Turbulent Flow Friction Coefficients," *ASME J. Fluids Eng.*, **110**, pp. 380–384.
- Hosni, M. H., Coleman, H. W., and Taylor, R. P., 1991, "Measurements and Calculations of Rough-Wall Heat Transfer in the Turbulent Boundary Layer," *Int. J. Heat Mass Transf.*, **34**(4/5), pp. 1067–1082.
- Scaggs, W. F., Taylor, R. P., and Coleman, H. W., 1988, "Measurement and Prediction of Rough Wall Effects on Friction Factor — Uniform Roughness Results," *ASME J. Fluids Eng.*, **110**, pp. 337–342.
- Bogard, D. G., Schmidt, D. L., and Tabbita, M., 1998, "Characterization and Laboratory Simulation of Turbine Airfoil Surface Roughness and Associated Heat Transfer," *ASME J. Turbomach.*, **120**(2), pp. 337–342.
- Barlow, D. N., and Kim, Y. W., 1995, "Effect of Surface Roughness on Local Heat Transfer and Film Cooling Effectiveness," *ASME Paper No. 95-GT-14*.
- Kitcart, M. E., and Klett, D. E., 1997, "Heat Transfer and Skin Friction Comparison of Dimpled Versus Protusion Roughness," *NASA N97-27444*, pp. 328–336.
- Sigal, A., and Danberg, J., 1990, "New Correlation of Roughness Density Effect on the Turbulent Boundary Layer," *AIAA J.*, **28**(3), pp. 554–556.
- Nikuradse, J., 1933, "Laws for Flows in Rough Pipes," *VDI-Forschungsheft 361*, Series B, Vol. 4. (English trans. NACA TM 1292, 1950).
- Antonia, R. A., and Luxton, R. E., 1971, "The Response of a Turbulent Boundary Layer to a Step Change in Surface Roughness. Part 1: Smooth to Rough," *J. Fluid Mech.*, **48**, pp. 721–726.
- Taylor, R. P., and Chakroun, W. M., 1992, "Heat Transfer in the Turbulent Boundary Layer with a Short Strip of Surface Roughness," *AIAA Paper No. 92-0249*.
- Schultz, D. L., and Jones, T. V., 1973, "Heat-transfer Measurements in Short-duration Hypersonic Facilities," *Advisory Group for Aerospace Research and Development*, No. 165, NATO.
- Drab, J. W., and Bons, J. P., 2002, "Turbine Blade Surface Roughness Effects on Shear Drag and Heat Transfer," *AIAA Paper No. 2002-0085*.
- Mills, A. F., *Heat Transfer*, 1st Edition, 1992, Irwin, IL.
- White, F. M., *Viscous Fluid Flow*, 2nd Edition, 1991, McGraw-Hill, New York, NY.
- Kays, W. M., and Crawford, M. E., *Convective Heat and Mass Transfer*, 3rd Edition, 1993, McGraw-Hill, New York, NY.
- Schlichting, H., *Boundary Layer Theory*, 7th Edition, 1979, McGraw-Hill, New York, NY.
- Dipprey, D. F., and Sabersky, R. H., 1963, "Heat and Momentum Transfer in Smooth and Rough Tubes at Various Prandtl Numbers," *Int. J. Heat Mass Transfer*, **6**, pp. 329–353.
- Wassel, A. T., and Mills, A. F., 1979, "Calculation of Variable Property Turbulent Friction and Heat Transfer in Rough Pipes," *ASME J. Heat Transfer*, **101**, pp. 469–474.
- Mahmood, G. I., Hill, M. L., Nelson, D. L., Ligrani, P. M., Moon, H.-K., and Glezer, B., 2000, "Local Heat Transfer and Flow Structure on and Above a Dimpled Surface in a Channel," *ASME Paper No. 2000-GT-230* presented at ASME TURBOEXPO, Munich, Germany, May.
- Pinson, M. W., and Wang, T., 2000, "Effect of Two-Scale Roughness on Boundary Layer Transition over a Heated Flat Plate: Part I — Surface Heat Transfer," *ASME J. Turbomach.*, **122**, pp. 301–307.
- Pedisius, A. A., Kazimekas, V. A., and Slanciauskas, A. A., 1979, "Heat Transfer from a Plate to a High-Turbulence Air Flow," *Soviet Research*, **11**, pp. 125–134.
- Maciejewski, P. K., and Moffat, R. J., 1992, "Heat Transfer with Very High Free-Stream Turbulence: Part I — Experimental Data," *ASME J. Heat Transfer*, **114**, pp. 827–833.
- Blair, M. F., 1983, "Influence of Free-Stream Turbulence on Turbulent Boundary Layer Heat Transfer and Mean Profile Development: Part II — Analysis of Results," *ASME J. Heat Transfer*, **105**, pp. 41–47.
- Baskaran, V., Abdellatif, O. E., and Bradshaw, P., 1989, "Effects of Free-Stream Turbulence on Turbulent Boundary Layers with Convective Heat Transfer," presented at the 7th Symposium on Turbulent Shear Flows, Stanford Univ., CA, Aug.
- Simonich, J. C., and Bradshaw, P., 1978, "Effect of Free-Stream Turbulence on Heat Transfer Through a Turbulent Boundary Layer," *ASME J. Heat Transfer*, **100**, pp. 671–677.
- Thole, K. A., and Bogard, D. G., 1985, "Enhanced Heat Transfer and Shear Stress due to High Free-Stream Turbulence," *ASME J. Turbomach.*, **117**, pp. 418–424.
- Sahm, M. K., and Moffat, R. J., 1992, "Turbulent Boundary Layers with High Turbulence: Experimental Heat Transfer and Structure on Flat and Convex Walls," *Stanford University Report HMT-45*.

# Separated Flow Transition Under Simulated Low-Pressure Turbine Airfoil Conditions—Part 1: Mean Flow and Turbulence Statistics

**Ralph J. Volino**

Mem. ASME,  
Department of Mechanical Engineering,  
United States Naval Academy,  
Annapolis, MD 21402  
e-mail: volino@usna.edu

*Boundary layer separation, transition and reattachment have been studied experimentally under low-pressure turbine airfoil conditions. Cases with Reynolds numbers ( $Re$ ) ranging from 25,000 to 300,000 (based on suction surface length and exit velocity) have been considered at low (0.5%) and high (9% inlet) free-stream turbulence levels. Mean and fluctuating velocity and intermittency profiles are presented for streamwise locations all along the airfoil, and turbulent shear stress profiles are provided for the downstream region where separation and transition occur. Higher  $Re$  or free-stream turbulence level moves transition upstream. Transition is initiated in the shear layer over the separation bubble and leads to rapid boundary layer reattachment. At the lowest  $Re$ , transition did not occur before the trailing edge, and the boundary layer did not reattach. Turbulent shear stress levels can remain low in spite of high free-stream turbulence and high fluctuating streamwise velocity in the shear layer. The beginning of a significant rise in the turbulent shear stress signals the beginning of transition. A slight rise in the turbulent shear stress near the trailing edge was noted even in those cases which did not undergo transition or reattachment. The present results provide detailed documentation of the boundary layer and extend the existing database to lower  $Re$ . The present results also serve as a baseline for an investigation of turbulence spectra in Part 2 of the present paper, and for ongoing work involving transition and separation control.*

[DOI: 10.1115/1.1506938]

## Introduction

Modern low-pressure (LP) turbine airfoils are subject to increasingly stronger pressure gradients as designers impose higher loading in an effort to improve efficiency and lower cost by reducing the number of airfoils in an engine. If the adverse pressure gradient on the suction side of these airfoils becomes strong enough, the boundary layer will separate. Separation bubbles, particularly those which fail to reattach, can result in a significant loss of lift and a subsequent degradation of engine efficiency (e.g., Hourmouziadis [1], Mayle [2], and Sharma et al. [3]). The problem is particularly relevant in aircraft engines. Airfoils optimized to produce maximum power under takeoff conditions may still experience boundary layer separation at cruise conditions, due to the thinner air and lower Reynolds numbers at altitude. A component efficiency drop of 2% may occur between takeoff and cruise conditions in large commercial transport engines, and the difference could be as large as 7% in smaller engines operating at higher altitudes. Component life may also be affected by more than an order of magnitude (Hodson [4]). Because the LP turbine produces the bulk of the net power in many engines, changes in its component efficiency can result in nearly equal changes in overall engine efficiency (Wisler [5]). There are several sources for losses in an engine, including secondary flows, but the suction side boundary layer has been identified as the primary source of losses in the LP turbine (Curtis et al. [6]). Prediction and control of suction side separation, without sacrifice of the benefits of higher loading, is therefore, necessary for improved engine design.

Separation on LP turbine airfoils is complicated by boundary layer transition. Turbulent boundary layers are much more resis-

tant to separation than laminar boundary layers. A substantial fraction of the boundary layer on both sides of a turbine airfoil may be transitional (Mayle [2]), so accurately predicting transition location is crucial for accurate prediction of separation. Transition prediction for turbine airfoils is complex and can depend on a number of factors, including the free-stream turbulence intensity (FSTI), streamwise pressure gradient, airfoil curvature, surface roughness, and the unsteadiness associated with passing wakes from upstream stages. Several transition mechanisms are possible under engine conditions. Mayle [2] classified the modes of transition as “natural transition” involving Tollmien-Schlichting waves; “bypass” transition caused by high free-stream turbulence or other large disturbances; “separated flow” transition of the shear layer over a separation bubble; “periodic-unsteady” transition, which might also be called wake-induced transition; and reverse transition. If transition occurs far enough upstream, it can prevent separation. If transition occurs in the shear layer over a separation bubble, it will tend to induce boundary layer reattachment. The lower the Reynolds number, the farther downstream transition will tend to occur, hence the problems associated with performance at altitude.

Boundary layer transition has been studied extensively, and in recent years several studies have focused on transition in the LP turbine. Halstead et al. [7] present a study from a rotating cascade with multiple stages and FSTI characteristic of engine conditions. The adverse pressure gradients in this study were not strong enough to induce separation, however. Solomon [8] subsequently modified the facility and provides documentation of separation from a more aggressive airfoil. Gier and Ardey [9] provide another example from a rotating facility. Boundary layers and separation bubbles on flat plates subject to adverse pressure gradients have been considered in several studies. Recent work has included the studies of Hatman and Wang [10], Sohn et al. [11], Lou and Hourmouziadis [12], Volino and Hultgren [13] and Yaras [14]. On

Contributed by the International Gas Turbine Institute and presented at the International Gas Turbine and Aeroengine Congress and Exhibition, Amsterdam, The Netherlands, June 3–6, 2002. Manuscript received by the IGTI, January 22, 2002. Paper No. 2002-GT-30236. Review Chair: E. Benvenuti.

airfoils, either in cascade or single-passage cascade-simulators, studies have included Murawski et al. [15], Qiu and Simon [16] and Simon et al. [17]. Cascades with moving wakes, simulating the effect of upstream blade rows, were utilized by Brunner et al. [18], Stadtmüller et al. [19], Howell et al. [20] and Kaszeta et al. [21]. Numerical studies have included the work of Dorney et al. [22], Chernobrovkin and Lakshminarayana [23], Huang and Xiong [24], and Thermann et al. [25]. A few studies have included attempts to control transition and separation. Howell et al. [20] studied modified airfoil shapes, Van Treuren et al. [26] utilized vortex generators, and Lake et al. [27] considered various passive devices including dimples. Bons et al. [28] showed considerable success using both steady and pulsed vortex generator jets. The preceding list of studies, while long, is by no means inclusive. It is merely a sample of recent work, biased toward the most recent studies.

Much has been learned from the work to date, but the nature of separated flow transition is still not completely clear, and existing models are still not as robust as needed for accurate prediction. The present study expands the existing database. The flow through a single-passage cascade-simulator is documented under both high and low FSTI conditions at several different Reynolds numbers. The geometry of the passage corresponds to that of the “Pak-B” airfoil, which is an industry supplied research airfoil that is representative of a modern, aggressive LP turbine design. This geometry was used in several of the studies mentioned above ([15–17,21,23,24,27,28]), and the pressure profile from the suction side of this airfoil was matched in the flat plate study of Volino and Hultgren [13]. Previous work has included documentation at Re (based on suction surface length and exit free-stream velocity) as low as 50,000 (e.g., [13,16,21]). The present work includes the first complete documentation (to the author’s knowledge) of cases with Re as low as 25,000. Also new is documentation of the turbulent shear stress in the boundary layer under both high and low FSTI.

Details of the experimental facility and results of the study follow. The present paper focuses on mean and statistical quantities. Part 2 of this work [29] includes turbulence spectral results, providing evidence of the important transition mechanisms.

## Experiments

Experiments were conducted in a low speed wind tunnel, described by Volino et al. [30]. Briefly, air enters through blowers and passes through a series of screens, a honeycomb, two settling chambers, and a three-dimensional contraction before entering the test section. At the exit of the contraction, the mean velocity is uniform to within 1%. The FSTI is  $0.5 \pm 0.05\%$ . Nearly all of this free-stream “turbulence” is actually streamwise unsteadiness at frequencies below 20 Hz and is not associated with turbulent eddies. The rms intensities of the three components of the unsteadiness are 0.7, 0.2, and 0.2% in the streamwise, pitchwise and spanwise directions, respectively. For low FSTI cases, the test section immediately follows the contraction. For high FSTI, a passive grid is installed at the contraction exit followed by a 1 m long rectangular settling chamber. Details of the grid are available in Volino et al. [30]. At the inlet to the test section the high FSTI mean flow and turbulence are spatially uniform to within 3 and 6%, respectively. The free-stream turbulence is nearly isotropic with rms intensities of 8.8, 8.9, and 8.3% in the streamwise, pitchwise and spanwise directions. The integral length scales of these components are 3, 1.6, and 1.4 cm. The integral scales were computed from the power spectra of each component.

The test section, shown in Fig. 1, consists of the passage between two airfoils. Details are listed in Table 1. Cascade simulators of this type have been used in studies such as Chung and Simon [31], more recently in the present facility by Aunapu et al. [32], and with the PakB geometry by Qiu and Simon [16] and Kaszeta et al. [21]. A large span to chord ratio of 4.3 was chosen to insure two-dimensional flow at the spanwise centerline of the

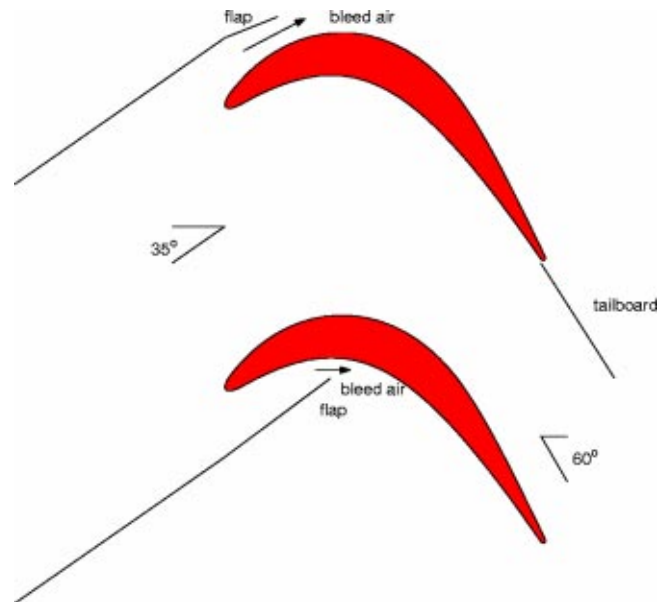


Fig. 1 Schematic of the test section

airfoils, where all measurements were made. Upstream of each airfoil are flaps, which control the amount of bleed air allowed to escape from the passage. These are adjusted to produce the correct leading edge flow and pressure gradient along the airfoils. A tailboard on the pressure side of the passage also aids in setting the pressure gradient.

Single passage test sections have several advantages. For a given wind tunnel with fixed maximum flow rate, the single passage can be considerably larger than a passage in a multi-blade facility. The larger size and simpler geometry can also result in better probe access. Previous studies (e.g., [31,32]) demonstrated that the full flow field, including the three-dimensional secondary flows near the endwalls, in a single passage can be set to match that in a corresponding multi-blade cascade. The present test section also has some advantages over flat plate test sections. First, the airfoil curvature is matched. Second, with an adverse pressure gradient, suction is often needed to prevent separation on the wall opposite a flat test plate (e.g., Volino and Hultgren [13]). A cascade simulator does not require suction due to the favorable pressure gradient on the pressure side of the passage.

Single passages also have disadvantages. It is, of course, impossible to establish periodicity. Stage losses cannot be directly determined since there is flow only on one side of each airfoil and the downstream wake is, therefore, unlike that in a multi-blade facility. This limitation, however, is not prohibitive for the present study. Primary concern is with boundary layer separation and transition, which occur *in the passage*. Although the downstream wake may be different, the flow in the passage does match that of a multi-blade facility.

Ten different cases have been documented including high and low FSTI cases at five Reynolds numbers ( $Re=25,000, 50,000, 100,000, 200,000, \text{ and } 300,000$ ). The Reynolds number range is representative of conditions from cruise to takeoff. The FSTI levels in an engine may vary considerably, but the values in the present work are believed to span the range of most interest. Solomon [8] surveyed several studies that included wake effects and

Table 1 Test section parameters

Axial Chord [mm]	True Chord [mm]	Pitch [mm]	Span [mm]	Suction side, $L_s$ [mm]	Inlet flow angle	Exit flow angle
153.6	170.4	136.0	660.4	228.6	35°	60°



**Table 2 Measurement stations locations, local acceleration (inviscid soln.), and measured local free-stream turbulence**

Station	$s/L_s$	$ReK$	Low FSTI $u'/U_\infty$ [%]	Low FSTI $v'/U_\infty$ [%]	High FSTI $u'/U_\infty$ [%]	High FSTI $v'/U_\infty$ [%]
1	0.111	1.58	0.44		5.2	
2	0.194	1.20	0.39		4.6	
3	0.278	0.86	0.37		4.0	
4	0.361	0.75	0.38		3.5	
5	0.444	0.62	0.39		3.2	
6	0.528	-0.02	0.41		2.8	
7	0.611	-0.81	0.47	0.05	2.9	5.9
8	0.694	-0.95	0.47	0.12	3.0	6.2
9	0.777	-0.58	0.48	0.14	3.4	6.6
10	0.861	-0.53	0.54	0.11	3.8	6.8
11	0.944	-0.18	0.51	0.11	4.0	6.8

found FSTI values ranging from 1 to 5% between wakes and from 3 to 23% within wakes. Wakes can affect transition and separation in the boundary layer in three ways. First, the FSTI rises during a wake passage compared to the between-wake value. Second, a calmed region follows wake induced transition. The calmed flow is nonturbulent, but unlike a steady nonturbulent flow, it can be very resistant to separation. Finally, independent of the FSTI effect, each wake includes a mean velocity deficit, resulting in temporal deceleration and acceleration as the wake passes. Lou and Hourmouziadis [12] separated this temporal effect from the wake turbulence effect, using downstream control to create an oscillating velocity in their test section. In the present study, only steady flow is considered. While the significant effects of temporal acceleration and calming are not present, the high and low FSTI cases of the present study do allow a means for evaluating the effect of wake turbulence level.

**Measurements.** Pressure surveys were made for each case using a pressure transducer (0–870 Pa range Validyne transducer) and a Scanivalve. Stagnation pressure was measured with a pitot tube upstream of the passage inlet, and eleven pressure taps were located on each airfoil along their spanwise centerlines. Locations of the taps on the suction side are listed in Table 2 along with measured local FSTI components, and the  $ReK$  product at these stations based on a nonseparating, inviscid solution. The pressure distribution on the upstream portion of the suction side always closely matched the inviscid solution for flow over the airfoil. This allowed the use of the measured static pressure at the third pressure tap on the suction side, along with the inviscid flow solution for the passage and the upstream stagnation pressure, to determine the nominal passage exit velocity, which was used to normalize the measured pressure distributions. More conventionally the measured inlet velocity and the inlet and exit flow angles are used to compute the exit velocity. Because the velocity at the third tap is 1.9 times that at the passage inlet, and therefore easier to measure, using the third tap velocity reduced the bias uncertainty in the pressure coefficients, particularly at the lower Reynolds numbers. The uncertainty in the suction side pressure coefficients was 7% at the lowest  $Re$ , and below 4% in other cases. Most of this uncertainty was due to bias error. Stochastic error was minimized by averaging pressure transducer readings over a 10-s period.

Velocity profiles were measured at eleven streamwise stations along the suction side at the locations given in Table 2. Profiles were measured near but not at the spanwise centerline of the airfoil to insure that the pressure taps did not interfere with the velocity measurements. Profiles were acquired with a hot-wire anemometer (TSI model IFA100) and a single sensor boundary layer probe (TSI model 1218-T1.5). The sensor diameter is 3.8  $\mu\text{m}$ , and the active length is 1.27 mm. At each measurement location, data were acquired for 26 seconds at a 20 kHz sampling

rate ( $2^{19}$  samples). All raw data were saved. The high sampling rate provides an essentially continuous signal, which is needed for intermittency and spectral post-processing. The long sampling time results in low uncertainty in both statistical and spectral quantities. Data were acquired at 60 wall normal locations in each profile, extending from the wall to the free-stream, with most points concentrated in the near wall region. The closest point was 0.1 mm from the wall, which corresponds to  $y/L_s = 0.0004$  and between 0.01 and 0.2 boundary layer thicknesses. Flow direction in a separation bubble cannot be determined with a single-sensor hotwire, but velocity magnitude can be measured and was found to be essentially zero within the bubbles of the present cases. Determining the direction was not, therefore, considered essential. At locations where the boundary layer was attached, local wall shear stress was computed from the near wall profile using the technique of Volino and Simon [33]. Uncertainties in the mean velocity are 3–5%, except in the very near wall region ( $y^+ < 5$ ) where near-wall corrections (Wills [34]) were applied to the mean velocity. Uncertainties in the momentum and displacement thicknesses computed from the mean profiles are 10%. Uncertainty in the shape factor,  $H$ , and the wall shear stress are both 8%.

The uncertainty in the fluctuating streamwise velocity is below 10%, except in the very near wall region, where spatial averaging effects become important in some cases. Ligrani and Bradshaw [35,36] showed that spatial averaging over the length of a hot-wire sensor can result in low apparent  $u'$ . Their experiments were done in a fully-turbulent boundary layer with  $Re_\theta = 2600$ . The spatial averaging effects become important when the sensor length is longer than the width of the smaller near wall streaks in a turbulent boundary layer. Ligrani and Bradshaw [35,36] found that the spatial averaging effects become small when the dimensionless sensor length,  $l/u_\tau/\nu$ , is less than about 25. The error also becomes smaller as the sensor is moved away from the wall. This is expected since the average size of the turbulent eddies should increase with distance from the wall. The Ligrani and Bradshaw [35,36] results suggest that when the distance from the wall,  $y$ , is larger than the sensor length,  $l$ , that spatial averaging errors are under 10% even for large  $l/u_\tau/\nu$ . Closer to the wall they showed errors in  $u'$  as large as 30% when  $l/u_\tau/\nu = 60$ .

In the present study,  $l/u_\tau/\nu$  remains below 25 in all cases with  $Re < 200,000$ . Spatial averaging is not, therefore, expected to be a problem, even near the wall. For the  $Re = 200,000$  cases,  $l/u_\tau/\nu$  is above 25 at Station 11 of the low FSTI case and at Stations 9–11 of the high FSTI case, reaching values as high as 60. Spatial averaging should not be significant for  $y > 1$  mm ( $y/L_s > 0.004$ ), but may cause errors as high as 30% closer to the wall. It is not certain that the errors are this large, however. The momentum thickness Reynolds numbers in the present cases are all below 700, which is significantly below the  $Re_\theta = 2600$  value of the Ligrani and Bradshaw [35,36] study. This may indicate less developed turbulence in the present study, which could imply fewer small-scale eddies and lower averaging errors. For the  $Re = 300,000$  cases,  $l/u_\tau/\nu$  reaches values as high as 90 at Stations 10 and 11 of the low FSTI case and Stations 9–11 of the high FSTI case. As in the  $Re = 200,000$  cases, errors should be small when  $y > 1$  mm, but may be larger closer to the wall.

A boundary layer cross-wire probe (TSI model 1243-T1.5) was used to measure profiles of the wall normal velocity and turbulent shear stress at Stations 7–11 for each case. The upstream boundary layer was too thin for cross-wire measurements. Data were acquired at 25 locations in each profile, beginning 1 mm from the wall and extending to the free-stream. Sampling rates and times were the same as for the single sensor probe. Uncertainty in the turbulent shear stress is 10%.

Measurements with the cross-wire probe are subject to spatial averaging errors due to the length of the sensors (1.27 mm active length) and the spacing between the two sensors (1 mm). Applying the results of Ligrani and Bradshaw [35,36] and Ligrani et al. [37] to the present cases, spatial averaging may be significant at

locations very near the wall, particularly for the high Reynolds number cases. At locations farther from the wall than 1 mm, however, the errors should become small and within the 10% uncertainty estimate given in the foregoing. Hence, no measurements were made at  $y$  locations below 1 mm. Because all measurements were at  $y > 1$  mm and a boundary layer type probe was used, probe blockage effects were not expected to be significant.

The intermittency,  $\gamma$ , is the fraction of time the flow is turbulent within the transition region, and was determined at each measurement location using the technique described in Volino et al. [30] with an uncertainty of 10%. Turbulent flow in the boundary layer is defined here as flow which includes a range of large and small scales, turbulence production, and dissipation. Using this definition, a boundary layer may be characterized by significant fluctuations, but still be nonturbulent if these fluctuations are induced by an external source which does not cause near-wall turbulence production. Such is often the case under high FSTI conditions. Free-stream eddies “buffet” the boundary layer, inducing nonturbulent boundary layer fluctuations. Buffeting may occur through pressure fluctuations. Boundary layer fluid is pushed in the wall normal direction across the mean gradient in the streamwise velocity, resulting in significant  $u'$  fluctuations. This type of motion was termed “inactive” by Bradshaw [38] since it does not result in momentum transport, in spite of potentially high  $u'$  levels. In addition to buffeting, some free-stream eddies may penetrate into the boundary layer and cause some mixing. As described in Volino [39], the eddies which have the greatest effect, whether through buffeting or penetrating the boundary layer, will be the larger, energy containing eddies. The nonturbulent boundary layer subject to these external effects will be characterized by large-amplitude, low-frequency fluctuations. Transition to turbulence is characterized not so much by large increases in  $u'$  levels, which may remain essentially constant, but by the appearance of higher frequencies superimposed on the low frequencies. The higher frequencies signal the generation of turbulence in the near wall region. Volino et al. [30] provide examples of an intermittent flow switching in time between disturbed nonturbulent and turbulent states.

The presence or absence of high frequencies in a signal is used to distinguish between turbulent and nonturbulent flow, using the algorithm presented by Volino et al. [30]. The algorithm is similar to others found in the literature. Briefly, the time derivative of a signal is computed and compared to a threshold. Rapid (high-frequency) fluctuations result in high derivatives. When the derivative is larger than the threshold, the flow is declared instantaneously turbulent and the intermittency function is assigned a value of 1. When the derivative is below the threshold, the intermittency is assigned a value of 0. The time average of the function is the intermittency,  $\gamma$ . Volino et al. [30] showed that intermittency can be computed based on  $u'$  or  $u'v'$  signals with essentially the same result. Results based on  $u'$  are presented in this paper.

## Results

**Pressure Profiles.** Pressure coefficients for all ten cases are shown in Fig. 2. At the upstream stations on the suction side, there is good agreement between the data at all Reynolds numbers and the inviscid flow solution. Separation appears to occur at  $s/L_s$  of about 0.6 in all cases. These results agree with those of Volino and Hultgren [13], who also observed that the separation location did not depend strongly on the Reynolds number or FSTI. They are in contrast to other studies, such as Qiu and Simon [16], which showed that the separation location depended more strongly on Re. Reattachment depends strongly on both Re and FSTI. With low FSTI (Fig. 2(a)), the boundary layer appears to be separated in all cases at Stations 8 and 9. It reattaches by Station 10 for the Re=200,000 and 300,000 cases, reattaches by Station 11 for the Re=100,000 case, and does not reattach at all for the Re=25,000 and 50,000 cases. Reattachment for the high FSTI cases

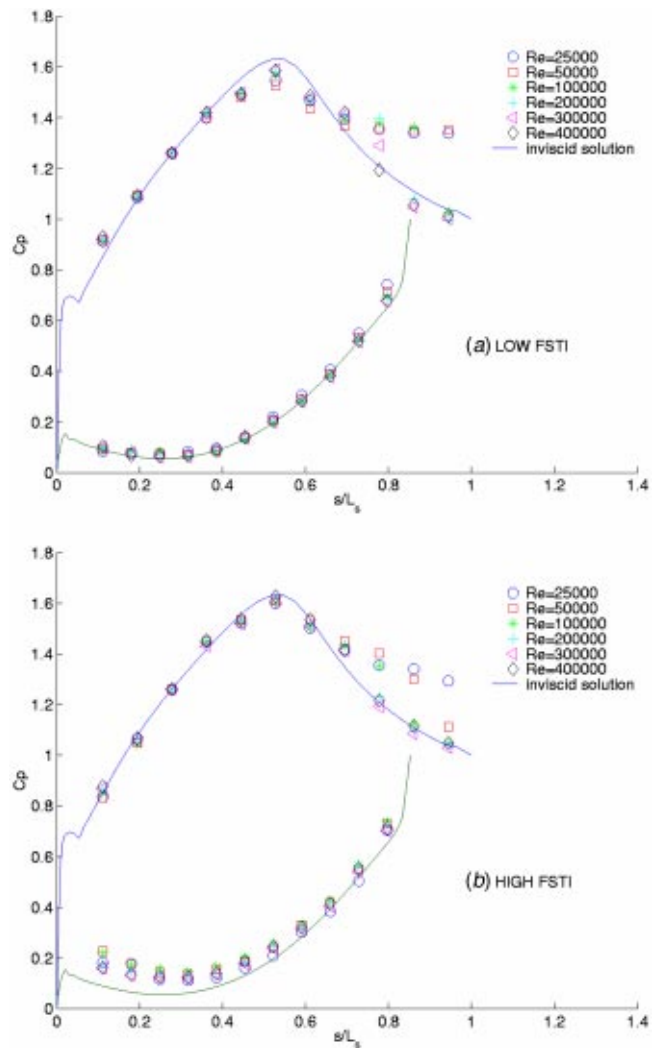


Fig. 2  $C_p$  profiles: (a) low FSTI, (b) high FSTI

(Fig. 2(b)) occurs upstream of the low FSTI locations. The boundary layer appears to be separated in all cases at Station 8, but has already reattached by Station 9 in the Re=200,000 and 300,000 cases. Reattachment has occurred by Station 10 for the Re=100,000 case, and appears to be beginning at Station 11 for the Re=50,000 case. The boundary layer does not appear to reattach when Re=25,000, in spite of the high FSTI. Results for the low FSTI cases are very similar to the flat plate results of Volino and Hultgren [13]. The present high FSTI results appear to show about a 10% larger separation region than the flat plate cases of [13]. The differences are small and of the order of the resolution of the measurement stations. Any differences between the studies are presumably due to differences in the free-stream turbulence. Although the high FSTI in both studies was about 8%, the inlet free-stream turbulence was more anisotropic in Volino and Hultgren [13], and the integral length scales of the free-stream turbulence in [13] were about double those in the present study. The larger length scale presumably caused earlier transition in the Volino and Hultgren [13] study, resulting in a slightly shorter separation bubble. Comparison to the high FSTI cases of Simon et al. [17] shows reattachment about 14% farther upstream in [17] than in the present study. With low FSTI, Simon et al. [17] did not observe reattachment at all when Re=100,000, while it was observed in the present study. For the low FSTI Re=200,000 case, they indicate reattachment about 6% farther upstream than the present study. Although the streamwise pressure gradients were

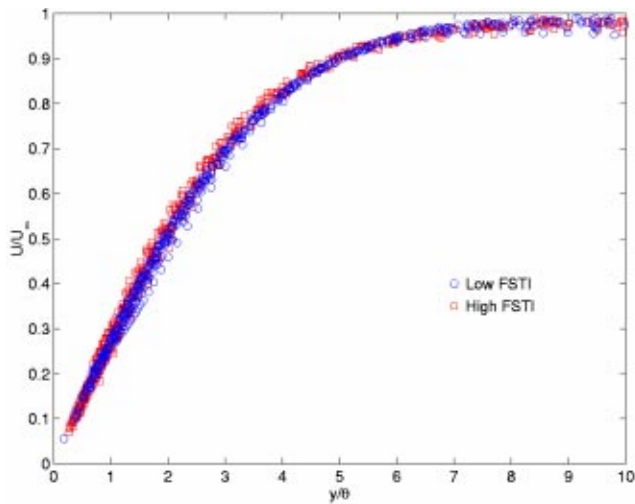


Fig. 3 Mean velocity profiles from Station 1–5, all cases

nominally the same in the present study and Simon et al. [17], small differences in the pressure gradients along with differences in the intensity and length scales of the free-stream turbulence were apparently responsible for the differences in reattachment location.

**Upstream Boundary Layer.** The local free-stream velocities at Station 1–5 for all 10 cases closely followed the equation

$$\frac{U_\infty}{U_e} = 1.48 \left( \frac{s}{L_s} \right)^{0.214} \quad (1)$$

which corresponds to the free-stream velocity distribution for a Falkner-Skan wedge flow. Figure 3 shows that the 50 mean velocity profiles from all 10 cases at these stations collapse onto the same Falkner-Skan profile. Skin friction coefficients, shown in Fig. 4, which were computed using the near wall profiles, also follow the Falkner-Skan solution. There is no significant difference between the low and high FSTI cases. Agreement with the flat plate data of Volino and Hultgren [13] is good. For the low FSTI cases, it is not surprising that the laminar boundary layer closely follows the expected laminar solution. Under the same high FSTI inlet conditions, however, Volino et al. [30] showed that a non-turbulent boundary layer may be strongly influenced by

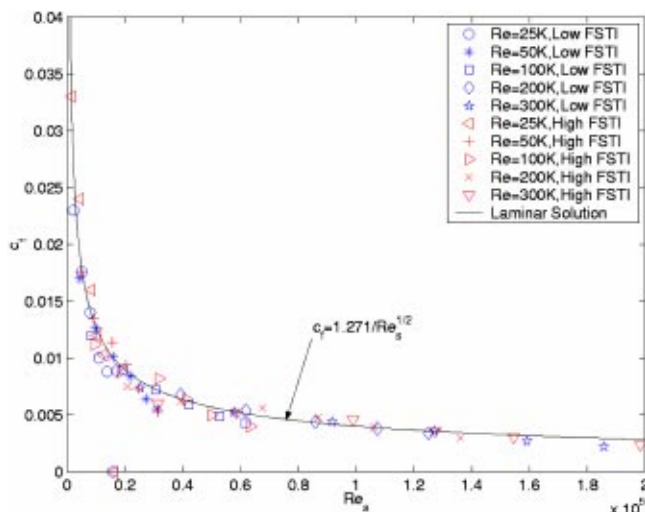


Fig. 4 Skin friction coefficients from Station 1–6, all cases

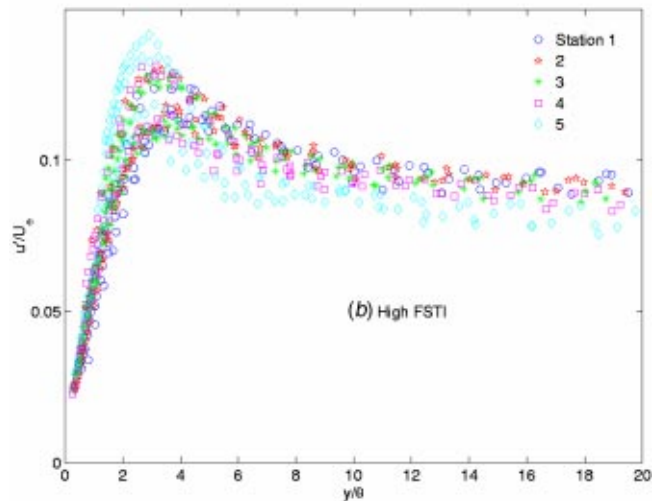
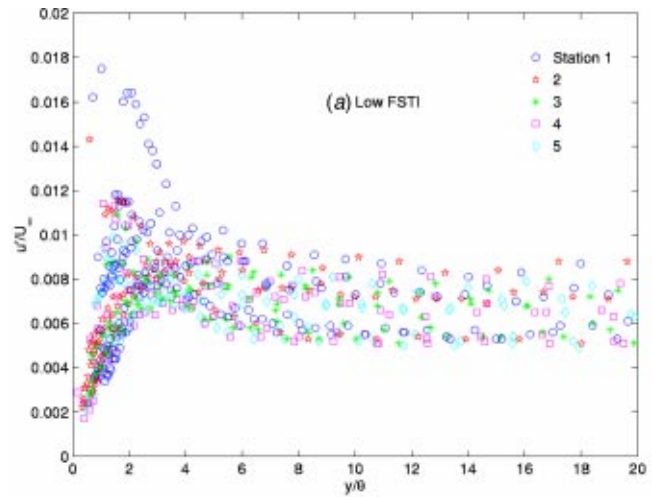
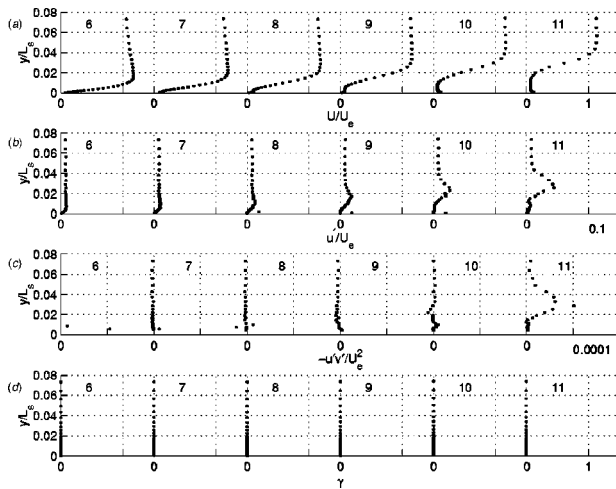


Fig. 5 Boundary layer  $u'$  profiles from Stations 1–5—(a) low FSTI cases, (b) high FSTI cases

the free-stream turbulence and exhibit large deviation from laminar behavior. In the present study, the acceleration parameter,  $K$ , is in some of the cases over 10 times larger than in the Volino et al. [30] study, and the boundary layer thickness is as little as 1/5 that in [30]. These differences apparently limit the free-stream effect on the upstream boundary layer, resulting in the observed laminar-like behavior.

Figure 5 shows profiles of the rms fluctuating streamwise velocity,  $u'$ , for the 50 upstream profiles. The low FSTI  $u'$  is mainly streamwise unsteadiness that scales with the local  $U_\infty$ . Values are low everywhere, increasing slightly from the free-stream value to a peak at  $y/\theta=3$  and then dropping to zero at the wall. For the high FSTI cases the free-stream  $u'$  level does not change significantly within the test section and scales with  $U_e$ . Since the boundary layer fluctuations are caused by the free-stream fluctuations, the  $u'$  profiles collapse when normalized on  $U_e$ . The collapse is not perfect since the free-stream  $u'$  does drop somewhat as the eddies are strained in the accelerating flow. Qualitatively the behavior is the same as in the low FSTI cases, with high values in the free-stream rising to a peak at  $y/\theta=3$  and dropping to zero near the wall. The peak in  $u'$  has lower magnitude and is farther from the wall than would be expected in a turbulent boundary layer. In all cases the boundary layer is clearly laminar-



**Fig. 6 Station 6–11 profiles for low FSTI, Re=25,000 case—(a) mean velocity, (b)  $u'$ , (c)  $-u'v'$ , (d) intermittency**

like in spite of the high  $u'$  level. This is shown in both the mean velocity profiles (Fig. 3) and the local skin friction coefficients (Fig. 4) which follow laminar flow solutions.

**Low FSTI Transition.** Downstream of Station 6, the pressure gradient becomes adverse and separation and transition occur. Figures 6 through 10 show profiles at Stations 6–11 of  $U$ ,  $u'$ , the turbulent shear stress,  $-u'v'$ , and the intermittency,  $\gamma$ , for the five low FSTI cases. The  $v'$  profiles are qualitatively very similar to the  $-u'v'$  profiles in all cases and are not shown. In the Re = 25,000 case (Fig. 6), the mean velocity profile has just separated at Station 7, and the separation bubble grows continuously larger at the downstream stations. There is no reattachment, but rather a massive separation with a burst bubble at the trailing edge. The intermittency is nearly zero everywhere, indicating that the shear layer remains essentially laminar. Although the flow is laminar,  $u'$  is nonzero. The  $u'$  peak grows as the flow moves downstream, and its location is concurrent with the inflection point in the mean profile. The  $-u'v'$  values remain near zero through Station 10, but then rise at Station 11 with a peak in the shear layer at the same location as the  $u'$  peak. The magnitude of this peak is extremely low; the eddy viscosity at the peak is only about 1/30th of the molecular kinematic viscosity. Although not significant in terms of eddy transport, this peak may signify the beginning of transition.

Figure 7 shows the profiles for the Re=50,000 case. Results are very similar to the Re=25,000 case of Fig. 6. The boundary layer does not reattach. The  $-u'v'$  profile at Station 11 again exhibits a low level peak. The dimensionless value of this peak is about three times that of the peak in Fig. 6, indicating that the Re = 50,000 case may be closer to transitioning.

Results for the Re=100,000 case are shown in Fig. 8. The mean velocity profiles show that the boundary layer is on the verge of separating at Station 7, but is still attached. It has separated by Station 8, and the separation bubble grows through Station 10, although it does not become as thick as in the lower Re cases. At Station 10, the mean velocity near the wall rises slightly above zero, indicating the beginning of reattachment. At Station 11 the boundary layer is clearly reattached. The intermittency is near zero through Station 10, and then suddenly increases to 1 at Station 11, indicating fully turbulent flow as the boundary layer reattaches. The peak in the intermittency is well away from the wall, indicating that transition begins in the shear layer over the separation bubble. The  $u'$  profiles exhibit a peak in the shear layer at Stations 8 and 9, similar to the behavior at the lower Re. At Station 10 there is an increase in  $u'$  near the wall as reattachment

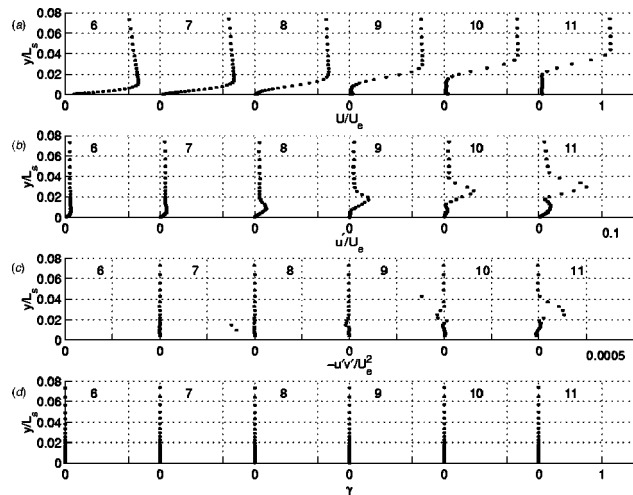


**Fig. 7 Station 6–11 profiles for low FSTI, Re=50,000 case—(a) mean velocity, (b)  $u'$ , (c)  $-u'v'$ , (d) intermittency**

begins. The turbulent shear stress profile rises above zero at Station 10 with a dimensionless value that is an order of magnitude larger than the peak shown in Fig. 7 for the Re=50,000 case. At Station 11 the magnitude of the peak has increased by another order of magnitude and the boundary layer is clearly turbulent. The peak in  $-u'v'$  is well away from the wall, indicating that while the boundary layer is turbulent and reattached, it has not yet recovered to fully developed turbulent conditions.

Figure 9 shows the profiles for the Re=200,000 case. The mean velocity profiles indicate that separation does not occur until near Station 8. There is a clear separation bubble at Station 9, and the boundary layer is reattached by Station 10. By Station 11 the mean profile appears to have recovered to a fully developed turbulent shape. The intermittency jumps from near 0 at Station 9 to 1 at Station 10, indicating a rapid transition and reattachment. The magnitude of  $u'$  increases similarly, from a small peak near the inflection point of the mean profile at Station 9 to high values throughout the boundary layer at Station 10. The turbulent shear stress profiles show the same sudden increase between Stations 9 and 10, and the peak is still away from the wall at Station 11, indicating that recovery from separation may not be fully complete.

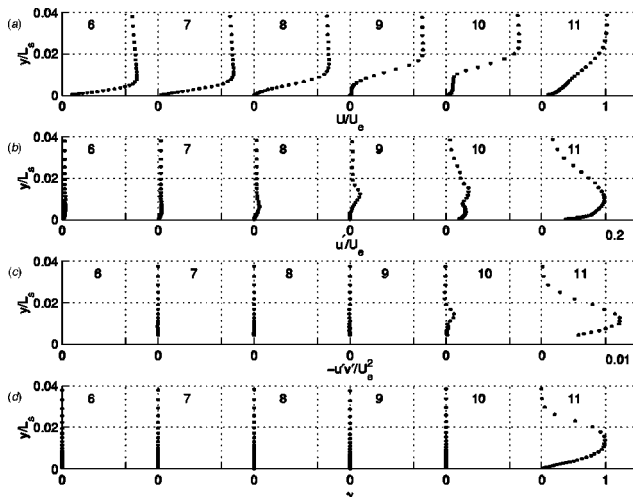


**Fig. 8 Station 6–11 profiles for low FSTI, Re=100,000 case—(a) mean velocity, (b)  $u'$ , (c)  $-u'v'$ , (d) intermittency**

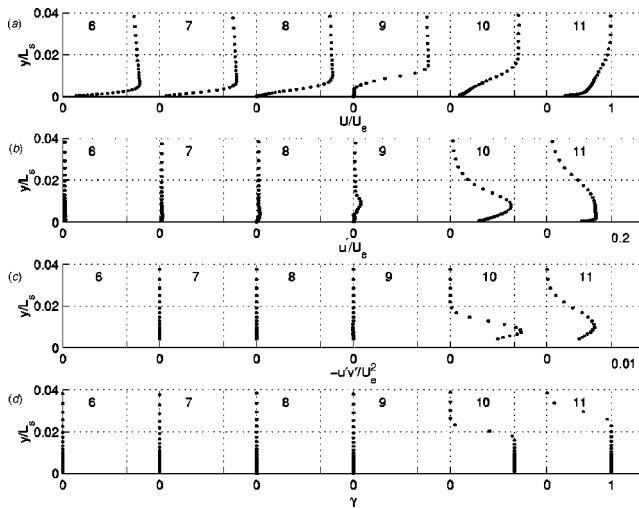


**Fig. 9 Station 6–11 profiles for low FSTI, Re=200,000 case— (a) mean velocity, (b)  $u'$ , (c)  $-u'v'$ , (d) intermittency**

The Re=300,000 case profiles are shown in Fig. 10. Separation again occurs near Station 8. By Station 9 the separation bubble has clearly grown and the nonzero mean velocities near the wall indicate that the boundary layer is on the verge of reattachment. The  $u'$  values increase greatly between Stations 8 and 9. The  $u'$  profile has a peak in the shear layer over the separation bubble and a second peak near the wall, which is indicative of reattachment. The intermittency profile at Station 9 shows this same double peak. The boundary layer is reattached and fully turbulent by Station 10. The turbulent shear stress profile rises to a small but discernable nonzero level at Station 9, corresponding to the beginning of reattachment and the rise of the intermittency. By Station 11,  $-u'v' = u_\tau^2$  near the wall, which would be expected for a fully developed, attached turbulent boundary layer.

The velocity data of Figs. 6–10 agree with the pressure profiles of Fig. 2(a). The separation locations agree, although the velocity profiles provide better resolution and indicate that separation does move downstream somewhat as Reynolds number increases. The reattachment locations indicated by the pressure profiles correspond to locations where the velocity profiles have clearly reattached. Incipient reattachment is visible in the mean velocity one station upstream of full reattachment in some cases. In all cases

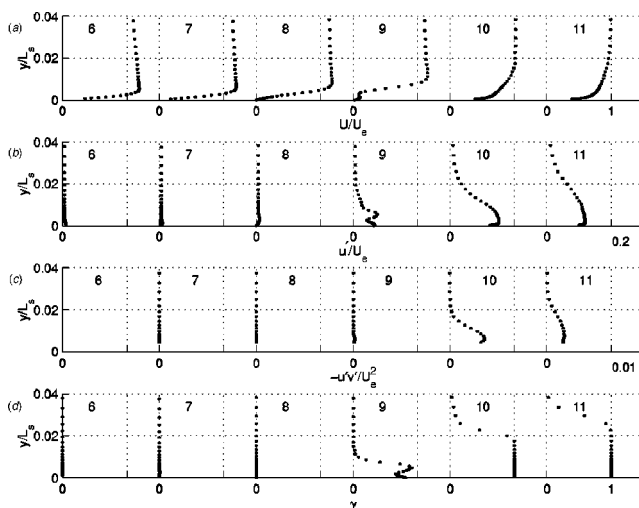


**Fig. 10 Station 6–11 profiles for low FSTI, Re=300,000 case— (a) mean velocity, (b)  $u'$ , (c)  $-u'v'$ , (d) intermittency**

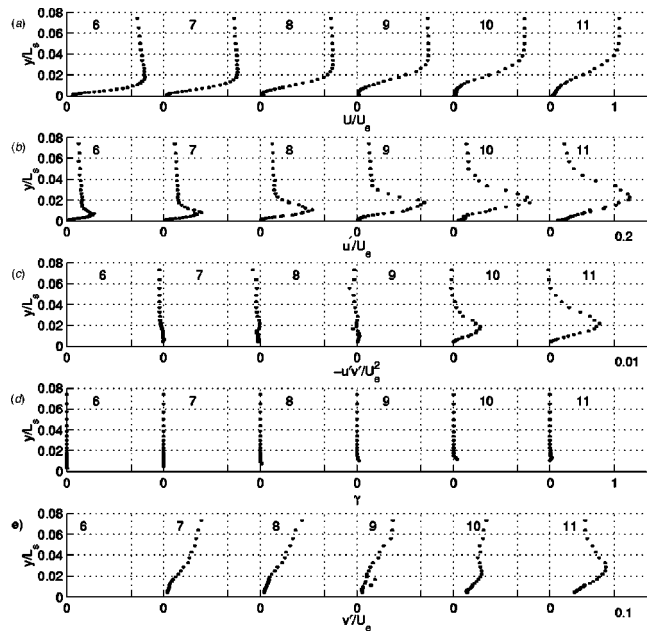


**Fig. 11 Station 6–11 profiles for high FSTI, Re=25,000 case— (a) mean velocity, (b)  $u'$ , (c)  $-u'v'$ , (d) intermittency, (e)  $v'$**

the magnitude of  $u'$  begins to increase in the shear layer after separation. At first this increase in  $u'$  occurs without a corresponding increase in  $-u'v'$ , which remains near zero, and the shear layer remains laminar. As the flow continues downstream, low but nonzero  $-u'v'$  values eventually appear in the shear layer, and at the higher Reynolds numbers this is quickly followed by a rapid rise of  $-u'v'$ , sudden transition to turbulence, and almost immediate reattachment of the boundary layer. At the two lowest Reynolds numbers, the initial rise in  $-u'v'$  was detected, but it occurred so far downstream that transition and reattachment never occurred. The present results are consistent with those of Hatman and Wang [10], Lou and Hourmouziadis [12], and Volino and Hultgren [13], who also considered low FSTI separated flow transition. They also reported rapid transition and attributed it to the breakdown of a Kelvin-Helmholtz-type instability of the shear layer. The transition mechanism in the present study will be discussed in more detail in Part 2 [29].

**High FSTI Transition.** Profiles for the high FSTI cases are shown in Figs. 11–15. For the Re=25,000 case (Fig. 11), the mean velocity profiles show that the boundary layer has separated by Station 6. The boundary layer appears on the verge of reattaching at Stations 10 and 11, but is not clearly reattached. The  $u'$  level rises rapidly after separation, with a peak in the shear layer at each station. The free-stream buffets the shear layer, forcing fluid across a large mean velocity gradient,  $dU/dy$ , which causes high  $u'$  levels. The same effect is present in the attached boundary layer upstream (Fig. 5b), but is damped somewhat by the wall. Free-stream buffeting and high  $u'$  do not necessarily imply turbulent transport, and the turbulent shear stress remains low through Station 9. The  $-u'v'$  level rises to high levels at Stations 10 and 11, but the peak is in the shear layer and drops to zero at the wall. Perhaps at this very low Reynolds number, even significant transport in the shear layer is insufficient to promote full reattachment of the boundary layer. Turbulent reattachment may be an intermittent phenomenon, related to and much like transition. At the lower Re it may occur over an extended distance. The intermittency indicates that the flow remains nonturbulent, in spite of the high levels of  $-u'v'$  at the downstream stations. The intermittency function, as defined above, only declares the flow turbulent when

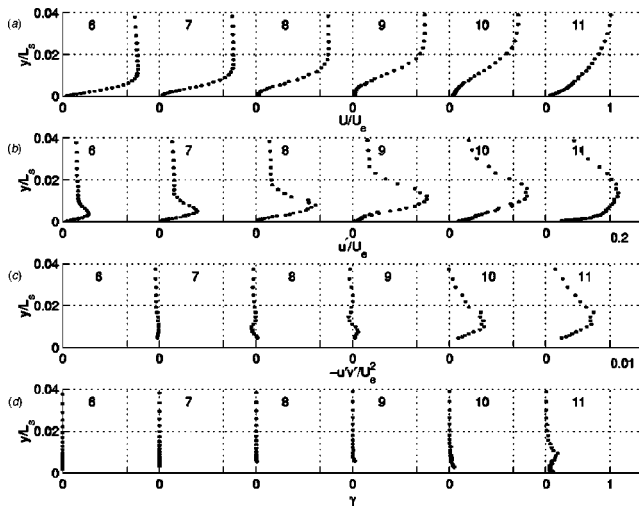


**Fig. 12 Station 6–11 profiles for high FSTI, Re=50,000 case—(a) mean velocity, (b)  $u'$ , (c)  $-u'v'$ , (d) intermittency**

the velocity fluctuations include a full range of both large and small scales. The apparent mismatch between the  $-u'v'$  and  $\gamma$  profiles of Fig. 11 may indicate that the fluctuations which cause the turbulent shear stress initially do not include this range of scales. Turbulent shear stress spectra are presented in Part 2 [29]. Profiles of the wall normal fluctuating velocity,  $v'$ , are also shown in Fig. 11. At Stations 7–9, high free-stream values drop to zero at the wall, with no peak corresponding to the peak in  $u'$ . The free-stream buffeting effect on  $v'$  is damped by the wall, a phenomenon also observed in attached, nonturbulent boundary layers under high FSTI conditions (Volino et al. [30]). A peak emerges in  $v'$  in the shear layer at Station 10 and 11, corresponding completely with the rise in  $-u'v'$  at these stations. The link between  $v'$  and  $-u'v'$  was clear at all Re, making it unnecessary to present both  $v'$  and  $-u'v'$  for the remaining cases.

The Re=50,000 case of Fig. 12 is very similar to the Re=25,000 case. Reattachment is clearer, however, at Station 11, and the intermittency is nonzero at this station. Figure 13 shows the Re=100,000 case. In this case the intermittency indicates that transition has begun by Station 9, which corresponds to an initial rise in  $-u'v'$ . The mean profile shows that the boundary layer is

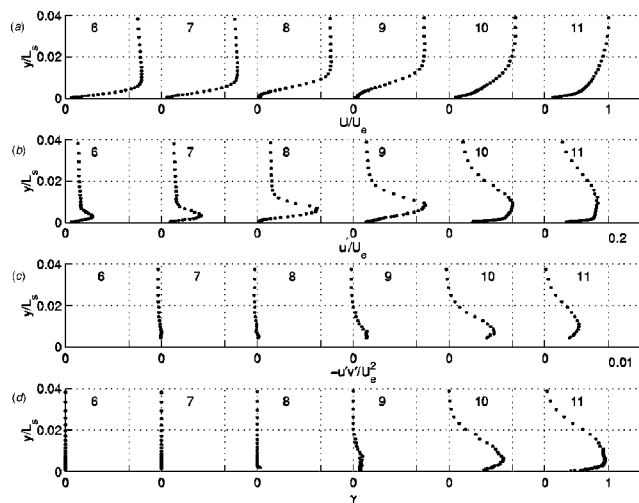


**Fig. 13 Station 6–11 profiles for high FSTI, Re=100,000 case—(a) mean velocity, (b)  $u'$ , (c)  $-u'v'$ , (d) intermittency**

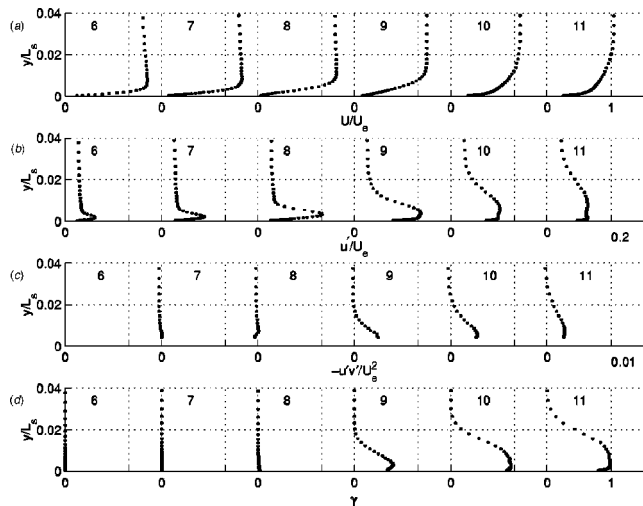


**Fig. 14 Station 6–11 profiles for high FSTI, Re=200,000 case—(a) mean velocity, (b)  $u'$ , (c)  $-u'v'$ , (d) intermittency**

reattached at the last two stations. The high  $-u'v'$  peaks away from the wall indicate that the boundary layer has not fully recovered from the separation at Station 11.

It is not clear that separation occurs in the Re=200,000 case (Fig. 14), but the velocity mean profile at Station 8 has an inflection point and appears to be close to separating. By Station 9 the boundary layer is clearly attached, the intermittency indicates transition is underway,  $u'$  is high even near the wall, and  $-u'v'$  has risen to a turbulent level. At Station 11,  $-u'v'$  reaches a maximum equal to  $u_e^2$  near the wall, indicating a fully developed attached turbulent flow.

The Re=300,000 results of Fig. 15 are very similar to those at Re=200,000. Transition begins slightly earlier at Re=300,000, with the intermittency greater than zero at Station 8. The thin boundary layer at Re=300,000 results in peaks in  $-u'v'$  at Stations 9 and 10 that are too close to the wall to resolve with the cross-wire probe.

In general, transition in the high FSTI cases began upstream of the locations in the corresponding low FSTI cases, and the transition region length was longer with high FSTI. This agrees with the observations of Volino and Hultgren [13], who also observed

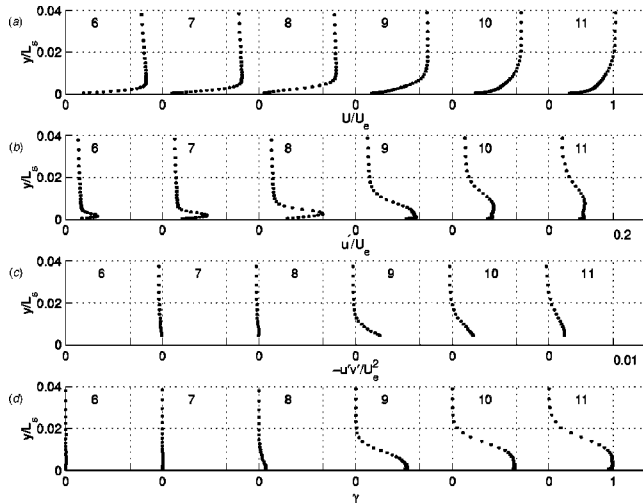


**Fig. 15 Station 6–11 profiles for high FSTI, Re=300,000 case—(a) mean velocity, (b)  $u'$ , (c)  $-u'v'$ , (d) intermittency**

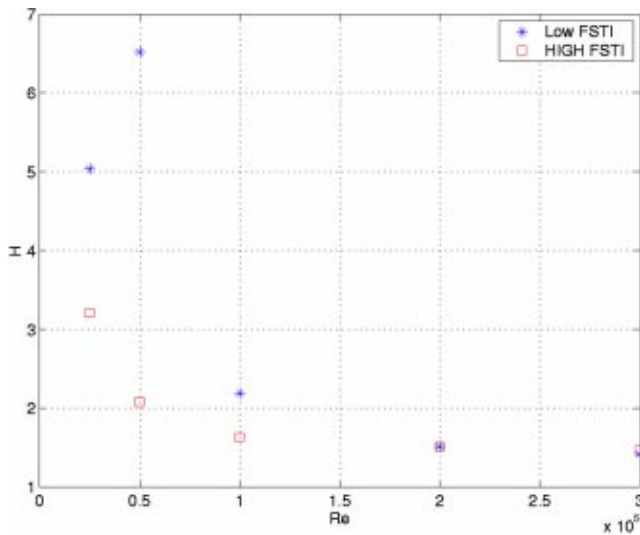


Fig. 16 Shape factor at Station 11

that transition was less abrupt with high FSTI. Boundary layer  $u'$  levels are much higher with high FSTI, but the turbulent shear stress magnitude remains low until transition begins and does not appear to depend strongly on FSTI.

**Shape Factor and Momentum Thickness.** As discussed above, stage losses cannot be determined quantitatively using a single passage test section, but is possible to compute the momentum thickness of the suction side boundary layer at the trailing edge. As explained by Howell et al. [20], this momentum thickness is proportional to the suction side profile loss when the boundary layer shape factor and passage exit angle remain constant. For those cases in which the boundary layer reattaches and recovers to a fully developed turbulent shape,  $H$  is approximately equal to 1.4. In these cases the suction side profile loss is likely the dominant loss mechanism (Howell et al. [20]). In those cases in which the boundary layer does not fully reattach, or reattaches near the trailing edge, the shape factor will be very large due to a large displacement thickness. The momentum thickness may be relatively small compared to the displacement thickness in these cases, since the wall shear is essentially zero and  $\theta$  will not grow significantly in the free-shear layer. Large losses would then be expected in the wake, downstream of the airfoil.

Figure 16 shows the shape factor at Station 11 ( $s/L_s = 0.94$ ) as a function of  $Re$ . In the  $Re = 200,000$  and  $300,000$  cases, the shape factor is approximately 1.4, indicating that the boundary layer is reattached and that the momentum thickness is a good indicator of overall losses. For the lower  $Re$  cases,  $H$  is significantly higher, particularly in the low FSTI cases. The lower  $H$  in the high FSTI cases indicates that high FSTI helps to keep the separation bubble thinner by promoting more mixing in the shear layer over the bubble and by inducing earlier transition and reattachment. Figure 17 shows the Station 11 momentum thickness as a function of  $Re$ . High FSTI helps keep the separation bubble thinner, as shown above in the mean velocity profiles of Figs. 6–15, which tends to result in lower  $\theta$  and lower losses when the boundary layer reattaches. High FSTI also promotes increased mixing, however, which tends to increase  $\theta$ . For the  $Re = 300,000$  cases, Fig. 17 indicates that the second effect is more significant and  $\theta$  is higher for the high FSTI case. Transition and reattachment occur sufficiently far upstream in the low FSTI case that the effect of the high FSTI in promoting even earlier reattachment is not enough to counter the enhanced mixing effects. This suggests that small, controllable separation bubbles may be acceptable or even desirable in some cases, as proposed by Hourmouziadis [1] for controlled diffusion blading. For the  $Re = 200,000$  and  $100,000$  cases,

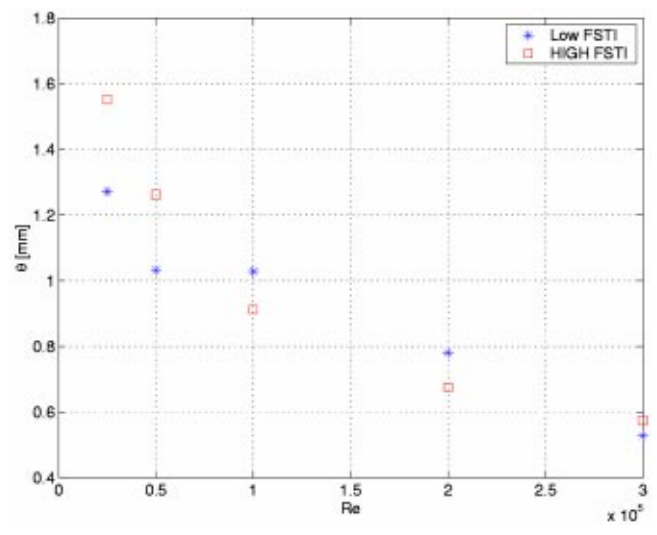


Fig. 17 Momentum thickness at Station 11

the earlier reattachment caused by high FSTI is more significant and  $\theta$  is lower for the high FSTI cases. This result is consistent with the observation in several studies that unsteady wakes from upstream airfoils result in lower losses. Enhanced mixing in the shear layer explains the higher  $\theta$  for the high FSTI cases at  $Re = 25,000$ . These momentum thicknesses do not relate directly to losses since the shear layer does not reattach in either of the  $Re = 25,000$  cases.

**Comparison to Correlations.** Hatman and Wang [10] discuss three modes of separated flow transition. Based on their criteria, the present cases all fall into their laminar-separation long-bubble category. The data support this; separation occurred before transition. Hatman and Wang [10], Mayle [2] and others suggest that the Thwaites [40] criteria,  $Re_\theta^2 K = -0.082$ , is a good predictor for laminar separation. A laminar, attached flow solution would put  $Re_\theta^2 K = -0.082$  between Stations 6 and 7 in all cases of the present study. The presence of the separation bubble changes the local acceleration, however, which tends to move the location where  $Re_\theta^2 K = -0.082$ . Volino and Hultgren [13] found the Thwaites criteria to be a good predictor of separation and it appears to work well for the present study as well. Exact prediction of the separation point is not straightforward, however, due to the interdependence of local  $K$  values and the separation bubble location.

Prediction of transition and reattachment is more difficult. Hatman and Wang [10] present a transition correlation based on low FSTI data which predicts that transition should not occur in any of the present cases. Clearly, however, transition and reattachment do occur. The  $-u'v'$  profiles indicate that transition is imminent even in the low FSTI, low  $Re$  cases. Volino and Hultgren [13] drew comparisons to correlations from Mayle [2] and Davis et al. [41] with mixed results. Comparisons to the present data are similarly mixed. The Mayle correlations predict the distance from the separation point to the onset of transition based on  $Re_\theta$  at the separation location. He presents a correlation for short separation bubble length and a correlation for long bubble length, which is 3.3 times the short bubble length. The Davis et al. [41] correlation also predicts the distance from separation to transition onset, but as a function of the FSTI. Table 3 presents the distance from separation to the start of transition, normalized on the suction surface length, for all cases of the present experiments and as predicted by the Mayle [2] and Davis et al. [41] correlations. The finite spacing between the measurement stations results in uncertainty in  $Re_\theta$  at separation and in the exact locations of separation and transition, so a range of values is given for each quantity in

**Table 3 Distance from separation location to start of transition as a fraction of  $L_s$ ; measured values and correlation predictions for each case**

FSTI	$Re \times 10^{-3}$	Measured	Mayle [2] short bubble	Mayle [2] long bubble	Davis et al. [41]
Low	25	> 0.41	0.25	0.83	1.54
	50	> 0.33	0.16-0.19	0.53-0.64	0.77
	100	0.17-0.33	0.12-0.14	0.39-0.48	0.38
	200	0-0.17	0.09-0.11	0.31-0.36	0.19
	300	0-0.08	0.07-0.08	0.23-0.28	0.13
High	25	> 0.33	0.27-0.29	0.89-0.98	0.17
	50	0.17-0.33	0.16-0.18	0.53-0.61	0.08
	100	0.08-0.17	0.12-0.14	0.39-0.48	0.04
	200	0-0.08	0.07-0.12	0.25-0.39	0.02
	300	0-0.08	0.06-0.09	0.19-0.31	0.02

the table. The results of the present cases lie between the Mayle long and short bubble correlations to within the resolution of the measurement locations. The Davis et al. correlation tends to predict too long a distance for the low FSTI cases and too short a distance for the high FSTI cases.

Existing correlations appear to give reasonable rough estimates of separated flow transition in some cases, but they are not particularly accurate or robust predictors. The general agreement between the similar cases of the present study, Volino and Hultgren [13], and Simon et al. [17] suggests that prediction of separated flow transition should be possible to some extent. The differences between the results of these studies, noted above, suggest that very accurate prediction of the flow may prove difficult and strongly dependent on small differences in boundary conditions. It is doubtful that a simple, robust correlation can be developed to incorporate all relevant boundary condition effects and provide very accurate predictions. It is also questionable whether the boundary conditions could be specified accurately enough for actual engine conditions. Perhaps they can, with addition research, however, and it may be possible to improve predictions with advanced computational schemes. The difficulty of predicting transition suggests that it may be advantageous to develop flow control schemes to force transition to occur at desired locations rather than try to predict it under existing conditions.

## Conclusions

Separated flow transition has been documented for cases with Reynolds numbers ranging from 25,000 to 300,000 at both high and low FSTI. The following conclusions can be drawn from the results.

1 The start of boundary layer reattachment occurs near the start of transition, and both depend strongly on Re and FSTI.

2 High FSTI results in competing effects with regard to losses. It causes enhanced mixing, which tends to promote boundary layer growth and increase losses. At the same time, it promotes earlier transition and reattachment, which reduces boundary layer thickness and losses. At the highest Re, reattachment occurred shortly after separation regardless of FSTI level, and high FSTI resulted in higher losses. At the intermediate Re, high FSTI reduced losses. At the lowest Re, the boundary layer did not reattach even with high FSTI, so losses would be high regardless of FSTI level.

3 The turbulent shear stress level can remain near zero in spite of high FSTI and high  $u'$  in the boundary layer. The beginning of a rise in  $-u'v'$  signals the beginning of transition. In the lowest Re cases, transition did not occur and the boundary layer did not reattach, but the beginning of a rise in  $-u'v'$  was observed near the trailing edge. This hints that it may be possible to induce transition even at very low Re.

4 The present results agree roughly with similar studies from the literature and existing correlations but there are significant differences. Attempts to control transition and force its location may prove more fruitful than prediction of unmodified flow. The present study provides an extensive, detailed baseline data set for ongoing flow control experiments.

## Acknowledgments

This work was sponsored by the NASA Glenn Research Center. The grant monitor is Dr. David Ashpis. Additional matching support was provided through a U.S. Naval Academy Recognition Grant. Mr. Dale Boyer of the Technical Support Department at the Naval Academy fabricated the airfoils for the test section.

## Nomenclature

- $C_f$  = skin friction coefficient
- $C_p = 2(P_T - P)/\rho U_e^2$ , pressure coefficient
- FSTI = free-stream turbulence intensity
- $H = \delta^*/\theta$ , shape factor
- $K = (\nu/U_\infty^2)(dU_\infty/ds)$ , acceleration parameter
- $L_s$  = suction surface length
- $l$  = hot-wire sensor length
- $P$  = pressure
- $P_T$  = upstream stagnation pressure
- $Re = U_e L_s/\nu$ , exit Reynolds number
- $Re_s = U_\infty s/\nu$ , local Reynolds number
- $Re_\theta$  = momentum thickness Reynolds number
- $s$  = streamwise coordinate, distance from leading edge
- $U$  = mean streamwise velocity
- $U_\infty$  = local free-stream velocity
- $U_e$  = nominal exit free-stream velocity, based on inviscid solution
- $u'$  = rms streamwise fluctuating velocity
- $u_\tau = \sqrt{\tau_w/\rho}$ , friction velocity
- $-u'v'$  = time averaged turbulent shear stress
- $v'$  = rms wall normal fluctuating velocity
- $y$  = cross-stream coordinate, distance from wall
- $y^+$  =  $yu_\tau/\nu$ , distance from wall in wall coordinates
- $\delta^*$  = displacement thickness
- $\gamma$  = intermittency, fraction of time flow is turbulent
- $\nu$  = kinematic viscosity
- $\rho$  = density
- $\tau_w$  = wall shear stress
- $\theta$  = momentum thickness

## References

- [1] Hourmouziadis, J., 1989, "Aerodynamic Design of Low Pressure Turbines," AGARD Lecture Series, 167.
- [2] Mayle, R. E., 1991, "The Role of Laminar-Turbulent Transition in Gas Turbine Engines," ASME J. Turbomach., **113**, pp. 509-537.
- [3] Sharma, O. P., Ni, R. H., and Tanrikut, S., 1994, "Unsteady Flow in Turbines," AGARD Lecture Series 195, Paper No. 5.
- [4] Hodson, H. P., 1991, "Aspects of Unsteady Blade-Surface Boundary Layers and Transition in Axial Turbomachines," *Boundary Layers in Turbomachines*, VKI Lecture Series 1991-2006.
- [5] Wisler, D. C., 1998, "The Technical and Economic Relevance of Understanding Boundary Layer Transition in Gas Turbine Engines," *Mimowbrook II, 1997 Workshop on Boundary Layer Transition in Turbomachines*, J. E. LaGraff and D. E. Ashpis, eds., NASA/CP-1998-206958, pp. 53-64.
- [6] Curtis, E. M., Hodson, H. P., Banieghbal, M. R., Denton, J. D., Howell, R. J., and Harvey, N. W., 1996, "Development of Blade Profiles for Low-Pressure Turbine Applications," ASME Paper 96-GT-358.
- [7] Halstead, D. E., Wisler, D. C., Okiishi, T. H., Walker, G. J., Hodson, H. P., and Shin, H.-W., 1997, "Boundary Layer Development in Axial Compressors and Turbines: Part 3 of 4—LP Turbines," ASME J. Turbomach., **119**, pp. 225-237.
- [8] Solomon, W. J., 2000, "Effects of Turbulence and Solidity on the Boundary Layer Development in a Low Pressure Turbine," ASME Paper 2000-GT-0273.
- [9] Gier, J., and Ardey, S., 2001, "On the Impact of Blade Count Reduction on Aerodynamic Performance and Loss Generation in a Three-Stage LP Turbine," ASME Paper 2001-GT-0197.
- [10] Hatman, A., and Wang, T., 1999, "A Prediction Model for Separated Flow Transition," ASME J. Turbomach., **121**, pp. 594-602.



- [11] Sohn, K. H., DeWitt, K. J., and Shyne, R. J., 2000, "Experimental Investigation of Boundary Layer Behavior in a Simulated Low Pressure Turbine," *ASME J. Fluids Eng.*, **122**, pp. 84–89.
- [12] Lou, W., and Hourmouziadis, J., 2000, "Separation Bubbles Under Steady and Periodic-Unsteady Main Flow Conditions," *ASME J. Turbomach.*, **122**, pp. 634–643.
- [13] Volino, R. J., and Hultgren, L. S., 2001, "Measurements in Separated and Transitional Boundary Layers Under Low-Pressure Turbine Airfoil Conditions," *ASME J. Turbomach.*, **123**, pp. 189–197.
- [14] Yaras, M. I., 2001, "Measurements of the Effects of Pressure-Gradient History on Separation-Bubble Transition," *ASME Paper 2001-GT-0193*.
- [15] Murawski, C. G., Sondergaard, R., Rivir, R. B., Simon, T. W., Vafai, K., and Volino, R. J., 1997, "Experimental Study of the Unsteady Aerodynamics in a Linear Cascade with Low Reynolds Number Low Pressure Turbine Blades," *ASME Paper 97-GT-95*.
- [16] Qiu, S., and Simon, T. W., 1997, "An Experimental Investigation of Transition as Applied to Low Pressure Turbine Suction Surface Flows," *ASME Paper 97-GT-455*.
- [17] Simon, T. W., Qiu, S., and Yuan, K., 2000, "Measurements in a Transitional Boundary Layer Under Low-Pressure Turbine Conditions," *NASA/CR-2000-209957*.
- [18] Brunner, S., Fottner, L., and Schiffer, H.-P., 2000, "Comparison of Two Highly Loaded Low Pressure Turbine Cascades Under the Influence of Wake-Induced Transition," *ASME Paper 2000-GT-268*.
- [19] Stadtmüller, P., Fottner, L., and Fiala, A., 2000, "Experimental and Numerical Investigation of Wake-Induced Transition on a Highly Loaded LP Turbine at Low Reynolds Numbers," *ASME Paper 2000-GT-0269*.
- [20] Howell, R. J., Ramesh, O. N., Hodson, H. P., Harvey, N. W., and Schulte, V., 2001, "High Lift and Aft-Loaded Profiles for Low-Pressure Turbines," *ASME J. Turbomach.*, **123**, pp. 181–188.
- [21] Kaszeta, R. W., Simon, T. W., and Ashpis, D. E., 2001, "Experimental Investigation of Transition to Turbulence as Affected by Passing Wakes," *ASME Paper 2001-GT-195*.
- [22] Dorney, D. J., Ashpis, D. E., Halstead, D. E., and Wisler, D. C., 1999, "Study of Boundary Layer Development in a Two-Stage Low Pressure Turbine," *AIAA Paper 99-0742*; also *NASA TM-1999-208913*.
- [23] Chernobrovkin, A., and Lakshminarayana, B., 1999, "Turbulence Modeling and Computation of Viscous Transitional Flow for Low Pressure Turbines," *ASME J. Fluids Eng.*, **121**, pp. 824–833.
- [24] Huang, P. G., and Xiong, G., 1998, "Transition and Turbulence Modeling of Low Pressure Turbine Flows," *AIAA Paper 98-0339*.
- [25] Thermann, H., Müller, M., and Niehuis, R., 2001, "Numerical Simulation of the Boundary Layer Transition in Turbomachinery Flows," *ASME Paper 2001-GT-0475*.
- [26] VanTreuren, K. W., Simon, T., von Koller, M., Byerley, A. R., Baughn, J. W., and Rivir, R., 2001, "Measurements in a Turbine Cascade Flow Under Ultra Low Reynolds Number Conditions," *ASME Paper 2001-GT-0164*.
- [27] Lake, J. P., King, P. I., and Rivir, R. B., 2000, "Low Reynolds Number Loss Reduction on Turbine Blades With Dimples and V-Grooves," *AIAA Paper 00-738*.
- [28] Bons, J. P., Sondergaard, R., and Rivir, R. B., 2001, "Turbine Separation Control Using Pulsed Vortex Generator Jets," *ASME J. Turbomach.*, **123**, pp. 198–206.
- [29] Volino, R. J., 2002, "Separated Flow Transition under Simulated Low-Pressure Turbine Airfoil Conditions: Part 2—Turbulence Spectra," *ASME J. Turbomach.*, **124**, pp. 656–664.
- [30] Volino, R. J., Schultz, M. P., and Pratt, C. M., 2001, "Conditional Sampling in a Transitional Boundary Layer Under High Free-Stream Turbulence Conditions," *ASME Paper 2001-GT-0192*.
- [31] Chung, J. T., and Simon, T. W., 1990, "Three-Dimensional Flow Near the Blade/Endwall Junction of a Gas Turbine: Visualization in a Large-Scale Cascade Simulator," *ASME Paper 90-WA/HT-4*.
- [32] Aunapu, N. V., Volino, R. J., Flack, K. A., and Stoddard, R. M., 2000, "Secondary Flow Measurements in a Turbine Passage With Endwall Flow Modification," *ASME J. Turbomach.*, **122**, pp. 651–658.
- [33] Volino, R. J., and Simon, T. W., 1997, "Velocity and Temperature Profiles in Turbulent Boundary Layers Experiencing Streamwise Pressure Gradients," *ASME J. Heat Transfer*, **119**, pp. 433–439.
- [34] Wills, J. A. B., 1962, "The Correction of Hot-Wire Readings for Proximity to a Solid Boundary," *J. Fluid Mech.*, **12**, pp. 65–92.
- [35] Ligrani, P. M., and Bradshaw, P., 1987, "Spatial Resolution and Measurement of Turbulence in the Viscous Sublayer Using Subminiature Hot-Wire Probes," *Exp. Fluids*, **5**, pp. 407–417.
- [36] Ligrani, P. M., and Bradshaw, P., 1987, "Subminiature Hot-Wire Sensors: Development and Use," *J. Phys. E*, **20**, pp. 323–332.
- [37] Ligrani, P. M., Westphal, R. V., and Lemos, F. R., 1989, "Fabrication and Testing of Subminiature Multi-Sensor Hot-Wire Probes," *J. Phys. E*, **22**, pp. 262–268.
- [38] Bradshaw, P., 1994, "Turbulence: the Chief Outstanding Difficulty of Our Subject," *Exp. Fluids*, **16**, pp. 203–216.
- [39] Volino, R. J., 2002, "An Investigation of the Scales in Transitional Boundary Layers Under High Free-Stream Turbulence Conditions," *ASME Paper GT-2002-30233*.
- [40] Thwaites, B., 1949, "Approximate Calculations of the Laminar Boundary Layer," *Aeronaut. Q.*, **7**, pp. 245–280.
- [41] Davis, R. L., Carter, J. E., and Reshotko, E., 1985, "Analysis of Transitional Separation Bubbles on Infinite Swept Wings," *AIAA Paper 85-1685*.

# Separated Flow Transition Under Simulated Low-Pressure Turbine Airfoil Conditions—Part 2: Turbulence Spectra

Ralph J. Volino

Mem. ASME,  
Department of Mechanical Engineering,  
United States Naval Academy,  
Annapolis, MD 21402  
e-mail: volino@usna.edu

*Spectral analysis was used to investigate boundary layer separation, transition and reattachment under low-pressure turbine airfoil conditions. Cases with Reynolds numbers ranging from 25,000 to 300,000 (based on suction surface length and exit velocity) have been considered at low (0.5%) and high (9% inlet) free-stream turbulence levels. Spectra of the fluctuating streamwise velocity and the turbulent shear stress are presented. The spectra for the low free-stream turbulence cases are characterized by sharp peaks. The high free-stream turbulence case spectra exhibit more broadband peaks, but these peaks are centered at the same frequencies observed in the corresponding low turbulence cases. The frequencies of the peaks suggest that a Tollmien-Schlichting instability mechanism drives transition, even in the high turbulence cases. The turbulent shear stress spectra proved particularly valuable for detection of the early growth of the instability. The predictable nature of the instability may prove useful for future flow control work.*

[DOI: 10.1115/1.1506939]

## Introduction

In Part 1 of the present study [1], the significance of boundary layer separation, transition, and reattachment to the flow over modern low-pressure turbine airfoils was discussed. Measured mean velocity and statistical turbulence quantities were presented for cases with high and low free-stream turbulence intensity (FSTI) and Reynolds numbers (based on suction surface length and exit velocity) ranging from 25,000 to 300,000. The separation point tended to move downstream somewhat as Reynolds number increased. Transition and reattachment locations moved upstream significantly as  $Re$  or FSTI were increased.

While the statistical quantities presented in Part 1 [1] provide a quantitative description of what happens under different  $Re$  and FSTI conditions, they do not explain the transition mechanism. To better explain the transition process and accurately predict or control it, an understanding of the physics which cause the results observed in Part 1 [1] is needed. The present paper uses spectral analysis to investigate separated flow transition.

Mayle [2] classified the modes of transition as “natural transition,” “bypass” transition; “separated flow” transition of the shear layer over a separation bubble; “periodic-unsteady” transition, which might also be called wake-induced bypass transition; and reverse transition. Under low FSTI, zero streamwise pressure gradient conditions, natural transition is expected. This type of transition has been extensively documented and can be predicted with linear stability analysis. As described by Schlichting [3], when the displacement thickness Reynolds number exceeds a critical value, the boundary layer becomes unstable to small disturbances, which begin to grow as Tollmien-Schlichting (TS) waves. These waves eventually become three dimensional and result in turbulent spots. Under high FSTI, zero pressure gradient conditions, large disturbances can cause a bypass of the linear growth stages of transition, resulting in the sudden appearance of turbulent spots. At intermediate FSTI, elements of both bypass and natural transition may be observed. Sohn and Reshotko [4],

for example, presented data for a 1% FSTI case, showing both spectral peaks at possible TS frequencies and broadband unsteadiness more typical of bypass transition.

In some cases, transition is observed even though linear stability theory predicts that the boundary layer should not develop TS waves. Volino [5], for example, considered a favorable pressure gradient case with high FSTI that clearly underwent transition. The boundary layer thickness remained low in this case due to the acceleration, resulting in  $Re_{\delta^*}$  below the critical limit for linear instability.

Separated flow transition could potentially include elements of either natural or bypass transition. In separated flow cases the pressure gradient is adverse, resulting in a boundary layer or shear layer that typically is unstable to TS waves. High FSTI, however, might be the dominant factor in a separated shear layer, overwhelming the effect of any TS waves and producing bypass transition. Hughes and Walker [6] list several studies with FSTI below 0.9% in which TS waves were detected in adverse pressure gradient cases. They also note that Halstead et al. [7] did not detect TS waves in the flow through a rotating cascade with more representative, higher FSTI. Solomon and Walker [8], however, provide evidence of TS waves under conditions similar to those of Halstead et al. [7]. Hughes and Walker [6] considered a flow with wakes, in which the FSTI between wakes ranged from less than 1% to about 3%, and the FSTI in the wakes was about 8%. They provide clear evidence of TS waves.

Hatman and Wang [9], Volino and Hultgren [10], and Lou and Hourmouziadis [11] all considered low FSTI, adverse pressure gradient flows and observed transition in the shear layer over separation bubbles. Spectral data in all three studies showed clear evidence of an instability along with harmonics. It was expected that this instability was very similar to the Kelvin-Helmholtz instabilities observed in free shear layers, although the unstable frequencies were somewhat different than expected for free shear layers since the separation bubbles were bounded by the wall on one side. Volino and Hultgren [10] also considered high FSTI cases and observed broadband unsteadiness in the spectra of the streamwise fluctuating velocity,  $u'$ . Spikes at discreet frequencies, which were observed in the low FSTI cases, were not present. They stated that transition in the high FSTI cases appeared to be through a bypass mode.

Contributed by the International Gas Turbine Institute and presented at the International Gas Turbine and Aeroengine Congress and Exhibition, Amsterdam, The Netherlands, June 3–6, 2002. Manuscript received by the IGTI, January 22, 2002. Paper No. 2002-GT-30237. Review Chair: E. Benvenuti.

Clearly there is some disagreement regarding the transition mechanism in separated boundary layers, particularly under high FSTI conditions. Some of these differences may stem from physical differences in the boundary conditions between the various studies. The present study addresses the issue through spectral analysis of flows over a range of Reynolds numbers at both high and low FSTI. Included in the analysis are spectra of the turbulent shear stress, which were not considered in previous studies.

## Experiments

The experimental facility and the cases considered are described in detail in Part 1 [1]. A low-speed wind tunnel supplies air to a single-passage cascade-simulator with geometry and flow angles matching those for the industry supplied Pak-B airfoil. For the low FSTI cases, the background turbulence level for the wind tunnel is nominally 0.5%, and consists primarily of low frequency unsteadiness. A passive grid is used to generate a high inlet FSTI of 8.7%.

Velocity data were acquired at 11 streamwise measurement stations along the spanwise centerline of the suction side of the passage. Station locations are given in Table 1. At each station, instantaneous streamwise velocity was measured at 60 locations as a single sensor hot-wire probe was traversed from the airfoil surface to the free-stream. The voltage from the hot-wire was offset and amplified by a factor of 10 and low pass filtered at 10 kHz using signal conditioners (TSI model 157). At each location, data were acquired for 26 s at a 20 kHz sampling rate ( $2^{19}$  samples). The high sampling rate provides an essentially continuous signal, which is needed for spectral processing. The long sampling time results in low uncertainty in both statistical and spectral quantities. Two component velocity measurements were made at Stations 7–11 with a cross-wire probe. The upstream boundary layer was too thin for cross-wire measurements. Data were acquired at 25 locations in each profile, beginning 1 mm from the wall and extending to the free-stream. Sampling rates and times were the same as with the single sensor probe. Power spectra of  $u'$ , the wall normal fluctuating velocity,  $v'$ , and the turbulent shear stress,  $-u'v'$ , were computed for the data from all measurement locations. Uncertainties in the  $u'$ ,  $v'$  and  $-u'v'$  spectra are all 10%. Frequencies are resolved from 4.88 to 10 kHz in 4.88 Hz increments using a 4096 point Fast Fourier Transform to compute the spectra. As a check, the spectra were integrated with respect to frequency and found to equal the corresponding time averaged Reynolds stresses.

Data sets were acquired for cases at high and low FSTI with exit Reynolds numbers of 25,000, 50,000, 100,000, 200,000 and 300,000. The upstream boundary layer through Station 6 remained laminar in all of these cases, with the mean velocity following a Falkner-Skan wedge flow solution. Downstream of Station 6 the pressure gradient becomes adverse. Separation occurred between Stations 6 and 8, with the separation point moving downstream as Re increased. Reattachment did not occur in the high or low FSTI, Re=25,000 cases or the low FSTI, Re=50,000 case. In all other cases the boundary layer did reattach, and the reattachment point moved upstream as Re or FSTI was increased. Details are available in Part 1 [1]. The  $u'$  level rose in the shear layer in each case after the boundary layer separated, but the turbulent shear stress remained near zero until transition began. Transition began in the shear layer and quickly led to boundary layer reattachment. In the Re=25,000 cases, low but non-zero turbulent shear stress was

observed at the most downstream stations, indicating that although the shear layer was still non-turbulent and separated, it was showing signs of the start of transition.

As discussed in Part 1 [1], the finite length of the hot-wire sensors (1.27 mm) will result in some spatial averaging and could result in attenuation of the measured fluctuating velocity components. Based on the results of Ligrani and Bradshaw [12,13], it was explained in Part 1 that the errors in the rms fluctuating quantities are within the 10% uncertainty estimates in the majority of cases in the present study. Exceptions occur for the Re=200,000 cases at Station 11 of the low FSTI case and Stations 9–11 of the high FSTI case. For the Re=300,000 cases, larger errors are expected for Stations 10–11 of the low FSTI case and Stations 9–11 of the high FSTI case. For these cases, errors may be as large as 30% near the wall, but should be under 10% at  $y$  locations greater than 1 mm. As explained by Ligrani et al. [14], measurements with the cross-wire probe are subject to potentially larger errors due to the finite spacing (1 mm) between the two sensors. These errors will be largest near the wall, but become smaller than the 10% uncertainty for  $y$  locations above 1 mm. For this reason, cross-wire measurements were only made for  $y > 1$  mm.

The spectra in the present paper are presented to show the energy content of the fluctuating quantities as a function of frequency. The average errors in these spectra, therefore, should be the same as those given in the foregoing for the corresponding rms quantities. The errors will not be uniform with respect to frequency across the spectra, however. As explained by Ligrani and Bradshaw [13], spatial averaging effects will be most severe for the smallest scales (highest frequencies) in the flow. Applying the spectral results of Ligrani and Bradshaw [13] to the present study, errors due to spatial averaging at  $y$  locations above 1 mm will rise above 10% at frequencies above 150, 300, 600, 1200, and 1800 Hz for the Re=25,000, 50,000, 100,000, 200,000, and 300,000 cases respectively. Below these frequencies the errors should be under 10%. These frequencies are all above the frequencies of the spectral peaks in the results presented below, so the peaks should not be significantly attenuated. For the Re=25,000 and 50,000 cases, all significant energy in the spectra is below the frequencies given above, so there is no significant attenuation of the results at any frequency. For the Re=100,000 case, only the high frequency “tail” of the spectra will be subject to significant error. Magnitudes at these high frequencies may be as much as 30% low. Similarly for the Re=200,000 and 300,000 cases, errors will only rise above 10% at frequencies about twice those of the spectral peaks. Magnitudes at the highest frequencies may be as much as 40% low in these cases.

## Frequencies of Interest

Transition in the shear layer over the separation bubble could be initiated by Tollmien-Schlichting waves originating in the boundary layer upstream of separation. Upstream of Station 6, the pressure gradient is favorable and the boundary layer should not develop TS waves at any frequencies. At Station 6 the flow begins to decelerate and immediately becomes unstable. Walker [15] provides the following equation for the frequency of maximum amplification rate for TS waves:

$$2\pi\nu f/U_\infty^2 = 3.2 \text{Re}_{\delta^*}^{-3/2} \quad (1)$$

The TS frequencies predicted by Eq. (1) are listed in Table 2. Values are given for Stations 6 and 7 for the cases in which the boundary layer is still attached at these stations.

Another possible path to transition is breakdown of the shear layer through a Kelvin-Helmholtz-type instability. The frequency of the instability should scale with the velocity change across the shear layer and inversely with the shear layer thickness. Since the velocity in the separation bubble is nearly zero, the velocity difference across the shear layer equals the local free-stream velocity. The shear layer thickness,  $\delta_s$ , is determined from the mean

Table 1 Measurement stations

Station	1	2	3	4	5	6
$s/L_s$	0.111	0.194	0.278	0.361	0.444	0.527
Station	7	8	9	10	11	$L_s=228.6$
$s/L_s$	0.611	0.694	0.778	0.861	0.944	mm

**Table 2 Most unstable Tollmien-Schlichting frequencies prior to separation and  $U_\infty/\delta_s$  values in shear layer**

FSTI	$Re \times 10^{-3}$	TS freq. [Hz]		$U_\infty/\delta_s$ [ $s^{-1} \times 10^{-3}$ ]					
		Station		Station					
		6	7	6	7	8	9	10	11
Low	25	80		1.0	0.8	0.6	0.5	0.4	0.4
	50	176			2.1	1.5	1.3	1.2	1.0
	100	443	266			3.9	3.2	3.8	
	200	1175	645			11	8.7		
	300	1554	1134			22	20		
High	25	60		1.1	0.8	0.6	0.4	0.4	0.3
	50	174		3.1	2.4	1.6	1.1	0.8	
	100	408	272			4.1	3.1		
	200	1138	732			15			
	300	1747	1195			25			

velocity profiles presented in Part 1 [1]. Table 2 lists the quantity  $U_\infty/\delta_s$  for each station where the boundary layer is separated.

**Results**

**Free-Stream Spectra.** The  $u'$  and  $v'$  free-stream spectra are shown in Fig. 1 for each station of the low FSTI,  $Re=300,000$  case. Frequency is plotted on a log scale versus frequency times

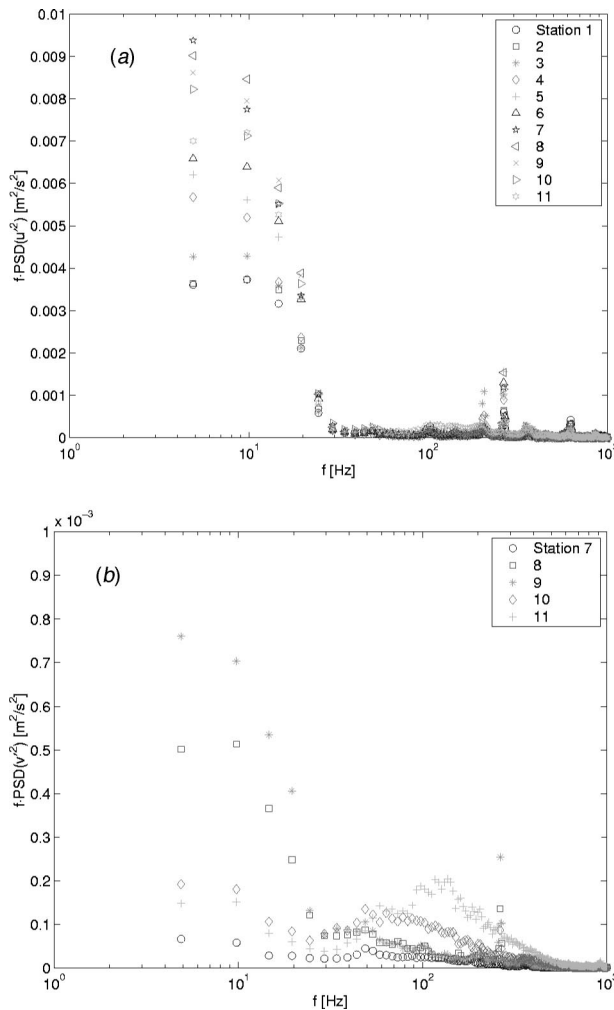


**Fig. 1 Free-stream spectra for low FSTI,  $Re=300,000$  case—(a)  $u'$ , (b)  $v'$**

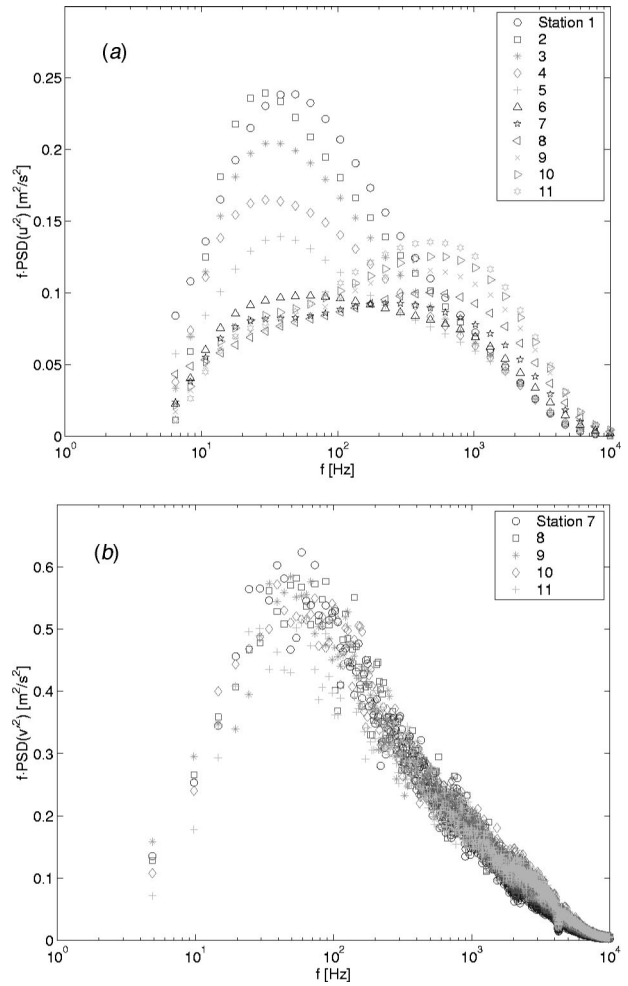


**Fig. 2 Free-stream spectra for high FSTI,  $Re=300,000$  case—(a)  $u'$ , (b)  $v'$**

power spectral density on a linear scale. In these coordinates the area under the curve in any frequency band is proportional to the contribution to the quantity of interest in that band. The  $u'$  spectra are dominated by low amplitude unsteadiness at frequencies below 20 Hz. The  $u'$  spectra for the lower  $Re$  cases (not shown) have proportionately lower amplitudes, but the frequency range remains the same. The frequencies associated with turbulent eddies would be expected to scale with the free-stream velocity. Since the frequencies in the present cases remain constant as  $Re$  is changed, the unsteadiness in the wind tunnel is most likely not associated with turbulent eddies. The  $v'$  spectra show the same low frequencies as  $u'$  but at  $1/10^{th}$  the magnitude. A second lower peak is centered at about 100 Hz. This peak is also present with the same magnitude in  $u'$ , and is visible in an expanded version of Fig. 1(a). The frequency of this second peak scales with the free-stream velocity and is proportionately lower for the lower  $Re$  cases. Its magnitude is very low, and by itself would correspond to an rms turbulence level of about 0.01%. It is likely the residual turbulence remaining after the wind tunnel screens.

The  $u'$  and  $v'$  free-stream spectra for the high FSTI  $Re=300,000$  case are shown in Fig. 2. The magnitude of  $u'$  is about 25 times larger than in the low FSTI case of Fig. 1(a). At the upstream stations there is a peak at about 30 Hz. This peak decays due to streamwise straining of the flow as it is accelerated through Station 6. In the adverse pressure gradient region downstream of Station 6, a broadband peak emerges centered at about 700 Hz. In the lower  $Re$  cases, the  $u'$  spectra is qualitatively the same, but

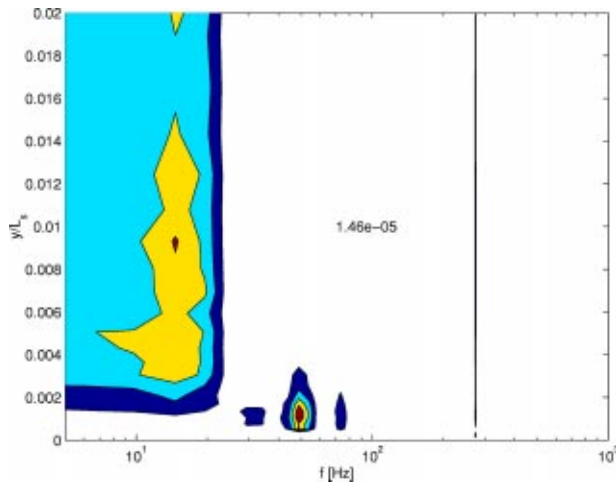


Fig. 3 Contours of  $fPSD(u'^2)$ , low FSTI,  $Re=100,000$ , Station 4; outer contour magnitude and contour spacing indicated by numerical value in field of figure

the magnitudes scale with  $U_\infty^2$  and the frequencies scale with  $U_\infty$ . The  $v'$  spectra of Fig. 2(b) all appear similar with a broadband peak centered at 60 Hz. As with  $u'$ , the magnitudes and frequencies of the  $v'$  spectra in the lower Re cases scale with the free-stream velocity, and appear qualitatively similar to those of Fig. 2(b).

**Upstream Boundary Layer.** Contours of the boundary layer  $u'$  spectra from Station 4 of the low FSTI  $Re=100,000$  case are shown in Fig. 3. Frequency in Hz is shown on the horizontal axis on a log scale, and distance from the wall normalized on the suction surface length is on the vertical axis on a linear scale. The frequency is left dimensional since there is no single appropriate normalization for all regions of the flow. The contours in Fig. 3 show the dimensionless magnitude of the spectra as  $f \cdot PSD(u'^2)/U_\infty^2$ . A slice through the data of Fig. 3 at a fixed distance from the wall would produce a spectrum in the coordinates of Fig. 2, except with dimensionless magnitude. The number (1.46e-05), which appears in the center of the figure, indicates the magnitude of the outermost contour and the contour spacing. Hence, the outermost contour value is  $1.46 \times 10^{-5}$ , the next contour value is  $2.92 \times 10^{-5}$ , the next is  $4.38 \times 10^{-6}$ , etc. The same format is used in all the figures which follow. Figure 3 shows a peak near the wall centered at 50 Hz and unsteadiness below 20 Hz extending from the free-stream to near the wall. The results shown in Fig. 3 are typical of the behavior at Stations 1–6 in all the low FSTI cases. The 50 Hz peak was also visible in the  $Re=200,000$  and  $300,000$  cases, but not at the two lower Re. This peak did not appear to have any significant effect on the downstream boundary layer.

Figure 4 shows the spectra from Station 4 of the high FSTI  $Re=300,000$  case in the coordinates of Fig. 3. The Fig. 4 spectra are typical of the spectra at Stations 1–6 of all the high FSTI cases. There is a near wall peak at 100 Hz, which is 1.7 times the frequency of the free-stream  $v'$  frequency peak shown in Fig. 2(b). The distance of the peak from the wall is larger in the lower Re cases, scaling with the boundary layer thickness. The frequency of the peak scales with Re, and is consistently 1.7 times the dominant  $v'$  frequency in the free-stream. This indicates that the boundary layer unsteadiness is induced by free-stream buffeting. Volino [5] discusses free-stream buffeting of boundary layers in more detail.

**Low FSTI Transition.** Upstream of Station 6, the boundary layer unsteadiness is attributable to low amplitude streamwise unsteadiness in the low FSTI cases, and free-stream buffeting in the

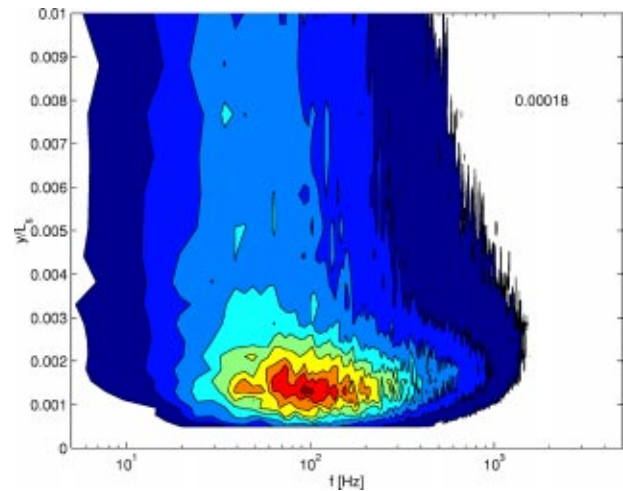


Fig. 4 Contours of  $fPSD(u'^2)$ , high FSTI,  $Re=300,000$ , Station 4; outer contour magnitude and contour spacing indicated by numerical value in field of figure

high FSTI cases. Buffeting, as explained in Part 1 [1], refers to the effect of free-stream pressure fluctuations on the boundary layer as fluid is pushed in the wall normal direction across the gradient in the mean streamwise velocity. Downstream of Station 6, the pressure gradient becomes adverse, and the spectra become more interesting. Figure 5 shows the  $u'$  spectra contours for Stations 7–11 of all the low FSTI cases. The coordinates of each subplot are the same as those of Fig. 3. In the  $Re=25,000$  case (top row of Fig. 5), the contours at Station 7 show the low frequency unsteadiness observed at the upstream stations. Between Stations 7 and 10, the magnitude of the peak increases by an order of magnitude. The peak at each station moves away from the wall. Comparison to the mean velocity profiles presented in Part 1 [1] shows that the location of the peak corresponds, not surprisingly, to the shear layer over the separation bubble. The  $Re=50,000$  case (row 2) shows similar behavior through Station 10, but a second peak emerges at about 78 Hz at Station 11. This second peak is indicative of transition.

In the  $Re=100,000$  case (row 3 of Fig. 5), a sharp peak appears at Station 10 at 273 Hz. The contour spacing increases by two orders of magnitude between Stations 9 and 10, indicating a similar increase in the magnitude of the peak. The peak is so sharp and so large that it appears as a line in the contour plot. Figure 6 shows this  $Re=100,000$ , Station 10 data in the same coordinates as Fig. 5, but three dimensionally. The low frequency unsteadiness visible at Station 9 is still present, but since its magnitude is only  $1/50^{\text{th}}$  that of the 273 Hz peak, it is barely visible in Fig. 6. The sharp peak in the shear layer is typical of all the low FSTI cases.

In the  $Re=200,000$  case (row 4 of Fig. 5), a small peak appears in the shear layer at 698 Hz at Station 9. By Station 10 this peak has increased in size by two orders of magnitude and is becoming more broadband as the boundary layer reattaches and becomes turbulent. Although not clear in Fig. 5, the sharp spectral peak remains in the center of this broadband turbulence and is clear in the format of Fig. 6. Similar behavior is apparent in the  $Re=300,000$  case, but the spectral peak and subsequent turbulence are centered at 922 Hz.

Contours of the normalized turbulent shear stress spectra,  $f \cdot PSD(-u'v')/U_\infty^2$ , for the low FSTI cases are shown in Fig. 7. The format is the same as in Fig. 5. The shear layer is laminar at Stations 7 and 8 in all cases, and the turbulent shear stress is near zero. The  $Re=25,000$  case shows a low magnitude, 15 Hz peak at Station 10. The peak was obscured in the  $u'$  spectra of Fig. 5 due to the presence of other streamwise unsteadiness at similar frequencies. The magnitude of the 15 Hz shear stress peak increases

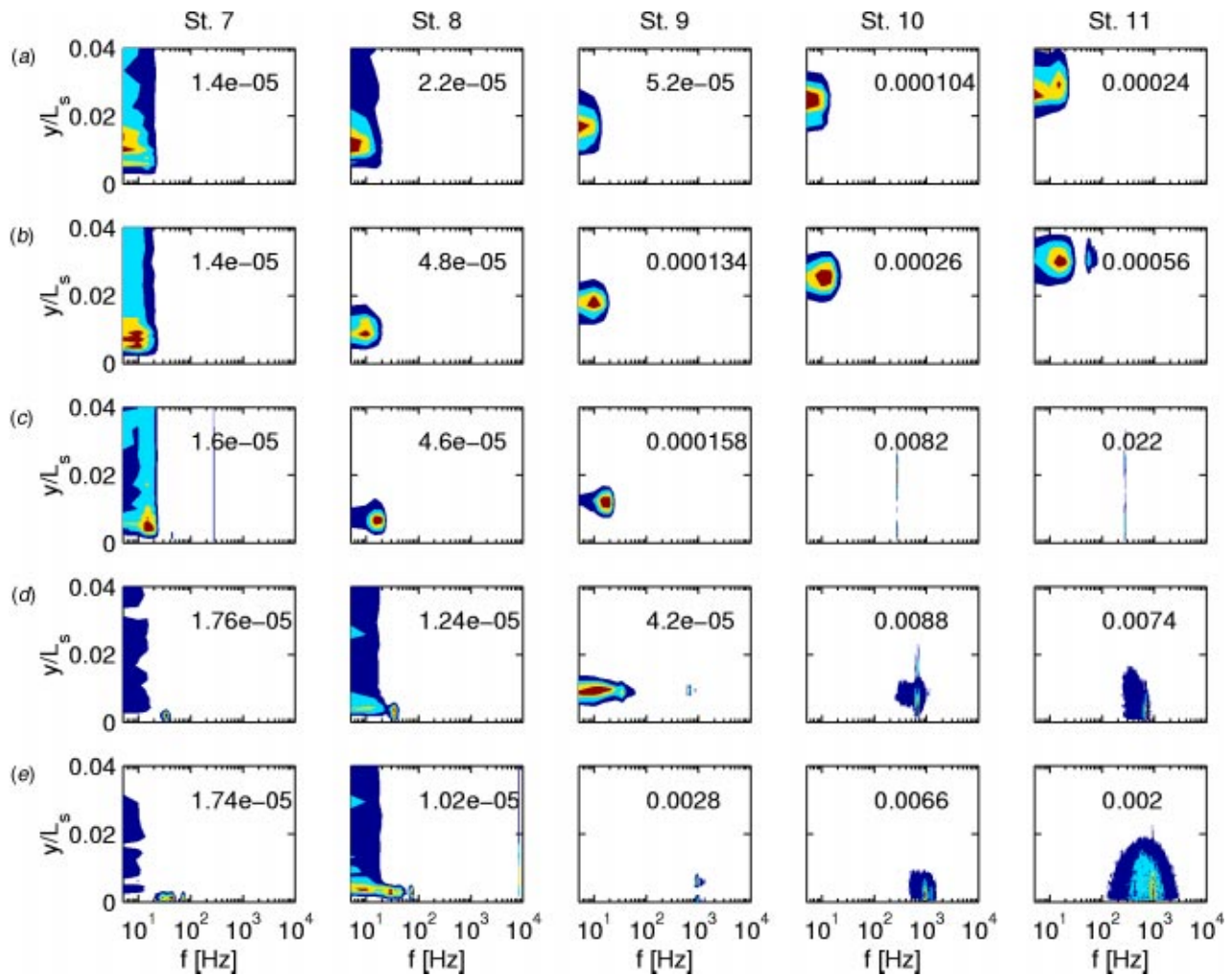


Fig. 5 Contours of  $f$ -PSD( $u'^2$ )/ $U_\infty^2$ , low FSTI cases; station number indicated above each column; by row—(a)  $Re=25,000$ , (b)  $Re=50,000$ , (c)  $Re=100,000$ , (d)  $Re=200,000$ , (e)  $Re=300,000$ ; outer contour magnitude and contour spacing indicated by numerical value in field of each subplot, 5 contours shown in each subplot

by a factor of 15 between Station 10 and 11, but its amplitude is still quite low. Close inspection of the  $u'$  spectra (Fig. 5) at Station 11 shows a double peak, with one peak at 15 Hz. The mean profiles of Part 1 [1] indicate that transition may be imminent, but the shear layer is still laminar at Station 11.

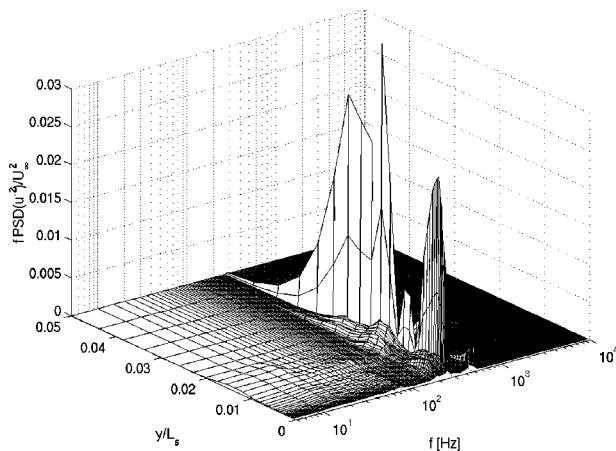


Fig. 6 Spectra of  $f$ -PSD( $u'^2$ )/ $U_\infty^2$ , low FSTI,  $Re=100,000$ , Station 10

The  $Re=50,000$  case shows similar behavior to that at  $Re=25,000$ . A turbulent shear stress peak appears at Station 10 and is 37 times larger by Station 11. This peak did not become visible until Station 11 in the  $u'$  spectra. Similarly, in the  $Re=100,000$  case a sharp turbulent shear stress peak emerges at Station 9, one station upstream of its appearance in  $u'$ . The shear stress peak appears at Station 9 in the  $Re=200,000$  and  $300,000$  cases. In all cases, the peak appears at the same frequency in  $u'$  and  $-u'v'$ , but tends to become visible earlier in the  $-u'v'$  spectra due to the lower magnitude of the low-frequency “noise” in  $-u'v'$ .

The frequencies of the spectral peaks are listed for all cases in Table 3. Also indicated in the table are the stations at which these frequencies were determined. The frequencies of the peaks did not change significantly in the streamwise direction. Because the peaks do not appear until after the boundary layer has separated, there is some reason to believe that a Kelvin-Helmholtz-type in-

Table 3 Measured peak frequencies in spectra

FSTI	$Re \times 10^{-3}$	25	50	100	200	300
Low	Station	10	10	9	9	9
	$f$ [Hz]	15	78	273	698	922
High	Station	9	9	9	9	9
	$f$ [Hz]	20	85	230	600	1100

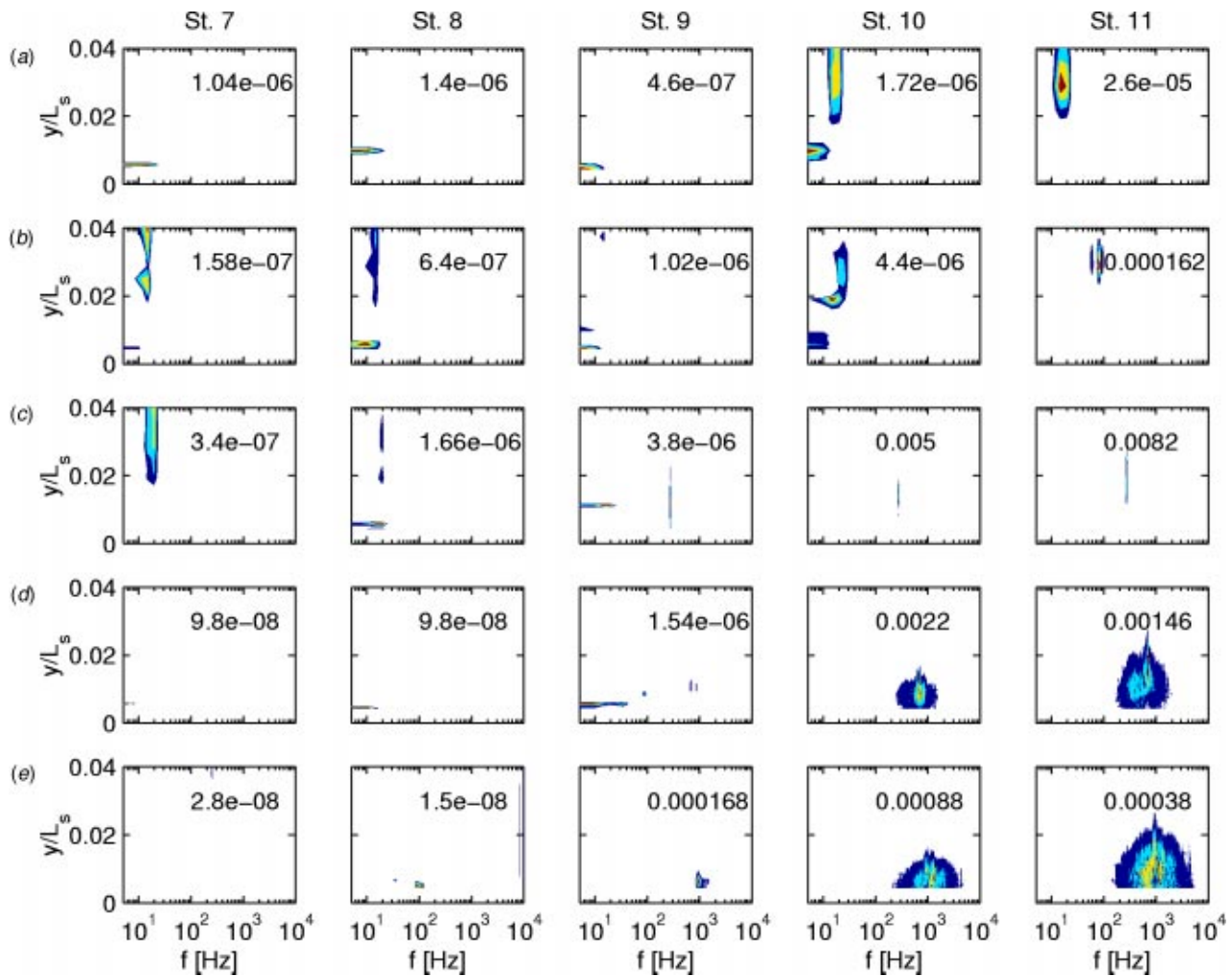


Fig. 7 Contours of  $f\text{-PSD}(-u'v')/U_\infty^2$ , low FSTI cases; see Fig. 5 caption for further explanation

stability may be involved. For the low FSTI cases, comparison of the spectral peak frequencies to the  $U_\infty/\delta_S$  values in Table 2 shows that the spectral frequencies and  $U_\infty/\delta_S$  values both increase with Re, as expected. The ratio of the measured frequency to  $U_\infty/\delta_S$  is not a constant, however, ranging from about 0.04 to about 0.08. Comparison of the measured frequencies to the TS frequencies of Table 2 shows better correlation. At the three highest Re, the measured frequencies agree with the TS frequencies at Station 7 (the last station before separation) to within 20%. The boundary layer is already separated at Station 7 in the Re = 25,000 and 50,000 cases, so the frequency comparison must be made at Station 6. Agreement with the TS frequencies is not as good in these cases as at the high Re. Hughes and Walker [6] note that since the most unstable TS frequency changes with streamwise position, the frequency observed in the shear layer need not equal the TS value at any single upstream position.

**High FSTI Transition.** Contours of the  $u'$  spectra for the high FSTI cases are shown in Fig. 8. In the Re=25,000 case (top row), there is low frequency unsteadiness at the same frequencies observed upstream (Fig. 4). As in the low FSTI cases, the peak  $u'$  location is in the shear layer over the separation bubble. In the Re=50,000 case, the outermost contour at Station 10 extends to higher frequencies than at the upstream stations, and by Station 11 a new peak has emerged at 60 Hz, extending from the shear layer down to the wall. The magnitude of this new peak is about equal to the magnitude of the original, low-frequency peak, which is also still visible. Similar behavior is clear for the Re=100,000

case. Higher frequencies begin to emerge at Station 9, and a large, clear peak centered at 260 Hz is visible at Stations 10 and 11. In the Re=200,000 and 300,000 cases, some signs of higher frequencies are already visible at Station 8, and a double peak is clear at Station 9. At Stations 10 and 11, the higher frequency peak overwhelms the lower frequencies.

Comparing Fig. 8 to Fig. 5, the contour levels in the high FSTI case are about 2 orders of magnitude higher than in the low FSTI case at Stations 7 and 8. This is expected and due to the higher  $u'$  caused by free-stream buffeting in the high FSTI case. Farther downstream, however, after the higher frequencies emerge, the contour levels are higher for the low FSTI cases. This is somewhat misleading, as the rms  $u'$  levels are actually very similar in the high and low FSTI cases at these stations. The lower contour levels in the high FSTI case result because the  $u'$  fluctuations are distributed over a wider frequency band. The spectral peaks of Fig. 8 are much broader than the corresponding peaks of the low FSTI cases shown in Figs. 5–7. Figure 9 shows the  $u'$  spectra at Station 10 of the high FSTI, Re=100,000 case. Comparing to Fig. 6, the high FSTI case exhibits much more low frequency activity due to free-stream buffeting, and the peak is clearly broader in frequency than the 273 Hz spike of the low FSTI case.

Figure 10 shows contours of the turbulent shear stress spectra for the high FSTI cases. Values at Stations 7 and 8 are low, in spite of the high FSTI, indicating that much of the  $u'$  unsteadiness observed in Fig. 8 does not involve turbulent transport. Distinct, broadband peaks emerge by Station 9 in all cases. As in the low

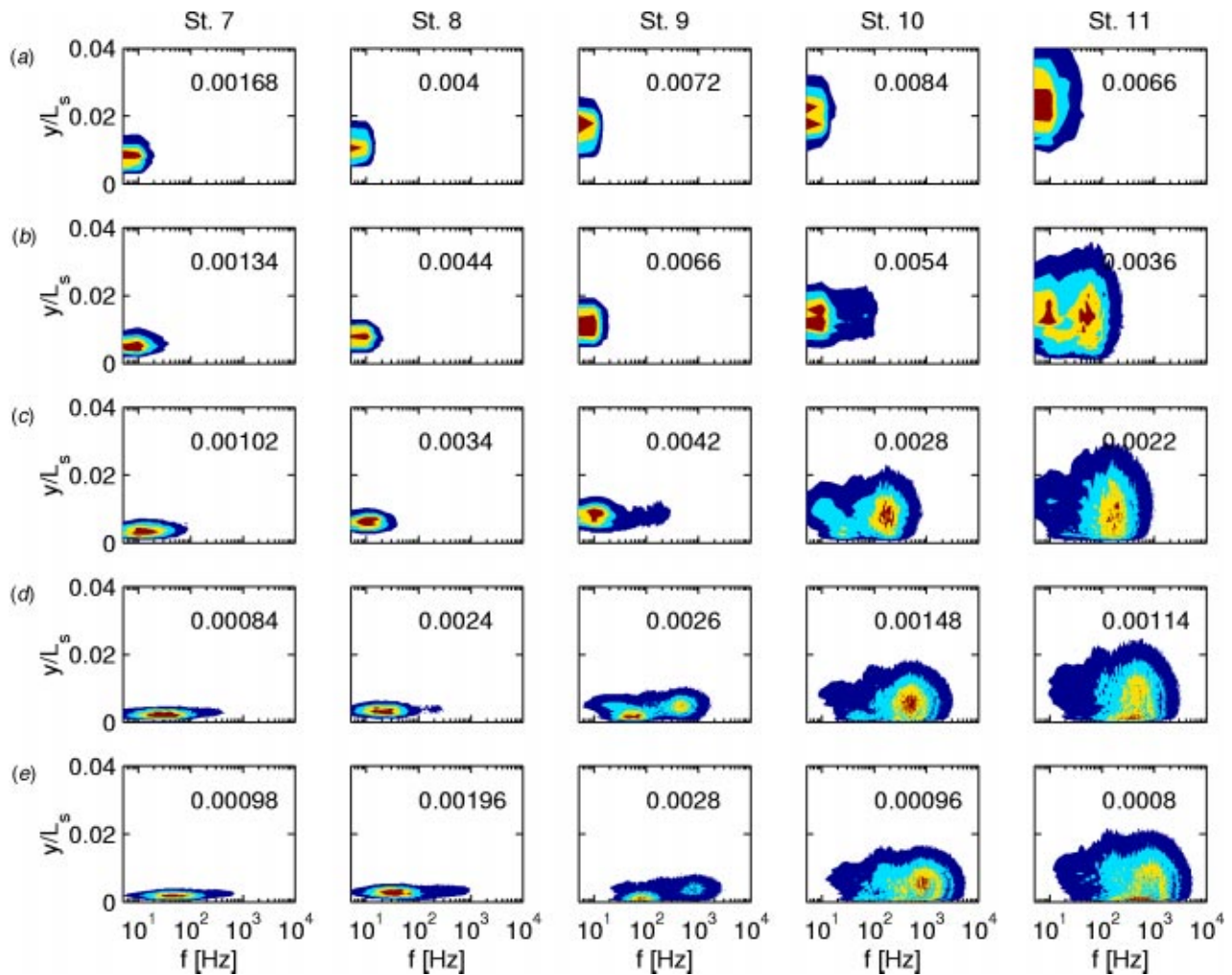


Fig. 8 Contours of  $f \cdot \text{PSD}(u'^2)/U_\infty^2$ , high FSTI cases; see Fig. 5 caption for further explanation

FSTI cases, these peaks are visible in  $-u'v'$  farther upstream than they are in  $u'$ . The peak becomes visible in  $-u'v'$  soon after it forms, but the  $u'$  peak must grow to become larger than the free-stream induced fluctuations before it is discernible.

The broad peaks in the high FSTI cases might suggest that transition occurs through a bypass mode. This was the conclusion

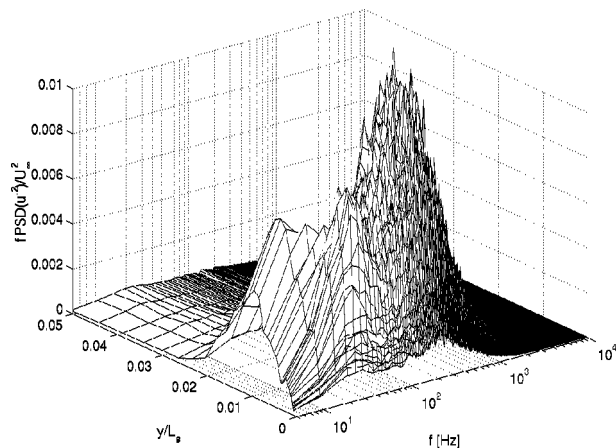


Fig. 9 Spectra of  $f \cdot \text{PSD}(u'^2)/U_\infty^2$ , high FSTI,  $Re=100,000$ , Station 10

of Volino and Hultgren [10]. Closer inspection, however, reveals strong similarity to the low FSTI cases. The frequencies of the peaks in the high FSTI cases are listed in Table 3. The broad nature of the high FSTI case peaks, as shown in Fig. 9, result in an uncertainty of about 20% in the frequency values in Table 3. With this uncertainty, the frequency at each  $Re$  is essentially the same as in the corresponding low FSTI case. Comparison to the TS frequencies in Table 2 show the same good agreement observed in the low FSTI cases. Close inspection of Fig. 10 reveals that at the four highest  $Re$ , the peak in  $-u'v'$  begins to appear, with very low magnitude, at Stations 7 and 8. The boundary layer is still thin at these stations, so part of the peak lies closer to the wall than can be measured with the cross-wire probe. The closest measurement to the wall with the cross-wire was at  $y=1$  mm, which corresponds to  $y/\delta_{99.5}$  between 0.2 and 0.65 at the stations in question. What is visible, however, is at the same frequencies as present downstream. Since the boundary layer is still attached at Station 7, it is doubtful these fluctuations could be induced by a Kelvin-Helmholtz-type instability. Instead, it appears that a TS instability plays a role, even in the high FSTI cases. This agrees with the findings of Hughes and Walker [6], who used instantaneous wall shear measurements to identify wave packets both within and between wakes in an unsteady flow. Although it appears that TS waves play a role in the high FSTI cases, it should be noted that it is also possible that transition occurs through a bypass mode, and



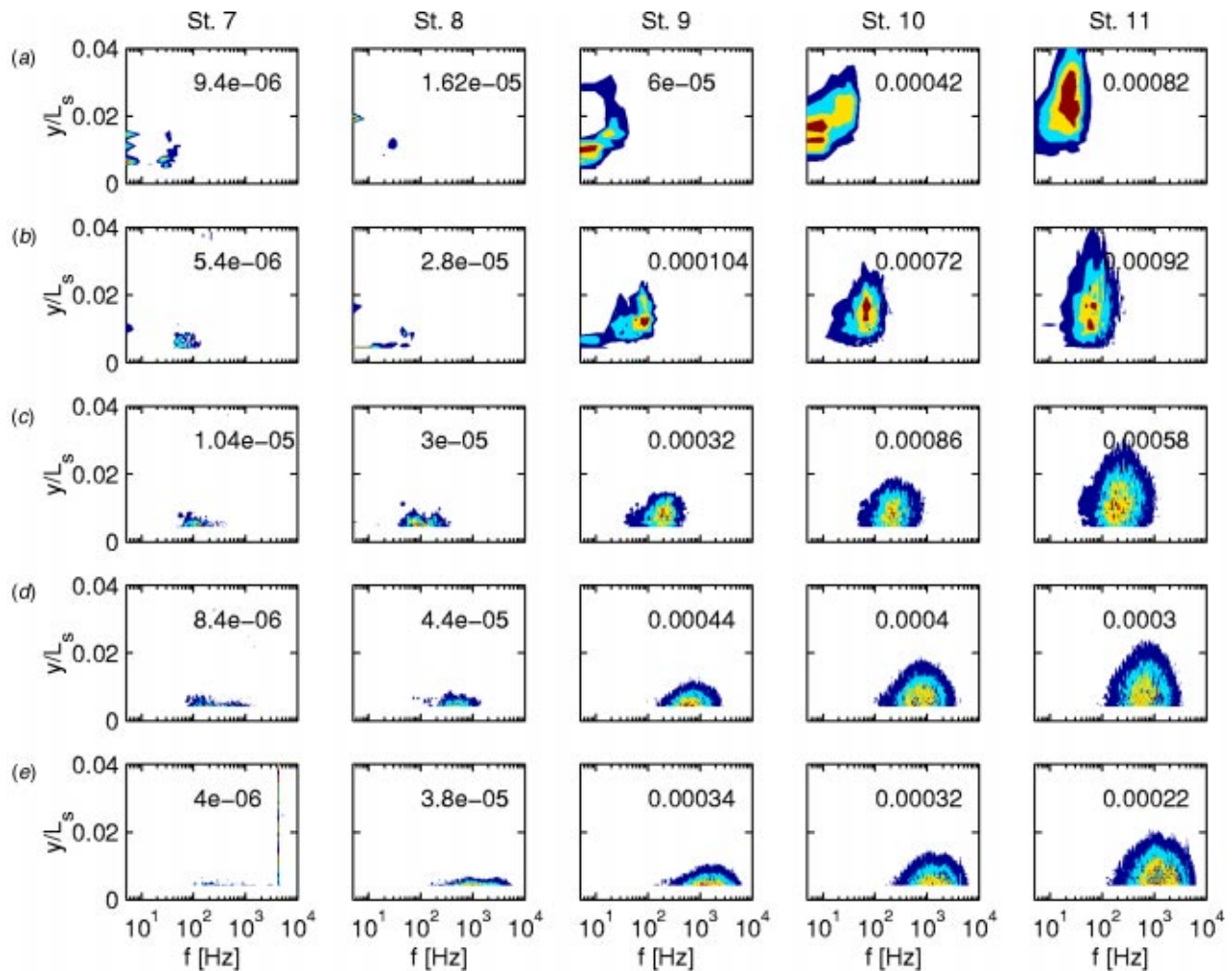


Fig. 10 Contours of  $f$ -PSD( $-u'v'$ )/ $U_\infty^2$ , high FSTI cases; see Fig. 5 caption for further explanation

that the spectral peaks are due not to TS waves, but to the turbulence within turbulent spots. Perhaps both TS and bypass modes play a role, as suggested by Mayle [2].

## Conclusions

Turbulence spectra provide valuable insights into the transition mechanism. Clear sharp peaks were observed in the spectra of the low FSTI cases, at frequencies indicating a probable TS instability mechanism for the breakdown of the shear layer over the separation bubble to turbulence. The spectra were more broadband for the high FSTI cases, but the peaks of these spectra occurred at the same frequencies as in the corresponding low FSTI cases, suggesting a possible similar transition mechanism at high and low FSTI. The turbulent shear stress spectra were valuable for detection of instabilities upstream of the location where peaks became discernable in the  $u'$  spectra. In the high FSTI cases, low magnitude peaks were detected in  $-u'v'$  upstream of separation, further supporting the argument for a TS transition. Larger initial disturbances in the high FSTI cases resulted in detectable  $-u'v'$  farther upstream than in the low FSTI cases. Since the adverse pressure gradient boundary layer is unstable to disturbances over a broad range of frequencies and the free-stream turbulence contains a range of scales, broad peaks emerge in the boundary layer spectra of the high FSTI cases. These peaks contrast with the sharp peaks of the low FSTI cases, which result from the growth of small disturbances at the most unstable fre-

quencies. The presence and predictability of the shear layer instability may prove useful in future attempts to induce transition for separation control.

## Acknowledgments

This work was sponsored by the NASA Glenn Research Center. The grant monitor is Dr. David Ashpis. Additional matching support was provided through a U.S. Naval Academy Recognition Grant.

## Nomenclature

FSTI	=	free-stream turbulence intensity
$f$	=	frequency in Hz
$L_s$	=	suction surface length
PSD	=	power spectral density of $u'^2$ or $-u'v'$
Re	=	$U_e L_s / \nu$ , exit Reynolds number
$Re_{\delta^*}$	=	$U_\infty \delta^* / \nu$ displacement thickness Reynolds number
$s$	=	streamwise coordinate, distance from leading edge
$U_\infty$	=	local free-stream velocity
$U_e$	=	nominal exit free-stream velocity
$u'$	=	streamwise fluctuating velocity
$-u'v'$	=	turbulent shear stress
$v'$	=	wall normal fluctuating velocity
$y$	=	cross-stream coordinate, distance from wall
$\delta^*$	=	displacement thickness

$\delta_S$  = shear layer thickness  
 $\delta_{99.5}$  = 99.5% boundary layer thickness  
 $\nu$  = kinematic viscosity

## References

- [1] Volino, R. J., 2002, "Separated Flow Transition Under Low Pressure Turbine Airfoil Conditions: Part 1 - Mean Flow and Turbulence Statistics," *ASME J. Turbomach.*, **124**, pp. 645–655.
- [2] Mayle, R. E., 1991, "The Role of Laminar-Turbulent Transition in Gas Turbine Engines," *ASME J. Turbomach.*, **116**, pp. 509–537.
- [3] Schlichting, H., 1979, *Boundary Layer Theory*, 7th ed., McGraw Hill, New York, NY.
- [4] Sohn, K. H., and Reshotko, E., 1991, "Experimental Study of Boundary Layer Transition with Elevated Freestream Turbulence on a Heated Flat Plate," NASA CR 187068.
- [5] Volino, R. J., 2002, "An Investigation of the Scales in Transitional Boundary Layers Under High Free-Stream Turbulence Conditions," ASME Paper GT-2002-30233.
- [6] Hughes, J. D., and Walker, G. J., 2001, "Natural Transition Phenomena on an Axial Compressor Blade," *ASME J. Turbomach.*, **123**, pp. 392–401.
- [7] Halstead, D. E., Wisler, D. C., Okiishi, T. H., Walker, G. J., Hodson, H. P., and Shin, H.-W., 1997, "Boundary Layer Development in Axial Compressors and Turbines: Part 3 of 4—LP Turbines," *ASME J. Turbomach.*, **119**, pp. 225–237.
- [8] Solomon, W. J., and Walker, G. J., 1995, "Incidence Effects on Wake-Induced Transition on an Axial Compressor Blade," *Proc. 12th Int. Symposium on Air Breathing Engines*, Melbourne, Australia, pp. 954–964.
- [9] Hatman, A., and Wang, T., 1999, "A Prediction Model for Separated Flow Transition," *ASME J. Turbomach.*, **121**, pp. 594–602.
- [10] Volino, R. J., and Hultgren, L. S., 2001, "Measurements in Separated and Transitional Boundary Layers Under Low-Pressure Turbine Airfoil Conditions," *ASME J. Turbomach.*, **123**, pp. 189–197.
- [11] Lou, W., and Hourmouziadis, J., 2000, "Separation Bubbles Under Steady and Periodic-Unsteady Main Flow Conditions," *ASME J. Turbomach.*, **122**, pp. 634–643.
- [12] Ligrani, P. M., and Bradshaw, P., 1987, "Spatial Resolution and Measurement of Turbulence in the Viscous Sublayer Using Subminiature Hot-Wire Probes," *Exp. Fluids*, **5**, pp. 407–417.
- [13] Ligrani, P. M., and Bradshaw, P., 1987, "Subminiature Hot-Wire Sensors: Development and Use," *J. Phys. E*, **20**, pp. 323–332.
- [14] Ligrani, P. M., Westphal, R. V., and Lemos, F. R., 1989, "Fabrication and Testing of Subminiature Multi-Sensor Hot-Wire Probes," *J. Phys. E*, **22**, pp. 262–268.
- [15] Walker, G. J., 1989, "Transitional Flow on Axial Turbomachine Blading," *AIAA J.*, **27**, pp. 595–602.

# Predicting Transition Without Empiricism or DNS

**Mark W. Johnson**

Department of Engineering,  
University of Liverpool,  
Liverpool L69 3GH, UK

*A numerical procedure for predicting the receptivity of laminar boundary layers to freestream turbulence consisting of vortex arrays with arbitrary orientation has been developed. Results show that the boundary layer is most receptive to those vortices which have their axes approximately in the streamwise direction and vortex wavelengths of approximately  $1.2 \delta$ . The computed near wall gains for isotropic turbulence are similar in magnitude to previously published experimental values used to predict transition. The new procedure is therefore capable of predicting the development of the fluctuations in the laminar boundary layer from values of the freestream turbulence intensity and length scale, and hence determining the start of transition without resorting to any empirical correlation. [DOI: 10.1115/1.1506940]*

## Introduction

For many years, engineers have used empirical correlations (e.g., Abu-Ghannam and Shaw [1]) to predict transition on gas turbine blades. These correlations are generally fairly reliable for attached flows and where the flow is at least approximately two-dimensional, but for separated flow or where strong blade curvature or sweep is present there are no reliable correlation procedures. Furthermore, the collection and correlation of experimental data to encompass all the possible flow scenarios encountered on a gas turbine blade would appear to be an exhaustive task. In the last few years, direct numerical simulation techniques have been used successfully to predict transition for simple geometries. These methods do have the potential to predict transition accurately for situations where correlations can not. However, currently DNS is computationally too expensive to be used for engineering design calculations.

Work by Johnson and co-workers [2,3] and Mayle and co-workers [4,5] has improved physical understanding of the bypass transition process. They recognized that the growth of low-frequency streamwise velocity fluctuations in the pre-transitional boundary layer is directly responsible for the generation of turbulent spots. This resulted in the derivation of transition prediction procedures for both zero pressure gradient flows [5] and favorable and adverse pressure gradients (Johnson and Ercan [3]). Although these procedures were successful, they still require empirical correlation procedures to predict the velocity fluctuations in the pre-transitional boundary layer. Therefore, although the methods provide an improved understanding of bypass transition, their extension to more complex flow situations is not possible without further extensive empirical correlation data.

The purpose of the current work was to develop a numerical procedure to determine the velocity fluctuations in the pre-transitional boundary layer resulting from a prescribed freestream turbulence structure. The objective was to understand the mechanisms through which the fluctuations are generated, and hence to identify a means of prediction for general three dimensional boundary layers.

## Theory

Experimental work [3] has demonstrated that the amplitude of velocity fluctuations in the pre-transitional boundary layer scales with the amplitude of the freestream turbulence which induces them. This suggests that the fluctuations can be reasonably pre-

dicted through a linear perturbation method. Furthermore, the majority of empirical correlations for start of transition use purely local boundary layer conditions. This suggests that although historical effects do exist (e.g., leading edge geometry), these are of secondary importance. For simplicity therefore it has been assumed in the current work that the laminar fluctuations can be approximated as linear perturbations to a nondeveloping (inviscid) boundary layer whose profile is given by the polynomial

$$\frac{u}{U} = 2\left(\frac{y}{\delta}\right) - 5\left(\frac{y}{\delta}\right)^4 + 6\left(\frac{y}{\delta}\right)^5 - 2\left(\frac{y}{\delta}\right)^6 \quad (1)$$

The momentum equations governing the linear perturbation are then

$$u'_t + \frac{1}{\rho} p'_x + uu'_x + u_y v' - \nu \nabla^2 u' = 0 \quad (2)$$

$$v'_t + \frac{1}{\rho} p'_y + uv'_x - \nu \nabla^2 v' = 0 \quad (3)$$

$$w'_t + \frac{1}{\rho} p'_z + uw'_x - \nu \nabla^2 w' = 0 \quad (4)$$

and the continuity equation is

$$u'_x + v'_y + w'_z = 0 \quad (5)$$

The perturbation to be considered will be periodic in  $x$ ,  $z$ , and  $t$ , but must also decay in the streamwise direction through viscous dissipation. Therefore, if spanwise symmetry about  $z=0$  is assumed, the perturbation will be given by

$$\frac{u'}{U} = u_p e^{i\Omega_x(X-cT)} \cos(\Omega_z Z) e^{-\beta X} \quad (6)$$

$$\frac{v'}{U} = v_p e^{i\Omega_x(X-cT)} \cos(\Omega_z Z) e^{-\beta X} \quad (7)$$

$$\frac{w'}{U} = w_p e^{i\Omega_x(X-cT)} \sin(\Omega_z Z) e^{-\beta X} \quad (8)$$

$$\frac{p'}{\rho U^2} = p_p e^{i\Omega_x(X-cT)} \cos(\Omega_z Z) e^{-\beta X} \quad (9)$$

where the coefficients  $u_p$ ,  $v_p$ ,  $w_p$ , and  $p_p$  are complex functions of  $Y$ ,  $\Omega_x$ , and  $\Omega_z$  are the angular frequencies in the streamwise and spanwise directions, respectively,  $c$  is the perturbation convection velocity and  $\beta$  is the streamwise decay coefficient. The dimensionless spatial and temporal co-ordinates  $X$ ,  $Y$ ,  $Z$ , and  $T$  are defined in the Nomenclature.

Contributed by the International Gas Turbine Institute and presented at the International Gas Turbine and Aeroengine Congress and Exhibition, Amsterdam, The Netherlands, June 3-6, 2002. Manuscript received by the IGTI, April 10, 2001. Paper No. 2002-GT-30238. Review Chair: E. Benvenuti.

Substituting these expressions for the perturbation into the equations of motion (Eqs. (2)–(5)) leads to

$$\left[ -\frac{u}{U}\beta + i\left(\frac{u}{U} - c\right)\Omega_X + \frac{1}{\text{Re}}(\Omega_X^2 - D^2 + \Omega_Z^2 - \beta^2 + i2\beta\Omega_X) \right] u_p + \frac{(Du)}{U}v_p + (i\Omega_X - \beta)p_p = 0 \quad (10)$$

$$\left[ -\frac{u}{U}\beta + i\left(\frac{u}{U} - c\right)\Omega_X + \frac{1}{\text{Re}}(\Omega_X^2 - D^2 + \Omega_Z^2 - \beta^2 + i2\beta\Omega_X) \right] v_p + Dp_p = 0 \quad (11)$$

$$\left[ -\frac{u}{U}\beta + i\left(\frac{u}{U} - c\right)\Omega_X + \frac{1}{\text{Re}}(\Omega_X^2 - D^2 + \Omega_Z^2 - \beta^2 + i2\beta\Omega_X) \right] w_p - \Omega_Z p_p = 0 \quad (12)$$

$$(i\Omega_X - \beta)u_p + Dv_p + \Omega_Z w_p = 0 \quad (13)$$

where  $D \equiv d/dY$

**Freestream Perturbations.** In the freestream  $Du=0$ , and so through the elimination of the velocity fluctuations between Eqs. (2) to (5) it can be shown that the Laplacian of the pressure fluctuation is zero

$$\nabla^2 p' = 0 \quad (14)$$

Hence substituting from Eq. (9) and assuming a periodic variation of frequency  $\Omega_y^2$  in the  $Y$  direction

$$(\Omega_X^2 + \Omega_Y^2 + \Omega_Z^2 - \beta^2 + i2\beta\Omega_X)p_p = 0 \quad (15)$$

The only viable solution for a freestream disturbance where  $\Omega_x \neq 0$  is that  $p_p = 0$ . Equation (10) now becomes

$$\left[ -\beta + i(1-c)\Omega_X + \frac{1}{\text{Re}}(\Omega_X^2 + \Omega_Y^2 + \Omega_Z^2 - \beta^2 + i2\beta\Omega_X) \right] u_p = 0 \quad (16)$$

Identical forms of this equation also result from Eqs. (11) and (12) for the  $v$  and  $w$  velocity components, and so for a nonzero solution for the perturbation velocity field

$$c = 1 + \frac{2\beta}{\text{Re}} \quad (17)$$

and

$$\beta^2 + \text{Re}\beta - (\Omega_X^2 + \Omega_Y^2 + \Omega_Z^2) = 0 \quad (18)$$

or for positive  $\beta$

$$\beta = \frac{-\text{Re} + (\text{Re}^2 + 4(\Omega_X^2 + \Omega_Y^2 + \Omega_Z^2))^{0.5}}{2} \quad (19)$$

For typical boundary layers and frequencies

$$\text{Re} \gg (\Omega_X^2 + \Omega_Y^2 + \Omega_Z^2) \quad (20)$$

so

$$\beta \approx \frac{(\Omega_X^2 + \Omega_Y^2 + \Omega_Z^2)}{\text{Re}} \quad (21)$$

The convection velocity (Eq. (17)) can now be rewritten as

$$c \approx (1 + 4(F_x^2 + F_y^2 + F_z^2))^{0.5} \quad (22)$$

where  $F_x = \Omega_x/\text{Re} = f_x u/U^2$ ,  $F_y = f_y v/U^2$  and  $F_z = f_z w/U^2$ .

The amplitude of a perturbation  $A$  with spatial frequencies  $F_x$ ,  $F_y$ , and  $F_z$  is then given by

$$A = A_0 \exp[0.5 \text{Re}_x(1 - [1 + 4(F_x^2 + F_y^2 + F_z^2)]^{0.5})] \quad (23)$$

where  $A_0$  is its amplitude at some arbitrary  $X=0$  datum. For typical windtunnel conditions the dimensionless frequencies  $F_x$ ,  $F_y$ , and  $F_z$  will be much less than unity, and so  $A$  can be approximated as

$$A \approx A_0 \exp[-\text{Re}_x(F_x^2 + F_y^2 + F_z^2)] \quad (24)$$

This equation suggests that the frequency spectra for the perturbations is only a function of  $\text{Re}_x(F_x^2 + F_y^2 + F_z^2)$ , and hence that the turbulent length scale will vary as  $x^{0.5}$  which has been confirmed in wind tunnel experiments (Roach [6]). The overall turbulent decay can also be determined as

$$Tu^2 = Tu_0^2 \int_0^x \int_0^x \int_0^x A^2 dF_z dF_y dF_x \quad (25)$$

$$\text{which results in } Tu = Tu_0 \text{Re}_x^{-0.75} \quad (26)$$

This result does not agree exactly with the experimental results of Roach who observed a power law decay, but with a coefficient of  $-0.714$ .

**Boundary Layer Fluctuations.** The momentum equations (10)–(12) can now be simplified using the relationships (17) and (18) to obtain

$$\left[ -\frac{1}{\text{Re}}(D^2 + \Omega_Y^2) + (i\Omega_X - \beta)\left(\frac{u}{U} - 1\right) \right] u_p + \frac{(Du)}{U}v_p + (i\Omega_X - \beta)p_p = 0 \quad (27)$$

$$\left[ -\frac{1}{\text{Re}}(D^2 + \Omega_Y^2) + (i\Omega_X - \beta)\left(\frac{u}{U} - 1\right) \right] v_p + Dp_p = 0 \quad (28)$$

$$\left[ -\frac{1}{\text{Re}}(D^2 + \Omega_Y^2) + (i\Omega_X - \beta)\left(\frac{u}{U} - 1\right) \right] w_p - \Omega_Z p_p = 0 \quad (29)$$

The response of the laminar boundary layer to the freestream fluctuations defined by the ordinary differential Eqs. (13), (27)–(29) can now be sought. Fourth-order finite difference approximations using a uniform grid spacing of  $\Delta Y = 0.01$  was used with a Gauss Seidel elimination procedure. This system of equations requires seven boundary conditions as the equations are second order in  $u_p$ ,  $v_p$ , and  $w_p$  and first order in  $p_p$ . Four of these boundary conditions are provided at the wall, viz.,  $u=v=w=0$  and  $Dv=0$ . The remaining three boundary conditions result from the three velocity components in the freestream vortex array.

**Freestream Turbulence.** In the current work the response of the boundary layer to homogeneous isotropic freestream turbulence is sought. The momentum Eq. (27)–(29) are satisfied in the freestream by any periodic variation in  $Y$  of frequency  $\Omega_y$ , but the amplitude of this variation must also satisfy the continuity Eq. (13). The solution for an array of vortices is

$$\frac{u_1}{U} = 0 \quad (30)$$

$$\frac{v_1}{U} = \frac{e^{-\beta X}(\Omega^2 + \beta^2 b_x^2)^{0.5} \cos(\Omega Y_1 - \alpha_Y) \cos(\Omega Z_1)}{(2\Omega^2 + \beta^2(n_x^2 + b_x^2))^{0.5}} \quad (31)$$

$$\frac{w_1}{U} = \frac{e^{-\beta X}(\Omega^2 + \beta^2 n_x^2)^{0.5} \sin(\Omega Y_1) \sin(\Omega Z_1 - \alpha_Z)}{(2\Omega^2 + \beta^2(n_x^2 + b_x^2))^{0.5}} \quad (32)$$

where  $u_1$ ,  $v_1$ , and  $w_1$  are the velocity components in the  $X_1$ ,  $Y_1$ , and  $Z_1$  coordinate directions, which are given by

$$\begin{pmatrix} X_1 \\ Y_1 \\ Z_1 \end{pmatrix} = \begin{pmatrix} a_x & a_y & a_z \\ n_x & n_y & n_z \\ b_x & b_y & b_z \end{pmatrix} \begin{pmatrix} X \\ Y \\ Z \end{pmatrix} \quad (33)$$

and the lags  $\alpha_y$ ,  $\alpha_z$  resulting from the viscous decay are

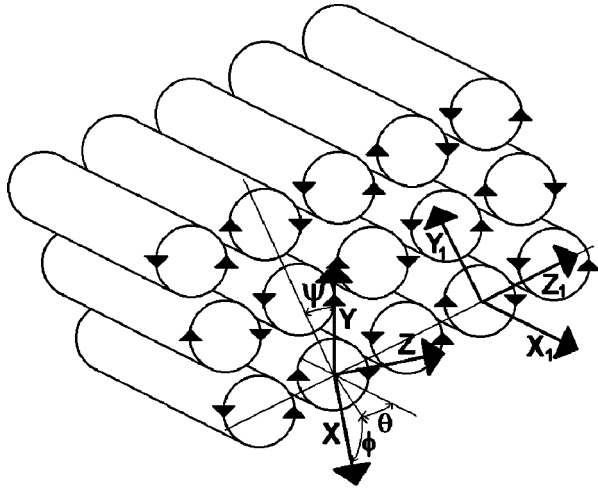


Fig. 1 Definition of the vortex coordinate system

$$\sin \alpha_Y = \frac{\beta n_X}{(\Omega^2 + \beta^2 n_X^2)^{0.5}} \quad \text{and} \quad \sin \alpha_Z = \frac{\beta b_X}{(\Omega^2 + \beta^2 b_X^2)^{0.5}}$$

Here the vortex and boundary layer coordinate systems are related through the unit vectors

$$\begin{pmatrix} a_X \\ a_Y \\ a_Z \end{pmatrix} = \begin{pmatrix} \cos \theta \cos \phi \\ \sin \phi \\ \sin \theta \cos \phi \end{pmatrix}$$

$$\begin{pmatrix} n_X \\ n_Y \\ n_Z \end{pmatrix} = \begin{pmatrix} \cos \theta \sin \phi \sin \psi + \sin \theta \cos \psi \\ -\cos \phi \sin \psi \\ \sin \theta \sin \phi \sin \psi - \cos \theta \cos \psi \end{pmatrix}$$

$$\begin{pmatrix} b_X \\ b_Y \\ b_Z \end{pmatrix} = \begin{pmatrix} \cos \theta \sin \phi \cos \psi - \sin \theta \sin \psi \\ -\cos \phi \cos \psi \\ \sin \theta \sin \phi \cos \psi + \cos \theta \sin \psi \end{pmatrix} \quad (34)$$

such that the orientation of the vortex axes are given by the angles  $\theta$  and  $\phi$  and the relative orientation of each vortex axis to its neighbors in the array by the angle  $\psi$  as shown in Fig. 1.

The boundary layer response to this freestream vortex array is given by a combination of two solutions of the Eqs. (13), (27)–(29) for frequencies of

$$\begin{pmatrix} \Omega_{X1} \\ \Omega_{Y1} \\ \Omega_{Z1} \end{pmatrix} = \Omega \begin{pmatrix} n_X + b_X \\ n_Y + b_Y \\ n_Z + b_Z \end{pmatrix}$$

and

$$\begin{pmatrix} \Omega_{X2} \\ \Omega_{Y2} \\ \Omega_{Z2} \end{pmatrix} = \Omega \begin{pmatrix} n_X - b_X \\ n_Y - b_Y \\ n_Z - b_Z \end{pmatrix} \quad (35)$$

Solutions were obtained for 100 vortex frequencies from 0 to  $2U/\delta$  Hz, 40  $\phi$  angles from 0 to 90 deg, 19  $\theta$  angles from 0 to 90 deg, and 45  $\psi$  angles from 0 to 45 deg. The value of  $\beta$  is such that freestream fluctuations above the upper limit frequency can be assumed to have decayed to a negligible amplitude.

**Near Wall Gain.** Johnson and Ercan [3] showed that in the near wall region (approximately  $Y < 0.2$ ) the near wall velocity fluctuations have an invariant frequency spectra and scale with the mean velocity. They therefore defined the near wall gain as

$$G = \frac{uU}{(U^2 + V^2)^{0.5}u} \quad (36)$$

as a measure of the receptivity of the boundary layer to freestream turbulence at a particular frequency. It should be noted that the hot wire used by Johnson and Ercan responded to both streamwise and normal velocity components but  $v=0$  near the wall.

## Results

Figure 2 shows the orientation averaged near wall velocity gain variation with the freestream vortex wavelength. The figure shows that the boundary layer is most responsive to a number of specific wavelengths. The values of the gain are however strongly influenced by the vortex orientation as shown in Fig. 3. These results have only been averaged over the array orientation angle  $\psi$  and clearly show that it is vortices with axes in or close to the streamwise direction that are most effective in generating near wall velocity fluctuations.

Figure 4 shows  $Y$ - $Z$  plane velocity and pressure plots for a near streamwise vortex array at 25 and 50% points in the vortex cycle. The freestream vortex possesses a very low streamwise velocity component, but as the vortex interacts with the strong shear in the boundary layer, the normal velocity  $v$  component carries high  $u$  velocity fluid into the boundary layer and although there is a rapid decay in the  $v'$  component this induces a change in pressure which extends to the wall. This change in pressure results in a corresponding  $u'$  component which is greatest near the wall where the steady velocity is least. It is therefore the pressure fluctuation which induces the strong streamwise velocity fluctuations near the wall. These streamwise “streaks” actually possess only weak streamwise vorticity as indicated by the small  $v'$  and  $w'$  velocity components. The lower diagram in Fig. 4 shows that there is a phase lag between the pressure and streamwise velocity fluctuations. The amount of lag will depend on the relative magnitudes of  $\Omega_x$  and  $\beta$  which determine the relative magnitude of the real and imaginary terms in the governing Eqs. (13) and (27)–(29)

The streamwise velocity fluctuations or streaks have also been observed in experimental boundary layer studies (e.g., Kit-tichaikam et al. [7] and Westin et al. [8]) and in DNS results Voke [9]. Westin et al. observed that the vortex spacing was approximately  $1.2 \delta$  which correlates closely with one of the peaks observed in Fig. 2. Vortices with wave numbers less than one will decay rapidly in the freestream as indicated by Eq. (24), so although the gain for these vortices is high their amplitude in the freestream and the boundary layer will be low. It is clear that the near wall streaks induced by freestream streamwise vortices have an important role in the transition process. It is also clear that if

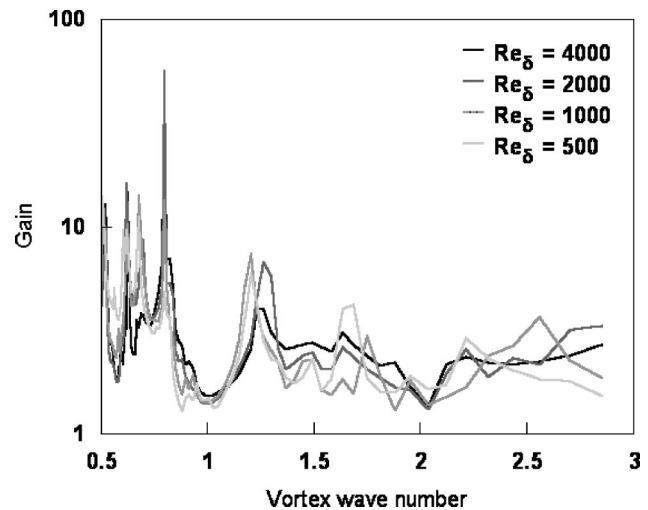


Fig. 2 Vortex orientation averaged near wall gain as a function of freestream vortex wave number

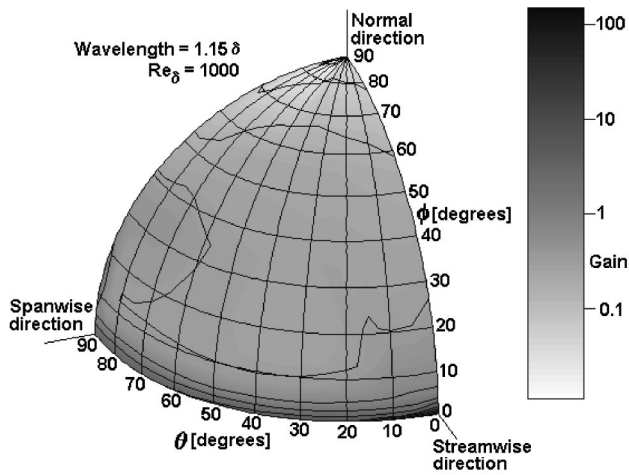


Fig. 3 Effect of vortex axis direction on the near wall gain for a vortex wave number of 1.15 and a  $Re_\delta=1000$

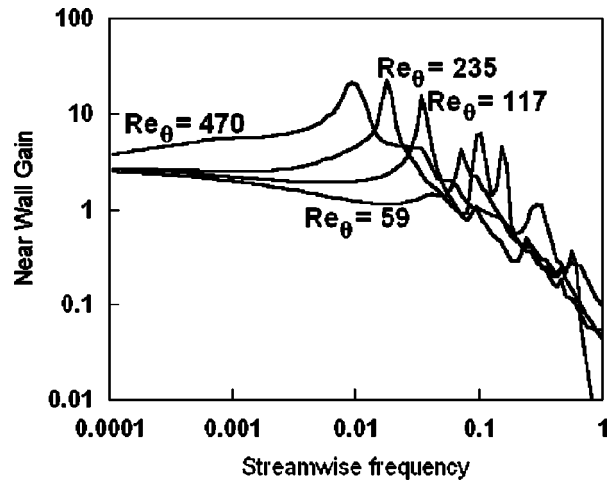


Fig. 5 Near wall gain for isotropic turbulence. (Turbulence generating grid to plate leading edge Reynolds number of 500,000.)

the receptivity of the boundary layer to these vortices can be reduced, then transition can be delayed and it seems likely that this is how drag reduction techniques such as polymers, riblets, and surface dendricles are successful.

**Streamwise Velocity Fluctuations.** Equation (35) indicates that a vortex with a frequency  $\Omega$  will contribute velocity fluctuations in the three coordinate directions with frequencies between 0 and  $\sqrt{2}\Omega$  dependent on the vortex orientation. In particular, the vortices with streamwise or near streamwise axes ( $\theta$  small and  $\phi$  small) to which the laminar boundary layer is particularly receptive and have relatively high  $\Omega_Y$  and  $\Omega_Z$  frequencies will have very low streamwise frequencies. This results in the highest gains being observed at the lowest streamwise frequencies as indicated in Fig. 5, which shows the orientation averaged gain values plotted against the streamwise frequency  $\Omega_X$ . The current results therefore identify the freestream streamwise vortices as being the source of these low frequencies. Mayle et al. [4,5] also determined that the low streamwise frequencies (wavelengths of 17–19  $\delta$ ) were responsible for generating the majority of the near wall velocity fluctuations. The predicted gains in Fig. 5 are close to the measured values obtained by Johnson and Ercan shown in Fig. 6 for frequencies above 0.01. For lower frequencies the predicted values tend to decrease whereas the measured values are almost constant. The reason for this is probably that the frequency resolution of the current results is insufficient as the discrepancy at low frequencies was observed to worsen when lower numbers of vortex frequencies were used for the predictions. Figure 2 indi-

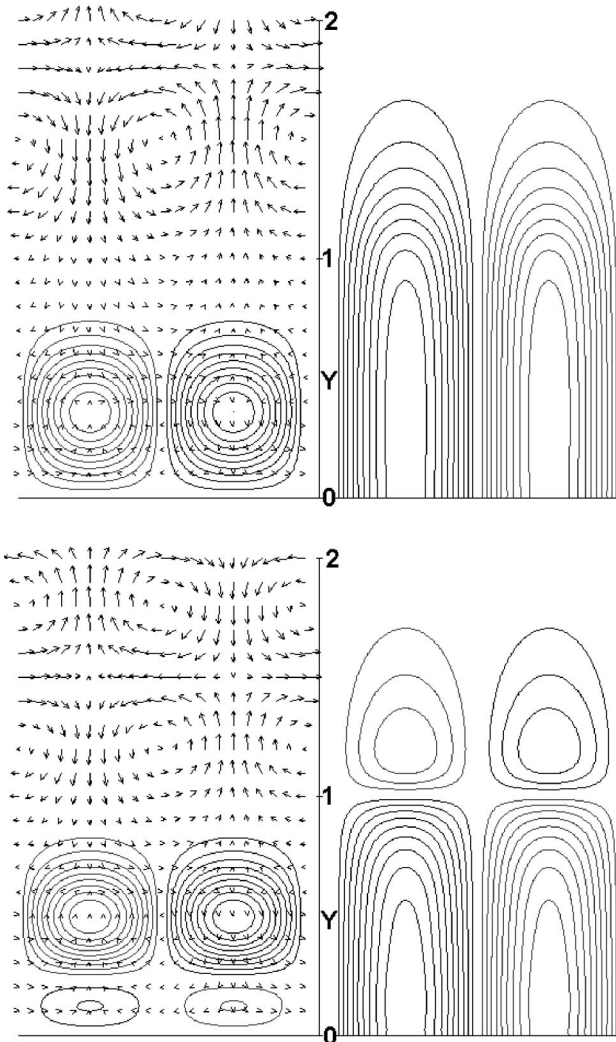


Fig. 4 Y-Z cross section of approximately streamwise vortices  $\theta=0$  deg,  $\phi=1$  deg. Left-hand diagrams show velocity perturbation and right hand diagrams show pressure perturbation. Contours: grey—negative, black—positive.

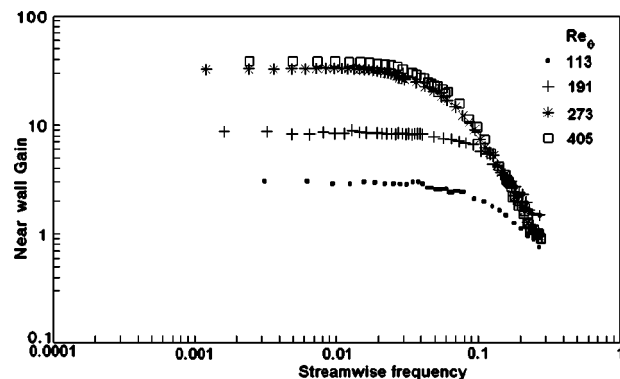


Fig. 6 Experimental near wall gain results from [3]

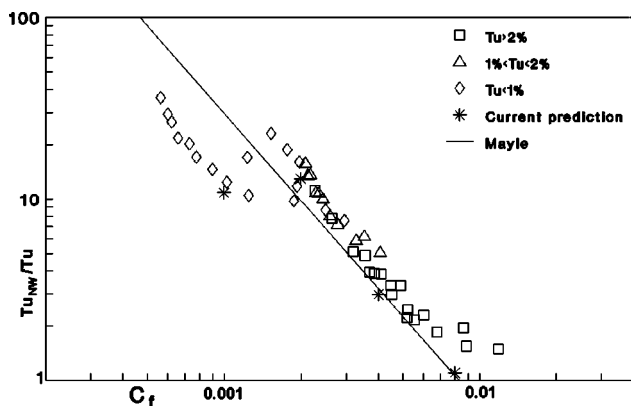


Fig. 7 Ratio of near wall to freestream turbulence levels

ated that resonant peaks exist in the frequency response and if these peaks are not accurately resolved significant errors may result in their contribution to the gain.

**Transition Prediction.** When the results from Fig. 5 are integrated over the full frequency range, the ratio of the near wall to freestream turbulence level is found. These values are shown in Fig. 7 together with experimental values from the ERCOFTAC zero pressure gradient test cases [10]. Mayle's zero pressure gradient transition correlation [11] is also plotted on this figure where it has been assumed that the near wall turbulence level reaches 23% at start of transition as suggested by Fasihfar and Johnson [2]. At higher values of  $C_f$  the current predictions lie very close to the Mayle line, however at lower values of  $C_f$  corresponding to start of transition where  $Tu < 1\%$ , the current predictions would result in transition at a higher Reynolds number than given by Mayle. The predicted values are however within the range of the ERCOFTAC data. Johnson and Ercan deduced that start of transition is more likely to be influenced by the freestream turbulent length scale at low  $C_f$  (i.e., low freestream turbulence level) and this is believed to be responsible for the differences observed here.

## Conclusions

1 A linear perturbation technique has been developed which is capable of predicting the receptivity of laminar boundary layers to isotropic turbulence consisting of vortex arrays at arbitrary orientation.

2 Laminar boundary layers are most receptive to freestream vortices which have their axes in approximately the streamwise direction. These vortices induce strong pressure fluctuations within the boundary layer which induce streamwise velocity fluctuation streaks near the wall. These streaks have preferred spanwise spacings which concur with experimental observations.

3 The predicted near wall gain variation with streamwise fluctuation frequency agrees with previously published hot wire measurements.

4 The current results lead to a predictive procedure for start of transition from values of the freestream turbulence intensity and length scale which does not require any empirical information, but is much simpler than DNS. The method can also be extended to predict spot generation rates and hence transition length.

## Future Work

The present paper is restricted to zero pressure gradient boundary layers on flat plates, however the receptivity of any two-dimensional boundary layer can be predicted simply by altering

the boundary layer profile given in Eq. (1). Future work will therefore consider boundary layers subjected to streamwise pressure gradients including those that have undergone separation. The current procedure can be extended to three-dimensional boundary layers, and hence the effects of flow features such as secondary flow on receptivity and hence transition can be studied. It is also planned to use the procedure to investigate the effects of compliant surfaces and riblets on receptivity with a view to optimizing drag reduction.

## Nomenclature

- $a_x, a_y, a_z$  = unit vector in freestream vortex axis direction  
 $b_x, b_y, b_z$  = unit vector in freestream vortex binormal direction  
 $c$  = fluctuation convection velocity  
 $f_x, f_y, f_z$  = fluctuation frequencies in  $x$ ,  $y$ , and  $z$  directions  
 $F_x, F_y, F_z$  = dimensionless fluctuation frequencies  
 $n_x, n_y, n_z$  = unit vector in freestream vortex normal direction  
 $p'$  = fluctuating pressure  
 $Re$  = boundary layer thickness Reynolds number  
 $Re_x$  = streamwise distance Reynolds number  
 $t$  = time  
 $T$  = ( $= Ut/\delta$ ) dimensionless time  
 $u$  = streamwise time mean velocity  
 $u, v, w$  = streamwise, normal, and spanwise fluctuating velocity components  
 $U$  = freestream time mean velocity  
 $U, V, W$  = freestream fluctuating velocity components  
 $x, y, z$  = streamwise, normal and spanwise coordinates  
 $X, Y, Z$  = ( $= x/\delta, y/\delta, z/\delta$ ) dimensionless streamwise, normal, and spanwise coordinates  
 $\beta$  = fluctuation decay coefficient  
 $\delta$  = boundary layer thickness  
 $\nu$  = kinematic viscosity  
 $\rho$  = fluid density  
 $\Omega_x, \Omega_y, \Omega_z$  = dimensionless fluctuation frequencies in  $X$ ,  $Y$  and  $Z$  directions

## Subscripts

- $t, x, y, z$  = derivatives in  $t$ ,  $x$ ,  $y$  and  $z$   
 $p$  = Fourier coefficient

## References

- [1] Abu-Ghannam, B. J., and Shaw, R., 1980, "Natural Transition of Boundary Layers—The effects of Turbulence, Pressure Gradient and Flow History," *J. Mech. Eng. Sci.*, **22**, pp. 213–228.
- [2] Fasihfar, A., and Johnson, M. W., 1992, "An Improved Boundary Layer Transition Correlation," ASME Paper No. 92-GT-245
- [3] Johnson, M. W., and Ercan, A. H., 1999, "A Physical model for Bypass Transition," *Intl. Jnl. of Heat and Fluid Flow*, **20**, pp. 95–104.
- [4] Mayle, R. E., and Schultz, A., 1997, "The path to predicting bypass transition," *ASME J. Turbomach.*, **119**, pp. 405–411.
- [5] Mayle, R. E., Dullenkopf, K., and Schultz, A., 1998, "The Turbulence That Matters," *ASME J. Turbomach.*, **120**, pp. 402–409.
- [6] Roach, P. E., 1987, "The Generation of nearly Isotropic Turbulence by means of Grids," *Int. J. Heat Fluid Flow*, **8**, pp. 82–92.
- [7] Kittichaiakarn, C., Ireland, P. T., Zhong, S., and Hodson, H. P., 1999, "An investigation on the onset of wake-induced transition and turbulent spot production rate using thermochromatic liquid crystals," ASME Paper 99-GT-126.
- [8] Westin, K. J. A., et al., 1994, "Experiments in a boundary layer subjected to freestream turbulence. Part 1. Boundary layer structure and receptivity," *J. Fluid Mech.*, **281**, pp. 193–218.
- [9] Voke, P. R., 1995, "Laminar/turbulent transition of boundary layers influenced by freestream disturbances," *Euromech 330*, Prague.
- [10] Savill, A. M., 1991, A synthesis of T3 test case predictions. Proc., 1st ERCOFTAC workshop, Cambridge University Press.
- [11] Mayle, R. E., 1991, "The Role of Laminar-Turbulent Transition in Gas Turbine Engines," *ASME J. Turbomach.*, **113**, pp. 509–537.

# Evaluation of Pressure Side Film Cooling With Flow and Thermal Field Measurements—Part I: Showerhead Effects

**J. Michael Cutbirth**

William B. Morgan Large Cavitation Channel,  
Naval Surface Warfare Center,  
Carderock Division,  
Memphis, TN 38113

**David G. Bogard**

Mechanical Engineering Department,  
University of Texas at Austin,  
Austin, TX 78712

*The goal of this study was to determine how showerhead blowing on a turbine vane leading edge affects the performance of film cooling jets farther downstream. An emphasis was placed on measurements above the surface, i.e., flow visualization, thermal field, and velocity field measurements. The film cooling performance on the pressure side of a simulated turbine vane, with and without showerhead blowing, was examined. Results presented in this paper are for low mainstream turbulence; high mainstream turbulence effects are presented in the companion paper. At the location of the pressure side row of holes, the showerhead coolant extended a distance of about  $3d$  from the surface ( $d$  is the coolant hole diameter). The pressure side was found to be subjected to high turbulence levels caused by the showerhead injection. Results indicate a greater dispersion of the pressure side coolant jets with showerhead flow due to the elevated turbulence levels.*

[DOI: 10.1115/1.1504441]

## Introduction

Film cooling of a turbine vane typically involves ejection of a large amount of coolant from a “showerhead” region of holes around the leading edge of the vane. Due to dispersion of the resulting coolant film, additional coolant is ejected along the surface at various intervals along the airfoil. Consequently, the coolant flow from the showerhead region interacts with the coolant jets located downstream affecting the performance of these downstream jets. Although there have been a few studies of the adiabatic effectiveness performance of these downstream film cooling holes, there have been no previous studies of the thermal field, and mean and turbulent velocity fields at the downstream location due to showerhead injection. Measurement of these thermal and velocity fields gives insight into how the showerhead blowing affects downstream film cooling performance.

One objective of this study was to determine whether the showerhead flow is reasonably simulated as a turbulent boundary layer at the downstream location. The vast majority of previous film-cooling studies have assumed a turbulent boundary layer as an approach condition. Some previous studies (e.g., [1]) have investigated the effect of varying the approach boundary layer for a row of film cooling holes. Increasing the boundary layer thickness was found to generally decrease the film cooling performance. This is due to a thicker boundary layer being less effective in turning the coolant jet and keeping it attached to the surface.

Previous studies, such as [2–5], have investigated the effect of showerhead flow on downstream cooling performance using adiabatic effectiveness and heat transfer coefficients. Drost and Böls [3] and Polanka et al. [5] studied the effects of a showerhead injection on the pressure side cooling of a simulated turbine vane. Both studies found that the combined effect of showerhead and pressure side coolant injection was not well predicted using a superposition model, suggesting that the performance of the pressure side coolant jets were affected in some way by the showerhead coolant flow. However, because measurements in these pre-

vious studies were confined to surface measurements, these studies failed to yield the physical mechanisms of the interaction between the coolant flows.

This paper presents Part I of a two-part study in which the “off-the-wall” flow visualization, thermal field and velocity field techniques described in Cutbirth and Bogard [6] were used to investigate the interaction of showerhead coolant flow with downstream film cooling. For Part I of the study, a low mainstream turbulence level was used, while the companion Part II paper [7] focuses on showerhead effects on downstream cooling with high mainstream turbulence. Although high mainstream turbulence is more realistic, the mainstream turbulence can be a dominating influence. Hence, use of low mainstream turbulence in this study allows a focus on the showerhead effects alone.

## Facilities and Experimental Conditions

The test facility for this study consisted of a closed-loop, low-speed wind tunnel, driven by a 50-hp variable pitch fan. The test section, shown in Fig. 1, consisted of a simulated three-vane and two passage turbine vane cascade with outer by-pass passages and adjustable walls to assure proper flow about the center model test vane. A full description of the facility is given by Polanka [8].

The geometry of the airfoil was a large-scale model of a first stage modern commercial inlet guide vane. The model vane had a chord length of 59.4 cm and a span length of 54.9 cm. The test vane was constructed using a polyurethane foam selected for low conductivity,  $k=0.048$  W/m·K, and structural strength. The leading edge of the vane had a wall thickness of 1.37 cm. The coolant hole diameter and pitch were constant throughout the vane and were  $d=4.11$  mm and  $p=5.55d$ , respectively.

The configuration of the coolant holes used in the current study is shown in Fig. 2. The results for this study focus on the film cooling performance of the first row of coolant holes on the pressure side of the vane located at  $x/d=-25$  where  $x=0$  was the position of the stagnation line at the leading edge of the vane. The showerhead region consisted of six rows of holes, spaced  $3.33d$  apart, with staggered hole positions between rows. For these measurements, the stagnation line of the flow was positioned at the center of the third row from the pressure side. Therefore, partial coolant from this row, and the two remaining coolant rows on the pressure side, provided the showerhead coolant flow directed along the pressure side of the vane. Each of the coolant holes in

Contributed by the International Gas Turbine Institute and presented at the International Gas Turbine and Aeroengine Congress and Exhibition, Amsterdam, The Netherlands, June 3–6, 2002. Manuscript received by the IGTI, November 2, 2001. Paper No. 2002-GT-30174. Review Chair: E. Benvenuti.



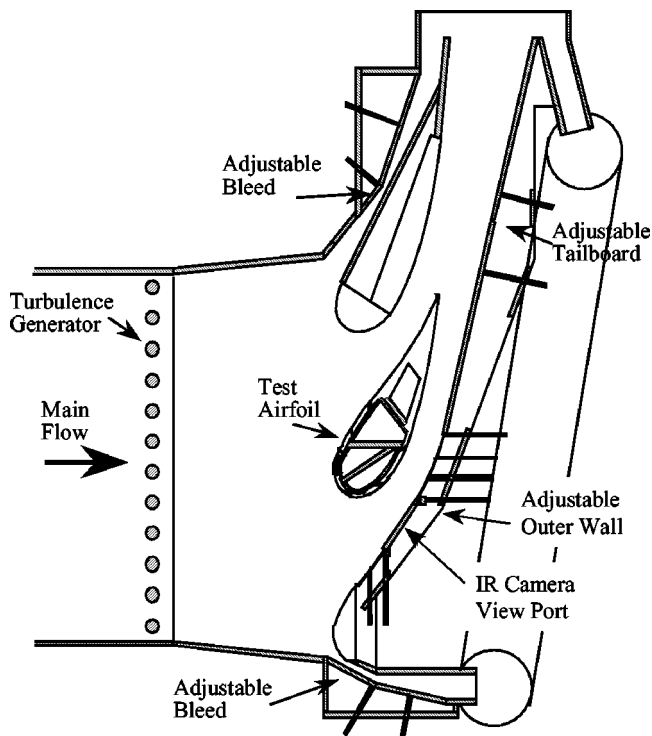


Fig. 1 Turbine vane test section

the showerhead that contributed to the coolant flow towards pressure side coolant holes of interest, had an injection angle of  $\phi=25$  deg, and were oriented laterally (downward,  $-z$  direction) with a streamwise angle of  $\theta=90$  deg. The coolant configuration for the pressure side row of holes consisted of an injection angle of  $\phi=25$  deg with a streamwise angle of  $\theta=45$  deg.

As is evident in Fig. 2, the vane test model used in this study had a “cross-over” region in the showerhead where the orientation of the film cooling holes reversed direction. All results presented in this paper were obtained in a “two-dimensional region” located above any influence by the cross-over region.

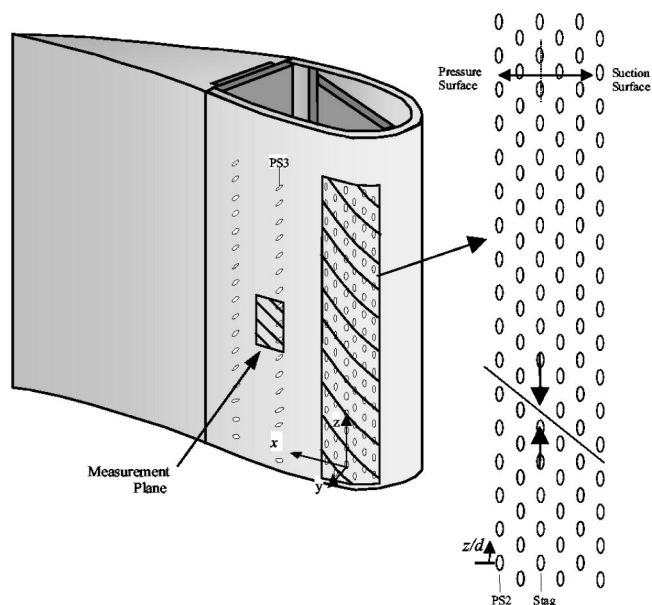


Fig. 2 Film-cooling hole configuration and location of measurement plane

Separate interior plenums fed the showerhead and pressure region allowing for independent control of the blowing ratio as well as independent seeding for flow imaging. To insure proper flow entering the coolant holes, the interior of the test airfoil included impingement plates consisting of 1-mm-thick stainless steel plates spaced 5.5 mm from the inner surface of the airfoil and molded to fit the contour of the turbine vane geometry. The impingement holes were 7.8 mm in diameter with a pitch of  $5.55d$ .

The coolant temperature was maintained at 167 K for the effectiveness tests, yielding a density ratio of  $DR=1.8$  and approximating actual engine conditions. However, thermal field and velocity field measurements were done using a density ratio of  $DR=1.2$ . Cutbirth [9] showed that film cooling performance for these two density ratio conditions were best matched using the mass flux ratio,  $M$ , for the showerhead while matching the momentum flux ratio,  $I$ , for the pressure side coolant holes, at a location of  $x/d=-28$ . In this study, our focus was on a low momentum flux ratio,  $I=0.2$ , for which the coolant jets remain attached to the surface, and a high momentum  $I=1.2$ , for which the coolant jets are expected to be separated from the surface. At a density ratio of  $DR=1.8$ , the associated mass flux ratios for the  $I=0.2$  and  $1.2$  conditions are  $M=0.6$  and  $1.5$ , respectively; while for  $DR=1.2$ , the associated mass flux ratios for the  $I=0.2$  and  $1.2$  conditions are  $M=0.5$  and  $1.2$ , respectively. For these two blowing conditions, adiabatic effectiveness performance was nominally the same for  $DR=1.8$  and  $DR=1.2$ .

The surface temperatures on the center vane model were measured using an infrared camera, Inframetrics 600L, with a spatial resolution of  $0.7d \times 0.7d$ . Calibration of the captured images was performed using type T thermocouples. Using this method, the uncertainty of the surface temperatures were determined to be  $\pm 1.0$  K for  $T_{aw} > 220$  K and  $\pm 2.6$  K for  $T_{aw} < 220$  K. A full description of the technique is given by Witteveld et al. [10].

The measured surface temperatures, coolant jet temperature, and mainstream temperature were used to calculate the adiabatic effectiveness as defined in Eq. (1).

$$\eta = \frac{(T_{\infty} - T_{aw})}{(T_{\infty} - T_c)} \quad (1)$$

The uncertainty in effectiveness (95% confidence interval) was  $\delta\eta=0.02$  for  $\eta > 0.4$ ,  $\delta\eta=0.01$  for  $\eta < 0.4$ , and  $\delta\bar{\eta}=0.01$  for all  $\bar{\eta}$ . The uncertainty of the blowing ratio was  $\delta M_{sh} = \pm 0.03$  for the showerhead cooling and varied from  $\delta I_{ps} = 0.01$  to  $\delta I_{ps} = 0.05$  for blowing conditions of  $I_{ps} = 0.2$  to  $I_{ps} = 1.2$ , respectively, for the pressure side cooling.

Prediction of the combined performance of the showerhead cooling and the pressure side cooling was done using the superposition model given by Sellers [11]. The superposition prediction is given by Eq. (2), where  $\eta_1$  and  $\eta_2$  refer to the showerhead only and pressure side only conditions, respectively.

$$\eta = \eta_1 + (1 - \eta_1) \cdot \eta_2 \quad (2)$$

Velocity measurements were performed using a three-component laser Doppler velocimeter constructed using TSI components. For these measurements, collection was performed in noncoincident mode using side-scatter with  $1\text{-}\mu\text{m}$ -dia titanium dioxide used as seed particles. Fluidized beds were used to seed the flow within the coolant line and mainstream. Details of the laser Doppler velocimeter system are presented in Cutbirth [9].

The temperature probe used in this study consisted of twelve type E thermocouples suspended by two 1.5-mm-dia prongs. The prongs were spaced two pitches,  $4.6$  cm,  $11.1d$ , apart. The thermocouples were  $80\text{-}\mu\text{m}$ -dia wires with  $0.4\text{-mm}$ -dia Teflon insulation. The thermocouples were stripped bare for the center  $2.0$  mm of the probe, with a  $1\text{-mm}$  overlap between the Constantan and Chromel wire, and tack welded. This yielded an array of  $0.16\text{-mm}$ -dia,  $1\text{-mm}$ -long temperature sensors. The thermal field data were normalized using Eq. (2) and the uncertainty in the measured  $\Theta$  values (95% confidence interval) was  $\delta\Theta=0.01$ .

$$\Theta \equiv \frac{(T_\infty - T)}{(T_\infty - T_c)} \quad (3)$$

For flow visualization, a 1-mm-thick laser sheet of light was used to illuminate titanium dioxide seed particles within the pressure side coolant flow. Imaging and recording of the flow visualization was performed using a commercial camcorder and VCR. The image processing was performed using the NIH Image software. Images were recorded at a rate of 30 frames per second. For the time-averaged flow visualization images, 8 images collected over an interval of one second were used.

All experiments were conducted with a mainstream approach velocity of  $U_0 = 5.8$  m/s, which established a Reynolds number matching that of actual engine operation ( $Re = 1.2 \times 10^6$ , based on chord length and exit velocity).

## Results

In the following presentation of results the effect of the showerhead blowing on the downstream flow is illustrated using flow visualization, and quantified with velocity field and thermal field measurements. These results are followed with adiabatic effective-

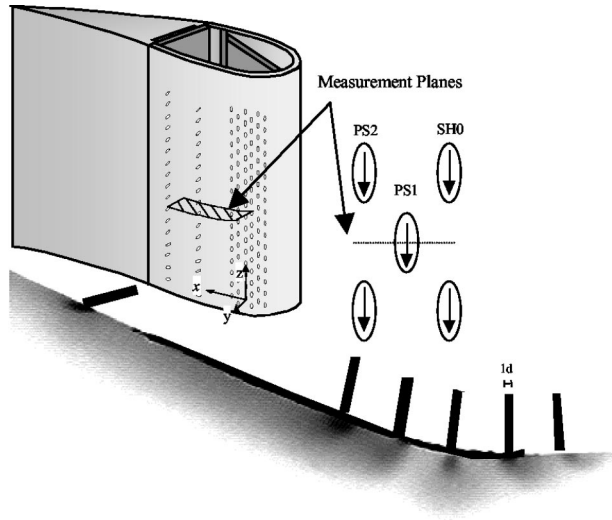


Fig. 3 Flow visualization of the showerhead film cooling with  $z/p = 7.5$  and  $M_{sh}^* = 1.5$

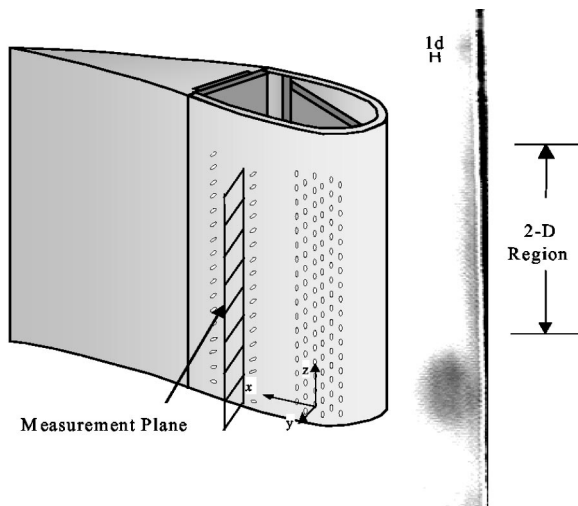


Fig. 4 Flow visualization of the upstream flow field for the pressure side film cooling with  $I_{ps} = 0.0$  and  $M_{sh}^* = 1.5$

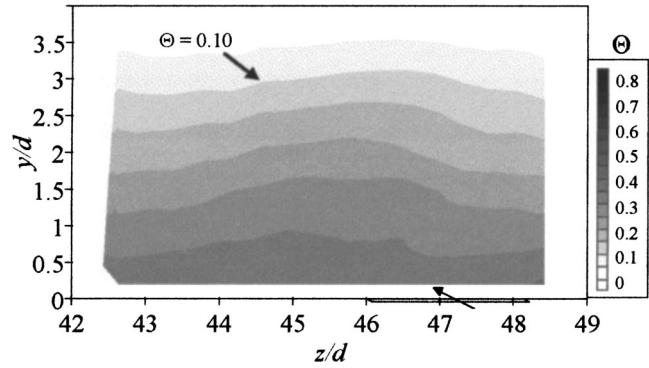
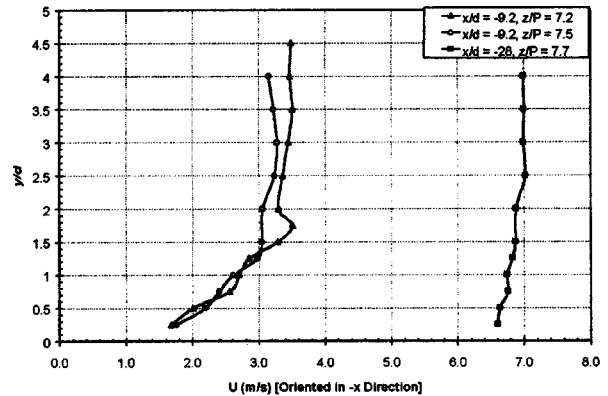


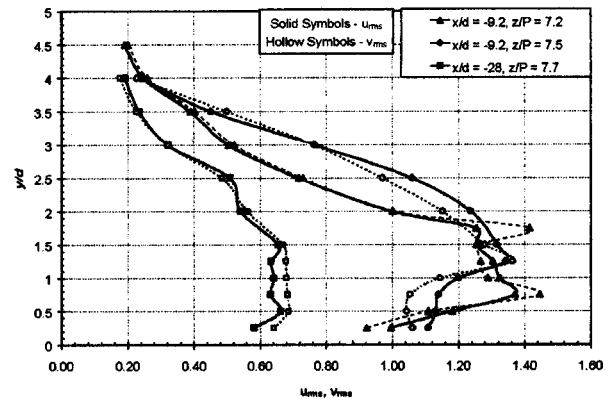
Fig. 5 Thermal profile of the showerhead coolant flow immediately upstream of the pressure side coolant row with  $M_{sh}^* = 1.5$  and  $x/d = -22$

ness measurements following the first row of holes, without and with showerhead blowing. Finally, the process by which the showerhead blowing interacts with the pressure side film cooling is detailed with flow visualization, thermal field measurements, and velocity field measurements.

**Effect of Showerhead Blowing on Approach Flow.** For this study the showerhead region of the simulated vane was operated with a blowing ratio of  $M_{sh}^* = 1.5$ . This is a blowing ratio giving good adiabatic effectiveness performance in the showerhead region (see Polanka et al. [12]). Flow visualization of the coolant



(a)



(b)

Fig. 6 Showerhead (a) mean and (b) rms profiles at  $x/d = -9$  and  $-28$  with  $M_{sh}^* = 1.5$

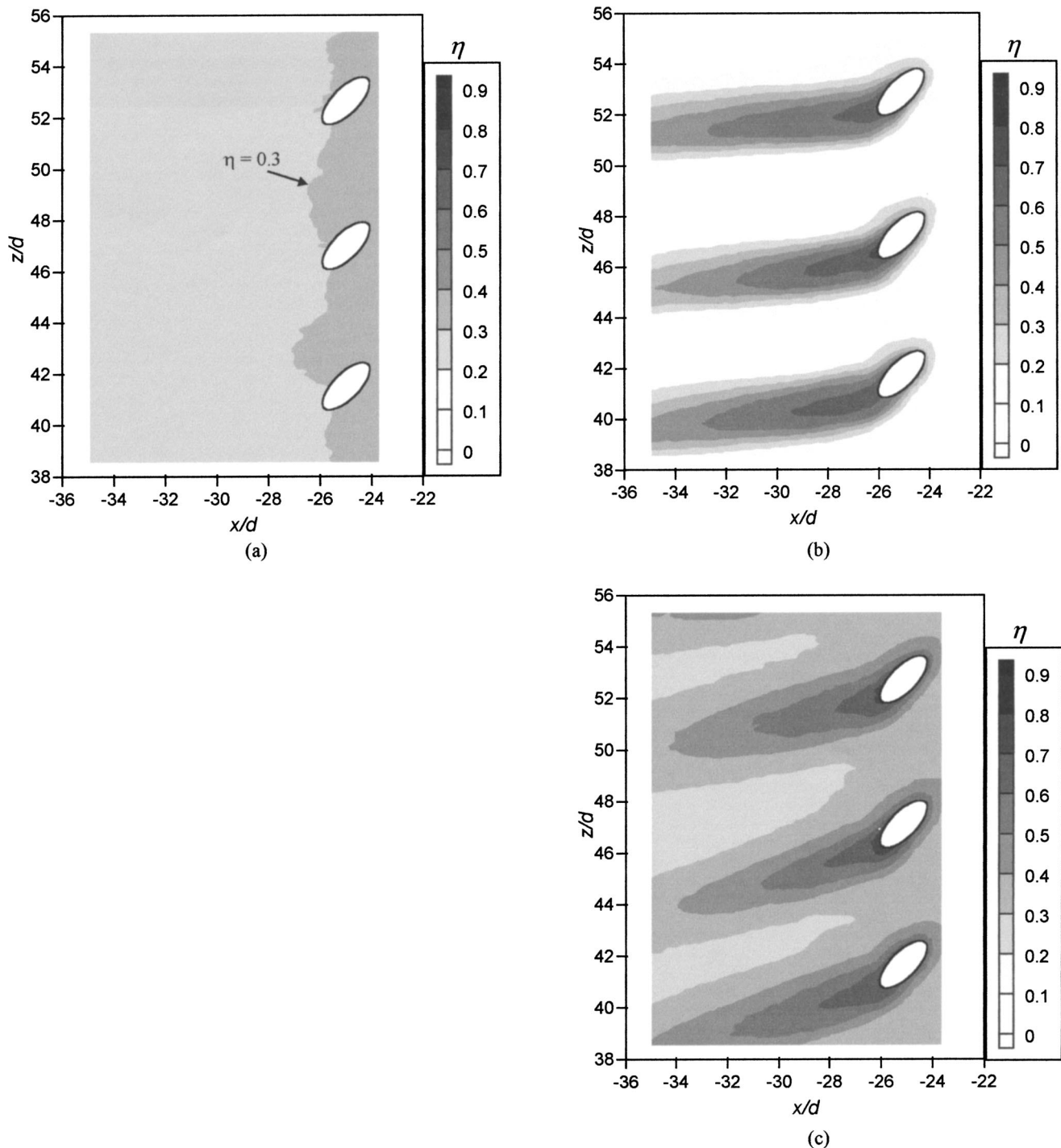


**Fig. 7 Comparison of upstream coolant conditions for (a)  $I_{ps}=0.0$  and  $M_{sh}^*=1.5$ , (b)  $I_{ps}=0.2$  and  $M_{sh}^*=0.0$ , and (c)  $I_{ps}=0.2$  and  $M_{sh}^*=1.5$**

emanating from showerhead, shown in Fig. 3, gives graphic evidence of how far into the mainstream the coolant is projected. In the showerhead region the coolant projects approximately  $5d$  from the surface, and significant coolant levels are still evident at  $4d$  from the surface downstream at the position of the first pressure side row of holes. For this study, measurements were confined to the “2-D region” identified in the flow visualization image shown in Fig. 4. This figure shows the spanwise coolant distribution at a position of  $x/d=-28$ , with the showerhead blowing ratio of  $M_{sh}^*=1.5$ , and no blowing from the pressure side holes. The large accumulation of coolant at the lower end of the

image is due to an interaction of coolant from jets directed downwards and jets on the lower portion of the airfoil that were directed upwards. The three-dimensional region caused by this opposing jet region, and the subsequent effects downstream, are the subject of a separate study.

Quantitative measurements of the extent of the coolant emanating from the showerhead are shown in terms of contours of non-dimensional temperature,  $\Theta$ , in Fig. 5. These temperature contours, measured at  $x/d=-23$  immediately upstream of the pressured side coolant holes, show a relatively uniform distribution of coolant over a spanwise distance equal to the spanwise

hole pitch. With  $\Theta = 0.05$  at a distance of  $3.5d$  from the surface, these thermal field measurements confirm the extent of the coolant away from the surface.

Profiles of the mean and rms velocities measured immediately downstream of the showerhead,  $x/d = -9$ , and immediately downstream of the pressure side row,  $x/d = -28$ , are presented in Fig. 6. Data at  $x/d = -28$  were taken between the holes and so were not affected by the coolant flow from the pressure side row. This figure shows that showerhead injection causes a region of very high turbulence levels to extend  $2d$  to  $3d$  from the surface immediately downstream of the showerhead. By  $x/d = -28$ , the  $u_{rms}$  and  $v_{rms}$  turbulence levels are still above  $0.6$  m/s, or  $u_{rms}/U > 0.08$ . Furthermore, these mean and turbulence velocity profiles are not characteristic of a turbulent boundary layer flow. The mean velocity approaching the wall is much higher than occurs for a turbulent boundary layer with an equivalent boundary layer thickness of nominally  $\delta = 2d$ . More importantly, the high turbulence levels extending to  $y/d > 2$ , the apparent edge of the boundary layer, are not at all characteristic of a turbulent boundary layer. The much higher turbulence levels than would occur with a turbulent boundary layer would be expected to increase the dispersion of the coolant.

### Adiabatic Effectiveness Results

The following adiabatic effectiveness results contrast the film cooling performance on the pressure side without and with showerhead blowing. For the condition of no showerhead blowing, the showerhead holes were covered with tape, resulting in laminar boundary layer flow approaching the pressure side holes. Radomsky and Thole [13], in a study with a vane geometry that was the same as used in this study, but with no film cooling, found that the boundary layer was laminar and very thin along the pressure side of the vane. In this study, we contrasted the effects of the natural laminar boundary layer with a turbulent boundary layer approach flow induced by using a boundary layer trip (0.38-mm-dia wire placed at  $x/d = -10$ ). Measurement of the adiabatic effectiveness on the pressure side with laminar and turbulent boundary layer flows (with no-showerhead) showed a slightly greater adiabatic effectiveness with the laminar boundary layer. Since disturbances in the showerhead region would generally promote a transition to a turbulent boundary layer, we elected to use the tripped turbulent boundary layer condition as the standard for the no-showerhead case. Hence, differences due to showerhead blowing would be attributed to the blowing effects rather than a simple tripping of the laminar boundary layer to a turbulent boundary layer.

Adiabatic effectiveness contours shown in Fig. 7 are for three operating conditions: (a) blowing with the showerhead alone using  $M_{sh}^* = 1.5$ , (b) blowing from the pressure side row of holes at  $M_{ps} = 0.6$  ( $I_{ps} = 0.2$ ) without showerhead blowing, and (c) combined blowing from the showerhead and pressure side row of holes. Not surprisingly, the main difference between adiabatic effectiveness distributions downstream of the pressure side holes with and without showerhead blowing is an increase in adiabatic effectiveness between the coolant jets. The contours indicate that between the coolant jets, the effectiveness levels are similar to the showerhead only condition. Also evident from the contours in Fig. 7 is a change in the angle of the coolant jets when the showerhead is blowing. As will be shown by the velocity field measurements, this is due to a lateral flow induced by the inclined holes in the showerhead.

Laterally averaged adiabatic effectiveness,  $\bar{\eta}$ , distributions downstream of the pressure side row of holes are presented in Fig. 8 for conditions without (a) and with (b) showerhead blowing. In both cases, maximum  $\bar{\eta}$  occurred at  $M_{ps} = 0.4$ , with decreasing performance at higher blowing ratios; presumably due to increasing jet separation. However, the decrease in performance with increasing blowing ratio was found to be much less for the

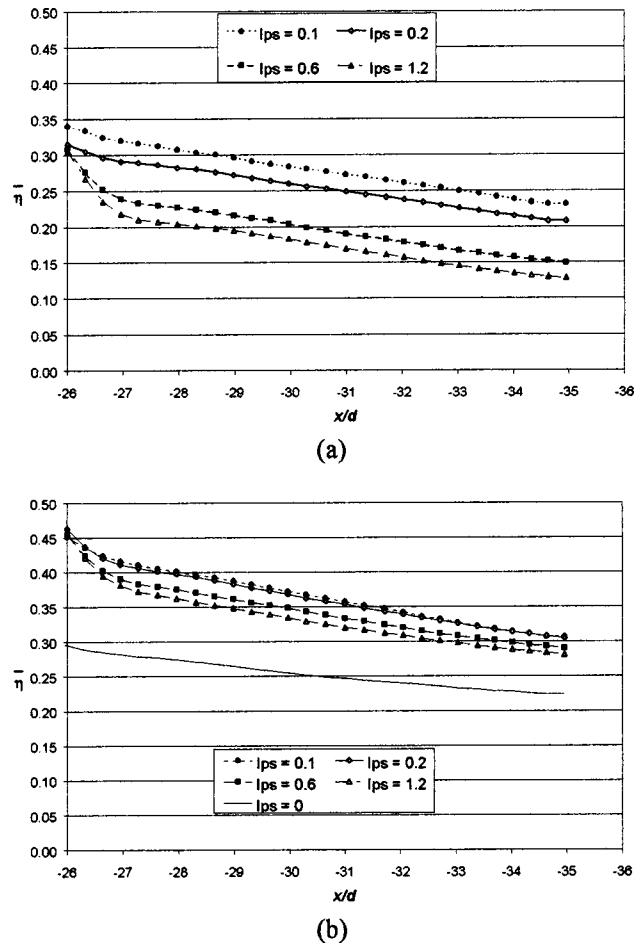
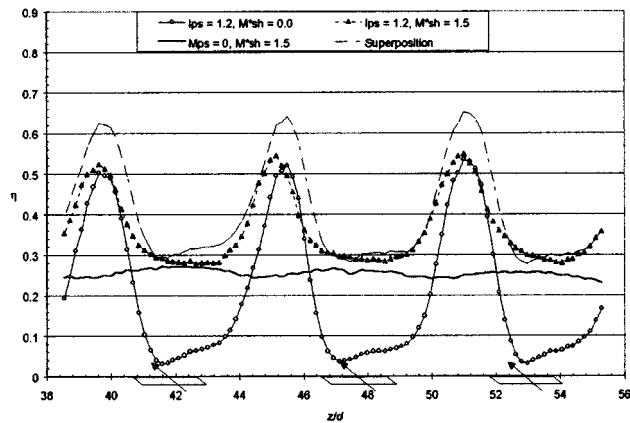


Fig. 8 Laterally averaged effectiveness for the pressure side film cooling for (a)  $M_{sh}^* = 0.0$ , and (b)  $M_{sh}^* = 1.5$

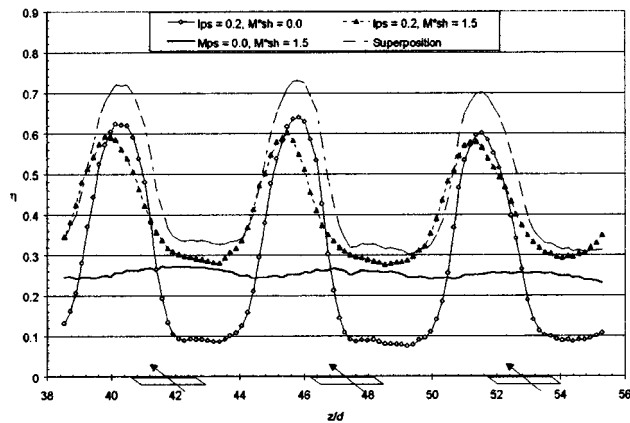
case with showerhead blowing than with no showerhead, indicating that showerhead blowing mitigated the effects of coolant jet separation.

Obviously, the  $\bar{\eta}$  levels were much larger for the showerhead blowing case due to the combined effects of the showerhead coolant and the coolant from the pressure side row of holes. However, as noted in the previous study [12], the increase in  $\bar{\eta}$  with the combined showerhead and pressure side blowing was not as much as would be predicted using superposition, which indicates an interaction between the coolant flow from the showerhead and the pressure side coolant jets. The failure of the superposition prediction is best seen with the lateral distributions of  $\eta$  as shown in Fig. 9. At a position of  $x/d = -28$ , i.e.,  $2d$  downstream of the exit of the pressure side holes, the peak  $\eta$  was found to be much less than predicted by superposition, even decreasing with showerhead blowing rather than increasing due to the added cooling effect of the showerhead coolant. The “off-the-wall” measurements were used to detail the interaction between the showerhead and pressure side coolant flows, which caused a decrease in performance of the pressure side coolant jets.

**Combined Coolant Flow “Off-the-Wall” Measurements.** Flow visualization, thermal field, and velocity field measurements were made to determine how the showerhead coolant flow was affecting the coolant jets from the pressure side row of holes. Comparing the flow visualization images for the pressure side



(a)



(b)

**Fig. 9** Lateral distribution of effectiveness for the combined coolant flow and predicted superposition at  $x/d = -28$ , and (a)  $I_{ps} = 0.2$ , and (b)  $I_{ps} = 1.2$

cooling jet with and without showerhead blowing, shown in Fig. 10, shows that for  $I_{ps} = 1.2$  the distance the coolant ejects away from the wall is similar for both conditions. Furthermore, the vortex pattern typical of compound angle holes is apparent from the swirling coolant pattern evident for the no-showerhead flow condition. However, a similar swirling pattern was not observed for the showerhead blowing condition.

Thermal profiles for  $I_{ps} = 0.2$  and  $1.2$ , Fig. 11, provide a quantitative measure of the coolant distribution above the surface. For the no-showerhead condition, the coolant jet for the  $I_{ps} = 0.2$  condition is confined to a very thin region near the wall. In contrast, the  $I_{ps} = 1.2$  coolant jet had some coolant projected to as much as  $1.5d$  above the surface of the vane.

Figures 11(c) and (d) show the thermal fields for the showerhead blowing condition. These figures show that the coolant jets for  $I_{ps} = 0.2$  and  $1.2$  are well within the  $3.5d$  extent of the coolant from the showerhead. Comparing the no-showerhead and showerhead blowing conditions at the lower momentum flux ratio of  $I_{ps} = 0.2$ , the coolant jets have a similar flat distribution, but the reduced  $\Theta$  levels for the showerhead blowing condition indicates a greater dispersion of the pressure side coolant jets. For  $I_{ps} = 1.2$ , the core of the coolant jet appears to be displaced from the wall significantly more for the showerhead blowing condition, but maximum  $\Theta$  levels are similar.

Mean velocity vectors in a lateral plane at  $x/d = -28$  for the no-showerhead and showerhead blowing conditions and the higher momentum flux ratio of  $I_{ps} = 1.2$  are shown in Fig. 12. The main difference between the no-showerhead and showerhead blowing conditions is a significant lateral velocity, as much as 2

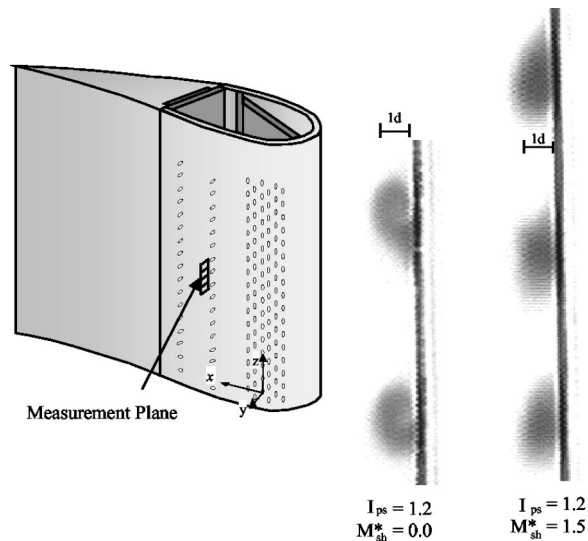


**Fig. 10** Flow visualization of the pressure side film cooling with and without showerhead flow

m/s or  $0.3U$ , for the showerhead blowing condition. This lateral flow, induced by the inclined jets in the showerhead, extends to about  $1.5d$  from the surface, and is responsible for the change in the angle of the coolant jet as discussed previously. For the no-showerhead condition, the vortex within the coolant jet is evident, while the showerhead blowing condition yields a flow pattern without a vortex. However, if the spanwise component of the showerhead flow is removed, the velocity field suggests a slight rotational movement, though not as strong as for the no-showerhead condition.

Contours of the turbulence field measurements,  $u_{rms}/U_\infty$ ,  $v_{rms}/U_\infty$ ,  $w_{rms}/U_\infty$ , are given in Fig. 13 for the no-showerhead and showerhead blowing conditions with  $I_{ps} = 1.2$ . In each case the core of the coolant jet shows increased turbulence levels with similar levels for  $u_{rms}/U_\infty$ ,  $v_{rms}/U_\infty$ , and  $w_{rms}/U_\infty$ . Maximum levels of  $u_{rms}/U_\infty > 0.18$  occurred for the no-showerhead condition, and slightly higher levels of  $u_{rms}/U_\infty > 0.20$  for the showerhead blowing condition. For the showerhead blowing condition, turbulence levels surrounding the coolant jet due to the showerhead injection were generally isotropic, with levels of  $u_{rms}/U_\infty > 0.08$ ; but close to the wall the lateral component had an in-

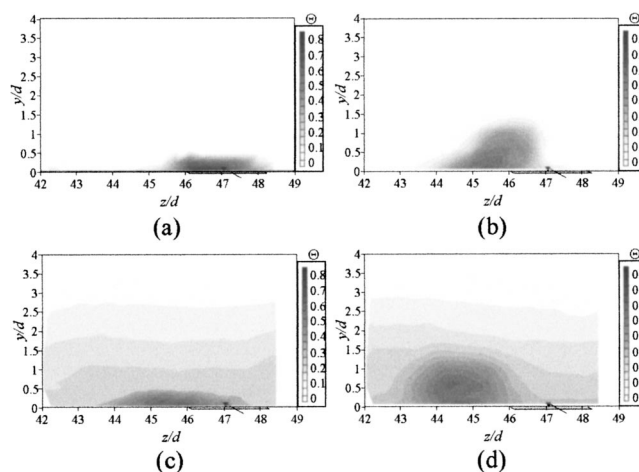


**Fig. 11** Thermal profile of the pressure side coolant jet with  $Tu_\infty = 0.5\%$ , and  $x/d = -28$  with  $M_{sh}^* = 0.0$  for (a)  $I_{ps} = 0.2$ , (b)  $I_{ps} = 1.2$ , and  $M_{sh}^* = 1.5$  for (c)  $I_{ps} = 0.2$ , and (d)  $I_{ps} = 1.2$

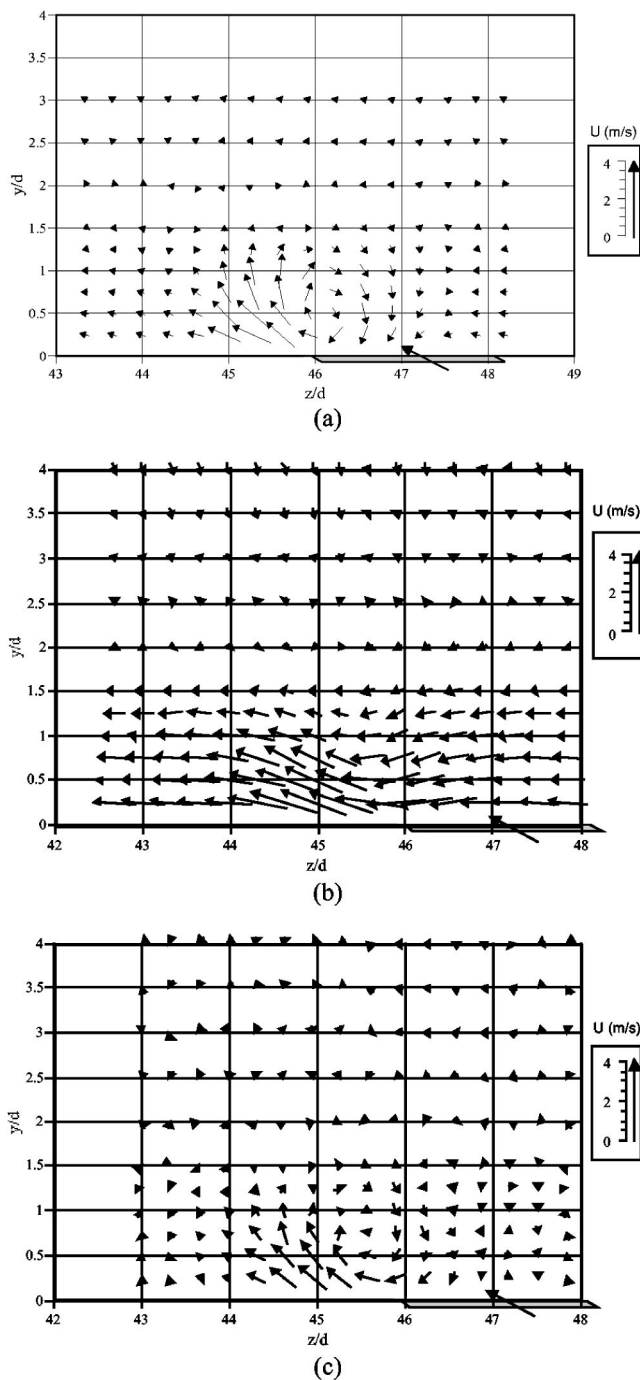


Fig. 12 V-W velocity vectors representing the velocity field for the pressure side film cooling (PS3) at  $x/d = -28$  for (a)  $M_{sh}^* = 0.0$ ,  $I_{ps} = 1.2$ , and  $M_{sh}^* = 1.5$ ,  $I_{ps} = 1.2$  for (b) actual flow, and (c) embedded structure

creased level of  $w_{rms}/U_\infty > 0.12$ . The increased levels of  $w_{rms}/U_\infty$  is consistent with the previous study of the showerhead region (Polanka et al. [14]) that showed generation of larger levels  $w_{rms}/U_\infty$  in the showerhead region. There were also differences within the coolant jets for the no-showerhead and showerhead blowing conditions. For no-showerhead, the  $u_{rms}/U_\infty > 0.16$  contours extended a significantly larger distance from the wall than the  $v_{rms}/U_\infty$  and  $w_{rms}/U_\infty$  contours. In contrast, for the condition with showerhead blowing, the  $v_{rms}/U_\infty$  levels were noticeably higher than  $u_{rms}/U_\infty$  and  $w_{rms}/U_\infty$  contours.

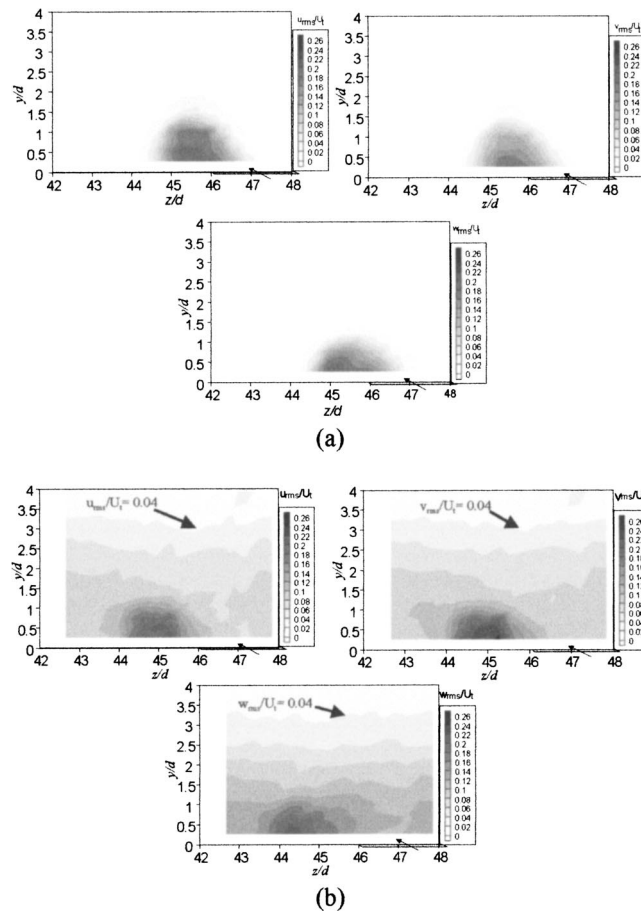


Fig. 13 Turbulence levels of the pressure side film cooling with  $I_{ps} = 1.2$  and  $x/d = -28$  for (a)  $M_{sh}^* = 0.0$ , and (b)  $M_{sh}^* = 1.5$

## Conclusions

This study was performed to provide more detailed measurements of the interaction of the showerhead coolant injection with the pressure side film cooling performance for a simulated turbine vane. The study was motivated by desire to determine the mechanism by which the showerhead coolant injection degraded the adiabatic effectiveness performance of coolant jets injected on the pressure side of the vane. Three-component LDV measurements, thermal profile measurements, and flow visualization, allowing determination of the nature of the flow and the thermal fields above the surface provided insight into these mechanisms.

An important finding from this study is that showerhead blowing at a typical operational level of  $M_{sh}^* = 1.5$ , causes high turbulence levels that are still at levels of  $u_{rms}/U_\infty > 0.08$  at the position of the first cooling holes on the pressure side. The mean velocity and turbulence profiles at this position were very different than would occur with a turbulent boundary layer. Increased levels of turbulence extend beyond  $3d$  from the surface. This was consistent with the extent of the coolant from the showerhead that was found to extend to  $3.5d$  from the surface. Adiabatic effectiveness measurements showed decreased peak values of adiabatic effectiveness with combined showerhead and pressure side cooling flows compared to pressure side coolant injection alone. Of course, this decrease in adiabatic effectiveness performance is contrary to a superposition prediction. The velocity field measurements showed that the primary reason for the degraded performance as compared to a superposition prediction is the high tur-

bulence generated by showerhead injection. This high turbulence probably greatly increases the dispersion of the coolant jets on the pressure side.

## Acknowledgments

We are most grateful to the sponsors of this work, Advanced Gas Turbine Systems Research Consortium and Pratt & Whitney. We would also like to thank Pratt & Whitney for supplying the turbine vane geometry.

## Nomenclature

$d$  = coolant hole diameter, 4.11 mm  
 $DR$  = density ratio,  $(\rho_c/\rho_\infty)$   
 $I$  = momentum flux ratio  $(\rho_c \cdot U_c^2/\rho_\infty \cdot U_\infty^2)$   
 $M$  = blowing ratio based on local freestream velocity  $(\rho_c \cdot U_c/\rho_\infty \cdot U_\infty)$   
 $M^*$  = blowing ratio based on local approach velocity  $(\rho_c \cdot U_c/\rho_0 \cdot U_0)$   
 $p$  = coolant hole-to-hole pitch, 5.6d  
 $t$  = time  
 $T$  = temperature  
 $U$  = mainstream mean velocity  
 $u, v, w$  = fluctuating velocity components  
 $x, y, z$  = surface coordinates; streamwise, normal, and lateral, respectively  
 $\phi$  = injection angle  
 $\eta$  = adiabatic effectiveness  $(T_\infty - T_{aw}/T_\infty - T_c)$   
 $\bar{\eta}$  = laterally averaged adiabatic effectiveness  
 $\theta$  = streamwise angle  
 $\Theta$  = nondimensional temperature  $(T_\infty - T/T_\infty - T_c)$   
 $\rho$  = density

## Subscripts

$aw$  = adiabatic wall  
 $c$  = coolant  
 $ps$  = pressure side  
 $sh$  = showerhead

0 = approach flow  
 $\infty$  = local freestream

## References

- [1] Ericksen, V. L., and Goldstein, R. J., 1974, "Heat Transfer and Film Cooling Following Injection Through Inclined Circular Tubes," *ASME J. Heat Transfer*, **96**, pp. 239–245.
- [2] Muska, J. F., Fish, R. W., and Suo, M., 1976, "The Additive Nature of Film Cooling from Rows of Holes," *ASME J. Eng. Power*, **98**, pp. 457–474.
- [3] Drost, U., and Böls, A., 1999, "Performance of a Turbine Airfoil with Multiple Film Cooling Stations Part I: Heat Transfer and Film Cooling Effectiveness," ASME Paper No. 99-GT-171.
- [4] Ethridge, M. I., Cutbirth, J. M., and Bogard, D. G., 2001, "Scaling of Performance for Varying Density Ratio Coolants on an Airfoil with Strong Curvature and Pressure Gradient Effects," *ASME J. Turbomach.*, **123**, pp. 1–7.
- [5] Polanka, M. D., Ethridge, M. I., Cutbirth, J. M., and Bogard, D. G., 2000, "Effects of Showerhead Injection on Film Cooling Effectiveness of Downstream Rows of Holes," ASME Paper No. 2000-GT-240.
- [6] Cutbirth, J. M., and Bogard, D. G., 2001, "Thermal Field and Flow Visualization Within the Stagnation Region of a Film Cooled Turbine Vane," ASME Paper No. 2001-GT-401.
- [7] Cutbirth, J. M., and Bogard, D. G., 2002, "Evaluation of Pressure Side Film Cooling With Flow and Thermal Field Measurements—Part II: Turbulence Effects," *ASME J. Turbomach.*, **124**, pp. 678–685.
- [8] Polanka, M. D., 1999, "Detailed Film Cooling Effectiveness and Three Component Velocity Field Measurements on a First Stage Turbine Vane Subject to High Freestream Turbulence," Ph.D. Dissertation, The University of Texas at Austin.
- [9] Cutbirth, J. M., 2000, "Turbulence and Three-Dimensional Effects on the Film Cooling of a Turbine Vane," Ph.D. dissertation, The University of Texas at Austin.
- [10] Witteveld, V. C., Polanka, M. D., and Bogard, D. G., 1999, "Film Cooling Effectiveness in the Showerhead Region of a Gas Turbine Vane Part I: Stagnation Region and Near-Suction Side," ASME Paper No. 99-GT-49.
- [11] Sellers, J. P., 1963, "Gaseous Film Cooling with Multiple Injection Stations," *AIAA J.*, **1**, No. 9, pp. 2154–2156.
- [12] Polanka, M. D., Witteveld, V. C., and Bogard, D. G., 1999, "Film Cooling Effectiveness in the Showerhead Region of a Gas Turbine Vane Part I: Stagnation Region and Near-Pressure Side," ASME Paper No. 99-GT-48.
- [13] Radomsky, R. W., and Thole, K. A., 1998, "Effects of High Freestream Turbulence Levels and Length Scales on Stator Vane Heat Transfer," ASME Paper No. 98-GT-236.
- [14] Polanka, M. D., Cutbirth, J. M., and Bogard, D. G., 2001, "Three Component Velocity Field Measurements in the Stagnation Region of a Film Cooled Vane," ASME Paper No. 2000-GT-240.

# Evaluation of Pressure Side Film Cooling With Flow and Thermal Field Measurements—Part II: Turbulence Effects

**J. Michael Cutbirth**

William B. Morgan Large Cavitation Channel,  
Naval Surface Warfare Center,  
Carderock Division,  
Memphis, TN 38113

**David G. Bogard**

Mechanical Engineering Department,  
University of Texas at Austin,  
Austin, TX 78712

*This study focused on the film cooling performance on the pressure side of a turbine vane subjected to high mainstream turbulence levels, with and without showerhead blowing. Whereas previous studies have measured the adiabatic effectiveness and heat transfer at the surface of the airfoil, the goal of this study was to examine the flow and thermal fields above the surface. These measurements included flow visualization, thermal profiles, and laser Doppler velocimetry. For comparison, adiabatic effectiveness was also measured. A mainstream turbulence level of  $Tu_\infty=20\%$ , with integral length scale of seven hole diameters, was used. Particularly insightful is the discovery that the large-scale high mainstream turbulence causes a lateral oscillation of coolant jet resulting in a much wider time average distribution of coolant. Even with high mainstream turbulence, showerhead blowing was found to still cause a significantly increased dispersion of the pressure side coolant jets. [DOI: 10.1115/1.1504442]*

## Introduction

In an actual gas turbine engine, devices such as swirlers and dilution jets are added to the combustor to sufficiently mix the air and fuel for optimum combustion. However, this mixing creates highly elevated levels of turbulence. This turbulence is then transported downstream to the inlet of the turbine. Therefore, for laboratory simulation of the film cooling of an inlet guide vane, high mainstream turbulence is a necessity. However, to allow for the comparison between different studies, the turbulence field is conditioned to be uniform and isotropic, and can be characterized by the turbulence intensity,  $u_{rms}/U$ , and a length scale.

In determining realistic values of the turbulence intensity and length scale, Moss and Oldfield [1] have shown that the energy spectra exiting several types of combustors were independent of the combustion reaction. Hence, nonreaction, “cold,” tests are reasonable predictors of the turbulence characteristics. Goldstein et al. [2] and Koutmos and McGuirk [3] performed measurements using can-type combustors with swirlers and dilution jets. These reports indicated turbulence levels from 15% to over 30% at the exit of the combustor with non-uniformity in the axial velocity and temperature spanning a factor of two. Radomsky and Thole [4] also report that a typical integral length scale entering the turbine passage relative to the pitch between airfoils is on the order of  $0.10 < \Lambda_x/P < 0.14$ . These length scales are based on measurements from Moss [5] and Ames [6] who used various combustor designs. Converting this length scale into coolant hole diameters for the current study yields  $11 < \Lambda_x/d < 16$ .

Numerous studies have been performed investigating the effects of turbulence on the film cooling performance for turbine blades and vanes. As described in Polanka et al. [7], there are distinct differences between vanes and blades in the curvature and acceleration for the leading edge region. Furthermore, for each of these airfoils, characteristics of the pressure side of the airfoil tend to be quite different than the suction side. The pressure side generally has much weaker pressure gradients and negligible curvature effects, whereas the suction side generally has strong curvature effects. This study focused on film cooling of the pressure side of a

turbine vane, with particular attention placed on the effects of high mainstream turbulence and of showerhead blowing.

The following results encompass the results from various turbine vane studies, [8–10]. Mainstream turbulence effects on the pressure side of a turbine vane with a single row of cooling jets, and with/without showerhead blowing, were reported by Polanka et al. [8]. This study indicated that high mainstream turbulence,  $Tu_\infty=20\%$  and  $\Lambda_x/d=10$ , caused a 20% decrease in effectiveness for fully attached jets, but a 20% increase in effectiveness for separating jets. These results were with no showerhead blowing. With combined showerhead and pressure side blowing, high mainstream turbulence levels caused decreases in adiabatic effectiveness levels for all blowing ratios. An important result from this previous study was that the adiabatic effectiveness for the combined showerhead and pressure side film cooling was always less than predicted by superposition of the individual contributions of the showerhead blowing and the pressure side blowing.

Other airfoil studies report only decreases of the effectiveness with increased levels of turbulence. Ames [9] reported decreases in adiabatic effectiveness of 25–40% as the turbulence level is increased from  $Tu=1$  to 12% and  $\Lambda_x/C=0.46$  (where  $C$  refers to the airfoil chord for the reported study), for a single and double row of holes located on the pressure side. Drost and Bölc [10] report small differences in the effectiveness levels, 5–10% decrease, as the turbulence level increases from  $Tu=5.5$  and 20% and  $\Lambda_x/C=0.32$  and 0.17, respectively, for pressure side film cooling. It should be noted that for the current study, the integral length scale is provided in terms of the coolant hole diameter. However, for these previous studies, the dimensions for the coolant holes were not provided.

Each of these studies consisted of surface measurements that provided only the “foot prints” of the interaction between the coolant flow and the turbulent mainstream, but fail to provide insight into the physical mechanisms involved in the interaction. This study focuses on expanding the surface measurements by using “off-the-wall” techniques such as thermal profiles, flow visualization, and velocity field measurements. This paper is Part II of a two-part sequence of papers. Part I [11] focuses on the effects of showerhead blowing with low mainstream turbulence on the pressure side cooling performance. This paper focuses on the high mainstream turbulence effects, and the combined showerhead blowing and high mainstream turbulence effects.

Contributed by the International Gas Turbine Institute and presented at the International Gas Turbine and Aeroengine Congress and Exhibition, Amsterdam, The Netherlands, June 3–6, 2002. Manuscript received by the IGTI, November 2, 2001. Paper No. 2002-GT-30175. Review Chair: E. Benvenuti.



## Facilities and Experimental Conditions

The test facility, airfoil, coolant configuration, test apparatus and test conditions for this study are described in [11]. The thermal data for this study are presented in the forms of adiabatic effectiveness,  $\eta$ , for surface measurements and non-dimensional temperature,  $\Theta$ , for the thermal field above the surface, defined in the following equations:

$$\eta \equiv \frac{(T_\infty - T_{aw})}{(T_\infty - T_c)} \quad (1)$$

$$\Theta \equiv \frac{(T_\infty - T)}{(T_\infty - T_c)} \quad (2)$$

Flow visualization was done by seeding jets with titanium dioxide powder, and illuminating with a laser sheet. Thermal fields were measured with a rake of miniature thermocouples. Velocities were measured with a three-component laser Doppler velocimeter. Details of these techniques were presented in [12] and [13]. The uncertainties for these measurements are given in [11].

All experiments were conducted with a mainstream approach velocity of  $U_\infty = 5.8$  m/s, which established a Reynolds number matching that of actual engine operation ( $Re = 1.2 \times 10^6$ , based on chord length and exit velocity). These tests were run with low,  $Tu_\infty = 0.005$ , and high mainstream turbulence. The high mainstream turbulence generator, described by Cutbirth [12], consisted of 20 vertical, 2.5-cm-dia rods located 14.8 rod diameters upstream of the vane leading edge. The turbulence generator was designed to provide a turbulence level, at a distance of 14.8 rod diameters, of  $Tu_\infty = 0.20$ , with an integral length scale of  $\Lambda_f/d = 7$ . This turbulence field was isotropic and uniform; details of the turbulence field are described in [7], [8], and [13].

## Results

Results from this study are presented first for high mainstream turbulence condition with no showerhead blowing. The combined effects of high mainstream turbulence and showerhead blowing follow this. In each case, adiabatic effectiveness measurements are presented first, followed by measurements of the flow and thermal fields overlaying the surface.

### High Mainstream Turbulence Effects With No Showerhead Blowing

**Adiabatic Effectiveness.** Laterally averaged effectiveness values, averaged over three coolant hole pitches, for the pressure side coolant row are presented in Fig. 1 for both low,  $Tu_\infty = 0.5\%$ , and high,  $Tu_\infty = 20\%$ , mainstream turbulence levels. At low momen-

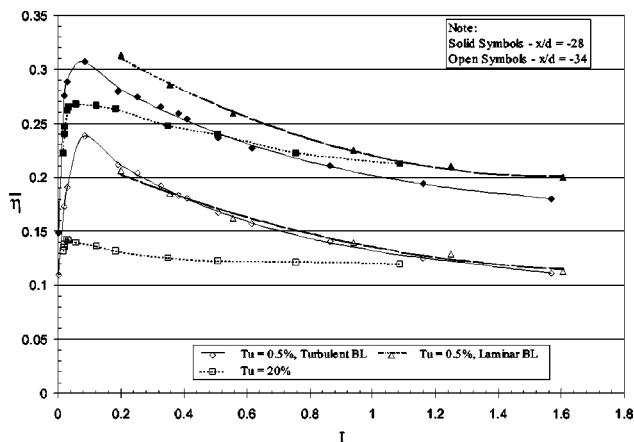


Fig. 1 Effect of turbulence on the pressure side film cooling as a function of blowing ratio for  $Tu_\infty = 20\%$  with integral length scale,  $\Lambda_x/d = 7$

tum flux, in which fully attached jets are expected, a 15% ~20% reduction in the effectiveness with high mainstream turbulence occurs  $3d$  downstream of the coolant row,  $x/d = -28$ , while a 25~40% reduction in the effectiveness occurs  $10d$  downstream,  $x/d = -34$ . The reduction in  $\bar{\eta}$  indicates an increased dispersion of the coolant jet due to increased turbulence. However, as the momentum flux,  $I$ , is increased; the high level of turbulence causes a slight increase in the adiabatic effectiveness. This increase in  $\bar{\eta}$  is caused by the increased dispersion of the coolant jet with high turbulence transporting coolant back to the surface for the condition of partially/fully separated coolant jets. For high

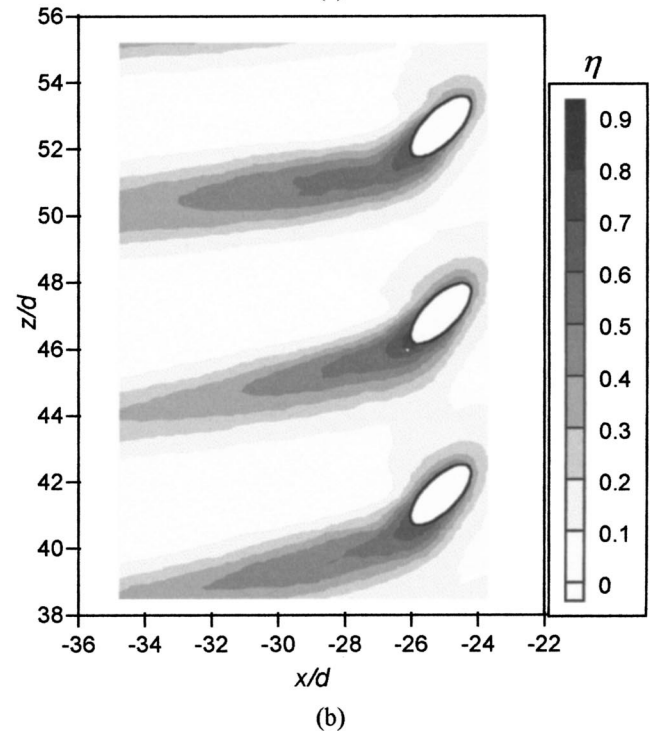
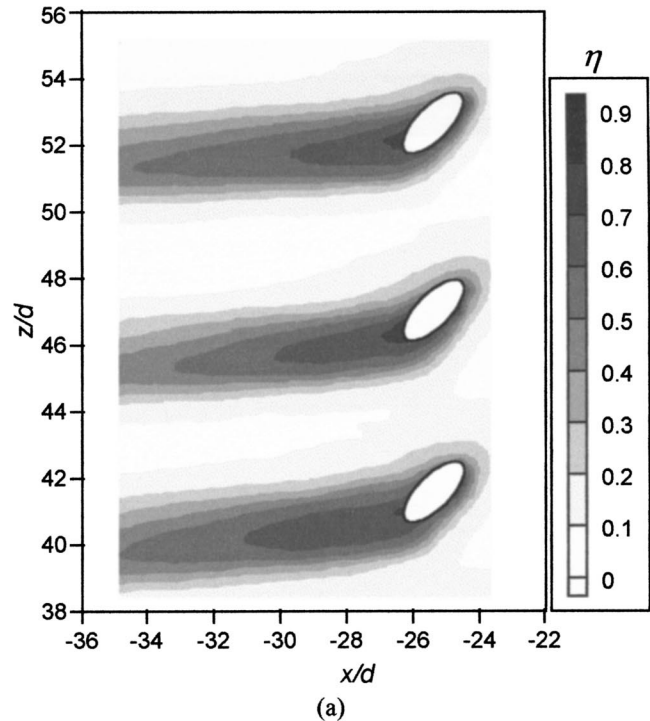
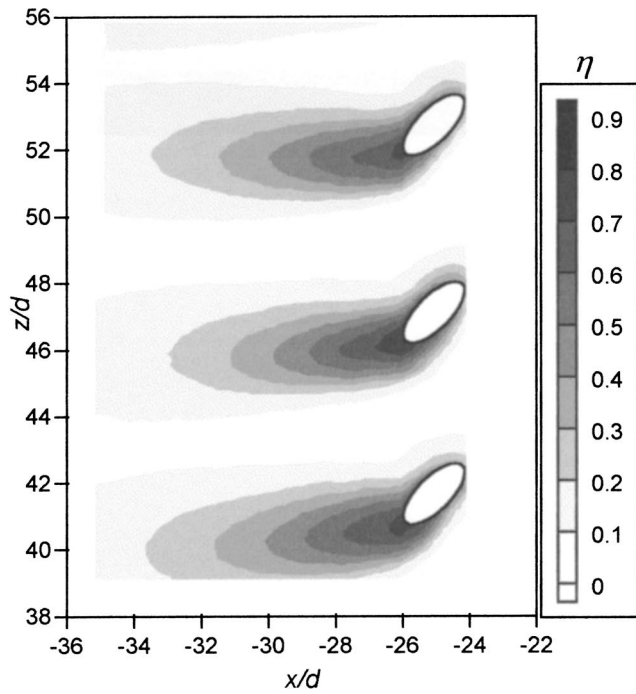
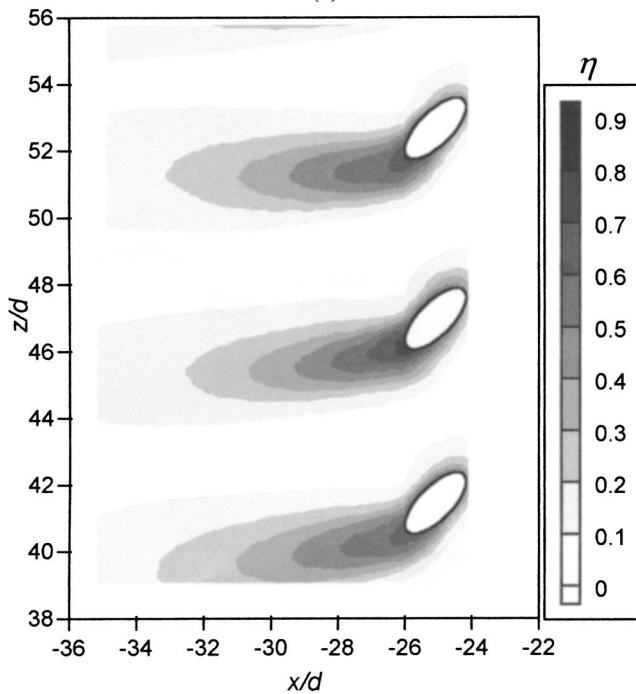


Fig. 2 Effect of turbulence on the pressure side film cooling with  $Tu_\infty = 0.5\%$ ,  $M_{sh} = 0.0$ , and (a)  $I_{ps} = 0.09$ , and (b)  $I_{ps} = 1.2$



(a)



(b)

**Fig. 3** Effect of turbulence on the pressure side film cooling with  $M_{sh}=0.0$ ,  $Tu_{\infty}=20\%$ , and (a)  $I_{ps}=0.11$ , and (b)  $I_{ps}=1.2$

mainstream turbulence levels, the balance of increased dispersion with turbulence and further jet separation with increased momentum flux results in relatively constant levels of  $\bar{\eta}$  for a wide range of momentum flux ratios.

More insight into the effects of high mainstream turbulence on the adiabatic effectiveness performance is given by the contours of adiabatic effectiveness shown in Figs. 2 and 3 for low and high mainstream turbulence, respectively. In Fig. 2, the transition from a fully attached jet,  $I_{ps}=0.09$ , to a partially attached jet,  $I_{ps}=1.2$  is apparent by the relative width of the coolant footprint. In

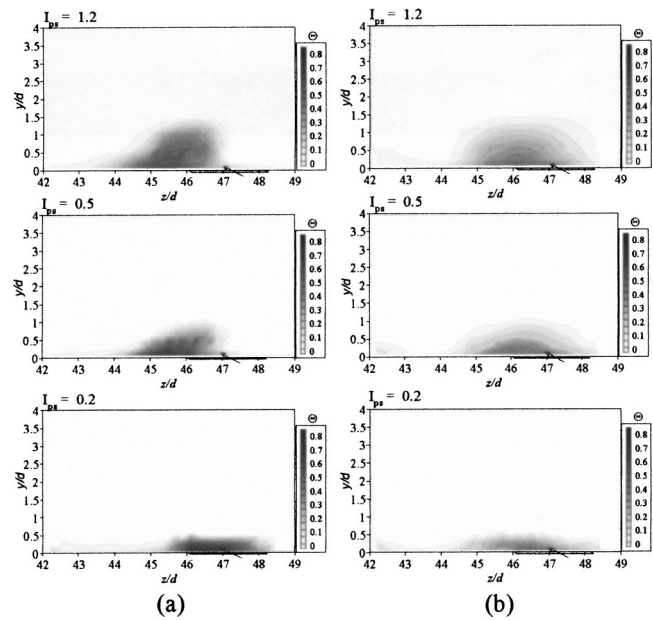


**Fig. 4** Thermal profiles for the pressure side film cooling with  $M_{sh}=0.0$  at  $x/d=-28$  for (a)  $Tu_{\infty}=0.5\%$  and (b)  $Tu_{\infty}=20\%$

contrast, with high mainstream turbulence the adiabatic effectiveness contours for  $I_{ps}=0.11$  and  $1.1$  remain similar. For both blowing conditions, a greater decay rate is evident for the high mainstream turbulence cases compared to the low mainstream turbulence cases. Another striking difference between the low and high mainstream turbulence cases is the much greater lateral spread of coolant for the high mainstream turbulence cases. Recall that, at high blowing rates of  $I_{ps}>1$ , there was little difference in  $\bar{\eta}$  values for the low and high mainstream turbulence conditions. However, the  $\eta$  contours in Figs. 2 and 3, for  $I_{ps}\approx 0.1$ , indicate a very marked difference between the two mainstream turbulence conditions. From these contour plots it is evident that the  $\bar{\eta}$  values for the high mainstream turbulence case are similar to the values for the low mainstream turbulence case because of the greater lateral distribution of coolant. This increase in width balances the lower effectiveness levels within the coolant jet, resulting in similar  $\bar{\eta}$  levels.

*Flow Visualization, Thermal and Velocity Fields.* The thermal profiles for low and high mainstream turbulence are given in Fig. 4 for a range of blowing conditions at a streamwise location of  $x/d=-28$  ( $2d$  downstream of the pressure side holes). The momentum flux ratios presented in Fig. 4 are  $I_{ps}=0.2, 0.5$  and  $1.2$ , representing a low, intermediate, and high blowing ratio, respectively. Contrasting thermal contours for the low and high turbulence levels, the vertical extents of the coolant were similar for each momentum flux ratio, but the lateral extent was slightly greater for the high turbulence condition. The main differences in the thermal contours for the low and high turbulence conditions were the shape and the thermal gradients. With low mainstream turbulence, the  $\Theta$  contours are inclined towards the right, which is a result of the interaction of the mainstream with the oblique injection angle of the coolant jets. However, with high mainstream turbulence the  $\Theta$  contours are symmetric. Temperature gradients were weakened (indicated by the greater spacing between contour lines) for the high turbulence conditions relative to the low turbulence conditions. The weakened temperature gradients can be attributed to increased dispersion of the coolant by the larger mainstream turbulence.

The time resolved flow visualization recordings provided insight into the dynamic effects of the high mainstream turbulence on the pressure side coolant jets. Figure 5 contrasts the instanta-

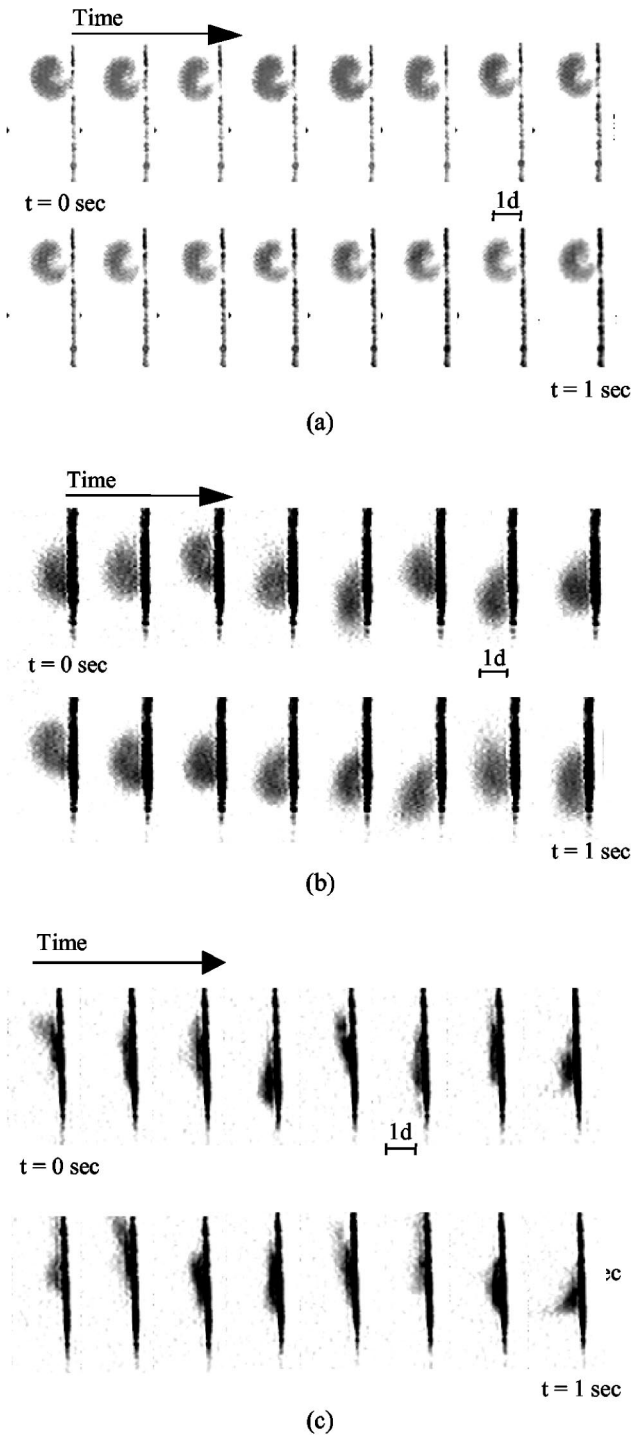


Fig. 5 Instantaneous flow visualization at  $x/d = -28$  with  $M_{sh} = 0.0$  and (a)  $I_{ps} = 1.2$ ,  $Tu_\infty = 0.5\%$ , (b)  $I_{ps} = 1.2$ ,  $Tu_\infty = 20\%$ , and (c)  $I_{ps} = 0.2$ ,  $Tu_\infty = 20\%$

neous snapshots of coolant jets for low and high turbulence, respectively, over a time period of 1.0 s with a time step of 1/15 s. For the low turbulence condition at a momentum flux of  $I_{ps} = 1.2$ , each snapshot shows the coolant jet in exactly the same position, indicating steady behavior of the coolant jet. Also evident is the vortical structure of the coolant jet. For the high turbulence condition at momentum fluxes of  $I_{ps} = 0.2$  and 1.2, the instantaneous images show a bodily movement of the coolant jets by as much as  $\pm 1d$ . Recall that the mainstream turbulence had an integral length scale of  $\Lambda_f = 7d$ , which accounts for the bodily

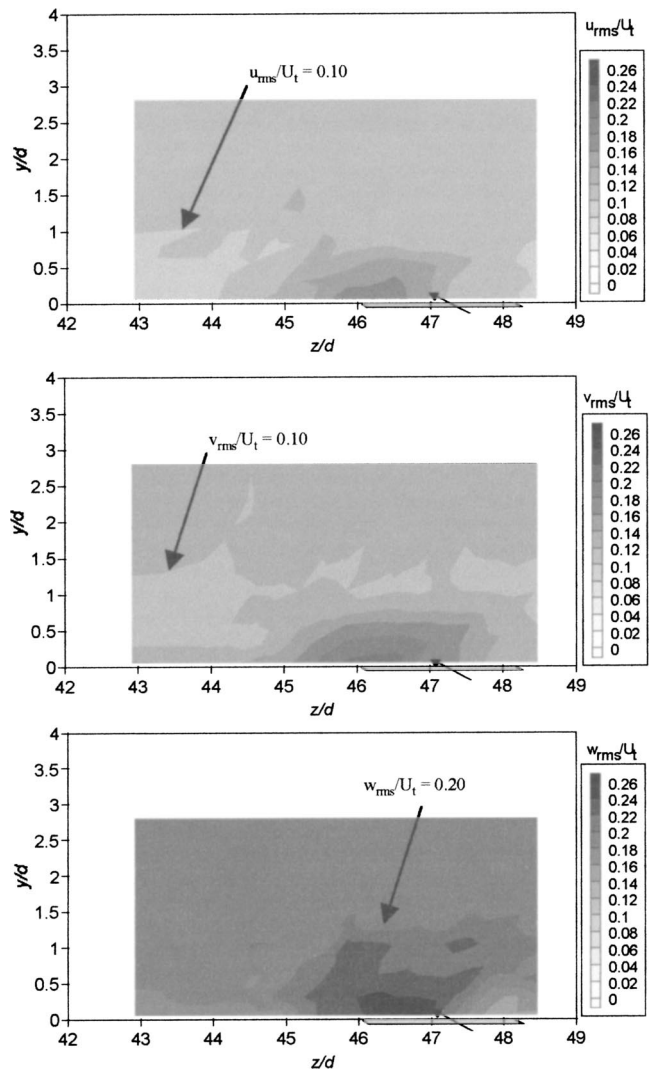


Fig. 6 RMS values at a location of  $x/d = -28$  for  $I_{ps} = 1.2$  and  $M_{sh} = 0.0$

movement of the coolant jets rather than a break-up of the jets. For  $I_{ps} = 0.2$ , there was some lifting of the coolant away from the wall, but the vertical displacement of the coolant jets with  $I_{ps} = 1.2$  was barely noticeable. This would suggest much greater lateral velocity fluctuations than vertical fluctuations.

The lateral oscillation of the coolant jet discovered with the flow visualization snapshots provided an explanation for the broader adiabatic effectiveness and thermal field distributions that occurred with the high mainstream turbulence. These distributions represent the time average jet position, and therefore are broader than the actual jet width because the time average encompasses the range of oscillations.

Measurements of the turbulent fluctuations,  $u_{rms}/U_\infty$ ,  $v_{rms}/U_\infty$ ,  $w_{rms}/U_\infty$ , are presented in Fig. 6 for the high mainstream turbulence condition (similar turbulence fluctuation results for the low mainstream turbulence conditions are presented Part I [11]). Turbulence levels surrounding the coolant jets for the  $u_{rms}/U_\infty$  and  $v_{rms}/U_\infty$  components were in excess of 12%, while  $w_{rms}/U_\infty$  turbulence levels surrounding the coolant jet were in excess of 20%. Radomsky and Thole [14] found a similar greater increase in  $w_{rms}$  near the wall for a simulated vane similar to that used in our facility. When the mainstream turbulence interacts with the wall, the normal component of turbulence,  $v_{rms}$ , is suppressed, and the turbulent energy in this component is redirected into components of turbulence parallel to the surface, i.e.,  $u_{rms}$  and

$w_{rms}$ . However, because of the streamwise acceleration, components parallel to the flow direction are suppressed, and components normal to the flow direction are enhanced. This causes a substantial increase in  $w_{rms}$  relative to  $u_{rms}$ . Since the integral length scale of the mainstream turbulence was  $\Lambda_f = 7d$ , these effects are expected to occur within a region extending to  $7d$  from the surface. Although this is thin region relative to the chord length of the airfoil, it is thick region relative to the coolant jets, and hence has a large effect on the coolant jets.

For the  $u_{rms}/U_\infty$  and  $v_{rms}/U_\infty$  components, turbulence levels in the core of the coolant jets are similar for the low and high turbulence cases; however, the  $w_{rms}$  level in the core of the jets was increased in the high mainstream turbulence case. This can be attributed to a superposition of the large-scale  $w_{rms}$  fluctuations due to the mainstream turbulence and the small-scale  $w_{rms}$  fluctuations inherent in the core of the coolant jet.

#### Combined High Turbulence and Showerhead Blowing.

The combined mainstream turbulence and showerhead blowing conditions represents the operating condition that is most realistic. In Part I [11], we described how the showerhead blowing with low mainstream turbulence caused a significant increase in mainstream turbulence levels at the position of the pressure side cooling holes, i.e.,  $u_{rms}/U_\infty$  and  $v_{rms}/U_\infty > 0.08$ , and  $w_{rms}/U_\infty > 0.12$ . Results presented in the previous section showed that for the high mainstream turbulence condition, the mainstream turbulence levels were twice these levels. Consequently, for the combined high mainstream turbulence and showerhead blowing case, a particular issue was whether the very high mainstream turbulence conditions would dominate so that no effects from the showerhead blowing would be evident.

**Adiabatic Effectiveness.** In the previous study by Polanka et al. [8], the effects of the combined high mainstream turbulence and showerhead blowing on the adiabatic effectiveness for the pressure side was examined. Results presented in that paper showed that showerhead blowing caused a degradation of film cooling performance on the pressure side of the vane. These adiabatic effectiveness results were confirmed in this study. However, the primary objective of this study was to gain an understanding about the mechanisms by which the showerhead blowing continues to affect the pressure side film cooling performance under high mainstream turbulence conditions.

Film-cooling adiabatic effectiveness contours, on the pressure side with showerhead blowing, are presented for low and high mainstream turbulence in Fig. 7. The relative effects of high mainstream turbulence and showerhead blowing are seen when comparing the contour plots shown in Fig. 7 with showerhead blowing to the previously presented contour plots with no showerhead blowing in Figs. 2 and 3. From this comparison it is clear that the broader coolant distribution with increased decay rate due to high mainstream turbulence is the dominant characteristic regardless of whether the showerhead is blowing or not. The lateral variation of  $\eta$  was examined at a position of  $x/d = -28$ , as shown in Fig. 8, to evaluate whether the adiabatic effectiveness performance for the combined showerhead and pressure side coolant injection is predictable with superposition. Consistent with the previous study by Polanka et al. [8], the adiabatic effectiveness levels with combined showerhead and pressure side coolant injection was found to be significantly less than would be expected using superposition. In fact, the peak adiabatic effectiveness levels were found to decrease with the addition of coolant flow from the showerhead.

**Flow Visualization, Thermal and Velocity Fields.** The effect of the high mainstream turbulence on the coolant film from the showerhead and approaching the pressure side row of holes is shown in Fig. 9 in which low and high mainstream turbulence effects on the thermal field are contrasted. The position for these thermal field measurements,  $x/d = -22$ , was immediately before pressure side row of holes. Evident from these thermal field contours is the much larger dispersion for the high mainstream turbu-

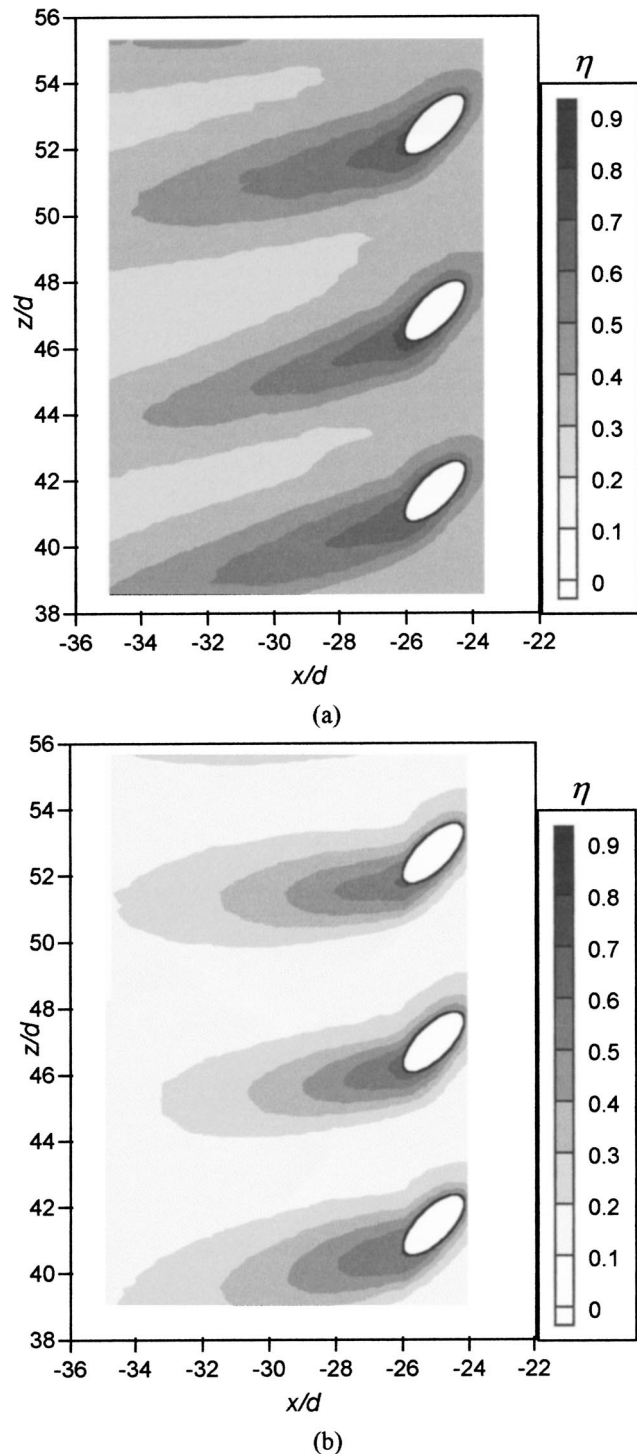


Fig. 7 Effect of turbulence on the mid-span pressure side film cooling with  $M_{sh}^* = 1.5$ ,  $I_{ps} = 0.2$ , and (a)  $Tu_\infty = 0.5\%$ , and (b)  $Tu_\infty = 20\%$

lence case resulting in much lower  $\Theta$  levels near the wall, i.e.,  $\Theta \sim 0.15$  for the high turbulence case compared to  $\Theta \sim 0.30$  for the low turbulence case. For both low and high mainstream turbulence cases, the coolant from the showerhead was uniform at this position immediately upstream of the pressure side holes (the spanwise position for these measurements was near the center of the airfoil where the coolant flow from the showerhead was two-dimensional).

Thermal profiles for the pressure side coolant jets with concu-

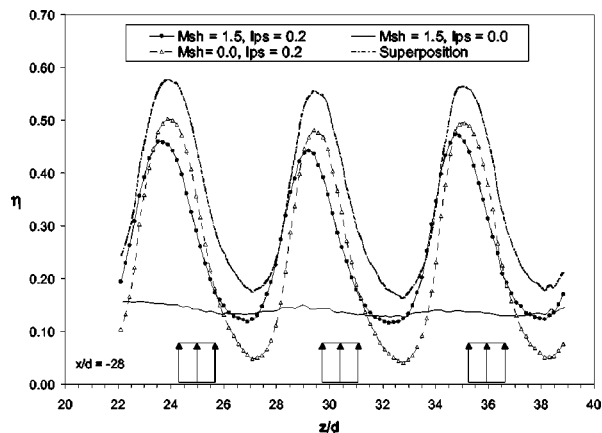


Fig. 8 Superposition of the showerhead,  $M_{sh}^* = 1.5$ , and pressure side film cooling with  $Tu_\infty = 20\%$  shown by the lateral distribution of effectiveness

rent showerhead blowing are presented in Fig. 10 for  $I_{ps} = 0.2$ , 0.5, and 1.2, representing a low, intermediate, and high blowing ratio, respectively. Comparing these thermal profiles with the thermal profiles for the coolant jets without the showerhead, given previously in Fig. 4, the cores of the coolant jets ( $\Theta > 0.2$ ) were very similar to that for the high mainstream turbulence with no showerhead blowing case. However, with showerhead blowing the cores of jets for  $I_{ps} = 0.5$  and 1.2 were larger and projected a greater distance from the wall. For  $I_{ps} = 0.2$  the core of the jet was very close to the wall for showerhead blowing and no-showerhead case, but the  $\Theta$  levels were decreased for the showerhead blowing

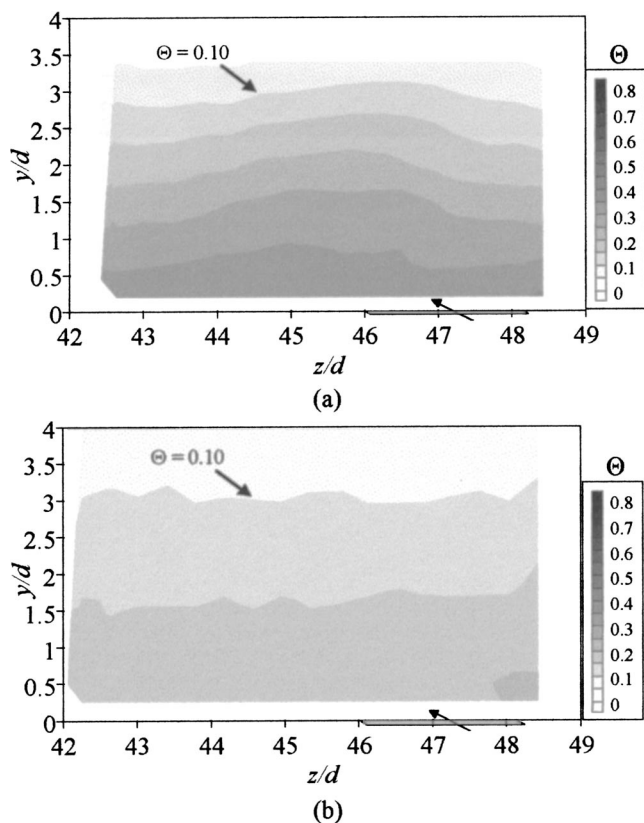


Fig. 9 Thermal fields due to showerhead injection measured immediately upstream of the pressure side holes ( $x/d = -22$ ) for (a)  $Tu_\infty = 0.5\%$ , and (b)  $Tu_\infty = 20\%$

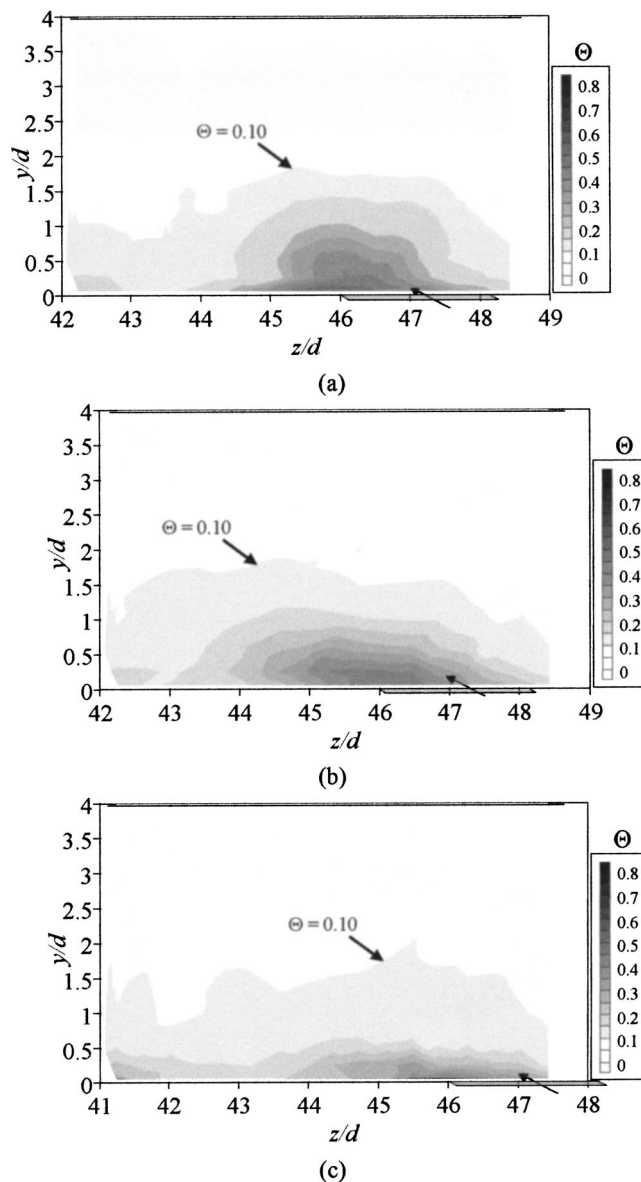


Fig. 10 Thermal profiles for the pressure side film cooling with  $Tu_\infty = 20\%$ ,  $x/d = -28$ ,  $M_{sh} = 1.5$ , and (a)  $I_{ps} = 1.2$ , (b)  $I_{ps} = 0.5$ , and (c)  $I_{ps} = 0.2$

case. Recognize that for the showerhead blowing case the pressure side coolant jets are surrounded with fluid at a  $\Theta$  level greater than 0.15, so the core jet temperatures would be expected to be  $\Delta\Theta \sim 0.1$  greater than the no-showerhead case. Since the coolant jet cores have no increase or have a decrease in  $\Theta$  level for the showerhead blowing case, the showerhead coolant flow must be causing a further increase in coolant dispersion beyond the dispersion caused by the high mainstream turbulence.

Insight into the difference between the mainstream turbulence effects and the showerhead-generated turbulence effects was obtained by contrasting the flow visualization of the pressure side coolant jets subjected to showerhead coolant flow with low and high mainstream turbulence, shown in Fig. 11. The images shown on Fig. 11 are a sequence of instantaneous snapshots highlighting fluctuations in the coolant jet positions for  $I_{ps} = 1.2$ . For low mainstream turbulence with showerhead blowing, Fig. 11(a), the coolant jets do not show any variation in position, but for high turbulence with showerhead blowing, Fig. 11(b), the coolant jets show the same lateral movement as discussed previously for the high

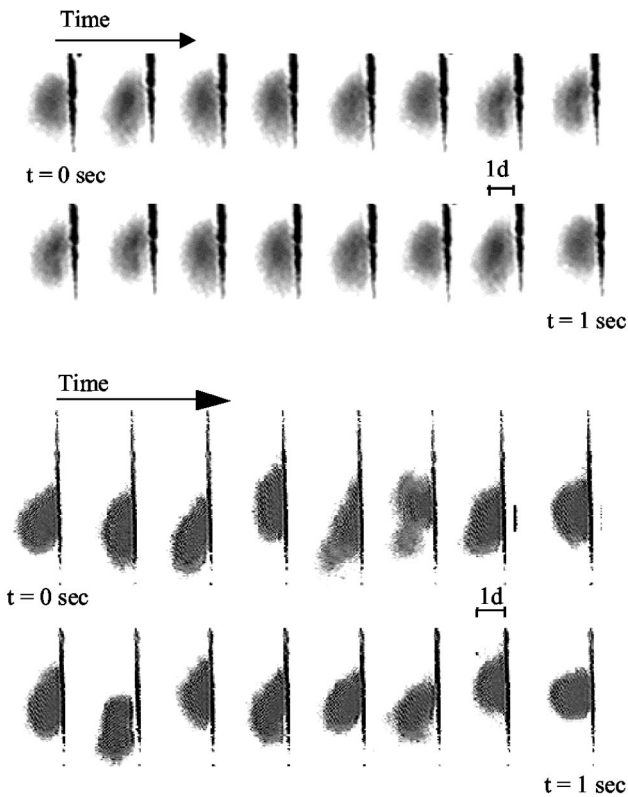


Fig. 11 Instantaneous flow visualization with  $I_{ps}=1.2$ ,  $M_{sh}^*=1.5$ , for (a)  $Tu_\infty=0.5\%$ , and (b)  $Tu_\infty=20\%$  at  $x/d=-28$

turbulence, no-showerhead condition, Fig. 5(c). These results indicate that the showerhead generated turbulence is not of large enough scale to cause bodily lateral movement of the coolant jets. Furthermore, the showerhead blowing does not disrupt the primary effect of the large scale mainstream turbulence of causing oscillations in the coolant jets.

Direct measurements of the turbulence  $u_{rms}/U_\infty$ ,  $v_{rms}/U_\infty$ , and  $w_{rms}/U_\infty$  levels for the high mainstream turbulence with showerhead blowing case are shown in Fig. 12 for  $I_{ps}=1.2$ . Comparing these profiles with the profiles for the high turbulence, no-showerhead case presented previously, Fig. 6, the major characteristic of the mainstream turbulence, i.e., much higher  $w_{rms}/U_\infty$  levels, was found to be preserved. Maximum rms levels were found to be similar for the no-showerhead and showerhead blowing cases, but the high turbulence regions were more extensive for the showerhead blowing case. This larger region of high turbulence may account for the increased dispersion of coolant for the showerhead blowing case.

## Conclusions

This study was performed to provide an understanding of how the film cooling of the pressure side of a vane is influenced by high mainstream turbulence and showerhead flow. Previous adiabatic effectiveness measurements showed a deterioration of the performance of the coolant jets subjected to these conditions. In this study, flow visualization, thermal field, and velocity field measurements provided insight into the interaction of the pressure side coolant jets with the surrounding highly turbulent flow.

Not surprisingly, high mainstream turbulence increases the dispersion of the pressure side coolant jets. In this study, we found that interaction of the mainstream turbulence with the airfoil results in an accentuation of the lateral velocity fluctuations relative to the streamwise and wall-normal velocity fluctuations. Furthermore, because of the large scale of the mainstream turbulence,

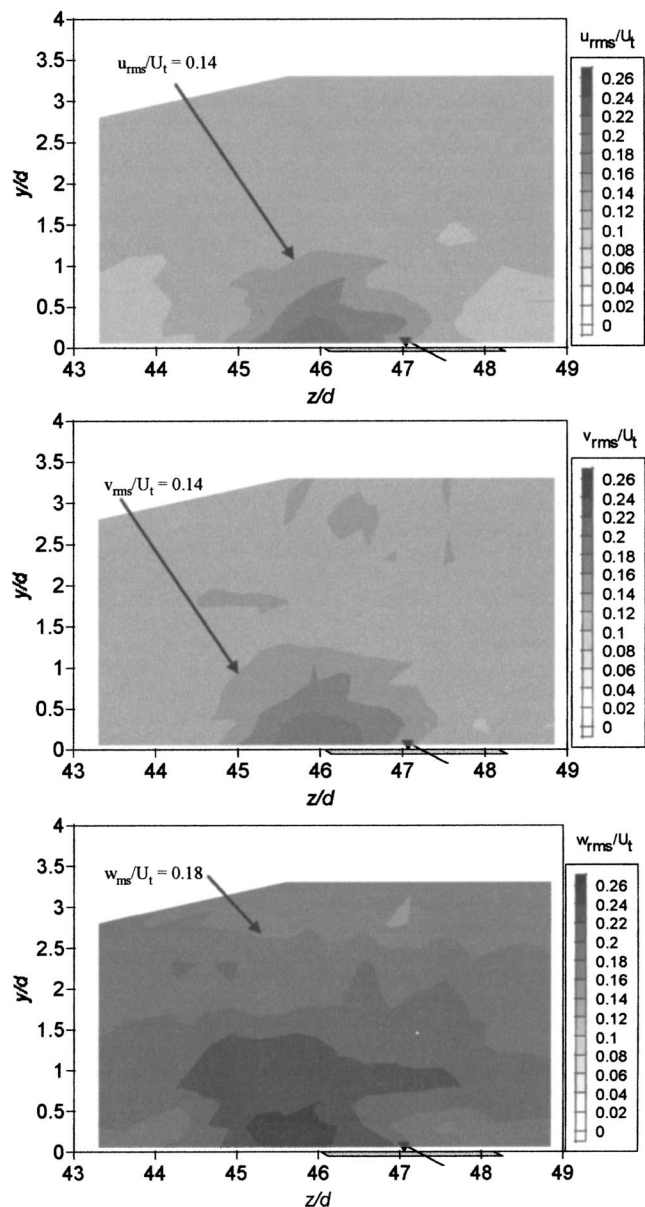


Fig. 12 RMS values at a location of  $x/d=-28$  for  $I_{ps}=1.2$  and  $M_{sh}^*=1.5$

$\Lambda_f=7d$ , the turbulence causes a lateral oscillation of the coolant jets rather than a break-up of the jets. This lateral fluctuation causes a broader adiabatic effectiveness distribution. This result is particularly important for guiding computational modeling efforts.

The high mainstream turbulence level used in this study,  $Tu_\infty=0.2$ , was significantly larger than the turbulence levels generated by the showerhead coolant injection. This suggested the possibility that the showerhead injection might not affect the pressure side coolant injection because of the dominance of the high mainstream turbulence effects. However, the showerhead coolant flow was found to still cause an increased dispersion of the pressure side coolant jet. Turbulence generated by the showerhead does not induce lateral oscillation of the coolant jets, suggesting that this is much smaller scale turbulence than the mainstream turbulence (purposely generated to have an integral scale of  $7d$ ). However, combining showerhead blowing with high mainstream turbulence results in larger regions of high turbulence, and hence increased dispersion of coolant jets on the pressure side of the vane.

## Acknowledgments

We are most grateful to the sponsors of this work, Advanced Gas Turbine Systems Research Consortium and Pratt & Whitney. We would also like to thank Pratt & Whitney for supplying the turbine vane geometry.

## Nomenclature

- $d$  = coolant hole diameter, 4.11 mm  
 $DR$  = density ratio,  $(\rho_c/\rho_\infty)$   
 $I$  = momentum flux ratio  $(\rho_c \cdot U_c^2/\rho_\infty \cdot U_\infty^2)$   
 $M$  = blowing ratio based on local freestream velocity  $(\rho_c \cdot U_c/\rho_\infty \cdot U_\infty)$   
 $M^*$  = blowing ratio based on local approach velocity  $(\rho_c \cdot U_c/\rho_0 \cdot U_0)$   
 $p$  = coolant hole-to-hole pitch, 5.6d  
 $P$  = airfoil-to-airfoil pitch, 457 mm  
 $t$  = time  
 $T$  = temperature  
 $Tu$  = turbulence intensity  $(u_{rms}/U_\infty)$   
 $U$  = mainstream velocity  
 $x, y, z$  = turbine vane surface coordinates  
 $\eta$  = adiabatic effectiveness  $(T_\infty - T_{aw}/T_\infty - T_c)$   
 $\bar{\eta}$  = spanwise averaged adiabatic effectiveness  
 $\Lambda_f$  = integral length scale  
 $\Theta$  = nondimensional temperature  $(T_\infty - T/T_\infty - T_c)$   
 $\rho$  = density

## Subscripts

- $aw$  = adiabatic wall  
 $c$  = coolant  
 $ps$  = pressure side  
 $sh$  = showerhead  
 $0$  = approach flow

$\infty$  = local freestream

## References

- [1] Moss, R. W., and Oldfield, L. G., 1991, "Measurements of Hot Combustor Turbulence Spectra," ASME Paper No. 91-GT-351.
- [2] Goldstein, R. J., Lau, K. Y., and Leung, C. C., 1983, "Velocity and Turbulence Measurements in Combustion Systems," *Exp. Fluids*, **1**, pp. 93–99.
- [3] Koutmos, P., and McGuirk, J. J., 1989, "Isothermal Flow in a Gas Turbine Combustor—A Benchmark Experimental Study," *Exp. Fluids*, **7**, pp. 344–354.
- [4] Radomsky, R. W., and Thole, K. A., 1998, "Effects of High Freestream Turbulence Levels and Length Scales on Stator Vane Heat Transfer," ASME Paper No. 98-GT-236.
- [5] Moss, R. W., 1992, "The Effects of Turbulence Length Scale on Heat Transfer," University of Oxford, Department of Engineering Science, Report No. OUEL 1924, Ph.D. Dissertation.
- [6] Ames, F. E., 1997, "The Influence of Large Scale High Intensity Turbulence on Vane Heat Transfer," ASME J. Turbomach., **119**, pp. 23–30.
- [7] Polanka, M. D., Witteveld, V. C., and Bogard, D. G., 1999, "Film Cooling Effectiveness in the Showerhead Region of a Gas Turbine Vane—Part I: Stagnation Region and Near-Pressure Side," ASME Paper No. 99-GT-48.
- [8] Polanka, M. D., Ethridge, M. L., Cutbirth, J. M., and Bogard, D. G., 2000, "Effects of Showerhead Injection on Film Cooling Effectiveness of Downstream Rows of Holes," ASME Paper No. 2000-GT-240.
- [9] Ames, F. E., 1998, "Aspects of Vane Film Cooling with High Turbulence: Part II—Adiabatic Effectiveness," ASME J. Turbomach., **120**, pp. 777–784.
- [10] Drost, U., and Bölcs, A., 1999, "Performance of a Turbine Airfoil with Multiple Film Cooling Stations Part I: Heat Transfer and Film Cooling Effectiveness," ASME Paper No. 99-GT-171.
- [11] Cutbirth, J. M., and Bogard, D. G., 2002, "Evaluation of Pressure Side Film Cooling With Thermal Field Measurements—Part I: Showerhead Effects," ASME J. Turbomach., **124**, pp. 670–677.
- [12] Cutbirth, J. M., 2000, "Turbulence and Three-Dimensional Effects on the Film Cooling of a Turbine Vane," Ph.D. dissertation, The University of Texas at Austin.
- [13] Cutbirth, J. M., and Bogard, D. G., 2001, "Thermal Field and Flow Visualization within the Stagnation Region of a Film Cooled Turbine Vane," ASME Paper No. 2001-GT-401.
- [14] Radomsky, R., and Thole, K. A., 2000, "Flowfield Measurements for a Highly Turbulent Flow in a Stator Vane Passage," ASME J. Turbomach., **122**(2), pp. 255–262.

# Correlation of Film-Cooling Effectiveness From Thermographic Measurements at Enginelike Conditions

S. Baldauf

M. Scheurlen

Siemens Power Generation,  
45473 Mülheim an der Ruhr, Germany

A. Schulz

S. Wittig

Lehrstuhl und Institut für Thermische  
Strömungsmaschinen,  
Universität Karlsruhe (TH),  
76128 Karlsruhe, Germany

*Adiabatic film-cooling effectiveness on a flat plate surface downstream of a row of cylindrical holes is investigated. Highly resolved two-dimensional surface data were measured by means of infrared thermography and carefully corrected for local conduction and radiation effects. These locally acquired data are laterally averaged to give the streamwise distributions of the effectiveness. An independent variation of the flow parameters blowing rate, density ratio, and turbulence intensity as well as the geometrical parameters streamwise ejection angle and hole spacing is examined. The influences of these parameters on the lateral effectiveness is discussed and interpreted with the help of surface distributions of effectiveness and heat transfer coefficients presented in earlier publications. Besides the known jet in cross-flow behavior of coolant ejected from discrete holes, these data demonstrate the effect of adjacent jet interaction and its impact on jet lift-off and adiabatic effectiveness. In utilizing this large matrix of measurements the effect of single parameters and their interactions are correlated. The important scaling parameters of the effectiveness are shaped out during the correlation process and are discussed. The resulting new correlation is designed to yield the quantitatively correct effectiveness as a result of the interplay of the jet in crossflow behavior and the adjacent jet interaction. It is built modularly to allow for future inclusion of additional parameters. The new correlation is valid without any exception within the full region of interest, reaching from the point of the ejection to far downstream, for all combinations of flow and geometry parameters. [DOI: 10.1115/1.1504443]*

## Introduction

The typical design process of advanced turbine components relies on thermal and structural finite element analyses. A reliable and quantitatively correct prescription of thermal boundary conditions on hot gas exposed surfaces of turbine components is crucial for a successful design. The precise prediction of wall temperatures is imperative for a proper evaluation of the part lifetime and the structural integrity. In modern high-efficiency designs, where materials are stressed close to their critical temperatures, a difference as low as 15 K from the predictions may halve the lifetime and cause part failure. Film cooling of hot gas exposed surfaces is a widely used design element to control material temperatures. However, the complex three-dimensional flow situation from discrete hole coolant ejection renders the prediction of according wall surface boundary conditions extremely difficult.

The thermal boundary conditions introduced to an FE-analysis are derived from flow and/or boundary layer computations or correlations. A major shortcoming of a computational approach is the pronounced dependence on the quality of specific input parameters. This dependence can feature chaotic results in sensitive areas like laminar turbulent boundary layer transition. Large changes of the predictions are caused by only minor differences in the input. A more robust and, therefore, commonly utilized source of boundary conditions are correlations. These are derived from, and validated by, experimental investigations. A major goal of the ongoing study is to provide detailed results for the flow reference temperature in the presence of film cooling in terms of the adiabatic film-cooling effectiveness [1,2]

Contributed by the International Gas Turbine Institute and presented at the International Gas Turbine and Aeroengine Congress and Exhibition, Amsterdam, The Netherlands, June 3–6, 2002. Manuscript received by the IGTI, November 29, 2001. Paper No. 2002-GT-30180. Review Chair: E. Benvenuti.

$$\eta = \frac{T_G - T_{AW}}{T_G - T_C} \quad (1)$$

The present part of the study concentrates on laterally averaged film-cooling effectiveness. The effectiveness is specific to the ejection case and depends on the ejection parameters, characterized by similarity numbers of the flow. A similarity and sensitivity study of Baldauf et al. [3] identified the set of parameters that is governing the laterally averaged effectiveness from rows of streamwise inclined ejection holes

$$\bar{\eta} = f\left(M, P, Tu, \frac{x}{D}, \alpha, \frac{s}{D}, \frac{\delta_1}{D}, \frac{L}{D}\right) \quad (2)$$

Whereas the local values, recorded and processed with high resolution (see [1]), give an in depth understanding of the cooling air distribution, these laterally averaged values allow for a direct and quantitative comparison of different measurements. They provide a precise categorization by the characteristics of different parameter ranges and, therefore, enable the evaluation and quantification of single jets versus interacting jets effects. Furthermore, the overall temperature reduction over the cooled surface becomes instantaneously obvious from the area enclosed by a laterally averaged effectiveness curve.

## Experimental Apparatus and Data Processing

The experiments were conducted in an open circuit hot wind tunnel of the Institute for Thermal Turbomachinery at the University of Karlsruhe. The experimental setup employs a scaled up geometry at steady-state measurement conditions. Special care was taken to assure similarity of the flow conditions to real engine applications [3]. A schematic of the experimental facility is shown in Fig. 1. A radial compressor and 270 kW electric heating system provide a hot gas mass flow of 1.3 kg/s at a temperature of 550 K.



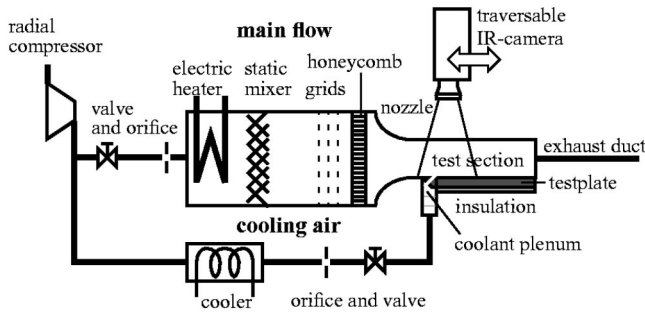


Fig. 1 Hot wind tunnel scheme

Two different sets of grids and flow straighteners produce low and elevated levels of the turbulence intensity at the entrance of the test section. A secondary air flow is conditioned by a cooler, orifice, and valve system, and delivered into an ejection plenum at the bottom of the test section. The test plate made from a low-conductivity semi-crystalline thermoplast (TECAPEK) approximates an adiabatic bottom wall of the test section. Exchangeable ejection modules carry the different ejection geometry. The ejection holes diameter is  $D = 5$  mm resulting in a cross-sectional area of the test section of  $21 \times 44 D$ . The instrumented part of the testplate, connected directly to the ejection module, extends  $82D$  downstream of the ejection location. The operating conditions and the range of parameters are given in Table 1.

Infrared thermography was used for mapping the surface temperature field of the test plate. Coating of the test plate with a constant emissivity dye and an in-situ calibration procedure (Martiny et al. [4]) utilizing surface thermocouple measurements assure quantitatively correct 2-D surface temperature distributions. The thermography data from a region of several hole pitches are reduced to one half pitch. Since a real temperature ratio experiment impedes real adiabatic wall conditions, a careful heat flux analysis of the testplate is imperative. A finite element approach is used to model the half-pitch stripe of the testplate and compute the 3-D plate internal heat flux. The wall normal heat flux result at the testplate surface combined with a radiation exchange analysis of test surface and test channel enables the evaluation of the local adiabatic effectiveness. The error of the local adiabatic film cooling effectiveness  $\bar{\eta}$  is kept well below 5%. For a more detailed description of the experimental facilities, data processing, and numerical analysis, see [1].

### Results of Laterally Averaged Effectiveness

The downstream distributions of the laterally averaged effectiveness are obtained by spanwise integration of the local values. This evaluation is performed for the complete downstream range starting from the hole axis at  $x/D = 0$  and extending to the end of the test plate at  $x/D = 82$ . The measuring data within the ejection hole openings do not display surface conditions. Therefore, only the measurement data outside and in between the hole openings are used for the integration of the laterally averaged values. In the following, the overall effectiveness is addressed as a measure for

Table 1 Operating parameters

Geometry:	$\alpha$	= 30°, 60°, 90°
	$s/D$	= 2, 3, 5
	$L/D$	= 6
Hot gas flow:	$Re_D$	= 6800 - 14000
	$\delta_1/D$	= 0.1
	$Tu$	= 1.5%, 4%
Coolant flow:	$M$	= 0.2 - 2.5
	$P$	= 1.2, 1.5, 1.8

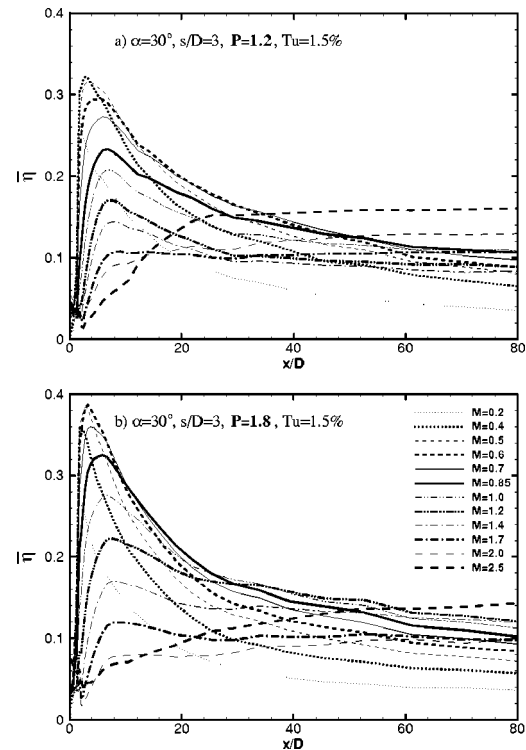


Fig. 2 Variation of the blowing rate at low and high density ratio

the total downstream surface temperature reduction. The overall effectiveness is defined as the area enclosed by the laterally averaged effectiveness curve. The laterally averaged effectiveness is integrated over the stated downstream range, which is considered to cover the surface area of major interest for the application.

**Variation of the Blowing Rate.** Figure 2 shows the results of the laterally averaged effectiveness for a variation of the blowing rate from very low values of  $M = 0.2$  to values as high as  $M = 2.5$ . The plots display results of an application typical case with a shallow ejection angle of  $\alpha = 30$  deg and a hole spacing of  $s/D = 3$ . In Fig. 2(a) the results for a low-density ratio of  $P = 1.2$  are shown, typical for experimental results at ambient temperature conditions. Figure 2(b) envisions the results at an engine-like high-density ratio of  $P = 1.8$ . A typical adiabatic effectiveness development with downstream distance can be observed:

- The value of  $\bar{\eta}$  is zero at the ejection position, since the adiabatic surface between the ejection holes is not covered by cooling air.
- $\bar{\eta}$  increases when the cooling air laterally spreads with downstream distance. A maximum is reached where the best surface coverage is obtained and the formation of a closed cooling film can be expected.
- Downstream of the maximum, the beneficial effect of the cooling air spread, yielding an increased surface coverage, is overbalanced by the adverse effect of an increasing cooling film temperature. The effectiveness is decaying due to the entrained hot gas.

The arrangement of the curves relative to each other is dominated by the effects of a single cooling air jet's mixing behavior in the hot gas crossflow. These effects are discussed by means of the effectiveness distributions shown in Fig. 2(b) for application conditions.

At very low blowing rates the coolant jets spread on the wall surface immediately after exiting the holes. This results in a high effectiveness peak close to the ejection location. The small cool-

ant mass flow is diluted fast by the hot gas flow and, therefore, a rapid decay of the effectiveness follows downstream of the maximum. The overall effectiveness is low, as can be seen from the area enclosed by the curves.

At low to moderate blowing rates both the maximum and the overall effectiveness increase due to the increased coolant mass flow that slows down the cooling film temperature rise. The effectiveness peak is moving downstream since the more compact jets require some downstream distance to spread on the surface. The highest effectiveness peak of  $\bar{\eta}=0.385$  is attained at a blowing rate of  $M=0.6$ .

At moderate blowing rates beyond  $M=0.6$ , the effectiveness peak is decreasing again. This is caused by the effects of beginning jet lift-off and its tendency to entrain hot gas underneath the coolant jet. Downstream of the maximum, the laterally averaged effectiveness is still rising with blowing rate. Here, the adverse effect of jet lift-off that tends to drive the jets away from the surface with increasing blowing rate is still outweighed by the beneficial effect of the additional coolant thermal capacity. An optimum is obtained at a blowing rate of  $M=1.0$ , indicated by the highest overall effectiveness. Further increasing the blowing rate now causes more pronounced lift-off effects. Whereas the higher coolant mass flow does not result in a substantial downstream effectiveness increase, the decreasing maximum effectiveness deflates the overall temperature reduction.

Proceeding to high blowing rates causes a slight change in the general curve characteristics. The continuous downstream decay characteristic is lost at a blowing rate of  $M=1.4$ . The downstream effectiveness rather tends to stabilize around values of  $\bar{\eta}=0.12$ . At higher blowing rates the effectiveness peak is still decreasing and a minimum overall effectiveness is given at  $M=1.7$ . The effectiveness peak is vanishing as the coolant jets detach from the surface at the hole exit. For the actual ejection case and  $M=1.7$  the effectiveness rises to a second maximum downstream of  $x/D=25$ , which is stretched out far downstream. This second maximum is slowly increasing with a further increase of the blowing rate. From local effectiveness and heat transfer coefficient distributions [1,2] it can be seen that adjacent jets of a row of holes interact to form a thickened, closed film at these conditions. This massive film layer with its high thermal capacity prevents intense hot gas entrainment and early cooling film degradation. The change of the effectiveness behavior indicates a change in the coolant flow structure. The flow structure was dominated by the jet in crossflow mixing and resulting lift-off effects at low to moderate blowing rates. At high blowing rates of  $M=1.7$  and beyond, it is dominated by the adjacent jet interaction. Note that these flow structural regimes and their effects are closely related to the actually discussed flow case. They will, of course, change with a variation of geometry, density ratio or other parameters. Nonetheless, the configuration displayed in Fig. 2(b) is considered as a typical application. Therefore, the specific flow structures related to this case are of practical interest.

**Density Ratio Effect.** Figure 2(a) shows results of a low-density ratio test case at  $P=1.2$  on the same range of blowing rates and identical geometrical ejection conditions. In general, the same characteristics of the laterally averaged effectiveness distribution can be observed. High and narrow maximum peaks close to the ejection location are followed by a fast decay at low blowing rates. An optimum overall effectiveness is attained at moderate blowing rates and a degradation of the peak effectiveness at higher blowing rates due to lift-off effects reflect a single jet in crossflow-dominated flow. At the high end of the examined blowing rates, again a stretched and stable maximum is displayed downstream. This is due to a dominating adjacent jet interaction within the cooling film flow at high blowing rates.

The impact of the low density ratio becomes obvious by a closer inspection of the curves. The highest effectiveness peak is now shifted to blowing rates of  $M=0.4$  to  $0.5$ , attaining a lower maximum value of  $\bar{\eta}=0.32$ . This lower peak value is expected,

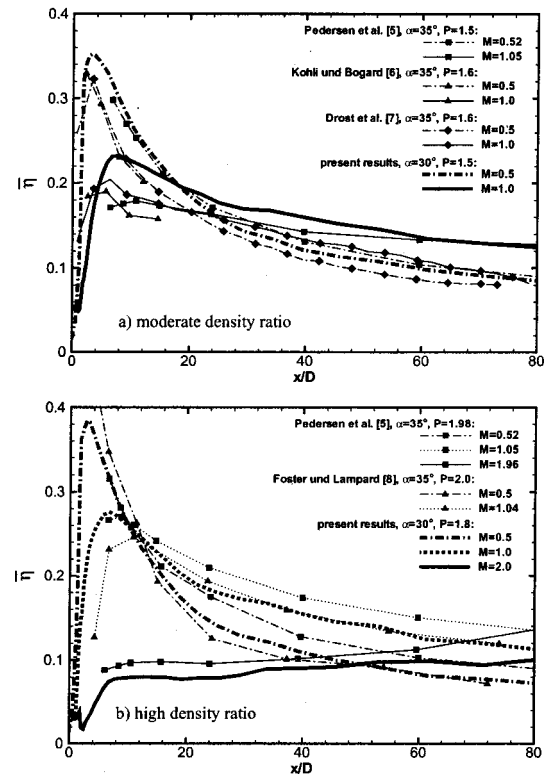


Fig. 3 Comparison with literature results

since the higher momentum ratio of the coolant jets tends to drive the jets off the wall. This is in accordance with an optimum overall effectiveness attained early at  $M=0.7$ . The optimum overall effectiveness, however, is almost the same as in the high density ratio test case at  $M=1.0$ . The range of decreasing peak values with increasing blowing rates is shifted to considerably lower values of the blowing rate. The lowest overall effectiveness still occurs at about  $M=1.7$  and at levels of  $\bar{\eta}=0.1$ . Beyond that blowing rate, the downstream effectiveness maximum is more pronounced than for high density ratio. The curves of the laterally averaged effectiveness commence their rise at considerably lower  $x/D$  and reach higher downstream effectiveness levels up to  $\bar{\eta}=0.16$ . At lower density ratios the higher momentum ratio intensifies the jet vortices. At the same time, the higher velocity ratios promote the shear layer effects around the coolant jets. The combination of both effects enhances the adjacent jet interaction. At very high blowing rates, this rather tends to stabilize the cooling film layer than driving it away from the wall.

**Comparison With Literature Data.** Especially for the geometrical configuration of the two ejection cases displayed in Fig. 2; that is, a shallow ejection angle and a typical three-hole diameter spacing—a number of laterally averaged effectiveness data sets are available in the literature. The present findings are compared to such results in Fig. 3. Two sets of measurements comprising (a) moderate level of density ratio tests at near application conditions and (b) high level of density ratio tests, considered application typical flow conditions, are regarded.

At moderate density ratio (Fig. 3(a)), two blowing rates offering the broadest basis for comparison are selected. At the low blowing rate of  $M=0.5$ , the chart displays an almost perfect match of results from literature with the present result. At the moderate blowing rate of  $M=1.0$ , the curve representing the present results is slightly elevated in the maximum peak region and converges back to the other results further downstream. This meets the expectations, since the present measurements are conducted at a slightly lower ejection angle of  $\alpha=30$  deg with re-

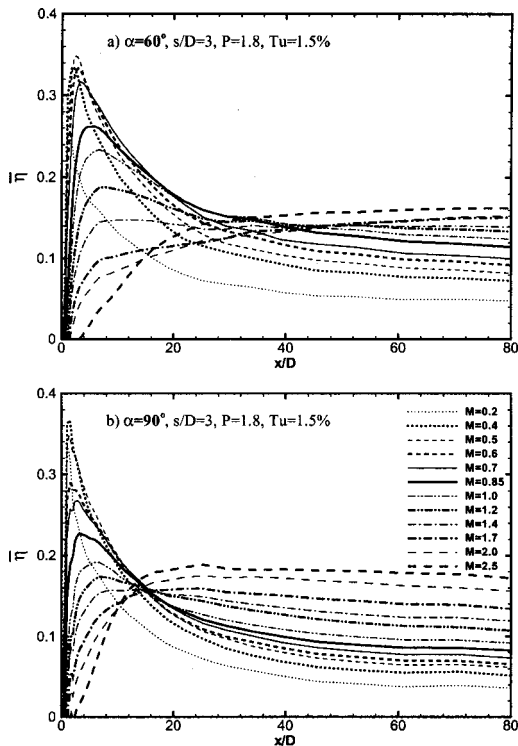


Fig. 4 Effect of the blowing angle

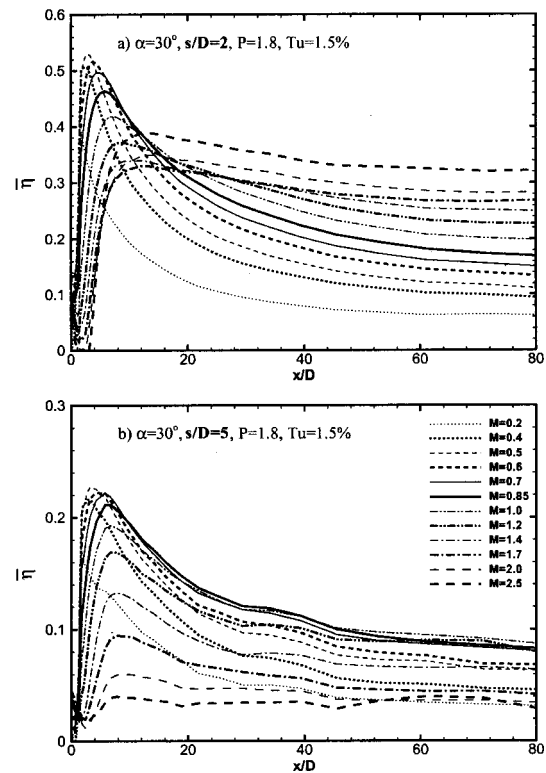


Fig. 5 Effect of the hole spacing

spect to the typically preferred  $\alpha=35$  deg. Therefore, the present results should display slightly less effectiveness loss due to jet lift-off.

For the high density ratio set in Fig. 3(b), three blowing rates are selected for comparison. For all three values the present results are well in the range of the scatter band of the other authors' measurements. At high blowing rate, the values of Pedersen et al. [5] seem to display a systematic offset from the present result. However, their results mark the top edge of the scatter band at all three blowing rates. The comparison reveals that the available literature data match the present results quantitatively and qualitatively. Therefore, the measured effectiveness is regarded both, typical for, and transferable to, real engine conditions.

**Effect of the Ejection Angle.** The normal ejection at a high density ratio of  $P=1.8$  and a standard hole spacing of  $s/D=3$  shown in Fig. 4(b) is considered an extreme case of angle variation. The maximum effectiveness peaks of the single jet in crossflow characteristic are found at lower downstream distances than for the inclined ejection. This is considered an effect of the very intense mixing of the coolant jets without a downstream velocity component. At low blowing rates, the peaks are extremely steep and narrow, reaching a greatest height of  $\bar{\eta}=0.37$  at a blowing rate as low as  $M=0.4$ . The effectiveness decays sooner than for an inclined ejection, yielding a smaller overall effectiveness area below the curves.

Within the examined range of  $x/D$  two regions of different flow behavior and structure can be identified in Fig. 4(b). Upstream a crossing point of all laterally averaged effectiveness curves at  $x/D=13$  and  $\bar{\eta}=0.16$ , maximum peaks of the single jet in crossflow characteristic are present. The peak effectiveness is decreasing monotonously with an increase of coolant mass flow in this region. Downstream of  $x/D=13$ , the extended maxima of the adjacent jet interaction characteristic appear and the effectiveness is increasing monotonously with an increase of the coolant mass flow. A closed cooling film and a high and stable downstream maximum is established at high blowing rates. At that crossing point, the adjacent jet interaction flow pattern takes over at much

lower downstream distances as for inclined ejection. It is assumed that the intense mixing of the surface normal jets in the hot gas crossflow promotes immediate spreading and subsequent intense interaction of adjacent coolant jets. At about  $M=1.4$ , the effectiveness peak near the ejection vanishes and the adjacent jet interaction pattern dominates the complete downstream range. The overall effectiveness values at very high blowing ratios are greater than those of an inclined ejection and reach a level of  $\bar{\eta}=0.18$ . The early and intense adjacent jet interaction seems to prevent as well the expected deep jet penetration as the related extensive hot gas entrainment into the cooling film.

The steep angle ejection results displayed in Fig. 4(a) fit well in between the characteristics of the shallow angle ejection and the normal ejection. A distinct crossing point dividing the cooled surface into a single jet in crossflow-dominated region and an adjacent jet interaction-dominated region is not yet established. The effects of jet interaction, as pictured by the effectiveness curves rising to the extended downstream maximum at high blowing rates, appear earlier than for shallow angle ejection. The downstream effectiveness at high blowing rates fits well in between the levels of the shallow angle and normal ejection.

A comparison with Fig. 2 shows that the optimum overall effectiveness is coupled to the lift-off effects of a jet in crossflow-dominated flow pattern. As soon as the adjacent jet interaction is becoming dominant in the vicinity of the ejection position, the lift-off behavior is significantly influenced. An optimum coolant mass flow with respect to the effectiveness then is no longer existent. Higher blowing rates directly yield higher overall effectiveness in this situation. (See references [6,7].)

**Effect of the Hole Spacing.** Figure 5 shows the laterally averaged effectiveness at shallow ejection angle, high density ratio, and two different hole spacings of  $s/D=2$  and 5, respectively. At a small hole spacing of  $s/D=2$  (Fig. 5(a)) the laterally averaged effectiveness is well above the values achieved at  $s/D=3$ , attributed to the larger coolant mass flow per surface area. However, at lower blowing rates, the positions of the maximum effectiveness

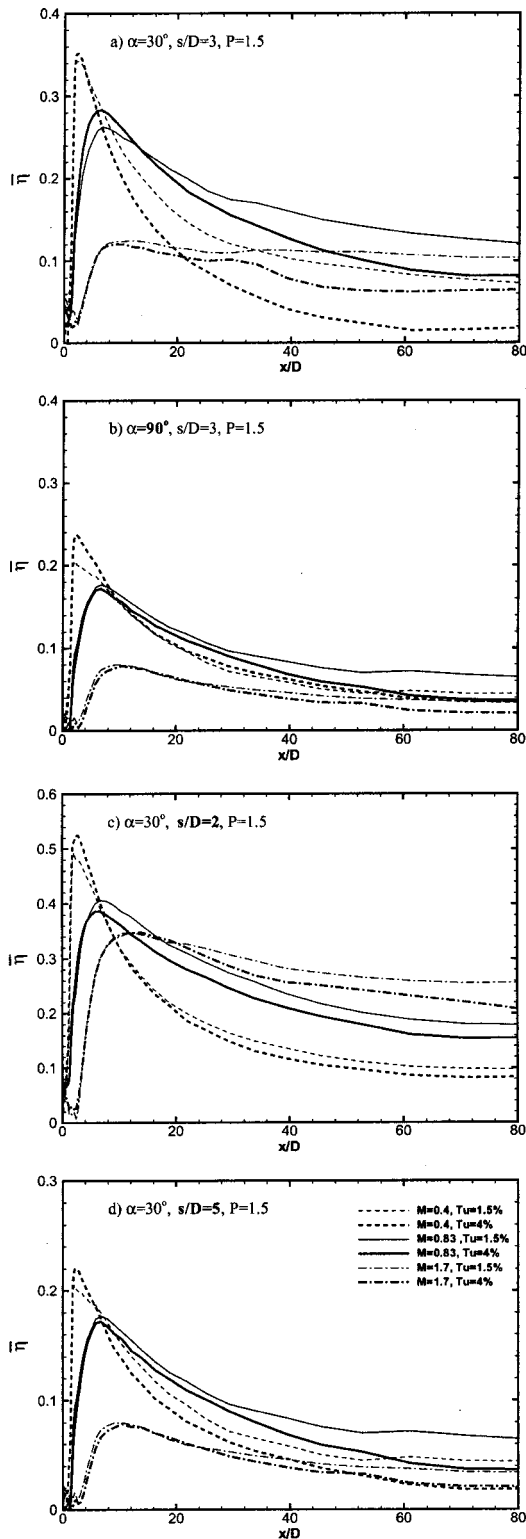


Fig. 6 Effect of the turbulence intensity

peaks have merely changed with respect to those of larger hole spacings. The highest maximum now occurs at a blowing rate of  $M=0.5$  reaching  $\bar{\eta}=0.53$ . At high blowing rates, the development of the maxima with increasing  $M$  is qualitatively similar to the normal ejection case at  $s/D=3$ . The single jet in crossflow maximum peak is decreasing and at least vanishing, or rather blinded out, by an increasing downstream maximum resulting from the adjacent jet interaction. Hence, the flow situation is com-

pletely taken over by the adjacent jet interaction at a blowing rate of  $M=1.7$ . For the narrow hole spacing, these downstream maxima also occur at very short downstream distances. Different from the three-diameter hole spacing, they display a distinct peak position and subsequent gradual decay instead of an almost constant value over a large downstream distance. Considering the overall effectiveness area below the curves, an obvious optimum coolant mass flow can not be identified. Downstream of  $x/D=20$  a monotonous increase of the effectiveness with increasing blowing rate takes place at high levels of  $\bar{\eta}=0.3$  and above.

For a large hole spacing of  $s/D=5$  (Fig. 5(b)), the laterally averaged effectiveness values are considerably lower than for  $s/D=3$ . This again is expected from the much lower coolant mass flow per surface area. The position of the effectiveness peaks are merely shifted with respect to the smaller hole spacing of  $s/D=3$ . A distinct optimum of the overall effectiveness occurs at blowing rates of about  $M=0.85$ . Further increasing the blowing rate causes a monotonous decrease of the effectiveness due to pronounced lift-off of the isolated jets. Within the examined downstream range, the laterally averaged effectiveness data are not influenced by adjacent jet interaction. (See reference [8].)

**Effects of Increased Hot Gas Flow Turbulence.** Figure 6 shows a comparison of low and elevated turbulence conditions at a moderate density ratio of  $P=1.5$ . Three blowing rates are chosen, representing low, moderate, and high blowing conditions. Displayed are the effects of different geometry, comprising normal ejection and different hole spacings with respect to the typical application case of  $s/D=3$  and  $\alpha=30$  deg (Fig. 6(a)).

Near the ejection position and at low blowing rates, the effectiveness peaks are higher at elevated turbulence conditions for all cases. It is assumed that a higher crossflow turbulence promotes the coolant jet in crossflow mixing and, therefore, jet spreading in the vicinity of the ejection position. At high blowing rates and close to the ejection location, the jet in crossflow mixing situation is dominated by the high turbulence levels within the coolant jet. Accordingly, the maximum effectiveness levels are not affected by the increased turbulence at high blowing rates. The adverse effect of additional hot gas entrainment, due to enhanced turbulent mixing, is compensated by the favorable effect of faster jet spreading and subsequently better surface coverage. At moderate blowing rates one or the other effect is dominant, depending on the specific flow situation.

Far downstream, the additional coolant into hot gas mixing at elevated turbulence levels causes an effectiveness loss for all geometry and blowing rates. The effect is most pronounced at lower blowing rates and shallow ejection angles, where the turbulence generation from the jet in crossflow mixing itself is low. This introduces a considerable effectiveness loss at typical moderate blowing rate shallow angle ejection situations, both at standard pitch (Fig. 6(a)), and at large pitch (Fig. 6(d)). The opposite applies for the small hole spacing and normal ejection situations (Figs. 6(b), (c)), where the turbulence generation by jet interaction and mixing dominates within the cooling film flow and the crossflow turbulence impact is moderate.

### Effectiveness Correlation

The screening of the open literature for experimental results still reveals missing data, especially concerning consistent studies of geometry variations and precise near ejection surface measurements. This often prevents a proper effectiveness prediction. The actual study represents a database covering a large range of all dominating ejection parameters at consistent and carefully controlled experimental conditions. Therefore, excellent conditions for the development of correlations including the complete surface area and all parameter interactions are at hand. The systematic findings of the flow and geometry variations discussed before, have to be formulated as empirical equations.

Important hints for suitable approaches were found by reviewing existing effectiveness correlations. An overview over early

correlation approaches, concentrating on slot ejection, is given by Goldstein [9]. Further approaches introducing more specific geometry are given by, e.g., Sturgess [10,11], Pai and Whitelaw [12], and Muckerjee [13]. A compilation of these later approaches is provided by Lefebvre [14]. A common basis of slot ejection correlations can be described as follows:

- At the ejection position a total coverage of the surface by the coolant is assumed, providing an effectiveness of  $\bar{\eta}=1$ .
- The total coverage situation of  $\bar{\eta}=1$  is sustained over a certain downstream distance presuming a cooling film core flow.
- The subsequent mixing and temperature rise of the cooling film is modeled by an exponential decay function, in which the exponent is evaluated experimentally.

Typical approaches for the ejection from rows of discrete holes adopt this model, skipping the cooling film core flow presumption. The exponential decay behavior is determined in experiments and extrapolated backwards to the ejection position. The correlations yield reasonable results for specific ejection situations further downstream of the ejection position (e.g., Metzger and Fletcher [15], Jabbari and Goldstein [16], Kruse [17], Forth and Jones [18]). However, these approaches give an unrealistic maximum at the ejection position and enforce a monotonic decay. At the ejection position, the local temperature load on the surface is inadmissibly underestimated. Hence, the vicinity of the ejection is usually excluded. Often a typical geometry, i.e.,  $\alpha=30-35$  deg and  $s/D=3$ , is presumed. Mostly the approaches cover only low to moderate blowing rates or employs different equations for low and high blowing rate regimes, respectively.

It is well known from locally resolved measurements of the adiabatic surface temperature in the vicinity of ejection holes that the film-cooling effectiveness builds up by the spreading of the ejected jets on the surface. More recent correlations of the laterally averaged effectiveness account for this initial downstream length required for the formation of a cooling film (e.g., L'Ecuyer and Soechting [19], Baldauf et al. [20]). These models aim on a complete description of the effectiveness behavior from the ejection position to far downstream for a large variety of ejection geometry and flow parameters.

From the present measurement results is concluded that the development of the cooling effectiveness is governed by the interplay of two phenomena. These are the single jet in crossflow mixing and the adjacent jet interaction. The cooling film development is distinctively determined by the ejection geometry, characterized by hole angle and spacing, and influenced by the density ratio. Therefore, even the modeling of basic effects needs to account for the whole database. The characteristic feature of the large majority of all measurements is the peak of the laterally averaged effectiveness curves due to the single jet in crossflow behavior. Obviously, all row of holes ejection situations must feature such peaks due to the fact of initially ejecting single jets. The correlation of L'Ecuyer and Soechting [19] already demonstrated that effectiveness curves of different ejection situations often can be considered similar, and the laterally averaged effectiveness level can be characterized by the value of the peak. Using these findings, the new effectiveness correlation will be set up as follows:

- The basic jet in crossflow behavior forms a typical base curve. It displays rising effectiveness towards a peak value, due to coolant spreading and closed cooling film formation, followed by an exponential decay downstream. The typical height of this peak depends on the ejection situation and necessitates a systematic description of the specific peak value and position. Normalizing all single curves by their maxima should bring all similar curves of jet in crossflow characteristic on top of each other. The collapsed curves should yield the laws for the effectiveness rise and decay of the base curve.
- The ejection cases dominated by the adjacent jet interaction

must deviate from this base curve after normalization. Especially their maximum peaks are not expected to match the description lined out before. The systemized divergence of the maximum peaks should allow for a common description of all cases on one base curve.

- With all curves pinched to common maximum values, deviations of the downstream decay due to the adjacent jet interaction will remain. A final systemization of these deviations should yield one common curve and correlation of laterally averaged adiabatic effectiveness.

Thus, the goal of the correlation process is to find transformation and scaling laws that allow the definition of a single functional relation. It yields an effectiveness representation over a downstream length representation of the kind

$$\eta^* = f(\xi) \quad (3)$$

Given the ejection parameters, the parameter specific backscaling and transforming of this base curve produces the required effectiveness distribution as a prediction of the corresponding ejection situation. The parametric scaling and transformation functions feature coefficients and reference values based on physical effects and allow an in depth interpretation of film cooling behavior. The coefficients themselves are functions of the ejection parameters

$$\text{coefficients} = f\left(M, P, \alpha, \frac{s}{D}\right) \quad (4)$$

The coefficient functions need to fit the measured distributions. They must reasonably interpolate between sampling points as given by the examined ejection parameter matrix. Furthermore, they should be non-critical at the edges of the parameter ranges. These coefficient functions are no longer physically meaningful. They result from curve fit procedures as given in the Appendix.

**Base Curve Evaluation.** The laterally averaged effectiveness curves are plotted over a common downstream length representation to find the similarities. It is known from early slot film cooling effectiveness measurements that the curves from different flow rates collapse by scaling the downstream length with slot width and blowing rate. This approach was transferred to the ejection from rows of holes (i.e., Louis [21], Kruse [17], L'Ecuyer and Soechting [19]) by introducing an equivalent slot width

$$s_e = \frac{\pi D^2}{4 s} \quad (5)$$

The scaled downstream length results in

$$\xi_M = \frac{x}{M s_e} \quad (6)$$

Still, the effectiveness resulting from discrete hole ejection at typically moderate blowing rates is dictated by the coolant jet lift-off effects. The penetration depth of a jet in crossflow corresponds to the relative jet momentum (e.g., Abramovic [22]), suggesting the momentum ratio as a scaling parameter.

$$\xi_I = \frac{x}{I s_e} \quad (7)$$

Thereabout is a perpetual discussion within the film cooling community, whether one ( $M$ ) or the other ( $I$ ) scaling parameter is characterizing the film cooling results. The typical outcome from using the different parameters is shown in Fig. 7 on a double logarithmic scale. Figure 7(a) confirms that the common downstream decay of the effectiveness curves, i.e., the farfield of the coolant ejection, is characterized by the blowing rate. This is expected from known results of slot ejection. The exponent of the decay function is given by the gradient of a straight line. Furthermore, Fig. 7(a) reveals that for the displayed case the downstream position of the maxima of all measurements are characterized by the blowing rate scaling. If the curves are scaled to the momentum

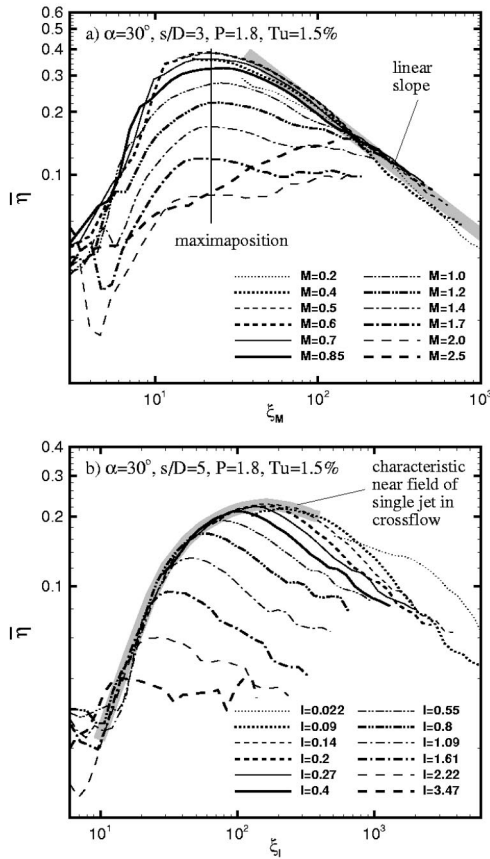


Fig. 7 Effectiveness plotted versus different downstream scales

ratio, it becomes obvious from Fig. 7(b) that the curves of the given case collapse for short downstream distances. Thus, the near field of the coolant ejection is characterized. All measurements follow the characteristic curve, until they branch, highest momentum ratio first. The branching curves fall to lower effectiveness values because of the coolant jet lift-off. Note that this ideal picture of the near field character applies only to the undisturbed single jet in crossflow flow behavior resulting from a large pitch ejection.

Since the blowing rate seems better suited to characterize the effectiveness peaks, these peak values are first hand plotted versus  $M$  to enable a classification. Figure 8 shows a compilation of the effectiveness peak values from all examined geometry, ordered by

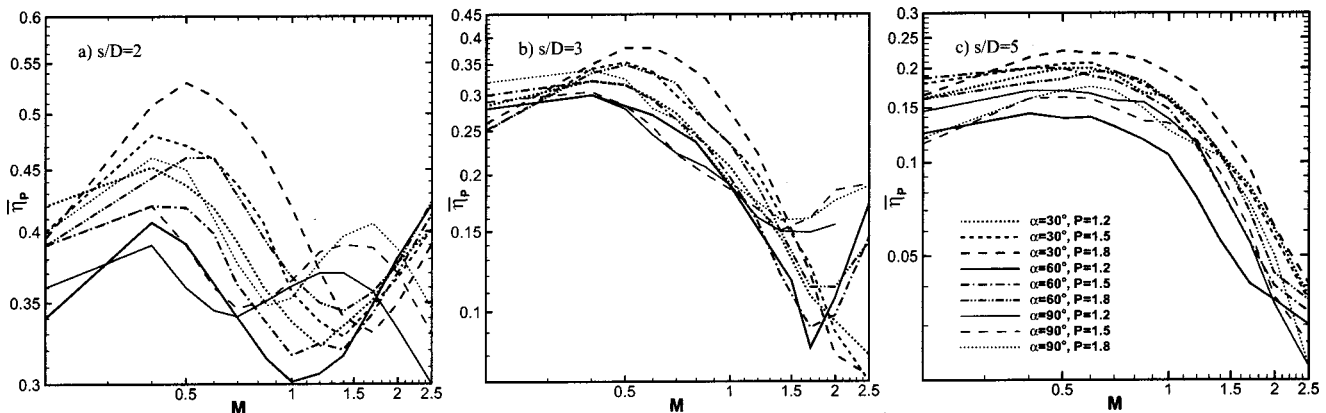


Fig. 8 Laterally averaged effectiveness peaks of all measurements

hole spacing. It can be seen that the peak development with the coolant mass flow is similar for the three hole spacings examined. The common picture is a rising peak value at low blowing rates and a decreasing peak value at moderate and high blowing rates, due to jet lift-off. Small pitch geometry yields steeply rising and falling curves at high levels. Large pitch geometry yields smoothly rounded curves at low levels. Regarding the medium and small pitch plots, one can observe the effect of the adjacent jet interaction causing rising maximum effectiveness at high blowing rates. At such conditions the peak resulting from the single jet in crossflow characteristic is vanishing and the absolute maximum is taken over downstream by the adjacent jet interaction. However, there is a special behavior at small pitch normal ejection. Here, the adjacent jet interaction evoked maximum also reaches a highest value at blowing rates of about  $M = 1.4-1.7$ . It then descends again with approximately the same gradient as the single jet in crossflow characterized maximum of these cases at lower blowing rates.

The next step is the scaling of the peak values  $\bar{\eta}_p$  and the blowing rate to bring the maxima development curves on top of each other. Therefore, scaling functions depending on blowing angle, hole spacing, and density ratio are generated. The scaled peak effectiveness  $\eta_{c,p}$  and coolant flow parameter  $\mu$  are defined as follows:

$$\eta_{c,p} = \bar{\eta} \frac{(\sin \alpha)^{0.06 \frac{s}{D}}}{P^{0.9/\frac{s}{D}}} \quad (8)$$

$$\mu = UP^{0.8} \left( 1 - \left[ 0.03 + 0.11 \left( 5 - \frac{s}{D} \right) \right] \cos \alpha \right) \quad (9)$$

Note that  $\mu$  is no longer referring to the blowing rate, but to the discriminated effects of velocity and density ratios.

Figure 9 shows the scaled curves of Fig. 8 together with a curve fit to correlate the common characteristic of the maximum development. The describing equation is

$$\eta_p^* = \frac{\eta_{c0} \left( \frac{\mu}{\mu_0} \right)^a}{\left[ 1 + \left( \frac{\mu}{\mu_0} \right)^{(a+b)c^{-1/c}} \right]} \quad (10)$$

As sketched in Fig. 9(b), the following physical meaning can be assigned to coefficients in Eq. (10):

- $a$  is the gradient of the ascending branch of the peak effectiveness.
- $b$  is the gradient of the descending branch of the peak effectiveness.

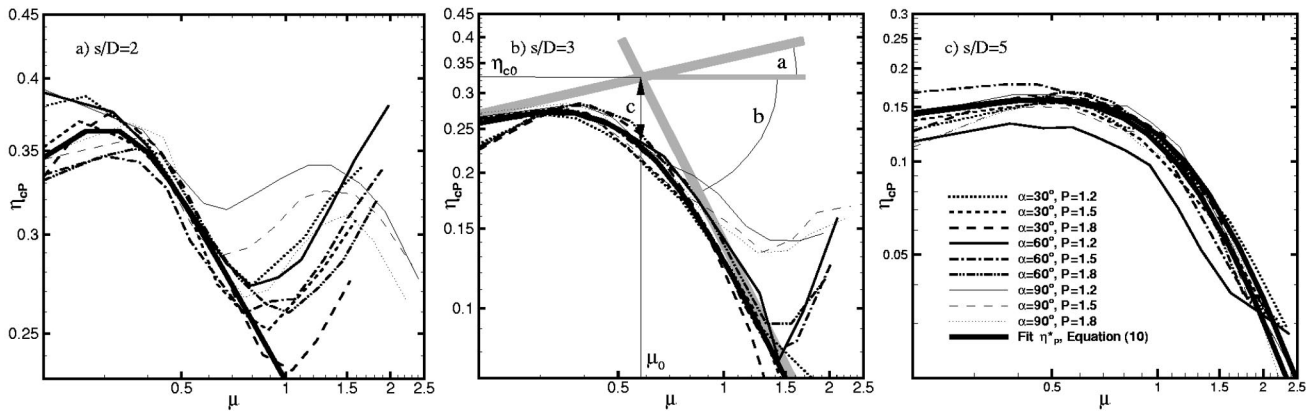


Fig. 9 Normalized effectiveness peaks of all measurements

- $c$  defines how close and sharp bowed the fit curve is leaning to the straight lines describing the rise and fall of the peak effectiveness.
- $\mu_0$  is the coolant mass flow parameter value where the ascending and descending straight lines intersect and, therefore, characterizes the highest maximum flow parameter.
- $\eta_{c0}$  is the according scaled peak effectiveness value of the intersection point characterizing the common maximum height.

The values of these coefficients are determined for each examined hole spacing and fitted by the following functions:

$$a = 0.2 \quad (11)$$

$$b = \exp \left[ 1.92 - 7.5 \left( \frac{s}{D} \right)^{-1.5} \right] \quad (12)$$

$$c = 0.7 + 336 \exp \left( -1.85 \frac{s}{D} \right) \quad (13)$$

$$\mu_0 = 0.125 + 0.063 \left( \frac{s}{D} \right)^{1.8} \quad (14)$$

$$\eta_{c0} = \frac{0.465}{1 + 0.048 \left( \frac{s}{D} \right)^2} \quad (15)$$

The peak effectiveness values  $\eta_p^*$  given by Eq. (10) and the coefficient functions normalize all laterally averaged effectiveness distributions to the same level for further examination.

This still leaves the question, if those curves should be plotted versus the downstream length scaled by the blowing rate or by the momentum ratio. A closer inspection of those two parameters reveals that they both are a linear combination of the ratios of velocity and density

$$I = \frac{(\rho u^2)_C}{(\rho u^2)_G} = P U^2 = (P U) U = M U \quad (16)$$

The downstream length scaling of measurement results at identical geometry and density ratio by  $M$  or  $I$  differs only by the weighting of the velocity ratio with an exponent of either one or two. The density ratio component is just an additional constant factor in the scaling of a set of measurements at constant  $P$ . The relative arrangement of the curves results only from the velocity ratio component. Keeping this in mind, the normalized effectiveness curves are plotted versus a downstream length scaled with the velocity ratio weighted with a variable exponent. It is found that the exponents have to be adjusted to the different hole spacings, but not to different density ratios. Figure 10 displays the normalized effectiveness curves for the shallow angle and high density ratio ejection. For the lower blowing rates these plots already display an almost perfect match of the different measurements and distinctly pronounce the path of the searched base

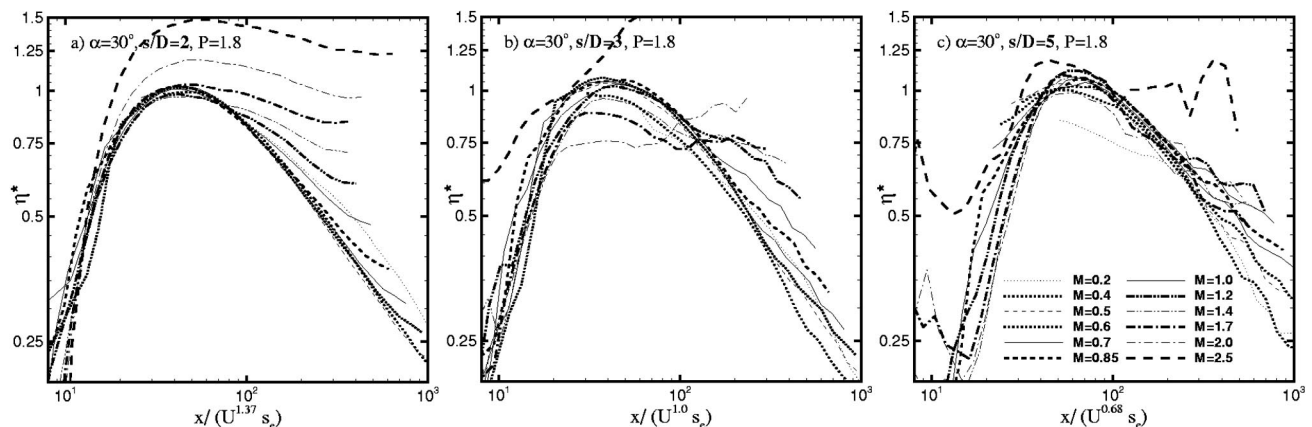


Fig. 10 Normalized effectiveness curves at different hole spacing

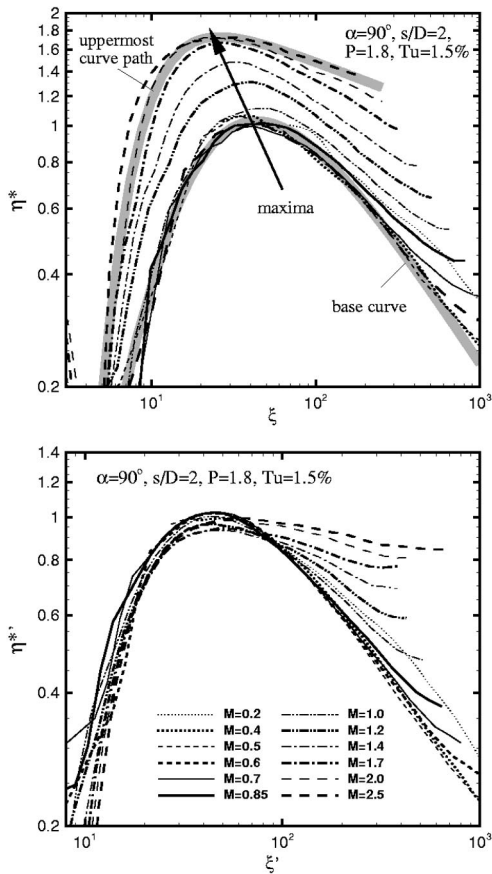


Fig. 11 Scaling of the peak effectiveness maximum

curve. Curves of higher blowing rates systematically deviate to higher normalized effectiveness as an effect of the adjacent jet interaction. In cases where the complete cooling film flow is dominated by the adjacent jet interaction, that is especially at small pitch, the normalized maxima of the high blowing rate curves also tend to higher values.

The curves are now scaled to the velocity ratio with exponents that result from a best fit solution for all measurements at different hole spacings. As can be seen, an exponent of 1.0 is appropriate for the typical three diameter hole spacing and shallow angle ejection. Amazingly, this coincides with the blowing rate scaling that was applied to typical row of hole ejection results in the past. At a small hole spacing of  $s/D=2$  a higher velocity ratio exponent of 1.37 is needed, and at a large hole spacing of  $s/D=5$  a smaller velocity ratio exponent of 0.68 fits the curves. The density ratio  $P$  has no significant effect on the streamwise alignment of the normalized curves. The ejection angle is found to cause a scaling of the downstream length representation and is introduced to an additional factor  $\xi_c$ . This combines to a downstream length parameter

$$\xi = \frac{x s}{DD} \xi_c \quad (17)$$

$$\xi = \frac{\pi}{4} U^{(s/D)^{-0.75}}$$

$$\xi_c = 0.6 + \frac{0.4(2 - \cos \alpha)}{1 + \left(\frac{s/D - 1}{3.3}\right)^6} \quad (18)$$

The equation of the base curve (ref. Fig. 11) is very similar to

Table 2 Constants of the base curve fit

$\xi_0$	$\eta_0$	$a^*$	$b^*$	$c^*$
9	5.8	4	0.7	0.24

the description of the peak effectiveness development and is defined as

$$\eta^* = \frac{\eta_0 \left(\frac{\xi}{\xi_0}\right)^{a^*}}{\left[1 + \left(\frac{\xi}{\xi_0}\right)^{(a^* + b^*)c^*}\right]^{1/c^*}} \quad (19)$$

Herein  $a^*$  and  $b^*$  represent the gradients of the ascending and descending branches of the base curve.  $\xi_0$  and  $\eta_0$  give the intersection point of the straight line descriptions of those branches, as typical downstream length and normalized effectiveness value, respectively. Finally,  $c^*$  fits the base curve apex to the value of  $\eta^* = 1.0$ . All these coefficients are constant numbers, as displayed in Table 2, since the base curve is valid for all geometry and density ratios.

**Complete Correlation.** So far, only the laterally averaged effectiveness of the single jet in crossflow-dominated cases is used to determine a base curve and parameter specific transformation of effectiveness and downstream length. This system predicts the effectiveness of cases with the typical single jet in crossflow characteristic. It utterly fails to predict effects of the adjacent jet interaction that is dominating ejection situations featuring a combination of high blowing rate, small pitch, and steep ejection angle. In the following, the deviations of the corresponding ejection situations are systemized and included into the description.

A fact that heavily obstructs a common description of single jet in crossflow-dominated and adjacent jet interaction-dominated cases, is the inflated effectiveness peak values of the latter. Showing the results of the normal ejection at small pitch and high density ratio, Fig. 11(a) nicely demonstrates that the curves of these adjacent jet interaction dominated situations are completely diverging. However, a close inspection of this plot confirms an assumption resulting from the discussion of Fig. 8: The normalized effectiveness curves in Fig. 11(a) cumulate on two paths, the lower being the base curve and the upper defining some highest possible effectiveness value from the adjacent jet interaction. The existence of this second prominent curve path confirms that, with increasing flow parameter, the decay characteristics of the adjacent jet interaction maximum are the same as the decay characteristics of the single jet in crossflow peaks (ref. Fig. 8(a)). A scaling of the overshooting maxima depending on flow parameters must transfer them back to the base curve apex. Such a scaling should be adoptable to all other cases and should allow for a common maximum description. The scaling procedure is formulated as follows

$$\xi' = \xi \xi_s \quad (20)$$

$$\eta^{*'} = 0.1 \left(\frac{\eta^*(\xi')}{0.1}\right)^{\eta_s} \quad (21)$$

The exponents  $\xi_s$  and  $\eta_s$  within these expressions perform a linear scaling of the curves on the logarithmic scale with respect to a base point (1,0.1). The scaling exponents need to run from a value of 1.0 at single jet ejection dominated conditions to limits valid for the uppermost effectiveness curve path, described by  $\hat{\xi}$  and  $\hat{\eta}$ . The transition functions are given as

$$\xi_s = 1 + \frac{\hat{\xi}}{1 + \left(\frac{UP^g}{k}\right)^{-5}} \quad (22)$$



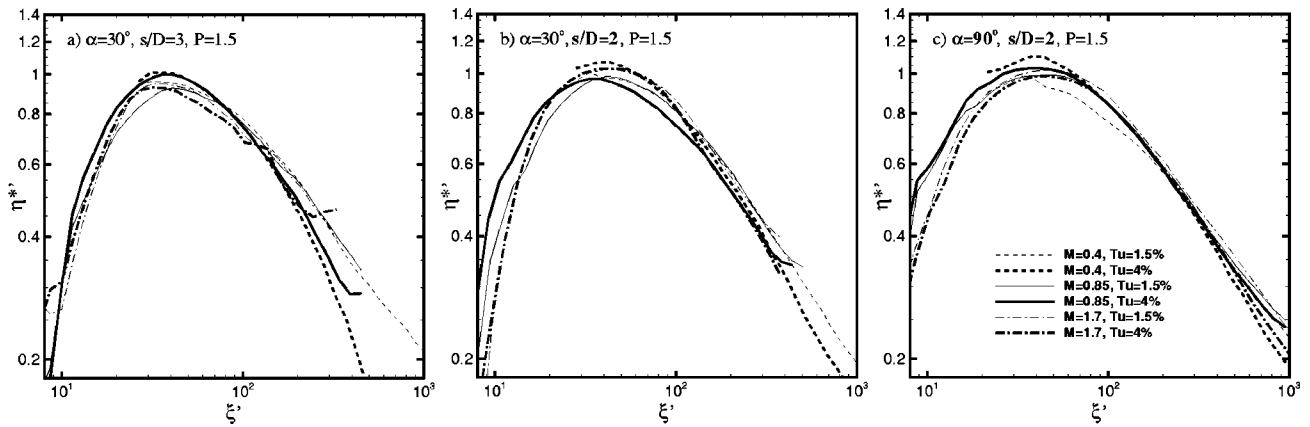


Fig. 12 Normalized and scaled effectiveness curves at low and elevated turbulence level

$$\eta_s = 1 + \frac{\hat{\eta}}{1 + \left(\frac{UP^g}{k}\right)^{-5}} \quad (23)$$

Herein the weighting  $g$  of the density ratio effect and the flow parameter magnitude  $k$  where transition takes place are defined by

$$g = 0.75[1 - e^{-0.8(\frac{s}{D}-1)}] \quad (24)$$

$$k = 2[1 - e^{0.57(1-\frac{s}{D})}] + 0.91 \cos^{0.65} \alpha \quad (25)$$

Functions for the limit values  $\hat{\xi}$  and  $\hat{\eta}$  are

$$\hat{\xi} = 1.17 \left[ 1 - \frac{\left(\frac{s}{D} - 1\right)}{1 + 0.2\left(\frac{s}{D} - 1\right)^2} \right] (\cos 2.3\alpha + 2.45) \quad (26)$$

$$\hat{\eta} = 0.022 \left(\frac{s}{D} + 1\right) (0.9 - \sin 2\alpha) - \left[ 0.08 + \frac{0.46}{1 + \left(\frac{s}{D} - 3.2\right)^2} \right] \quad (27)$$

It is assumed that in cases where the uppermost curve path could not be identified from the measurement results, it occurs at blowing rates beyond the experimentally examined range. The scaling parameter limits  $\hat{\xi}$ ,  $\hat{\eta}$ , and according transition function coefficients then are chosen to result in a best fit of the transition functions in Eqs. (22), (23) for the available measurements.

Figure 11(b) shows the same ejection case after the scaling of the overshoot maxima. It confirms that the described procedure is capable to collapse both the single jet-dominated and the adjacent jet interaction influenced maxima on the base curve. Figure 11(b) indicates only one remaining pattern of effectiveness curves deviating from the base curve: The high blowing rate curves branch from the downslope of the base curve towards higher effectiveness values. To account for this deviation pattern a modification is introduced to Eq. (21) resulting in

$$\eta^{*'} = 0.1 \left( \frac{\left(\frac{\eta^*}{0.1}\right)}{1 + \left[\frac{\xi'}{\hat{\xi}_1}\right]^{b_1 c_1}} \right)^{\eta_s} \quad (28)$$

The coefficients within the corrective Eq. (28) have the following physical meaning:

- $\hat{\xi}_1$  is the downstream position where the deviation occurs first and the correction is initiated.

- $b_1$  defines the magnitude of the required correction. Note that the exponent  $b_1$  is a direct counterpart to compensate  $b^*$  of the base curve definition of  $\eta^*$ .
- $c_1$  describes the smoothness of the curve branching at the downstream position  $\hat{\xi}_1$ .

These coefficients are also functions of the flow and geometry parameters and are given by the following equations:

$$\hat{\xi}_1 = \frac{65}{\left(\frac{M}{2.5}\right)^{a_1}} \quad (29)$$

$$a_1 = 0.04 + 0.23 \frac{s}{D} + \left(0.95 - 0.19 \frac{s}{D}\right) \cos 1.5\alpha \quad (30)$$

$$b_0 = 0.8 - 0.014 \left(\frac{s}{D}\right)^2 + \left(1.5 - \frac{2}{\sqrt{\frac{s}{D}}}\right) \times \sin \left(0.86\alpha \left[1 + \frac{0.754}{1 + 0.87\left(\frac{s}{D}\right)^2}\right]\right) \quad (31)$$

$$b_1 = \frac{b_0}{1 + M^{-3}} \quad (32)$$

$$c_1 = 7.5 + \frac{s}{D} \quad (33)$$

Finally, an attempt is made to include the findings of the elevated turbulence measurements into the new correlation. A compilation of the normalized effectiveness from measurements at low and elevated turbulence is shown in Fig. 12. The apex as well as most of the ascending branch of the elevated turbulence curves match those of the low turbulence curves. Systematic deviations of the elevated turbulence curves are found at the descending branch of the curves (Fig. 12(a)). Assuming that low turbulence conditions are described properly by the base curve, the elevated turbulence curves decay faster, requiring a higher decay exponent. In situations of high ejection induced turbulence, e.g., from adjacent jet interaction effects (Fig. 12(b)), the differences between elevated and low turbulence results diminish. Proceeding to situations of excessive turbulence production, e.g., small pitch normal ejection (Fig. 12(c)), the hot gas turbulence influence becomes insignificant. To get a broader basis for the formulation of the turbulence effects further measurements from Bons et al. [23] and

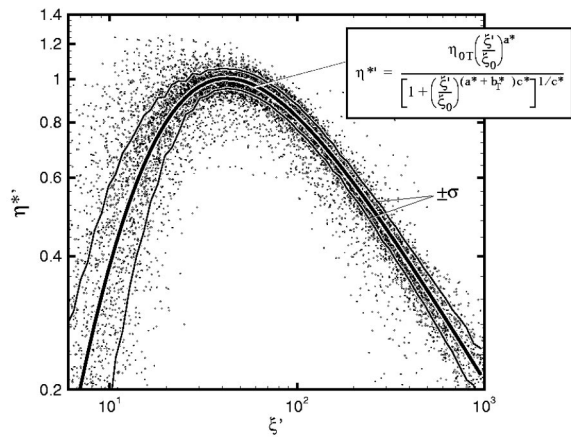


Fig. 13 Final laterally averaged effectiveness correlation

Schmidt and Bogard [24] at higher turbulence levels are used. The turbulence intensity dependent slope  $b_T^*$  could be described by

$$b_T^* = 0.7 \left( 1 + \left[ \frac{1.22}{1 + 7 \left( \frac{s}{D} - 1 \right)^{-7}} + 0.87 + \cos 2.5\alpha \right] \right) \times \exp \left[ 2.6Tu - \frac{0.0012}{Tu^2} - 1.76 \right] \quad (34)$$

Unfortunately, the variable descending branch slope  $b_T^*$  influences the choice of the intersection coordinates  $\xi_0$  and  $\eta_0$  of the ascending and descending straight line descriptions of the base curve. To retain the proper apex at  $\eta'^* = 1.0$ , the value of  $\eta_0$  is modified accordingly to

$$\eta_{0T} = 2.5 \left( \frac{5.8}{2.5} \right)^{\frac{b_T^*}{0.7}} \quad (35)$$

This concludes the definition of transformations to form the laterally averaged effectiveness correlation. To evaluate the accuracy of the new correlation RMS values of the deviation of the measurements from the base curve path are determined. Figure 13 displays the normalized and scaled measurement data, resolved into single points and compared to the base curve. Obviously, the measurements are heavily massing around the base curve path, confirming the high accuracy of the correlative description. The overall RMS deviation of the measurements is  $\sigma = 5.5\%$  representing the same accuracy as found by the measurement error estimation (see [1]). The  $\pm\sigma$  lines of the downstream parameter dependent gliding RMS deviation in Fig. 13 display that within the important range of the maximum and decay even lower deviations are achieved. They range from 5% at the apex position to 3% on the descending branch. The calculation procedure of reproducing an effectiveness distribution from an arbitrary set of describing parameters is explicitly presented in the Appendix.

## Conclusions

Downstream distributions of the laterally averaged adiabatic film cooling effectiveness are evaluated from an integration of high resolution local thermographic results. The quantitative discussion of the downstream effectiveness effects by means of the laterally averaged results confirm the characteristic impact from two different cooling film flow patterns on the downstream effectiveness distribution. These two different flow patterns are the single jet in crossflow mixing and the adjacent jet interaction. The former dominates the cooling film flow at short downstream dis-

tances and lower blowing rates and governs the jet lift-off. The latter dominates further downstream and at higher blowing rates, as soon as sufficient jet spreading causes the adjacent jets to interact. The novel approach of this study is the quantitative description of the interplay of these patterns. The flow from a typical ejection geometry of  $s/D = 3$ ,  $\alpha = 30$  deg. is mostly dominated by the jet in crossflow mixing. But, the adjacent jet interaction introduces important quantitative influences at high blowing rates and large downstream distances. Geometry of steeper ejection angles and smaller hole spacing is mostly dominated by the adjacent jet interaction. It requires a completely different approach to describe the observed effectiveness distributions.

Based on these two different basic flow features, a new correlation for the prediction of the laterally averaged film cooling effectiveness is presented. It applies for a row of cylindrical, streamwise inclined holes and a wide range of ejection parameters. The complete downstream distance is covered, none of the typical constraints and exceptions are necessary. The correlation process revealed the velocity ratio  $U$  as the most important scaling parameter for this row of holes ejection situation. Only the  $U$ -related scaling allows a common description of sets of measurements with different coolant mass flow and enables a correlation of the geometry influence. With this new correlation a powerful tool is given for the prediction of external temperature distributions in presence of film cooling. They represent an essential boundary condition for a cooled wall temperature analysis. The corresponding heat transfer coefficient correlation to complete such a set of boundary conditions is presented in a companion article [25].

## Acknowledgments

This study was partly funded by the Secretary of Research and Technology of the Federal Republic of Germany through the German joint research program AG Turbo and Siemens AG PG, Mülheim a. d. Ruhr, Germany.

## Nomenclature

- $a, b, c$  = correlation coefficients
- $D$  = ejection hole diameter, m
- $g, k$  = correlation coefficients
- $I$  = momentum ratio, Eq. (16)
- $L$  = ejection hole length, m
- $M$  = blowing rate, Eq. (16)
- $P$  = coolant to hot gas density ratio, Eq. (16)
- $Re$  = Reynolds
- $s$  = ejection hole spacing, m
- $T$  = temperature, K
- $Tu$  = turbulence intensity
- $U$  = velocity ratio, Eq. (16)
- $u$  = velocity, m/s
- $x$  = streamwise coordinate, m
- $\alpha$  = blowing angle
- $\delta_1$  = displacement thickness of the boundary layer, m
- $\eta$  = film cooling effectiveness, Eq. (1)
- $\mu$  = flow rate parameter for peak correlation, Eq. (10)
- $\rho$  = density, kg/m<sup>3</sup>
- $\xi$  = downstream distance parameter, Eq. (6)

## Subscripts

- 0 = without ejection, reference values
- 1 = downstream interaction correction
- AW = adiabatic wall
- C = coolant
- c = scaled maximum peak values
- D = hole diameter based
- e = equivalent slot
- f = cooling film
- G = hot gas
- I = momentum ratio based

$M$  = blowing rate based  
 max = maximum  
 $p$  = peak  
 $s$  = maximum scaling due to jet interaction  
 $T$  = turbulence dependent  
 $W$  = wall

### Superscripts

$'$  = modified approach  
 $*$  = normalized  
 $\wedge$  = upper limits  
 $-$  = lateral average

### Appendix

The lateral-averaged effectiveness correlation presented in this study forms an extensive set of equations. Especially the coefficient functions, not offering a physical interpretation, are difficult to verify and to control. Therefore, an explicit application example is given incorporating the numerical values for all variables and coefficients. This provides a means of verification for the correct reproduction of the correlation equations.

#### Correlating the Effectiveness From the Ejection Parameters

The example shall be of typical geometry conditions ejection into a low turbulence hot gas flow at high blowing rate and low density ratio. This is known to cause significant lift-off effects and adjacent jet interaction as well near the ejection location as downstream. Ejection parameters are stated in Table 3. The equations were reproduced in a spread sheet calculation. All numerical values of the coefficients are given to the according precision, as stated in Table 4.

Starting point for the determination of specific effectiveness values is the base curve from the jet in crossflow mixing behavior. Deriving  $\eta_{0T}$  and  $b_T^*$  from Eqs. (34), (35) and using the constants of Table 2, the turbulence-dependent base curve is calculated by

**Table 3 Ejection parameter example**

M	$\alpha$ [°]	s/D	P	Tu
2.0	30	3	1.2	0.015

**Table 4 Numerical coefficients**

Base curve	
$b_T^* = 0.70138176$	$\eta_{0T} = 5.809643$
Transformation to specific maximum	
$\xi_c = 1.0321731$	
$\eta_{c0} = 0.32472067$	$a = 0.2$
$\mu = 1.5108774$	$b = 1.6106283$
$\mu_0 = 0.58015447$	$c = 2.0061856$
Adjacent jet interaction effects	
on maximum	downstream
$\hat{\xi} = -0.36508783$	$\xi_1 = 81.226444$
$\hat{\eta} = -0.51931793$	$a_1 = 0.99870058$
$g = 0.59857761$	$b_0 = 0.61626073$
$k = 2.1891363$	$b_1 = 0.54778731$
$\xi_s = 0.88819413$	$c_1 = 10.5$
$\eta_s = 0.84096213$	

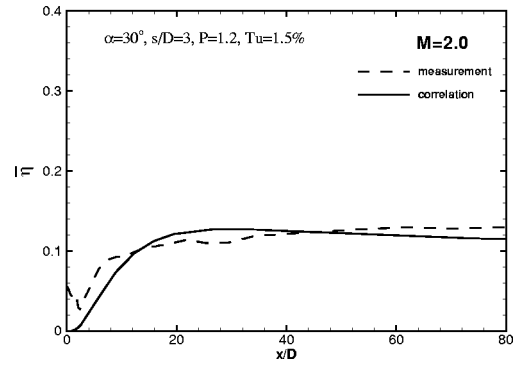


**Fig. 14 Comparison measurement versus correlation**

$$\eta^{*'} = \frac{\eta_{0T} \left( \frac{\xi'}{\xi_0} \right)^{a^*}}{\left[ 1 + \left( \frac{\xi'}{\xi_0} \right)^{(a^* + b_T^*)c^*} \right]^{1/c^*}} \quad (36)$$

The range of  $\xi'$  should cover values of 1 to 1000 to result in a useful  $x/D$  downstream length for most applications. The apex and descending branch of the base curve needs modification to account for the adjacent jet interaction. (See Fig. 14.) Scaling by  $\eta_s$ , from Eq. (23), employing the coefficients  $\hat{\eta}$ ,  $g$ ,  $k$ , from Eqs. (24), (25), (27), and using coefficients  $\xi_1$  (from  $a_1$ ),  $b_1$  (from  $b_0$ ),  $c_1$ , from Eqs. (29)–(33), returns a curve

$$\eta^* = 0.1 \left( \frac{\eta^{*'}}{0.1} \right)^{1/\eta_s} \left[ 1 + \left( \frac{\xi'}{\xi_1} \right)^{b_1 c_1} \right]^{1/c_1} \quad (37)$$

This normalized curve is blown up to the characteristic peak effectiveness development according to Eq. (10), employing the coefficients  $a$ ,  $b$ ,  $c$ ,  $\mu_0$ ,  $\eta_{c0}$ , from Eqs. (11)–(15)

$$\eta_c = \frac{\eta_{c0} \eta^* \left( \frac{\mu}{\mu_0} \right)^a}{\left[ 1 + \left( \frac{\mu}{\mu_0} \right)^{(a+b)c} \right]^{1/c}} \quad (38)$$

Backscaling to the specific peak effectiveness of the given ejection conditions according to Eq. (8) yields

$$\bar{\eta} = \eta_c \frac{P^{0.9/\bar{D}}}{(\sin \alpha)^{0.06/\bar{D}}} \quad (39)$$

These values of the laterally averaged effectiveness are plotted over the downstream length  $x/D$ . Employing the scaling exponent  $\xi_s$ , from Eq. (22), by use of the coefficients  $g$ ,  $k$ ,  $\hat{\xi}$ , from Eqs. (24)–(26), and  $\xi_c$ , from Eq. (18), results for all values  $\xi'$  in

$$\frac{x}{D} = \frac{\xi'^{1/\xi_s} \frac{\pi}{4} U^{(s/D/3)^{-0.75}}}{\frac{s}{D} \xi_c} \quad (40)$$

### References

- [1] Baldauf, S., Schulz, A., and Wittig, S., 1999, "High-Resolution Measurements of Local Effectiveness From Discrete Hole Film Cooling," *ASME J. Turbomach.*, **123**, pp. 758–765.
- [2] Baldauf, S., Schulz, A., and Wittig, S., 1999, "High Resolution Measurements of Local Heat Transfer Coefficients From Discrete Hole Film Cooling," *ASME J. Turbomach.*, **123**, pp. 749–757.
- [3] Baldauf, S., and Scheurlen, M., 1996, "CFD Based Sensitivity Study of Flow Parameters for Engine Like Film Cooling Conditions," *ASME Paper 96-GT-310*.
- [4] Martiny, M., Schiele, R., Gritsch, M., Schulz, A., and Wittig, S., 1996, "In Situ

- Calibration for Quantitative Infrared Thermography," Quirt '96 Eurotherm Seminar No. 50, Stuttgart, Germany, September 2–5.
- [5] Pedersen, D. R., Eckert, E. R. G., and Goldstein, R. J., 1977, "Film Cooling With Large Density Differences Between the Mainstream and the Secondary Fluid Measured by the Heat-Mass Transfer Analogy," *ASME J. Heat Transfer*, **99**, pp. 620–627.
- [6] Kohli, A., and Bogard, D. G., 1997, "Adiabatic Effectiveness, Thermal Fields, and Velocity Fields for Film Cooling With Large Angle Ejection," *ASME J. Turbomach.*, **119**, pp. 352–358.
- [7] Drost, U., Bolcs, A., and Hoffs, A., 1997, "Utilization of the Transient Liquid Crystal Technique for Film Cooling Effectiveness and Heat Transfer Investigations on a Flat Plate and a Turbine Airfoil," *ASME Paper 97-GT-26*.
- [8] Foster, N. W., and Lampard, D., 1980, "The Flow and Film Cooling Effectiveness Following Injection Through a Row of Holes," *ASME J. Eng. Power*, **102**, pp. 584–588.
- [9] Goldstein, R. J., 1971, "Film Cooling," *Adv. Heat Transfer*, **7**, Academic Press, pp. 321–379.
- [10] Sturgess, G. J., 1968, "Correlation of Data and Prediction of Effectiveness from Film Cooling Injection Geometries of Practical Nature," *Proc. Cranfield International Propulsion Symposium Series*, Vol. 2, pp. 229–250.
- [11] Sturgess, G. J., 1968, "Film Cooling Optimization for Minimum Cooling Airflow in Aircraft Gas-Turbines," *Proc. Cranfield International Propulsion Symposium Series*, Vol. 2, pp. 347–376.
- [12] Pai, B. R., and Whitelaw, J. H., 1971, "The Prediction of Wall Temperature in the Presence of Film Cooling," *Int. J. Heat Mass Transf.*, **14**, pp. 409–426.
- [13] Mukherjee, D. K., 1976, "Film Cooling With Injection Through Slots," *ASME J. Eng. Power*, pp. 556–559.
- [14] Lefebvre, A. H., 1983, *Gas Turbine Combustion*, Hemisphere Publ., New York, NY.
- [15] Metzger, D. E., and Fletcher, D. D., 1971, "Evaluation of Heat Transfer for Film-Cooled Turbine Components," *J. Aircr.*, **8**, pp. 33–38.
- [16] Jabbari, M. Y., and Goldstein, R. J., 1978, "Adiabatic Wall Temperature and Heat Transfer Downstream of Injection Through Two Rows of Holes," *ASME J. Eng. Power*, **100**, pp. 303–307.
- [17] Kruse, H., 1985, "Effects of Hole Geometry, Wall Curvature and Pressure Gradient on Film Cooling Downstream of a Single Row," *Heat Transfer and Cooling in Gas Turbines*, AGARD Conf. Proc., AGARD CP-390, Paper 8.
- [18] Forth, C. J. P., and Jones, T. V., 1986, "Scaling Parameters in Film Cooling," *Proc. 8th International Heat Transfer Conference*, Vol. 3, pp. 1271–1276.
- [19] L'Ecuyer, M. R., and Soechting, F. O., 1985, "A Model for Correlating Flat Plate Film Cooling Effectiveness for Rows of Round Holes," *Heat Transfer and Cooling in Gas Turbines*, AGARD Conf. Proc. AGARD-CP-390, Paper 19.
- [20] Baldauf, S., Scheurlen, M., Schulz, A., and Wittig, S., 1997, "An Overall Correlation of Film Cooling Effectiveness From One Row of Holes," *ASME Paper 97-GT-46*.
- [21] Louis, J. F., 1977, "Systematic Studies of Heat Transfer Coefficient and Film Cooling Effectiveness," *Heat Transfer and Cooling in Gas Turbines*, AGARD Conf. Proc., AGARD-CP-299, Paper 28.
- [22] Abramovic, G. N., 1963 *The Theory of Turbulent Jets*, MIT Press, Cambridge, MA.
- [23] Bons, J. P., MacArthur, C. D., and Rivir, R. B., 1994, "The Effect of High Freestream Turbulence on Film Cooling Effectiveness," *ASME Paper 94-GT-51*.
- [24] Schmidt, D. L., and Bogard, D. G., 1996, "Effects of Free-Stream Turbulence and Surface Roughness on Film Cooling," *ASME Paper 96-GT-462*.
- [25] Baldauf, S., Scheurlen, M., Schulz, A., and Wittig, S., 2002, "Heat Flux Reduction From Film Cooling and Correlation of Heat Transfer Coefficients From Measurements at Enginelike Conditions," 2002-GT-30181 *ASME J. Turbomach.*, **124**, pp. 699–709.

# Heat Flux Reduction From Film Cooling and Correlation of Heat Transfer Coefficients From Thermographic Measurements at Enginelike Conditions

S. Baldauf

M. Scheurlen

Siemens Power Generation,  
45473 Mülheim an der Ruhr, Germany

A. Schulz

S. Wittig

Lehrstuhl und Institut für Thermische  
Strömungsmaschinen,  
Universität Karlsruhe (TH),  
76128 Karlsruhe, Germany

*Heat transfer coefficients and the resulting heat flux reduction due to film cooling on a flat plate downstream a row of cylindrical holes are investigated. Highly resolved two-dimensional heat transfer coefficient distributions were measured by means of infrared thermography and carefully corrected for local internal testplate conduction and radiation effects. These locally acquired data are processed to lateral average heat transfer coefficients for a quantitative assessment. A wide range variation of the flow parameters blowing rate and density ratio as well as the geometrical parameters streamwise ejection angle and hole spacing is examined. The effects of these dominating parameters on the heat transfer augmentation from film cooling are discussed and interpreted with the help of highly resolved surface results of effectiveness and heat transfer coefficients presented earlier. A new method of evaluating the heat flux reduction from film cooling is presented. From a combination of the lateral average of both the adiabatic effectiveness and the heat transfer coefficient, the lateral average heat flux reduction is processed according to the new method. The discussion of the total effect of film cooling by means of the heat flux reduction reveals important characteristics and constraints of discrete hole ejection. The complete heat transfer data of all measurements are used as basis for a new correlation of lateral average heat transfer coefficients. This correlation combines the effects of all the dominating parameters. It yields a prediction of the heat transfer coefficient from the ejection position to far downstream, including effects of extreme blowing angles and hole spacing. The new correlation has a modular structure to allow for future inclusion of additional parameters. Together with the correlation of the adiabatic effectiveness it provides an immediate determination of the streamwise heat flux reduction distribution of cylindrical hole film-cooling configurations. [DOI: 10.1115/1.1505848]*

## Introduction

The lateral mean heat transfer coefficients on a film-cooled wall are the essential entity for the prediction of the wall heat flux and, subsequently, the blade material temperature. To enable heat flux predictions, the database for correlations must comprise experimental results of the adiabatic effectiveness and the according results of heat transfer coefficients at identical ejection conditions. The present study provides the distributions of the adiabatic effectiveness as well as the heat transfer coefficients for a large variety of ejection cases and for the complete matrix of dominating parameters. From this comprehensive database, correlations of the lateral mean values of both the effectiveness and the heat transfer are developed [1,2].

The local heat transfer coefficient depends on the local temperature situation described by a dimensionless wall temperature

$$\theta = \frac{T_G - T_C}{T_G - T_W} \quad (1)$$

Referring to the temperature difference between hot gas flow and the wall surface, the heat flux can be written as

$$q_w = h(\theta)(T_G - T_W) \quad (2)$$

It was shown by several authors that the relationship  $h(\theta)$  is linear in incompressible flow regimes [3–6]. Furthermore, it was confirmed that  $h(\theta)$  can be regarded linear with negligible deviations even for film cooling applications with enginelike gas property variations [7–9]. The linear dependence can be determined by the linear superposition of two known results of the local heat transfer coefficient; i.e., two known specific measurements determine the straight line  $h(\theta)$  of a distinct ejection situation at a distinct location on the film-cooled surface. Gritsch et al. [10] demonstrated the applicability of the linear superposition approach, experimentally and numerically, also for lateral mean values of  $\bar{h}(\bar{\theta})$  at varying downstream locations in variable property flows. A special representation of the linear superposition approach is referring to two particular points on the straight line  $h(\theta)$ . It employs the adiabatic film cooling effectiveness as one point

$$\eta = \frac{T_G - T_{AW}}{T_G - T_C} \quad (3)$$

As second point the heat transfer coefficient  $h_f$  from the near wall cooling film flow to the surface determines the same heat flux as Eq. (2)

$$q_w = h_f(T_{AW} - T_W) \quad (4)$$

The first particular point in this approach denotes the “adiabatic” situation of zero heat flux  $q_{AW} = 0$ , where the adiabatic wall temperature gives  $\theta_{AD} = 1/\eta$ . The second particular point designates the “isothermal” situation of  $\theta = 0$ , denoting that the cooling film

Contributed by the International Gas Turbine Institute and presented at the International Gas Turbine and Aeroengine Congress and Exhibition, Amsterdam, The Netherlands, June 3–6, 2002. Manuscript received by the IGTI, October 29, 2001. Paper No. 2002-GT-30181. Review Chair: E. Benvenuti.

temperature has no effect on the heat transfer coefficient at  $h(\theta = 0) = h_f$ . Note that the vanishing effect of the cooling film temperature is not equivalent to a vanishing temperature difference between hot gas and ejected coolant. Assuming the validity of the linear superposition approach connotes identically both, the linearity of  $h(\theta)$  and a constant value  $h_f$  at varying  $\theta$ , in the typical variable property flow situation. The transformation from the straight line representation to the two points representation was formulated by Eckert [11]

$$h(\theta) = h_f(1 - \eta\theta) \quad (5)$$

This demonstrates that even accepting the constraints of a linear approach in either representation, the heat flux evaluation in a film-cooling situation necessitates the knowledge of at least one pair of measurement results. These may be either two arbitrary data pairs  $h(\theta)$ , or the two particular values  $\eta$  at  $h(1/\eta) = 0$ , and  $h_f$  at  $h_f = h(\theta = 0)$  (see detailed discussion by Gritsch et al. [10]). The latter choice of parameters results in well defined conditions for the two points to define the straight line  $h(\theta)$ . It is, therefore, preferred by most authors and will be used for the further discussion.

The present documentation concentrates on the lateral mean values of the heat transfer coefficient that are crucial for the quantitative evaluation of heat flux. To enable the application and comparison of heat transfer results, a dimensionless representation of the heat transfer coefficient is imperative. It is well known that the laterally averaged film-cooling effectiveness  $\bar{\eta}$  depends on the ejection situation, i.e., geometry and flow parameters. Since the lateral mean value of  $\bar{h}_f$  is, in principal, just an other point on the same line  $\bar{h}(\theta)$ , it must depend on the same geometrical and flow parameters of the ejection. Referring to a similarity and sensitivity analysis of the discussed film cooling situation (see [12]), this dependence can be formulated as a functional relation of similarity numbers. Employing the Stanton number as dimensionless heat transfer coefficient yields

$$\bar{St} = f\left(\bar{\theta}, M, P, Tu, \frac{x}{D}, \alpha, \frac{s}{D}, \frac{\delta_1}{D}, \frac{L}{D}\right) \quad (6)$$

In the presence of film cooling, the influence of the ejection on the heat transfer situation is of particular interest. Therefore, the ratio of the heat transfer coefficients on the surface with and without film ejection is regarded. Since the Stanton numbers of both cases should refer to the hot gas flow properties, the dimensionless augmentation ratio fulfils

$$\frac{\bar{St}_f}{\bar{St}_0} = \frac{\bar{h}_f}{h_0} \quad (7)$$

## Experimental Apparatus and Data Processing

The measurements were performed in an open circuit hot wind tunnel of the Institute of Thermal Turbomachinery, University of Karlsruhe. Engine like flow conditions were established for steady-state heat transfer measurements on a film cooled surface in a scaled up test section. Proper temperature ratios of hot gas to cooling air are applied to obtain realistic density gradients and heat flux directions. A schematic of the test facility is given in Fig. 1. A detailed description of its basic features is provided by Baldauf et al. [2]. For heat transfer measurements an additional cooling circuit was installed, which is detailed by Baldauf et al. [1]. It generates a heat sink on the back surface of the testplate inducing heat flux from the hot gas into the test surface.

The cooling air is fed from a plenum through cylindrical ejection holes of  $D = 5$  mm diameter. The cross sectional area of the test duct measures  $21 \times 44 D$ . Different ejection geometry is realized by modules fitting into the coolant plenum duct. The modules approximate adiabatic conditions at the ejection position. The testplate is directly connected to the ejection module. It consists of machinable ceramic material (Corning Macor) with a thickness of

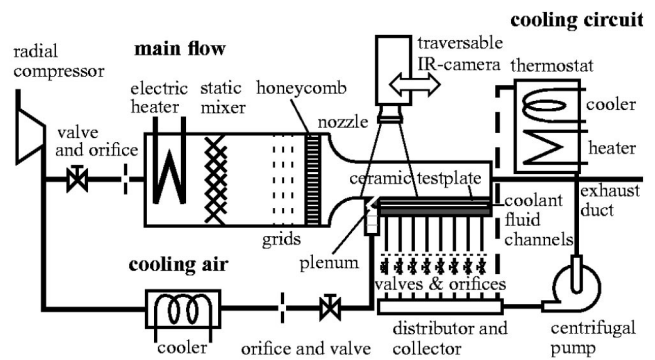


Fig. 1 Extended hot wind tunnel scheme with cooling circuit

$2D$  extending from  $2D$  to  $82D$  downstream of the ejection position. The cooling fluid supply channels are machined into the test plate's support for a direct contact of cooling fluid and ceramic. The thermostatic cooling circuit provides coolant fluid at an adjustable preset temperature to enable a wall temperature variation without influencing the flow conditions. In this way sets of measurement data with different dimensionless wall temperatures  $\theta$  at identical flow conditions are generated. A compilation of the dimensionless operating parameters is given in Table 1.

The local surface temperatures were measured with a high resolution IR-camera system. A careful *in situ* calibration of the IR-camera images by surface mounted thermocouples (Martiny et al. [13]) and a constant emissivity dye coating of the surface assure a quantitatively correct mapping of 2-D surface temperatures. The data of corresponding local points of several complete hole pitches are reduced to one half pitch stripe of the periodically symmetric ejection situation. The local surface heat flux is obtained by a 3-D finite element analysis of a half pitch model of the testplate and ejection module, considering their different thermal properties. IR-data is utilized as a temperature boundary condition on the test surface. Thermocouple readings from the coolant fluid exposed back surface of the testplate are applied to the backside of the FE-model as a temperature boundary condition. The computation yields the local surface heat flux  $q_w$  into the testplate with an error of about 1%. For a detailed description of the experimental facilities, data processing, and numerical analysis, see [1].

A laterally averaged heat transfer coefficient differs from the lateral mean value based on laterally averaged heat flux and wall temperature. For a correct averaging, Eq. (2) is formulated for the lateral mean value of the heat flux and rearranged to give the heat transfer coefficient

$$\bar{h}(\bar{\theta}) = \frac{\bar{q}_w}{T_G - \bar{T}_w} \quad (8)$$

This relation obviously requires the laterally integrated heat flux, referring to the mean wall temperature. The resulting lateral mean

Table 1 Operating parameters

Geometry:	$\alpha = 30^\circ, 60^\circ, 90^\circ$
	$s/D = 2, 3, 5$
	$L/D = 6$
Hot gas flow:	$Re_D = 6800 - 14000$
	$\delta_1/D = 0.1$
	$Tu = 1.5\%$
Coolant flow:	$M = 0.2 - 2.5$
	$P = 1.2, 1.5, 1.8$
	$\theta = 1.6 - 4$

value of the heat transfer, based on the average dimensionless wall temperature  $\bar{\theta}$ , returns the same heat flux as the spanwise integration of the local heat flux. The  $\bar{\theta}$ -dependent heat transfer coefficients are each normalized by their specific reference  $h_0$  without ejection. The heat transfer without ejection is correlated for flat plate flow considering an uncooled starting length and variable property effects due to large temperature ratios as proposed by Kays and Crawford [14]

$$h_0 = (\rho u c_p) 0.03 \text{Re}^{-0.2} \text{Pr}^{-0.67} \left[ 1 - \left( \frac{x_s}{x + x_s} \right)^{0.9} \right]^{-1/9} \left( \frac{T_w}{T_G} \right)^{-0.25} \quad (9)$$

For every downstream coordinate the  $\bar{h}(\bar{\theta})/h_0$  points and a laterally average adiabatic effectiveness value (see companion paper [15]), are then combined. All combined data are taken from measurements with identical ejection conditions, i.e., identical blowing rate  $M$  and density ratio  $P$ . For each such set of data, the linear relation  $\bar{h}(\bar{\theta})/h_0$  is derived from a linear regression and the  $\bar{\theta}$  independent value of  $\bar{h}_f/h_0$  of the high temperature ratio flow is extrapolated. Further details of the evaluation of heat transfer coefficients are provided by [1] and [10]. For typical measurement conditions, the error of the resulting heat transfer coefficient  $\bar{h}(\bar{\theta})$  is less than 3.5%. The error of the extrapolated heat transfer coefficient ratio  $\bar{h}_f/h_0$  is kept below 7%.

## Results of the Heat Transfer Measurements

The results of the lateral mean value of  $\bar{h}_f/h_0$  are available right from the beginning of the active testplate at  $x/D=2$  to far downstream at  $x/D=80$ . At the junction of the uncooled ejection module and the cooled test surface at  $x/D=2$ , a very high and extremely sharp maximum of the heat transfer occurs for all cases. These extreme values are not physical. They result from the finite element analysis, where realistic junction conditions between the two parts could not be modeled.

**Variation of the Blowing Rate.** Figure 1 shows the lateral mean heat transfer augmentation due to a typical coolant ejection at a shallow angle of  $\alpha=30$  deg, and a standard hole spacing of  $s/D=3$ . In general the lateral mean heat transfer curves are not as smooth as the laterally averaged effectiveness presented in the companion paper [15]. This is due to the larger error in the heat transfer coefficient determination, compared to the error of the adiabatic effectiveness values [1,2]. Furthermore, the deviation of the heat transfer coefficient ratio from the unity base value is relatively small for the majority of the examined cases. To display and discuss the results in detail the scale is stretched hereby also magnifying all perturbations. Smoothing of the curves is deliberately not considered, since it is not possible to assure if smoothed out wiggles are of statistical nature or real, systematic effects.

First, the results for an application like high density ratio of  $P=1.8$  are discussed (Fig. 2(b)). In general, the heat transfer ratio curves feature high values near the ejection location. They decay with downstream distance by settling of the flow perturbations introduced by the coolant ejection. As expected, rising blowing rates in principle yield higher heat transfer values. As already known from the discussion of the local heat transfer results [1], only minor effects on the overall heat transfer are observed as long as the coolant jet stays attached to the wall. Such a situation is given up to  $M=0.85$ . The heat transfer augmentation relative to the unblown case stays well below 10% with highest values at about  $x/D=20$ , where the attached jets act on the surface. With the coolant jets lifting from the surface a significant rise of the heat transfer augmentation takes place, beginning at  $M=1.2$ . From the local heat transfer distributions of this configuration can be seen that the coolant jets detach from the surface at about  $x/D=10$ . There, relatively low values of the heat transfer are reasonable. The coolant jets reattach at a downstream distance of about  $x/D=30$  and, consequently, elevated heat transfer values

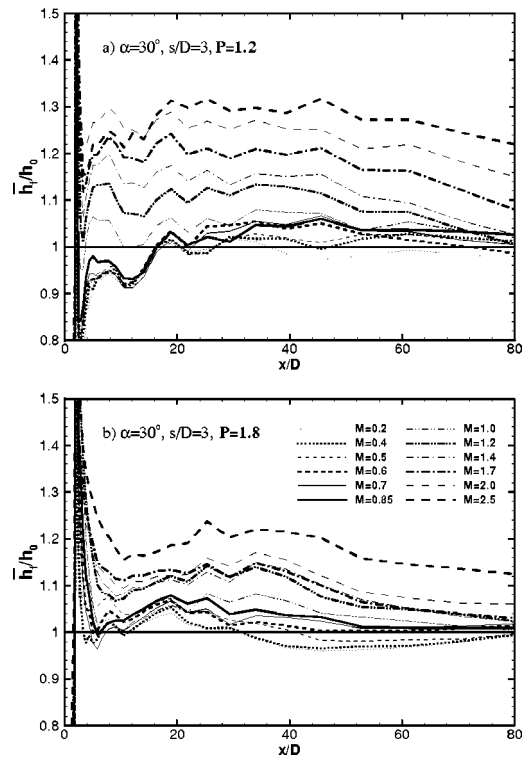


Fig. 2 Effect of the density ratio on the heat transfer augmentation

occur in this area. Heat transfer augmentation of 25% is attained for the highest examined blowing rate of  $M=2.5$ . Except for the highest blowing rates, the area of severely augmented heat transfer extends up to around  $60D$  downstream of the ejection.

**Density Ratio Effect.** Results of the same geometrical configuration at a typical low density ratio of  $P=1.2$  are shown in Fig. 2(a). In general, the downstream distributions of the heat transfer have a similar characteristic as for the engine like high density ratio case. However, the severe augmentation of the heat transfer at higher blowing rates extends further downstream, covering the whole examined test surface. The values range up to a 30% augmentation for the highest blowing rate of  $M=2.5$ . At short downstream distances, low blowing rates exhibit a reduction of the heat transfer coefficients below the unblown level. The coolant jet impact on the surface seems less intense than in the high density ratio case. Even less convection than from the unblown reference seems possible because of the low coolant velocity.

**Comparison With Literature Data.** Lateral mean values of heat transfer augmentation of other authors are compared to the present results in Fig. 3. Sufficient data matching the present experimental conditions are only available for typical shallow angle ejection and standard hole spacing of  $s/D=3$ . All authors agree on minor effects of the coolant ejection on the lateral average value of the heat transfer at low blowing rates. Therefore, this comparison emphasizes on moderate to high blowing rates. Measurements at near unity density ratios are compared in Figs. 3(a) and (b). Only few measurements at elevated density ratios are found and compared in Figs. 3(c) and (d). Note that the present measurements have a high local resolution and no attempt is made to smooth the data.

The whole of the available measurements at low density ratio and moderate blowing rate, Fig. 3(a), suggest an augmentation of the heat transfer coefficient level of about 5 to 10% approving the present results. Considering the comparison of effectiveness mea-

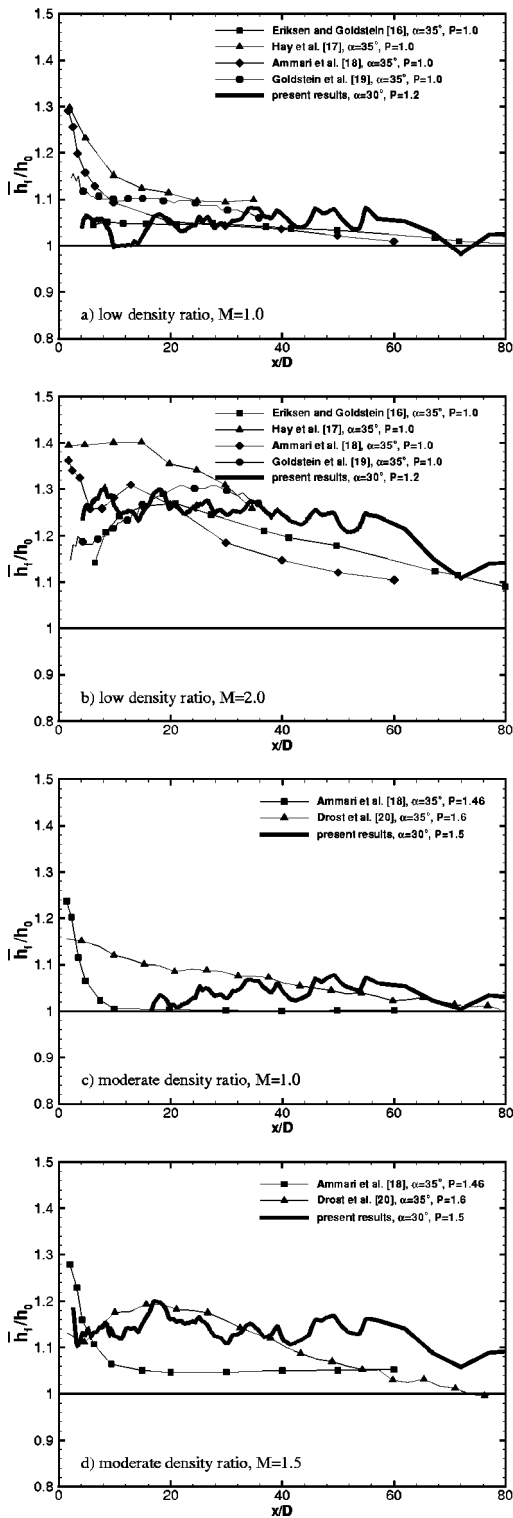


Fig. 3 Comparison with literature results

measurements, the heat transfer measurements of different authors show much larger deviations and even contradicting tendencies. Depending on the reference, either a stable value close to the ejection location or a steep raise of the heat transfer towards the ejection location is found. At high blowing rates and the same low-density ratio conditions, a good match of the majority of the available data, especially at shorter downstream distances, is given, Fig. 3(b). These data describe a heat transfer augmentation of about 25 to 30%. Most interesting, the general tendency at high

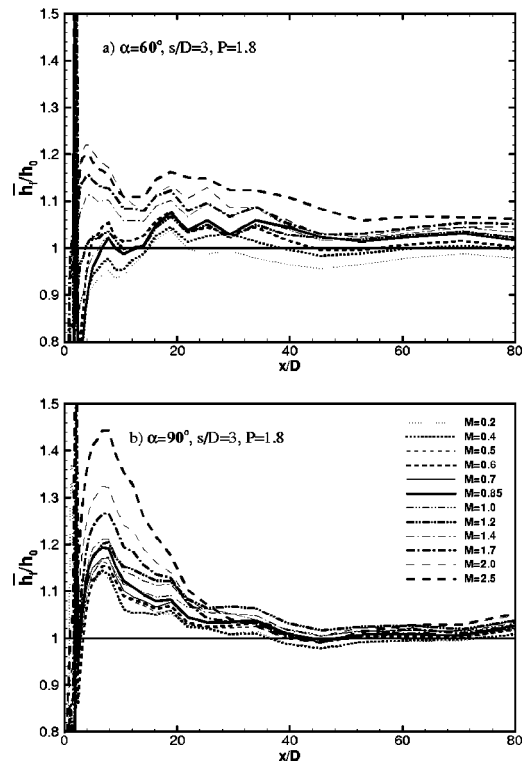


Fig. 4 Effect of the blowing angle on the heat transfer augmentation

blowing rate and low-density ratio is not a steep raise of the heat transfer towards the ejection location. From the ejection location downstream, the values are rather gradually increasing with downstream distance towards a maximum near  $x/D=20$ .

The data from the two references offering heat transfer values at elevated density ratio frame the present data as can be seen in Figs. 3(c) and (d). However, the results of Drost et al. [20] display high values, while the results of Ammari et al. [18] exhibit very low values for both blowing rates. The data of those two authors differ by up to 15 percentage points. The trend of the former authors' data is almost constant level to distinctly lower data values towards the ejection location, whereas the latter authors' data display a high upstream peak.

Hence, the levels of the reference data match the present data. The heat transfer behavior within the direct vicinity of the ejection position can not be determined by the present data nor by the compilation of reference data. Special care will be given to this issue within the correlation process.

**Effect of the Ejection Angle.** The extreme of a steep angle ejection is the surface normal ejection displayed in Fig. 4(b). Distributions from high density ratio and standard hole spacing are shown. Obviously, the downstream extension of augmented heat transfer is much shorter than at shallow angle ejection (ref. Fig. 2). At  $25D$  to  $30D$  downstream of the ejection position, the heat transfer augmentation drops back to unity for all examined blowing rates. A maximum of all curves can be found at  $x/D=7$ . Up to moderate blowing rates of  $M=1.0$  the curves are lumped together, as also seen for shallow angle ejection. Normal ejection at small blowing rate yet causes an augmentation of the heat transfer of 13 to 15%. The curves of  $M=1.2$  and beyond successively rise to significantly higher heat transfer levels than those of the shallow angle ejection. They attain values of up to 45% over the unblown case for the highest blowing rate examined.

In contrast to the findings at normal ejection, the steep angle ejection at  $\alpha=60$  deg (Fig. 4(a)) does not cause an augmentation of the heat transfer values with respect to the shallow angle ejection.



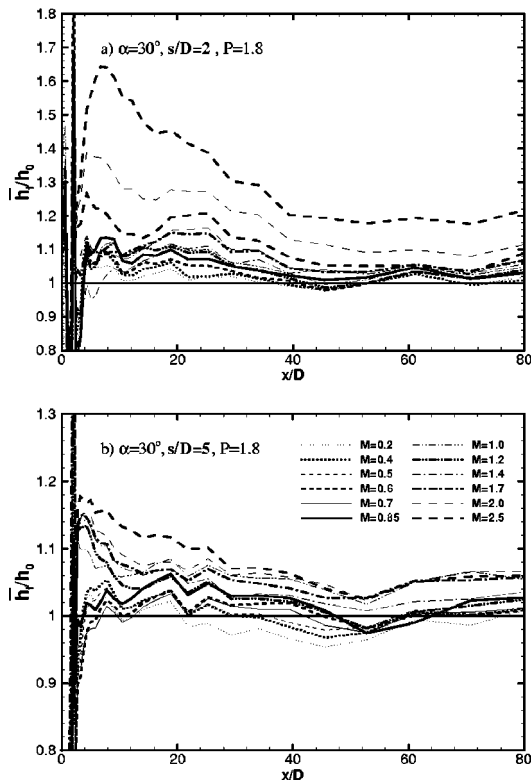


**Fig. 5 Effect of the hole spacing on the heat transfer augmentation**

tion. The heat transfer values are back to normal at around  $x/D = 50$ , an intermediate value between the shallow angle and normal ejection results. This suggests that a more intense jet in crossflow interaction from a steep ejection angle does not produce an equally intense surface impact of the resulting vortices. The dominating effect of the increased blowing angle is a shortened downstream extension of high heat transfer levels. The locally resolved heat transfer results [1] confirm that only the normal ejection causes a significant change in the cooling film flow pattern, resulting in high heat transfer values shown in Fig. 4(b).

**Effect of the Hole Spacing.** The small pitch ejection shown in Fig. 5(a) envisions a completely different situation. Different to steep blowing angles, the more intense interaction of adjacent jets generate a cooling film flow with much higher surface impact and, subsequently, intensified heat transfer. Note that the ordinates in Fig. 5 are different from previously discussed results. A relatively small blowing rate already causes an augmentation of the heat transfer of 10%. An enormous increase of the heat transfer takes place at  $M = 1.4$  and beyond. The highest values exceed 60% heat transfer augmentation at  $M = 2.5$ . This is due to the intense vortex flow pattern from the closely spaced jets as known from the locally resolved results [1]. The locally resolved results also display that this intense contact of adjacent jet vortices causes an early decay of high heat transfer, compared to the standard pitch situation. Most of the curves are back to unity at around  $x/D = 40$  to 50. Only the highest blowing rates seem to generate enough flow perturbations farther downstream, where the heat transfer augmentation still reaches values of 20% above the unblown case.

Heat transfer augmentation at large pitch ejection of  $s/D = 5$  (Fig. 5(b)) is much lower than in the  $s/D = 3$  standard case. The locally resolved heat transfer results [1] already showed that surface areas of augmented heat transfer are closely confined to the hole centerline region, because of the missing jet interaction. The values of the heat transfer augmentation range from below 5% for smaller blowing rates, to a maximum value of 18 percent at the

highest examined blowing rate. Most of the curves exhibit a maximum very close to the ejection location as expected from the missing adjacent coolant jet interaction. They fall back to unity at around  $x/D = 40$  to 50. Only at  $M = 0.85$  where jet lift-off is initiated, lower values are found close to the ejection location, while the maximum is located around  $x/D = 20$ .

**Turbulence Effects.** The flow conditions of the heat transfer experiments are deliberately adjusted to low turbulence levels. Enhanced heat transfer levels caused by high background turbulence that could cover the coolant jet effects should be avoided. However, the elevated turbulence influence can be estimated from the mechanisms of coolant jet mixing and cooling film development detailed in the present study. It is expected that a situation of dominating jet in crossflow mixing is significantly affected by enhanced hot gas turbulence. Jet spreading should be accelerated and increased hot gas entrainment and turbulent viscosity should damp the development of intense counterrotating coolant jet vortices. These assumptions are confirmed by the locally resolved results of the effectiveness [1]. They suggest a lower overall augmentation of the heat transfer over the already enhanced unblown level, due to the less pronounced coolant jet structures. Normal and/or small pitch ejection at higher blowing rates induce flow situations of intense adjacent jet interaction and mixing. Here the ejection dominates the local turbulence level, and the hot gas turbulence should have a minor impact on the resulting heat transfer augmentation. Results of Burd et al. [21] confirm that the structure of such coolant films is merely influenced by the elevated turbulence environment.

## Results of the Heat Flux Reduction

The intention of ejecting large amounts of coolant, of course, is to achieve intense film cooling by best possible surface coverage. Reviewing the effectiveness results [15] confirms that it indeed is possible to produce high overall effectiveness by the excessive use of coolant. The present results of the heat transfer measurements indicate that configurations causing the highest heat transfer augmentation in general coincide with those configurations yielding the best overall effectiveness. Obviously, it is necessary to combine the measurements of both parameters to determine the wall temperature governing the heat flux reduction. Only a comparison based on the heat flux reduction allows for a final decision for one of several competing ejection configurations. The results of the present study offer the unique possibility of combining effectiveness and heat transfer from measurements at identical flow conditions on a very broad database. Locally resolved results of the heat flux reduction are obtained, but are mostly very similar to the local effectiveness distribution. This is typical for ejection at moderate blowing rates where only a gradual heat transfer augmentation takes place. The heat flux is governed by the local effectiveness under these conditions. Emphasizing on the quantitative prediction by means of design tools, the lateral mean values of the heat flux reduction over the downstream length are discussed.

Sen et al. [22] introduced the concept of the net heat flux reduction (NHFR) to evaluate film cooling in terms of its wall heat flux effect

$$\text{NHFR} = 1 - \frac{q_w}{q_0} \quad (10)$$

Best cooling is achieved for large values of NHFR, indicating maximum reduction of the heat flux into the film cooled wall  $q_w$  compared to that without cooling film  $q_0$ . Using the definitions of the heat flux into the cooled and the uncooled wall leads to

$$\text{NHFR} = 1 - \frac{h_f}{h_0} (1 - \eta\theta) \quad (11)$$

Given the values of the heat transfer augmentation  $h_f/h_0$  and the effectiveness  $\eta$ , NHFR is obtained for a preset, dimensionless wall temperature  $\theta$ . The flaw of this approach is the possibility of

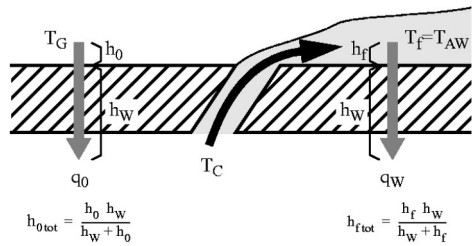


Fig. 6 Heat transfer through the diabatic wall

generating arbitrary NFHR values by presetting of the a priori unknown wall temperature. Comparing results of different experimentalists may become virtually meaningless considering this possibility of NHFR tuning.

The way out of this dilemma is to regard the heat transfer all through the cooled wall to the internal coolant flow (Fig. 6). Given identical internal flow situations with and without ejection, the heat transfer coefficient  $h_w$  from the wall surface into the backside coolant is invariant. Furthermore, assuming a dominant wall normal heat flux component, the heat flux reduction in analogy to Eq. (10) is given by

$$\Theta = 1 - \frac{h_{f \text{ tot}}(T_{AW} - T_C)}{h_{0 \text{ tot}}(T_G - T_C)} = 1 - \frac{h_f(h_w - h_0)}{h_0(h_w + h_f)}(1 - \eta) \quad (12)$$

Unknown is  $h_w$ , depending on the local part geometry and backside cooling characteristic. It still is imperative to determine the locally specific heat flux to get the accurate and also locally specific result of the heat flux reduction. However, it is possible to estimate  $h_w$  to a fraction of the unblown external heat transfer coefficient  $h_0$

$$h_w = \vartheta h_0 \quad (13)$$

Introducing this assumption yields

$$\Theta = 1 - \frac{(1 + \vartheta)(h_f/h_0)}{\vartheta + (h_f/h_0)}(1 - \eta) \quad (14)$$

Actual designs aim to meet the distribution of the external heat loads by the intensity of the internal cooling. Assuming a constant factor  $\vartheta$ , on basis of a 1-D approach as sketched in Fig. 6 should result in a good initial guess for the wall temperature distribution. This handy equation gives a reasonable estimate of the heat flux reduction of typical applications and assists the comparative evaluation of the total effects of film cooling. For both reasons of simplicity and to match the present experimental situation, a value of  $\vartheta = 1$  was used in this study.

**Effect of the Density Ratio.** Figure 7 compares heat flux reduction results of the typical geometry of shallow angle ejection and standard hole spacing for low (Fig. 7(a)), and high (Fig. 7(b)) density ratios. As mentioned before, the downstream distributions of the lateral mean values of the heat flux reduction are very similar to the effectiveness distributions. The curves appear somewhat roughened compared to effectiveness curves due to the roughness of the heat transfer data. An optimum cooling effect in terms of the enclosed area becomes much more obvious from the heat flux reduction curves than from the effectiveness curves. The decay of the effectiveness at high blowing rates due to lift-off is amplified by the simultaneous rise of the heat transfer coefficient. At low blowing rates, the high effectiveness peak close to the ejection location (see [15]) is also put into perspective by the augmented heat transfer values in that area. As a result, the benefit of moderate blowing rates is pronounced.

Optimum overall heat flux reduction is obtained at  $M = 0.6$  for low density ratio and  $M = 0.85$  at high density ratio. This differs from the optimum overall effectiveness observed at  $M = 0.7$  and

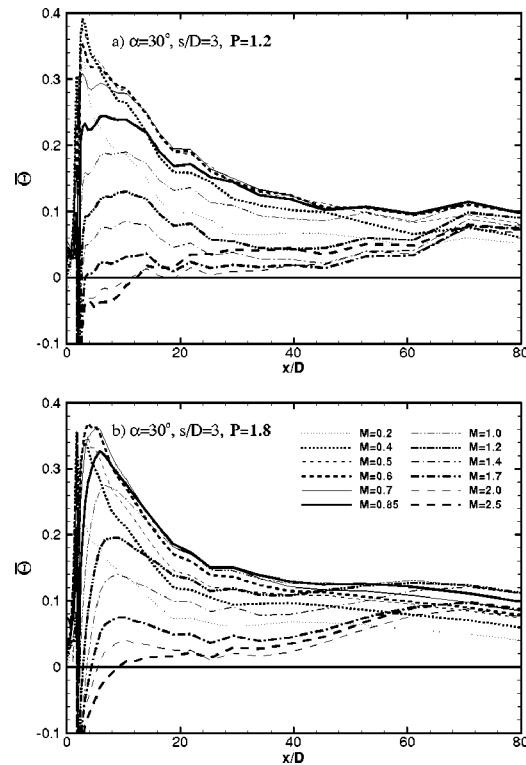


Fig. 7 Effect of the density ratio on the heat flux reduction

$M = 1.0$ , respectively. The optimum of the heat flux reduction can be related to the velocity ratio. Best ejection conditions for the actual geometry correspond to a velocity ratio of  $U = 0.5$ . The maximum heat flux reduction obtained is about 35% close to the ejection and 10 to 12% downstream, gradually increasing with density ratio. At higher density ratios, more coolant has to be ejected for optimum cooling.

At high blowing rates, the cooling effect upstream  $x/D = 40$  to  $50$  is gradually decreasing due to the high heat transfer values. Blowing rates of  $M = 1.7$  and beyond yield heat flux reductions in the order of 2 to 5%, indicating that a large amount of coolant is ejected without any beneficial effect. Only the decay of heat transfer and a simultaneous formation of a closed cooling film due to adjacent jet interaction assists heat flux reduction far downstream. A rise towards a 10% level at  $x/D = 60$  to  $70$  can be observed.

**Effect of the Ejection Angle.** With steep angle and normal ejection, as displayed in Fig. 8 for an engine like high density ratio, the effect of the adjacent jet interaction becomes more pronounced. Along the film-cooled surface, the areas of dominating single jet in crossflow mixing and adjacent jet in crossflow interaction downstream can be clearly distinguished. For the steep angle ejection Fig. 8(a), the adverse effect of a rising blowing rate can be observed upstream  $x/D = 30$  for lower blowing rates with a shift to  $x/D = 50$  for high blowing rates. For normal ejection, a distinct crossing point of all curves is present at  $x/D = 18$ . It obviously separates the single jet dominated region close to the ejection from the film flow dominated region downstream (Fig. 8(b)). The steep angle ejection features an optimum cooling situation at a blowing rate of about  $M = 1.0$ . In agreement with measurements at the same geometry but lower density ratios, the velocity ratio of  $U = 0.55$  represents the optimum flow condition. The optimum is less pronounced than for shallow angle ejection. At normal ejection, no optimum cooling configuration can be determined. For this ejection situation, the coolant mass flow has to be adjusted according to the downstream position where the heat flux reduction is needed. A particular effect is the downstream coordinate

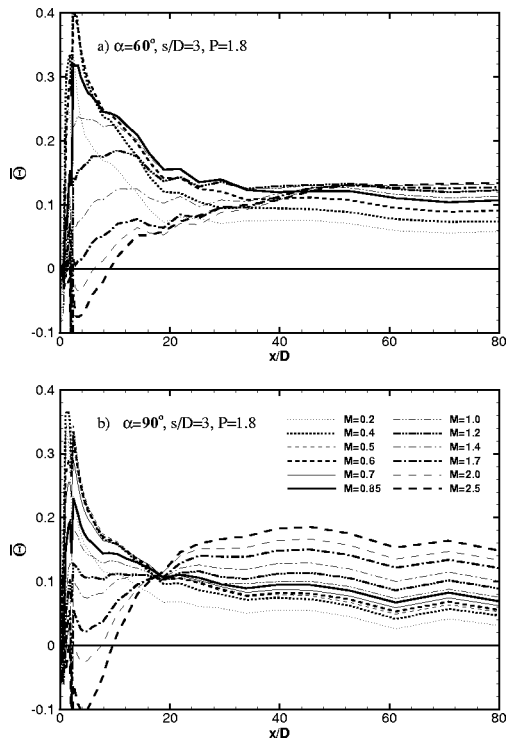


Fig. 8 Effect of the blowing angle on the heat flux reduction

independent heat flux reduction at a 10% level at  $M=1.2$ . It occurs for standard hole spacing and independent from density ratio. Negative values of the heat flux reduction, i.e. heat flux augmentation, are found at locations upstream of  $x/D=10$  for the highest examined blowing rate at normal ejection. They indicate, in fact, an additional heat load of up to 10 percent on this surface area due to coolant ejection.

**Effect of the Hole Spacing.** Figure 9 shows the results of small pitch and large pitch ejection at typical shallow ejection angles and engine like high density ratios. Note that the scale of the small pitch ejection is twice the scale of the large pitch ejection. At a hole spacing of  $s/D=2$  (Fig. 9(a)) the heat flux reduction is monotonically increasing with blowing rate over most of the regarded downstream length. This documents the dominance of the adjacent jet interaction at small pitch resulting in stable cooling films. In contrast to the findings at larger hole spacings, the heat flux reduction is especially high at high blowing rates. Only upstream of  $x/D=10$  a considerable decrease of the heat flux reduction peaks due to the jet in crossflow typical lift-off effect is found. With the exception of the near vicinity of the ejection position a virtually constant level of almost 30 percent is attained at high blowing rates. However, the blowing rate proportional increase is stagnating beyond  $M=1.7$ . This effect can be attributed to the massive increase of the heat transfer coefficients at very high blowing rates of this configuration (see Fig. 5(a)). At lower density ratios this plateau level is already reached for lower blowing rates, suggesting an optimum cooling effect at a velocity ratio of  $U=0.7$ . At ejection conditions of steeper angles and small hole spacing, such a plateau is not recognized within the examined range of blowing rates. Therefore, a distinct optimum can not be identified.

The large pitch ejection, Fig. 9(b), displays a completely different behavior. The almost purely jet in crossflow structured situation obviously exhibits optimum cooling conditions at a blowing rate of  $M=0.85$ . At lower density ratios the optimum is shifted to lower blowing rates, indicating most favorable flow conditions at  $U=0.45$ . The maximum heat flux reduction at these optimum

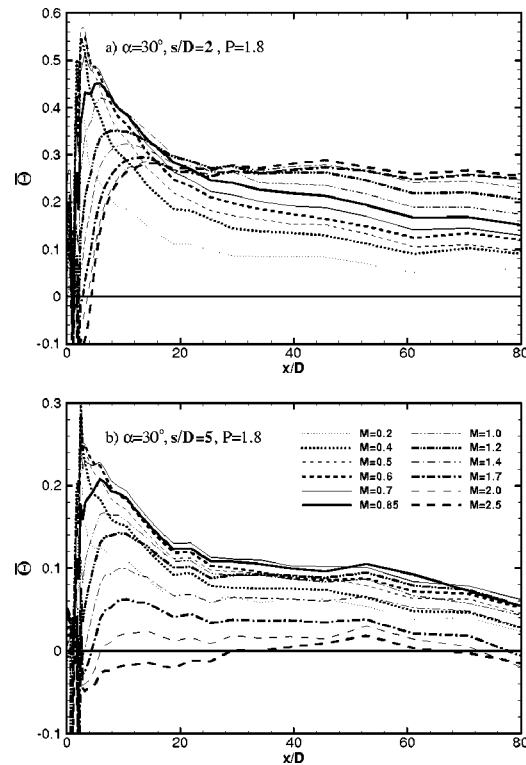


Fig. 9 Effect of the hole spacing on the heat flux reduction

conditions is 20% close to the ejection, falling back to 10% at downstream distances of  $x/D=30$  to 50. High blowing rates cause a severe degradation of the heat flux reduction. At  $M=2.5$ , the overall heat flux reduction from coolant ejection is zero, with a tendency towards negative values upstream of  $x/D=30$ . The alarming outcome is that coolant ejection at such conditions makes no sense and does not yield any film-cooling effect at all. Besides the ejection inherent efficiency loss of the thermodynamic process and supplement deterioration of the aerodynamic performance due to flow perturbation, there is even a sever potential of creating additional heat load on the affected surface.

### Correlation of the Heat Transfer Coefficient

To enable the required prediction of the heat flux reduction as discussed above, a correlation of the heat transfer coefficients is imperative. It should be given by a set of empirical equations with the ejection parameters as variables according to the effectiveness correlation presented in the companion paper [15]. Existing approaches for heat transfer coefficients from slot ejection can assist in characterizing the complex flow from discrete hole ejection. In the literature various correlations for the slot situation are documented (e.g., Hartnett et al. [23], Metzger et al. [3], Forth and Jones [24]). Studies of Seban [25], Jabbari and Goldstein [26], and Bittlinger et al. [27] show the importance of the ejection velocity to the heat transfer coefficient. A decay of the heat transfer effects with downstream distance results from the wall jet flow character of a slot ejection with velocity overshoot or deficit.

The heat transfer distributions from discrete hole ejection rely on much more complex flow patterns requiring more sophisticated descriptions. Approaches are available from, e.g. Metzger and Fletcher [4], Forth et al. [8], or Ammari et al. [18]. Those approaches share the constraint of limited applicability with respect to geometry and flow conditions. They have in common that a very high peak of the lateral mean value of the heat transfer coefficient at the ejection position is followed by an exponential decay downstream. However, the near vicinity of the ejection location is explicitly excluded from the prediction. From detailed

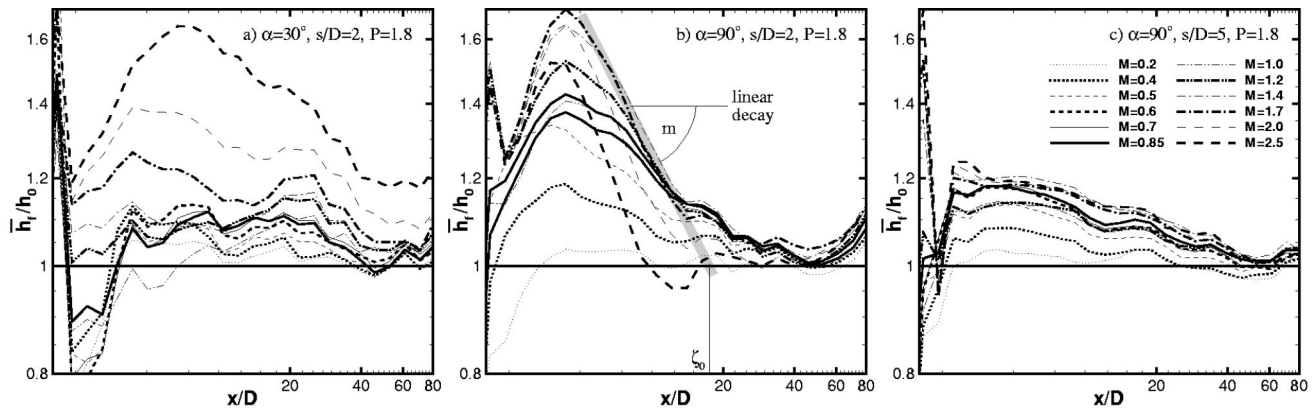


Fig. 10 Lateral mean values of the heat transfer augmentation on double logarithmic scales

results of Goldstein and Taylor [28] it is known that no extreme peaks but well defined maxima of the heat transfer coefficient are present at the ejection location. This finding, as well as the effects of all geometrical and flow parameters examined, need to be included in the new correlation.

As mentioned earlier, the curves of laterally averaged effectiveness from the present study (see [15]) are smoother, due to less uncertainties caused by the evaluation process. The heat transfer behavior is more difficult to characterize from the comparatively rough curves and the correlations, therefore, are more general than those for the effectiveness. Nonetheless, the database exploited is by far the broadest in the open literature and offers the unique opportunity of a complete description of all dominating parameter effects and their interactions. In the same way as for the effectiveness a functional relation has to be generated of the form

$$\frac{h_f^*}{h_0} = f(\zeta) \quad (15)$$

The required function features coefficients and reference values that have a physical meaning and depend on the ejection parameters

$$\text{coefficients} = f\left(M, P, \alpha, \frac{s}{D}\right) \quad (16)$$

The coefficients must fit the measured distributions. They need to interpolate sampling points, given by the examined ejection parameter matrix, and they have to exhibit a good-natured behavior at the edges of the parameter ranges. The coefficient functions, however, have no physical interpretation. They are the result of curve fit procedures and given in the appendix.

As for the effectiveness, the assumption of exponential decay laws suggests double logarithmic scales for a systematic description of the heat transfer characteristic. Figure 10 shows the results of three sets of measurements with different geometry in this way. The extreme of a small pitch normal ejection with very pronounced adjacent jet interaction displays a very intense heat transfer that is confined to an area upstream of  $x/D = 20$  (Fig. 10(b)). The results of this situation also confirm that the heat transfer is not increasing arbitrarily with the blowing rate. A maximum level is attained at blowing rates of about  $M = 1.7$ . For higher blowing rates the heat transfer is sagging, indicating a change in the flow character that is not structured by individual jets any more (see [1]). Taking Fig. 10(b) as a reference, it can be seen that a decrease of the ejection angle, Fig. 10(a), as well as an increase of the pitch (Fig. 10(c)) result in a downstream extension of the high heat transfer area. This confirms the observations made with different ejection angles and pitch as discussed earlier. An increase of the pitch typically has a less pronounced effect. The values are back to unity at about  $x/D = 40$  in Fig. 10(c), while they stay at an

elevated level up to  $x/D = 80$  in Fig. 10(a). Some dependences of this downstream extension on the density ratio are observed, being neither systematic nor very pronounced. Therefore, a scaling of the downstream distance by a geometry depending parameter is formed

$$\zeta = \left(\frac{x}{D}\right)^\varepsilon \quad (17)$$

The geometry dependent scaling exponent  $\varepsilon$  is expressed as

$$\varepsilon = 1.2 - 0.05 \frac{s}{D} + \left(\frac{s}{D} - 4\right) \frac{\cos 1.5\alpha}{10\sqrt{2}} + 2.91(\sin 1.38\alpha - 0.99) \times \left[ \frac{\frac{s}{D} - 1.7}{1 + \left(\frac{s}{D} - 1.7\right)^2} - 0.277 \right] \quad (18)$$

All the curves scaled in this way feature high levels of heat transfer close to the ejection position with a distinct maximum. Downstream the decay of the heat transfer augmentation can be described with sufficient accuracy by a straight line on the double logarithmic scale. The straight line intersects with a unity value line, indicating the unblown base level, at a position  $\zeta_0$  (see sketch in Fig. 10(b)). The behavior of this descending part of the heat transfer curve can be described by

$$\frac{h_f^*}{h_0} = \frac{\frac{h_f}{h_0} \left(\frac{\zeta}{\zeta_0}\right)^m}{\left[1 + \left(\frac{\zeta}{\zeta_0}\right)^{mn}\right]^{1/n}} \quad (19)$$

The position  $\zeta_0$  was found to depend mainly on the ejection angle  $\alpha$

$$\zeta_0 = 45 - 250 \cos \alpha \quad (20)$$

Within Eq. (19)  $m$  denotes the slope of the straight line. Figure 10 reveals a coolant flow dependent individual slope of the curves from one set of measurements. The best approach for  $m$  is found as a function of the blowing rate weighted with density ratio, both scaled depending on the geometry

$$m = m_0 M^{m_1} P^r \quad (21)$$

The functions for the scaling and weighting coefficients  $m_0$ ,  $m_1$ , and  $r$ , are defined as

$$m_0 = (2.22 - 1.48 \cos^{0.28} \alpha) [0.027 + 1.35 e^{-(1.6 + 0.5 \sin 2\alpha)s/D}] \quad (22)$$

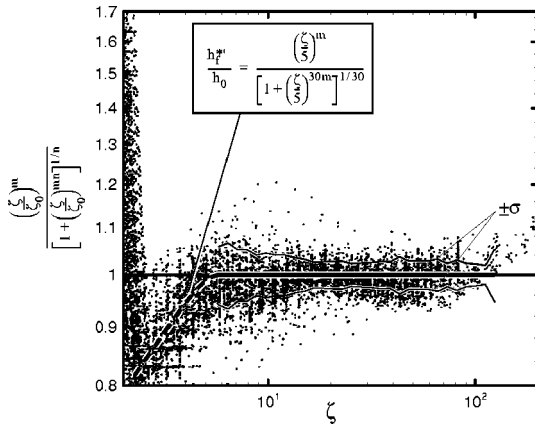


**Fig. 11 Correlation of the lateral mean heat transfer coefficients**

$$m_1 = 0.6 \left[ 1 + \frac{2.08 + 1.47 \cos 1.5 \alpha}{1 + 0.172 \left( \frac{s}{D} - 2.5 \right)^2} \right] \quad (23)$$

$$r = 1 - \frac{\cos 1.5 \alpha}{\sqrt{2}} \quad (24)$$

The transition from the augmented heat transfer to the unblown base level is described by the constant  $n$  within Eq. (19). It characterizes how close the resulting curve leans to the straight line slope and the unity value at  $\zeta_0$  with

$$n = 50 \quad (25)$$

Additional care is given to the description of the breakdown of the flow situation, as seen in Fig. 10(b) for blowing rates beyond  $M = 1.7$ . Accordingly, Eq. (19) is extended by a reduction factor to form

$$\frac{h_f^{*'}}{h_0} = \gamma \frac{h_f^*}{h_0} \quad (26)$$

To obtain unity  $\gamma$  except for small pitch normal ejection,  $\gamma$  becomes a function of the slope  $m$  and the scaled downstream length

$$\gamma = 1 - \frac{(2.1m)^4}{1 - \left( \frac{\zeta}{0.6\zeta_0} \right)^7} \quad (27)$$

To evaluate the accuracy of the new correlation versus measurement data, all results are normalized using Eqs. (19) and (26), reducing the downslope part of the curves to the unity unblown base value. In Fig. 11 the normalized and scaled curves are resolved into data points and gliding RMS values  $\sigma$  over the downstream distance parameter are indicated. As expected, the data scatters close to the constant value of one, with an overall RMS deviation of 3.8% within the indicated range of  $\zeta$ .

As mentioned before, the measurements exhibit a distinct maximum upstream of the exponential slope. This part of the curves is not described by the normalization as represented by Eqs. (19) and (26). Therefore, the normalized values are over-corrected upstream of about  $\zeta = 5$  and drop below unity. From Fig. 11 it becomes obvious that the scatter band still highlights a particular path, as indicated by the fit curve, that can be described by

$$\frac{h_f^{*'}}{h_0} = \frac{\left( \frac{\zeta}{5} \right)^m}{\left[ 1 + \left( \frac{\zeta}{5} \right)^{30m-1/30} \right]} \quad (28)$$

The fit curve shown in Fig. 11 is drawn as dashed line to indicate that the term depending on the slope  $m$  results in an individual curve for each ejection situation. Using Eq. (28) to compensate the described over correction near the ejection location yields reasonable heat transfer coefficients in the close vicinity of the ejection. The calculation procedure of reproducing a heat-transfer distribution from an arbitrary set of describing parameters is explicitly presented in the appendix.

## Conclusions

Downstream distributions of the lateral mean values of the heat transfer coefficient are determined from high-resolution local thermographic measurements of the diabatic film-cooled wall. The quantitative discussion of the heat transfer results reveals systematic impact of the ejection parameters on the heat transfer augmentation. The typical finding is a downstream length scaling of the augmented heat transfer region with the ejection angle and an increasing heat transfer with decreasing hole spacing. Based on these findings, a new correlation for the heat transfer coefficient augmentation is presented. It applies for a wide range of ejection parameters and the complete downstream distance, without any of the typical constraints and exceptions. It employs a large base of realistic temperature ratio measurement data at variable property flow conditions. Unique in the open literature, these flow conditions are completely consistent with those of corresponding effectiveness measurements and the according effectiveness correlation [15]. The combination of both correlations define convective heat transfer boundary conditions in the presence of film cooling as a powerful design tool for wall temperature analyses.

A new approach for the heat flux reduction is developed to evaluate the total film cooling effect on the heat flux balance at the cooled wall, prior to a specific component FE-analysis. Different to the known model of NHFR, this new approach does not depend on an arbitrary value of the temperature ratio  $\theta$ , i.e. a preset wall surface temperature. This model enables the derivation of the heat flux reduction due to coolant ejection. The actual heat flux reduction is derived by combining the heat transfer coefficients with the adiabatic film cooling effectiveness distributions measured at identical flow conditions.

In agreement with the commonly shared expectations, the best cooling potential is found at shallow ejection angles and moderate blowing rates. The crucial advancement of this study is the precise definition of optimum flow conditions for a lowest possible heat flux, i.e., the optimum material temperature reduction. The flow structure, and subsequently, the resulting surface impact, is most closely related to the velocity ratio. The optimum conditions at typical ejection situations of shallow ejection angles and a hole spacing of  $s/D = 3$  exist at a velocity ratio of  $U = 0.5$ . The hole pitch influences this optimum velocity ratio, resulting in higher values of  $U = 0.7$  for  $s/D = 2$  and lower values of  $U = 0.45$  for  $s/D = 5$ , respectively. Steep ejection angles promote the interaction of adjacent coolant jets and shift the optimum velocity ratio to higher values.

The results clearly demonstrate that ejection at high blowing rates has to be applied very carefully. If high blowing rates are employed and a small pitch can not be realized, steeper blowing angles may yield a heat flux reduction superior to shallow angle ejection. High blowing rates always have the potential of creating additional heat load onto the surface, i.e., surface heating instead of the intended surface cooling. Such additional heat load occurs right there, where the most intense cooling is intended, directly downstream of the ejection location.

## Acknowledgments

This study was partly funded by the Ministry of Research and Technology of the Federal Republic of Germany through the German joint research program AG Turbo and Siemens AG PG, Mülheim a. d. Ruhr, Germany.

## Nomenclature

$c_p$	= thermal capacity
$D$	= ejection hole diameter, m
$h$	= heat transfer coefficient, $W/(m^2K)$
$I$	= momentum ratio, $(\rho u^2)_C/(\rho u^2)_G$
$L$	= ejection hole length, m
$M$	= blowing rate, $(\rho u)_C/(\rho u)_G$
$m, m_1$	= correlation coefficients
NHFR	= net heat flux reduction, Eq. (11)
$n, r$	= correlation coefficients
$P$	= coolant to hot gas density ratio, $\rho_C/\rho_G$
Pr	= Prandtl number
$q$	= heat flux, $W/m^2$
Re	= Reynolds number
St	= Stanton number
$s$	= ejection hole spacing, m
$T$	= temperature, K
Tu	= turbulence intensity
$U$	= velocity ratio, $u_C/u_G$
$u$	= velocity, m/s
$x$	= streamwise coordinate, m
$\alpha$	= blowing angle
$\delta_1$	= displacement thickness of the boundary layer, m
$\varepsilon, \gamma$	= correlation coefficients
$\eta$	= film-cooling effectiveness, Eq. (3)
$\Theta$	= heat flux reduction, Eq. (14)
$\theta$	= dimensionless wall temperature, Eq. (1)
$\vartheta$	= wall heat transfer factor, Eq. (13)
$\rho$	= density, $kg/m^3$
$\zeta$	= downstream distance parameter, Eq. (17)

## Subscripts

0	= without ejection, reference values
AW	= adiabatic wall
C	= coolant
f	= cooling film
G	= hot gas
s	= starting length
tot	= total
T	= turbulence dependent
W	= wall

## Superscripts

'	= modified approach
*	= normalized
-	= laterally averaged

## Appendix

In the following an example is given for the evaluation of the lateral mean heat transfer augmentation from the presented correlation. Since the employed coefficient functions cannot be physically interpreted, numerical values are stated to enable a verification of the correct implementation.

**Correlating the Heat Transfer Augmentation From the Ejection Parameters.** The example refers to the same ejection situation as the according effectiveness correlation example within the companion paper [15], with parameters as stated in Table 2. A spreadsheet calculation was used to reproduce the equations and all values are given to the according precision in Table 3.

A range of  $\zeta$  covering values of 1 to 100 is chosen for a useful downstream distance  $x/D$ . Referring to Fig. 12, the values of the specific lateral mean heat transfer augmentation are given by

$$\frac{\bar{h}_f}{h_0} = \frac{1}{\gamma} \left( \frac{\zeta_0}{5} \right)^m \frac{\left[ 1 - \left( \frac{\zeta}{\zeta_0} \right)^{mn} \right]^{1n}}{\left[ 1 + \left( \frac{\zeta}{5} \right)^{m30} \right]^{1/30}} \quad (29)$$

Table 2 Ejection parameter example

M	$\alpha$ [°]	s/D	P	Tu
2.0	30	3	1.2	0.015

Table 3 Numerical coefficients

flow parameters / distance	downstream slope
$\varepsilon = 0.80270505$	$m = 0.084750932$
$\zeta_0 = 261.50635$	$m_0 = 0.023977279$
$r = 1.5$	$m_1 = 2.3945045$

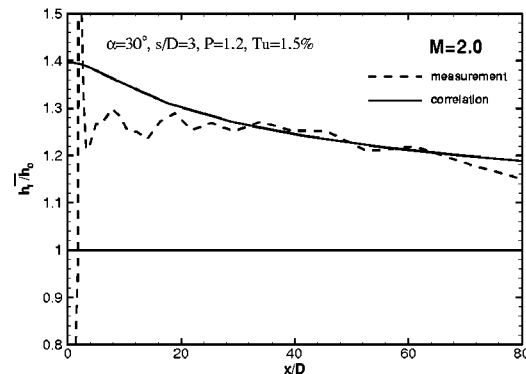


Fig. 12 Comparison measurement versus correlation

Herein the straight line slope  $m$ , as indicated in Fig. 10, is obtained by Eq. (21), employing the coefficients  $m_0$ ,  $m_1$ ,  $r$ , from Eqs. (22)–(24), and  $\xi_0$ ,  $\gamma$ , from Eqs. (20), (27). Using coefficient  $\varepsilon$  from Eq. (18) these values are plotted over

$$\frac{x}{D} = \zeta^{1/\varepsilon} \quad (30)$$

## References

- [1] Baldauf, S., Schulz, A., and Wittig, S., 2001, "High Resolution Measurements of Local Heat Transfer Coefficients From Discrete Hole Film Cooling," ASME J. Turbomach., **123**, pp. 749–757.
- [2] Baldauf, S., Schulz, A., and Wittig, S., 2001, "High-Resolution Measurements of Local Effectiveness From Discrete Hole Film Cooling," ASME J. Turbomach., **123**, pp. 758–765.
- [3] Metzger, D. E., Carper, H. J., and Swank, L. R., 1968, "Heat Transfer With Film Cooling Near Nontangential Injection Slots," ASME J. Eng. Power, **80**, pp. 157–163.
- [4] Metzger, D. E., and Fletcher, D. D., 1971, "Evaluation of Heat Transfer for Film-Cooled Turbine Components," ASME J. Eng. Power, **8**, pp. 181–184.
- [5] Metzger, D. E., Carper, H. J., and Warren, J. M., 1972, "Predicted Film Cooling Near Flush Slots-Comparison With Experiment," J. Aircr., **9**, pp. 857–863.
- [6] Choe, H., Kays, W. M., and Moffat, R. J., 1974, "The Superposition Approach to Film-Cooling," ASME Paper 74-WA/HT-27.
- [7] Loftus, P. J., and Jones, T. V., 1983, "The Effect of Temperature Ratios on the Film Cooling Process," ASME J. Eng. Power, **105**, pp. 615–620.
- [8] Forth, C. J. P., Loftus, P. J., and Jones, T. V., 1985, "The Effect of Density Ratio on the Film Cooling of a Flat Plate," Heat Transfer and Cooling in Gas Turbines, AGARD-CP-390, Paper 10.
- [9] Teekaram, A. J. H., Forth, C. J. P., and Jones, T. V., 1989, "The Use of Foreign Gas to Simulate the Effects of Density Ratios in Film Cooling," ASME J. Turbomach., **111**, pp. 57–62.
- [10] Gritsch, M., Baldauf, S., Martiny, M., Schulz, A., and Wittig, S., 1999, "The Superposition Approach to Local Heat Transfer Coefficients in High Density Ratio Film Cooling Flows," ASME Paper 99-GT-168.
- [11] Eckert, E. R. G., 1984, "Analysis of Film Cooling and Full-Coverage Film Cooling of Gas Turbine Blades," ASME J. Eng. Gas Turbines Power, **106**, pp. 206–213.
- [12] Baldauf, S., and Scheurlen, M., 1996, "CFD Based Sensitivity Study of Flow Parameters for Engine Like Film Cooling Conditions," ASME Paper 96-GT-310.
- [13] Martiny, M., Schiele, R., Gritsch, M., Schulz, A., and Wittig, S., 1996, "In Situ

- Calibration for Quantitative Infrared Thermography,” Quirt’96 Eurotherm No. 50, Stuttgart, Germany, Sept. 2–5.
- [14] Kays, W. M., and Crawford, M. E., 1980, *Convective Heat and Mass Transfer*, McGraw Hill, New York, NY.
- [15] Baldauf, S., Scheurlen, M., Schulz, A., and Wittig, S., 2002, “Correlation of Film-Cooling Effectiveness From Thermographic Measurements at Engine-like Conditions,” GT-2002-30180, ASME J. Turbomach., **124**, pp. 686–698.
- [16] Eriksen, V. L., and Goldstein, R. J., 1974, “Heat Transfer and Film Cooling Following Injection Through Inclined Circular Tubes,” ASME J. Heat Transfer, **96**, pp. 239–245.
- [17] Hay, N., Lampard, D., and Saluja, C. L., 1985, “Effects of Cooling Films and the Heat Transfer Coefficient on a Flat Plate With Zero Mainstream Pressure Gradient,” ASME J. Eng. Gas Turbines Power, **107**, pp. 105–110.
- [18] Ammari, H., Hay, N., and Lampard, D., 1990, “The Effect of Density Ratio on the Heat Transfer Coefficient From a Film-Cooled Flat Plate,” ASME J. Turbomach., **112**, pp. 444–450.
- [19] Goldstein, R. J., Jin, P., and Olson, R. L., 1998, “Film Cooling Effectiveness and Mass/Heat Transfer Downstream of One Row of Discrete Holes,” ASME Paper 98-GT-174.
- [20] Drost, U., Bölcs, A., and Hoffs, A., 1997, “Utilization of the Transient Liquid Crystal Technique for Film Cooling Effectiveness and Heat Transfer Investigations on a Flat Plate and a Turbine Airfoil,” ASME Paper 97-GT-26.
- [21] Burd, S. W., Kaszeta, R. W., and Simon, T. W., 1996, “Measurements in Film Cooling Flows: Hole L/D and Turbulence Intensity Effects,” ASME Paper 96-WA/HT-7.
- [22] Sen, B., Schmidt, D. L., and Bogard, D. G., 1996, “Film Cooling with Compound Angle Holes: Heat Transfer,” ASME J. Turbomach., **118**, pp. 800–806.
- [23] Hartnett, J. P., Birkebak, R. C., and Eckert, E. R. G., 1961, “Velocity Distributions, Temperature Distributions, Effectiveness and Heat Transfer for Air Injected Through a Tangential Slot Into a Turbulent Boundary Layer,” ASME J. Heat Transfer, **83**, pp. 293–306.
- [24] Forth, C. J. P., and Jones, T. V., 1986, “Scaling Parameters in Film Cooling,” Proc. 8th Int. Heat Transfer Conference, Vol. 3, pp. 1271–1276.
- [25] Seban, R. A., 1960, “Heat Transfer and Effectiveness for a Turbulent Boundary Layer With Tangential Fluid Injection,” ASME J. Heat Transfer, **82**, pp. 309–312.
- [26] Jabbari, M. Y., and Goldstein, R. J., 1978, “Adiabatic Wall Temperature and Heat Transfer Downstream of Injection Through Two Rows of Holes,” ASME J. Eng. Power, **100**, pp. 303–307.
- [27] Bittlinger, G., Schulz, A., and Wittig, S., 1994, “Film Cooling Effectiveness and Heat Transfer Coefficients for Slot Injection at High Blowing Ratios,” ASME Paper 94-GT-182.
- [28] Goldstein, R. J., and Taylor, J. R., 1982, “Mass Transfer in the Neighborhood of Jets Entering a Crossflow,” ASME J. Heat Transfer, **104**, pp. 715–721.

# Combined 3-D Flow and Heat Transfer Measurements in a 2-Pass Internal Coolant Passage of Gas Turbine Airfoils

**D. Chanteloup**

e-mail: denis.chanteloup@epfl.ch

**Y. Juaneda**

e-mail: juaneda@imft.fr

**A. Bölc**

e-mail: albin-boelcs@epfl.ch

EPFL-LTT, 1015 Lausanne-Switzerland

*A study of the flow and heat transfer in a stationary model of a two-pass internal coolant passage is presented, which focuses on the flow characteristic effects on the wall heat transfer distribution. Results are given in the upstream fully developed region. Heat transfer measurements were made with a transient technique using thermochromic liquid crystal technique to measure a surface temperature. The technique allows full surface heat transfer coefficient measurements on all the walls. Flow measurements were made with a stereoscopic digital PIV system, which measures all three-velocity components simultaneously. The coolant passage model consists of two square ducts, each having a 20 hydraulic diameter length. The ducts are connected by a sharp 180 deg bend with a rectangular outer wall. 45 deg ribs are mounted in a staggered arrangement on the bottom and top walls of both legs. The height of the ribs is equal to 0.1 hydraulic diameters. They are spaced 10 rib heights apart. The flow and heat transfer measurements were obtained at one flow condition with an inlet flow Reynolds number, based on the hydraulic diameter, of 50,000. The paper presents detailed measurement results of the flow characteristics and of the heat transfer distribution in the upstream straight leg of the passage and describes how the main and secondary flows influence the heat transfer distribution in the fully developed regions of the channel. [DOI: 10.1115/1.1506176]*

## Introduction

For the design of gas turbine blades, a detailed knowledge of the physical phenomena in the passage is necessary. To improve the performance of the CFD codes, a validation of the predictions is necessary, and detailed measurements of the flow structure and heat transfer distribution in the passages are required for comparison.

Rib arrays inside an internal cooling channel are often used in heat exchanger systems to enhance the heat transfer rate. When ribs are oblique to the channel, the main flow can more easily climb over the ribs and generate stronger secondary flow, as shown in Schabacker [1]. Heat transfer characteristics have been measured in 45 deg rib arrangement in literature. Several references describe area averaged results performed mainly with thermocouples (Mochizuki et al. [2] and Han [3]). Correlations presented in Han [4] and Han and Chandra [5], have been built in single pass channel for several Re numbers and geometrical characteristics. Detailed full surface heat transfer measurements are also published. Some results are compared to flow measurements in the vicinity of the walls (Wang [6]). Rau [7] showed the impact of rib pitch parameter in channels with a parallel 45-deg rib arrangement. Studies of the flow characteristics in the coolant channels. Schabacker et al. [8] showed velocity (PIV) measurements in the turn region of 2-pass coolant channels. Bonhoff et al. [10] and Hermanson et al. [11] showed the capability of CFD codes to simulate flow characteristics and heat transfer in ribbed channels.

Although detailed heat transfer measurements in coolant channels are available in literature, to the authors knowledge, the direct combination of flow measurements and heat transfer distribution in such ducts has not been described. In the present study, the particle-image-velocimetry (PIV) measurement method was em-

ployed for the investigation of the flow field in models of a stationary two-pass coolant passage. The measurement error introduced in high 3-D flows, can be avoided by using a stereoscopic PIV setup. A stereoscopic digital PIV system, based on the angular displacement method, was used for the present investigation (Schabacker and Bölc [12]). This PIV system measures all three instantaneous velocity components. Subsequently, an ensemble average of the velocity data, in identical spatial windows, is calculated to determine the mean and fluctuating velocity field.

Full surface heat transfer measurements were made on all the outer walls of the channel. The transient liquid crystal technique described in Wang et al. [13], is suitable for full surface heat transfer measurements in regions with high heat transfer gradients. Because in long test channels, the gas temperature is not a perfect step, the Duhamel theorem was used to process the gas temperature (Ekkad and Han [14]). The information was processed with a full digital system as presented in Vogel and Bölc [15].

This paper presents initial results from the Brite-Euram project, for Internal Cooling of Turbine Blades (ICTB). The main objective of Chanteloup and Bölc [16] was to present flow results in the present configuration. The specific objectives of the present paper are to determine and present the influence of the flow characteristics on the heat transfer distribution in the fully developed region of a 2-pass coolant channel with a 45-deg rib arrangement.

## Experimental Setup

**Test Facility.** A sketch of the test section is shown in Fig. 1 and geometry characteristics are given in Table 1. Air was the working medium and was supplied by a continuously running compressor. The air enters the settling chamber with an inner diameter of 600-mm via a 150-mm tube and a conical entrance section with an angle of 30 deg. The settling chamber is equipped with a combination of perforated plates, honeycombs and meshes to reduce unsteadiness and swirl in the flow. A bell mouth entry leads the air from the settling chamber to the test channel. The

Contributed by the International Gas Turbine Institute and presented at the International Gas Turbine and Aeroengine Congress and Exhibition, Amsterdam, The Netherlands, June 3–6, 2002. Manuscript received by the IGTI, October 29, 2001. Paper No. 2002-GT-30214. Review Chair: E. Benvenuti.



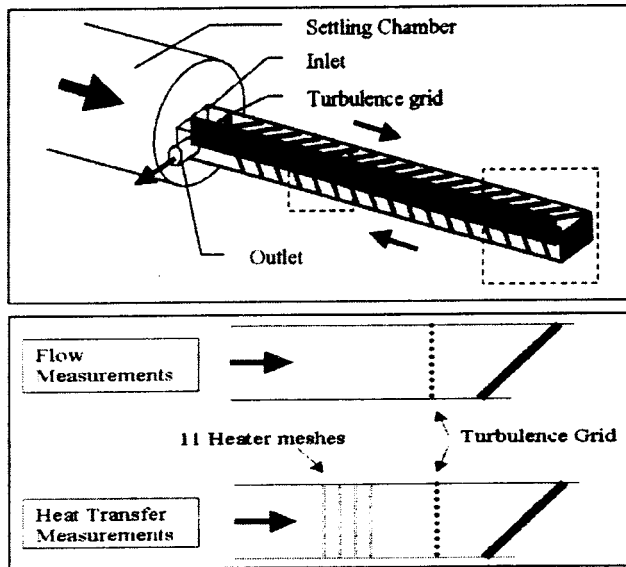


Fig. 1 The internal coolant passage test facility and inlet region details

settling chamber outlet is equipped with heaters for heat transfer measurements. During the flow measurements, the heaters are removed from the channel. A turbulence grid is placed downstream of the heaters in both flow and heat transfer measurements to reach the same turbulence level at the channel inlet.

The test section is a two-pass, cooling passage model of a gas turbine blade. The flow path in the downstream and upstream passages has a cross-section of  $100 \times 100 \text{ mm}^2$  with a corresponding hydraulic diameter,  $D_H = 100 \text{ mm}$ , and a length of  $20D_H$ . The outer walls of the test section are made of 5-mm-thick extruded Plexiglas to obtain good optical properties for the PIV experiment. In the straight-corner bend, the clearance between the tip of the divider plate and the outer wall is equal to  $1 Dh$ . The thickness of the divider plate or web between the two passages is  $0.2D_H$ . The tip of the divider plate is cylindrically shaped with a  $0.1D_H$  radius. Square ribs with an angle of 45 deg to the passage centreline, rib heights of 0.1 hydraulic diameters ( $e/D_H = 0.1$ ), and rib spacing of 10 rib heights ( $P/e = 10$ ) are mounted in a staggered arrangement on the top and bottom wall of the passage. The ribs in the bend region and the dimensions of the bend are shown in Fig. 2. Eighteen ribs are mounted on each of the top and bottom walls in each of the upstream and downstream passages of the model ( $18 \times 4$ ).

Table 1 The coolant passage geometry characteristic

Test section length	L	$20 D_h$
Height & Width of passage legs	D	$1 D_h$
Bend cross-section	S	$1 D_h$
Length of divider plate		$19 D_h$
Thickness of divider plate	B	$0.2 D_h$
Rib cross-section		$0.01 D_h^2$
Rib pitch	P	$1 D_h$
Rib height	c	$0.1 D_h$
Rib angle of attack		45deg

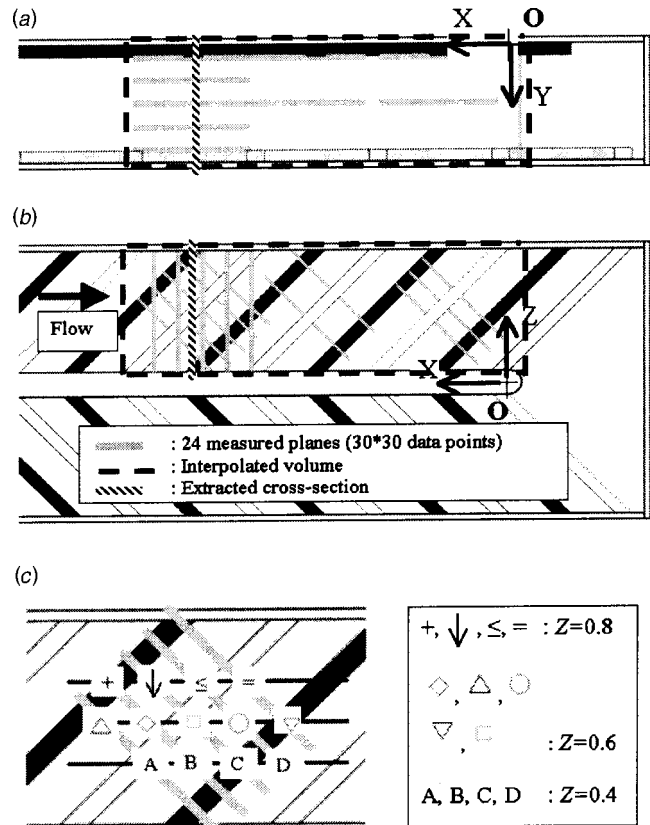


Fig. 2 Measurement sections. The symbols represent the measurement lines (Y direction) that will be analyzed in the next sections (Fig. 5)—(a) data sets perpendicular to X-Y plane, (b) data sets perpendicular to X-Z plane, (c) symbol details for velocity profiles

A modular concept was chosen for the test section that allows an easy exchange of the components. The total model test section including the test section entrance is turned 90 deg around the x-axis to obtain additional measurement planes without changing the flow conditions in the passage. This allows an easy optical access to the positions of interest for the PIV measurements.

**Flow Conditions, Measurement Program, and Coordinate Systems.** The measurements were obtained with air as working medium, at a flow Reynolds number of 50,000 (corresponding to a bulk velocity:  $U_b = 7.58 \text{ m/s}$ ), at the entrance of the test section. The Reynolds number is based on the 0.1 m hydraulic diameter with an air temperature of  $18^\circ\text{C}$ . Upstream of the test-rig, the mass flow is measured by means of a 5864S Brooks flow meter with a 1-percent accuracy. The turbulence level is approximately 3 percent at the model inlet. An experimental study was conducted to assess the effect of varying test section orientation on the flow. The small variations between the flow conditions are within the measurement uncertainty and can therefore be neglected for the experiments.

Static pressure measurements in the configurations have been performed with a DRUCK LPM 5480 differential pressure transmitter, with a  $6\text{N/m}^2$ -accuracy.

Detailed measurements of the flow structure in the passage have been obtained in the bend, upstream ( $3D_H$ ) and downstream ( $4D_H$ ) of the 180 deg bend. A total of 24 measurement planes provided with nine hundred measurement points (30 by 30), were taken in the region of interest. Fifteen planes parallel to the Y-axis and nine planes parallel to the XZ-plane allowed to give a description of the 3-D flow field in the fully developed region. An inter-

polation of all planes, based on an inverse distance algorithm, allowed obtaining streamlines from measured data in the entire volume, as shown in Fig. 1.

The definition of the coordinate systems in the test facility is shown in Fig. 2. A Cartesian coordinate system is used for the straight passages and a cylindrical coordinate system is used for the bend region. The origin for both coordinate systems is set on the bottom wall at the center of the rounded end of the divider plate. In the Cartesian ( $X, Y, Z$ ) system,  $X$  is defined as positive in the streamwise direction of the flow downstream of the bend exit,  $Y$  is defined positive vertically upwards in the horizontal test section orientation, and  $Z$  is defined as shown.

**Flow Measurements.** Particle image velocimetry (PIV) was chosen as a flow measurement technique. A homemade stereoscopic PIV system was used, which allowed to obtain the mean velocity fields as well as the turbulence quantities in approximately a hundred planes in each test configuration.

Di-ethyl-hexyl-sebacate (DEHS) from TOPAS is used as light scattering droplets for the PIV experiments. A DLR-made Aerosol Generator using Laskin Nozzles generates 1–3- $\mu\text{m}$ -dia DEHS droplets. The droplets are injected upstream of the settling chamber to guarantee a homogeneous seeding density in the test section.

A 1.2-mm-thick light sheet that illuminates the particles is created by a Quantel Twins B Nd-Yag double oscillator pulsed laser. A plano-concave lens (–30 mm focal length) combined with two plano-cylindrical lenses (76.2 and 300 mm focal length) transform the beam into the vertical light sheet.

The imaging system consists of two independent Kodak ES1.0 cameras, each having its own PC. A Nikon Nikkor 55 mm lens is mounted on each camera. For a typical recording situation, the cameras are placed with an oblique angle of 4.3 deg at a distance of 0.7 m from the light sheet plane. The pulse separation time is about 40  $\mu\text{s}$ . The frame grabber is an Imaging Technology PCI frame grabber with 2 MB memory onboard. During the PIV measurement series, 10 images are written in real time into the PC's RAM memory and subsequently saved on the hard disk. The automation of the process allows storing of 5000 frames per measurement plane. The laser components (flash lamp and Q-switch) and the cameras are triggered by 10 Hz TTL signals that are dispatched to all the elements with specific delays.

The 3-D PIV measurements are obtained from the combination of two 2-dimensional vector fields. From the processed vector fields, the instantaneous three-dimensional velocity field can be reconstructed. Matlab homemade reconstruction software was developed at the EPFL-LTT. With angular PIV systems, where both cameras observe the light sheet from the same side, the corresponding interrogation positions in the right and left images do not match in general. Therefore, a calibration of the camera system is performed which also corrects for the distortion of the images in the lenses and the Plexiglas walls of the passage. In order to obtain PIV measurements in the presented forms, the statistical distribution of the velocity components is determined in identical spatial windows from a series of instantaneous PIV measurements. From these statistical distributions, the ensemble average is calculated to determine the desired mean-velocity field.

**Heat Transfer Measurements.** For the present study, transient heat transfer experiments were performed using liquid crystals to determine the surface temperature. The transient technique is well described in Wang [17]. The transient liquid crystal technique consists of monitoring the surface temperature evolution in time with a step change in the gas temperature. Eleven fine, fast response, mesh heaters were fitted to the duct inlet to produce the step change in gas temperature. This heater comprises a mesh of stainless steel wires, 40  $\mu\text{m}$  in diameter woven at a pitch of approximately 100  $\mu\text{m}$ , with an open area of 38% (see [13] for more details). The meshes were connected in series to the 10 kW power supply (256A, 40V). Figure 3 shows a typical variation of tem-

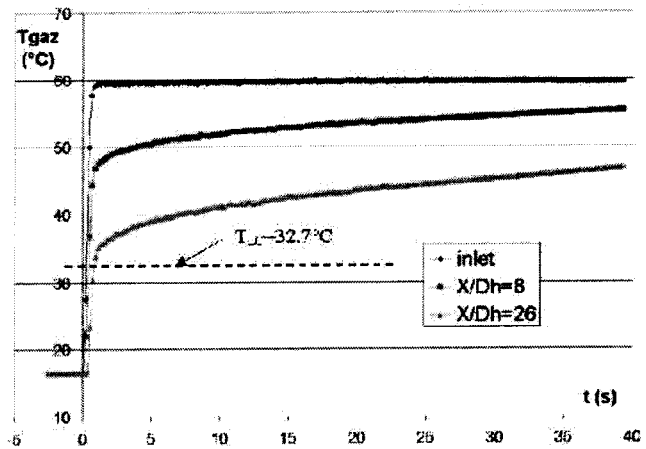


Fig. 3 Gas temperature increase at different  $X/D$  locations for heat transfer post processing

perature with time in the test channel. At the inlet, the heaters provide a step change in temperature of 75 and 99% of the total temperature increase, in 0.4 and 0.6 s, respectively. The temperature distribution across the inlet section is constant with a spatial variation of less than 3% of the total temperature step.

In the present experiments, the heat transfer coefficient  $\alpha$  is obtained by using the 1-D unsteady heat conduction equation, and treating the wall material as “semi-infinite” which limits the allowable measurement time. Vogel and Weigand [18] showed, that the maximum allowable measurement time can be calculated from  $t_{\max} = L^2 / (0.25 \cdot \Lambda)$ , where  $L$  is the model thickness and  $\Lambda$  the thermal diffusivity of the model material. In the present study, a 5-mm-thick Plexiglas model was used to obtain good optical properties for PIV experiments; the maximum allowable time is  $t = 64$  s, which is longer than the typical measurement duration of 38 s.

The transient heat transfer measurement method consists of monitoring the surface temperature evolution by acquiring the color signal of a liquid crystal coating applied on the test section. By using a single layer of narrow-band thermo-chromic liquid crystals (Hallcrest BM/R30.5C0.7W/C17-10), the evolution of the local surface temperature  $T_{\text{wall}}(y, z, t) = T_{LC}$  is obtained from a hue capturing technique. Several miniature color CCD cameras mounted around the test section record the color change of the liquid crystal coating. The video signal of each view is digitally stored on DV (digital video) tapes. The use of the DV format storage ensures precise color image signal restitution at constant image frequency and without any noise generation. Video sequences of each camera are transferred subsequently to a computer where the image processing and the data reduction are performed.

The liquid crystals are painted directly on the channel inner Plexiglas surface. A black paint coating covers the liquid crystals to provide a good color background for image acquisition. A validation procedure was conducted to ensure that the black coating doesn't affect the quality of the results.

The 1-D transient conduction equation, with classical initial conditions and boundary conditions on the test surface, is used to obtain the nondimensional temperature at the convective boundary surface

$$\frac{T_{\text{wall}}(t) - T_i}{T_G - T_i} = 1 - \exp^{-\alpha^2 \Lambda \cdot t / \lambda^2} \operatorname{erfc} \left( \frac{\alpha \sqrt{\Lambda \cdot t}}{\lambda} \right) \quad (1)$$

The initial temperature  $T_i$  was measured in the Plexiglas model, after a thermal balance was reached between the gas temperature and the model outer surface temperature.

Thermocouples were placed along the channel to measure the gas temperature. They were located in the center of one of the secondary flow vortex ( $Y=0.67$ ,  $Z=0.43$  in the upstream leg). Tests based on numerical simulations showed that at this cross-section location, the gas temperature is closer to the bulk temperature than the centreline temperature, with  $|T_{\text{measured}} - T_{\text{bulk}}| < 1^\circ\text{C}$  along the entire channel. The thermocouples were separated  $1D_H$  from another in the region of interest. A linear interpolation of the gas temperature in  $X$  direction was performed for every location between the thermocouples.

The use of heater grids yields a double dependence of the gas temperature on time and  $X$ -location (see Fig. 3). Downstream of the inlet, due to heat exchange the temperature increase is no longer a step. For a given  $X$ , the gas temperature is an increasing function of time (Ekkad and Han [14]). It can be shown that, when the gas temperature change can be expressed as series of  $n$  summed step functions, the Plexiglas surface temperature  $T_{\text{wall}}(t) = T_{LC}$  is

$$T_{\text{wall}}(t) = T_{LC} = T_i + \sum_{j=1}^n (T_{G,j} - T_{G,j-1}) \cdot F(t - t_j) \quad (2)$$

with

$$F(t - t_j) = \left\{ 1 - \exp^{-\alpha^2 \Lambda \cdot (t - t_j) / \lambda^2} \operatorname{erfc} \left( \frac{\alpha \sqrt{\Lambda \cdot (t - t_j)}}{\lambda} \right) \right\} \quad (3)$$

An iterative procedure is used to determine the value of the heat transfer coefficient from the above equations.

**PIV Uncertainty Analysis.** Schabacker et al. [8–10] demonstrated the applicability of the presented stereoscopic PIV technique in details. Using the method of Bendal and Piersol [19], the mean value of the measured velocities is calculated by taking the instantaneous velocity measurements of the sample, summing the values, and dividing by the number of samples ( $N=1250$  per measurement plane in the present study)

$$\bar{x} = \frac{1}{N} \sum_{i=1}^N x_i \quad (4)$$

In a similar manner, a measure of the fluctuating velocities can be obtained from the sample variance

$$s^2 = \frac{1}{N-1} \sum_{i=1}^N (x_i - \bar{x})^2 \quad (5)$$

In the equations  $\bar{x}$  and  $s^2$  are the *sample mean* and *sample variance*, respectively. The number of observations  $N$  used to compute the estimates is called the *sample size*. Using the method of Bendal and Piersol [19], the uncertainty for the mean velocity values of the present measurements is of order of 1 percent with a confidence level of 95%. The uncertainty of the mean velocity depends on the normal stresses and as a consequence is higher in regions where the turbulence level is high. The uncertainty level of the normal stresses of the Reynolds tensor, with a confidence level of 95%, is 8 percent of the normal stress values. The uncertainty of the normal stresses depends only on the number of samples and on the confidence level. Further details of the uncertainty method are given in [10].

**Heat Transfer Uncertainty Analysis.** The error in the heat transfer measurements has been calculated considering the method described in Höcker [20]. It showed that the error can be minimized by adjusting measurement parameters as the model material and the dimensionless temperature  $T = (T_{LC} - T_i) / (T_G - T_i)$ . In the present study, the heat transfer coefficients are of the order of  $20 \text{ W/m}^2\text{K}$  to  $200 \text{ W/m}^2\text{K}$ . Using the method of Höcker [20], this leads to optimum dimensionless temperatures between  $0.2 < T < 0.4$ . Thus it was chosen to set the different temperature at  $T_i \approx 18^\circ\text{C}$ ,  $T_G \approx 70^\circ\text{C}$ ,  $T_{LC} \approx 32.7^\circ\text{C}$ , in order to obtain an aver-

**Table 2 Fully developed friction factor compared to Han [4] correlation**

$Re = 50\,000$	Results	Han
$f$	0.066	0.047

age dimensionless temperature  $T=0.28$ . The maximum error can be estimated to  $\pm 8\%$  on the heat transfer coefficient under the assumption that the heat transfer coefficient is constant during the experiment.

## Results and Discussion

The objectives of the present paper are:

- to present complete flow and heat transfer sets of data in the fully developed region of a 2-pass internal coolant channel,
- to relate the flow and heat transfer distributions in a coolant channel with 45-deg ribs,
- to show how the vortex structure influences the heat transfer distribution in the fully developed region of a 2-pass coolant channel with 45-deg rib arrangements.

**Flow Characteristics.** A comparison of velocity components in the developed flow region of a similar coolant passage was presented by Bonhoff et al. [10]. The measurements showed that the flow with a 45-deg rib arrangement differs from the flow in a similar passage with a 90-deg rib arrangement [8]. With 90-deg ribs, a developed flow condition in terms of mean velocity and turbulent kinetic energy was achieved after 3 rib modules. The flow in the passage with 45-deg rib arrangement requires a longer development length; at least 8 rib modules are needed to achieve a developed flow condition for the mean velocity components and 12 rib modules are required for the turbulent kinetic energy of the flow. In the present configuration, 18 rib-modules are placed in the upstream leg, to produce a developed flow field before the 180-deg bend.

The velocity components downstream of the 16th rib module are judged to be in a developed flow region.

Table 2 shows a comparison between the present channel friction factor and a correlation for 45-deg rib-arrangements presented in [4]. The correlation was extrapolated beyond Han's test range ( $0.047 < e/D_H < 0.078$ ). The result from the present study is an average of measurements in the fully developed section of the first leg. The Han correlation is 30% lower than the present results. Measurements and numerical simulations of Haasenritter et al. [21] showed a friction factor approximately equal to that measured in the present study. The differences with the Han [4] correlation are thought to be due to geometrical differences between the test channels, especially the rib height and blockage ratio.

It has been shown [16,8] that the vortices behind inclined ribs move along the ribs and then join the main flow. This interaction between main flow and rib-induced vortices causes a strong secondary flow motion in the passage leg. The secondary flow consists of two counter-rotating vortices that drive fluid from the duct center towards the web along the center plane and to the sidewall along the ribbed walls as shown in Fig. 4. Note that the web is placed on the right hand side of the figure.

It was shown in [16] that the secondary flow field impinges on two main areas in the channel. Flow with velocity as high as  $0.3U_b$  impinges on the outer wall at approximately one rib height above the ribbed walls ( $Y=0.15$  and  $Y=0.85$ ). Flow with lower velocities ( $0.1U_b$ ) impinges on the web along the center plane  $Y=0.5$ . The streamwise velocity characteristics in Fig. 6(b) show three regions of high streamwise velocity. Two are located in the secondary vortex core. The third is less obvious and is located adjacent to the web, and limits the impingement velocity of the secondary flow.

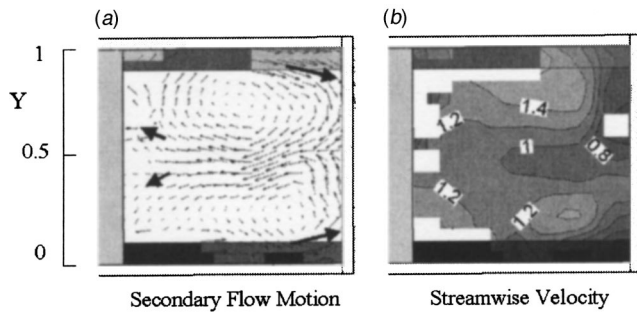


Fig. 4 Streamwise and secondary flow motion in a fully developed flow cross section of a coolant channel with 45-deg rib arrangement

The streamwise ( $U$ ), cross-stream ( $W$ ) and normal ( $V$ ) velocity profiles at selected streamwise and cross-stream locations are shown in Fig. 5. The streamwise locations are between  $X=2.1$  and  $3.1$  (All the distances are normalized by  $D_H$ ). The cross-stream locations are at  $Z=0.4, 0.6$ , and  $0.8$ . Note that the web wall location is at  $Z=0.1$ . Data from values of  $Y=0.06$  to  $0.94$  are plotted except at the rib surfaces where the closest value of has a  $\Delta Y=0.06$ . The measurement procedures with this PIV set of

Z	Streamwise Velocity	Cross-stream Velocity	Vertical Velocity
0.4	a.1.	b.1.	c.1.
0.6 (passage center)	a.2.	b.2.	c.2.
0.8	a.3.	b.3.	c.3.

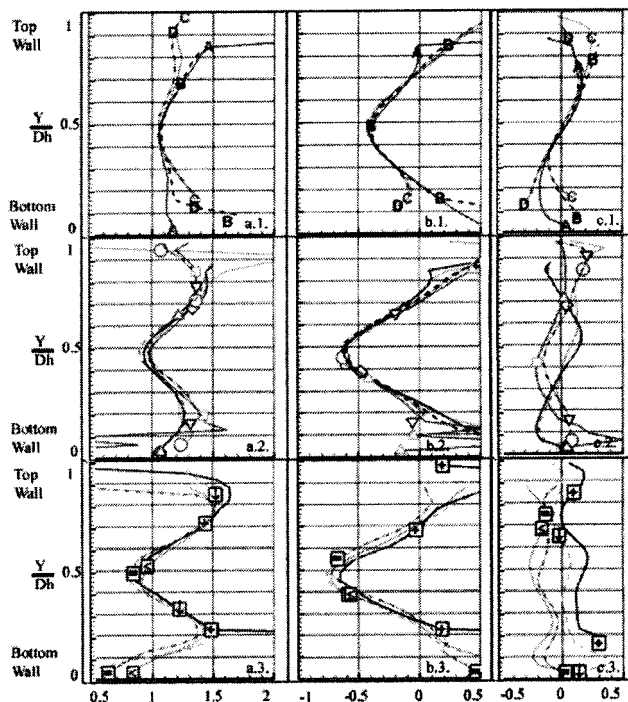


Fig. 5 Velocity profiles in the 16th rib module, normalized by  $U_b$ . See Fig. 2 for exact locations in the rib module. (a) overview of the graphs in the next figure, (b) velocity profiles.

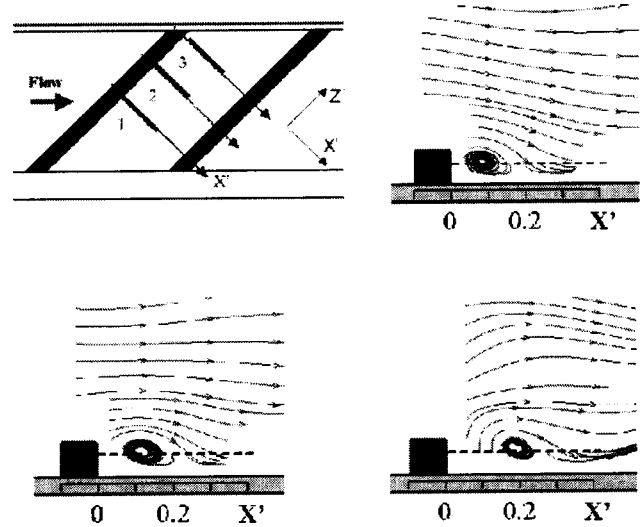


Fig. 6 Streamline details in the vicinity of a rib.—(a) locations, (b) location 1, (c) location 2, (d) location 3

optics has a probe dimension of  $\Delta Y=0.06$ . For  $Y$  values closer than  $0.06$  to the wall, spurious results were obtained due to wall light reflections.

The streamwise velocity profiles in Figs. 5(a2) and (a3) have two peaks at values of  $Y$  approximately equal  $0.2$  and  $0.8$ . These are attributed to the acceleration of the flow as it crosses the ribs at  $Y=0.1$  and  $0.9$  for the ribbed walls, respectively. In the region near the downstream wall,  $X=0.8$  (Fig. 5(a1)), the velocity profiles are close to a single shape. The velocity at the centerline is near  $0.9$ . The two peaks in the rib region are between  $1.3$  and  $1.6$ . The flow at the centerline of the passage,  $X=0.6$  and  $Y=0.5$ , also has a streamwise velocity of approximately  $0.9$ . The streamwise velocities in the peak regions vary from  $1.25$  to  $1.6$  or more. This large variation is attributed to measurement locations close to the ribs, e.g.,  $X=2.63$ . The streamwise velocities at  $Z=0.4$ , have a common minimum of  $U=1.07$ . The velocity profiles nearer the walls vary depending upon streamwise location [10].

The cross-stream velocity profiles (Figs. 5(b1), (b2), (b3)) show a well-behaved increase in velocity as the fluid moves from the web or upstream wall to the outer or downstream wall. The peak velocities of  $0.4$  at  $Z=0.4$  increase to  $0.65$  at  $Z=0.8$ .

The velocities normal to the ribbed walls (Figs. 5(c1), (c2), (c3)) have a more complex shape, which reflects the secondary flow pattern caused by the ribs. The velocity directions near the walls, e.g.,  $Y=0.1$  and  $0.9$  are compatible with the single large secondary flow cell.

Figure 6 shows streamline pattern over and downstream a rib in the 16th rib module. Data are extracted from measurement planes normal to the ribs. The streamlines are plotted along the local  $X'$ -axis. Due to reflection, no measurements are available in the vicinity of the walls and ribs.

As  $Z'$  increases from location 1 towards location 3, the recirculation cell evolves including the main stream flow above it, and the stagnation point on the bottom wall. The vortex center moves from both the downstream edge of the rib and the ribbed wall. The recirculation cell size increases.

The vertical velocities at  $Y=0.06$  are shown in Fig. 7 for the same planes as in Fig. 6. The profiles are extracted from the plane  $Y=0.06$ , represented by dashed lines in Figure 6. Note that negative and positive velocities indicate impinging flow and motion away from the wall, respectively.

As the flow moves along the rib from the web towards the outer wall, the recirculation cell increases in size as it moves from the downstream wall of the rib. The center location of the vortex, characterized by  $V$  zero-values, are located at  $X'=0.11$  in plane-1

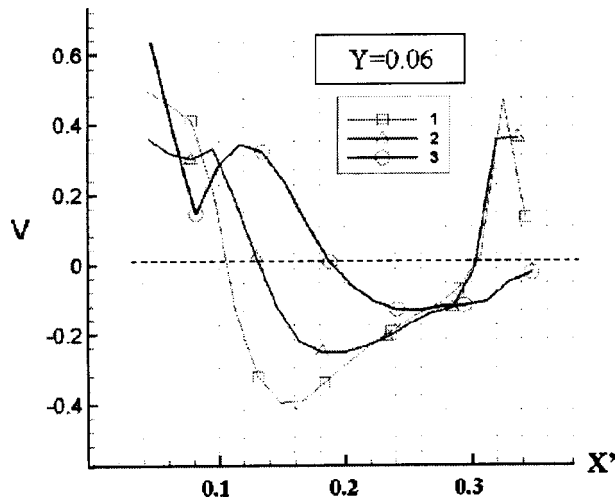


Fig. 7 Velocity profiles downstream of a rib normal to the bottom wall (see Fig. 6 for exact location)

and at  $X' = 0.19$  in plane-3. The angle of the vortex centerline to the ribs increases from 4 deg between plane-1 and plane-2, to 11 deg between plane-2 and plane-3.  $V$  minima, indicating impinging velocity maxima, are shifted away from the rib. The  $V$  minima shift angle increases from 7 deg between plane-1 and plane-2, to 12 deg between plane-2 and plane-3. The length of the negative velocity region, indicating the impinging area of the flow, also increases as the flow moves towards the outer wall. The absolute values of the impinging velocity decrease as the impinging area increases.

The results presented in the previous section provide a set of measurements that can be used to evaluate codes and turbulent transport models in the developed flow region of a ribbed channel. This flow in this region is as “periodic” as will probably be obtained in most coolant channels. The data provide a good test for codes to predict flow and heat transfer with various turbulence models and wall approximations.

The upstream fully developed region extends from  $X = 3.5$  to  $X = 0.5$ . The ribbed wall ( $Y = 0$ ) and the outer wall ( $Z = 1.1$ ) are shown. Note that the view direction goes through the web, which is not plotted here to clarify the figure. Streamlines extracted from the full set of PIV measurements are plotted in Fig. 8; they were chosen to start at several locations in order to identify characteristics of the flow field in the fully developed region. The streamline color helps to distinguish the start location.

Streamlines plotted downstream of the ribs show the location and size of the recirculation cell. In the rib-module-a, streamlines (blue) start in the core of the recirculating cell, pointing at the recirculating cell itself. In the rib-module-b, the streamlines (red) start just above the upper rib surface; they go over the recirculating cell and underline the flow reattachment downstream of the recirculating cell.

In the rib-module-a upstream corner between the rib and the web, a recirculating cell starts. As  $Z$  increases, the flow inside the recirculating cell is directed along the rib with a convective velocity of  $1.2U_b$ . The flow develops into a vortex shape along the rib; this is the rib-induced vortex typically mentioned in literature on heat transfer with 45-deg rib arrangements. As also shown in [1] and in Fig. 6, the vortex size is increasing as the distance to the divider increases. The vortex center is directed in the streamwise direction as  $Z$  increases, yielding in greater reattachment distances from the rib downstream wall. Figure 8(b) in rib (a) shows the location of the vortex relative to the rib.

As the vortex is approaching the outer wall, the vortex strength decreases and the streamlines impinge on the outer wall. The streamlines from the bottom rib region are guided along the outer

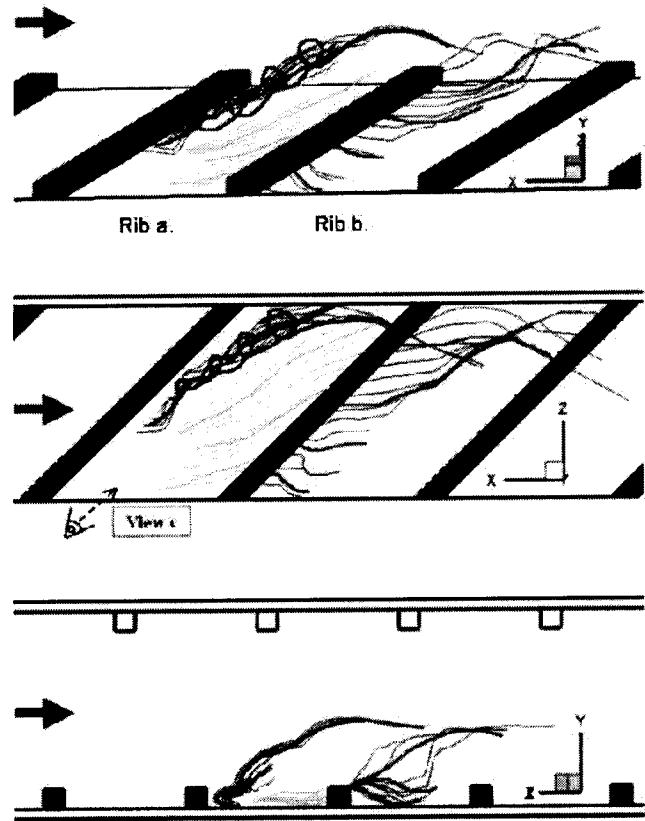


Fig. 8 3-D streamlines in the near bottom wall region—(a) upstream fully developed streamlines; 3-D view, (b) X-Z plane view, (c) view normal to the upstream ribs

wall up to  $Y = 0.5$ , and meet the flow coming from the top wall. This produces two counter-rotating cells already described in [16] and shown on Fig. 4. The streamlines go as a sheet in the center of the channel, towards the web. They reach the web  $2D_H$  downstream of the impact area on the outer wall.

The part of the flow located above the ribbed wall (green streamlines), between the reattachment line and the next rib, is divided in two regions, separated by a line linking the web-upstream rib corner and the outer wall-downstream rib corner. The part of the flow located upstream of this line undergoes the vortex influence and is directed towards the outer wall. This portion of the flow impinges on the outer wall in the region  $1.9 > X > 2.4$ ,  $Y < 0.3$ . The part of the flow located downstream of the separation line, undergoes the effect of the mainstream flow. This region is characterized by low impingement. The flow is directed towards the downstream rib, with velocities parallel to the ribbed wall.

The conclusion from these data is that the complex flow induced by the 45-deg rib arrangement causes the development of a secondary vortex behind each rib. The main source of the flow characteristics in the straight legs is the vortex induced by the ribs. This vortex structure must be accurately predicted to obtain accurate local heat transfer simulations from the CFD predictions. The previous sections give details that can be used to evaluate CFD calculations.

**Heat Transfer Measurements.** Heat transfer measurements were conducted in the same model to accompany the flow results. Following are data and discussion on the heat transfer results in the fully developed region (16th and 17th rib module).

Figure 9 shows the heat transfer distribution in the 16th and 17th rib modules, located at  $3.5 > X > 1$  in the upstream leg. Two walls are shown, the bottom and the outer walls  $Nu/Nu_0$  contours are plotted, where  $Nu_0$  is the Dittus-Boelter correlation value for a

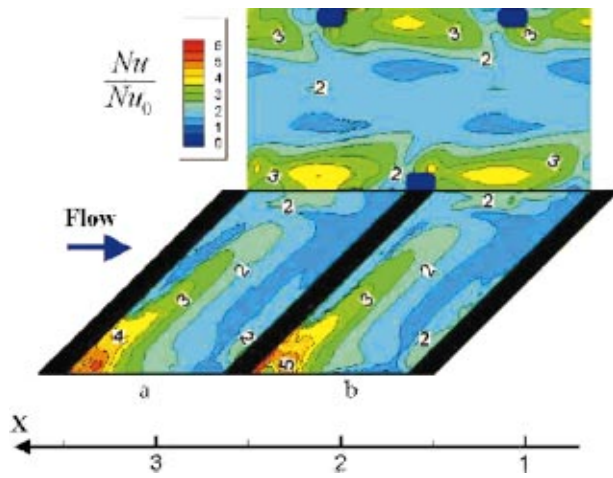


Fig. 9 2-D view heat transfer distribution on the bottom and outer walls in the fully developed region

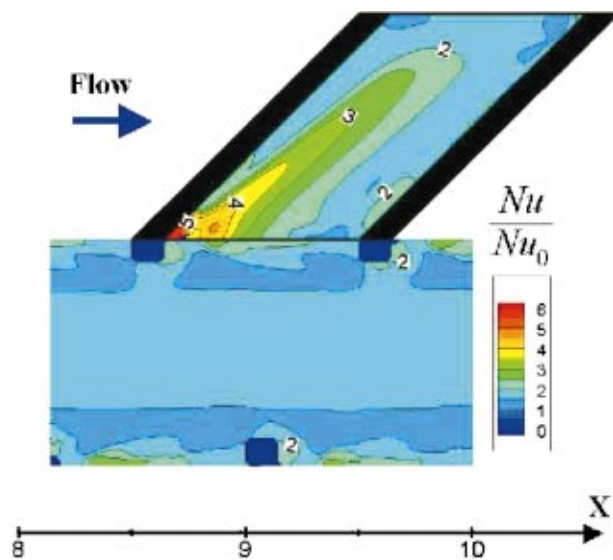


Fig. 10 2-D view heat transfer distribution on the bottom and outer walls.  $10D_H$  downstream of the bend

smooth channel:  $Nu_0 = 0.023 \cdot Re^{0.8} \cdot Pr^{0.4}$ ; in the present study,  $Nu_0 = 114.5$ . The periodic heat transfer distribution from rib to rib shows the region's near fully developed. Small differences may also be attributed to the presence of the turn ( $1D_H$  downstream).

On the ribbed wall, four regions can be identified in the rib-module heat transfer distribution. Along the upstream rib, an area of high heat transfer occurs. The  $Nu/Nu_0$  ratio decreases from the web towards the outer wall. The maxima values (up to six times  $Nu_0$ ), are located between  $0.1$  to  $0.2D_H$  from the rib downstream wall. The angle of the maxima line to the rib is approximately  $14$  deg. Next to the outer wall, another region of relatively high heat transfer occurs;  $Nu/Nu_0$  values reach  $2.5$ . A similar region is located next to the downstream rib. Between these three regions, in the rib-module center, low heat transfer occurs: The  $Nu/Nu_0$  values are between  $1$  and  $1.5$ , which are almost the same as in a smooth channel.

On the first side wall where the vortex impacts, two regions are clearly detectable. A region of high  $Nu/Nu_0$  values is located at mid distance between the ribs. It is  $0.5D_H$  long and occupies the space  $0.3 > Y > 0$  on the outer wall.  $Nu/Nu_0$  values are over  $3$  in this region. Small differences occur near the top wall due to the

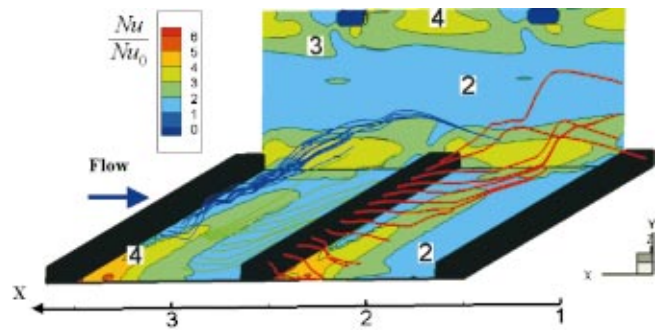


Fig. 11 Combined heat transfer distribution and streamlines in the vicinity of the bottom and outer walls: 3-D view

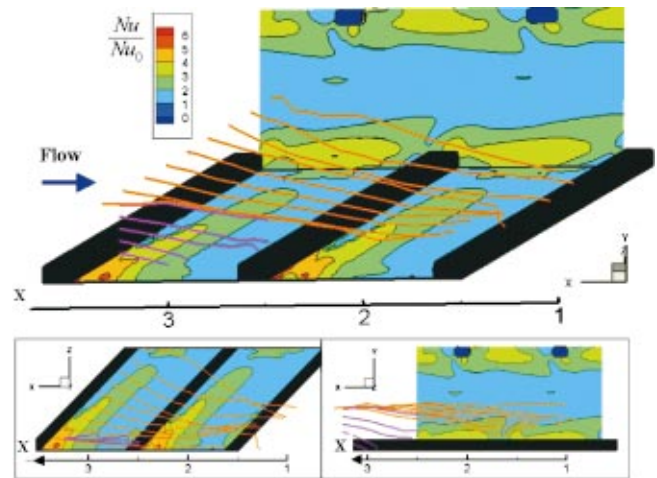


Fig. 12 Combined heat transfer distribution and streamlines in the vicinity of the  $Y=0.5$  plane and web: 3-D and 2-D views

channel geometry. Around the channel center plane ( $Y=0.5$ ), heat transfer is lower with  $Nu/Nu_0$  values between  $1$  and  $2$ .

Results on the same walls were presented in [7] with a directly opposing  $45$ -deg rib arrangement. The distribution was similar to the present study on the bottom wall with the same order of magnitude of  $Nu/Nu_0$ . On the outer wall, some differences between the present results and [7] occurred due to the symmetric, instead of the staggered rib arrangement in the present experiments.

Due to optical access restrictions, measurements on the web or second side wall weren't obtained in the first leg of the model. However, measurements were taken  $10D_H$  downstream of the bend in the second leg of the model. The rib arrangement in the configuration is such that the web of the upstream leg and the downstream outer wall of the second leg, have a similar position, compared to the channel flow field. The ribbed wall heat transfer distributions in Figs. 9 and 10 are very similar and [16] showed that at  $X=4$ , the flow has almost reached fully developed conditions. Thus measurements on the outer wall in the second leg (Fig. 10) are representative of the upstream web heat transfer.

The differences between the side walls in Figs. 9 and 10 outer walls are noticeable. The heat transfer levels are much higher on the wall where the vortex, behind the ribs, impinges. Two regions are present: A low heat transfer region is located near the ribbed walls, with values  $1 < Nu/Nu_0 < 1.5$ . Around the centerline, a region of higher heat transfer values occurs ( $1.5 < Nu/Nu_0 < 2$ ). Note that in Table 3, the downstream outer value is identified as *Sts web*.

**Table 3 Fully developed area average Stanton numbers compared to Han [4] correlation**

<i>Re</i> = 50 000	Results	Han
<i>Str</i>	0.0091	0.0085
<i>Sts outer</i>	0.0073	0.0067
<i>Sts web</i>	0.0054	0.0067

Rau [7] also noted big differences between both smooth walls in its configuration. The 45-deg rib arrangement leads to high inhomogeneous heat transfer between all channel walls; ribbed walls area-averaged values are 25 and 40% higher than the outer and web walls, respectively. The conclusion is that the rib-induced flow has a great impact on the heat transfer distribution, between the ribs on the ribbed walls, and on the sidewalls.

Table 3 gives values of area-average Stanton number. Measurements were normalized by the projected area to compare with the correlations. *Str*, *Sts outer* and *Sts web* represent the ribbed wall, outer and web walls area average Stanton numbers respectively. Note that smooth wall values were obtained as the mean value of both smooth walls [4]. Present heat transfer results and correlations are in good agreement, taking into account the measurement and correlation uncertainties ( $\pm 8\%$  and  $\pm 10\%$ , respectively), and the blockage ratio differences between [4] and the present geometries.

#### Combination of Flow and Heat Transfer Measurements.

3-D-views of the flow streamlines superimposed on the heat transfer distribution are shown in Figs. 11 and 12. Note that for readability reasons, only seven  $Nu/Nu_0$  contour values are plotted. This combination shows the strong influence of the rib-induced secondary flow on the heat transfer. Regions of high  $Nu/Nu_0$  values can be explained by the shape and location of the rib-induced vortex. In Fig. 11, the streamlines of Fig. 8(b) are superimposed on the heat transfer distribution of Fig. 9. Note that the symmetrical channel geometry, which yields to two separate flow regions placed around the  $Y=0.5$  plane, yields a symmetrical heat transfer distribution in the two channel regions:  $Y<0.5$  and  $Y>0.5$ .

Near the web behind the rib, the vortex begins in the region of highest heat transfer, up to six times the smooth channel Dittus-Boelter correlation value. The vortex develops along the rib, it coincides on the bottom wall with the U-shape high heat transfer area behind the rib. The reattachment zone corresponds to the high heat transfer region on the bottom wall. The varying reattachment length leads to a high Nusselt number region at 30-deg angle to the streamwise direction. This corresponds to the angle of the maximum impinging velocity shown in Fig. 7. The decrease of the impinging velocity leads to a negative Nusselt number gradient in the  $Z$  direction. As the vortex impinges on the outer wall, another region of high heat transfer occur, yielding a high heat transfer area on the sidewall ( $Nu/Nu_0>3$  for  $Y<0.3$ ). Around the  $Y=0.5$  plane on the outer wall, velocity vectors are away from the outer wall (Fig. 4), which leads to a low heat transfer region.

Part of the flow, which is not directed in the rib-induced vortex, remains parallel to the walls. It induces lower heat transfer regions on the walls. The flow passes over the recirculating cell in the upstream rib vicinity, and goes towards the bottom wall in the middle of the rib-module. It induces a region of low Nusselt number.  $Nu/Nu_0$  values reach 1, which indicates that the heat transfer coefficient is approximately the same as in a smooth channel.

Figure 12 shows the same region with the heat transfer results of Fig. 10 and with streamlines plotted from the center of the channel. These streamlines are not previously shown. They are representative of the part of the flow that goes towards the web in the middle of the channel around the  $Y=0.5$  plane (see Fig. 4). Two 2-D views are added to Fig. 12 to identify the streamline 3-D locations (along  $X-Y$  and  $X-Z$  planes). The streamlines do not

show any vortex in the middle of the channel. The flow crosses the channel as sheets parallel to the ribbed walls. The flow is smoothly directed towards the downstream direction by the mainstream motion. The impact on the web is weaker than on the outer wall. This explains the relatively low heat transfer coefficient on the web shown in Fig. 10;  $Nu/Nu_0$  values between 1 and 2 in the web center part.

## Conclusions

Three-dimensional velocity measurements and heat transfer measurements were obtained in a two-legged blade coolant passage model with ribs orientated 45 deg to the passage. The model length, the rib locations and the geometry of the web between the coolant passage legs was more representative of aero or land-based gas turbine cooling designs than previously available geometries. The results from these flow and heat transfer measurements were combined, to show the impact of the flow field on the heat transfer distribution in the fully developed region of a 2-pass internal coolant passage. The measurements provide data to compare with CFD predictions, to evaluate mesh strategies, turbulence or wall treatment models.

Measurements in the developed flow region show details in the three velocity profiles. The measurements showed the tendency of the streamwise and cross-stream velocities to be similar for various streamwise locations at the same cross-stream location. The two secondary vortices in channel cross sections are due to the interaction of the rib-induced and the mainstream flows. A secondary motion divides the flow along the channel into two separate regions. The flow in the two halves ( $Y<0.5$  and  $Y>0.5$ ) is constrained to remain in the same region along both straight legs.

A rib-induced vortex develops downstream of the ribs, impinges on the outer wall along the bottom wall, flows towards the top wall along the outer wall for  $Y<0.5$ , and goes back towards the web along the  $Y=0.5$  plane. As the vortex develops along the rib, the vortex size increases, and the center moves from the rib and from the ribbed wall.

Ribs at 45 deg increase the average heat transfer gradients. Several regions of different heat transfer levels are identified on the ribbed and sidewalls. The ratio of high to low Nu numbers goes up to 6 in the U-shaped heat transfer distribution downstream of the ribs. High heat transfer gradients occur between the four channel walls in the area-averaged values between the walls (Table 3), which are required to cool the expected walls. Gradients also occur in the heat transfer distributions on each wall surface, which causes high temperature gradients and thermal stresses in the blade.

The complex phenomenon of the vortex and mainstream flow combination, which governs the heat transfer distribution in the straight legs of the coolant passage with inclined ribs have been connected from the combined flow and heat transfer measurements. The impinging velocity induced by the vortex, and more generally by the secondary flow, are strongly linked with the regions of high heat transfer. The present work provides results to understand how to use the secondary flow and especially the inclined rib-induced vortex, in order to reduce the high heat transfer gradients on the channel walls.

## Acknowledgments

This study was funded by the Swiss Office of Science in cooperation with the BriteEuram Internal Cooling of Turbine Blades project (contract number: BRPR-CT97-0600, project number: BE97-4022).

## Nomenclature

- $X$  = Cartesian coordinate in axial duct direction
- $Y$  = Cartesian coordinate in cross duct direction
- $Z$  = Cartesian coordinate in horizontal duct direction
- $U$  = mean velocity component in  $x$  direction

$V$  = mean velocity component in  $y$  direction  
 $W$  = mean velocity component in  $z$  direction  
 $U_b$  = bulk mean-velocity  
 $L$  = test section length  
 $D$  = height and width of passage legs,  $D = 100$  mm  
 $D_H$  = hydraulic diameter  $D_h = D$   
 $B$  = thickness of divider plate  
 $P$  = rib pitch  
 $e$  = rib height  
 $S$  = section length in bend at 90 deg section  
 $\alpha$  = heat transfer coefficient  
 $\lambda$  = plexiglas thermal conductivity  
 $\Lambda = \lambda / (\rho \cdot C_p)$  Plexiglas thermal diffusivity  
 $T = (T_{LC} - T_i) / (T_G - T_i)$  dimensionless temperature  
 $f = \Delta P / L \cdot D_H / 1/2 \rho U_{b,in}^2$  = friction factor  
 $Nu$  = Nusselt number  
 $St = Nu / (Re \cdot Pr)$  = Stanton number

## References

- [1] Schabacker, J., 1998, "PIV Investigation of the Flow Characteristics in an Internal Coolant Passages of Gas Turbine Airfoils With Two Ducts Connected by a Sharp 180 deg Bend," Ph.D. thesis, Ecole Polytechnique fédérale de Lausanne, Vol. no. 1816.
- [2] Mochizuki, S., Murata, A., and Fukunaga, M., 1997, "Effects of Rib Arrangements on Pressure Drop and Heat Transfer in a Rib-roughened Channel with a Sharp 180 deg Turn," ASME J. Turbomach., **119**(3), pp. 610–616.
- [3] Han, J. C., Zhang, P., and Lee, 1991, "Augmented Heat Transfer in Square Channels With Parallel, Crossed, and V-shaped Angled Ribs," J. Heat, **113**, pp. 590–596.
- [4] Han, J. C., and Park, J. S., 1988, "Developing Heat Transfer in Rectangular Channels With Rib Turbulators," J. Heat Mass Transf., **31**, pp. 183–195.
- [5] Han, J. C. and Chandra, P. R., 1987, *Local Heat/Mass Transfer and Pressure Drop in a Two-Pass Rib-Roughened Channel for Turbine Airfoil Cooling*, Lewis Research Center NASA.
- [6] Wang, Z., Ireland, P. T., Kohler, S. T., and Chew, J. W., 1996, "Heat Transfer Measurements to a Gas, Turbine Cooling Passage With Inclined Ribs," Proc. International Gas Turbine & Aeroengine Congress & Exhibition, Birmingham, UK 96-GT-542.
- [7] Rau, G., 1998, Einfluss der Rippenanordnung auf das Strömungsfeld und den Wärmeübergang in einem Kühlkanal mit quadratischem Querschnitt. Ph.D. thesis (Technischen Universität Darmstadt), Vol. D17.
- [8] Schabacker, J., Bölcs, A., and Johnson, B. V., 1999, "PIV Investigation of the Flow Characteristics in an Internal Coolant Passage With 45 deg Rib Arrangement," Proc., International Gas Turbine & Aeroengine Congress & Exhibition, Indianapolis, IN. 99-GT-120.
- [9] Schabacker, J., Bölcs, A., and Johnson, B. V., 1998, "PIV Investigation of the Flow Characteristics in an Internal Coolant Passage With Two Ducts Connected by a Sharp 180 deg Bend," Proc., International Gas Turbine & Aeroengine Congress & Exhibition, Stockholm, Sweden. 98-GT-544.
- [10] Bonhoff, B., Schabacker, J., Parneix, S., Leusch, J., Johnson, B. V. and Bölcs, A., 1998, "Experimental and Numerical Study of Developed Flow and Heat Transfer in Coolant Channels With 45 and 90 Degree Ribs," Proc. Turbulent Heat Transfer II, Manchester, UK, 99-GT-123.
- [11] Hermanson, K., Parneix, S., Von Wolfersdorf, J., and Semmler, K., 2000, "Prediction of Pressure Loss and Heat Transfer in Internal Cooling Passages," Proc., Turbine-2000: International Symposium on Heat Transfer in Gas Turbine Systems, Cesme, Izmir, Turkey. 934, 448–455.
- [12] Schabacker, J., and Bölcs, A., 1996, "Investigation of Turbulent Flow by means of the PIV Method," Proc., 13th Symposium on Measuring Techniques for Transonic and Supersonic Flows in Cascades and Turbomachines, Zurich, Switzerland.
- [13] Wang, Z., Gillepsie, D. R. H., and Ireland, P. T., 1996, "Advances in Heat Transfer Measurements Using Liquid Crystals," Turbulent Heat Transfer (Engineering Foundation), 1–25. San Diego, CA.
- [14] Ekkad, S. V., and Han, J. C., 1995, "Local Heat Transfer Distributions Near a Sharp 180 deg Turn of a Two-Pass Smooth Square Channel Using a Transient Liquid Crystal Image Technique," J Flow Visualisation and Image Processing, **2**, pp. 285–297.
- [15] Wang, Z., Gillepsie, D. R. H., and Bölcs, A., 2000, "A Novel Digital Image Processing System for the Transient Liquid Crystal Technique Applied for Heat Transfer and Film Cooling Measurements," Proc. International Symposium on Heat Transfer in Gas Turbine Systems, Izmir, Turkey.
- [16] Chanteloup, D., and Bölcs, A., 2001, "PIV Investigation of the Flow Characteristics in 2-leg Internal Coolant Passages of Gas Turbine Airfoils," Proc., Euroturbo, 4th European conference on turbomachinery fluid dynamics and thermodynamics, Firenze, Italy.
- [17] Wang, Z., 1991, "The Application of Thermochromic Liquid Crystals to Detailed Turbine Blade Cooling Measurements," thesis, Department of Engineering Science, Oxford.
- [18] Vogel, G., and Weigand, B., 2001, "A New Evaluation Method for Transient Liquid Crystal Experiments," Proc., National Heat Transfer Conference Anaheim, CA. NHTC01-1511.
- [19] Bendat, J. S., and Piersol, A. G., 1986, "Random Data," Random Data John Wiley & Sons, Inc., New York, NY.
- [20] Höcker, R., 1996, "Optimization of Transient Heat Transfer Measurements Using Thermochromic Liquid Crystals Based on an Error Estimation," Proc., International Gas Turbine & Aeroengine Congress & Exhibition, Birmingham, UK. 96-GT-235.
- [21] Haasenritter, A., Amro, M., and Weigand, B., 2001, "An Experimental and Numerical Study of the Heat Transfer Performance of Sharp-Edged and Rounded Ribs in Square Ducts," Proc., 9th International Symposium on Transport Phenomena and Dynamics of Rotating Machinery, Honolulu, HI.